Molecular Simulation of Hydrogen Systems: From Properties and Methods to Applications and Future Directions

Rahbari, A.; Hulikal Chakrapani, Thejas; Shuang, F.S.; Krokidas, Panagiotis; Habibi, P.; Lagerweij, V.J.; Ramdin, M.; Vlugt, T.J.H.; Hajibeygi, H.; Dey, P.

DOI
10.1021/acs.chemrev.5c00617

Publication date
2025

Document Version
Final published version

Published in
Chemical Reviews

CHEMICAL REVIEWS

Review

Molecular Simulation of Hydrogen Systems: From Properties and Methods to Applications and Future Directions

Ahmadreza Rahbari,[○] Thejas Hulikal Chakrapani,[○] Fei Shuang, Panagiotis Krokidas, Parsa Habibi, V. Jelle Lagerweij, Mahinder Ramdin, Thijs J. H. Vlugt, Hadi Hajibeygi, Poulumi Dey, Ioannis N. Tsimpanogiannis, and Othonas A. Moultos*

Cite This: *Chem. Rev.* 2025, 125, 11878−12029

ABSTRACT: This extensive review highlights the central role of classical molecular simulation in advancing hydrogen (H_2) technologies. As the transition to a sustainable energy landscape is urgently needed, the optimization of H_2 processes, spanning production, purification, transportation, storage, safety, and utilization is essential. To this end, accurate prediction of thermodynamic, transport, structural, and interfacial properties is important for overcoming engineering challenges across the entire H_2 value chain. Experimental measurements, despite being the traditional way of obtaining these properties, can be limited by the distinctive nature of H_2, harsh operating conditions, safety constraints, and extensive parameter spaces. Free from such limitations, classical molecular simulations, in the general frameworks of Monte Carlo and Molecular Dynamics, provide an optimal balance between computational efficiency and accuracy, bridging the gap between quantum mechanical calculations and macro-scale modeling. This review also systematically covers molecular simulation methods and force fields for computing key properties of H_2 systems, such as phase and adsorption equilibria and transport coefficients. Beyond property prediction, we explore how molecular simulation reveals fundamental mechanisms governing hydrate formation and dissociation, membrane permeations, and H_2 embrittlement. When possible, data from multiple sources are compared and critically assessed, while effort is put on evaluating the force fields used and methodological approaches followed in the literature. Finally, this review aims at identifying research gaps and future opportunities, emphasizing emerging approaches, such as molecular simulation in the era of artificial intelligence.

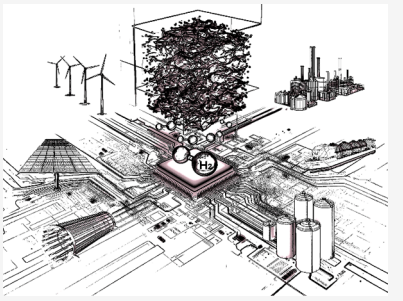

CONTENTS

Published: December 10, 2025

https://doi.org/10.1021/acs.chemrev.5c00617
Chem. Rev. 2025, 125, 11878−12029

https://doi.org/10.1021/acs.chemrev.5c00617
Chem. Rev. 2025, 125, 11878−12029

1. INTRODUCTION

1.1. Background and Motivation

Hydrogen (H_2) is a fundamental commodity in the chemical industry, serving as a building block of numerous products and processes in many different sectors. Characteristic examples are ammonia production, methanol synthesis, hydrocracking, steel and cement production, space exploration, and aerospace propulsion systems.[1−9] In the past decade, H_2 has gained significant attention as a clean energy carrier because it can be stored on the TWh scale.[10] H_2 can be produced via various methods, such as thermochemical processes, water electrolysis, direct solar water splitting, and geological and biological pathways.[11,12] Currently, the chemical industry primarily relies on fossil fuels to produce H_2, mostly without treatment of the emitted CO_2 (e.g., via natural hydrocarbon cracking, steam methane reforming, coal gasification or reforming processes).[1,13] This is the so-called grey H_2, which accounts for ca. 96% of the total H_2 supply. If the CO_2 emitted during H_2 production from fossil fuels is captured and stored, the result is the so-called blue H_2.[2] The transition to a sustainable energy landscape, with H_2 as an essential part, necessitates the efficient and economic production of the so-called green (i.e., via electrolysis of water using renewable energy sources) or low carbon H_2, in sharp contrast to H_2 produced from fossil sources.[14]

The European Union (EU) has reached the consensus that by 2030, 42% of the H_2 utilized in the industrial sector must be derived from renewable non-biological sources. This figure should increase to 60% by 2035. This decision is in alignment with the EU initiative "Fit for 55", which aims at a 55% reduction in greenhouse gas emissions by 2030. Thus, efforts focusing on scaling up the production and use of H_2 as a green energy carrier are becoming urgent in the context of chemical industry and mitigation of environmental impacts.[13,15−17] Such efforts, however, are hindered by technological challenges such as the high cost of green H_2 production,[16,18,19] the inefficient separation/purification methods of H_2 streams, the lack of safe transportation due to e.g., boil-off (the evaporation of liquid H_2 due to heat leakage into cryogenic storage tanks, causing continuous product loss[20]) and H_2 embrittlement,[17,21] the lack of commodity high-energy-density storage systems,[22,23] and the low efficiency, and often durability, of electrolyzers and fuel cells.[24] These challenges span the whole H_2 value chain, which in this review is going to be described by five different stages, i.e., H_2 production, purification, transport, storage, and utilization as shown in Fig. 1. Although, this categorization is not unique, it offers a practical view of the predominant H_2 technologies.

To overcome the engineering challenges in each stage of the H_2 value chain and to devise optimized processes that will allow for H_2 to play a central role in the energy mix of the future, accurate predictions of thermodynamic, transport, structural, mechanical, and electrochemical properties of H_2 systems are essential.[19,22,25,26] Such properties are phase equilibria and transport coefficients of gaseous mixtures and aqueous electrolyte solutions of H_2 (crucial for water electrolysis, fuel cells, deoxygenation, temperature/pressure swing adsorption), adsorption and absorption energies of H_2/adsorbents and storage capacities of different storage media (for physical storage), kinetic, structural and thermodynamic properties of hydrates (for physical storage and separations) and hydrides (chemical storage), electroosmotic drag coefficients in membranes (important for fuel cells and electrochemical compressors), interfacial tension and wettability (i.e., contact angles) of H_2/solid/liquid/gas systems (for subsurface storage), permeabilities of H_2 gas streams through nanoporous materials, membranes (separations of multicomponent H_2 streams) and geological media (subsurface storage), and phenomena such as H_2 embrittlement mechanisms in metals (safe transport in pipelines and storage in vessels). Aside from the plethora of required properties, the parameter space of

https://doi.org/10.1021/acs.chemrev.5c00617
Chem. Rev. 2025, 125, 11878−12029

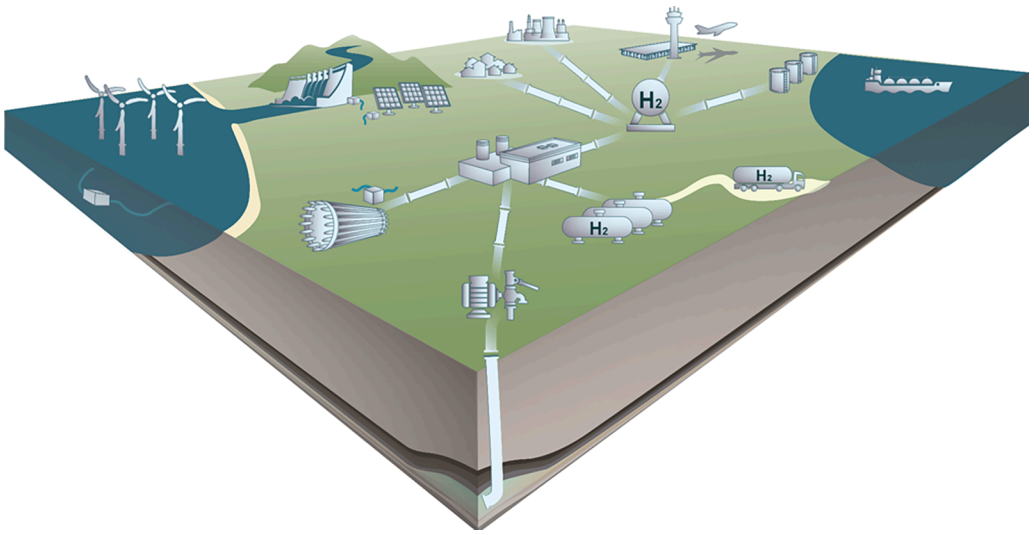

Figure 1. Schematic representation of a green hydrogen value chain spanning the production via water electrolysis using renewable energy sources, purification and compression of the hydrogen stream, storage in the liquid and gaseous form in tanks and in the subsurface, transportation via pipelines, trucks, and ships, and domestic and industrial utilization. Classical molecular simulation plays an important role as a reliable predictive tool for thermo-physical properties necessary for the design and optimization of the processes involved in all the stages in the hydrogen value chain.

temperatures, pressures, mixture compositions, and type of systems is extensive. This renders the total number of necessary physicochemical data extremely high, and therefore, makes data acquisition a challenging endeavor.

Traditionally, thermophysical properties are obtained via experimental measurements, often complemented by macroscale modeling. Nevertheless, due to the numerous different systems, the extremely broad state-point space, and the harsh conditions involved (e.g., high temperatures and/or pressures, corrosive and/or dangerous species) in H_2 processes, experiments become costly, and often, not possible to perform at in-situ conditions due to the necessity for adherence to safety standards (e.g., Atmosphères Explosibles − ATEX) and Pressure Equipment Directive (PED) norms.[27,28] As a consequence, thermophysical data of H_2 systems remain scarce, especially at high pressures, temperatures, and electrolyte molalities (e.g., for alkaline/acidic electrolytes).[29,30] The lack of such datasets is particularly important because due to the low volumetric energy density of H_2 gas, high pressures (usually >200 bar) are necessary for many H_2 applications. Another experimental shortcoming is the limitation in spatial resolutions of the available experimental techniques, which makes the detection of atomic hydrogen in alloys challenging.[31] It is also important to note that experimental measurements alone, rarely guarantee deep insight into the fundamental physical and chemical mechanisms of the H_2 systems. Understanding these mechanisms at the molecular scale is paramount for overcoming engineering hurdles, optimizing processes and materials, and coming up with novel technologies. Complementary to experimental measurements, equation of state (EoS) modeling is a popular and efficient approach, mainly for predicting the phase behavior of single- or multi-component H_2 mixtures.[32−37] However, cubic EoS encounter difficulty in accurately predicting the phase diagrams of H_2 systems, while more advanced EoS such as the ones of SAFT, PC-SAFT, and Mie families, have been designed to mainly reproduce properties of long chain, polar, and hydrogen bonding molecules, and therefore, these models are not expected to have an improvement over simple cubic EoS.[38−45] Moreover, EoS modeling alone cannot directly yield structural and transport properties of H_2 systems.

Due to these inherent limitations of experiments and EoS modeling, molecular simulation, performed in the general frameworks of Monte Carlo (MC) and Molecular Dynamics (MD), has emerged as an alternative powerful tool for computing thermophysical properties of H_2 systems at a wide parameter space range, and for providing unique insight into the molecular scale. Molecular simulations also guarantee safety and relatively low budget, since commodity computer clusters have become widely accessible. While performing molecular simulations to study H_2 systems and processes is a potent research route, it is not without limitations.[46−53] The first step in every molecular simulation is to choose the level of theory for simulating the material or system.[54] Options span accurate quantum-mechanical potentials derived from wave function or density-functional theory (DFT), classical fully atomistic potentials fitted to DFT or experimental data, united atom two-body potentials, and coarse-grained models.[51,55−58] The more detailed the model, the higher the accuracy, but the lower the computational efficiency. This means that although performing quantum mechanical simulations (e.g., DFT, Ab initio MD) will always yield the most precise results, such a modeling approach is only limited to small system sizes and time-scales. On the other side of the spectrum, although coarse-grained simulations (e.g., simulations using the Martini[59,60] potentials or dissipative particle dynamics - DPD[61]) allow access to much higher length- and time-scales, the computed properties can only serve as a qualitative measure, since the atomistic detail is omitted. Combining the best of both worlds, classical molecular simulation offers distinct advantages such as relatively high computational efficiency and accurate prediction of thermophysical properties. In this sense, classical simulations play an important role in filling the gap between computationally intensive ab initio simulations and not-as-precise coarse-grained models or EoS. For these reasons, an extensive, but in some cases scattered, literature body of atomistic molecular simulations of H_2 systems is available to date. In this review, we attempt to

https://doi.org/10.1021/acs.chemrev.5c00617
Chem. Rev. 2025, 125, 11878−12029

summarize these studies, and highlight the crucial role of molecular simulations, alongside experimental measurements, macro-scale modeling, and engineering approaches, in designing and refining H_2 technologies. Lately, tremendous efforts by researchers in academia and industry is put in blending Machine Learning (ML) (or even broader, Artificial Intelligence - AI) with molecular simulation techniques towards improving the predictive ability of models, and accelerate simulations and/or material screening. This upcoming paradigm shift in the way we perform molecular simulations, is also discussed in this review, focusing on the case of H_2 systems.

1.2. What to Expect from This Review and How to Read It

The scope of this review is to showcase the importance of classical molecular simulation studies in advancing technologies spanning the whole H_2 value chain (Fig. 1). The focus is on covering the most relevant properties of H_2 systems that can be computed with molecular simulation throughout the different aspects of the H_2 economy, i.e., we focus on properties important to H_2 production via water electrolysis, storage (e.g., in porous media, in hydrates, in the subsurface), H_2 compression for storage and mobility, membrane- and hydrate-based separations of H_2 streams, and H_2 embrittlement of metal pipelines. We provide a comparative assessment of the results of various properties of H_2 systems, obtained from different sources, while stretching the limitations and possible misalignment in the available literature.

An overview of the available simulation methods, and a critical discussion on most important concepts for computing H_2 properties is also provided. In more detail, we review different simulation techniques such as MC sampling methods for phase and adsorption equilibria, ways to compute hydrate three-phase (thermodynamic) equilibria, transport coefficients such as diffusivities, viscosities, and conductivities from MD simulations, kinetic MC simulations to obtain diffusion coefficients of H_2 in materials, and high-throughput screening of materials using classical simulation combined with ML. Another important contribution of this review is the comprehensive analysis of the advantages and limitations of the available force fields for different species involved in H_2 technologies (e.g., H_2, aqueous electrolytes, substrate materials, organic components).

Based on the thorough discussion of the different H_2 systems and properties, we also present an outlook for future research directions, especially in light of emerging approaches involving AI. When possible, we provide datasets of available properties of H_2 systems in tables and figures. These datasets can serve both as a reference point and as a motivation for future research. The raw data along with tables summarizing the availability of different properties (and corresponding ranges) can also serve as a bridge between industrial applications and academic research, e.g., to aid constructing engineering correlations, and as feed to process design tools.

In a nutshell, the goals of this review are the following:

- Inform the reader regarding the capabilities of molecular simulation for computing thermophysical properties central to the H_2 value chain.
- Provide an overview of the available literature and point the reader towards the appropriate molecular simulation studies relevant to various technologies across H_2 economy.
- Introduce the main molecular simulation methods and associated techniques for computing thermodynamic, transport, and interfacial properties of H_2 systems.
- Engage into a comprehensive discussion on the fundamental and engineering insights provided from molecular simulation of H_2 systems.
- Contribute tables and figures containing available thermophysical data compiled from different sources.
- Bring forth a pragmatic and useful outlook that will motivate and guide future research in the field, focusing on aspects that have not been sufficiently studied or require improvement.

This review aspires to cover a substantial part of literature on molecular simulation of H_2 systems. There are no restrictions on the years of literature (our literature review search covers studies until early 2025) or the type of systems considered. It is, however, important to note that we limit our attention only to classical molecular simulation, meaning that studies reporting quantum mechanical calculations are not discussed here (e.g., DFT, AIMD), except from some specific topics, for which the combination of DFT and classical molecular simulation is used as a norm. This choice was made due to the extremely high number of available studies using quantum mechanical approaches to study catalytic systems (e.g., H_2 evolution reactions) and surface reactions (e.g., H_2 storage on materials). In fact, these topics are already covered by several review articles. Nevertheless, to present a multi-scale perspective, the validity range and limitations of classical interaction potentials are discussed in detail, even for the cases where quantum effects of H_2 play a significant role. Similarly, studies using reactive force fields or methods (e.g., quantum MC and MD) are not discussed, except for a few cases which are rendered unique or complementary to the topics presented here (e.g., liquefaction, membranes).

Another topic that is not exhaustively discussed in this review is H_2 adsorption on all possible (two-dimensional) 2D and (three-dimensional) 3D (nano-)porous materials. Substantial research efforts have been focused on studying H_2 adsorption and separation using various materials, such as zeolites, metal organic frameworks (MOFs), covalent organic frameworks (COFs), graphene derivatives, borophane, boron nitride, and hydrides. Given the great number of available studies (in the order of thousands or more), we provide a focused overview primarily emphasizing recent advances in high-throughput screening using ML techniques. The permeation behavior of H_2 through polymeric matrices and minerals is covered up to an extensive degree, with the focus being on materials and processes relevant to storage in high−pressure tanks and the subsurface. Again, a thorough analysis of all available studies involving the interaction of H_2 with these families of materials is not feasible since a great number of polymeric and composite systems have been studied using molecular simulation to assess their performance as separation membranes. The latter application is discussed here, however, only with the purpose of providing an overview and a qualitative comparison between polymeric and other porous media for separations.

An area not discussed in this review is molecular modeling of H_2 interactions with plasma-facing materials (PFMs), a crucial research direction for realizing fusion energy as a sustainable power source.[62] At the atomistic scale, MD simulations have been performed by different research groups to reveal the mechanisms of H_2 trapping and intragranular blister formation

https://doi.org/10.1021/acs.chemrev.5c00617
Chem. Rev. 2025, 125, 11878−12029

mainly in Tungsten (W) (i.e., the leading PFM material[63−65]) primarily using many-body (e.g., Brenner-type[66,67]), and recently also ML potentials.[62,64,68] Despite its importance for fusion materials research, the study of H_2-PFM lies outside the scope of the present review. For a comprehensive study on this topic, the reader is referred elsewhere.[63]

Given the extent and high density of information provided in this review, we have organized the manuscript in the following manner: In Section 2, the role of molecular simulation as a tool for predicting thermophysical properties, and for obtaining fundamental insight into each aspect of the H_2 value chain is elaborated upon. Section 2 also constitutes a comprehensive map of the review, containing a brief overview of the most important properties, relevant conditions, and methods regarding each H_2 technology considered, and referring the reader to the relevant sections in the rest of the manuscript, where more information and data are provided. Section 3 focuses on molecular simulation methods and models. Initially, an extensive discussion on the use, parameterization, and limitations of classical force fields used in MC and MD simulations is provided, followed by an outline of techniques that can be used in the frameworks of MD and MC to compute phase equilibria of gaseous and liquid mixtures of H_2, transport coefficients, wettability and interfacial tension, hydrate properties, gas permeabilities in materials, and quantities related to H_2 embrittlement. Section 4 constitutes a comprehensive review of available thermophysical properties of H_2 systems computed with molecular simulation. Examples of the data reviewed and discussed are two-component vapor-liquid equilibria (VLE) of H_2-H_2O, three-phase (hydrate) equilibria of H_2-H_2O, self- and mutual diffusivities, electro-osmotic drag coefficients in membranes, adsorption of H_2 onto materials, thermodynamic properties of wet compressed H_2, adsorption of H_2 onto rock formations, properties of hydrates (e.g., structural, kinetic, equilibria), liquid-vapor interfacial tensions of gas mixtures, high-throughput screening of materials for separations of H_2 containing streams, and H_2 embrittlement mechanisms. The discussion on the available literature also aims at identifying aspects that have not been sufficiently studied or discrepancies between different studies. Discussion on the role of AI and ML is also provided when applicable. Finally, in Section 5 a future outlook is compiled aiming to motivate new research in molecular simulations of H_2 systems.

2. ROLE OF MOLECULAR SIMULATION IN ADVANCING HYDROGEN TECHNOLOGIES: PROCESSES, PROPERTIES, AND RELEVANT CONDITIONS

In this section, we provide an overview of the role of molecular simulation in each stage of the H_2 value chain, i.e., production, purification, transport, storage, and utilization. The focus is on the important properties that can be computed with molecular simulation and the respective relevant conditions for each technology/application. Since many thermophysical properties are relevant to multiple applications and aspects in the H_2 value chain, this section serves as a comprehensive map for the rest of the review. To this purpose, every section below, aside from providing background information for different H_2 technologies, it also points the reader to the appropriate segment in Section 4, where the relevant properties are reviewed in detail.

2.1. Hydrogen Production, Compression, and Utilization in Electrochemical Systems

H_2 is commonly categorized based on the production pathway followed and the related emissions.[69,70] Grey H_2, the most prevalent form, is produced from natural gas via steam methane reforming. This process releases CO_2 into the atmosphere. The process for producing black and brown H_2 from coal emits both CO_2 and CO, and is considered the most harmful to the environment. When combined with CO_2 capture and sequestration, grey H_2 becomes blue H_2, where CO_2 emissions are partly avoided. Blue H_2 can act as a transitional stage between grey and green, enabling continued use of existing infrastructure during the transition. The production pathway via methane pyrolysis, yields the so-called turquoise H_2, which has solid carbon as a by-product. In this review, the focus is on green H_2 processes (production via water electrolysis using renewable sources). Nevertheless properties, and relevant methods to compute, e.g., phase equilibria, chemical reactions, and transport properties are equally applicable to the other H_2 production routes.

The design and wide use of efficient electrolysis systems capable of replacing fossil-based H_2 production with green H_2 signifies a crucial step towards the future energy landscape.[13] Achieving this necessitates the utilization of process modeling and precise understanding of the thermodynamic, electrochemical, and transport properties in various components of the electrolysers, including the balance of plant (BoP).[15,25,71−76] However, the cost competitiveness of green H_2 production poses a key challenge compared to fossil-based methods.[15] Fuel cells, which convert stored H_2 into electrical energy via the reverse process of electrolysis, complement the green H_2 energy cycle. Fuel cell technology shares fundamental electrochemical and thermodynamic principles with water electrolysis, where modeling membrane morphology, water management, and ion transport are key areas into which molecular simulations can provide valuable insights. Similarly, electrochemical H_2 compression (EHC),[77] an innovative method for compressing H_2 using electrochemical splitting and recombination of H_2, operates on comparable principles. The physical insights into these technologies derived from molecular simulations are examined collectively in this review due to their shared fundamental principles and similar H_2 mixtures involved.

EHC performs on similar electrochemical principles as a PEM fuel cell. The key difference is in the functions of the two devices, i.e., compressors are used to increase H_2 pressure e.g., for storage and transport, while PEM fuel cells generate electricity and water from H_2 and O_2, serving as a power source.[78] EHC requires optimal membrane hydration to maintain efficient charge transport through the membrane. This leads to a saturated H_2 stream at the outlet of the compressor. Proper water management is therefore essential to ensure optimal performance and longevity of the membrane. The presence of even low water content in H_2 introduces challenges for downstream of the EHC, for example the design of H_2 refueling stations, which must adhere to the standard limit of 5 ppm water content.[79,80] While minimizing humidity is critical for efficient H_2 refueling, increased humidity in the inlet gas of the fuel cell improves its performance. In fuel cells, a decrease in membrane humidity leads to an increase in ionic resistance and ohmic losses.[81] The application of molecular simulations becomes necessary in comprehending the inner workings of electrochemical compressors, wherein the

https://doi.org/10.1021/acs.chemrev.5c00617
Chem. Rev. 2025, 125, 11878−12029

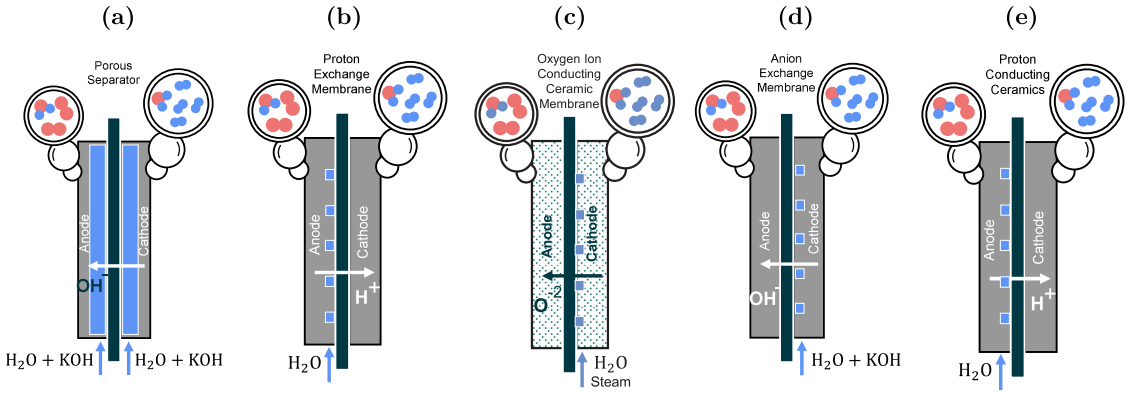

Figure 2. Schematic representations of different electrolyzer technologies for H_2 production: (a) alkaline water electrolysis, (b) proton-exchange membrane water electrolysis, (c) solid oxide electrolysis cell, (d) anion exchange water electrolysis, and (e) proton conducting ceramic electrolysis. To design, optimize, and obtain fundamental understanding of hydrogen production technologies, molecular simulation is used to compute properties, common to all electrolysis processes, e.g., solubilities of hydrogen, oxygen, and electrolytes, mass transport of these species to and from the electrodes, viscosity of the aqueous electrolytes, electrical conductivity, and electro-osmotic drag in the membranes.

fundamental mechanism involves the dissociation of H_2 molecules to protons on the anodic side, and the subsequent formation of H_2 on the cathodic side using electrical current.[77]

In the context of H_2 production (electrolysis), utilization (fuel cell), and electrochemical hydrogen compression (EHC), molecular simulation is important for property prediction to aid the process modeling of these electrochemical systems. Due to the shared electrochemical principles between these technologies, our focus of discussion is mainly on electrolyzers. Without delving into the details of the different available electrolyzer technologies, the following types of electrolysis are currently available[82] as shown in Fig. 2: alkaline water electrolysis (AWE), proton-exchange membrane water electrolysis (PEMWE), anion exchange water electrolysis (AEMWE), solid oxide electrolysis cell (SOEC), and proton conducting ceramic electrolysis (PCCEL).[82] Using molecular simulations to predict properties of and obtain physical insight into charge transport and phase behavior of electrolyte solutions is particularly relevant since such solutions are the common element in all these electrochemical systems. The range of relevant conditions and the solution compositions vary depending on the type of electrochemical system and operating mode, as discussed in more detail later on.

The high costs of green H_2 production are largely driven by elevated electricity prices and regulatory challenges.[15] While electricity costs are outside the scope of system design, efforts can focus on optimizing other factors impacting cost of green H_2 such as enhancing the efficiency and safety of electrolysis systems.[73,74,83,84] While the development of a cost-efficient electrolysis system also relies on factors such as the standardization of components, economies of scale, and efficient integration with renewable sources, these are not the focus of this review. Instead, we emphasize how molecular simulations can provide accurate thermodynamic and transport properties which are critical for optimizing green H_2 production and utilization in electrochemical systems to further drive cost reduction. Typical thermodynamic properties necessary for process modeling of water electrolysis are electrolyte densities, solubilities of gaseous species (e.g., H_2, O_2) in aqueous electrolyte solutions, surface tension of concentrated liquid electrolytes, and partial pressures of water vapor.[75,76] Thermodynamic and transport properties of aqueous potassium hydroxide (KOH), sodium hydroxide (NaOH), and sodium chloride (NaCl) solutions are particularly relevant for electrolysis and fuel cells.[85−89] The dynamic viscosity of liquid electrolytes, mass transport expressed by the self- and mutual-diffusivities of all the species in the solution,[25,71,90,91] and ion transport in membranes are representative examples of important transport properties required for the process modeling of electrolyzer cells. These properties can be computed with molecular simulations using different methods. A detailed list of thermodynamic and transport properties of various H_2 systems relevant to electrochemical applications (i.e., production and utilization of H_2) computed via molecular simulations and reported in literature is provided in Table 1 along with the respective ranges of conditions (e.g., temperatures, pressures, hydration of membranes). For each system listed in Table 1, we also refer the reader to the relevant methodology and detailed discussion in Section 3 and Section 4.

Membrane electrode assemblies (MEAs) are critical components in electrochemical systems.[92] The membranes allow proton transport in acidic environments and hydroxide ion transport in alkaline environments while blocking the passage of gases, ensuring efficient charge transport and water management.[93] The conductivity of a polymer in a PEM/EHC is influenced by its crystallinity, equivalent weight, hydration level, side chain length, and morphology, making the optimization process complex and time-consuming due to the wide range of parameters involved. Effective water management in MEAs (hydration level) is essential, balancing electro-osmotic drag and back diffusion of water at different current densities. Electro-osmotic drag causes water to move across the membrane as protons migrate through the membrane under the influence of the imposed electric field.[92,94] Concurrently, back diffusion occurs due to the difference in water concentration between the cathodic and anodic compartments. Another related critical topic is understanding and mitigating degradation in MEAs. As an example, the contamination of ionomer membranes by e.g., CO^{2+}, Na^+, can significantly disrupt the morphology of the membrane, specifically blocking ion exchange sites. The presence of contamination can impair the flow of reactant gases in the catalyst layer. Additionally, it can hinder the diffusion of hydronium ions (H_3O^+) and water molecules, which are critical for maintaining proton conductivity and

https://doi.org/10.1021/acs.chemrev.5c00617
Chem. Rev. 2025, 125, 11878−12029

Table 1. Thermodynamic and Transport Properties Related to H_2 Production and Utilization in Electrochemical Systems Computed with Molecular Simulation in Different Studies[i]

Property	System[Method]	Conditions
Fugacity Coefficient	H_2-H_2O[a,110]	264−323 K, 10−1000 bar
Chemical Potential	H_2-H_2O-KOH[a,111]	298−423 K, 10−400 bar, 0−8 mol KOH/kg H_2O
	H_2-H_2O-NaCl[a,111]	298−423 K, 10−400 bar, 0−6 mol KOH/kg H_2O
Solubility	H_2-H_2O[a,110]	310−423 K, 10−1000 bar
Vapor-Liquid Equilibrium,	H_2-H_2O[a,47]	264.21−272.4 K, 100−1000 bar
Activity	H_2-H_2O[b,48]	423, 477.59 K, 60.9−182.9 bar
	H_2-H_2O-KOH[a,111]	298−423 K, 10−400 bar, 0−8 mol KOH/kg H_2O
	H_2-H_2O-NaCl[a,111]	298−423 K, 10−400 bar, 0−6 mol KOH/kg H_2O
	H_2/O_2-H_2O-KOH[a,112]	298−353 K, 1−100 bar, 0−8 mol KOH/kg H_2O
	H_2/O_2-H_2O-NaOH[a,112]	298−353 K, 1−100 bar, 0−8 mol NaOH/kg H_2O
	H_2-H_2O-$NaB(OH)_4$[a,113]	298−353 K, 1 bar, 0−5 mol $NaB(OH)_4$/kg H_2O
	O_2-H_2O, Nafion, Aquivion/Pt[d,114]	353.15 K, 2.92 < λ < 13.83
Joule-Thomson Coefficient	H_2-H_2O[c,47]	323 K, 100−1000 bar
Thermal Expansivity	H_2-H_2O[c,47]	323 K, 100−1000 bar
Heat Capacity		
Self-diffusion	Nafion, 3M, Hyflon[d,e93]	300, 353 K, 5 < λ < 14
	Dry Nafion[d,115]	150−600 K
	Hydrated Nafion[d,f116]	300 K, 3.44 < λ < 11.833
	Hydrated Nafion[d,117]	300, 350 K, 3.5 < λ < 16
	H_2, O_2, Nafion[g,118,119]	298 K, λ = 1
	H_2, O_2, H_2O, SPEEK[d,120,121]	298−353 K, 4.9 < λ < 11.1
	H_2O, H_3O^+, Ph-SPEEK[d,122]	300−400 K, 3.5 < λ < 40
	H_2O, H_3O^+, CH_3OH, Ph-SPEEK[d,123]	360 K, 8 < λ < 28
	H_3O^+, PFSA type membranes[d,124]	300 K, λ = 3
	H_2O, Nafion, Aquivion[d,125]	298 K, 3 < λ < 18
	H_2-H_2O-KOH[a,112]	298−353 K, 1−100 bar, 0−8 mol KOH/kg H_2O
	H_2-H_2O-NaOH[a,112]	298−353 K, 1−100 bar, 0−8 mol NaOH/kg H_2O
	O_2-H_2O-KOH[a,112]	298−353 K, 1−100 bar, 0−8 mol KOH/kg H_2O
	O_2-H_2O-NaOH[a,112]	298−353 K, 1−100 bar, 0−8 mol NaOH/kg H_2O
	H_2-H_2O-$NaB(OH)_4$[a,113]	298−353 K, 1 bar, 0−5 mol $NaB(OH)_4$/kg H_2O
Electrical conductivity	H_2O-$NaB(OH)_4$[a,113]	298−353 K, 1 bar, 0−5 mol $NaB(OH)_4$/kg H_2O
	Dry Nafion[d,115]	150−600 K
	H_2, O_2, Nafion[g,118,119]	298 K, λ = 1
	H_2O, H_3O^+, Ph-SPEEK[d,122]	300−400 K, 3.5 < λ < 40
	H_2O, H_3O^+, CH_3OH, Ph-SPEEK[d,123]	360 K, 8 < λ < 28
	H_3O^+, PFSA type membranes[d,124]	300 K, λ = 3
Thermal Conductivity	H_2O, Nafion[d,126]	300−350 K, 3 < λ < 20
Electro-osmotic drag	H_2O, cylindrical pore of Nafion 117[d,127]	298 K, < 7.65 λ < 20.9
	H_2O, Nafion 117[h,128]	287.15−364.65 K, λ = 20
	H_2O, H_3O^+, Nafion[g,129]	363 K, 4.25 < λ < 12.75
	H_2O, H_3O^+, Nafion[g,94]	330−420 K, 5 < λ < 20
	H_2O, H_3O^+, Nafion[g,94]	350 K, 1 < λ < 2

[a]Continuous fractional component Monte Carlo. [b]Monte Carlo. [c]Ensemble fluctuations. [d]Grand-equilibrium method; molecular dynamics. [e]Multistate empirical valence bond. [f]Reversible reference system propagator algorithms. [g]Molecular dynamics with reactive force fields. [h]Non-equilibrium molecular dynamics. [i]The superscripts in the table denote the simulation method used for each system. λ is the water content in the systems with membranes (see Eq. (31)). The table points the reader to the appropriate sections in this review where the relevant methods and discussion are provided. The relevant methods and in-depth discussions per property can be found in this review in the following sections: Fugacities, chemical potentials, solubilities, activities, and vapor-liquid equilibrium: Section 3.3.1 (methods), Sections 4.1.2.1, 4.1.2, and 4.1.1 (discussion). Joule-Thomson coefficient, thermal expansivity, and heat capacities: Section 3.3.4 (methods) and Section 4.1.4 (discussion). Diffusivities: Sections 3.2.4 and 3.2.3 (methods), and Section 4.1.5 and Section 4.1.7 (discussion). Electroosmotic drag: Section 3.2.12 (methods) and Section 4.1.6 (discussion).

hydration within the membrane. Such effects can be rigorously studied and understood via molecular simulations, which offer detailed insights into the structural and transport properties of ionomers under various contamination scenarios. To this purpose, molecular simulations are performed to model membrane morphologies, sorption, percolation, densities, glass transition temperatures, and ion transport.[92,94−101] The influence of these contributions can be isolated in molecular simulations which is challenging to achieve in experiments.[93] Classical MD simulations can capture the vehicular mechanism of charge transport, while reactive force fields and Ab-initio MD[102−105] can potentially capture the Grotthuss mechanism, since bond breaking and formation during the simulation is required.[93] Molecular simulations have also been used in the literature for modeling the membrane and ion transport within the membrane of electrochemical compressors.[92,97] Additionally, molecular simulations can be used to determine the water content in and the thermodynamic properties of the compressed H_2 downstream of the electrochemical compressor.[47,106−110] Fig. 3 highlights various thermophysical properties which are crucial for the process design and optimization of two widely used electrochemical technologies (AWE and EHC) computed with molecular simulation.

2.2. Purification and Separation of Hydrogen Streams

2.2.1. Separations with Membranes. Membranes provide a potentially sustainable alternative to traditional separation methods of H_2 streams.[130−132] An important property of membranes is permeability (P_i). Membrane permeability quantifies the molecular-level transport of substances across thin barriers and differs significantly from other types of permeabilities reported in the literature, such as Darcy's permeability,[133] widely used in subsurface storage and porous media research. Membrane permeability is defined as $P_i = S_iD_i$, where S_i is the solubility of species i (which reflects its affinity with the membrane material) and D_i is the diffusivity (which is a measure of the rate of molecular transport of the

https://doi.org/10.1021/acs.chemrev.5c00617
Chem. Rev. 2025, 125, 11878−12029

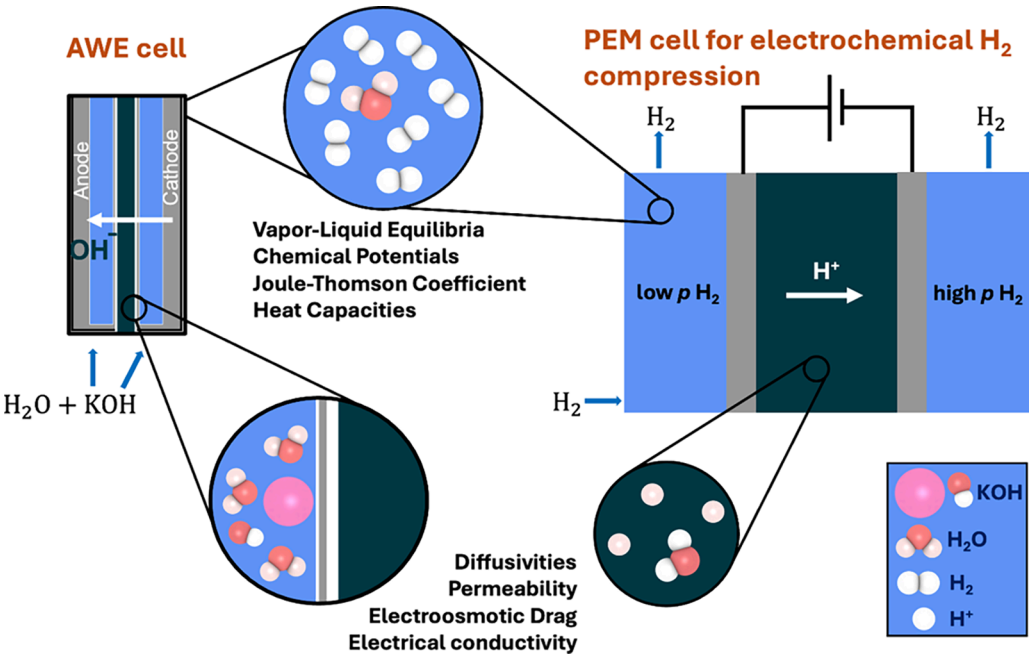

Figure 3. Schematic of alkaline water electrolysis and electrochemical H_2 compression in a proton exchange membrane cell highlighting areas where molecular simulations are crucial, e.g., electrical conductivity, electro-osmotic drag, heat capacity, Joule-Thomson coefficients, and vapor-liquid equilibrium.

species within the membrane). P_i is commonly expressed in Barrer, a unit named after Richard L. Barrer,[134] a pioneer in membrane science. One Barrer represents the permeability of a membrane of 1 cm thickness that allows the passage of molecules occupying 1 cm^3 at standard temperature and pressure (STP: 273.15 K and 1 atm) per second through a 1 cm^2 of membrane area under a pressure difference of 1 cmHg. A related property, membrane permeance, measures the flux of a substance per unit driving force and membrane thickness. It is typically expressed in Gas Permeance Units (GPU), where 1 GPU corresponds to the permeance of a membrane that allows 1 cm^3 of gas (STP) to pass through 1 cm^2 under a pressure difference of 1 cmHg. Expressing permeability in GPU is convenient because the definition inherently accounts for membrane thickness, which can be useful when this parameter is unknown or varies between samples.

In membrane science, selectivity is expressed as the ratio of the permeabilities, P_i/P_j, of two species i and j, as schematically shown in Fig. 4. While this ratio must be high enough to comply with the needs of a given process, at the same time a minimum permeability for the fast-permeating gas (e.g., P_i) should be ensured. Otherwise the overall process is regarded as of discouragingly low performance for industrial applications.

Polymeric membranes are extensively used in industrial-scale separations due to ease of fabrication, cost-effectiveness, and scalability. Polymeric membranes are classified into isotropic, which have a uniform composition and pore structure throughout their thickness, and anisotropic, which have varying pore structures and compositions across their cross-section.[135] Gas separation in polymeric membranes is driven by both solubility and diffusivity selectivity. While the well−known permeability/selectivity trade−off is fundamentally diffusion-dominated,[136] chemical modifications often improve performance by increasing solubility selectivity. For example, introducing polar or CO_2 − philic groups can enhance the uptake of condensable gases (e.g., CO_2, CH_4, O_2) and shift

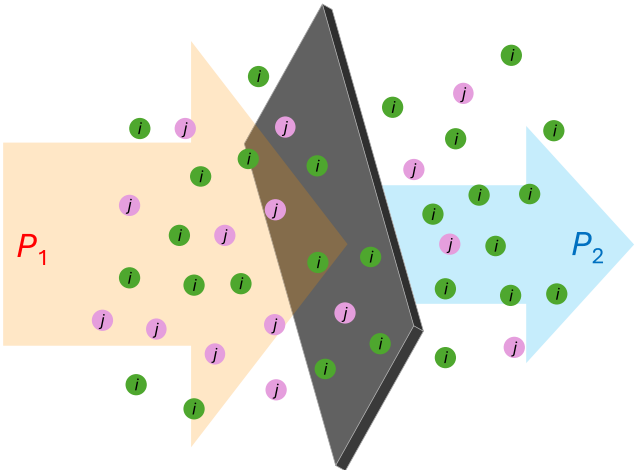

Figure 4. Schematic representation of a membrane separation process, showing the feed side of a mixture i and j at higher pressure (P_1), permeate at lower pressure (P_2) across the membrane.

materials upward relative to the Robeson limits. For H_2 − related separations, this has asymmetric consequences. Because H_2 is a non-condensable gas, and its solubility is difficult to increase, membranes aiming for high H_2 permeation selectivity (H_2/CO_2, H_2/CH_4) remain largely controlled by diffusion. In contrast, increasing the solubility of the heavier partner can substantially improve CO_2/H_2 or CH_4/H_2 selectivity, which explains why many polymer modifications benefit processes focused on capturing CO_2 or CH_4 from H_2 − rich streams but have limited impact on designing highly H_2 − selective membranes.

This observation creates a significant trade-off between permeability and selectivity, as it is shown in Fig. 5 where experimental results from the literature for separations of H_2/CH_4 (Fig. 5(a)) and H_2/CO_2 (Fig. 5(b)) mixtures with

https://doi.org/10.1021/acs.chemrev.5c00617
Chem. Rev. 2025, 125, 11878−12029

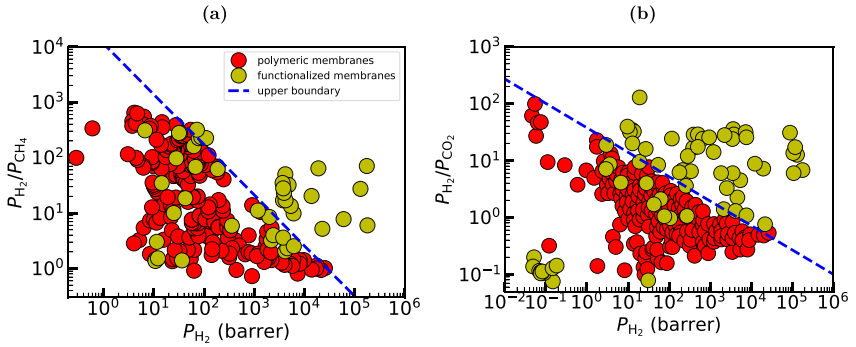

Figure 5. Representative performance assessment in the form of Robeson plots for (a) H_2/CH_4 and (b) H_2/CO_2, comparing experimental results on polymeric and functionalized nanoporous membranes (e.g., MOFs, COFs, zeolites, carbon-based, mixed matrix membranes). Polymeric membranes literature results taken from the seminal work of Robeson.[136] The data from literature for the functionalized materials were collected from an extended survey of the authors and can be found in Tables 15 and 16.

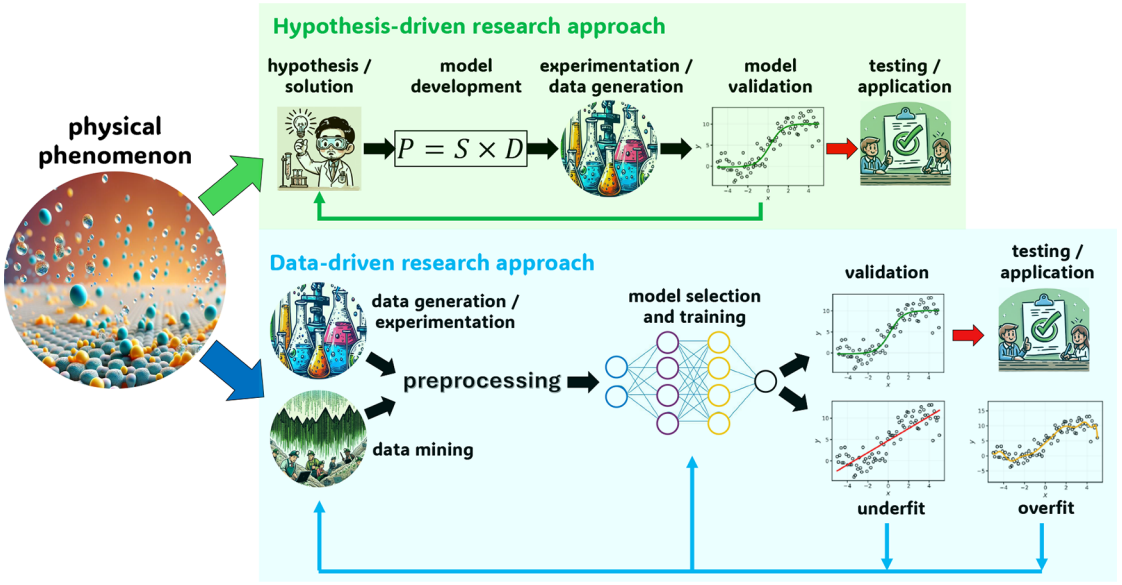

Figure 6. Schematic showing hypothesis (traditional) and data (modern)-driven research approaches. In the traditional route, a hypothesis is usually made in the beginning. Based on this hypothesis models are devised, and experiments are performed to test its validity. In the modern route, data are produced, analyzed, processed, and used to train machine-learning models. The outcomes of these models are validated and used to fine-tune the model. This approach is revolutionizing the study of H_2 processes involving porous materials. The figure is inspired from Fig. 2 of ref 150.

polymeric membranes are indicated with red color. This limitation hinders the widespread use of polymeric membranes for separations of H_2 streams, and has spurred research into exploring alternative materials that can overcome these intricacies.

Crystalline nanoporous materials have surfaced as a prominent class of candidates for addressing the drawbacks of polymeric membranes. These materials have high permeability and selectivity due to their unique structure. Nano-porous materials achieve separations of mixtures via primarily size and shape exclusion. This is due to the small, well-defined windows or apertures connecting internal cavities or narrow channels within the structures of the materials. The apertures act like molecular sieves, allowing smaller molecules to pass through while blocking larger ones.[137,138] The rigid structure of crystalline nanoporous materials provides more precise control over which molecules can pass, unlike polymeric membranes that typically rely on diffusion through flexible, less structured pathways.

While zeolites and activated carbons are widely used materials for H_2 gas separations in the industry,[139−143] due to the limited tunability of pore sizes of zeolites, attention has been directed towards exploring functionalized materials. The most prominent classes of such materials are MOFs (i.e., materials consisting of metal clusters linked with organic ligands)[144] and COFs (i.e., materials composed ogranic molecules connected through covalent bonds).[145] Membranes can be made solely based on MOFs or COFs, or in a hybrid form by using polymers as a matrix and nanoporous materials as fillers, resulting in the so-called mixed-matrix membranes (MMMs).[146] One of the most fascinating features of MMMs is that they can be modified at the molecular level (by using e.g., different fillers, varying filler compositions, different polymer matrices) to tailor their macroscopic properties.[147]. This versatility opens an almost boundless array of possibilities for achieving desired separation results within the H_2 value chain.[148] This also becomes evident by the increased performance of functionalized membranes made of MOFs

https://doi.org/10.1021/acs.chemrev.5c00617
Chem. Rev. 2025, 125, 11878−12029

Table 2. Structure and Properties of the Three Most Common Types of Clathrate Hydrates in Nature[161]

hydrate structure	sI		sII		sH		
crystal system	Primitive cubic		Face-centered cubic		Hexagonal		
space group	*Pm3n*		*Fd3m*		*P6/mmm*		
cavity type (notation)	small (S)	large (L)	small (S)	large (L)	small (S)	medium (M)	large (L)
Description	5^{12}	$5^{12}6^2$	5^{12}	$5^{12}6^4$	5^{12}	$4^35^66^3$	$5^{12}6^8$
cavity radius (Å)	3.95	4.33	3.91	4.73	3.94	4.04	5.79
cavities/unit cell, $n_{i,k}$	2	6	16	8	3	2	1
H_2O/unit cell, $N_{w,k}$	46		136		34		
Unit cell formula	$2S \cdot 6L \cdot 46\ H_2O$		$16S \cdot 8L \cdot 136\ H_2O$		$3S \cdot 2M \cdot 1L \cdot 34\ H_2O$		

and COFs, compared to the limited performance of pure polymeric membranes shown in Fig. 5.

Due to the virtually limitless ways of tailoring the separation performance of these materials through functionalization, achieving the desired results solely in the laboratory is a strenuous, time-consuming, and financially demanding process. Therefore, molecular simulation has emerged as a powerful computational tool for exploring modification-performance correlations and aiding the development of highly H_2-selective membranes.[149] MC and MD simulations are particularly valuable for computing properties related to performance metrics in membrane separations. Such properties are the solubilities, diffusivities, permeabilities, selectivities, and heats of adsorption of H_2 and other gases in the membranes. A brief but comprehensive review of the literature regarding these properties for pure H_2 and different mixtures (with e.g., CO_2, CH_4, N_2, He,) is provided in Section 4.6 for various materials (i.e., MOFs, COFs, MMMs, and zeolites). This discussion also covers properties such as the storage capacities, which are mainly useful for the design and evaluation of H_2 storage systems as briefly covered in Section 2.3.2. Relevant details on models and methods widely used to perform simulations of nanoporous materials and membranes are provided in Sections 3.1.4, 3.2.5, and 3.3.2.

With the advent of high performance computing, the execution of hundreds or even thousands of simulations is now feasible, allowing the exploration of wide design spaces of functionalized materials.[149] Assisted by ML techniques, these complex correlations become easier to uncover, as discussed in more detail in Sections 4.6.1 and 4.6.2. As shown in Fig. 6, ML leads to a paradigm shift in the development of separation membranes, enabling the transition from a hypothesis-driven approach, limited to trial-and-error, to a data-driven approach.[150−158]

In addition to membrane-based separations, large-scale H_2 purification is frequently carried out using adsorption processes such as pressure-swing adsorption (PSA) and temperature-swing adsorption (TSA). Both these processes rely on packed beds of porous adsorbents, often zeolites or activated carbons, and comprise the industrial state-of-the-art for H_2 recovery from complex mixtures. Although PSA/TSA operate on different principles than selective transport across membranes, both approaches benefit from molecular−scale insights into adsorption equilibria, energetics, and diffusion. Discussion on how high−throughput molecular simulations combined with ML approaches can be an important tool for selecting high−performing adsorbents for PSA and TSA processes is provided in Sections 4.6.1 and 4.6.2. For details relevant to PSA process design and optimization, the reader is referred to the studies of Park et al.[159] and Ribeiro et al.[160]

2.2.2. Hydrate-Based Separations. Clathrate hydrates, or simply hydrates, are crystalline, non-stoichiometric, inclusion compounds consisting of a hydrogen-bonded network of water molecules that form three dimensional cavities (cages) inside which guest molecules of appropriate size can be enclathrated (i.e., encaged).[161,162] The water molecules can self-assemble into forming cages under appropriate conditions (i.e., high pressures and/or low temperatures). The cages are further stabilized by weak van der Waals interactions between the water molecules in the lattice and the encaged guest molecules. The most common hydrate structures in nature are the sI, sII, and sH, which result from combinations of different numbers and types (i.e., pentagonal dodecahedron, 5^{12}; tetrakaidecahedron, $5^{12}6^2$; hexacaidecahedron, $5^{12}6^4$; icosahedron, $5^{12}6^8$; irregular dodecahedron, $4^35^66^3$) of cages which form the unit cell of each hydrate structure. Table 2 shows the structural characteristics of the sI, sII, and sH hydrate structures.

Hydrates have attracted significant interest from the industry and academia due to their ability to selectively incorporate particular molecules of appropriate size in their crystal structure. This makes hydrates attractive candidates for a number of industrial applications, including the storage/transport of energy carriers such as H_2 and CH_4[163−166] and environmental gases such as CO_2,[167,168] gas mixture separations, water purification,[169] and desalination.[170] In particular, two industrial applications of hydrates are of significant importance within the H_2 value chain: (i) the storage (stationary or mobile applications) and transportation of H_2 inside hydrates[171,172] (i.e., hydrate slurries or solid hydrates in pellet form), and (ii) hydrate-based separation of the H_2/CO_2 binary gas mixture resulting from the so-called integrated coal gassification cycle (ICGC) plants, where the CO_2 is captured before fuel combustion (i.e., precombustion capture[173]). A hydrate-based separation of a gas mixture is the direct result of the selective incorporation of gas molecules from the mixture of appropriate size in the hydrate crystal structure.[174] Fig. 7 shows a cartoon representation of a single-stage hydrate-based separation for the general case of a gas mixture consisting of components A and B. The process works as follows: Initially, a gas mixture of A and B is in contact with water. The pressure and temperature conditions are tuned to induce hydrate formation, which is followed by separation of the solid hydrate phase and the subsequent hydrate dissociation. Two gas streams, an A-rich (i.e. the "unreacted" gas mixture which remained after hydrate formation), and a B-rich (i.e., resulting from hydrate dissociation), are produced, each of which has different compositions from the initial one. After implementing a number of hydrate formation/dissociation stages, gas streams having a certain degree of required purity are obtained. For extensive discussions on the

https://doi.org/10.1021/acs.chemrev.5c00617
Chem. Rev. 2025, 125, 11878−12029

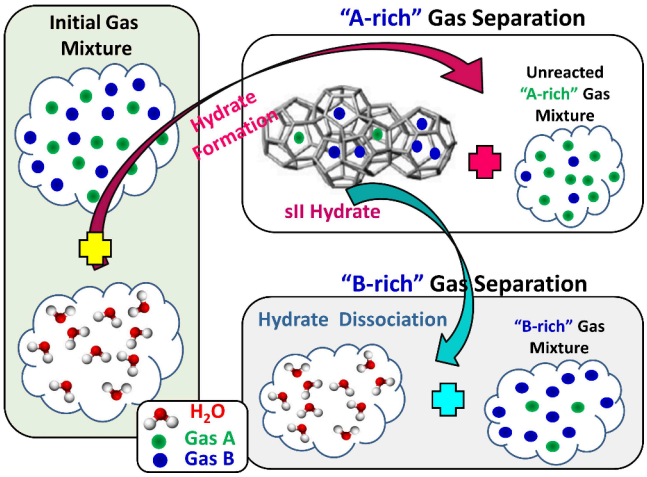

Figure 7. Schematic of a single-stage, hydrate-based, separation of a binary gas mixture "A + B", where A and B are the two gas components.

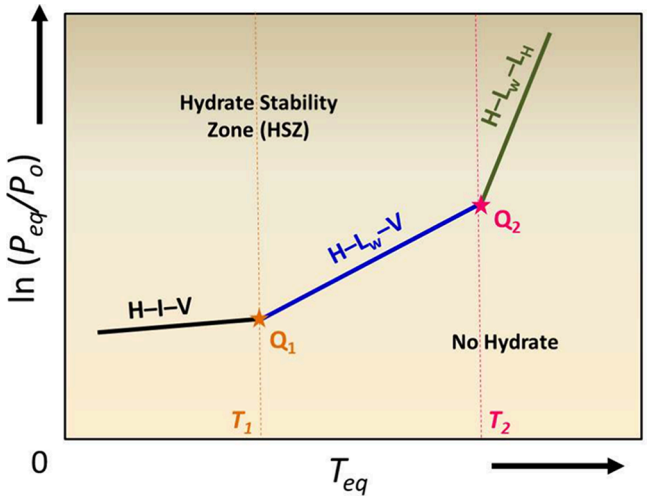

Figure 8. Pressure-equilibrium temperature diagram showing the three-phase equilibria curves for a hydrate-former with lower (Q_1) and upper (Q_2) quadruple points. Phase notation: H − hydrate; L_w − liquid water; I − ice; V − vapor; L_H − liquid hydrate-former.

experimental and computational aspects of hydrate-based H_2-mixture separations, the reader is referred to the review articles by Babu et al.,[173] Tsimpanogiannis et al.,[175] and Hassanpouryouzband et al.[176]

Molecular simulation is an important tool for computing various thermodynamic, transport, kinetic, and structural properties of interest to H_2 hydrate-related applications. Table 3 shows a number of such properties that can be obtained via MD and MC simulations. Table 3 also guides the reader to the corresponding sections in this review where particular properties and methods are further discussed for the case of pure or mixed H_2 hydrates. It should be noted that some of these properties can also be obtained by means of first principle calculations (e.g., DFT[177]). For detailed discussions on DFT-based calculations relevant to H_2 hydrates, the reader is referred elsewhere.[178−182]

Table 3. Important Thermophysical, Transport and Structural Properties for Pure or Mixed H_2 Hydrates[a]

Property	Methodology	Discussion
Phase (p, T) equilibria	Section 3.2.14	Section 4.8.1
Structure	Section 3.2.15	Section 4.8.3
H_2 diffusivities	Section 3.2.3	Section 4.8.8
Kinetic rates	Section 3.2.15	Section 4.8.2
Promoter identification	Section 4.8.7	
Storage capacities	Section 3.3.3	Sections 4.8.5 and 4.8.4

[a]The reader is referred to the sections in this review where the respective methods (methodology) and review (Discussion) of the available literature are located.

Three-phase equilibria is among the most important thermodynamic properties for the design stages of hydrate-based processes. Fig. 8 shows a typical phase diagram of a hydrate-forming system that has a lower (Q_1) and an upper (Q_2) quadruple point. The solid lines indicate where the three-phases are at equilibrium, while the two stars indicate the quadruple points, i.e., where four-phase equilibria occurs. Certain hydrate-forming systems, such as CH_4, N_2, and Ar, exhibit only Q_1, while others, e.g., CO_2, H_2S, C_2H_6, C_3H_8, exhibit both Q_1 and Q_2. Experimental measurements, continuum scale modeling and molecular simulations can be used for the estimation of hydrate phase equilibria. The vast majority of continuum scale modeling studies has been performed by an approach that couples van der Waals−Platteeuw statistical theory,[183] used for describing the solid solution, with an EoS that describes the vapor-liquid equilibria. The seminal work of Parrish and Prausnitz,[184] and the later modifications,[185,186] introduced to overcome some of the initial limitations of the theory, are capable of providing a satisfactory description of the phase equilibria for the most common hydrate systems. For a detailed review on this, the reader is referred to the study by Medeiros et al.[187]

The study of hydrate equilibria with MC and MD simulations can provide a deeper understanding of the related microscopic phenomena. Such molecular-scale methodologies can be used in a complementary role to the experimental and continuum-scale approaches to aid the design of new hydrate-related processes. Additional properties of interest reported in literature are the enthalpies of hydrate dissociation (ΔH^{dissoc}), the enthalpies of enclathration (ΔH^{encl}), isobaric heat capacities (C_p), hydrate lattice expansivities, and separation efficiencies. Interestingly, no molecular simulation data regarding these properties are available for H_2 containing systems, despite the fact that these properties are essential for the design/optimization of industrial processes involving hydrate-based systems. This clearly shows that ample room is available for future computational studies of H_2-containing mixtures capable of forming hydrates.

2.2.3. Separations Using Ionic Liquids. As discussed earlier, membranes comprising polymeric and nanoporous materials can be used to efficiently separate H_2 streams under various conditions and for different applications. High selectivities and adsorption capacities, have also been reported using solvents based on ionic liquids (ILs) and deep eutectic solvents (DES). ILs are salts (comprising only ions) with melting temperatures orders of magnitude lower than common salts, e.g., NaCl. The melting T of ILs is below 100 °C, and for some components (the so-called room temperature ILs) it can even be below ambient T. The broad liquid range, combined with other properties such as the negligible vapor pressures, thermal stability, and high degree of tunability, makes ILs an

https://doi.org/10.1021/acs.chemrev.5c00617
Chem. Rev. 2025, 125, 11878−12029

interesting class of materials for a wide variety of processes. In addition, in the past 50 years ILs have been considered for use in industrial applications as an environmentally friendlier solvent compared to common organic components.

ILs have found application also in extraction (e.g., liquid-liquid) and separation (e.g., gas) processes, usually in the form of IL-supported membranes. For more details on ILs and their applicability the reader is referred elswhere.[188−191] To the best of our knowledge, no molecular simulation studies investigating relevant H_2/DES properties are available in literature. Contrary, studies on sorption, diffusivities, and interfacial properties of H_2 (and mixtures of H_2 with other gases) in ILs computed via MC and MD simulations are available. Nevertheless, the number of these studies is limited compared to e.g., CO_2/ILs or CH_4/ILs systems. Evidently, the main motivation for performing molecular simulations of H_2/ILs is the study of CO_2/H_2 separation, which is crucial for pre-combustion processes. Predicting properties for H_2 separations from N_2 and CH_4 are also common in the available molecular simulation literature owing to the importance of these mixtures for the design of carbon capture technologies. Since mixed-gas experiments are usually challenging to conduct, molecular simulations offer a compelling and efficient complementary method for predicting and understanding the absorption selectivities of IL/gas systems.

Based on our review of the available molecular simulation literature, H_2 appears to have very low solubilities in ILs compared to other gases, which increases with temperature (contrary to some experimental findings). CO_2/H_2 selectivity in ILs dramatically decreases with temperature, while, computations of H_2 diffusivities show that it diffuses up to 12 times faster than CO_2. The full review of this topic is provided in Section 4.5, along with details regarding discrepancies between simulations and experimental data. For relevant methods and models, the reader is referred to Sections 3.1.3, 3.2, and 3.3.1.

2.3. Hydrogen Storage

The high gravimetric energy density of H_2 (ca. 120 MJ/kg), nearly two and a half times higher than conventional fossil-based fuels such as methane, propane, diesel, and gasoline (see Fig. 9), makes it an attractive energy carrier. However, focusing solely on gravimetric energy density does not provide a complete picture regarding the widespread application of H_2, due to the storage challenges associated with its low volumetric density (ca. 0.010 MJ/L at 20 °C).[22,192] Typically, commercially compressed H_2 gas (CHG) is stored at pressures up to 700 bar. CHG at 300 bar has a density of 24 kg/m^3 at 15 °C, while at 700 bar and the same temperature, the density increases to 40 kg/m^3 as shown in Fig. 10.

Liquid H_2 (LH) at cryogenic temperatures has densities up to 70 kg/m^3. Subcooled liquid H_2 (SLH), which achieves a density of 62 kg/m^3 at -245 °C and 16 bar, is produced by slightly increasing the pressure of LH using state-of-the-art compression systems.[195,196] SLH storage faces challenges due to boil-off, estimated to last between 10 and 200 hours depending on the state of charge of the system.[195] Cryo-compressed H_2 (CCH), combining low temperatures with high pressures, and LH are other storage types, although the technology readiness level (TRL) for CCH remains low.[195]

Cost-effective, high energy density H_2 storage is a crucial part of the future sustainable energy landscape. The need to discover (at the material level) and design (at the system level)

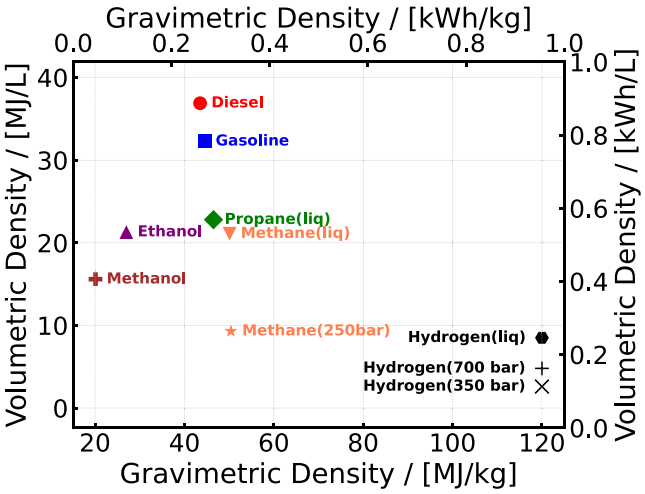

Figure 9. Gravimetric and volumetric energy densities of hydrogen compared to other fuels at ambient temperature. The data are extracted from refs 38 and 193.

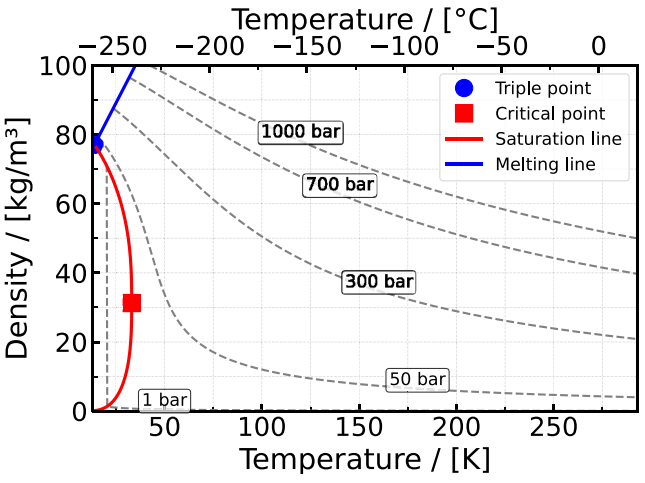

Figure 10. Hydrogen density - temperature diagram for different isobars. Data are taken from NIST.[194]

improved media for H_2 storage is specifically emphasized by the US Department of Energy (DOE).[22,197,198] Molecular simulations play a central role in addressing the material challenges and in modeling H_2 storage processes, especially under elevated pressures and temperatures (relevant to *e.g.*, underground storage), providing unique insights into the physical-chemical mechanisms governing the behavior of the systems at hand. Such insights are almost impossible to achieve through experimental methods alone, which are limited by both safety, cost, and resolution constraints. To this end, the prediction of relevant thermophysical properties and insights obtained from molecular simulations can guide the design of more efficient H_2 storage systems.[77,199−201] This review focuses solely on classical molecular simulations related to three different types of storage, namely compressed H_2 for vehicular applications, storage in materials, and underground H_2 storage. It is important to note that this work does not extensively cover H_2 storage in materials, since this field is already well-documented in the literature, particularly regarding the vast array of nanoporous and 2D nano-materials. However, several key references to comprehensive reviews are provided on this topic for further reading.

https://doi.org/10.1021/acs.chemrev.5c00617
Chem. Rev. 2025, 125, 11878−12029

2.3.1. High Pressure Storage of Gaseous Hydrogen in Tanks. The pathway to achieving a less carbon-intensive mobility sector relies on the use of battery electric vehicles (BEVs) and fuel cell electric vehicles (FCEVs). Usually, BEVs are most suitable for short-range commutes, while FCEVs are preferred for medium to long-haul applications.[193,195,202−206] Currently, CHG at 70 MPa and 35 MPa is used in light-duty vehicles, while an inlet pressure of up to 875 bar is required in on board H_2 storage tanks to refuel the FCEV within 3 to 4 minutes.[79,201,207−215]

In FCEVs of all types, e.g., trucks, light vehicles, buses, H_2 is stored at high pressures in different tanks of varying type and size. The main types of tanks are classified as I, II, III, IV, and V.[216,217] Type I tanks typically operate at a maximum pressure of 200 bar, with a gravimetric storage density of 0.01 to 0.02 kg_{H_2}/kg. Type II tanks, with a maximum pressure of 300 bar, reduce weight by 40% compared to type I tanks, but are still less efficient for H_2 storage due to a 50% increase in manufacturing costs.[216,217] Both types are unsuitable for mobility applications because of their low storage density. In contrast, type III and IV tanks, which operate between 450 and 700 bar, provide significantly higher H_2 storage capacity and are commonly used in fuel cell vehicles. Type IV tanks, in particular, are widely used due to their lightweight composite structure, capable of withstanding pressures up to 700 bar or higher.[216,217] Type V tanks, though still in development, are expected to offer even greater performance.[216,217]

Due to the high pressures in the tanks (e.g., 700 bar), H_2 gas experiences a strong driving force to escape. To mitigate this thermodynamic phenomenon, it is common that thermoplastic polymers and composite materials are used in the tanks as barrier materials (i.e., inner liners) that provide H_2 gas containment. To this purpose, developing polymers and composites with low inherent H_2 permeability is crucial. This requires extensive research involving a wide spectrum of materials tested under high pressures, which is not trivial to do with experiments alone. Molecular simulation can make a substantial contribution towards advancing H_2 storage systems under high pressures, which are essential for FCEVs.[218] The insights from molecular simulations allow for the understanding of H_2 interactions with the liner materials, which affect permeation resistance and gas barrier properties.[218] By studying these interactions at the nano-scale, molecular simulations help assess the suitability of polymeric and composite materials, thus, providing crucial insights into the performance and safety of H_2 storage systems. Molecular simulation studies in this field have mainly focused on studying H_2/polymer systems relevant to IV-type hydrogen tanks. The most common polymers in these tanks are polyamide-6 (PA6), polyethylene (PE) and high density polyethylene (HDPE), and composite materials such as graphene/PA6. Molecular simulation studies of synthetic rubbers, such as ethylene propylene diene monomer (EPDM), used mainly as sealing components (e.g., gaskets, hose liners, O-rings) in H_2 energy/storage infrastructure, are also available in the literature.

In Section 4.4 we provide a detailed review of the available molecular simulation literature reporting thermophysical properties of H_2/polymer (and composite) systems. These studies mainly report diffusivities (and diffusion mechanisms), solubilities (and sorption), permeabilities of H_2 in the solid phases, and polymer-specific properties such as the material fractional free volume (FFV), specific volume, and density. Our analysis of the available literature revealed that there is a large data variability among the simulation studies. For example, the computed H_2 solubilities and permeabilities span three orders of magnitude across different studies, despite using the same (or similar) force fields and methods. In addition, we show that while molecular simulations capture experimental permeabilities qualitatively, quantitative differences exceed three orders of magnitude clearly indicating that there is ample room for improved predictions. For a description of the relevant molecular models and methods for computing the thermodynamic and transport properties of H_2/polymer systems, the reader is referred to Sections 3.1.4, 3.2.4, 3.2.5, 3.3.1, and 3.3.2.

2.3.2. Storage in Materials. To avoid working at high pressures (as discussed in Section 2.3.1) and/or at low temperatures (see Section 2.4.3), H_2 can be stored in solids and liquids.[22] Materials can store H_2 via physical (physisorption, i.e., via weak electrostatic or Van der Waals interactions) or chemical (chemisorption, i.e., via formation of chemical bonds) sorption.[23] Characteristic examples are intermetallic hydrides, where H_2 is physically absorbed within the interstitial space in the solid, or complex hydrides where covalent/ionic interactions between H_2 and adsorption cites drive the H_2 storage process.[193] Other families of relevant materials are the so-called Liquid Organic Hydrogen Carriers (LOHCs),[219] 2D materials (e.g., graphene, borophene),[220−222] and nanoporous materials such as MOFs and COFs (introduced in Section 2.2).

DOE has issued requirements for the design and production of new onboard automotive H_2 storage systems.[197,199] The most important requirements comprise H_2 gravimetric capacities of 6.5 wt.% or higher, volumetric capacities of 0.05 kg H_2/L or higher, and system costs of 266 $/kg H_2 or cheaper.[197] The adsorption energy of H_2 with the material should optimally range from -0.20 to -0.40 eV/H_2 to avoid under- or over-binding of the H_2 molecules with the storage medium.[223−226] A detailed description of the requirements including the minimum durability of the storage unit can be found in ref 197. It is noteworthy that no existing material has yet met all the requirements of DOE for onboard H_2 storage. This is a major motivation, driving research in both academia and industry to discover and fabricate new materials and catalysts for H_2 storage systems.[197]

Physisorption on porous materials such as MOFs and zeolites generally results in fast H_2 release and capture kinetics, but suffers from low gravimetric and volumetric H_2 capacities.[227,228] Chemisorption on materials such as metal hydrides, reaches larger H_2 capacities but the release of H_2 (i.e., the dehydrogenation reaction) is energy intensive and has slow kinetics.[229,230] To make H_2 economy feasible, discovering and using suitable and cost-effective materials with high H_2 capacities and fast release/capture kinetics are essential. 2D materials and porous structures, such as MOFs, are frequently studied for H_2 storage and separation (see also Section 2.2.1) due to their high surface-to-volume ratio and chemical tunability, which allows for optimizing adsorption capacities and efficiencies (see Section 2.2.1). The number of possible new materials that can be potentially synthesized and used for H_2 storage is virtually unlimited.[198]

Even when considering specific classes of nanoporous media, such as MOFs or zeolites, the number of materials that has been theoretically predicted to date reaches the order of mangnitudes of hundreds to millions. This combined with the

https://doi.org/10.1021/acs.chemrev.5c00617
Chem. Rev. 2025, 125, 11878−12029

rapid rate that new families of materials are being discovered, synthesized, and considered for H_2 storage makes relying solely on experiments prohibitively costly and time-consuming.[231−235] Also, experimental measurements of H_2 systems require strict adherence to safety standards which involve protocols to prevent leaks, explosions, and contamination, especially at high-pressures.[197] To this end, atomistic molecular simulations have emerged as a robust and efficient approach to *in silico* screen extensive families of materials with respect to important properties governing H_2 storage. These properties include H_2 adsorption energies, gravimetric and volumetric storage capacities, and diffusion coefficients of H_2 in the materials.[51,236] This allows for early detection of unsuitable materials, either due to low storage capacities or material instability, but also for identifying key-performing media which can be further studied experimentally. Material properties such as the Young's modulus and thermal conductivity can also be predicted using molecular simulations[237,238] and used to evaluate potential H_2 storage systems. Considering the extensive body of literature on H_2 storage in 2D and 3D materials, and given the fact that this topic closely aligns with Section 2.2.1, in this review we present only a condensed discussion of H_2 sorption and storage in nanoporous media in Section 4.6. Focus is directed in the increasing coupling of AI techniques with classical molecular simulation to screen thousands of different materials Sections 4.6.1 and 4.6.2.

2.3.3. Storage in Hydrates. While gas hydrates have been known for more than 200 years, it was a common belief until recently that pure H_2 was not capable of stabilizing the hydrate structure due to the small size of the H_2 molecule. A major change in the dominant belief occurred in 1997, when Kuhs et al.[239] using neutron diffraction data of sII N_2 hydrates demonstrated experimentally that multiple occupancy of a hydrate cage was possible. The important study of Kuhs et al. was followed by a number of experimental studies that confirmed the possibility of multiple occupancies for N_2, O_2 and Ar (for more details the reader is referred to the relevant experimental studies discussed in the review by Tsimpanogiannis and Economou[240]). A few years later, MC studies confirmed the capability of molecular simulations to capture multiple occupancy phenomena. A detailed review of the relevant MC studies is presented in ref 240.

While experimental evidence of the existence of H_2 hydrates became available via a number of studies,[241−244] the interest in H_2 hydrates increased significantly only after Mao et al.[171] reported experimental measurements confirming the formation of pure H_2 hydrates at high pressures (i.e., 300 MPa at 280 K). At ambient pressure, pure H_2 hydrate was found to be stable at low temperatures (i.e., 150 K). Mao et al. performed energy-dispersive X-ray diffraction (EDXD) and neutron diffraction experiments to identify that H_2 hydrates are of type sII structure. Mao et al. also suggested that the 5^{12} (S-cages) could accommodate two H_2 molecules, while the $5^{12}6^4$ (L-cages) could accommodate up to four H_2 molecules. Such a configuration allows for a H_2 storage capacity equal to 5.0 wt.% H_2 on hydrates. This value is close to the US DOE target of 6.5 wt% and a volumetric density of 62 kg H_2/m^3 for H_2 storage in solid materials prior to 2001.[206] Fig. 11 shows a schematic of sII H_2 hydrate formation. Namely, when water and H_2 are brought together at appropriate pressure and temperature conditions, sII hydrate forms. This hydrate consists of two different types of cages (i.e., S-, and L-cage)

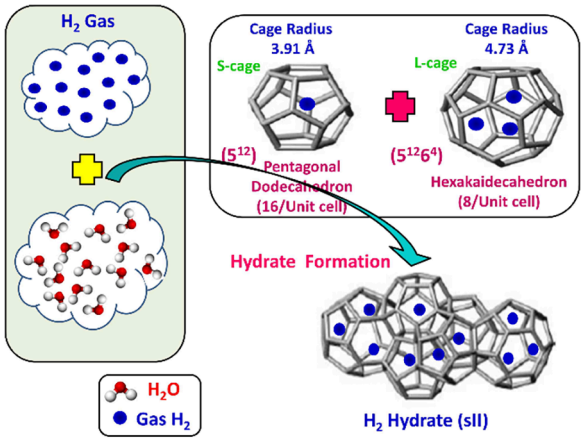

Figure 11. Schematic representation of H_2 hydrate (sII) formation. Sixteen pentagonal dodecahedron (5^{12}; S-cage) cages and eight hexacaidecahedron ($5^{12}6^4$; L-cage) cages combine in order to form a single unit cell of sII hydrate. The multiple occupancy of L-cages results in increasing the H_2 storage capacity of the hydrate.

as shown in the top right panel of Fig. 11. The possibility of multiple H_2 molecules occupying the L-cages (see bottom right panel of Fig. 11) results in a solid material with increased H_2 storage capacity compared to the case when all types of cages are occupied (at most) by a single H_2 molecule.

The high pressures (or the low temperatures) required for the formation of pure H_2 hydrates is a major limitation for the use of hydrates as H_2 storage materials for e.g., vehicular applications. Florusse et al.[245] reported experiments demonstrating that the high pressures (≈ 2000 bar) required for the formation of pure H_2 hydrates can be significantly reduced (e.g., 50 bar at 280 K) by using tetrahydrofuran (THF) as hydrate "promoter" (i.e., a component that promotes hydrate formation at moderate pressure and temperature conditions compared to the pure case[246]). The use of a promoter, however, results in lower H_2 storage capacity due to the promoter occupying the L-type cages (see Table 2 for cage notation). Lee et al.[247] reported the possibility of increasing the H_2 storage capacity of the mixed H_2/THF hydrate by "tuning" the hydrate. Namely, using less than the stoichiometric amount of THF, therefore succeeding in having partial occupancy of the L-cages by H_2, instead of being occupied completely by THF. However, hydrate tuning has been highly debated in the literature due to the difficulty in experimentally reproducing the process (i.e., see the detailed discussions by Alavi and Ripmeester[177] and Papadimitriou et al.[248]). Furthermore, an extensive discussion on the experimental and computational aspects of H_2 storage in hydrates can be found in a series of review studies,[172,177,249−256] while an excellent discussion on the statistical mechanics theory behind the thermodynamic stability of hydrates is provided by Tanaka and Matsumoto.[257]

From the discussion presented here it becomes evident that we are interested in identifying properties (thermodynamic, transport, and structural) and condition that affect the H_2 storage capacity of pure or mixed H_2 hydrates. Such are the following: (i) three-phase equilibrium conditions (i.e., higher pressures result in higher cage occupancies, therefore higher storage capacities, as a result of the fact that hydrates are not stoichiometric materials. Namely, not all cages are required to be occupied for hydrate stability), (ii) H_2 diffusivity within the

https://doi.org/10.1021/acs.chemrev.5c00617
Chem. Rev. 2025, 125, 11878−12029

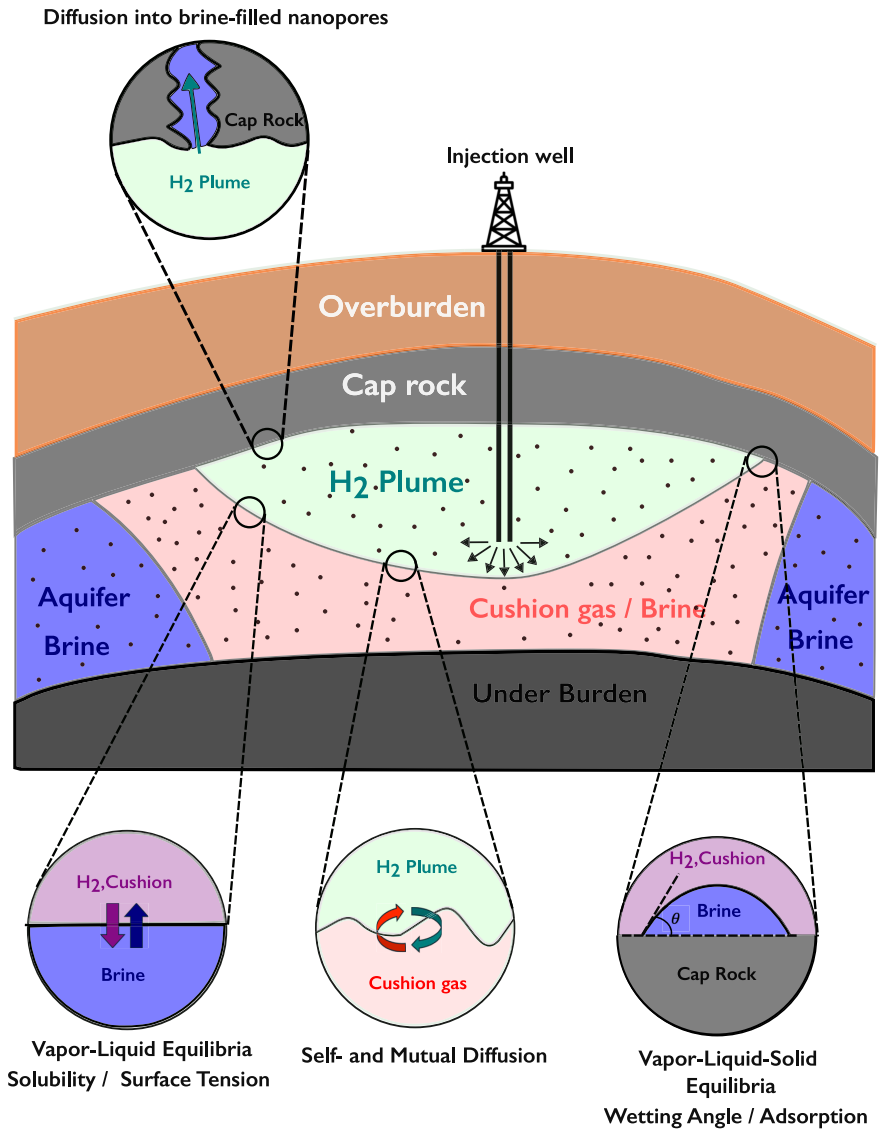

Figure 12. Schematic representation of key physical processes governing subsurface H_2 storage. We highlight areas where molecular simulations are crucial, e.g., the diffusion of H_2 into empty or brine-filled nanopores in the caprock, essential for assessing leakage risks, the dissolution of H_2-cushion gas mixtures into brines under reservoir conditions, where atomistic modeling enhances our understanding, the mixing of H_2 with cushion gas via molecular diffusion, potentially leading to contamination, and the three-phase contact angle between H_2-cushion gas mixtures, brine, and geological solids, determining the capillary pressure needed for hydrogen to invade brine.

hydrate crystal (i.e., H_2 can escape via diffusion from the hydrate solid structure, reducing the amount of H_2 stored in the hydrate), and (iii) hydrate lattice constants (i.e., the use of various promoters, having different sizes, can result in increasing the lattice constant, therefore, providing increased storage capacity).

2.3.4. Subsurface Storage. In 2021, the world energy consumption was estimated at 600 EJ.[258,259] This massive energy requirement highlights the need for extensive H_2 storage solutions. Given the limitations of surface storage facilities, e.g., holding the large volumes necessary for long-term energy storage, alternative solutions are explored. Geological formations, such as depleted reservoirs and salt caverns, offer storage capacities in the order of hundreds of gigawatt-hours, providing a feasible option for large-scale H_2 storage.[259−262]

Underground H_2 storage (UHS)[263,264] (also referred to as subsurface H_2 storage) involves injecting H_2 into geological formations where interactions with the surrounding gases, fluids, and solids occur. A cartoon representation of UHS is shown in Fig. 12. This process can include the use of a so-called cushion gas,[259−262] occupying up to 30% of the reservoir's volume, to maintain a minimum pressure and ensure mechanical stability. Brine (usually a mixture of water and sodium chloride) acts as a natural sealant preventing H_2 leakage into surrounding aquifers, maintaining the integrity and stability of the geological structure. Understanding the physical processes involved in subsurface H_2 storage is crucial for optimizing storage strategies and ensuring safety and efficiency. In past years, molecular simulation has been proven to be a necessary tool for investigating these processes at the molecular level, providing detailed insights into several key properties and physical mechanisms, while accessing state points and quantities which can be inaccessible without costly and complex experimental setups. For example, H_2 tends to form mixtures with other gases present in the reservoir, driven

https://doi.org/10.1021/acs.chemrev.5c00617
Chem. Rev. 2025, 125, 11878−12029

Table 4. Comprehensive List of Hydrogen Properties Relevant to Underground Storage (See Also Fig. 12), as Computed via MD Simulations[a]

Property	System	Condition
pVT	H_2	323-423 K, 5-50 MPa, 0-1 x_{H_2}
	H_2-CO_2	323-423 K, 5-50 MPa, 0-1 x_{H_2}
	H_2-CH_4	310-470 K, 15−30 MPa, 0-1 x_{H_2}
	H_2-CO_2	310-470 K, 15−30 MPa, 0-1 x_{H_2}
Self- and mutual-diffusivity	H_2-CO_2	323-423 K, 5-50 MPa, 0-1 x_{H_2}
Thermodynamic factor	H_2-CO_2	323-423 K, 5-50 MPa, 0-1 x_{H_2}
Interfacial tension	H_2-H_2O	0.1−160 MPa, 298−523 K, 0−5 mol
	H_2-NaCl Brine	0.1−60 MPa, 298−523 K, 0−5 mol
	H_2-$CaCl_2$ Brine	1−30 MPa, 298−373 K, 0−5 mol
	H_2-$MgCl_2$ Brine	1−30 MPa, 298−373 K, 0−5 mol
	H_2-KCl Brine	1−30 MPa, 298−373 K, 0−5 mol
	H_2-N_2-H_2O	1−70 MPa, 300−343 K
	H_2-CH_4-H_2O	10−60 MPa, 323−388 K
	H_2-CO_2-NaCl Brine	5−40 MPa, 298−373 K, 0−3 mol
Wetting angle	H_2-H_2O-Mica	5 and 20 MPa, 300 and 323 K
	H_2-H_2O-Gypsum	5 and 20 MPa, 300 and 323 K
	H_2-H_2O-Anhydrite	5 and 20 MPa, 300 and 323 K
	H_2-H_2O-Halite	5 and 20 MPa, 300 and 323 K
	H_2-H_2O-Silica (Q2 and Q4)	5−60 MPa, 320 K
	H_2-H_2O-Silica (Q3/Q4)	1−160 MPa, 298−523 K
	H_2-NaCl Brine-Quartz	20 MPa, 333 K, 1.5−3.5 mol
	H_2-NaCl Brine-Silica (Q2)	0.1−150 MPa, 300−423 K, 0−5.4 mol
	H_2-NaCl Brine-Humic Acid substrate (Q2)	0.1 MPa, 300 K, 0.5 mol
	H_2-NaCl Brine-Siloxane with defects	10 MPa, 323 K, 20 wt%
	H_2-NaCl Brine-Halite NaCl	5−25 MPa, 300−400 K, 0−1 mol
	H_2-NaCl Brine-Quartz	5−25 MPa, 300−400 K, 0−1 mol
	H_2-NaCl Brine-Calcite	5−25 MPa, 300−400 K, 0−1 mol
	H_2-NaCl Brine-Montmorillonite	5−25 MPa, 300−400 K, 0−1 mol
	H_2-KCl Brine-Silica (Q2)	14−150 MPa, 323−423 K, 0−5.4 mol
	H_2/CO_2-H_2O-Calcite	0.1−70 MPa, 298−373 K
	H_2/CO_2-H_2O-Quartz	0.1−70 MPa, 298−373 K
	H_2/CO_2-H_2O-Silica	10−30 MPa, 333−413 K
	H_2/CO_2-H_2O-Silica	10−30 MPa, 333−413 K
	H_2/CO_2-H_2O-Graphene	5−40 MPa, 292−343 K
	H_2/CH_4-H_2O-Calcite	0.1−70 MPa, 293−373 K
	H_2/CH_4-H_2O-Quartz	0.1−70 MPa, 293−373 K
	H_2/CH_4-H_2O-Silica	20 MPa, 373 K
	H_2/CH_4-H_2O-Graphene	5−40 MPa, 292−343 K
	H_2/N_2-H_2O-Silica	20 MPa, 373 K
	H_2/CO_2-NaCl Brine-Siloxane (Kaolinite)	5−80 MPa, 303−343 K, 1.7 mol
	H_2/CO_2-NaCl Brine-Talc	15 MPa, 333 K, 3.4 mol
	H_2/CO_2-KCl Brine-Talc	15 MPa, 333 K, 0.13 mol
	H_2/CO_2-NaCl Brine-Gibbsite (Kaolinite)	15 MPa, 333 K, 3.4 mol
	H_2/CO_2-KCl Brine-Gibbsite (Kaolinite)	15 MPa, 333 K, 0.13 mol
	H_2/CH_4-NaCl Brine-Siloxane (Kaolinite)	5−80 MPa, 303−343 K, 1.7 mol
	H_2/CH_4-NaCl Brine-Talc	15 MPa, 333 K, 3.4 mol
	H_2/CH_4-KCl Brine-Talc	15 MPa, 333 K, 0.13 mol
	H_2/CH_4-NaCl Brine-Gibbsite (Kaolinite)	15 MPa, 333 K, 3.4 mol
	H_2/CH_4-KCl Brine-Gibbsite (Kaolinite)	15 MPa, 333 K, 0.13 mol
Adsorption on clay-substrates	CH_4/H_2/H_2O-Na-Montmorillonite	343 K / -
	H_2-Kaolinite (Gibbsite and Siloxane)	300 K / 1.0−50.7 MPa
	H_2/CH_4-Kerogen	338 K / 0−27.6 MPa
	H_2/CH_4-Montmorillonite	323 K / up to 11.15 MPa
	H_2/CH_4/H_2O-Montmorillonite	323 K / up to 11.15 MPa
	H_2/H_2O-Kaolinite (Gibbsite and Siloxane)	298.15 K / 0.1−10 MPa
	H_2/CH_4-Hydroxylated Quartz	323.15−423.15 K / 1−50 MPa
	H_2/CO_2-Hydroxylated Quartz	323.15−423.15 K / 1−50 MPa
	H_2/H_2O-Hydroxylated Quartz	323.15−423.15 K / 1−50 MPa
	H_2-Kaolinite	303.15−353.15 K / 0−18 MPa
	H_2-Illite	303.15−353.15 K / 0−18 MPa
	H_2-Dolomite	303.15−353.15 K / 0−18 MPa
	H_2-Quartz	303.15−353.15 K / 0−18 MPa
	H_2-Calcite	303.15−353.15 K / 0−18 MPa
	H_2-SiO_2	300 K / 10−30 MPa
	H_2/CH_4-SiO_2	300 K / 10−30 MPa
	H_2/H_2O-SiO_2	300 K / 10−30 MPa
	H_2/CH_4/H_2O-SiO_2	300 K / 10−30 MPa
	H_2/CH_4/H_2O-Kaolinite	333.15 K / 30 MPa
	H_2/CO_2/H_2O-Kaolinite	333.15 K / 30 MPa
	H_2/CH_4-Montmorillonite	333 K / 15 MPa
	H_2/CO_2-Montmorillonite	333 K / 15 MPa
	H_2/CH_4-Illite	333 K / 15 MPa
	H_2/CO_2-Illite	333 K / 15 MPa
	H_2/H_2O-Kaolinite (Gibbsite and Siloxane)	298 K / 10 and 20 MPa
	H_2-Calcite	298−350 K / 1−10 MPa
	H_2-Hematite	298−350 K / 1−10 MPa
	H_2-Quartz	298−350 K / 1−10 MPa
	H_2/CH_4-Kaolinite	333.15 K / 30−15−10 MPa
	H_2/CH_4-Kerogen	333.15 K / 30−15−10 MPa
	H_2-Kerogen II-D	333.15 K / 3−18 MPa
	H_2/CH_4-Montmorillonite	333.15 K / 3−18 MPa
	H_2/CO_2-Montmorillonite	333.15 K / 3−18 MPa
	H_2-Kaolinite	323−403 K / 1−50 MPa
	H_2/CH_4-Kaolinite	323−403 K / 1−50 MPa
	H_2/CO_2-Kaolinite	323−403 K / 1−50 MPa

https://doi.org/10.1021/acs.chemrev.5c00617
Chem. Rev. 2025, 125, 11878−12029

Table 4. continued

Property	System	Condition
	H_2/CH_4-Quartz	339−400 K / 1−50 MPa
	$H_2/CH_4/H_2O$-Quartz	339−400 K / 1−50 MPa
	H_2-Kaolinite (Gibbsite and Siloxane)	303−423 K / 1−30 MPa
	H_2/H_2O-Kaolinite	318.15 K / 0.1−30 MPa
	CH_4/H_2O-Kaolinite	318.15 K / 0.1−30 MPa
	$H_2/CH_4/H_2O$-Kaolinite	318.15 K / 0.1−30 MPa
	H_2/H_2O-Pyrophyllite	300 K / 0.1 MPa
	CO_2/H_2O-Pyrophyllite	300 K / 0.1 MPa
	H_2/H_2O-Gibbsite	300 K / 0.1 MPa
	CO_2/H_2O-Gibbsite	300 K / 0.1 MPa
	H_2-Kerogen	363.15 K / 0.1−50 MPa
	CH_4-Kerogen	363.15 K / 0.1−50 MPa
	H_2/CH_4-Kerogen	363.15 K / 0.1−50 MPa
	H_2-Na-Montmorillonite	298−403 K / 1−50 MPa
	$H_2/CO_2/H_2O$-Na-Montmorillonite	298−403 K / 1−50 MPa
	$H_2/CH_4/H_2O$-Na-Montmorillonite	298−403 K / 1−50 MPa
	H_2/CO_2/Octane-Kaolinite (Gibbsite and Siloxane)	300 K / 5.1−30.4 MPa
	H_2/OMCTS-MCM-41 Silica	298 K / 0−1 MPa
	CO_2/OMCTS-MCM-41 Silica	298 K / 0−1 MPa
	H_2-Montmorillonite	333−413 K / 2−30 MPa
	H_2/H_2O-Montmorillonite	333−413 K / 2−30 MPa
	H_2/H_2O-Kaolinite	310−410 K / 30 MPa
	H_2/NaCl Brine-Kaolinite	310−410 K / 30 MPa
	$H_2/MgCl_2$ Brine-Kaolinite	310−410 K / 30 MPa
	H_2-Calcium Silicate Hydrate	300−370 K / 2.5−40 MPa
	H_2-Kerogen	360 K / 3−41 MPa
	$H_2/CH_4/H_2O$-Illite	326 K / 30.4 MPa
	$H_2/CH_4/CO_2/H_2O$-Illite	326 K / 30.4 MPa
	$H_2/CH_4/H_2O$-Kerogen	326 K / 30.4 MPa
	$H_2/CH_4/CO_2/H_2O$-Kerogen	326 K / 30.4 MPa
	H_2/H_2O-Pyrophyllite	368.15 K / 30 MPa
	H_2/H_2O-Montmorillonite	368.15 K / 30 MPa
	H_2/H_2O-Beidellite	368.15 K / 30 MPa
	H_2/H_2O-Calcite	353 K / 20 MPa

[a]For each property, the table contains the specific systems investigated and the conditions of the studies. The relevant methods and in-depth discussions per property can be found in this review in the following sections: *pVT*: Sections 3.2 and 3.3 (methods), Section 4.2 (discussion). Diffusivities and thermodynamic factors: Sections 3.2.3, 3.2.4, and 3.2.13 (methods), Section 4.2.5 (discussion). Interfacial tension: Section 3.2.16 (methods) and Section 4.9 (discussion). Wetting: Section 3.2.17 (methods) and Section 4.10 (discussion). Adsorption on clays: Section 3.3.2 (methods) and Section 4.7 (discussion).

by molecular diffusion (see Fig. 12) and hydrodynamic dispersion[265] caused by cyclic injection and production. The generalized Fick's law describes this multi-component diffusion, relating the mass flux of each component to the concentration gradients of the others, governed by the mutual diffusion coefficient.[266,267] These coefficients depend on thermodynamic state variables such as the pressure, temperature, and composition of the mixture. MD simulations can yield both accurate predictions of these coefficients, enhancing our understanding of the gas mixing behavior under various conditions relevant to subsurface H_2 storage.

H_2 and other gases in the reservoir interact with brine, leading to dissolution and exchange of molecules between the gas and liquid phases. The solubility of H_2 in the brine, which depends on factors such as pressure, temperature, and salinity, determines the mole fraction of dissolved H_2 and the moisture content in the gas phase at equilibrium (see Fig. 12). Accurate knowledge of these solubilities is critical for maintaining H_2 purity, and optimizing storage conditions. Molecular simulations offer a detailed view of these interactions, allowing for precise predictions of solubilities and the overall phase behavior. The interfacial tension between H_2 and brine significantly affects the stability and integrity of the storage system. The interfacial tension not only suppresses phase mixing, maintaining sharp gas-brine boundaries, and thus, reducing leakage,[259] but also promotes capillary trapping, in which H_2 becomes immobilized within brine-saturated pores on the grain scale. Although limiting phase mixing helps preserve the purity of stored H_2, capillary trapping within brine-filled pores diminishes the recoverable volume and thus hampers the effectiveness of underground hydrogen storage (UHS).[261] Because direct experimental measurements of such nanoscale forces are challenging, molecular simulations are indispensable for quantifying interfacial tension and elucidating the mechanisms of the H_2 brine interaction, thus guiding the design of safer and more efficient storage strategies.

Another property, important for UHS, is the contact angle between H_2, brine, and the solid geological matrix, which influences the wettability of the rock and the overall capillary pressure in the system (see Fig. 12). This, in turn, affects the storage capacity and retrievability of H_2. Molecular simulations can be performed to predict the wetting behavior and contact angles in these systems, offering insights into how to modify surface properties to improve storage performance. While atomistic simulations provide useful insight into inter- and intra-molecular forces, and capture the fundamental physics of the wetting phenomena, they cannot always provide accurate quantitative predictions. Therefore, coupling molecular simulations with higher scale modeling methods is essential for studying, and ultimately, improve UHS performance. Key transport and displacement processes unfold over pore networks that extend from millimeters to centimeters and feature tortuous throats and irregular geometries, length scales far beyond the reach of molecular dynamics because of the prohibitively large number of molecules needed for the simulations. To describe flow and capillary behavior in such media, one must therefore couple the interfacial properties (e.g., surface tension, contact angle, diffusion coefficients) computed from molecular simulations to mesoscale or continuum models, such as pore-network and lattice-Boltzmann frameworks, volume-of-fluid CFD solvers, or hybrid multiscale schemes. UHS is thus inherently multiscale, which means that only by integrating molecular-level data into coarser-scale simulations one can predict injectivity, storage capacity and H_2 retrievability relevant for UHS.

Understanding adsorption − the process by which gas molecules adhere to the surfaces of solids − is important for evaluating the feasibility and efficiency of UHS in geological formations. Adsorption can provide information related to the storage capacity, retention time, and potential leakage risks of H_2 within these formations, essential for ensuring both efficiency and safety.[268] Additionally, interactions between H_2

https://doi.org/10.1021/acs.chemrev.5c00617
Chem. Rev. 2025, 125, 11878−12029

and swelling clays at grain contacts, involving adsorption and desorption, can induce clay swelling.[261] This swelling may lead to small normal and shear strains, resulting in stresses between individual grains. Over the lifespan of a H_2 storage complex, such stresses could contribute to mechanical fatigue and permanent deformation of the reservoir, leading to induced seismicity.[261] Therefore, sorption processes not only influence the retrievability of stored H_2 but also play a significant role in the long-term stability and safety of the storage site. The complexity of the subsurface environment, with its variations in pressure, temperature, mineral compositions, and complex pore morphologies, makes predicting adsorption behavior of H_2 an arduous task. Performing experimental measurements to study adsorption under these challenging conditions is fraught with practical challenges and risks, such as the high flammability of H_2 and the difficulty of replicating complex subsurface conditions in the laboratory. Molecular simulations have emerged as a powerful tool to overcome these challenges. Molecular simulations can accurately model the interactions between H_2 molecules and the diverse mineral surfaces found in geological formations, such as shale, quartz, and kerogen.[268] By replicating subsurface conditions, molecular simulations help predict the adsorption capacity and behavior of H_2, including its interaction with other gases like CH_4 and CO_2. The computed adsorption isotherms can then be used as input to reservoir-scale simulators to predict the transport of multicomponent H_2 mixtures, thus, helping in building predictive models for UHS.

From the short discussion above, it becomes apparent that molecular simulations are indispensable for advancing our understanding of subsurface H_2 storage systems. By providing detailed insights into gas-gas mixing, vapor-liquid equilibrium, interfacial tensions, and wetting behaviors, molecular simulations enable the optimization of storage strategies, ensuring safe, efficient, and long-term H_2 storage in geological formations. In an effort to build a sustainable energy future, taking full advantage of the power that molecular simulations offer will be crucial in overcoming the challenges associated with large-scale H_2 storage. To facilitate navigation, Table 4 provides a summary of key properties relevant to UHS, indicating the sections where relevant computational methods are explained and where the discussion of related articles can be found in this review.

2.4. Hydrogen Transport

2.4.1. Transport in Polymer Pipelines. H_2 economy presents new opportunities and challenges for pipeline systems. Currently, H_2 is mainly transported in compressed pressure vessels, tube trailers, and pipelines. Pipeline transport offers advantages due to high capacity, extensive inter-connectivity, geographic coverage, and relatively low operational costs. While over 5,000 km of H_2 pipelines exist globally, these are primarily constructed of various steel grades that face significant challenges from hydrogen embrittlement as discussed in more detail in Section 2.4.2. For this reason, polymer pipelines are considered a plausible solution for the transport of gaseous H_2 due to intrinsic advantages over traditional metallic infrastructures, such as corrosion resistance, flexibility, cost-effectiveness, and the ability to form robust joints through fusion techniques.[269] Among the numerous available polymeric materials, PE (and HDPE) is the predominant choice for gas distribution networks, comprising 90-95% of new installations in Europe and the United States.[270] Despite their advantages, polymer pipelines face distinct challenges when transporting H_2. The most important drawback is the enhanced permeation rate of H_2 molecules through the polymer matrix, which can be up to five times higher than that of CH_4. The permeability is also heavily affected by the temperature and pressure conditions. Other disadvantages are the so-called blistering risk (i.e., H_2 absorbed by the polymer liner at high pressure cannot escape quickly enough during decompression, causing internal pressure buildup that creates blisters on the material), and various other possible material failure mechanisms which are outside the context of this review.[271] The semi-crystalline structure of PE consists of long polymeric chains with varying lengths and side branches. Pipeline performance is primarily determined by the base resin density, molecular weight of these chains, and their distribution. The viscoelastic properties of PE create complex creep and stress relaxation behaviors that make short-term tests inadequate for predicting long-term performance.

As with all aspects of H_2 technology discussed thus far, the safe and effective transport of H_2 through polymer pipelines requires deep understanding of material properties, manufacturing processes, and operational conditions. With the plans to expand H_2 infrastructure, developing polymer systems with enhanced barrier properties will be crucial for maintaining integrity and safety in transportation networks. Toward this goal, molecular simulation has become a widely used tool for studying H_2/polymer systems, as also discussed in Sections 2.2.1 and 2.3.1. As expected, the main body of the relevant molecular simulation literature focuses on PE/HDPE, which are the most adequate materials for pipelines. Nevertheless, H_2 interactions with other polymers such as ethylene-vinyl alcohol copolymer (EVOH) (a promising alternative to HDPE), poly(dimethylsiloxane) (PDMS), poly(chloro-p-xylene), polystyrene (PS), rubbery matrices, and polysaccharides have been studied via molecular simulation in a broader context spanning H_2 applications beyond transport in pipelines. The vast majority of these studies focus on the same properties (i.e., sorption, diffusion, and permeation), make use of similar methods (MC for computing sorption and MD for gas transport coefficients - see Section 3) and force fields (see Section 3.1.4). A representative selection of molecular simulation studies in this field is reviewed in Section 4.4.

2.4.2. Hydrogen Embrittlement of Metallic Pipelines. Numerous efforts for designing metallic pipelines such that they are compatible with H_2 are made by both the industry and scientific community. This is not a simple engineering task since the presence of atomic hydrogen (H) in metals (e.g., in steels used in existing natural gas pipelines) results in the deterioration of mechanical properties, such as strength and deformability. This phenomenon is known as hydrogen embrittlement (HE)[21,272−277] and can occur even at extremely low H_2 concentrations (in the order of 1 ppm). Therefore, HE poses a significant challenge to the safe transportation of gaseous H_2 via pipelines. The complexity behind understanding the fundamental mechanisms of HE lies in the fact that it requires an accurate description of the atomic H trapping and diffusion in the presence of different kinds of microstructural features. The diffusivity study, in particular, is crucial as the fact that the diffusible H causes embrittlement, is well established.[278,279] The minute amount of H present in a material, is attracted towards stress fields e.g., front of crack tip where it concentrates causing brittle fracture. Diffusion measurements e.g., permeation tests and Thermal Desorption

https://doi.org/10.1021/acs.chemrev.5c00617
Chem. Rev. 2025, 125, 11878−12029

Table 5. Thermophysical and Mechanical Properties Investigated in Relation to the Mechanisms Governing Hydrogen Embrittlement of Metals[a]

Properties	Materials	Relevant sections	
		Methods	Discussion
H diffusion	bcc Fe; fcc Ni; bcc MoNbTaW; fcc FeMnCrCoNi	3.2.7, 3.2.9, and 3.3.5	4.11.1, 4.11.6, and 4.11.7
H trapping and H-mediated vacancy behavior	Carbides; oxides; bcc Fe; fcc Cu and Pd; bcc MoNbTaW; fcc CrCoNi, FeMnCrCoNi	3.2.7 and 3.2.8	4.11.2, 4.11.6, and 4.11.7
Dislocation nucleation and mobility	fcc Ag, Ni, Pd; bcc Fe; fcc FeNiCr and FeMnCrCoNi	3.2.10 and 3.3.5	4.11.3, 4.11.6, and 4.11.7
Crack propagation and GB decohesion	fcc Ni; bcc Fe; fcc CrCoNi, CoNiV, CoCrFeNi and FeMnCrCoNi	3.2.7, 3.2.11, and 3.3.5	4.11.4 and 4.11.6
Complex deformation behavior	fcc Ni; bcc Fe; hcp Mg	3.2.7 and 3.3.5	4.11.5

[a]The sections that detail the methods and the subsequent discussion are indicated.[292]

Analysis (TDA),[280] have indicated that diffusible H can be trapped in microstructural features e.g., grain boundaries (GBs) and carbides. There is experimental evidence[281] that a material in service does not suffer from HE if the diffusible H can be controlled. This observation forms the basis of designing alloys with irreversible traps for immobilizing diffusible H.[281−283] Another effective way to reduce the amount of diffusible H in the material is by the usage of coatings, such as oxides and metallic alloys, which act as barriers against H thereby reducing the H uptake by the material.[283] The Slow Strain Rate Test (SSRT) performed within recent works[31,284] has shown that the stress-strain curves of H charged coated sample is similar to that of uncharged bare sample of X70 pipe steel. Most of the experimental techniques employed in the investigation of H in materials operate at the macro-scale and hence lack spatial resolution, thus, making the determination of H trapping sites difficult, especially when H is trapped in nano-sized precipitates. In this regard, Atom Probe Tomography (APT), which allows high spatial resolution, proves to be a reliable tool for nano-scale visualization of H distribution in steels.[285−288] Another useful experimental technique in this regard is the Small Angle Neutron Scattering (SANS).[289,290] The individual underlying mechanisms are, however, still hard to elucidate experimentally since the complexity of the steels implies combined effects.

HE in metallic pipelines is a multi-disciplinary phenomenon, involving chemical processes and mechanical deformation across a wide range of spatial and temporal scales.[291] At the chemical level, HE is initiated with H_2 adsorption and dissociation on metal surfaces, followed by atomic H diffusion into bulk lattices, vacancies, dislocation cores, and GBs. All involved processes, i.e., adsorption, absorption, desorption, and lattice diffusion, are governed by distinct thermodynamic and kinetic parameters, which strongly depend on the local microstructure. Concurrently, mechanical deformation involving crack propagation, GB decohesion, dislocation nucleation and motion, and vacancy formation interacts continuously with H diffusion, leading to coupled chemo-mechanical degradation.[292] Capturing these phenomena demands a hierarchical, multi-scale modeling approach: DFT simulations provide atomically accurate energetics and kinetics of H behavior at the sub-nanometer scale; MD simulations, with classical interatomic potentials, enable insights into defect-driven deformation processes at the nano-meter and nano-second scales; and Kinetic Monte Carlo (KMC) methods allow for the study of H diffusion and trapping processes over significantly longer, time-scales (i.e., milliseconds to seconds). Bridging these methodologies offers a powerful and comprehensive framework to unravel the fundamental mechanisms underlying HE, enabling more accurate predictions and effective mitigation strategies for metallic structural components in H-rich environments. Table 5 summarises the key properties investigated in HE, and the metallic systems considered, while referring the reader to the sections where the relevant methods and discussion are presented in this review.

2.4.3. Liquid Hydrogen. As already discussed earlier in this review, the implementation of green H_2 is currently seriously hindered by the challenges related to transport and storage. Gaseous H_2 has an extremely low volumetric energy density, which can be increased if H_2 is liquefied. However, liquefaction is an expensive process that normally requires very low temperatures (ca. 20 K). The specific liquefaction energy is roughly equal to 15 kWh/kg, which corresponds to 1.5 Euros/kg if a realistic electricity price of 0.1 Euros/kWh is used.[293] The high energy consumption is a consequence of the low liquefaction temperatures that can only be attained by complex refrigeration cycles, and the unique behavior of H_2 at very low temperatures (the so-called quantum effects).[294] The molecules of H_2 can exist in two forms depending on the spins on the two H nuclei. If both spins are symmetric, i.e., in the same direction, the molecule is called ortho-H_2 (o-H_2) and when the spins are anti-symmetric, the molecule is referred to as para-H_2 (p-H_2). o-H_2 molecules have a higher energy state than the p-H_2 molecules. H_2 at room temperature contains 75% o-H2 and 25% p-H2, but the para-fraction is increased to almost 100% as the temperature is reduced to the liquefaction temperature of ca. 20 K. Due to the difference in the energy state of the spins, the ortho-to-para conversion is highly exothermic and releases a huge amount of heat during liquefaction. The released heat should be removed, which increases the cooling demand (energy requirement) of the refrigeration cycle. However, the heat release is not linear but increases exponentially with decreasing temperature. An interesting conclusion from this physics exercise is that it would be beneficial if H_2 could be liquefied at higher temperatures, because that would reduce the cooling demand as most of the energy is consumed at the lower temperatures (due to increased heat release). This sounds almost impossible, because the liquefaction of H_2 is governed by its pressure-temperature diagram (saturation line), which states that H_2 can be at the liquid state only in a temperature range of 14 K (triple point) to 33 K (critical point). Interestingly, a molecular simulation study in 2005 by Han et al.[295] showed that H_2 can be liquefied at 80 K if the liquefaction is performed under confinement in a carbon nanotube (CNT). This phenomenon was attributed to the

https://doi.org/10.1021/acs.chemrev.5c00617
Chem. Rev. 2025, 125, 11878−12029

strong electrostatic interaction between the CNT and H_2 molecules, which induce local-ordering of the H_2 molecules and results in liquefaction. Note that such a finding does not necessarily violate thermodynamics, because the previously mentioned liquefaction temperature range of 14 to 33 K holds for bulk systems, which may be different for systems under confinement. However, the understanding of H_2 liquefaction under confinement is poorly studied and understood. To the best of our knowledge, no other theoretical or experimental studies to date were reported to verify the results of Han et al.[295] This showcases the power of molecular simulation not only as a predictive tool, complementary to experiments, but also as a vehicle for exploring new H_2 technologies. More details on this and a few other studies related to molecular simulation of liquid H_2 are provided in Section 4.3.

3. MOLECULAR SIMULATION METHODS FOR COMPUTING THERMOPHYSICAL PROPERTIES OF HYDROGEN SYSTEMS

In this section, we provide an overview of the most widely used methods and models for computing thermophysical properties of H_2 systems. Although a lot of ground related to thermodynamic, transport, interfacial, and structural properties, as well as physical mechanisms and force fields is covered here, a detailed discussion on statistical mechanics fundamentals, derivations of equations, and a full list of possible methods are out of the scope of this review. For such information, the reader is referred to relevant textbooks in the field of molecular simulation.[51,52,296−299]

3.1. Force Fields

To a great extent, the accuracy of classical molecular simulations, both MD and MC, relies on semi-empirical models, the so-called force fields, which describe the intra- and inter-molecular interactions between the atoms and molecules in the system. Thus, it is not surprising that rigorous effort has been put during the past five decades by numerous researchers to design "high-performance" force fields with varying complexity for almost all types of chemical species. "High-performance" entails that a force field is able to accurately reproduce as many experimentally measured thermophysical properties of a species as possible. Such a performance is usually tied to the strategy followed during the parameterization of the force field, e.g., the number and type of properties considered, the range of conditions, the functional forms used to approximate inter- and intra-molecular forces.

The main focus of force fields for important components, such as water, hydrocarbons, electrolytes, and bio-molecules, has been the replication of phase behavior, volumetric properties, structure, transport coefficients, and energies.[56,300−307] It is important to note that due to the fact that force fields are primarily fitted to experimental data, the abundance and accuracy of the available experimental data are crucial elements for accurate molecular simulations. Complementary, the significant attention put in performing MC and MD simulations for the prediction of many H_2 properties is a motivation for further experimental effort. In this review, we provide a brief discussion on force fields commonly used to perform molecular simulations of H_2 systems. The main focus is on the H_2 force fields, pure or in aqueous electrolyte solutions (important for electrochemical processes), systems involving H_2 and solid surfaces (important for storage), and organic components (important for separation applications).

Since this review paper mainly focuses on classical force fields, it is important to delineate the conditions under which quantum effects become significant and lead to noticeable deviations in the prediction of thermophysical properties using classical molecular simulations. The criteria discussed below serve as indicators for the onset of quantum mechanical contributions that should not be neglected. A commonly used criterion is based on the comparison between the thermal de Broglie wavelength and the characteristic interparticle spacing, approximated by mean nearest neighbor separation, $(V/N)^{\frac{1}{3}}$.[308] The de Broglie wavelength is given by

$$\Lambda = \left(\frac{h^2}{2\pi m k_B T}\right)^{1/2} \tag{1}$$

where h is Planck's constant, m is the particle mass, k_B is the Boltzmann constant, and T is the absolute temperature. Bartolomeu and Franco[308] report representative values for the ratio $\Lambda/(\frac{V}{N})^{\frac{1}{3}}$ as 0.36 at 100 K and 1000 bar, and 0.016 at 400 K and 1 bar. For liquid H_2, this ratio approaches 0.97, indicating that quantum effects are substantial and should be explicitly accounted for. A second criterion involves the comparison between the rotational temperature Θ_{rot} of molecular H_2 and the simulation temperature. Quantum effects in rotational degrees of freedom become significant when Θ_{rot} is comparable to or greater than the system temperature.[308] For molecular hydrogen, the rotational temperature is ca. 86 K, and is defined as

$$\Theta_{rot} = \frac{h^2}{8\pi^2 I k_B} \tag{2}$$

where I is the moment of inertia of the molecule. If either of these criteria is fulfilled, classical simulations may yield inaccurate results. A way to mitigate this drawback is using the so-called quantum corrections (discussed in Section 3.1.1).

3.1.1. Hydrogen. Many different classical force fields have been developed for H_2, differing on the experimental/ab-initio parameters they are trained on, the functional form, and the number of interaction sites.[48,309−314] While the discussion we are presenting here does not aim to be exhaustive, it covers several of the most frequently used H_2 models in molecular simulation studies. Our goal is to highlight key parameter choices, point out inconsistencies and ambiguities that have emerged in the literature, and identify points of attention for researchers aiming to ensure consistency and reproducibility in the application of H_2 force fields. It is important to acknowledge the detailed assessment by Barraco et al.[309], who systematically compared eight Lennard-Jones (LJ)−based models in the gas phase, at conditions relevant to H_2 storage in tanks. To ensure cohesion and provide a self−contained overview, we also summarize relevant aspects of their findings in this review.

In classical simulations, the most popular functional form describing the pairwise attractive (van der Waals) and repulsive (Pauli's exclusion) forces is the 12-6 LJ potential (U_{LJ})[51]

$$U_{LJ} = 4\epsilon_{ij}\left[\left(\frac{\sigma_{ij}}{r_{ij}}\right)^{12} - \left(\frac{\sigma_{ij}}{r_{ij}}\right)^{6}\right] \tag{3}$$

where ϵ_{ij} and σ_{ij} are the so-called energy and size parameters, respectively, and r_{ij} is the distance between species i and j.

https://doi.org/10.1021/acs.chemrev.5c00617
Chem. Rev. 2025, 125, 11878−12029

Although most H_2 force fields are based on the 12-6 LJ potential, the 9-6 LJ form has also been used e.g., in the IFF (9-6) force field[313] and the COMPASS force field of Yang et al.[315], Sun[316]. H_2 force fields using the 9-6 LJ potential have larger σ_{ij} values than the 12-6 LJ to compensate for the reduced repulsive interactions.[309] The LJ potential can be considered as a special case of the more general Mie potential:

$$U(r) = \frac{n}{n-m}\left(\frac{n}{m}\right)^{\frac{m}{n-m}} \times \varepsilon\left[\left(\frac{\sigma_{ij}}{r_{ij}}\right)^{n} - \left(\frac{\sigma_{ij}}{r_{ij}}\right)^{m}\right] \quad (4)$$

By setting $n = 12$ and $m = 6$, one recovers the familiar 12-6 LJ potential, while $n = 9$ and $m = 6$ yields the softer-repulsion 9-6 LJ variant. Bartolomeu and Franco[308] proposed a single-site Mie potential, known as the SAFT-γ Mie force field, using parameters previously optimized within the SAFT-VR Mie EoS framework.

To account for the electrostatic interactions, the most common approximation in H_2 force fields is Coulomb's law[51]

$$U_{\text{Coul}} = \frac{q_i q_j}{4\pi\epsilon_0 r_{ij}^{\,2}} \quad (5)$$

where q_i is the charge of species i, and ϵ_0 is the electric constant. Force fields that incorporate charges can be classified in two different categories, i.e., non-polarizable and polarizable. In non-polarizable force fields, H_2 is modelled using fixed point charges. Polarizable force fields account for the change in the charge distribution of a molecule depending on the environment.[314] Most of the H_2 models to date are non-polarizable.[309−311,313] For models with no intramolecular degrees of freedom, the total potential energy of the system follows from the summation of Eq. (3) and Eq. (5).[51,52] The combination of LJ and Coulombic potentials is not always sufficient to describe strong adsorption interactions of H_2 with materials.[317] In such cases, instead of the LJ, the Morse potential is used[318]

$$U_{\text{Morse}} = D_{ij}(1 - \exp[-\alpha(r_{ij} - r_{ij}^{*})]) \quad (6)$$

where D_{ij} and r_{ij}^{*} are the interaction and size parameters (analogous to ϵ_{ij} and σ_{ij} for the LJ potential), respectively. Parameter α controls the width of the potential well. This extra fitting parameter of the Morse potential allows for better reproducibility of H_2 adsorption onto materials with exposed metal centers, such as MOFs.[317] Another functional form of intermolecular potentials of H_2 is the so-called Exp-6 (Buckingham). Although such models have been already derived more than 70 years ago (see for example the work of Mason and Rice[319]), they are scarcely used in molecular simulations of H_2 systems, and therefore, we do not discuss them further.

Fig. 13 shows a schematic representation of single-, two-, and three-site H_2 force fields. In single-site force fields, H_2 is assumed to have only one effective interaction site (united atom approach), which interacts with the surrounding molecules using only two-body attractive and repulsive forces.[309,320] The model by Vrabec and co-workers[48] (also referred to as Köster), with $\epsilon/k_B = 25.84$ K and $\sigma = 3.0366$ Å, was fitted to reproduce speed of sound and PVT data in the 50-250 K range. In contrast, the potential by Buch[312] focuses on capturing orientational effects of H_2 at low temperatures (parameters: $\epsilon/k_B = 34.2$ K and $\sigma = 2.96$ Å). Hirschfelder et al.[321] proposed multiple sets of LJ parameters based on different datasets and methodologies: fitting to classical

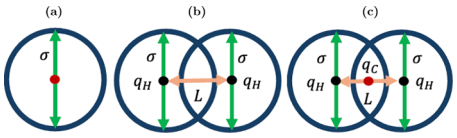

Figure 13. Schematic representations of (a) single-site, (b) two-site, and (c) three-site LJ-based H_2 force fields. The green arrows represent the σ value of the LJ potential, the pink arrows represent the bond distance (L) of H_2, and q_H and q_C represent the charges on the H-atom and the center of mass of H_2, respectively. The force fields developed by Buch,[312] Köster et al.,[48] and Hirschfelder et al.[321] are examples of one-site force fields, in which the LJ site is located at the center of mass of H_2. The force fields developed by Cracknell[311] and Wang et al.[313] are examples of two-site force fields, in which the LJ sites are separated by a bond length L. The force fields by Cracknell[311] and Wang et al.[313] are non-polarizable and do not use charges (i.e., $q_H = 0$). The force field by Marx and Nielaba[310] is an example of a three-site H_2 force field, which accounts for the quadruple moment of H_2. Three-site LJ force fields can have up to three different LJ sites. This figure is based on the work of Barraco et al.[309]

viscosity data yields either $\epsilon/k_B = 33.3$ K, $\sigma = 2.968$ Å or $\epsilon/k_B = 38.0$ K, $\sigma = 2.915$ Å, while fitting to second virial coefficients produces $\epsilon/k_B = 37.0$ K, $\sigma = 2.928$ Å (quantum-based) and $\epsilon/k_B = 29.2$ K, $\sigma = 2.87$ Å (classical). The authors recommend using the viscosity-based fits for transport property calculations, and the virial-based parameters for thermodynamic modeling. In their review, Barraco et al.[309] refer to the parameter set $\epsilon/k_B = 37.0$ K and $\sigma = 2.928$ Å, derived from fits to the second virial coefficients. Rzepka et al.[322] and Ferrando and Ungerer[323] used the classically derived parameters from Hirschfelder's viscosity-based model, i.e., $\epsilon/k_B = 33.3$K and $\sigma = 2.97$ Å. Similarly, Caviedes and Cabria[324] adopted this parameter set in their study of H_2 storage capacities in slit-shaped pores, nanotubes, and torusenes. In contrast, Rahbari et al.[110] used the alternative viscosity-based parameterization by Hirschfelder, namely $\epsilon/k_B = 38.0$ K and $\sigma = 2.915$ Å. The specific rationale for selecting among the four parameter sets proposed by Hirschfelder is not necessarily explicitly addressed in these studies; however, in most cases, the choice appears to align with the focus and requirements of the respective application.

Two-site force fields, such as the IFF force field by Wang et al.[313], provide a more realistic representation of the structure of H_2 by including explicit interaction sites for each atom. This also allows for the inclusion of intra-molecular interactions, often represented by harmonic potentials, which capture the H-H bond vibrations. These vibrations are particularly important for accurately predicting spectroscopic properties such as Raman and IR spectra. However, this approach, due to the high-frequency nature of vibrational modes, requires the use of smaller MD integration time steps (typically <1 fs) to maintain numerical stability due to the high-frequency nature of vibrational modes. Despite their importance for vibration-dependent properties, the use of two-sites in the H_2 force fields has limited impact on the prediction of bulk thermodynamic and transport properties, such as self-diffusivities, pVT relations, and physisorption of H_2, which are dominated by slower translational and rotational motions.[311] For many practical applications, the additional computational cost of resolving vibrations is unnecessary, and the use of simpler, rigid models (i.e., with a fixed bond length) is sufficient. Nevertheless, several two-site inter-molecular potentials have been

https://doi.org/10.1021/acs.chemrev.5c00617
Chem. Rev. 2025, 125, 11878−12029

Table 6. Overview of Selected Hydrogen Force Fields and Their Parameters[a]

Force Field	No. of Sites	Fitting Basis	ϵ/k_B	σ/Å	q_H/e	Q/DÅ	Temperature/ Pressure Range
Vrabec[48]	1	Speed of sound, PVT data, enthalpy of vaporization	25.84	3.0366			50−250 K
Buch[312]	1	Potential energy, para-ortho H_2 clusters	34.2	2.96			Low T (34 K)
Hirschfelder (a)[321]	1	Viscosity (classical)	33.3	2.968			Not specified
Hirschfelder (b)[321]	1	Viscosity (classical)	38.0	2.915			Not specified
Hirschfelder (c)[321]	1	2nd virial (quantum)	37.0	2.928			Not specified
Hirschfelder (d)[321]	1	2nd virial (classical)	29.2	2.87			Not specified
Mondal[334]	1		9.56	3.14			
Yang and Zhong[325]	2	PVT and self-diffusion	10.0	2.72			80−300 K, up to 600 bar
Cracknell[311]	2	Adsorption energy, Q_{st} in pores	12.5	2.59			298 K
Yang	2	Bulk PVT fit					
Sun[331]	3	VLE near-critical region	8.06	3.03	0.47		near critical region
SAFT-γ-Mie[308]	2	Heat capacity at constant pressure, speed of sound, PVT data	18.355	3.1586			
Marx and Nielaba[310]	2+Q	Bond length, enthalpy of adsorption, isochoric heat capacity	36.7	2.958		0.6369	Not specified
Bouanich[330]	2+Q	2nd virial coeff. fit	11.2544	2.68259	0.1108		98−773 K
TraPPE[331]	2+Q	VLE near critical	8.06	3.03	0.47		33 K
Belof[332]	3+Q	Ab initio, second virial coefficient, pressure-density relations	8.8516 (COM), 4.0659 (outer)	3.2293 (COM), 2.3406 (outer)	0.3732		50−500 K; 0−2000 atm

[a]For extended discussion on the paremeters and consistency issues, the reader is referred to Section 3.1.1. ϵ and σ are the LJ parameters (see Eq. (3)). Two- and three-site LJ force fields with a quadrupole are referred to as 2+Q and 3+Q, respectively.

developed to describe molecular H_2 based on different calibration targets. Yang and Zhong[325] proposed a H_2 model using parameters ϵ/k_B = 10 K and σ = 2.72 Å, with a fixed bond length of 0.74 Å. This model was calibrated using experimental *PVT* data and self-diffusion coefficients of H_2 over a temperature range of 80−300 K and pressures up to 600 bar. Cracknell[311] proposed a two-site intermolecular potential for H_2 with ϵ/k_B = 12.5 K, σ = 2.59 Å, and a fixed bond length of 0.74 Å. The LJ parameters were adjusted to reproduce H_2 adsorption behavior in graphitic slit pores, specifically targeting agreement with isosteric heats and adsorption isotherms obtained from earlier Path Integral Monte Carlo (PIMC) simulations.

The following models extend the two-site description of H_2 by incorporating electrostatic interactions via embedded quadrupoles, most commonly implemented through point-charge arrangements rather than explicit multipole sites. Most of the molecular simulation software packages do not support point multipole sites,[326] and thus, point charges are often preferred. Dipole moments can, in principle, be represented by a pair of closely spaced point charges $(+q, -q)$, yielding a dipole moment $\mu_d = qd$. Similarly, three point charges $(+q, -2q, +q)$ can be arranged to reproduce a quadrupole moment of the form $Q = 2qd^2$. Either the distance d or the charge q may be specified, and the choice of parameter is non-trivial.[326] In this review, most of the surveyed studies use point-charge models. In the case of the force field developed by Marx and Nielaba[310], some confusion has arisen regarding the specific charges used to reproduce the quadrupole moment, as noted by Barraco et al.[309] The parameters reported by Marx and Nielaba[310] are σ = 2.958 Å, ϵ/k_B = 36.7 K, and a reduced quadrupole moment of $Q/((\pi\epsilon_0 k_B)^{1/2}$=54.2 in units of $(KÅ)^{1/2}$. While this quadrupole can be implemented directly via a point-multipole interaction, it may also be represented using three point charges, if needed.[48] Köster et al.[48] refer to this value as Q = 0.6369 DÅ. Calculating the corresponding partial charge using the definition of the quadrupole yields q/e = 0.120746, as also reported by Barraco et al.[309], which is consistent with the original model.

Darkrim et al.[327] referenced a charge of $q = 0.615 \times 10^{-26}$ esu associated with quadrupole interactions between H_2 molecules. This appears to be a typographical or unit error. Interpreting this instead as $q = 0.615 \times 10^{-10}$ esu, an equivalent q/e = 0.1280 is obtained, which is close to the original charge of the force field.[309] Using the relation $Q = 2qd^2$ with d = 0.741 Å, the resulting quadrupole moment is Q = 0.675 DÅ, which is close to the value of 0.6369 DÅ reported by Köster et al.[48] In sharp contrast, using the originally stated[327] $q = 0.615 \times 10^{-26}$ esu underestimates the original quadrupole magnitude by several orders of magnitude. Ferrando and Ungerer[323] adopted the charge parameter of q/e = 0.4664 for the H_2 atom, which seems to deviate from the original force field by Marx, followed up by Darkrim. Similarly, Rahbari et al.[110] and Bartolomeu and Franco[308] adopted the LJ parameters from the Marx force field but used partial charges of q = +0.468 for H_2 and $-2q$ for the center of mass, which does not reproduce the quadrupole moment reported in Marx and Nielaba[328]. Another example of inconsistency appears in Li et al.[329] and Ferrando and Ungerer[323] who adopted the model by Darkrim et al.,[327] itself based on the Marx force field, and reported charges of q = 0.4664 for H_2 and $-2q$ for the center. It is unclear how this value was derived from the $q = 0.615 \times 10^{-26}$ esu cited in ref 327 as it does not reproduce the quadrupole originally reported by Marx and Nielaba. Bouanich[330] proposed another two-site H_2 LJ 12-6 potential with quadrupole having σ = 2.68259 Å, ϵ/k_B = 11.2544 K with a fixed bond length of 0.7508 Å. The partial charge supplemented on H_2 sites is q/e = 0.1108 with a $-2q$ charge

https://doi.org/10.1021/acs.chemrev.5c00617
Chem. Rev. 2025, 125, 11878−12029

in the center of mass. This force field was fitted using the experimental second-virial coefficients in the 98-773 K temperature range. Sun et al.[331] proposed a rigid three-site (H− M− H) potential for H_2 with LJ parameters σ = 3.03 Å and ϵ/k_B = 8.06 K, and an intramolecular H-H distance of 0.741 Å. Partial charges of q_H = +0.47 e are placed on each H atom and a compensating charge of q_M = −0.94 e on the central M-site. The force field parameters were fitted using Monte Carlo simulations to reproduc experimental VLE data of H_2 near the critical temperature (ca. 33 K). Although it is not always possible to trace the complete history of how force field parameters have been used, adopted or modified, it is important to emphasize the need for careful comparison with original references and to explicitly report any deviations or assumptions made by subsequent authors.

Three-site force fields add further complexity by introducing an additional interaction site, typically placed at the geometric center of the molecule or representing a pseudo-atom. This approach enables a better representation of the electronic charge distribution within H_2, capturing dipole-induced interactions and quadrupole effects more accurately. These effects are particularly relevant in systems where electrostatic interactions play a significant role, such as in the study of H_2 interactions with polar surfaces or within electric fields. Although three-site models improve the accuracy of intermolecular interactions, there is a higher computational cost compared to one-site and two-site models. Belof et al.[332,333] parameterized both polarizable and non-polarizable potentials for H_2, derived from first-principles calculations. The non-polarizable LJ 12-6 potential incorporates three LJ interaction sites along with an embedded quadrupole moment. A fixed bond (with length of 0.742 Å) is used at the ends of which the masses are placed along with a charge of q/e = 0.3732 each. The charge neutrality is conserved by the addition of a counter charge of $-2q$ at the center of mass. The LJ interaction site (ϵ/k_B = 8.8516 K and σ = 3.2293 Å) is also placed at center of mass. Two other LJ sites (ϵ/k_B = 4.0659 K, σ = 2.3406 Å, and m = 0) are also placed 0.329 Å from the center of mass (on the same axis with the sites carrying the masses). The validation of this force field was based on second virial coefficient data for temperatures ranging from 50 to 500 K. The pressure density curves were validated for pressures between 0 and 20 MPa and 0 to 200 MPa, at 298.15 K and 77 K, respectively. For a comparative summary of the selected H_2 force fields discussed above, including parameter values, number of interaction sites, and fitting approaches, see Table 6.

As for bulk systems, choosing suitable force fields is a crucial step towards obtaining accurate results in classical molecular simulations of H_2 hydrates. A force field often used in hydrate studies is Silvera−Goldman[335] (SG). This model has both LJ and electrostatic interactions but uses a rather complex functional form which is not easy to implement in molecular simulation software. An attempt to resolve this drawback is through the approach proposed by Alavi et al.[336] where SG is replaced by a three-site LJ-based force field developed to reproduce the experimental quadrupole moment of H_2. In this model, the two H atoms bear negative point charges, while the positive charge is placed on a "dummy" atom located at the center of mass of the molecule (see Fig. 13c). This force field is the most popular in the field of hydrates, having been used in more than 60% of the MC and MD studies in literature. In the studies of Levesque et al.[337] and Gu et al.[338], H_2 was modeled using an one-site LJ model which takes into account the quantum nature of H_2 via the Feynman−Hibbs (FH) correction[339]

$$U_{FH} = U_{LJ} + \frac{\beta\hbar}{24\mu}\left(\frac{d^2U_{LJ}}{dr^2} + \frac{2}{r}\frac{dU_{LJ}}{dr}\right) + \cdots \tag{7}$$

where $\beta = 1/(k_BT)$ (where k_B is the Boltzmann constant and T is temperature), $\mu = m/2$ (where m is the molecular mass of H_2), and $\hbar = h/(2\pi)$ (where h is the Planck constant). For computational efficiency in molecular simulations of hydrates, instead of using Eq. (7), the corrected potential is replaced by an equivalent LJ potential with temperature-dependent σ and ϵ parameters. This dependence is described using third degree polynomials. The use of higher order (e.g., quartic) terms in Eq. (7) has also been reported in literature.[340] However, such terms have been mostly ignored in hydrate studies. Figure 14 shows a comparison of different H_2 force fields used in studies of hydrate.

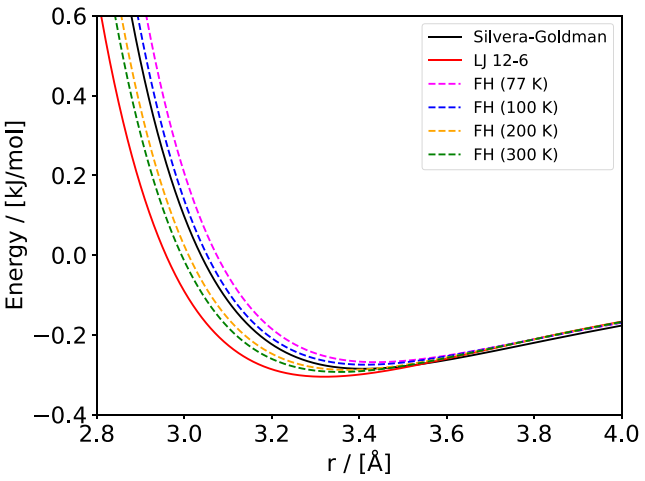

Figure 14. Comparison of different hydrogen potentials: Lennard-Jones (Eq. (3)), Feynman−Hibbs quantum effective potential (Eq. (7)) at different temperatures, and Silvera−Goldman force field. The data are taken from ref 341 (where more temperatures for the FH can be found).

Michalis et al.[342] in an effort to increase the accuracy of three-phase equilibrium calculations for the system H_2/H_2O used a modification factor, χ, to correct the Lorentz-Berthelot cross interaction energy parameter according to

$$\epsilon_{H(H_2)-O(H_2O)} = \chi\sqrt{\epsilon_{H(H_2)}\epsilon_{O(H_2O)}} \tag{8}$$

where $\epsilon_{H(H_2)}(H_2)$ and $\epsilon_{O(H_2O)}(H_2)$ are the LJ energy parameters of the H atom in H_2 and the oxygen atom in H_2O, respectively. The value of χ was obtained by minimizing the error in the calculation of aqueous H_2 solubility. Finally, a less used force field in hydrate studies is the one by Alavi et al.[343]. This model uses the anisotropic H_2/D_2 potential introduced by Wang[344], which was parametrized to account for quantum mechanical effects of H_2 motion at low temperatures (of order $\hbar^2$ in the second virial coefficient).

3.1.2. Water. Force fields for water are relevant for molecular modeling of processes such as hydrate formation, H_2 production (e.g., in alkaline electrolyzers), and H_2 storage (e.g., underground storage, where H_2 is in contact with aqueous NaCl solutions). Non-polarizable force fields with fixed point-charges are commonly used in molecular simulations of

https://doi.org/10.1021/acs.chemrev.5c00617
Chem. Rev. 2025, 125, 11878−12029

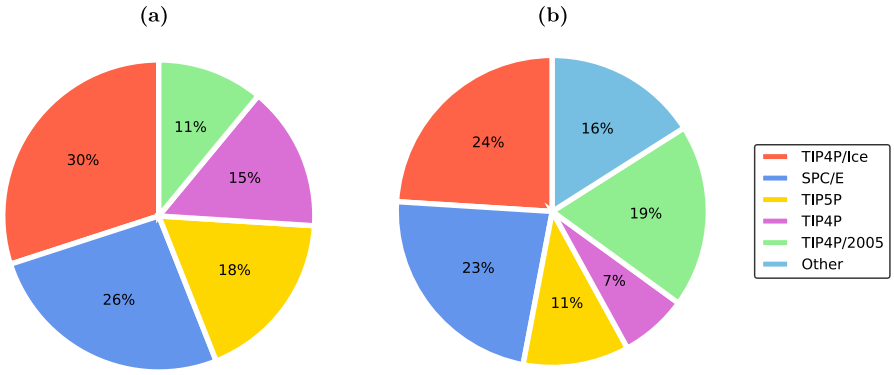

Figure 15. Overview of the relative popularity of the H_2O force fields used in the H_2-hydrate literature of (a) MC and (b) MD studies. In panel (b), "Other" includes TIP3P (4%), TIP4P-FQ/Ice (2%), q-TIP4P/F (2%), SPC (2%), and other force fields. The statistics are based on the studies considered in this review.

aqueous electrolytes.[345−348] Non-polarizable force fields of water such as SPC/E[346] and TIP4P/2005[349] accurately capture thermophysical properties such as densities, radial distribution functions (RDFs), viscosities, and self-diffusivities of water. TIP4P/2005 which outperforms other fixed charged force fields in predicting densities and transport properties,[348] overestimates the vaporization enthalpy and underestimates the excess chemical potential of water.[110,345,350] At 323.15 K, the chemical potentials for the TIP4P/2005 water model deviate from the IAPWS empirical EoS[351,352] by ca. −500 K/k_B. The underestimation of the excess chemical potential of liquid water leads to severe underestimations of the saturated vapor pressure of water compared to experiments, and the solubilities of water in H_2 compared to experiments.[350] The TIP3P, TIP4P, TIP4P/μ (see the Supporting Information of ref 47 and Section 4.1.2.1), and the SPC water force fields significantly outperform the TIP4P/2005 force field for computing chemical potentials of liquid water.[110,345] A comparison of the predicting ability of the chemical potential in the liquid phase at T = 323 K and pressures ranging between P = 10 and P = 1000 bar of different water force fields is provided in ref 110. The rigid, five-site TIP5P/Ew[353] water model has also been used in the literature to study high-pressure H_2 drying using zeolites.[143] Polarizable water force fields such as HBP,[354] BK3,[355] and AMOEBA[356] are on average ca. 3-5 times more computationally expensive compared to non-polarizable force fields (the newly developed polarizable force field of Xiong et al.[357] is an exception). Despite their improved accuracy for various properties of water, polarizable force fields have not gained the widespread popularity of non-polarizable force fields due to their increased computational cost and limited availability in open-source simulation software. For a relevant discussion, the reader is referred to study by Jiang et al.[354]

Already in 1987, Berendsen et al.[346] discussed that fitting non-polarizable force fields to the free energies of water (i.e., vaporization energies or excess chemical potentials) results in excluding the self-polarization energy of water. The inclusion of self-polarization energy results in accurate predictions for the transport properties of liquid water but at the cost of lower accuracy for the free energies of water. As such, not all thermodynamic and transport properties of aqueous systems can be described simultaneously using a single non-polarizable force field. Different water force fields can be chosen depending on the system or properties of interest. Force fields such as TIP4P/μ, which are trained on free energies and chemical potentials are more suitable than TIP4P/2005 for phase coexistence calculations, as accurate predictions for the chemical potentials of water is crucial for improving the prediction of vapor-liquid phase-coexistence compositions of $H_2O - H_2$ systems.[47] For computing transport properties of H_2 in liquid water, force fields such as TIP4P/2005 and SPC/E which are trained on liquid phase transport properties are more suitable, as accurate predictions for the viscosity of water ensures that drag forces that influence the transport of H_2 in water are accurately modeled.

Fig. 15 shows an overview of the relative popularity of the H_2O force fields used in MC and MD studies of H_2-hydrate studies. As can be seen, the order of popularity in MC studies (Fig. 15(a)) is TIP4P/Ice,[358] SPC/E,[346] TIP5P,[359] TIP4P/2005,[349] and TIP4P,[360] while the respective order for MD studies (Fig. 15(b)) is TIP4P/Ice, SPC/E, TIP4P/2005, TIP5P, and TIP4P. In MD studies, various other force fields have also been used to a lesser extent, e.g., TIP3P,[300] SPC,[361] q-TIP4P/F,[362] TIP4P-FQ/Ice[363] While the vast majority of H_2-hydrate studies is performed with non-polarizable H_2O force fields (which also ignore quantum effects), there are a few exceptions. Rick and Freeman[364] used the polarizable TIP4P-FQ/Ice H_2O,[363] which yields accurate predictions of the density and melting point of ice I_h. TIP4P-FQ/Ice is a reparameterization of the TIP4P-FQ model.[365] Cendagorta et al.[366] performed simulations for the quantum free energy profiles and rates of diffusion of H_2 and D_2 via the hexagonal face of two neighboring $5^{12}6^4$ hydrate cages considering the temperature range 8 K up to 200 K with q-TIP4P/F[362] H_2O, which is a modified version of TIP4P/2005. q-TIP4P/F is flexible and implicitly accounts for quantum effects.

During recent years, an increase in the use of TIP4P/Ice[358] H_2O force field in MD studies of hydrates is observed. TIP4P/Ice is a rigid and non-polarizable model which was designed to accurately reproduce the melting temperature of hexagonal ice (I_h). García Fernández et al.[367] reported a melting temperature of T_m = 270 ± 3 K. In a more recent study, Conde et al.[368] performed a systematic study to increase the accuracy of the direct phase coexistence approach (see Section 3.2.14), and recommended a value of T_m = 269.8 ± 0.1 K for I_h. These calculations, therefore, show a clear under-prediction of the melting point of TIP4P/Ice by 3.35 K. Conde and Vega[369] argued that the accurate calculation of the melting temperature of hexagonal ice is essential for the accurate calculation of the three-phase coexistence temperature of hydrate systems using the phase coexistence approach.

https://doi.org/10.1021/acs.chemrev.5c00617
Chem. Rev. 2025, 125, 11878−12029

3.1.3. Ionic Species. The presence of ions, such as Na^+, K^+, Cl^-, and OH^-, influences the thermophysical properties of water, which in turn affects the solubility, diffusivity, and phase behavior of H_2 in the system. Similarly to water, force fields for ions can be either non-polarizable or polarizable. Non-polarizable force fields of ions, such as Madrid-2019[370] and Joung-Cheatam,[371] assume fixed charges on the ions. Polarizable force fields for ions, such as the ones developed by Kiss and Baranyai[372] and Dočkal et al.[373], use more elaborate functional forms e.g., Gaussian charge distributions and the charge-on-spring model. In the "charge-on-spring" model a massless charge is attached to each ion by a harmonic spring. This allows the charge to move in response to the local electric field. As in the respective water force fields, the additional calculations required to determine the positions and forces on these charge-on-spring elements increase the complexity and the time requirements of the simulation (typically by a factor of 3-10).[372] Recent advances in polarizable force fields aimed at overcoming these limitations, striving to balance accuracy and efficiency.[357,373]

Until 2009, force fields of ions were primarily parameterized based on free hydration energies of salts and RDFs of ions and water (e.g., the location of the first peak and the number of water molecules in the first hydration layer).[371,374−377] A list of available ion force fields (until 2011) and the target properties, which are used for their validation is provided by Reif and Hünenberger[378]. The non-polarizable force field developed by Joung and Cheatham[371] for alkali (e.g., Li^+, Na^+, and K^+) and halide (e.g., F^-, Cl^-, and Br^-) ions is particularly popular in literature. The Joung-Cheatham[371] force field uses nominal charges (i.e., +1 [e] for Na^+ and −1 [e] for Cl^-) to model the electrostatic interactions of ions in the solution and can accurately predict the free hydration energies of ions in the aqueous solution along with the lattice energies (and constants) of the alkali halide salts in crystal form. Despite the success of the Joung-Cheatham force field for describing the free energies of ions, the dynamic properties (e.g., viscosities and self-diffusivities of ions and water) in concentrated salt solutions (i.e., beyond a molality of 1 mol salt / kg salt) cannot be accurately modeled with respect to experiments.

Since 2009, Leontyev and Stuchebrukhovhav have published several works using the concept of "scaled charges" for modeling ions in aqueous solutions.[379−382] Scaling down the charges of ions by a factor of 0.7-0.9 allows for accounting the dielectric screening of electrostatic charges in the aqueous medium.[370,381,383] Use of scaled charges has been shown to significantly improve the accuracy of predicting dynamical properties such viscosities, diffusion coefficients of water, and electrical conductivities for aqueous electrolyte solutions[112,113,370,384,385] at the cost of less accurate predictions for free hydration energies of salts. Several different force fields have been recently developed for modeling ions using scaled charges.[370,384] Madrid-2019, developed by Zeron et al.[370] in 2019, was parameterized based on the TIP4P/2005[349] water force field, and is particularly popular in literature of aqueous electrolytes due to its computational efficiency and accurate predictions of densities, RDFs, infinite dilution self-diffusivities of ions, and freezing point depression in aqueous electrolyte solutions. Madrid-2019 uses a charge scaling factor of 0.85 and has parameters for a wide array of ions such as Li^+, Na^+, K^+, Cl^-, and SO_4^{2-}), which are particularly important for H_2 applications. Despite its widespread use, Madrid-2019 force field cannot accurately predict all properties (e.g., free hydration energies of salts and the transport properties of concentrated aqueous solutions). Recently, the Madrid-Transport[384] (with a charge scaling factor of 0.75) has been developed for aqueous NaCl and KCl solutions, which outperform the Madrid-2019[347] in predicting the transport properties (i.e., viscosities, self-diffusivities of ions, and electrical conductivities). However, this force field yields less accurate results for interfacial tensions and activities of water in aqueous electrolyte solutions.

Despite being scarce, molecular simulation data for properties of systems involving H_2 and more complex ionic species, such as ionic liquids (ILs), have been reported. In these studies, common force fields for ILs are the ones developed by Maginn and co-workers,[386−388] the General Amber force field (GAFF),[307] the Optimized Potentials for Liquid Simulations-All Atom (OPLS-AA) for ILs by Sambasivarao and Acevedo[389], and the model by Koller et al.[390]. Usually, the atomic point charges of the atoms of ILs are derived from quantum mechanical calculations using e.g., the Restrained Electrostatic Potential (RESP) method.[391] Similarly to the monovalent ions discussed earlier, a common practice in simulations of ionic systems such as ILs and DES is to scale the charges obtained from RESP (or other QM-based methods) to reduce the charge screening, and hence, improve force field accuracy. For more details on this approach, the reader is referred to refs 389 and 392−396 and the discussion in Section 4.1.2.

A wide variety of force fields for other ions, important for modeling H_2 processes, such as the Delft-Force field (for OH^-, $B(OH)_4^-$, and BH_4^- ions),[113,397] have been developed recently. For a detailed overview of common ion models the reader is referred to the review by Nezbeda et al.[398] and refs 302, 370, and 385.

3.1.4. Nanoporous Materials, Membranes, and Solid Substrates. In the studies of H_2 separations or storage in nanoporous materials (e.g., MOFs, COFs, zeolites, CNTs), general force fields are mainly used. Among them, the Universal force field (UFF), developed in 1992 by Rappe et al.,[399] is designed to be applicable across the entire periodic table. UFF parameters are based on general rules that consider an element's hybridization and connectivity. Similarly, DREIDING by Mayo et al.[400] is a widely used generic force field aimed at predicting the structures and dynamics of organic, biological, and main-group inorganic molecules, making it a reasonable choice for polymer simulations. To better account for the wide structural space of specific functional materials families, more sophisticated approaches have been developed; QuickFF[401] is a force field parametrization protocol for MOFs and other nanoporous materials that produces force field parameters from first-principles calculations. UFF4MOF[402] is an extension of UFF aiming at improved accuracy for MOFs. IntraZIF-FF[403] and ZIF-FF[404] are specialized force fields for ZIFs, capturing their flexibility and dynamic behavior.

For representing both crystalline and amorphous polymeric materials (e.g., in studies of barrier materials in H_2 tanks, and as membranes for separations and in electrochemical processes), the most common force fields are the condensed-phase optimized molecular potentials for atomistic simulation studios (COMPASS),[315,316,405] the polymer consistent force field (PCFF),[406] and OPLS.[360] These popular polymer force fields are combined with different H_2 models, such as the ones

https://doi.org/10.1021/acs.chemrev.5c00617
Chem. Rev. 2025, 125, 11878−12029

discussed in detail in Section 3.1.1. It is also common that specially developed energy interaction parameters for the H_2[325,407] are used to study properties of H_2/polymer systems. It is noteworthy that despite being one of the most successful force fields for these systems, COMPASS is a proprietary model, part of the Direct Force Field software suite.[408] Other force fields used to model polymeric systems include the modified Adaptive Intermolecular Reactive Empirical Bond Order potential (AIREBO-M),[409] modified versions of the DREIDING force field (e.g., Mabuchi and Tokumasu[410]), and the model by Smith et al.[411]. Scarcely, the anisotropic united atom force field (AUA4)[412] is used to model polymeric materials.[413] It is important to note that many of these models, have also been used for zeolites and other nanoporous materials.

When computing the adsorption and storage capacities of H_2 in functionalized nanoporous materials, intramolecular interactions are often neglected.[198,317,414] Although MOFs are assumed to be rigid in most H_2 adsorption studies, it is important to note that the presence of gases, such as CO_2, in MOFs can induce swelling and phase transitions, which can result in changes to pore-sizes and adsorption properties.[415] To study these phenomena, flexible force fields are required. A review of flexible force fields for MOFs is provided by Heinen and Dubbeldam.[415] There is no general consensus as to which H_2 force field is most suitable for adsorption in MOFs.[414] For strong H_2 adsorption energies (especially for open metal and H_2 interactions), the Morse potential can be used to model the interatomic interactions between H_2 and the MOFs. The Morse potential has been shown to perform better than LJ in modeling stronger interatomic interactions.[317] Many studies in the literature underline the importance of quantum-corrections to classical potentials of H_2, with the most popular being the quasi-classical Feynmen-Hibbs correction[317] (see also Eq. (7) and Fig. 14). Without quantum corrections, the low temperature (below 70 K) adsorption capacity of H_2 can be overpredicted by ca. 20% as shown by Bobbitt and Snurr.[414] Although most H_2 force fields neglect the polarization of H_2 (primarily due to its small size), polarization can play an important role in H_2 adsorption especially when dealing with open metal adsorption sites. Polarization of H_2 significantly enhances the binding between H_2 and the adsorbent.[414] Thus, neglecting polarization by using non-polarizable H_2 force fields,[312] can result in inaccurate predictions of binding sites and capacities as shown by Franz et al.[416] In such cases, it is necessary to use polarizable force fields of H_2 or ab-initio simulations.[414,416] Getman et al.[317] and Bobbitt and Snurr[414] discuss in detail molecular simulations of H_2 adsorption on MOFs, and the use of appropriate force fields. In practice, researchers often need to make a compromise when choosing force fields, since the most accurate representation of adsorbate−organic group and adsorbate−metal interactions may not be equally well captured within a given model. While many studies adopt transferable force fields, others have introduced custom parameterizations in an effort to better capture the structural behavior of the frameworks of the porous media, particularly when new metals are present (see for example refs 417 and 418). Such refinements do not guarantee a universally improved adsorbate−framework description, but can enhance e.g., the accuracy of framework flexibility.

For guest gas molecules other than H_2 (e.g., CO_2, hydrocarbons), widely used force fields include the Transferable Potentials for Phase Equilibria (TraPPE), designed by Martin and Siepmann[301] to model phase equilibria of gases and hydrocarbons, emphasizing transferability and vapor-liquid coexistence properties, the Elementary Physical Model 2 (EPM2) by Harris and Yung[419] developed to accurately describe the phase behavior and thermodynamic properties of CO_2, making it suitable for gas adsorption studies, and OPLS.[360,420,421] In general, OPLS and GAFF[307] force fields are the most widely used force field for modeling hydrocarbons and guest molecules in porous materials.

MD studies related to H_2 storage in subsurface geological formations typically use classical force fields tailored to represent the structural and interaction properties of solids. Among these, CLAYFF (and its variations)[422−424] is the most prevalent, designed explicitly for layered minerals such as montmorillonite, kaolinite, pyrophyllite, beidellite, quartz, hematite, and calcium silicate hydrates. CLAYFF predominantly treats interactions through non-bonded potentials, capturing the essential physics of clays and related nanoporous materials with particular emphasis on hydration and surface interactions. UFF[399] is also frequently chosen to model inorganic solids such as kaolinite, illite, dolomite, quartz, and calcite, thanks to its wide applicability across the periodic table, and parametrization approach based on atomic hybridization and connectivity. The INTERFACE force field[425] extends popular biomolecular and organic force fields to accurately simulate inorganic oxide interfaces, as exemplified by its application to kaolinite. Other specialized force fields used in molecular simulations of H_2/substrate systems are the CVFF[426] and PCFF++[427] for modeling kerogen, OPLS[428] for graphene, and specialized models for silica-based mesoporous materials e.g., MCM-41.[429] Furthermore, force fields such as PCFF+[316,406,430] for SiO_2, and those specifically optimized for calcite (e.g., by Xiao et al.[431] and Raiteri et al.[432]), highlight the importance of targeted development of force fields to accurately capture specific structural, mechanical, or thermodynamic properties relevant to UHS.

3.1.5. Metal-Hydrogen Systems. Several classes of interatomic potentials have been developed to model metal−H interactions, including classical many−body methods such as the Embedded−Atom Method (EAM), its modified form (MEAM), Angular−Dependent Potentials (ADP), and Bond−Order Potentials (BOP), as well as modern machine−learning interatomic potentials (MLIPs). These methods represent a hierarchy of increasing complexity and accuracy in describing metal−H systems.

The EAM potential is a many−body framework that models metals by combining pairwise interactions with an embedding function representing the host electron density. Developed by Daw and Baskes,[433] EAM was groundbreaking in capturing metallic cohesion more accurately than simple pair potentials. Notably, the original work already addressed H in metals, employing EAM to study H interstitials, surface adsorption, and even the effect of H on Ni and Pd fracture.[434] This demonstrated the unique capability of EAM to model HE problems that pair potentials could not resolve. EAM potentials have been extensively parameterized for various metal−H systems, enabling detailed simulations of H trapping at defects and its weakening effect on metal bonds. Currently available EAM potentials for metal−H systems include Pd−Ag−H,[435] Al−Ni−H,[436] Fe−H,[437−439] Pd−H−He,[440] W−H−He,[441] Ni−H,[442] Pd−H,[440] W−H,[443] and Fe−Cr−Ni−H.[444]

The MEAM potential extends the EAM framework by incorporating directional bonding effects, addressing a key

https://doi.org/10.1021/acs.chemrev.5c00617
Chem. Rev. 2025, 125, 11878−12029

limitation of traditional EAM potentials. Developed by Baskes[445], MEAM was the first semi−empirical scheme able to treat fcc, bcc, hcp and diamond structures within one formalism, thereby capturing both metallic and covalent bonding. It has since been extended to second−nearest−neighbour (2NN−MEAM)[446] and multi-component versions and is now widely used for metal−H systems. Compared to EAM, the inclusion of angular terms in MEAM, provides enhanced accuracy in modeling HE phenomena across diverse metals, though at the cost of increased computational and parametric complexity. To date, MEAM potentials have been developed for various metal−H systems, including Al−H,[447] Al−V−H,[448] Fe−H,[449] Ni−H,[447] Ni−V−H,[448] V−H,[450] and Zr−H.[451]

ADPs offer a streamlined way to include directional bonding effects in metals, extending the EAM as a more tractable successor to MEAM. Introduced by Mishin et al.,[452] ADPs supplement the usual EAM energy with explicit dipole and quadrupole terms that penalize deviations from high-symmetry environments, capturing bond-angle dependence via analytic functions rather than the many−body screening routines of MEAM. These additional angular contributions span multiple coordination shells and employ smooth cutoffs for efficiency. Although initially parameterized for transition metals like bcc Fe and fcc Ni,[452] the same formalism has since been adapted successfully to a variety of alloys and metal−H systems. Currently available ADP parameterizations include Al−H,[453] Cr−Fe−H,[454] and Mg−H[455] systems.

BOPs derive from quantum mechanical principles, where bond strength depends explicitly on the local coordination environment. Unlike simpler approaches, BOPs incorporate multi−atom interactions (three− and four−body terms) that dynamically adjust bond energies based on atomic geometry.[456] This formulation provides superior description of directional bonding and bond-breaking/forming processes compared to ADP or MEAM, though at the expense of greater mathematical complexity. Developed initially for alloys and semiconductors,[457] BOP frameworks have been successfully extended to metal-H systems. Currently available BOP parameterizations for metal-H systems include Al-Cu-H[458] and Cu-H.[459]

MLIPs have emerged in the past decade as a transformative approach, leveraging data-driven models to achieve accuracy approaching that of DFT. The field was pioneered by Behler and Parrinello's neural network potential,[460] which demonstrated that high-dimensional neural networks could accurately reproduce DFT potential energy surfaces. Subsequent advances, including Gaussian approximation potential (GAP)[461] and moment tensor potential (MTP),[462] have broadened this methodology, enabling the modeling of complex multi-component systems through flexible functional forms. Unlike traditional empirical potentials, MLIPs are not constrained by predefined functional forms tied to specific theoretical frameworks (e.g., electron density or bond order). This allows MLIPs to achieve accuracies comparable to quantum-mechanics across diverse atomic environments. However, this comes at the cost of requiring extensive training data and reduced physical interpretability compared to conventional potentials.[463] For metal−H systems, MLIPs represent a significant breakthrough as they can simultaneously describe metallic, covalent, and even molecular interactions relevant to HE. Importantly, MLIPs serve as a unifying framework that can, in principle, replicate the behavior of EAM, MEAM, BOP, and other conventional potentials when trained on sufficient data, thereby bridging gaps between these established methodologies. With advancing computational power and algorithms, MLIPs are becoming indispensable tools for investigating HE across various metal systems with unprecedented detail. Successful applications include Pd-H,[464] Nb-H, W-H,[465] Ti-H,[466] Fe-H,[467] and multi-component systems like Mo-Nb-Ta-W-H,[468] and Fe-Co-Ni-Cr-Mn-H.[469]

The landscape of interatomic potentials for metal-H systems reveals two fundamentally distinct modeling philosophies. Traditional approaches (EAM, MEAM, ADP, and BOP) employ compact functional forms grounded in physical principles, with parameters carefully optimized against experiments or DFT reference data. These models incorporate essential physics through distinct mechanisms: electron-density embedding in EAM, angular corrections in MEAM and ADP, and bond-order dependence in BOP. These fundamental physical principles serve as a safeguard, ensuring that even beyond their fitted regimes, the potentials typically maintain reasonable metallic or covalent behavior. In contrast, MLIPs forgo explicit physical constraints in favor of complex, high-dimensional functions with thousands of parameters trained on extensive DFT datasets.[463] While this flexibility enables remarkable accuracy across diverse structural and chemical environments when training data is comprehensive, it carries an inherent risk: configurations outside the training domain may produce unphysical predictions that empirical potentials would naturally avoid. Recent efforts to develop hybrid approaches, such as physics-informed neural network potentials, aim to bridge this divide by embedding physical constraints within ML architectures.[470] However, these methods currently remain limited in scope (e.g., to pure Al[471] and Ta[472] systems), and have not yet been successfully extended to metal-H applications.

When selecting interatomic potentials for HE studies, users must carefully balance two critical factors: (1) the accuracy for target phenomena, and (2) computational efficiency. For physics-based potentials (EAM, MEAM, ADP, BOP), accuracy depends on proper parameterization for specific applications, as demonstrated by Song and Curtin,[276] who refined Fe-H and Ni-H EAM potentials to better capture H-defect interactions, highlighting how even established models may require reparameterization for certain HE mechanisms. For MLIPs, accuracy is intrinsically linked to training data coverage; for instance, an MLIP trained only on bulk H diffusion[465] cannot reliably predict H-defect interactions[469] absent from its training set. Computational cost varies significantly across methods as shown in Table 7: relative to EAM, ADP and MEAM increase costs by ca. 3× and 7×, respectively, while BOP reaches ca. 13×.[473] Modern MLIPs (e.g., ACE, MTP16) further escalate costs to 20−66×,[474] though they offer near-DFT accuracy. Thus, the choice hinges on the priorities of the study: empirical potentials provide transferable, computationally efficient frameworks with inherent physical safeguards, whereas MLIPs deliver higher fidelity at greater computational expense, provided their training data adequately represents the relevant atomic configurations for HE.

3.2. Computation of Hydrogen Properties from Molecular Dynamics Simulations

The past two decades, MD simulations have been proven to be an invaluable tool for studying properties of H_2 systems. In brief, MD performs numerical integration of Newton's

https://doi.org/10.1021/acs.chemrev.5c00617
Chem. Rev. 2025, 125, 11878−12029

Table 7. Comparison of Computational Costs for Different Interatomic Potentials, Normalized Relative to EAM[a]

Force field	CPU cost relative to EAM (times)
EAM	1
ADP	3
MEAM	7
BOP	13
ACE	20
MTP16	66

[a]Performance data for EAM, ADP, MEAM, and BOP potentials are obtained from LAMMPS benchmark tests,[473] while results for ACE and MTP16 (where 16 denotes the MTP level) are sourced from Shuang et al.[474]

equations of motion to yield the positions of particles over time. Unlike MC simulations, which are limited to computing thermodynamic ensemble averages, MD simulations provide insight into both equilibrium and transport properties of a system. The interactions between atoms are determined based on the chosen force field (discussed in detail in Section 3.1). Typically, an MD simulation starts by initializing the positions and velocities of all particles in the simulation box, followed by an equilibration period to bring the system at thermodynamic equilibrium. Then, a production run, usually in the order of ns, is performed to sample the relevant properties. For all details regarding MD simulations the reader is referred to the relevant textbooks.[51,52,297]

The most common open source MD simulation packages for modeling H_2 systems are the Large-scale Atomic/Molecular Massively Parallel Simulator (LAMMPS)[475] and Groningen Machine for Chemical Simulations (GROMACS).[476,477] The modular structure of these simulation tools (and especially of LAMMPS), allows for extensions to the main code (e.g., via the creation of plugins) to accommodate new or advanced computations which are not part of the package (for example the information in ref 478). Nevertheless, other open-source MD software such as DLPOLY[479] and RASPA[480] is also used for modeling H_2 systems. Aside from the simulation packages, visualization software, such as VMD,[481] AVOGADRO,[482] iRaspa,[483] and OVITO,[484] is an indispensable tool for not only visualizing simulations but also computing properties and creating initial configurations. These tools are used to visualize both MD and MC simulations.

3.2.1. Transport Properties: A Brief Introduction. Both equilibrium (EMD)[51,52] and non-equilibrium molecular dynamics (NEMD)[52,485] simulations are naturally suited, and thus, widely used for computing transport coefficients. In NEMD, transport coefficients are calculated using[485]

$$\gamma = \lim_{X\to 0}\lim_{t\to\infty}\frac{J}{X} \tag{9}$$

where γ is the transport coefficient (e.g., self-diffusion coefficient), X is (usually) a fictitious field that drives a conjugate flux, J (i.e., mass flux in case of self-diffusivity or momentum flux for the case of dynamic viscosity), and t is the simulation time.[485] In EMD, transport coefficients can be computed either by using the Green Kubo (GK) or the Einstein relations.[51,485,486] Following the GK approach, transport coefficients are computed from integrals of time-correlation functions of dynamical variables, according to[52,299,487]

$$\gamma = \int_0^\infty \langle \dot{A}(t')\,\dot{A}(0)\rangle \mathrm{d}t' \tag{10}$$

where $\dot{A}$ is the corresponding dynamic variable and the angle brackets $\langle\cdots\rangle$ denote an ensemble average. The Einstein method follows[52]

$$\gamma = \langle (A(t) - A(0))^2\rangle/2t \tag{11}$$

which is a linear relation between time (t) and the mean-squared displacement (MSD) of the dynamical variable. Eq. (11) is valid at time-scales where the slope of MSD(t) equals 1 in the logarithmic scale.[51,52] Using this as a criterion, one can specify the minimum simulation duration for computing transport coefficients using the Einstein method. Such a criterion is not present in the GK approach, where the tail of the time-correlation functions converges to zero regardless of how long the simulation is.[488,489] Thus, from a purely practical standpoint, the Einstein method is advantageous for computing transport properties. Nevertheless, both GK and Einstein methods should yield identical results.[490]

An advantage of using EMD over NEMD simulations is that a single simulation can be used to sample multiple different transport properties.[485,486] NEMD simulations often require multiple simulations at different field strengths (to extrapolate to 0 field) for each transport property.[94] An advantage of NEMD simulations is that, unlike EMD simulations, it can be used to simulate non-linear response behaviors such as the rheology of non-Newtonian fluids.[485] While EMD is well suited for studying spontaneous fluctuations in equilibrium, NEMD is particularly effective for investigating transport processes driven by external forces, such as electro-osmotic drag in polymer membranes. Since most of the systems reviewed in this work deal with aqueous Newtonian systems (such as alkaline electrolyte solutions), primarily EMD simulations are discussed in this work.

To compute transport properties using EMD in LAMMPS,[475] the OCTP plugin[491] or the PyLAT[492] post-processing tools can be used. In the OCTP plugin, Einstein relations are used in combination with the order-n algorithm[51] as implemented by Dubbeldam et al.[493] PyLAT[492] uses a combination of GK (for dynamic viscosity and ionic conductivity), and Einstein relation (for self-diffusivity) expressions.

3.2.2. Viscosity. Computing viscosity, η, via EMD is generally preferred over NEMD because it uses spontaneous fluctuations in pressure of an unperturbed system avoiding introducing external fields or shear flows, which can potentially induce non-linear effects.[51,52,490] As mentioned earlier for all transport properties, η in EMD can be computed by using either the GK approach or the Einstein relation.[490] The Einstein expression for η is as follows

$$\eta = \lim_{t\to\infty}\frac{\mathrm{d}}{\mathrm{d}t}\left[\frac{1}{20}\frac{V}{k_B T}\left\langle \sum_{\alpha\beta}\left(\int_0^t \mathrm{d}t' p_{\alpha\beta}^{\mathrm{Tr}}(t')\right)^2\right\rangle\right] \tag{12}$$

where t is time, V is the volume of the simulation box, k_B is the Boltzmann constant, T is the temperature, and $\langle\cdots\rangle$ indicates an ensemble average. $p_{\alpha\beta}^{\mathrm{Tr}}$ are the components of the traceless pressure tensor calculated using

$$p_{\alpha\beta}^{\mathrm{Tr}} = \frac{p_{\alpha\beta} + p_{\beta\alpha}}{2} - \delta_{\alpha\beta}\left(\frac{1}{3}\sum_k p_{kk}\right) \tag{13}$$

https://doi.org/10.1021/acs.chemrev.5c00617
Chem. Rev. 2025, 125, 11878−12029

where $\delta_{\alpha\beta}$ is the Kronecker delta. Eq. (12), allows viscosities to be computed directly from the slope of the MSD (term in the bracket) at long times.[490] This approach yields results identical with those obtained from the GK method, but avoids the complexity of fitting correlation functions, as discussed by Maginn et al.[490]

3.2.3. Self-Diffusivity. Self-diffusivity is the mass transport mechanism of a species driven by Brownian motion, occurring in the absence of chemical potential, temperature, or pressure gradients.[494] This review mainly deals with self-diffusivities in binary and multi-component gas/liquid mixtures containing H_2. In a multi-component mixture, the self-diffusivity can be calculated as follows

$$D_i^{\text{self,MD}} = \lim_{t\to\infty} \frac{\mathrm{d}}{\mathrm{d}t}\left[\frac{1}{2\mathrm{d}N_i}\left\langle \sum_{j=1}^{N_i} (\mathbf{r}_{j,i}(t) - \mathbf{r}_{j,i}(0))^2 \right\rangle\right] \tag{14}$$

where $\mathbf{r}_{j,i}(t)$ is the position of the j^{th} molecule of species i at time t, $\langle\cdots\rangle$ denotes an ensemble average, and d is the dimensionality of the system. Better statistical accuracy in the computation of $D_i^{\text{self,MD}}$ is achieved by considering the MSDs of all N_i molecules in Eq. 14. At early times ($t \to 0$), a molecule exhibits ballistic motion with MSD scaling as t^2, while at long times ($t \to \infty$), the MSD scales linearly with t, indicating diffusive behavior, during which self-diffusivities are computed. It is important to note that although the slope of unity in the log-log plot of MSD as a function of time is a necessary condition for computing self-diffusivities (and other transport coefficients), it is not always sufficient. According to Maginn et al.[490], the square root of the MSD should be comparable or larger than the simulation box size length. This is a common practice ensuring that the diffusing molecule has explored a substantial part of the configurational space. A similar rule of thumb has been recently proposed by Kärger et al.[495] for diffusivity in nanoporous materials, where the square root of the MSD should be at least equal to one unit cell. This criterion ensures that the molecule is diffusing and not simply vibrating around its position.

Self-diffusivities computed in MD simulations suffer from finite-size effects which arise from spurious hydrodynamic interactions between the particles in the simulation box with their periodic images. These effects can be substantial, depending on the system size and type, and particularly prominent in dense systems, i.e., liquids or compressed gasses.[496] To mitigate finite-size effects, one should either perform MD simulations with large system sizes or use analytical corrections.[497−500] The most widely used correction term, the so-called Yeh-Hummer correction (D^{YH}), was derived in the pioneering studies of Dünweg and Kremer[497] and Yeh and Hummer.[498] The self-diffusivity at the thermodynamic limit can be obtained via the following expression

$$D_i^{\text{self}} = D_i^{\text{self,MD}} + D^{\text{YH}}(T, \eta, L) = D_i^{\text{self,MD}} + \frac{k_B T \xi}{6\pi\eta L} \tag{15}$$

where D_i^{self} is the finite-size corrected self diffusivity of the i^{th} species, ξ is a dimensionless constant equal to 2.837298, and L is the box length of a cubic simulation box. η is the shear viscosity computed from MD simulations, which is shown to be independent of the size of the system.[496,498,501−503]

3.2.4. Maxwell-Stefan and Fick (Mutual) Diffusivities. Mutual diffusivities describe the collective diffusion of species which is commonly modeled using the MS (Maxwell-Stefan) and Fick frameworks. This review mainly focuses on mass transport phenomena in binary and multi-component gas/liquid mixtures containing H_2. The MS framework expresses diffusion in terms of chemical potential gradients, where the flux is driven by differences in the chemical potential, μ_i, of each species and characterized by the MS diffusivity, Đ, an inverse-friction coefficient.[266,321] On the other hand, the Fickian approach uses concentration gradients, with flux governed by the Fick diffusivity, D^{Fick}.[266,504] Despite the different gradients considered, MS and Fick frameworks describe the same physical process, and are mathematically connected by the so-called thermodynamic factor, Γ, for diffusion, according to[505−509]

$$D^{\text{Fick}} = \Gamma Đ^{\text{MS}} \tag{16}$$

As discussed in more detail in Section 3.2.13, Γ accounts for deviations from ideal behavior, and depends on the mixture's composition, pressure, and temperature.[510] While MS diffusivities are linked to chemical potentials, which are difficult to measure experimentally,[511] Fick diffusivities are more commonly reported due to their dependence on measurable concentration gradients.[266] Direct calculation of D^{Fick} using non-equilibrium molecular dynamics simulations is possible, but impractical as it requires setting up systems with large concentration gradients, yielding inaccurate predictions of D^{Fick} as discussed in the studies by Liu et al.,[506] Maginn et al.,[512] Tsige and Grest.[513,514]

In an N − component mixture, there are $N(N-1)/2$ unique MS diffusivities which can be represented as a symmetric matrix. By performing EMD, the MS diffusivity, Đ, in binary mixtures are computed by first obtaining the Onsager coefficients Λ_{ik} at zero total linear momentum.[505−507] Λ_{ik} is computed from the cross-correlations of the molecular displacements of species i and k[505−507,515]

$$\Lambda_{ik} = \lim_{t\to\infty} \frac{\mathrm{d}}{\mathrm{d}t}\left[\frac{1}{6N_{\text{tot}}}\left\langle \left(\sum_{l=1}^{N_i} (\mathbf{r}_{l,i}(t) - \mathbf{r}_{l,i}(0))\right) \times \left(\sum_{m=1}^{N_k} (\mathbf{r}_{m,k}(t) - \mathbf{r}_{m,k}(0))\right)\right\rangle\right] \tag{17}$$

where N_i, $N_k N_{\text{tot}}$ are the number of molecules of type i and k, and the total number of molecules in the system, respectively. $Đ^{\text{MS,MD}}$ for a binary mixture is then expressed as a linear combination of the Onsager coefficients,[505−507,515]

$$Đ^{\text{MS,MD}} = \frac{x_2}{x_1}\Lambda_{11} + \frac{x_1}{x_2}\Lambda_{22} - 2\Lambda_{12} \tag{18}$$

where x_1 and x_2 are the mole fractions of the components in the binary mixture.

As in the computation of self-diffusivities with EMD, finite-size effects are present also in MS diffusivities.[499,503] In a binary mixture, MS diffusivities can be corrected for finite-size effects using the term derived by Jamali et al.:[503]

$$Đ^{\text{MS}} - Đ^{\text{MS,MD}} = \frac{1}{\Gamma}\frac{k_B T \xi}{6\pi\eta L} = \frac{1}{\Gamma} D^{\text{YH}} \tag{19}$$

Fick diffusivities, $D^{\text{Fick,MD}}$, can be computed using Eq. (16). As shown by Jamali et al.,[516] extrapolation of $D^{\text{Fick,MD}}$ to its value at the thermodynamic limit follows from:

https://doi.org/10.1021/acs.chemrev.5c00617
Chem. Rev. 2025, 125, 11878−12029

$$D^{\text{Fick}} - D^{\text{Fick,MD}} = D^{\text{YH}} \tag{20}$$

Eq. (20) shows that the finite-size correction to Fick diffusivities equals the Yeh-Hummer correction term for self-diffusivities (Eq. (15)). Corrections for an N-component system, were derived by Jamali et al.[500]. In an N component mixture, unlike $Đ^{\text{MS}}$, there are $(N-1)^2$ distinct Fick diffusivities where label order matters, i.e $D_{ij}^{\text{Fick}} \neq D_{ij}^{\text{Fick}}$. For a binary mixture, however, $D_{12}^{\text{Fick}} = D_{21}^{\text{Fick}} = D^{\text{Fick}}$.

The discussion above focuses on mass fluxes in a molar reference frame, where velocities are mole-fraction-weighted. Mass fluxes can also be evaluated using mass- or volume-averaged velocities, yielding different Fick diffusivities.[266,517] The benefits of each reference frame are discussed in detailed in Taylor and Krishna[266] (Section 3.1), Bird et al.[517] (Section 17.7), and in refs 508, 510, 518. Notably, for binary mixtures, Fick diffusivities remain identical across reference frames.[266,517] The discussion provided here is not exhaustive, but is meant to showcase the main approach for computing mutual diffusivities of H_2 mixtures using EMD. For detailed discussions on the MS and Fick frameworks in multi-component mixtures, the reader is referred to refs 266, 267, 500, and 519−526.

3.2.5. Diffusivity in Nanoporous Materials. Diffusion inside nanoporous solids is studied extensively using experimental techniques such as frequency response methods, pulsed-field gradient NMR, and quasi-elastic neutron scattering.[527] These approaches define different, but closely related to each other types of diffusivities. Among these types, self-diffusivities in sorbents are convenient to compute via EMD using the methodology discussed in detail in Section 3.2.3. Transport diffusivity ($D_t(c)$, where c is the concentration of the species in the material) is one of the most widely computed quantities to quantify the propagation of diffusing species in sorbents. $D_t(c)$ can be obtained using the following expression:

$$D_t(c) = D_0 \left(\frac{\partial \ln f}{\partial \ln c} \right)_T \tag{21}$$

The second term on the right-hand side in Eq. (21) is the thermodynamic factor, i.e., the derivative of the logarithm of the fugacity of the bulk phase (f) with respect to the logarithm of the concentration of the adsorbed phase.[528] Fugacities can be calculated via MC simulations (see Section 3.3). T is temperature and D_0 is the so-called corrected diffusivity, which describes the displacement of the center of mass of the molecules propagating in the pores of the solid. Note that D_0 depends on c. Both self- and transport diffusivities, depend on the concentration or the guest loading. For a useful discussion on the subtle but critical differences between the measured and computed diffusivities, the approximations made in relating macroscopic and microscopic diffusion measurements, and the assumptions used in permeation models, the reader is referred to the work of Skoulidas and Sholl.[528]

Conventional MD faces challenges in accurately estimating diffusivity for orders of magnitude below 10^{-12} m^2/s[154,529] due to time-scale limitations. For this reason, other, non-conventional approaches are followed, that mostly fall under the category of enhanced sampling methods, addressing the problem as an activated process.[530] The most popular approach in the field is Transition State Theory (TST)[531] which can be coupled with umbrella sampling[532,533] to identify transition states of the propagation of H_2 gas molecules in the cages and apertures of the nanoporous material. Dynamically corrected TST (dcTST)[531,533,534] refines classical TST by applying a transmission coefficient (κ) to account for the fact that overcoming the energy barrier of the aperture does not always result in a successful cage−to−cage crossing, i.e., some jumps fail to thermalize in the destination cage and re−cross the aperture. κ (especially in the cases when it has a low value) can be efficiently computed following the approache of Ruiz-Montero et al.[530] Such effects can be even more pronounced when moving from rigid to flexible simulations (although κ is also needed in simulations of rigid lattices[531,535]), since dynamic motions of groups located near the exit side of the aperture (e.g., rotating methyl groups in ZIFs or flexible linker tails) may intermittently obstruct or deflect the trajectory of the penetrating molecule. In dcTST, the diffusivity of H_2 is approached by tracking "hops" of H_2 molecules from cage to cage via crossing the framework's apertures. After many attempts, a successful aperture crossing will be achieved. The success rate is then translated to the diffusivity via the following expression

$$D_0 = \frac{1}{2n} k_{\text{EXIT}} l^2 \tag{22}$$

where n is the dimensionality of diffusion (e.g., for 3D materials in which H_2 can diffuse in x, y, and z dimensions, n equals 3), k_{EXIT} is the total exiting rate of a molecule from a cage to any of the adjacent ones, and l is the distance between energy minima, which are the centers of cages. k_{EXIT} is estimated by

$$k_{\text{EXIT}} = n_{\text{apert}} k_{\text{cross}} \tag{23}$$

where n_{apert} is the number of available exiting apertures in a cage and k_{cross} is the rate of successful crossings of a molecule (e.g., H_2) through a given aperture, given by[536]

$$k_{\text{crossing}} = \frac{1}{\sqrt{2\pi m}} P(\lambda^*) \tag{24}$$

where m is the mass of the molecule, λ is the reaction coordinate which can be regarded as a function of the Cartesian coordinates.[536] $P(\lambda^*)$ is the probability of finding the molecule in the dividing surface, which is an orthogonal plane at $\lambda = \lambda^*$ vertical to the reaction axis, close to the energy barrier (or at the point where free energy is maximized). For the cases discussed in this review the energy barrier corresponds to the aperture's center. $P(\lambda^*)$ depends on the free energy barrier and can be computed from

$$P(\lambda^*) = \sqrt{\frac{k_B T}{2\pi m}} \frac{\exp^{-\beta F(\lambda^*)}}{\int_{-\infty}^{\lambda^*} \exp^{-\beta F(\lambda^*)}} \tag{25}$$

where F is the free energy, which can be computed by umbrella sampling.[51,52,532] k_{crossing} (Eq. (24)) does not account for some seemingly successful jumps to a new cage, which end up again back to origin cage.[531] To account for this, a dynamic correction factor must be calculated, called correction factor (κ). Thus, the actual, crossing rate is

$$k_{\text{cross}}^{\text{dc}} = \kappa k_{\text{cross}} \tag{26}$$

Details on the umbrella sampling technique and the estimation of the correction factor κ can be found in the work by Krokidas et al.[418]

3.2.6. Thermal Conductivity Using the WAVE Method. Cheng and Frenkel[537] introduced the so-called WAVE method to calculate thermal conductivity of liquid H_2 (and

https://doi.org/10.1021/acs.chemrev.5c00617
Chem. Rev. 2025, 125, 11878−12029

other systems) by analyzing density fluctuations rather than using the traditional GK method. According to the authors, this approach solves a significant limitation of GK methods when dealing with systems that have non-pairwise additive interactions (e.g., ML and DFT-derived potentials). The WAVE method uses Fourier components of density fields in the simulation cell, applies hydrodynamic theory that describes density fluctuations responsible for Rayleigh-Brillouin scattering, and uses the autocorrelation function of density waves to extract thermal conductivity. The width of the central Rayleigh peak in the power spectrum is proportional to thermal diffusivity (and thus thermal conductivity). In short, the scheme for computing thermal conductivity using the WAVE method involves the following elements: (i) Decomposing the density field into discrete Fourier components, (ii) analyzing the autocorrelation function or power spectrum of these components, (iii) fitting to hydrodynamic equations to extract conductivity $\lambda(k)$, and (iv) extrapolating $\lambda(k)$ to $k = 0$ to obtain the macroscopic thermal conductivity. Note that as stated by Cheng and Frenkel,[537] electronic effects are not accounted for since heat transfer in insulators occurs mainly due to the motion of nuclei (electrons are in the ground state and adiabatically follow the nuclei). The authors showed that the electronic contribution to the thermal conductivity of H_2 for the state points studied is negligible, i.e., ca. 0.002% of the computed value.

The method was validated with GK using a generalized LJ fluid over a wide range of temperature and density conditions (i.e., >20 different state points). The WAVE method only requires positional trajectories from MD simulations, making it usable as a post-processing step, there is no need to modify existing MD codes (classical or ab initio), while it works with any interaction potential, including many-body force fields, ML potentials, and DFT. According to the authors, the WAVE method eliminates the ambiguity in defining heat flux and atomic energy partitioning, and avoids potential issues with slowly decaying correlation functions in GK. Limitations of the WAVE method are the requirement of the system to be in the hydrodynamic regime (wavelengths larger than atomic dimensions), the possibility of large systematic errors due to extrapolations (although the statistical errors reported in ref 537) are small, and some discrepancies observed between GK and WAVE for bulk viscosity computations.

3.2.7. Identification of Hydrogen Segregation Sites at Defects. The first task in studying H trapping and its interaction with defects is to identify the stable H segregation sites and the diffusion pathways that connect them. In perfect crystals, H occupies the classical tetrahedral (T) and octahedral (O) interstitials in bcc and fcc lattices respectively, and migrates along the minimum-energy paths between these sites as determined by Nudged Elastic Band (NEB) calculations. However, in highly distorted regions such as GBs or dislocation cores, these ideal sites no longer correspond directly to the actual trapping sites, making their identification non-trivial.

A broadly applicable strategy is the pure Voronoi-vertex sweep, i.e., one computes a full 3D Voronoi tessellation of the atomic network and treats every Voronoi vertex as a prospective H site. In fcc Ni, this automatically recovers all the T and O bulk interstices plus any irregular GB-specific voids;[538] in bcc Fe, the same vertex list captures all T sites but must be augmented by the midpoints of each Fe-Fe next-nearest-neighbor bond to include the classical O sites before energy screening.[539]

By contrast, the polyhedral-centroid method first groups the GB region into its constituent convex packing units (e.g., tetrahedra, octahedra, pentagonal bipyramids, capped prisms) via a deltahedron-based tessellation, then places exactly one H candidate at the geometric center of each cell. This extra grouping step collapses thousands of raw vertices into a parsimonious set of physically meaningful "cages," each labeled by its polyhedral type and directly linked to local volume dilation, greatly enhancing interpretability and computational efficiency.[540,541]

Wang et al.[542] resort to a straightforward grid-scan of the GB region, placing H at regularly spaced points along and normal to the boundary and evaluating each binding energy. Although easy to implement, this brute-force line-grid approach is computationally intensive and its fixed spacing can overlook narrow or irregular traps, making it far less efficient and precise than geometry-driven methods like pure Voronoi sweeps or polyhedral-centroid tessellations.[542]

Having identified these distinct segregation sites, one can assemble the corresponding H-segregation energy spectrum for complex defect configurations, delineate the associated migration pathways, predict the equilibrium H distribution, and ultimately employ KMC simulations to model H diffusion.

3.2.8. Hydrogen Trapping and Interactions with Defects. The energetics of H incorporation and trapping in a metal can be quantified in terms of two key quantities: (1) the solution energy and (2) the segregation (or trapping) energy. The energy to dissolve one H atom in the host crystal (relative to H_2 gas) is

$$E_{\mathrm{sol}} = E_{\mathrm{host+H}} - E_{\mathrm{host}} - \frac{1}{2}E_{\mathrm{H_2}} \tag{27}$$

where $E_{\mathrm{host+H}}$ is the total energy of the supercell containing a single interstitial H atom, E_{host} is the total energy of the pristine (defect-free) supercell, and $E_{\mathrm{H_2}}$ is the total energy of an isolated H_2 molecule in vacuum. To assess the preference of H for a defect site versus a regular bulk interstitial, one evaluates

$$E_{\mathrm{seg}} = (E_{\mathrm{defect+H}} - E_{\mathrm{defect}}) - (E_{\mathrm{bulk+H}} - E_{\mathrm{bulk}}) \tag{28}$$

A negative value of E_{seg} indicates that H is energetically more stable at the defect site than in a bulk interstitial position.

Because the light mass of H gives rise to significant zero-point vibrational energy, one typically adds zero point energy (ZPE) corrections to the energies in the equations above. In practice, since the host and defect lattices contribute negligibly, the ZPE-corrected quantities reduce to[543,544]

$$E_{\mathrm{sol}}^{\mathrm{ZPE}} = E_{\mathrm{sol}} + E_{\mathrm{host+H}}^{\mathrm{ZPE}} - \frac{1}{2}E_{\mathrm{H_2}}^{\mathrm{ZPE}} \tag{29}$$

and

$$E_{\mathrm{seg}}^{\mathrm{ZPE}} = E_{\mathrm{seg}} + E_{\mathrm{defect+H}}^{\mathrm{ZPE}} - E_{\mathrm{host+H}}^{\mathrm{ZPE}} \tag{30}$$

where each E^{ZPE} is the sum of $\frac{1}{2}\hbar\omega_i$ over the three H vibrational modes. All of these energies can be obtained from zero-temperature (static) calculations by first relaxing the relevant structures and then performing vibrational analyses on the H atoms. Energy minimization is typically carried out with conjugate-gradient (CG) or fast inertial relaxation engine

https://doi.org/10.1021/acs.chemrev.5c00617
Chem. Rev. 2025, 125, 11878−12029

(FIRE) algorithms, either at the DFT level or using EAM or MLIP (see Section 3.1.5).

3.2.9. Hydrogen Diffusion in Metals. MD simulations provide a powerful approach for studying how H migrates through lattices in metals under realistic thermo-mechanical conditions. In a typical HE MD study, one integrates Newton's equations of motion for a large ensemble (10^3-10^6 atoms) using interatomic potentials parameterized to capture metal-H interactions, which range from EAM and MEAM to MLIP (see Section 3.1.5). H diffusion coefficients are then extracted from the MSD of H atoms via the Einstein relation (see Section 3.2.3). By performing simulations over a temperature range, one can obtain Arrhenius parameters (pre-exponential factor and activation energy). Periodic boundary conditions, a careful choice of time step, and sufficiently large simulation cells are crucial to minimize finite-size and sampling artifacts. Beyond pure lattice diffusion, MD naturally captures H trapping at microstructural features such as vacancies, dislocations, GBs, or free surfaces, enabling the observation of how these defects alter local diffusivity and cause transient trapping or "hopping" behavior.[538,545]

Path integral MD (PIMD), centroid MD (CMD) and ring-polymer MD (RPMD) represent three conceptually distinct ways to include nuclear quantum effects in atomistic simulations of H diffusion. In PIMD each H nucleus is replaced by a closed ring polymer of beads whose spring-bead system is thermostatted so as to sample the exact quantum canonical ensemble; because all beads move collectively, PIMD yields thermodynamic properties but does not correspond to real-time quantum dynamics. CMD and RPMD both build on the same ring-polymer framework but are tailored to approximate quantum dynamical observables: CMD propagates only the centroid (mean) position of each polymer under an adiabatic separation of internal modes, whereas RPMD evolves the full bead coordinates under Hamiltonian dynamics (with no thermostat on the real-time trajectories). Although the only formal differences among the three methods lie in the choice of fictitious bead masses and the thermostatting protocol, CMD and RPMD are based on different interpretations of how to extract time-correlation functions from the path-integral isomorphism. Both CMD and RPMD recover ordinary MD in the high-temperature limit, when the ring polymer collapses to a single point and quantum fluctuations become negligible.[465,546]

3.2.10. Hydrogen-Mediated Dislocation Nucleation and Mobility. Atomistic simulations, MD and transition-state calculations via the NEB method, offer powerful insight into how H modifies both the nucleation of dislocations at crack tips or free surfaces and the mobility of existing dislocations. H atoms must first be introduced at concentrations and lattice sites that mirror the intended service or experimental conditions. Equally critical is constructing a simulation cell that faithfully reproduces the target geometry, stress distribution and boundary conditions. For example, nanoindentation studies use MD to drive an indenter into a crystalline surface while monitoring the characteristic "pop-in" event in the load-displacement curve, which marks the onset of dislocation nucleation beneath the indenter[547] In a similar vein, constant-load compression of nanopillars with subsequent extended dynamic relaxation enables direct observation of dislocation emission from surfaces or edges under realistic loading rates and avoids artifacts associated with excessively high strain rates.[548,549] To probe H's effect on dislocation motion, MD simulations can measure the critical resolved shear stress required to mobilize pre-existing dislocations in H-charged lattices.[550] In all cases it is essential to choose a sufficiently large simulation cell to eliminate spurious image interactions, apply thermostats and loading protocols that isolate the active deformation region, and select boundary constraints (fixed, free or periodic) that replicate experimental stress gradients. When these MD results are combined with climbing-image nudged elastic band (CI-NEB) calculations of the minimum-energy pathways for dislocation loop or half-loop formation, the integrated approach yields both activation energies and critical stress thresholds. Such insights are essential for quantifying how H alters the atomic mechanisms underlying fracture toughness and surface-driven plasticity.

3.2.11. Hydrogen-Mediated Crack Propagation and Grain Boundary Decohesion. One of the most critical aspects in the study of HE mechanisms is the coupled study of crack propagation and GB decohesion in the presence of H. In this process, H diffusion and mechanical deformation interact continuously, i.e., stress concentrations at a crack tip or along a GB attract H, which in turn weakens interatomic bonds and alters the local stress field, accelerating crack advance and promoting intergranular fracture.[551] Capturing this feedback loop requires chemo-mechanical models that combine H transport with fracture mechanics. Direct atomistic simulation of this coupling is particularly challenging because H diffusion is manifested on timescales (microseconds to seconds) far longer than typical MD loading rates (nanoseconds). As a result, most studies decouple diffusion and deformation by first establishing an equilibrium H distribution under a given stress field and then applying mechanical loading.

Two widely used strategies accomplish this without explicit H charging. In the Grand Canonical Monte Carlo (GCMC) method (see Section 3.3.2), H atoms are added or removed under a prescribed chemical potential (or gas pressure), allowing the system to reach equilibrium coverage at surfaces, GBs and crack-tip regions before loading begins.[552] Alternatively, insertion-relaxation protocols emulate H arrival by placing individual H atoms at interstitial sites dictated by the local elastic field of the crack tip, then relaxing the entire system via MD to permit real-time diffusion into favorable sites. Song and Curtin[276] used a self-consistent stochastic insertion algorithm which can be summarized as follows: At each step, the energy cost to add one more H at every empty interstitial is computed and translated into an equilibrium occupancy probability. Then randomly populate sites until no further H can be inserted at that stress intensity. Both approaches generate near-equilibrium H distributions around evolving crack tips without ever simulating H_2 molecules, enabling subsequent MD or CI-NEB studies of crack advance and GB decohesion under realistic H coverages.

By choosing an appropriate method for generating H distributions under varying loads, one can study HE under more realistic, coupled conditions. GCMC is typically performed before any mechanical loading to establish equilibrium H coverages at surfaces, GBs and crack tips. Once deformation begins, whether via dislocation emission, cleavage or crack advance, it proceeds at MD strain rates many orders of magnitude higher than H diffusion rates, so further redistribution of H is negligible on the simulation timescale.[553] The downside is that GCMC is computationally expensive, and therefore, impractical to run different simulations for each small loading increment. As a result, it cannot capture any

https://doi.org/10.1021/acs.chemrev.5c00617
Chem. Rev. 2025, 125, 11878−12029

load-induced changes in H segregation. In contrast, self-consistent stochastic insertion algorithms rebuild the H distribution after each incremental increase in stress intensity. Although this still does not track H diffusion in real time, it captures the instantaneous interplay between evolving stress fields and H trapping at every load step, providing a practical compromise between physical fidelity and computational cost.[276]

3.2.12. Electroosmotic Drag Coefficient. Electro-osmotic drag (EOD) signifies the transport ratio of water to protons (H^+) in a membrane.[92] In hydrated membranes, H^+ are conveyed across the membrane in response to an electric field. H^+ do not migrate independently across the membrane; instead, they are stabilized as H_3O^+ or larger protonated clusters. Proton transport, therefore, occurs via the so-called proton hopping (Grotthuss mechanism)[554,555] and vehicular mechanism.[556] According to the vehicular mechanism, H^+ move between water molecules involving coordinated movement of H_3O^+ ions and water molecules. This differs from the Grotthuss mechanism, where protons hop through a chain of water molecules by breaking and forming hydrogen bonds. The combined effect of these two mechanisms results in the manifestation of ionic conductivity in hydrated membranes. EOD is influenced by the level of hydration (λ) which indicates how many water molecules are associated with each ion exchange site in the membrane. For a Nafion membrane, hydration is defined as

$$\lambda = \frac{N_{H_2O}}{N_{SO_3^-}} = \frac{N_{H_2O}}{N_{H_3O^+}} \tag{31}$$

where N_{H_2O}, and $N_{SO_3^-}$ are the numbers of water molecules and sulfonic acid groups in the membrane, respectively.

The EOD coefficient, ξ_D is a measure of the number of water molecules transported alongside each proton within its solvation shell, and is defined as

$$\xi_D = \frac{j_{H_2O}}{j_{H^+}} \tag{32}$$

where j_{H_2O} and j_{H^+} are the fluxes of water molecules and protons, respectively. Note that ξ_D is defined in the absence of concentration and/or pressure gradients, and at vanishing chemical potential gradients of water.[92,100,557,558] EOD coefficients are computed using NEMD, in which the driving force is imposed by an external electric field, **E**. The necessity for NEMD arises because the transport of water and ions are governed by both diffusion and the coupling of electrical and hydrodynamic forces. NEMD framework is therefore necessary, as the introduction of an electric field induces directional ion motion, which in turn influences water transport. In practice, the EOD coefficient is computed by applying external electric fields of varying magnitudes across one axis of the simulation box at a time and observing that ion velocities scale linearly with the field.[94] By analyzing the system's response to these external perturbations, the EOD can be extracted from the NEMD simulation in agreement with Eq. (32), from

$$\xi_D = \lim_{\mathbf{E}\to 0} \frac{j_{H_2O}}{j_{H^+}} \tag{33}$$

where each flux is obtained at vanishing **E**, ensuring the sampling occurs in the linear response regime. This definition is in alignment with the broader framework introduced in Eq. (9).

In a classical MD simulation, where proton hopping is absent, the flux of H_3O^+ perpendicular to one of the faces of the simulation box along the x, y, or z axis can be expressed as the product of the number of H_3O^+ and their average velocity along the respective axis, sampled during the production runs. Similarly, the flux of water molecules can be expressed as the product of the number of water molecules and their average velocity.[94] Consequently, Eq. (33) can be rewritten in terms of number density and velocity for the classical case where proton hopping does not occur

$$j_{H_3O^+} = N_{H_3O^+}\left\langle v_{H_3O^+}\right\rangle \tag{34}$$

where $j_{H_3O^+}$ is the flux of hydronium ions across the membrane. A similar expression applies to the molecular flux of water. Using the definition of λ in Eq. (31), one can substitute $N_{H_2O}=\lambda N_{H_3O^+}$ into Eq. (33), leading to

$$\xi_D = \lim_{\mathbf{E}\to 0} \frac{j_{H_2O}}{j_{H_3O^+}} = \lambda \times \lim_{\mathbf{E}\to 0} \frac{\left\langle v_{H_2O}\right\rangle}{\left\langle v_{H_3O^+}\right\rangle} \tag{35}$$

Eq. (35) enables the direct computation of the EOD coefficient from MD simulations by tracking the velocities of water and H_3O^+ under an applied electric field. The EOD coefficient is determined by interpolating the average velocities as **E** approaches zero.[94] It is evident that Eq. (35) represents a specific case of the more general formulation given in Eq. (33).

It is important to note that ξ_D can be computed using both classical simulations[94,127,559] and first principles MD of small systems.[129] The advantage of a first-principles simulation is that it captures the Grotthuss mechanism, in contrast to MD. Due to the fact that this mechanism becomes more dominant at higher water uptakes in the membrane, it is not a surprise that ξ_D of water computed via classical MD is in good agreement with experimental data[560] at lower water uptakes[94]

3.2.13. Thermodynamic Factor for Diffusion. The thermodynamic factor Γ for diffusion links MS and Fick diffusivities via Eq. (16). For an N-component mixture, the thermodynamic factor matrix $\boldsymbol{\Gamma}$[266,510] is defined as

$$\Gamma_{ij} = \delta_{ij} + x_i\left(\frac{\partial \ln \gamma_i}{\partial x_j}\right)_{T,P,\sum} \tag{36}$$

where x_i is the mole fraction, γ_i the activity coefficient, T the temperature, P the pressure, and δ_{ij} the Kronecker delta. The constraint $\sum$ enforces that during the differentiation, $\{x_i\}$ of all species remain constant, except for the n^{th} component, so that $\Sigma_{i=1}^{n} x_i = 1$[266,507,510]. The activity coefficient γ_i is related to the chemical potential as follows[266,510]

$$\ln\gamma_i = \frac{\mu_i - \mu_i^o}{k_B T} - \ln x_i \tag{37}$$

where μ_i^o is the chemical potential of pure component i. For a binary mixture, Eq. (36) reduces to a single thermodynamic factor Γ. $\Gamma = 1$ denotes an ideal mixture, while negative values indicate phase separation. In general, $\boldsymbol{\Gamma}$ for an N-component mixture is not symmetric,[267,510] and for ideal mixtures ($\gamma_i = 1$), $\Gamma_{ij} = \delta_{ij}$. $\boldsymbol{\Gamma}$ can be computed via molecular simulation in various ways; via Kirkwood-Buff integrals (KBIs),[561−565,565−570]

https://doi.org/10.1021/acs.chemrev.5c00617
Chem. Rev. 2025, 125, 11878−12029

simulations at the grand canonical (GC) ensemble,[571] and by using the Permuted Widom Test Particle Insertion (PWTPI) method.[572,573] Each approach has advantages and drawbacks. For example, KBIs yield thermodynamic factors without relying on activity coefficient models but require large system sizes to obtain accurate RDFs, especially for $n > 2$ components.[506,574] In contrast, PWTPI directly yields composition derivatives from a single simulation at a computational cost similar to WTPI,[51,575] but like WTPI and GC methods, it is inefficient at liquid-like densities due to the low probability of successful single-step particle insertions.[51] Recently, the CFCPWTPI method developed by Hulikal Chakrapani et al.[576] was used to compute thermodynamic factors for dense CO_2-H_2 mixtures using small systems (i.e., containing a few hundred molecules). Such innovations improve the feasibility and reliability of using molecular simulations to directly realize the theoretical definitions of thermodynamic factors.

3.2.14. Hydrate Phase Equilibria from the "Direct Phase Coexistence" Method. The "direct phase coexistence" method[577] has extensively been used to calculate the phase equilibria of systems such as ice[367,368] and hydrates.[342,369,578−581] The different phases that are at equilibrium (e.g., solid hydrate (H)/ice (I), liquid water (W), gas (G)/vapor (V)) are brought in contact, and the evolution of the potential energy of the system is sampled via MD simulations at the *NPT* ensemble. By performing a temperature scan (i.e., recording the potential of the system for each temperature considered) for any given, fixed pressure, the three-phase equilibrium temperature can be identified, as the average between the lowest value that hydrate dissociation occurs and the highest value that hydrate formation occurs. To increase the accuracy of the calculation, the equilibrium temperature should be the result of averaging multiple MD runs (replicas).

Fig. 16 is a schematic representation of the various steps of the "direct phase coexistence" approach. Typical configurations for the simulations, encountered in the literature, are the three-slab (WHG) or four-slab (WHWG) arrangement. A hydrate supercell ($K \times M \times N$) of the hydrate structure of interest is constructed by using K, M, and N unit cells in the $x-$, $y-$, and $z-$ directions, respectively. The positions of the oxygen atoms within the unit cell of the sII hydrate can be obtained from Mak and McMullan,[582] while the corresponding positions for sI hydrates, from McMullan and Jeffrey.[583] The positions of the hydrogen atoms can be found by minimizing the energy of the system while fixing the oxygen atoms, resulting in a structure that respects the Bernal and Fowler[584] rules. Such an approach has been suggested[585] as an alternative to finding a configuration that has the minimum dipole moment. Takeuchi et al.[586] provided a detailed discussion for sI, sII, and sH hydrates. The authors used the TIP4P water model, and reported the coordinates of water molecules in the unit cell of hydrates that have nearly zero net dipole moment. The reported coordinates have been used in many molecular simulation studies, and have been further adapted for use with different water force fields.

All the centers of the cages can be filled with a single guest molecule (i.e., 100% (full) cage occupancy). Alternatively, experimental measurements or MC simulations can be used for cases of examining partial (i.e., lower than 100%) or multiple (i.e., higher than 100%) cage occupancy. A typical procedure followed during these simulations involves the following steps:

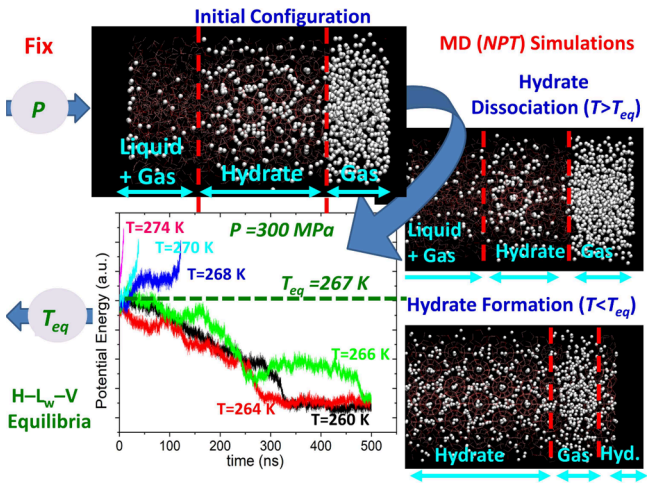

Figure 16. A schematic representation of the "direct phase coexistence" method. For a fixed P, an initial configuration (shown in the top left panel) consisting of three distinct slabs (i.e., (i) Liquid H_2O + dissolved H_2, (ii) hydrate crystal, and (iii) gaseous H_2) is constructed to perform MD simulations (*NPT* ensemble). The potential energy of the total system is recorded for various temperatures (shown in bottom left panel). For $T > T_{eq}$ (where T_{eq} is the equilibrium temperature) the potential energy increases, and the hydrate dissociates (top right panel), while for $T < T_{eq}$ the potential energy decreases, and the hydrate phase grows (bottom right panel). For the shown P, T_{eq} = 267 K is identified as the average between the lowest value (268 K) at which hydrate dissociation occurs and the highest value (266 K) at which hydrate formation occurs.

Initially, each slab is equilibrated separately at each different pressure. Next, all different slabs are connected with a buffer distance, followed by energy minimization to avoid overlaps, while keeping the oxygen positions frozen. The connection of the slabs is achieved with their interfaces normal to the x-direction. During the equilibration of the water and H_2 slabs, their y and z dimensions are kept equal to the equilibrated y and z dimensions of the hydrate slab.

3.2.15. Hydrate Structure and Kinetics. A number of methods have been reported for the calculation of the growth rate of hydrate crystals based on MD simulations. Such methods include: (i) the counting of the water molecules added to the hydrate phase,[587] (ii) plotting the potential energy as a function of time (until it reaches constant value) in order to estimate the growth time τ. The growth rate, u, is then simply obtained by dividing the length of the grown hydrate, ΔL, by 2τ due to the fact that there are two interfaces growing under periodic boundary conditions,[588] and (iii) tracking of the position of the hydrate-liquid interface.[589,590] To identify the type of structure each water molecule belongs to, order parameters have been defined. The order parameters can describe the hydrogen bond network within the water. In particular, F_3 expresses deviations from the tetrahedral angle within the hydrogen bond network.[591] An angle θ can be defined between the oxygen atoms in a $B_i - A - B_j$ triad and then used to calculate F_3 through the equation

$$F_3 = \left\langle (\cos\theta|\cos\theta| + \cos^2\theta_t)^2 \right\rangle \tag{38}$$

where θ_t is the tetrahedral angle (109.47°). The angular brackets denote an average over all unique pairs B_i, B_j and over all the designated central atoms A. Essentially, the order parameter probes oxygen atoms within the first solvation shell

https://doi.org/10.1021/acs.chemrev.5c00617
Chem. Rev. 2025, 125, 11878−12029

of the central oxygen atom (i.e., less than 0.35 nm from oxygen A). F_3 will be close to zero for tetrahedrally coordinated water and larger than zero otherwise.[592]

For the analysis of hydrate crystals Rodger et al.[593] concluded that it would be useful to have an order parameter that can distinguish between the different tetrahedral networks adopted by water, and introduced a new, four-body order parameter ($F_{4\phi}$) based on the H-O−O-H torsion angle, ϕ for two adjacent water molecules; for these purposes the hydrogen atoms have been defined as the outer-most H in the water dimer. ($F_{4\phi}$) is defined as

$$F_{4\phi} = \langle \cos 3\phi \rangle \tag{39}$$

Therefore, by comparing the set of instantaneous order parameters for any specific water molecule with the distribution of parameters found within various stable phases (see Table 8), it is possible to identify the local phase to each

Table 8. Order Parameters for Water Molecules in Various Phases

Phase	F_3	$F_{4\phi}$
Liquid	0.1	−0.04
Hydrate	0.01	0.7
Ice	0.01	−0.4

water molecule, and thereby to determine both the hydrate content of a system and the extent to which the water molecules with hydrate local phase are clustered.

Alternatively, some studies considered the time evolution of the number of 5^{12} or $5^{12}6^4$ cages to track the hydrate growth rate. In particular, in two H_2-hydrate-related studies (i.e., H_2 + CH_4;[594] H_2 + THF[595]), the hydrate growth process was monitored with the face-saturated incomplete cage analysis method (FSICA).[596] By performing an analysis of the network topology formed by the hydrogen bonds of water molecules, FSICA can identify all of the face-saturated hydrate cages in the system, where face-saturation means that the edge formed between two water molecules is shared by at least two faces (water rings).[596] Zhang et al.[594] showed that the calculation of the growth rate, either using the evolution of the number of 5^{12} cages, or using the evolution of the number of $5^{12}6^4$ cages produce identical results for the hydrate crystal growth rate. The hydrate growth rate in these studies was calculated using the following equation:

$$R = \frac{N_{500\text{ns}} - N_{100\text{ns}}}{L_x L_y 400} \tag{40}$$

where $N_{100\text{ns}}$ and $N_{500\text{ns}}$ represent the number of 5^{12} cages in the system at 100 and 500 ns of simulation duration, respectively. L_x and L_y represent the x − and y − direction lengths of the system box, respectively. Δt = 400 is the time span between the two measurements.

3.2.16. Interfacial Tension. Let us consider a planar slab of fluid with a planar area $\mathcal{A} = L_\parallel^2$, in contact with a gas inside a simulation box with dimensions $L_\parallel$, $L_\parallel$, $L_\perp$ in the x, y, z directions (box volume: $V = L_\parallel^2 \times L_\perp$), respectively. The thermodynamical definition of the interfacial tension of gas-liquid (or a liquid-liquid) interface in the canonical (NVT) ensemble is the change in the Helmholtz free-energy (F) of the system due to the change in the surface area of the interface[51,52,597]

$$\gamma = \left(\frac{\partial F(N, V, T)}{\partial \mathcal{A}}\right)_{N,V,T} \tag{41}$$

where the composition, volume, and temperature of the system are fixed. Interfacial tension in a system with fixed pressure, temperature, and composition is given by[51,52,597]

$$\gamma = \left(\frac{\partial G(N, p, T)}{\partial \mathcal{A}}\right)_{N,p,T} \tag{42}$$

where $G(N, p, T)$ is the Gibbs free energy of the system.

The mechanical definition of the surface tension using the microscopic pressure tensor for a planar fluid slab coexisting with a gas as proposed by Irving and Kirkwood is[597−599]

$$\gamma = \int_{-\infty}^{\infty} \mathrm{d}z [p_\perp(z) - p_\parallel(z)] \tag{43}$$

where $p_\perp$ and $p_\parallel$ follow from

$$p_\perp = p_{zz} \tag{44}$$

and

$$p_\parallel = \frac{1}{2}(p_{xx} + p_{yy}) \tag{45}$$

The integrand of Eq. 43 is non-zero only in the vicinity of interface separating the two phases and zero otherwise.[51,52,597] As stated in the review by Ghoufi et al.[597], the definition of γ from the thermodynamic route (Eq. (41)) and the mechanical route (Eq. (43)) are formally equivalent. It is important to note that Eq. (43) is valid for continuous pairwise-additive potentials.[51,52,597] It is readily shown that,

$$\int \mathrm{d}z\, p_{\alpha\beta} = L_\perp \langle p_{\alpha\beta} \rangle \tag{46}$$

where

$$p_{\alpha\beta} = \rho k_B T(\mathbf{I})_{\alpha\beta} + \frac{1}{V}\left\langle \sum_{i=1}^{N-1} \sum_{j>i}^{N} (\mathbf{r}_{ij})_\alpha (\mathbf{f}_{ij})_\beta \right\rangle \tag{47}$$

where $\rho = N/V$ is density, $\mathbf{I}$ is the identity matrix, $\mathbf{r}_{ij}$ and $\mathbf{f}_{ij}$ are the separation vector and the intermolecular force between molecule i and j, α, β = x, y, z and $\langle \cdots \rangle$ is the canonical (Boltzmann) average over the simulation run. Using Eq. (46) the interfacial tension in Eq. (43) can be rewritten as follows

$$\gamma = \frac{L_\perp}{2}\langle p_\perp - p_\parallel \rangle \tag{48}$$

where the factor 2 in the denominator signifies the presence of two interfaces. Equation 48 is also called the Kirkwood-Buff definition.[597,600]

3.2.17. Solid Gas/Liquid Contact Angle. Contact angles provide a quantitative measure of how a liquid, solid, and gas interact at their three-phase contact line.[52] As shown in Fig. 17, the contact angle is defined as the angle formed between the tangent to the liquid-gas interface and the solid surface at the point where they meet. Contact angle characterizes the wettability of the surface, i.e., small contact angles indicate a surface that is easily wetted, while large ones suggest poor wettability. By measuring contact angles, one can gain insights into surface chemistry, material properties, and fluid-solid interactions. Below, we describe how to compute contact angles for gas bubbles in MD simulations.

https://doi.org/10.1021/acs.chemrev.5c00617
Chem. Rev. 2025, 125, 11878−12029

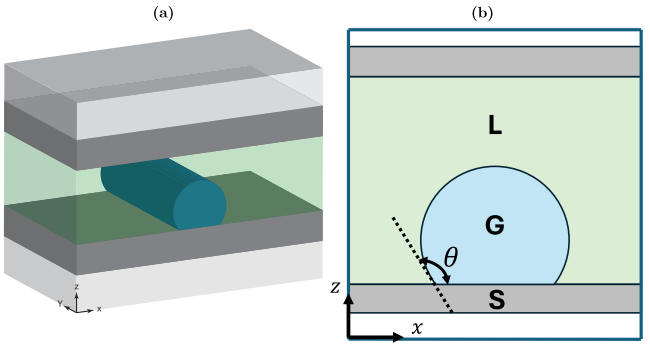

Figure 17. (a) A typical MD simulation setup for computing contact angles: A hydrogen nano-bubble (dark green) immersed in water/brine (transparent green), shaped cylindrically due to symmetry along the *y*-direction, is enclosed between solid surfaces (dark gray) at the top and bottom. The top wall serves as a piston (or barostat) to control gas-liquid pressure.[601,602] To prevent wall interactions across periodic boundaries, the simulation box length in the *z*-direction is (typically) several times longer than lateral dimensions.[602] The regions (in light gray) above the top wall and below the bottom wall are vacuum. (b) A cross section of the simulation box in the $x-z$ plane. The intersection between the solid surface (S), surface of the nanobubble (G) and the liquid medium (L) co-determines the contact angle θ.

To compute contact angles, MD simulations are performed in the *NVT* ensemble adopting the setup shown in Fig. 17(a).[602−609] A cylindrical slab composed of H_2 gas spanning the $y-$ direction is surrounded by water while directly contacting a "solid" slab beneath it. Typically, a gas nanobubble spanning the $y-$ direction is chosen to avoid the effects of line tension on the contact angle. By eliminating effects of line tension on the contact angle, a comparison with experiments is possible. Introducing another solid slab positioned at a distance *w* from the bottom slab confines the gas-liquid medium. Adjusting the distance *w* allows for variation in the confining pressure, effectively serving as a barostat, as depicted in Fig. 17(a). The volumes between the lower surface of the lower solid slab and the upper surface of the upper solid slab are vacuum. To ensure that the slabs do not interact via the periodic boundary in the *z*-direction the top and bottom wall are positioned far from each other. Finally, the gas nanobubble is equilibrated for a duration of several ns, after which the contact angle can be computed.

To determine the contact angle, 2D *xz* density maps (see Fig. 17(b)) are obtained by a binning procedure wherein the center-of-mass of the gas nanobubble in the simulation box are segregated into bins of a (typical) size of 0.5×0.5 Å^2, based on their position in the *xz* plane. Density maps are averaged over several ns to obtain a smooth density profile. A non-linear regression is performed to fit the iso-density curve of the gas nanobubble to a circle, and its intersection with the position of the wall in the *z* direction determines the contact angle, as shown in Fig. 17(b). For instance, the position of the wall in the *z*-direction is determined by averaging the positions of the outermost silica atoms if the wall is composed of silica as in the study by Chen and Xia.[605] The contact angle of a water droplet is the supplementary angle corresponding to the contact angle of the gas nanobubble, i.e., $\theta_{H_2O}=180-\theta$ in Fig. 17(b). A note of caution to the reader: in the absence of any pinning sites (or heterogeneities) the gas nanobubble tends to translate parallel to the wall, and its center of mass may vary with time. Thus, when generating density maps, it is important to reposition the the gas nanobubble about its center of mass.

3.3. Computation of Hydrogen Properties Using Monte Carlo Simulations

The past decades, MC simulations have been evolved into a powerful tool for computing thermodynamic properties of reactive and non-reactive H_2 systems. Representative examples of such properties are phase coexistence, chemical reactions, solubilities (in gas, liquid, and solid phases), densities, and chemical potentials. As in MD simulations, the interactions between atoms and molecules are determined based on the chosen force fields. Unlike MD simulations, MC simulations use a stochastic algorithm. The concept of "trial-moves" is used in MC simulations to sample the phase-space. Examples of trial-moves are displacements and rotations of molecules, particle insertions (or deletions), volume changes, and changes in bond lengths.[51,52] Trials moves can be accepted (or rejected) based on a probability (P_i), which is often proportional to the probability of occurrence of the given micro-state (i.e., metropolis algorithm). Trial moves can also be more complex, such as identity swaps, where one particle type is replaced by another. The flexibility of MC methods is a significant advantage compared to MD. MC simulations typically involve thousands to millions of cycles, where each cycle consists of *N* trial moves. The number of cycles needed depends on the property being studied, the size of the system, and the complexity of the force field. The properties listed in this section such as excess chemical potentials and solubilities can also be computed using MD. However, they are most commonly computed using MC simulations. For all details regarding MC simulations and statistical mechanics the reader is referred to the relevant textbooks.[51,52,296,298]

As for MD simulations, several high-quality open-source software packages have been developed through the years for performing MC simulations of H_2 (and other) systems. Prime examples are Towhee,[610] Cassandra, RASPA,[480] and BRICK-CFCMC,[611,612] however, the list of available codes is long. For a relevant discussion the reader is referred to ref 613. Visualization of MC simulations is an important feature allowing for both understanding of mechanisms and tracing of possible simulation errors. Examples of state-of-the-art visualization software for molecular simulations is discussed in Section 3.2.

Kinetic Monte Carlo (KMC) is a simulation technique that is used to model the time evolution of physical systems through stochastic processes, focusing on the dynamics and rates of transitions between states.[614,615] Unlike classical MC (described above), which primarily samples equilibrium configurations using acceptance probabilities based on energy differences, KMC explicitly tracks the temporal evolution of the system with transition rates, and associates time with each simulation step. KMC works by selecting transitions proportionally to their rates rather than attempting moves with uniform probability followed by accept/reject decisions, making it particularly well-suited for studying non-equilibrium processes and kinetic phenomena while classical MC excels at determining equilibrium thermodynamic properties. While MD simulations (see Section 3.2) are well-suited for studying fast processes such as the dislocation motion, they are limited in their ability to capture the long-timescale diffusion and segregation of H_2 in complex micro-structures. KMC methods complement MD by enabling the simulation of H_2 transport

https://doi.org/10.1021/acs.chemrev.5c00617
Chem. Rev. 2025, 125, 11878−12029

over experimentally relevant timescales (up to seconds or longer) while maintaining atomic-level resolution. In this review, we briefly describe properties computed with KMC related to HE.

3.3.1. Phase Equilibria of Hydrogen Systems. Based on vapor-liquid equilibrium (VLE), the solubilities of H_2 in different liquid mixtures, densities, and equilibrium gas compositions can be determined. Equilibrium is established when the chemical potentials of both phases are equal. At this point, the densities of each phase become stable, fluctuating around well-defined values. To compute VLEs of H_2 mixtures from molecular simulations, different methods can be used.

3.3.1.1. Gibbs Ensemble. A common approach for computing the VLE of a system with MC simulations is the Gibbs Ensemble (GE) method introduced by Panagiotopoulos[616] in 1987. Unlike most MC and MD methods, GE considers two distinct simulation boxes (without any interface), each containing the gas or the liquid phase. GE enables the determination of phase coexistence properties of multicomponent systems from a single simulation. To achieve equilibrium, a sufficient number of MC trial moves are performed to generate random configurations within each phase, along with the random transfer of molecules between them.[51] To assess whether the chemical potentials of the two phases have equilibrated, test particle insertion methods[617] are often employed. When one of the phases has a high density (e.g., liquid water at room temperature), VLE computations can become inefficient. This is primarily due to the frequent rejection of molecular exchanges between the simulation boxes in conventional single-molecule trial insertion and removal moves. In such cases, the Continuous Fractional Component Gibbs Ensemble (CFCGE) approach (GE expanded with fractional molecules) can be used to facilitate the equilibration of phase compositions (i.e., sampling densities at equilibrium) while also enabling direct sampling of chemical potentials.[618] This approach will be discussed further in Section 3.3.1.4.

3.3.1.2. Vapor–Liquid Equilibrium from Chemical Potentials. Although GE and CFCGE methods provide a straightforward approach to compute the VLE of H_2 systems, the chemical potential of each phase (or species) can also be independently sampled in separate simulations to determine VLE compositions. Rahbari et al.[110] performed CFCGE simulations to compute the VLE of $H_2O - H_2$ systems at high pressures. At low H_2 concentrations, either a simulation box with a large number of molecules is required or extended simulation cycles to adequately sample the equilibrium composition in each phase. In such cases, separate simulations for each phase are recommended to determine the chemical potential for phase equilibrium.

Accurately computing chemical potentials is crucial for obtaining solubilities and VLEs of H_2 systems using molecular simulations. The chemical potential of H_2 in each phase can be expressed as

$$\mu_{H_2} = \underbrace{\mu^0_{H_2}(T) + k_B T \ln\left(\frac{\langle \rho_{H_2} \rangle}{\rho_0}\right)}_{\text{ideal gas part: } \mu^{id}_{H_2}} + \mu^{ex}_{H_2} \tag{49}$$

where $\mu^0_{H_2}(T)$ represents the reference chemical potential, incorporating intramolecular contributions such as rotation, vibration, translation, and bond dissociation energy. The number density, ρ_{H_2}, is defined as the number of molecules per unit volume, with $\rho_0 = 1$ Å^{-3} serving as a reference to ensure a dimensionless logarithm. $\mu^0_{H_2}(T)$ is relevant when chemical reactions (bond breaking/formation) are considered in the simulations. The first two terms in Eq. (49) correspond to the ideal gas contribution ($\mu^{id}_{H_2}$), while the final term represents the excess chemical potential ($\mu^{ex}_{H_2}$), which quantifies the difference in the Gibbs free energy associated with the addition of a molecule or species of type i into an interacting molecular system compared to an ideal gas at the same temperature, pressure, and composition.[619] Different methods can be used to compute $\mu^{ex}_{H_2}$, and therefore, VLE and solubilities, in molecular simulations. Brief overviews of these methods are provided below.

3.3.1.3. Widom Test Particle Insertion Method. The Widom test particle insertion (WTPI) method, along with its adaptations, is widely used for computing $\mu^{ex}_{H_2}$ in both MC and MD simulations.[51,572,573,576,617,618,620−623] $\mu^{ex}_{H_2}$ is sampled using the WTPI method as

$$\mu^{ex}_{H_2} = - k_B T \ln\left\langle \exp[-\beta \Delta U_{H_2}{}^{+}] \right\rangle_{NVT} \tag{50}$$

where $\Delta U_{H_2}{}^{+}$ is the energy change of the system when a H_2 probe molecule (or any other species) is randomly inserted in the system. One should be aware that Eq. (50) faces challenges when simulating high-density systems or systems with a strong dependence on molecular orientation.[54,624,625] Variations of WTPI, in which the test particle is gradually inserted, are commonly used in expanded ensemble methods (in both MC and MD) to avoid the drawbacks of the single-step insertions.

3.3.1.4. Continuous Fractional Component Monte Carlo. The CFCMC[626,627] method is an adaptation of the expanded ensembles concept in MC simulations. A thorough review of this method is provided in.[618] In CFCMC, conventional ensembles such as *NPT*, *NVT*, GE or the reaction ensemble (RxMC), are expanded with a fractional molecule or a group of fractional molecules with scaled interactions. This leads to improving efficiency in cases where one phase has a high density or strong electrostatic interactions. Simultaneously, the excess chemical potentials of species in both phases are obtained. The interactions of the fractional molecules are scaled with a coupling parameter $\lambda \in [0, 1]$.[627−629] At $\lambda = 0$, the fractional molecule does not interact with the rest of the molecules in the system, while at $\lambda = 1$, the fractional molecule has fully scaled interactions. Staged insertions are performed during the simulation using random trial moves in λ space by increasing or decreasing the value of λ. To improve sampling in λ space (especially in dense systems, such as aqueous solutions), a biasing weight function is often applied[112,630] using the Wang-Landau algorithm.[631] Provided that sufficient sampling is performed at $\lambda = 0$ and $\lambda = 1$, $\mu^{ex}_{H_2}$ in the *NVT* or *NPT* ensemble follows from[627,632]

$$\mu^{ex}_{H_2} = - k_B T \ln\left(\frac{p(\lambda_{H_2} = 1)}{p(\lambda_{H_2} = 0)}\right) \tag{51}$$

where k_B is the Boltzmann constant, and T is the temperature in K. $p(\lambda_{H_2} = 1)$ and $p(\lambda_{H_2} = 0)$ are the probabilities of the coupling parameter λ of H_2 fractional molecules being equal to 1 and 0, respectively.

https://doi.org/10.1021/acs.chemrev.5c00617
Chem. Rev. 2025, 125, 11878−12029

Thermodynamic integration is an alternative method for computing excess chemical potentials in CFCMC simulations or in similar adaptations of expanded ensembles:[618]

$$\mu_{H_2}^{ex} = \int_0^1 \left\langle \frac{\partial U(\lambda_{H_2})}{\partial \lambda_{H_2}} \right\rangle d\lambda_{H_2} \tag{52}$$

In dense electrolyte solutions, performing random walks in the λ space can become difficult because of the strong electrostatic interactions in the mixture.[612] In such cases, it is difficult to sufficiently sample the λ space even using biasing weight functions constructed by the Wang-Landau algorithm. This is especially the case when computing μ^{ex} of ions, such as Na^+.[612] Thermodynamic integration can therefore be used in multiple simulations for fixed values of $\lambda \in [0, 1]$ to compute the excess chemical potentials.[612]

3.3.1.5. Solubility of Hydrogen in the Liquid Phase. The solubility of H_2 in the liquid phase can be computed based on the excess chemical potential of H_2 in the liquid phase. The ideal gas chemical potential of H_2 (and therefore the number density) in the liquid phase is obtained by imposing equal chemical potentials of H_2 in the gas phase and the liquid phase ($\mu_{H_{2(g)}} = \mu_{H_{2(l)}}$). The solubility of H_2 in the liquid phase follows from[47,110]

$$\frac{\langle \rho_{H_{2(l)}} \rangle}{\rho_0} = \exp\left[\frac{\mu_{H_{2(l)}}^{id} - \mu_{H_2}^0}{k_B T}\right] = \exp\left[\frac{\mu_{H_{2(g)}} - \mu_{H_{2(l)}}^{ex} - \mu_{H_2}^0}{k_B T}\right] \tag{53}$$

At low fugacities of H_2, the solubility of H_2 can also be computed using Henry coefficients (H):

$$\frac{\langle \rho_{H_{2(l)}} \rangle}{\rho_0} = \lim_{f_{H_2} \to 0} \frac{f_{H_2}}{H} \tag{54}$$

The Henry coefficient of H_2 can be computed directly based on $\mu_{H_{2(l)}}^{ex}$:

$$H = \rho_0 k_B T \exp\left[\frac{\mu_{H_{2(l)}}^{ex}}{k_B T}\right] \tag{55}$$

At sufficiently low H_2 densities, the ideal gas law can also be used (i.e., $f_{H_2}=P_{H_2}=\rho_{H_2}k_BT$). This significantly simplifies the computation of H_2 solubilities compared to Eq. (53), as no simulations are needed for the gas phase.

3.3.1.6. Grand Equilibrium Method. The grand equilibrium method computes VLE for multi-component systems by equilibrating the liquid phase in the *NPT* ensemble, where the chemical potential is sampled using Widom's test particle insertion method (explained in Section 3.3.1.3).[48] From the chemical potential, the Henry constant is calculated at infinite dilution. The chemical potential is then fitted as a function of pressure ($\mu(P)$) at constant temperature and mixture composition and approximated using a Taylor series expansion. This function is subsequently used in a pseudo-μVT ensemble simulation of the vapor phase to sample the vapor pressure. Köster et al.[48] applied this method to compute VLE for H_2 multi-component systems.

3.3.1.7. Fugacity Coefficient. The fugacity coefficient of H_2 can be computed from the $\mu_{H_2}^{ex}$ or probability distribution of λ (see Eq. (51)) in a mixture using

$$\phi_{H_2} = \frac{\exp\left[\frac{\mu_{H_2}^{ex}}{k_B T}\right]}{Z_{mix}} = \frac{1}{Z_{mix}} \times \frac{p(\lambda_{H_2} = 0)}{p(\lambda_{H_2} = 1)} \tag{56}$$

where $Z_{mix} = \frac{P\langle V \rangle}{N_t RT}$ is the compressibility factor of the mixture, and N_t is the total number of moles in the mixture.

3.3.2. Hydrogen Adsorption onto Nanoporous Materials. The Grand Canonical Monte Carlo (GCMC) method (system at constant μ,V, T) is widely used to study gas adsorption in nanoporous media such as polymers, MOFs, COFs, zeolites, and CNTs.[51,52,317] In GCMC, a simulation box with constant volume containing the adsorbent (e.g., solid) is used,[51,52] assuming contact with an infinite reservoir (not explicitly considered) that holds the adsorbate (e.g., H_2 or gas mixture) at a specified temperature, pressure, and composition. Gas molecules are randomly inserted and deleted (adsorbed/absorbed and desorbed) onto the material surface or in the pores. The chemical potential of each component in the reservoir (and therefore the solubility of the adsorbate), $\mu_i(p, T, x)$, can be computed using an EoS or WTPI method (see Section 3.3.1.3) in the *NPT* ensemble. This ensemble can also be extended with fractional H_2 molecules to compute solubility, phase coexistence, and equilibrium properties more efficiently, following the principles outlined in Section 3.3.1.4

An alternative way to compute the solubility coefficient is to use the WTPI method in MD trajectories of only the adsorbent (e.g., MOF, ZIF). The MD simulation generates representative host configurations (usually in the order of 10^3 simulation snapshots). In each of these frames, a sole molecule of the gas under investigation is randomly inserted at various positions, to get adequate statistics on the conformations of the guest-host system, and at each insertion the energy of the system is calculated. An average over these different conformations yields μ_i^{ex} of the inserted species according to Eq. (50). The solubility, S_i, of component i (e.g., H_2), can be then obtained from

$$S_i = \frac{22400\ \text{cm}^3\ \text{STP}}{\text{mol}} \frac{1}{RT} \exp\left(-\frac{\mu_i^{ex}}{RT}\right) \tag{57}$$

As already shown in Eq. (56) in Section 3.3.1.7, the excess chemical potential can lead to fugacity. This facilitates the production of adsorption isotherms, by linking the fugacity to the number of existing sorbed molecules.

3.3.3. Hydrogen Adsorption and Separation of Gas Mixtures in Hydrates. As discussed in the previous section, GCMC simulations are widely used to compute gas adsorption in solid nanoporous materials. Considering that gas hydrates have a fixed and well defined geometry, enables simulating their formation as a process of adsorption of H_2 gas inside a porous solid material (i.e., the different cages are considered as effective pores). Namely, the hydrate lattice is treated as a rigid porous solid substrate (i.e., H_2O molecules are fixed in their positions, not allowed to move) where an adsorption site can be positioned anywhere within a hydrate cage belonging to the hydrate lattice. To this end, MC simulations have been performed with either in-house or open-source software (e.g., MCCCS Towhee[610]). While studies using GCMC simulations consider H_2O molecules fixed in space, Brumby et al.[633] reported MC simulations in the GE (Section 3.3.1.1), allowing isotropic volume change moves (i.e., H_2O movement) in

https://doi.org/10.1021/acs.chemrev.5c00617
Chem. Rev. 2025, 125, 11878−12029

addition to the regular MC moves, and reported good agreement with the counterpart GCMC studies.[248]

To determine the average occupancy θ (i.e., average number of H_2 molecules per cavity) for every cavity type, each H_2 molecule is assigned to the cavity center whose center is the closest. For a hydrate structure that contains k types of cavities with $n_{i,k}$ cavities of type i together with N_w water molecules in a single unit cell, the gas (H_2) content, expressed as weight percentage (wt.%), is given by

$$(\text{wt. \%}) = \frac{MW_g \cdot \sum_{i=1}^{k} n_{i,k} \cdot \theta_i}{MW_g \cdot \sum_{i=1}^{k} n_i \cdot \theta_i + N_w \cdot MW_w} \times 100 \tag{58}$$

where MW_g and MW_w are the molecular weights of the guest gas (g) and water (w), respectively. In the more general case where a promoter (i.e., guest that contributes in hydrate formation under more favorable P and T conditions) is also present in the hydrate structure, the term $n_p \cdot \theta_p \cdot MW_p$ needs to be added to the denominator of Eq. (58), where it is assumed that the promoter has a molecular weight MW_p and occupies the cavities of type p, with an average occupancy θ_p. Usually it is assumed that all of the promoter-designated cavities are fully occupied by a single promoter molecule, therefore, $\theta_p = 1$.

The basic input for a GCMC run is the chemical potential of the adsorbate, which can be calculated via different methods. During the earlier hydrate-related MC studies, a simpler approach was utilized that was based either on (i) the use of general-purpose, cubic EoS,[634−637] which largely failed at computing the chemical potentials of H_2 at the conditions of interest for storage in hydrates since they were not developed using H_2 data, or (ii) on component-specific[638,639] EoS, which partially solved this problem. Later MC studies[248,341,640,641] used a more refined approach for the calculation of the chemical potential and the correlation of chemical potential to the pressure of the system. In particular, a series of MC simulations of bulk H_2 in the NVT ensemble is performed from which the virial pressure is calculated. In a subsequent step, the excess chemical potential is calculated with WTPI[617] as explained in Section 3.3.1.3. The reference value of chemical potential, μ_0, is calculated from an additional NVT run where all interactions are set to zero. The chemical potential is, thus, calculated as a function of pressure, at a constant temperature. This approach is more reliable and self-consistent than using EoS, however, it requires additional computational resources. In this way, each run corresponds to a certain H_2 density and for this density the pressure and chemical potential are calculated from the appropriate equations. This procedure allows for the determination of the relation between pressure and chemical potential, while simultaneously, provides the EoS for H_2. Additional details regarding the methodology can be found in refs 248 and 641.

The separation of gas mixtures (e.g., H_2/CH_4 and H_2/CO_2) via hydrate formation is based on the principle that the different components of the gas mixture have a different distribution within the hydrate crystal compared to the original mixture composition. Therefore, a series of GCMC simulations can be performed at different P and T conditions to calculate the separation efficiency of the hydrate-based process. The simulation protocol is identical to the one described for the calculation of the hydrate gas storage capacities, applied however for the gas mixture, instead of the pure H_2 gas.

3.3.4. Heat Capacities, Thermal Expansivity, Joule−Thomson Coefficient, and Speed of Sound from Ensemble Fluctuations. Thermal expansivity (α_P), isothermal compressibility (β_T), isobaric heat capacity (C_P), isochoric heat capacity (C_V), and the Joule-Thomson coefficient μ_{JT} are derivative properties defined in classical thermodynamics as pressure or temperature derivatives.[571,642,643] These thermodynamic properties of H_2 gas or for multi-component H_2 systems at high pressures are computed using the so-called ensemble fluctuations in molecular simulations.[47,51] For the computation of heat capacity, ones needs to consider both the ideal and the residual contributions[644,645]

$$C_P(T, P) = \left(\frac{\partial \langle H \rangle}{\partial T}\right)_P = C_P^{id}(T) + C_P^{res}(T, P) \tag{59}$$

where

$$C_P^{res}(T, P) = \frac{1}{k_B T^2}[\langle U^{ext}\hat{H}\rangle - \langle U^{ext}\rangle\langle \hat{H}\rangle + P(\langle V\hat{H}\rangle - \langle V\rangle\langle \hat{H}\rangle)] - Nk_B \tag{60}$$

where N is the number of molecules in the system. Eq. (60) is derived by using the enthalpy, H,[645]

$$H = H^{id} + H^{res} \Rightarrow$$
$$H = U^{int} + K + Nk_BT + U^{ext} + PV - Nk_BT \Rightarrow$$
$$H = \hat{H} + K \tag{61}$$

where H^{id} and H^{res} are the ideal and residual parts of H, and K is the kinetic energy. C_P^{id} can be obtained from thermodynamic reference tables[643,646] or quantum mechanical calculations.[53,647]

Thermal expansivity (α_P) and isothermal compressibility (β_T) from ensemble fluctuations follow from

$$\alpha_P = \frac{1}{\langle V\rangle}\left(\frac{\partial \langle V\rangle}{\partial T}\right)_P = \frac{1}{k_B T^2 \langle V\rangle}(\langle V\hat{H}\rangle - \langle V\rangle\langle \hat{H}\rangle) \tag{62}$$

$$\beta_T = -\frac{1}{\langle V\rangle}\left(\frac{\partial V}{\partial P}\right)_T = -\frac{1}{k_B T \langle V\rangle}(\langle V^2\rangle - \langle V\rangle^2) \tag{63}$$

Having obtained α_P and β_T, one can also calculate the isochoric heat capacity from

$$C_V = C_P - \frac{T\langle V\rangle \alpha_P{}^2}{\beta_T} \tag{64}$$

The Joule−Thomson coefficient (μ_{JT}) and speed of sound (c_{sound}) follow from

$$\mu_{JT} = \left(\frac{\partial T}{\partial P}\right)_H = -\left(\frac{\partial H}{\partial P}\right)_T \frac{1}{C_P} = \frac{1}{c_P}\left[T\left(\frac{\partial v}{\partial T}\right)_P - v\right] = \frac{v}{c_P}[T\alpha_P - 1] \tag{65}$$

and

$$c_{sound} = \sqrt{\frac{c_P}{c_V \times \beta_P \times \rho}} \tag{66}$$

where c_P, c_V and v are the specific heat capacities and the specific volume, respectively. In principle, the same fluctuation-based formulas and methods used to compute thermodynamic properties in MC simulations also apply to MD simulations performed in the same ensemble (e.g., see ref 308). Another example of using ensemble fluctuations in MD simulations is

https://doi.org/10.1021/acs.chemrev.5c00617
Chem. Rev. 2025, 125, 11878−12029

the study by Rahbari et al.[94] where partial molar volumes and partial molar enthalpies of water in Nafion membranes were computed at different water uptakes.

It is noteworthy that for multi-component systems, the analytical expressions for thermodynamic derivatives based on fluctuations become increasingly complex. In such cases, using alternative methods such as the multiple linear regression are more practical and conceptually straightforward as shown by Rahbari et al.[648].

3.3.5. Hydrogen Diffusivity in Metals via Kinetic Monte Carlo. KMC provides a framework for simulating H diffusion across experimentally relevant time scales (nanoseconds to seconds) while retaining atomistic resolution of individual hopping events.[649,650] The method is transferable across crystal structures. Here we illustrate with bcc and fcc lattices (such as Fe and Ni), though only the site topology and hop catalog require modification for other lattices. The simulation protocol begins by constructing a periodic supercell containing all symmetry-inequivalent interstitial sites (tetrahedral, octahedral) and defect traps (vacancies, dislocations, GBs). Each site i is assigned a solution energy E_i^{sol} from DFT or validated potentials. For each allowed transition $i \rightarrow j$, the CI-NEB calculations[651] are used to determine the saddle-point energy $E_{i\rightarrow j}^{\dagger}$, while harmonic transition-state theory yields the prefactor $\nu_{i\rightarrow j}$ (or a representative $\nu \approx 10^{13}$ s^{-1} when phonon calculations are unavailable).[652] Symmetry operations reduce equivalent hops to a minimal set stored for reuse. The hop rate follows from

$$k_{i\rightarrow j} = \nu_{i\rightarrow j} \exp\left[-\frac{E_{i\rightarrow j}^{\dagger} - E_i}{k_{\mathrm{B}}T}\right] \tag{67}$$

where $E_i = E_i^{\mathrm{sol}} + E_i^{\mathrm{int}} + E_i^{\sigma}$ combines solution, interaction (H-H or H-defect), and optional elastic terms. The residence-time algorithm proceeds by: (1) selecting events proportionally to their rates using $u_1 K$ ($u_1 \in (0, 1]$, $K = \sum_m k_m$), (2) advancing time by $\Delta t = -\ln u_2/K$ ($u_2 \in (0, 1]$), (3) updating affected rates and heap structure, and (4) recording observables. The diffusivity is computed using the method described in Section 3.2.3, while trap statistics emerge from waiting-time distributions at defect sites.

A fundamental limitation of conventional KMC is its dependence on a predefined event catalog, in which all possible hops and their associated barriers must be known in advance. This requirement is tractable in pristine bcc or fcc lattices or for simple defects such as isolated vacancies, where diffusion pathways can be exhaustively enumerated. However, it becomes prohibitive in materials exhibiting a rich variety of local environments, such as H at complex GBs or dislocation cores, and is further exacerbated in chemically disordered systems like high-entropy alloys (see Section 4.11.6), where the combinatorial explosion of distinct atomic configurations yields effectively infinite diffusion paths and barrier values. Two strategies promise to remove this bottleneck. (i) On-the-fly KMC (for example using the kinetic Activation-Relaxation Technique) triggers a local saddle search whenever the system enters a new atomic environment, stores the resulting barrier under a topological fingerprint, and reuses it on subsequent visits.[653] (ii) Machine-learning-assisted KMC trains a surrogate model (neural network) on a modest set of barriers from DFT or highly accurate interatomic potentials, predicts activation energies from local descriptors during the run.[468,654] These adaptive workflows dispense with a static catalogue and make KMC practical for H diffusion in chemically and structurally heterogeneous micro-structures.

GCMC (see Section 3.3.2), on the other hand, can be an efficient pre-equilibration method for multi-scale diffusion studies. GCMC "teleports" H atoms directly into deep traps such as vacancies, dislocation cores and GB sites, thereby establishing the equilibrium occupancy that ordinary diffusion would approach only after long KMC or MD times.[552] To generate KMC-ready H distributions one first fixes the external chemical potential μ_{H} (or the equivalent gas pressure) and builds a simulation cell, starting with a defect-free lattice to calibrate bulk solubility and later expanding it to include vacancies, dislocations, GBS or precipitates. A cavity-biased grand-canonical Monte Carlo (CB-GCMC) pre-equilibration then accelerates sampling: the lattice is scanned once to catalogue genuine interstitial cavities, after which each MC sweep attempts three move types, namely (i) small displacements of existing H atoms, accepted according to the Metropolis criterion; (ii) insertions of H atoms restricted to the pre-identified cavities; and (iii) deletions of cavity-hosted H atoms, with both insertion and deletion accepted or rejected by the grand-canonical rule. The thermodynamically consistent, trap-filled configurations produced by CB-GCMC can be used for subsequent MD simulations that target H-affected deformation such as crack propagation[553] and dislocation motion,[550] allowing those simulations to focus on the relevant kinetics rather than spending computational time on equilibration.

4. REVIEW OF THERMOPHYSICAL PROPERTIES OF HYDROGEN SYSTEMS COMPUTED WITH MOLECULAR SIMULATION

As discussed in Section 2, reliable thermophysical property predictions are essential for the design and optimization of all major H_2 processes, i.e., water electrolysis, compression, storage, transportation, liquefaction, and underground sequestration. The relevance of data derived from molecular simulations lies both in the ability to extract physical insight from molecular structures and interactions, and in the reduction of required experimental measurements under hazardous or challenging conditions, e.g., high pressures or toxic environments. To this extent, the use of molecular simulation in the process design of H_2 systems can greatly strengthen engineering workflows by providing reliable data on-demand. Here, we compile an extensive review of the available literature on classical molecular simulation of both pure H_2 and of H_2 systems involving other gases, liquids, and solids. Our discussion spans VLE of aqueous and non-aqueous H_2 solutions, electrolyte systems, thermophysical properties, transport coefficients, and interfacial phenomena. Due to the extended body of literature reporting properties of H_2 combined with porous and 2D materials (studied via both classical and quantum simulation methods), we limit the respective part of our review to mostly materials useful in UHS, hydrates, polymeric/composites, and metals. Nevertheless, a short overview of H_2/membrane/nanoporous systems is provided, espcecially in light of the new advancements in the field exploiting ML and AI approaches.

4.1. Thermodynamic and Transport Properties of Aqueous Hydrogen Solutions

4.1.1. Vapor−Liquid Equilibrium, Fugacity, and Henry Coefficients of Aqueous Hydrogen Solutions.

https://doi.org/10.1021/acs.chemrev.5c00617
Chem. Rev. 2025, 125, 11878−12029

Table 9. Representative List of Phase Equilibrium Calculations of H_2-Containing Systems Using Molecular Simulations, Along with Relevant Details on Systems, Force Fields, Conditions, and Methods[a]

		System Details		Thermodynamic Conditions		Simulation Method
Year	Study	System	Force Fields	Pressure	Temperature	
1993	Buch and Devlin[661]	H_2O(s), H_2(g)	Buch[661]		12 K	Diffusion MC, Path Integral MC
1994	Buch[312]	(para-D_2)$_3$(ortho-D_2)$_{10}$ and (para-D_2)$_{13}$ clusters	Buch[312]		1-3 K	Path Integral MC
1998	Rzepka et al.[322]	H_2(g), Carbon Slitpores, Carbon Nanotubes(s)	Rzepka (H_2)	10-30 MPa	50-600 K	GCMC
1999	Darkrim et al.[327]	N_2(g), H_2(g), Graphite(s)	Darkrim[327]	0-600 MPa (N_2: 0-500 MPa, H_2: 0-60 MPa)	77 and 293 K	GCMC
2001	Cracknell[311]	H_2(g), Graphitic Nanofibres (GNFs)(s)	Buch,[312] Cracknell[311]	1-112 bar	298 K	GCMC
2005	Urukova et al.[662]	CO_2(g), CO(g), H_2(g), [bmim][PF_6](l)	Cracknell[311]	Up to 9 MPa	293 - 393 K	GE
2007	Ferrando et al.[323]	H_2(g), n-Alkanes(g), Iso-Alkanes(g), Alkenes(g), Cycloalkanes(g), Aromatics(g), Polyaromatics(g)	Hirschfelder,[321] Corresponding State, Darkrim,[327] Cracknell	20.1-1200 bar	160-664.1 K	GE
2018	Köster et al.[48]	H_2, N_2, H_2O, Ar, O_2	Vrabec, Marx[310]	Up to 304.5 MPa	83.15-625 K	NPT, μ-VT
2019	Rahbari et al.[110]	H_2(g), H_2O(l)	Hirschfelder,[321] Buch,[312] Vrabec,[48] Cracknell,[311] Marx[310]	10-1000 bar	283-423 K	CFCMC
2020	Salehi et al.[663]	CO_2(g), H_2S(g), CH_4(g), CO(g), H_2(g), N_2(g), ChClU(l), ChClEg(l)	H_2 (Cracknell[311]), GAFF (ChClEg), OPLS (ChClEg)	1 bar	328 K	CFCMC
2021	Rahbari et al.[47]	H_2(g), H_2O(l), Ice Ih(s)	TIP3P, Modified TIP4P (TIP4Pμ); Marx,[310] Vrabec,[48] Cracknell,[311] Buch,[312] Hirschfelder (H_2)	50-1000 bar (VLE: 100-1000 bar)	264.21-423.15 K	CFCMC
2021	Liu et al.[664]	CO_2(g), SO_2(g), N_2(g), CH_4(g), H_2(g), Ionic Liquid(l)	Cracknell,[311] OPLS-AA (ILs)	1 bar	300 K	NPT(MD)-GCMC
2022	Caviedes et al.[324]	H_2(g), Carbon nano-pores(s)	Rzepka (H_2(g)), Steele,[665] Tjatjopoulos[666] and Siderius-Gelb[667] potentials for pore interactions	0.1-35 MPa	298.15 K	GCMC

[a]The data also contain non-aqueous systems for completeness.

https://doi.org/10.1021/acs.chemrev.5c00617
Chem. Rev. 2025, 125, 11878−12029

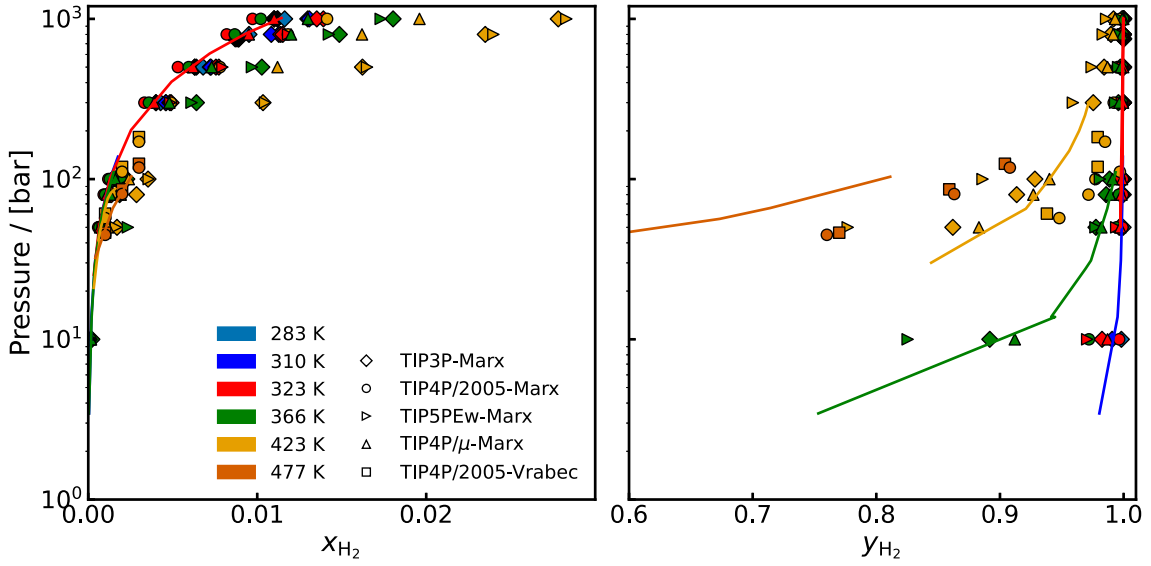

Figure 18. Isothermal phase diagram of the water-hydrogen system computed from molecular simulations, as reported in refs 47, 48, and 110. The solid lines represent experimental data. Simulation parameters and force field details are provided in refs 47, 48, and 110.

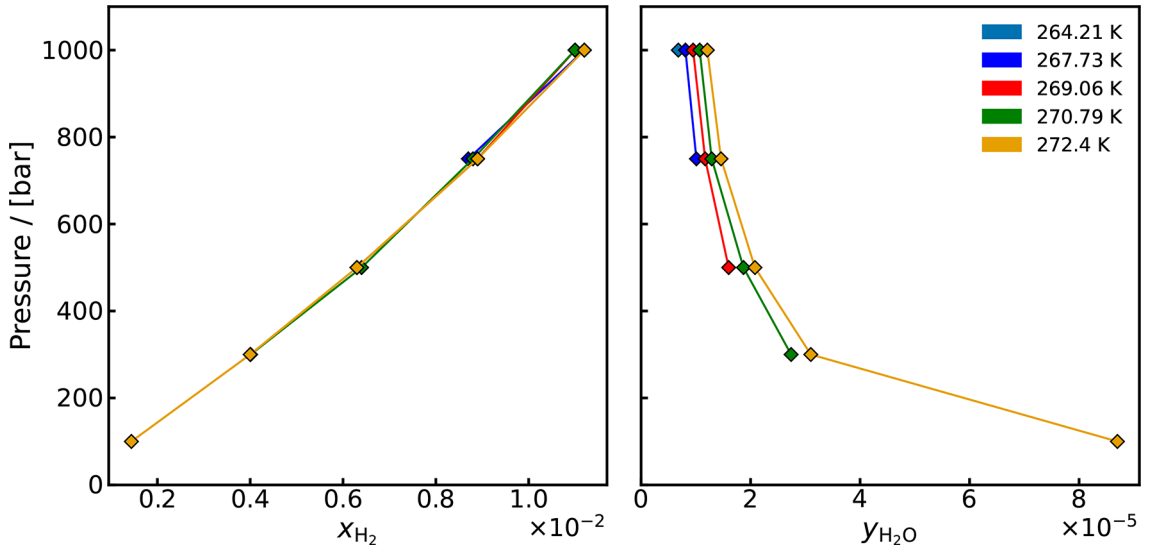

Figure 19. VLE of water hydrogen along the melting line of ice and higher pressures than the corresponding equilibrium pressure. The force field combination shown is TIP3P-Marx. The lines connecting the markers are drawn to guide the eye.

The knowledge of VLE of aqueous H_2 solutions is essential for the design and optimization of electrochemical systems and storage processes. In water electrolysis, the gas stream exiting the electrolyzer or separator tank typically consists of H_2 saturated with water vapor. Accurate determination of the partial pressure of water in H_2 is therefore critical for the design of downstream units such as knockout drums or dryers. Conversely, the solubility of H_2 in water or aqueous electrolyte solutions is necessary for modeling concentration gradients within the electrolyte phase, for instance when calculating gas crossover. An overview of representative molecular simulation studies reporting phase equilibria data of H_2 systems is provided in Table 9. The table includes both aqueous and non-aqueous systems (e.g., H_2-hydrocarbon systems) to provide the reader a view of the available literature.

Rahbari et al.[110] computed densities and fugacities of pure H_2, the VLE of H_2-water systems covering temperatures of 310, 323, 366, and 423 K, and pressures ranging from 10 to 1000 bar, and VLE at low temperatures along the melting line of ice I_h, corresponding to a temperature range of 264.21-272.4 K.[47] This low-temperature regime is particularly relevant for evaluating the thermodynamic behavior of H_2-water mixtures in refueling stations utilizing electrochemical compression. Several rigid, non-polarizable force fields were used in the CFCGE and CFC*NPT* ensembles (see Section 3.3.1.4). In the study by Köster et al.,[48] the Grand Equilibrium method (see methodology in Section 3.3.1.6) was used to calculate the VLE of binary H_2-water at 423 and 477.59 K for pressures in the range of 57 to 125 bar, as well as ternary mixtures of N_2-Ar-H_2 (which are discussed in Section 4.2). The solubilities of H_2-water systems at high pressures reported in refs 47, 48, and 110 are compiled in Fig. 18.

It is evident that experimental solubility data at elevated pressures remain limited. Available high-pressure solubility and VLE data have been compiled and reported in ref 110. For the gas phase, solubility measurements used for validation are in

https://doi.org/10.1021/acs.chemrev.5c00617
Chem. Rev. 2025, 125, 11878−12029

the following pressure ranges: 50-300 bar at 423 K, 3.45-110 bar at 366 K, 50-1013 bar at 323 K (the widest pressure range), and 3.44-138 bar at 310 K. For the liquid phase, experimental solubility data span 20-87 bar at 423 K, 3-110 bar at 366 K, up to 1013 bar at 323 K, and 3.45-138 bar at 310 K. These data, as visualized in Fig. 18, serve as a benchmark for evaluating the performance of various force field combinations in reproducing VLE behavior across different thermodynamic conditions. The raw solubility data from molecular simulations, used in Fig. 18, are provided in the Supporting Information of refs 47, 48, and 110 for several H_2 models, including Hirschfelder,[321] Vrabec,[48] Buch,[312] the two-site model of Cracknell,[311] and the multi-site model of Marx.[310] Fig. 18 shows that the TIP3P and TIP4P/μ (see Section 4.1.2.1) water models, when combined with the Marx force field for H_2, yield the best agreement with experimental gas-phase solubility data. For the liquid phase, solubilities are most accurately captured using the TIP4P/μ combined with the Marx force field;[47] however, this comes at the cost of reduced accuracy in predicting liquid water densities compared to the TIP4P/2005 model. These findings underscore that while specific force field combinations can be tuned to yield accurate phase composition predictions, this often involves trade-offs with other thermophysical properties.

In ref 47, the TIP3P and TIP4P/2005 force fields were used to compute the VLE of the H_2-water system along the ice melting line and at elevated pressures. The results are presented in Fig. 19. TIP3P was selected in that study due to its superior performance in reproducing gas-phase compositions, as previously demonstrated by Rahbari et al.[110] Given the low solubility of water in H_2 at low temperatures, the mole fractions of water are plotted in Fig. 19 (right panel), rather than showing the H_2 mole fraction, which approaches unity under these conditions. This representation is particularly relevant for applications involving deep-freezing of H_2, such as at refueling stations, where accurate knowledge or prediction of water content at low temperatures is essential. No experimental data were found in published literature for the H_2-water system at such high pressures, highlighting the value of molecular simulation as a powerful predictive tool to estimate VLE behavior where experimental data are lacking. For this, appropriately validated force fields is a prerequisite.

A notable advantage of the CFCMC method for VLE calculations is that in addition to determining phase coexistence, it enables direct sampling of the excess chemical potentials of each component in both phases through random walks in λ space. This facilitates the calculation of fugacity coefficients and Henry's law constants within the same simulation framework. The fugacity coefficients of pure H_2-calculated using the CFC*NPT* ensemble-and fugacity coefficients of H_2 in the gas phase from VLE simulations using the CFCGE or CFC*NPT* ensembles are presented in Fig. 20. As discussed earlier, fugacity coefficients and Henry's law constants are obtained inherently in these methods by introducing a fractional molecule and performing random walks in λ space.

H_2 solubilities in the liquid phase obtained from the excess chemical potential, can be reported in form of Henry coefficient. The Henry coefficient (in units of bar) in ref 48 was computed using the following thermodynamic relation:

$$H = \rho k_B T \exp(\mu^{inf}/(k_B T)) \tag{68}$$

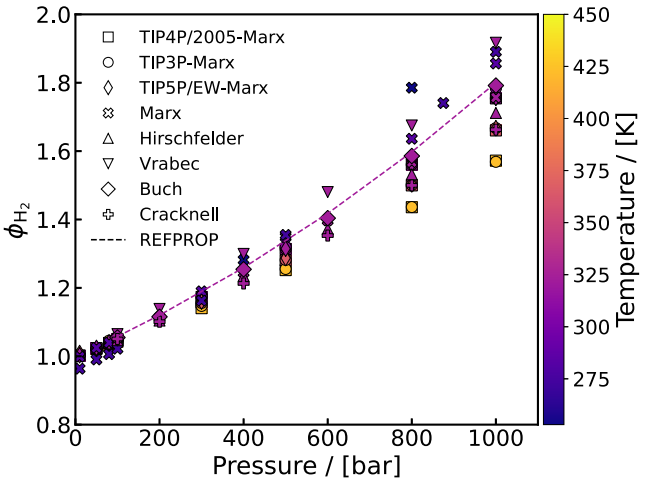

Figure 20. Fugacity coefficients of hydrogen computed for different force fields as a function of pressure. The data are obtained from legacy raw simulation data in refs 47 and 110 which have not been previously published, except for pure hydrogen at 323 K. As a reference, the fugacity coefficient of hydrogen at 323 K from REFPROP[352] is shown.

where μ^{inf} is the excess chemical potential at infinite dilution and ρ is the saturated liquid density of the solvent. In the MD simulation study by Zhang et al.[655], the Henry constant is reported in units of bar^{-1} and is calculated using

$$H_{MD} = \frac{\exp(-\mu^{inf}/(k_B T))}{\rho k_B T}. \tag{69}$$

Henry's law coefficients for H_2 in water reported by Köster et al.[48] were obtained over a broad temperature range of 280-625 K. These results exhibit the characteristic non-monotonic temperature dependence of H_2 solubility, with a clear maximum in the Henry's constant between 330 and 370 K, indicative of the low solubility of H_2 in water at intermediate temperatures. Zhang et al.[655] also calcualted the Henry coefficient of H_2 for different force fields of water and H_2 using MD simulations combined with the WTPI method (see Section 3.3.1.3).

Henry coefficients reported by Köster et al. and Zhang et al. are presented in Fig. 21. To ensure consistent units in the figure, the reported Henry coefficients by Zhang et al.[655] were converted to units of GPa. For completeness, the original correlation by the authors, valid at 273-433 K and 1 bar, is provided here as well:

$$H[\frac{x_{H_2}}{bar}] = 2.0369 \times 10^{-4} - 1.4628 \times 10^{-6} T + 3.6181 \times 10^{-9} T^2 - 2.8405 \times 10^{-12} T^3 \tag{70}$$

Experimental data compiled from refs 656 and 657 as cited by Zhang et al., are labeled as Exp. 1 in Fig. 21, while additional Henry coefficients reported by Zhang et al.[655], based on data from Alvarez,[658] are labeled as Exp. 2. The Exp. 1 dataset demonstrates internal consistency and excellent agreement with molecular simulation results. In contrast, the data from Alvarez significantly deviate from the other two sources, and are thus, distinguished as a separate experimental set, i.e., Exp. 2. Zhang et al. reported that the combination of TIP4P/2005 for water and the hydrogen model by Yang[325] yields excellent agreement with the Exp. 1 dataset. However, their reported

https://doi.org/10.1021/acs.chemrev.5c00617
Chem. Rev. 2025, 125, 11878−12029

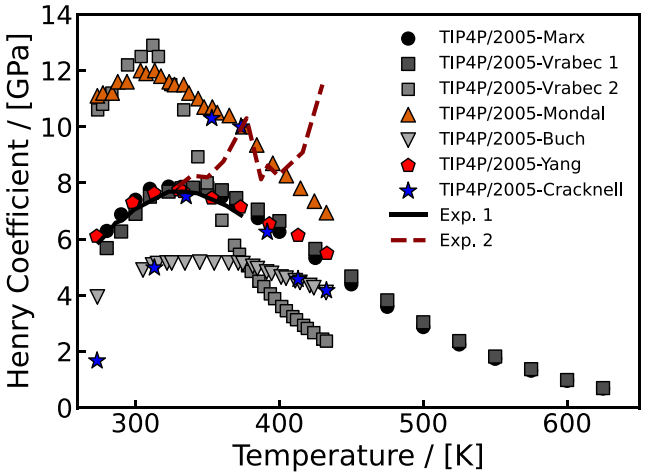

Figure 21. Henry coefficient of hydrogen in water as a function of temperature and pressure were compiled from refs 48 and 655. In ref 48, the Henry coefficients were calculated over a temperature range of 280-625 K. Zhang et al.[655] employed the TIP4P/2005 water model in combination with various hydrogen force fields, including those by Buch, Mondal, Yang, Cracknell, and Vrabec. To differentiate between the datasets corresponding to the TIP4P/2005-Vrabec force field combination, the results from Köster et al. are referred to as the first set, while those reported by Zhang et al. are designated as the second set. Exp. 1 are experimental data from refs 655−657 and Exp. 2 from refs 655 and 658.

Henry coefficients based on the TIP4P/2005-Vrabec force field combination show inconsistencies when compared to those by Köster et al., whose results align well with the experimental data. The H_2 force fields developed by Buch and Mondal reproduce the temperature dependence observed in the experimental data but systematically overpredict solubility across the entire temperature range. Nevertheless, both models are able to quantitatively capture the peak in the Henry coefficient between 300 and 350 K. Thermodynamic and structural properties of H_2 gas in bulk water computed via MC simulations have also been reported by Sabo et al.[659,660]

4.1.2. Vapor−Liquid Equilibrium of Aqueous Hydrogen Electrolyte Solutions. Obtaining accurate thermodynamic properties of aqueous electrolyte solutions is considered one of the most challenging modeling problems in applied thermodynamics due to the complex interactions between the dissolved ions and the solvent.[668−671] Nevertheless, this is highly relevant for developing H_2 technologies, which often involve electrolytes, e.g., alkaline solutions in electrolysis cells. Typical salts encountered in H_2 applications are NaCl, NaOH, and KOH. For example, the solubility of H_2 in aqueous NaCl solutions is relevant for underground storage of H_2, and therefore, the prediction of accurate data at high temperatures (up to 500 K) and pressures (up to 1000 bar) is central.[630,672]

The reduction in the solubility of non-polar gasses in water in the presence of salts (ofter referred to as the salting-out effect) is a well-established phenomenon.[656,673,674] The salting-out effect of H_2 in aqueous solutions has also been studied using molecular simulations.[112,113,630,672,675] van Rooijen et al.,[630] Zhang et al.,[676] Kerkache et al.,[672] and Lopez-Lazaro et al.[675] computed the solubility of H_2 in concentrated NaCl solutions using MC simulations. Lopez-Lazaro et al.[675] and Zhang et al.[676] used the WTPI method to estimate the excess chemical potential of H_2 in aqueous NaCl solutions (from which H_2 solubilities can be computed as discussed in detail in Section 3.3.1). van Rooijen et al.[630] and Kerkache et al.[672] both performed CFCMC simulations to compute excess chemical potentials. As shown in Fig. 22(a), which is a compilation of solubility data from different studies, the H_2 solubilities computed using the WTPI[675] have error bars ca. 5 times larger than the solubilities computed using CFCMC calculations.[630,672] This showcases that the gradual insertion using the CFCMC method allows for much better sampling of the excess chemical potentials compared to the WTPI (particularly in the liquid phase). The marginal differences between the solubilities computed in the different studies can be almost solely attributed to the choice of force fields, as discussed thoroughly later on.

It has been shown that scaling down the partial charges of ions can improve the accuracy in predicting thermodynamic and transport properties in systems involving electrolytes.[347,394,395] This holds true also for aqueous H_2 electrolyte solutions, where the choice of scaled or un-scaled force fields

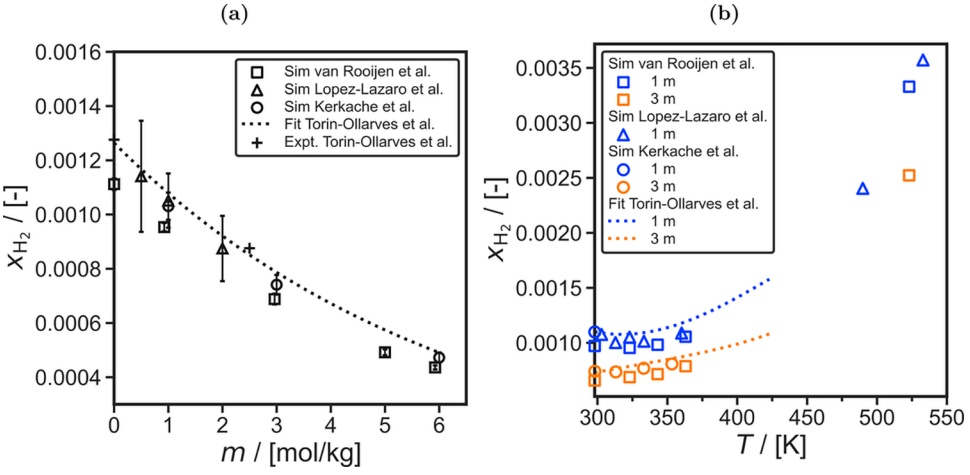

Figure 22. Solubilities of H_2 (x_{H_2}) in aqueous NaCl solutions at a H_2 fugacity of 100 bar at (a) 323 K as functions of salt molality m (in units of mol salt / kg water), and (b) as functions of temperature T. The MC simulation data of van Rooijen et al.[630] and Lopez-Lazaro et al.[675] are shown. The MC data of Kerkache et al.[672] for solubilities of Marx H_2 in TIP4P/2005 water and Madrid-2019[347] NaCl with adjusted interaction parameters (k_{ij} for H_2-H_2O) is also plotted. The experimental fit of Torin-Ollarves and Trusler[674] is shown for comparison.

https://doi.org/10.1021/acs.chemrev.5c00617
Chem. Rev. 2025, 125, 11878−12029

plays a dominant role. van Rooijen et al.[630] combined Marx (for H_2), TIP4P/2005 (for water), and the Madrid-2019 NaCl force fields. Kerkache et al.[672] tested several different model combinations for H_2O (i.e., TIP4P/2005, SPC/E, and TIP4P/EW), H_2 (i.e., Marx, Alavi, and Yang and Zhong), and NaCl (i.e., Madrid-2019, KBF, and OPLS). Madrid-2019 NaCl has scaled charges of +0.85 / -0.85 [e], while KBF and OPLS have charges of +1 / -1 [e]. Kerkache et al.[672] showed that NaCl force fields with un-scaled charges under-predict the solubilities of H_2 (thereby over-predicting the salting out effect), especially at higher salt molalities (≥ 4 mol salt / kg water). Lopez-Lazaro et al.[675] and Zhang et al.[676] also showed that the combination of Darkrim H_2 force field with TIP4P/2005 water, and OPLS, Joung-Cheatam, Smith, and Dang NaCl force fields (all having un-scaled charges) under-predict the solubility of H_2 in aqueous NaCl solutions by ca. 25%. Despite this, behavior of H_2 solubilities as a function of temperature is correctly predicted in refs 675 and 676. To accurately model the salting out of H_2 in aqueous NaCl solutions, Lopez-Lazaro et al.[675] adjusted the LB mixing rules for Na^+-H_2 and Cl^--H_2. Madrid-2019 NaCl force field with scaled charges of +0.85 / -0.85 [e] was shown to perform accurately in predicting the salting out of H_2 in aqueous NaCl solutions without any further fitting of mixing rules as shown in Fig. 22 and discussed in refs 630 and 672.

Habibi et al.[112] computed the solubilities of H_2 and O_2 in aqueous KOH and NaOH solutions using the scaled charge force fields Madrid-Transport (K^+ and Na^+) and the DFF/OH^- (developed in the same study). The authors performed CFCMC simulations at a temperature and pressure range of 298-353 K and 1-100 bar, respectively. The authors showed that thew newly developed DFF/OH^- model accurately predicts densities and viscosities (5 to 20% deviations) of the aqueous NaOH and KOH solutions up to molalities of 8 mol/kg. The expected salting-out effect with increasing electrolyte concentration was also captured. Engineering equations were fitted using the simulation data for both solubilities and diffusivities of the gases in the aqueous solutions. It is important to note that the solubilities of H_2 in water are ca. 1 order of magnitude smaller at a concentration of 8 mol KOH / L solution compared to the solubilities of H_2 in pure water. Therefore, the choice of the salt force field is crucial when computing the solubility of H_2 in the aqueous phase. This is also the main motivation for heavily discussing the performance of force fields in this section.

Hulikal Chakrapani et al.[677] performed molecular simulations to compute the solubilities of H_2-CO_2 mixtures in aqueous NaCl solutions over a wide range of pressures (5-50 MPa), temperatures (323.15-423.15 K), and salinities (0-2 molal NaCl). TIP4P/μ,[110] all-atom TraPPE,[678] and Marx[328] force fields were used for water, CO_2, and H_2, respectively. Using the CFCGE (see Section 3.3.1.1) method, solubilities of H_2, CO_2, and H_2O were computed by equilibrating chemical potentials between the gas and liquid phases, with a fixed initial 1:1 H_2:CO_2 gas phase ratio. CO_2 solubility in aqueous NaCl solutions increased with pressure and temperature, but decreased with salinity due to the salting-out effect (well captured by the Setschenow equation[679]). The decline in solubility followed a consistent slope of approximately −0.21, independently of pressure and temperature. At low pressures (<10 MPa), CO_2 solubility rose linearly, transitioning to a non-linear behavior at higher pressures. Simulations matched experiments within 5-10% at 423.15 K. Larger deviations were observed at lower temperatures.

In the study of Hulikal Chakrapani et al.[677] H_2, solubility increased with temperature across the range 323.15−423.15 K, at all pressures and salt concentrations. However, at a fixed pressure and temperature, the solubility of H_2 decreased with increasing salt concentration, exhibiting a Setschenow-type[679] slope of −0.11 to −0.19, corresponding to ca. 15% decrease in solubility per mole NaCl. The simulation results showed good agreement (within 5−10%) with experimental data at 323.15 K, though higher temperatures and pressures led to slight overestimations. In CO_2 − H_2 − H_2O − NaCl systems, CO_2 solubility was shown to be lower than in CO_2 − H_2O − NaCl (see Fig. 23a), whereas H_2 solubility increased (see Fig. 23b),

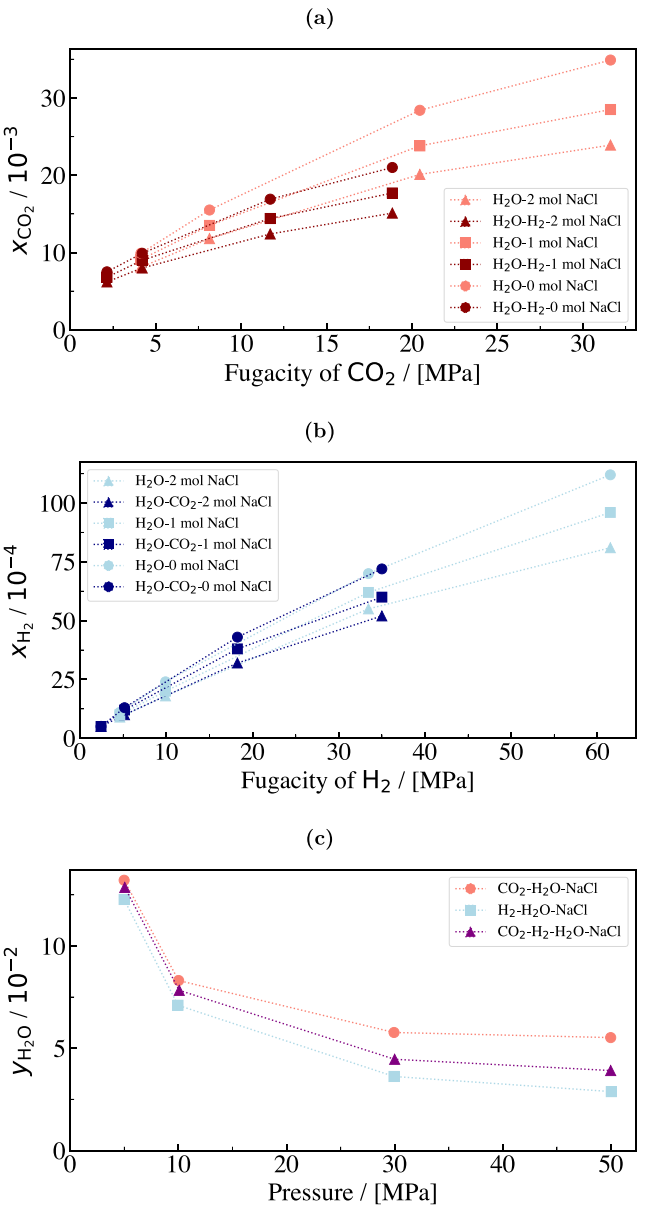

Figure 23. (a) The solubility of CO_2 in different aqueous NaCl solutions as a function of CO_2 fugacity. (b) The solubility of H_2 in different aqueous NaCl solutions as a function of H_2 fugacity. (c) The mole fraction of H_2O in the gas phase as a function of pressure for different aqueous NaCl-H_2 mixtures. The lines connecting the markers are drawn to guide the eye.

https://doi.org/10.1021/acs.chemrev.5c00617
Chem. Rev. 2025, 125, 11878−12029

suggesting a cooperative mechanism where H_2 promotes its own solubility while suppressing that of CO_2. Water content in the gas phase was computed to be between the values observed in the CO_2 and H_2 aqueous electrolyte systems (see Fig. 23c). At 423.15 K, water content decreased with pressure but showed little dependence on salt concentration. At 323.15 K, the water content remained nearly constant, while at 423.15 K it was found to be 20−40 times greater than the value at 323.15 K, when considered across all pressures.

The solubilities of H_2 in aqueous $NaB(OH)_4$ solutions were recently computed using CFCMC simulations at 298−363 K and 1 bar.[113] This electrolyte is relevant for applications related to hydrolysis of $NaBH_4$ solutions for H_2 storage. The presence of 5 mol $NaB(OH)_4$ / kg water is shown to significantly reduce both H_2 solubilities (by a factor of ca. 0.4) and the activities of water (by a factor 0.75). In a follow up work also focusing on $NaBH_4$ as a H_2 energy carrier, Postma et al.[680] developed a new force field (i.e., the DFF/BH_4^-, extending the DFF family) performed MD simulations to compute densities and viscosities of $NaBH_4$ (in the range 0 to 5 mol salt / kg water), $NaB(OH)_4$ (0 to 3 m), and 1 m NaOH aqueous solutions at 295 K. The predicted properties were within ca. 2% and 10% from the respective experimental data. The authors used the MD data to devise engineering correlations for densities, viscosities, and self-diffusivities for these systems which can be used as a fast model when data are required for e.g., $NaBH_4$ hydrolysis reactor design.

4.1.2.1. Force Field Performance and the Effective Charge Surface Approach. It is observed in the pervious section that obtaining accurate VLE data reequires careful selection of force field combinations for hydrogen and water. The results show that there is not a single combination of classical force fields that can predict all thermodynamic and transport properties accurately. An illustrative example is provided in Fig. 24,

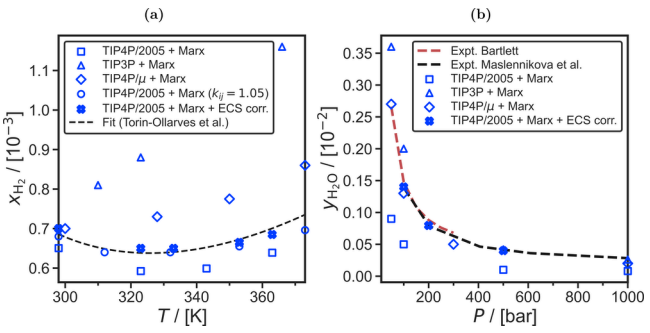

Figure 24. (a) Solubilities of H_2 (in units of mole fraction x_{H_2}) in liquid water at a H_2 fugacity of 50 bar as functions of temperature. (b) Solubilities of H_2O (in units of mole fraction y_{H_2O}) in gaseous H_2 at 323 K as functions of total pressure. The MC data for x_{H_2} and y_{H_2O} for the combination of Marx[310] H_2 force field and TIP4P/2005 and TIP3P water is obtained from Rahbari et al.[46] The MC data for x_{H_2} and y_{H_2O} of Marx[310] H_2 and modified TIP4P (herein referred to as TIP4P/μ) is obtained from refs 111 and 47, respectively. The MC data of Kerkache et al.[672] for solubilities of Marx H_2 in TIP4P/2005 with adjusted interaction parameters (k_{ij} for H_2-H_2O) is also shown in (a). The MC data for Marx[310] and TIP4P/2005 water force field including the ECS free energy correction as introduced by Habibi et al.[350] is obtained from ref 111. The experimental fit of Torin-Ollarves and Trusler[674] for x_{H_2} and the experimental data of Maslennikova et al.[681] and Bartlett[682] for y_{H_2O} are shown for comparison.

aiming to show the differences in performance as a result of different force field parameterization. Figure 24 shows the solubilities of H_2 in liquid water and the solubilities of water in gaseous H_2 computed using MC simulations at 323 K and pressures from 10 to 1000 bar.

In ref 110 it is shown that the TIP3P water force field[300] combined with the Marx[310] force field results in accurate predictions for the equilibrium water content in the gas phase but cannot accurately predict the solubilities of H_2 in the liquid phase. The TIP4P/2005 water force field and the Marx[310] force field result in accurate predictions for the solubility of H_2 in water (and the variations with respect to temperature), but the water content in H_2 is under-predicted with respect to experiments (e.g., by a factor of 3 at 323 K).[110] The TIP3P water force field paramters are fitted on the vaporization energy of water, and can thereby correctly predict the experimental vapor pressure of water and the water content in the gas phase.[110,350] The TIP4P/2005[349] water force field parameters are trained on the liquid phase properties such as densities, temperature of maximum density, and transport properties (e.g., shear viscosities of water), and can thereby predict the solubilities of H_2 in water (and their temperature dependence) accurately with respect to experiments.[110]

In ref 47, a modified version of TIP4P/2005 (i.e., using the same geometry) was employed by scaling the atomic charges by a factor of 0.955, resulting in a dipole moment of 2.2 D. Subsequently, the Lennard-Jones energy parameter ϵ for oxygen was adjusted to 79.86 K to better match the chemical potential of liquid water. The TIP4P/μ accurately models the excess chemical potential of water (i.e., with respect to the ideal gas reference state), and results in accurate modeling of the water content in H_2. The solubilities of the Marx H_2 force field[310] in water at 298 K are also accurately modeled. However, the temperature dependence of H_2 solubilities in water are not accurately captured (no minimum is observed in H_2 solubilities at ca. 323 K similar to experiments[683]).

The reason why it is difficult to model the VLE of H_2 and water systems using non-polarizable water force fields can be traced back to the paper of Berendsen et al.[346] in 1987. Berendsen et al.[346] discussed that non-polarizable water force fields cannot capture both the experimental vaporization energy of water (required for modeling the vapor pressures of water) and the effective interactions that result in accurate predictions of densities (required for modeling the solubility of H_2 in water) and transport properties of water, due to "the missing term in effective pair potentials" (i.e., the title of the paper by Berendsen et al.[346]). Recently, Habibi et al.[350] developed a new method in which the TIP4P/2005 water force field is used to model the effective interactions in the liquid phase and an additional effective charge surface (ECS) is used to compute the excess chemical potential of water. The excess chemcial potential of water obtained using the ECS is used to compute a free energy correction for the free energies of TIP4P/2005 at different temperatures. Applying a free energy correction to the partition function of the isolated water molecules allows for accurately computing the excess chemical potentials of water, without compromising the liquid phase properties. As shown in Figure 24 and ref 111 this energy correction can be used to accurately predict both the equilibrium water content in the gas phase and the solubilities of H_2 in the liquid phase with respect to experiments. The simulations are performed at 298-423 K, 10-500 bar, 0-6 mol NaCl/kg water, and 0-8 mol KOH/kg water. As discussed in

https://doi.org/10.1021/acs.chemrev.5c00617
Chem. Rev. 2025, 125, 11878−12029

ref 350 it is important not to model water vapor using non-polarizable water force fields trained on the liquid phase (e.g., TIP4P/2005 and TIP3P), as the second virial coefficients of water vapor (and thereby the excess chemical potentials of water in the gas phase) are not accurately modeled with respect to experiments.[684] It is advised to combine MC simulations with EoS, such that the MC simulations can be used to obtain the liquid phase chemical potentials and free energies and the EoS (such as the GERG-2008[685]) can be used to model H_2O-H_2 gaseous mixtures.

4.1.3. Pressure−Volume−Temperature Computations. Yang et al.[686] performed molecular simulations of aqueous $H_2/CO_2/H_2O$ systems to compute *pVT* data and densities at conditions close to the supercritical regime, for which no prior experimental data were available. The motivation for this molecular simulation study is the application of supercritical water gasification of coal for energy production, a process in which *pVT* properties are difficult to measure. The authors state that no experimental, theoretical, or simulation studies exist regarding the *pVT* properties of H_2O-H_2-CO_2 mixtures in the near-critical and supercritical regions of water. They tested both the Cracknell and Buch force fields for hydrogen, but the results presented in the paper are based on the Cracknell force field. In their H_2O-CO_2 binary-mixture validation, the authors report that the absolute average error of the PR EoS and MD simulation is 15.09% and 0.66%, respectively. Thus, the adopted MD simulation model appears to have significantly better predictive accuracy than the PR EoS in near-critical and supercritical regions of water. However, for the H_2O-H_2 binary system, they note that no experimental research has investigated the *pVT* properties of H_2O-H_2 mixtures under those conditions. Therefore, their MD results are only compared against Peng-Robinson calculations, with no direct experimental benchmark for H_2O-H_2 in the near-critical and supercritical regimes. The pressure calculations obtained for binary H_2O-H_2 and ternary H_2O-H_2-CO_2 mixtures are shown in Fig. 25. Temperatures vary from 673 to 973 K, and the mole fractions of hydrogen range from 0.05 to 0.20. The results obtained from MD simulations are potentially more accurate and can provide more insight than the PR EoS.

4.1.4. Thermal Expansivity, Heat Capacity, Joule-Thomson Coefficient, and Speed of Sound of Aqueous Hydrogen Mixtures. As discussed in Section 3.3.4, isothermal compressibility, thermal expansivity, heat capacity, speed of sound, and the Joule-Thomson coefficient are thermodynamic properties which can be computed from ensemble fluctuations in molecular simulations.[571,642,643] Alternatively, these properties can be calculated using the multiple linear regression method which have been shown to be mathematically equivalent.[648]

The study by Rahbari et al.[47], mainly motivated from electrochemical compression systems, focused on the effect of trace amounts of water on the thermodynamic properties of compressed H_2 using MD simulations. The authors computed thermal expansivity, heat capacity, Joule-Thomson coefficients, partial molar volumes and enthalpies and the VLE of pure H_2 and aqueous H_2 mixtures. The H_2-water data were obtained from a prior study by the authors[110] where equilibrium compositions were sampled at 366 - 423 K, and pressures up to 1000 bar. Importantly, the isothermal compressibility data were retrieved from the legacy simulation data in ref 47 and are presented in this review for the first time (Fig. 26 upper). TIP3P model was used for water, while a new force field, i.e.

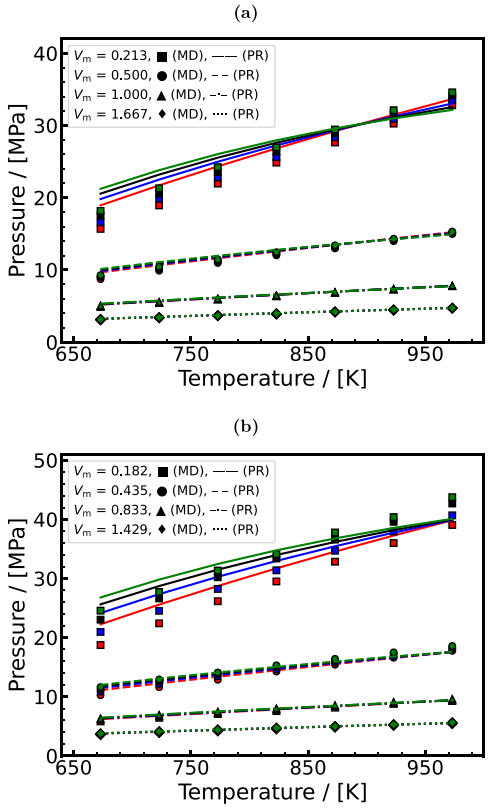

Figure 25. Pressure-temperature relation of (a) binary H_2O-H_2 mixtures and (b) ternary H_2O-H_2-CO_2 mixtures at different hydrogen mole fractions and molar volumes. MD simulation results are compared with predictions from the Peng-Robinson EoS. The different colors of the lines and markers correspond to different mole fractions of hydrogen (red: x_{H_2}=5%, blue: x_{H_2}=10%, black: x_{H_2}=15%, and green: x_{H_2}=20%).

TIP4P/μ was developed to yield improved solubilities (for more details the reader is referred to the Supporting Information of ref 47 and Section 3.1.2). H_2 was modelled with different force fields, with Marx showing the best overall performance. The molecular simulation results clearly indicated that at low pressures, the water content has significant influence on the thermodynamic properties of the H_2/H_2O mixtures (i.e., a positive Joule-Thomson coefficient for H_2O − H_2 mixtures and a negative value for pure H_2 mixtures at 423 K and 50 bar).[47] The effects become less pronounced as pressure increases, and become negligible above 700 bar. All computed properties (for different force field combinations) are shown in Fig. 26 along with available data from NIST (REFPROP92[352]) for pure H_2. These results underline the importance of accounting for trace water content when modeling hydrogen systems for storage and energy applications.

Bartolomeu and Franco[308] developed a single-site force field for H_2 using the SAFT-γ Mie potential, and validated it against existing LJ-type models (both 1-site and 2-site) for predicting thermophysical properties of supercritical H_2. Similarly to the study by Rahbari et al.,[47] the motivation of this study was high-pressure EHC applications. The authors reported both thermodynamic (i.e., densities, isochoric and isobaric heat capacities, thermal expansion coefficients, isothermal compressibilities, joule-Thomson coefficients, and speed of sound) and transport properties (i.e., diffusivities, viscosities, and thermal

https://doi.org/10.1021/acs.chemrev.5c00617
Chem. Rev. 2025, 125, 11878−12029

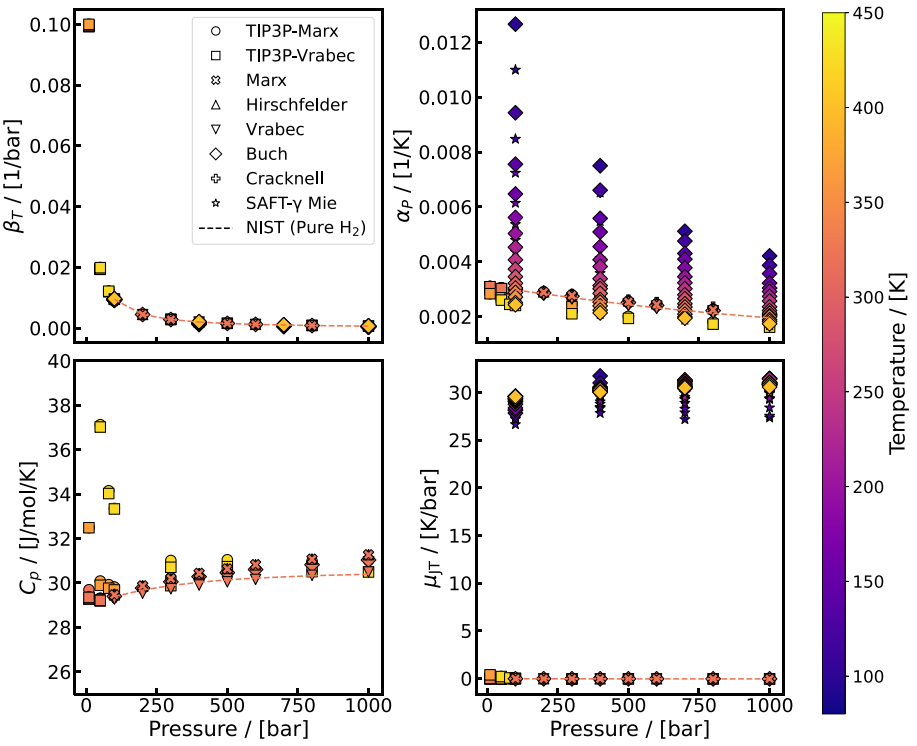

Figure 26. Comparison of different force fields in predicting the isothermal compressibility (top left), thermal expansivity (top right), isobaric heat capacity (bottom left), and Joule-Thomson coefficient (bottom right) of pure hydrogen in the gas phase over a pressure range of 10 to 1000 bar. Experimental data from NIST (REFPROP92[352]) are shown as lines. Raw simulation data are provided in the Supporting Information of ref 47. The error bars are smaller than the symbol size. For force field combinations with TIP3P, representing a gas phase saturated with water, the compositions at each temperature are directly taken from VLE simulations in ref 110 where the TIP3P force field was used for water and the Marx force field for hydrogen. The mole fraction of water in saturated hydrogen−water mixtures in the gas phase ranges from 0.004 to 0.138. Raw data from ref 308 were provided by the authors.

conductivities). The data from Bartolomeu and Franco[308] (provided to us by the authors) for the thermodynamic properties are shown in Fig. 26 and Fig. 27. This study emphasized that quantum effects are non-negligible at low temperatures, particularly when the de Broglie thermal wavelength approaches the inter-molecular distance or when the simulation temperature is below the rotational temperature of hydrogen (86 K). The authors observed that while a classical treatment may be acceptable for temperatures above 200 K, below this threshold, classical models increasingly deviate from experimental reference data. Among the tested models, the SAFT-γ Mie (which is a force field developed in the same study[308]) yielded the lowest average deviations, attributed to its softer repulsive potential and EoS-consistent parameterization, despite the absence of explicit quantum corrections.

4.1.5. Self-Diffusivity of Hydrogen in Aqueous Electrolyte Solutions. As discussed in detail in Section 2.1, reliable data of H_2 diffusivities in the aqueous phase are essential for the design and optimization of H_2 electrochemical systems such as water electrolyzers and fuel cells.[71] The diffusion of H_2 in the aqueous phase influences the bubble formation and growth rates, which in turn influence the ohmic resistance of the aqueous electrolyte and reduces the active electrode area.[71] The self-diffusivity of H_2 is also a relevant property in supercritical water gasification for conversion of biomass to fuel gasses.[687] Obtaining self-diffusivities of H_2 (and other gasses) at high pressures and temperatures (e.g., supercritical conditions) requires cumbersome and expensive

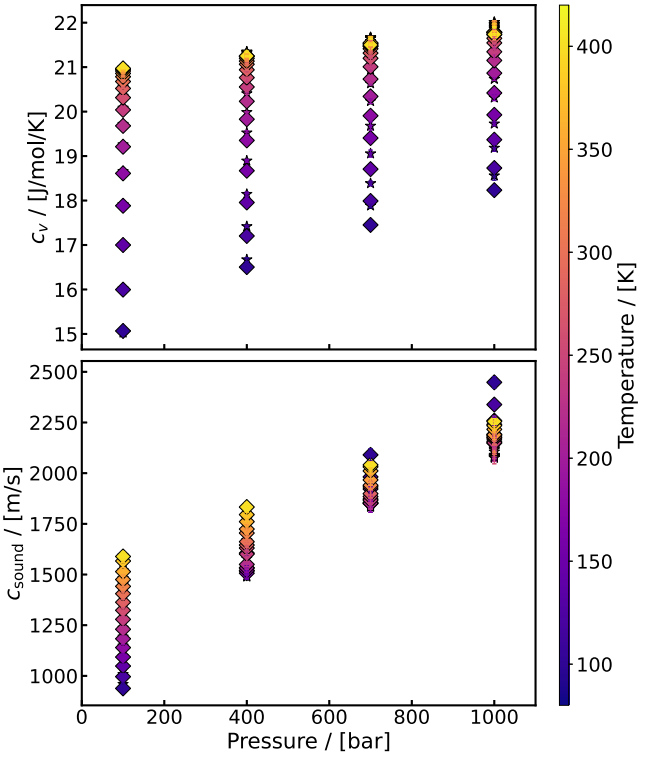

Figure 27. Isochoric heat capacity (top) and speed of sound (bottom) of supercritical hydrogen from ensemble fluctuations from MD simulations. Raw data from ref 308 was provided by the authors.

https://doi.org/10.1021/acs.chemrev.5c00617
Chem. Rev. 2025, 125, 11878−12029

experiments. Thus, molecular simulations have been widely used for obtaining these data over a large temperature and pressure range.[688,689] The relevant methods are described in Section 3.2.

Fig. 28 shows the temperature and pressure conditions for which data (MD and experimental) of H_2 self-diffusion

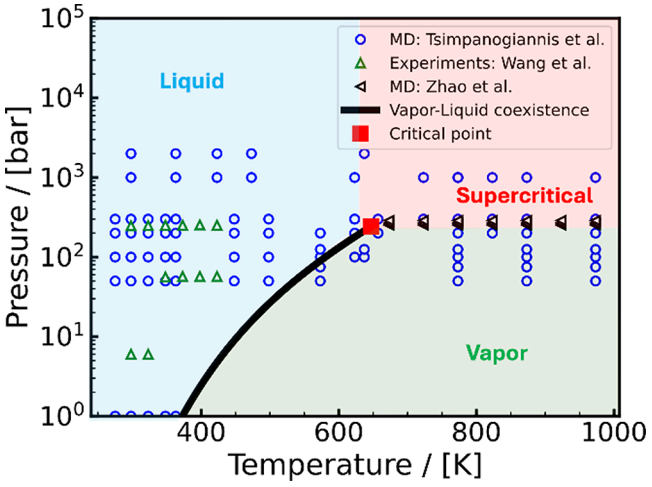

Figure 28. State points for which self-diffusivities of H_2 in water are available in literature. Experimental data ranges are from Wang et al.[690] which is the largest experimental dataset available. MD simulation data ranges are from the studies of Tsimpanogiannis et al.[688] and Zhao and Jin.[687]

coefficients in water are available.[687,688,690] The experimental dataset of Wang et al.[690] spans the most state points compared to the rest of the available experiments.[690] Additional experimental data at low pressures (0.1 MPa) have been collected and reported in ref 688. To the best of our knowledge, no experimentally measured self-diffusivities of H_2 in supercritical water are reported in open literature. Zhao and Jin[687] computed the diffusivity of H_2 in supercritical water while Tsimpanogiannis et al.[688] performed MD simulations to compute the diffusivities of H_2 and O_2 in water up to pressures of 2000 bar and 975 K. Kallikragas et al.[691] computed the diffusivity of H_2, O_2, OH radical, and H_2O in liquid water at a temperature range of 298 - 973 K and water densities spanning 0.1 g cm^{-3} to 1 g cm^{-3}. Since small gas molecules such as H_2 are sparsely soluble in liquid water (i.e., mole fractions of ca. 10^{-5} at 298 K and a H_2 pressure of 1 bar[112]), simulations of H_2 are often performed at near infinite dilution.[687,688,691] Therefore, to a great extent, the behavior of the solvent (e.g., density, viscosity) is the one dictating the diffusivity of the gas. This means that the choice of the water force field is crucial in these studies because the properties of the solvent need to be accurately modeled over a wide temperature and pressure range. Tsimpanogiannis et al.[688] and Zhao and Jin[687] used TIP4P/2005,[692] while Kallikragas et al.[691] used SPC/E. Both these water force fields perform well in modeling the density, viscosity, and self-diffusivity of liquid water.[345,348,692−694] As discussed in Section 3.1.2, TIP4P/2005 and SPC/E are rigid, non-polarizable force fields, ca. 3−10 times more computationally efficient than polarizable force fields.[354,355,695] The computational efficiency of non-polarizable force fields is a significant advantage compared to polarizable ones or quantum mechanical simulations (e.g., Born-Oppenheimer MD) for generating large datasets for transport properties of H_2 in aqueous mixtures. Polarizable force fields have been used by Śmiechowski[314] (i.e., AMOEBA combined the H_2 force by Śmiechowski[314]) to compute the diffusion of H_2 and H_2O in liquid water. However, these computations were carried out only at 298 K, and were not the main focus of the work by Śmiechowski[314] (i.e., calculation of Raman spectra for the hydrated H_2).[314]

To model H_2, Tsimpanogiannis et al.[688], used six different force fields for (i.e., Buch,[312] Marx,[310] Vrabec,[48] Cracknell,[311] Silvera-Goldman,[335] and Hirschfelder[321] H_2 force fields - see relevant discussion in Section 3.1.1). Depending on the H_2 model, the self-diffusivities varied by ca. 20−30%. Though this is a notable variation, it is comparable to the error of experimentally measured H_2 diffusivities found in literature.[348] The authors concluded that the Buch−TIP4P/2005 force field combination, performs the best, and proceeded in producing a wide range of data for H_2 and O_2 self-diffusivities in H_2O as shown in the Arrhenius-type plot of Fig. 29. Based on these

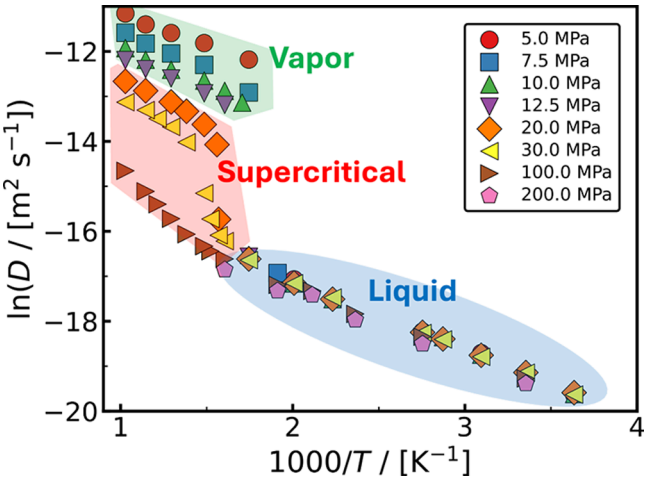

Figure 29. Arrhenius plot of the self-diffusion coefficients of H_2 in H_2O computed by Tsimpanogiannis et al.[688] using the Buch[312]−TIP4P/2005[305] force fields. The computed diffusion coefficients are corrected for system-size effects.[498−500] The identified self-diffusivity patterns of the H_2 in H_2O, in the vapor, liquid, and supercritical regions are highlighted. Data were collected from ref 688.

data, Tsimpanogiannis et al.[688] developed engineering correlations for the regions shown in Fig. 29 corresponding to vapor, liquid, and supercritical conditions. In a follow-up study, Moultos and Tsimpanogiannis[696] revised the proposed correlation of the vapor region to increase the accuracy of predictions for the lower pressure and higher temperature regions.

Available data from experiments and MD simulations for the self-diffusivities of H_2 in liquid H_2O have been considered to examine the validity of the Stokes-Einstein relation. Following the steps of Tsimpanogiannis et al.,[697] the analysis performed in ref 698 clearly indicates that the Stokes-Einstein relation is violated for both the experimental measurements and the MD simulation data. It is important to note that H_2 self-diffusivities computed from MD simulations are subject to finite-size effects[688] (see the relevant discussion in Section 3.2.3). The magnitude of these effects in the liquid phase depends on the temperature, number of molecules, and viscosity, as shown in Eq. (15).[498−500] The finite-size effects for diffusivities of H_2 in the aqueous phase are in the range 3-15% based on the studied

https://doi.org/10.1021/acs.chemrev.5c00617
Chem. Rev. 2025, 125, 11878−12029

by Tsimpanogiannis et al.,[688] Habibi et al.,[112] and Śmiechowski.[314] Accounting for these effects is necessary to ensure the reproducibility of the MD data.

In a recent study Kerkache et al.,[699] investigated H_2 diffusivity in water and NaCl brine over a wide range of thermodynamic conditions, including temperatures from 298 to 473 K, pressures from 1 to 1000 bar, and salt molalities up to 6 mol salt/kg solvent, focusing on self-diffusion coefficients relevant to infinitely diluted H_2 in aqueous solutions; the study primarily addressed H_2-H_2O and H_2-H_2O-NaCl systems. The results indicated that H_2 self-diffusion coefficients decrease with increasing salinity, for example from approximately 6.0×10^{-9} m^2/s in pure water to ca. 4.2×10^{-9} m^2/s at 6 mol/kg NaCl at 323 K and 200 bar, and increase with temperature and slightly decrease with pressure. No data on mutual diffusivities for H_2-CH_4 or H_2-CO_2 mixtures were provided. The physical mechanism underlying these findings is linked to the increasing structuring of the solvent and ions around the H_2 molecule, reflected by more negative two-body excess entropy values with higher salinity and pressure, leading to higher viscosity and thus lower diffusivity, while temperature weakens solvent structuring and enhances H_2 mobility. The solvent viscosity, accurately captured by the TIP4P/2005 water model combined with the Madrid-Transport salt force field, was found to be the dominant factor influencing H_2 diffusivity, consistent with the fractional Stokes-Einstein relation, having an exponent of ca. 0.83. The computed diffusion coefficients were compared qualitatively to limited experimental data available for H_2 diffusion in pure water and low salinity brine, showing good agreement in trends though experimental data remain sparse and uncertain at higher salinities and pressures. Finally, the study proposed both a fractional Stokes-Einstein model and an Arrhenius-type empirical correlation for H_2 self-diffusivity as functions of temperature, pressure, and NaCl molality, providing a reliable predictive framework for underground H_2 storage applications.

Molecular simulations have also been used to compute the diffusivity of H_2 in concentrated aqueous NaCl, NaOH, KOH, and $NaB(OH)_4$ solutions.[112,113,630,680] The data collected from literature are shown in Fig 30. These electrolyte solutions are primarily relevant for water electrolysis and H_2 storage (see also Section 2.1). As in the simulations of H_2/water systems discussed earlier, it is important to choose salt/water force field combinations that can accurately model the densities and transport properties of the aqueous electrolyte solvents. For example, salt force fields that cannot capture the change in viscosity as a function of salt molality, it is expected that they also fail in modeling the diffusivity (and other properties) of H_2, ions, or water at different salt loadings.[630] Blazquez et al.[700] has shown that non-polarizable force fields of NaCl and KCl that correctly predict the density and viscosity of the aqueous solution can accurately describe the diffusion coefficients of Na^+, K^+, Cl^-, and water. Similarly, Avula et al.[701] has shown that for predicting the anomalous increase in the water diffusivities in aqueous CsI solutions, the decrease in solution viscosities needs to be accurately captured. The data reported in the Supporting Information of van Rooijen et al.[630] show that the Madrid-2019 NaCl[370] force field overestimates the solution viscosities by ca. 20% at the solubility limit compared to Madrid-Transport,[384] and therefore, underestimates the diffusivities of H_2 in the aqueous solution.

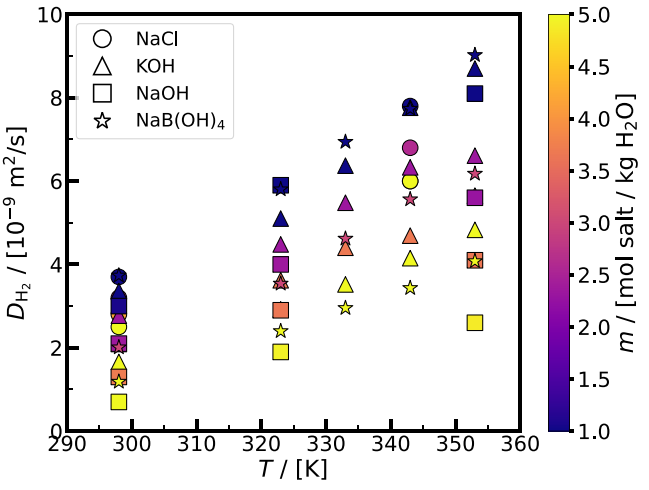

Figure 30. Self-diffusivities of H_2 in aqueous NaCl, KOH, NaOH, and $NaB(OH)_4$ solutions at different temperatures and salt molalities at 1 bar. The data are collected from refs 112, 113, and 630.

4.1.6. Electroosmotic Drag Coefficient. Din and Michaelides[127] computed EOD within a cylindrical pore examining both a flow of water molecules or ions, and the case of no macroscopic flow in the channel. The interactions between water molecules and wall atoms, and the interactions between hydrogen atoms (protons) and wall atoms were determined based on the work of Zhu and Robinson.[702] Din et al. established a linear connection between the EOD coefficient and water uptake. For $\lambda \in [7.65, 10.9, 12.2, 20.9]$, the EOD computed equals [7.34, 10.5, 12.0, 19.6], respectively. These results are shown in Fig. 31. The overestimation of the EOD possibly arises from the simplified pore model used in the simulations, which assumes uniform wall charge, straight cylindrical pores, and neglects structural complexity of the membrane. As a result, the simulations allowed for more water to be dragged by protons than what is observed in experiments with membranes. In addition, the proton hopping mechanism is missing from the model of the authors.

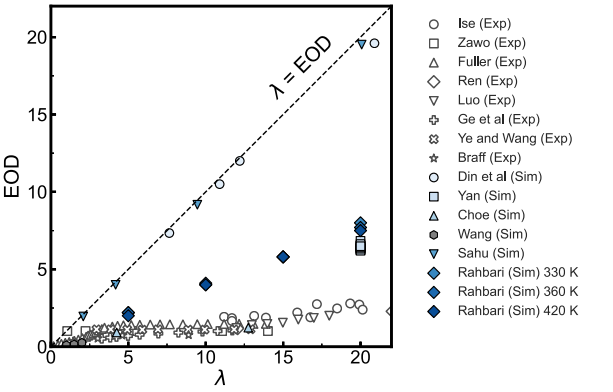

Figure 31. Electro-osmotic drag coefficients from MD simulations and experiments as a function of the hydration level, λ (defined in Eq. (31)). The dashed line denotes the ideal case where EOD equals λ, serving as a reference. Data are compiled from refs 92, 94, 98, and 127–129.

Yan et al.[128] performed atomistic MD simulations to compute the EOD coefficient with electric fields (up to 2 V/μm) for λ = 20. All-atom force-fields were used to model the hydrated PFSA oligomers, water molecules, and H_3O^+.[128,703]

https://doi.org/10.1021/acs.chemrev.5c00617
Chem. Rev. 2025, 125, 11878−12029

Table 10. Summary of Studies Calculating the EOD from Molecular Dynamics Simulations

		System Details		Thermodynamic Conditions		
Year	Study	Phases	Force Fields	Electric Field V/Å	Temperature	Method
1998	Din et al[127]	Nafion(s), H_2O(l), H^+(aq)	SPC/E, H^+,[127] Wall atoms (Nafion)	0.0592 to 0.3809	298	NEMD
2008	Choe et al.[129]	Nafion(s), H_2O(l), H_3O^+(aq)	SPC/E, Nafion (Dreiding, UFF)	0.05	363	NEMD/Ab initio
2008	Yan et al.[128]	Nafion(s), H_2O(l), H_3O^+(aq)	TIP3P, H^+,[127] Nafion	0.02 to 0.05	287.15-364.65	NEMD
2022	Wang et al.[98]	Nafion(s), H_2O(l), H^+(aq)	SPC/E, Nafion (AMBER/GAFF)	0.0001 to 0.0005	350	NEMD
2022	Rahbari et al.[94]	Nafion(s), H_2O(l), H_3O^+(aq)	PCFF (Class II), COMPASS (partial charges)	0.02, 0.05, 0.075, 0.100	330, 360, 420	NEMD
2025	Sahu et al.	Nafion(s), H_2O(l), H_3O^+(aq), Cu^+, Cu^{2+}, Cl^-	TIP4P/2005 (H_2O), DFT-derived charges (Nafion), LJ + Coulomb (ions), Nafion model from TURBOMOLE	0.00, 0.02, 0.05, 0.075, 0.10	298	NEMD (classical MD)

Every backbone comprised four side chains terminated with sulfonic acid groups. The EOD coefficient was computed using two approaches: one based on average transport velocities, and the other on peak shifting velocities. Both methods yielded comparable results.[128] The EOD was computed over a temperature range of 287.15 K to 364.65 K, showing no significant temperature dependence. An average value of 6.41 was obtained. These values are notably higher than most experimental values as shown in Fig. 31. The authors attributed this overestimation to the absence of proton hopping in their model, which omits the dissociation of O-H bonds, and therefore, excluding a major transport mechanism. While the authors suggested a correction, the discussion was and not further supported by additional simulations or quantitative analysis. The proposed correction was, thus, a qualitative estimate rather than a rigorously derived result, limiting the strength of the comparison with experimental values.

Choe et al.[129] computed the EOD coefficient of water at T = 363 K for λ values ranging from 4.25 to 12.75. Under a uniform electric field, the EOD coefficients were extracted from ab initio MD trajectories, yielding values of 0.92 and 1.23 for λ = 4.25 and λ = 12.75, respectively. These results are consistent with experimental measurements, as shown in Fig. 31. The model system comprised two Nafion monomers arranged around a central water cluster in a sandwich-like structure, with hydrophilic tails facing the water. The proton from the sulfonic acid end group was modeled as a hydronium ion. The Dreiding force field was used for intra-molecular interactions within Nafion, and UFF was applied for nonbonded interactions with water and hydronium (for more information on these force fields the reader is referred to Section 3.1.4). Classical MD simulations were first used to generate equilibrated configurations, which then served as initial states for AIMD. The authors attributed the nearly constant EOD across hydration levels to two opposing effects, i.e., the increased proton hopping at higher hydration, which tends to lower the drag, and the enhanced water mobility beyond the hydration shell, which tends to raise it. These effects largely offset each other, resulting in the observed invariance of the EOD with respect to water content. The study by Choe et al.[129] clearly demonstrates that combining ab initio calculations with classical MD enables a more accurate representation of the underlying transport physics (as also recently shown in ref 105). Although this review does not elaborate on QM methods, it is worth noting that such approaches are necessary for accurately predicting H_2 properties in electrochemical systems.

Rahbari et al.[94] computed the EOD coefficient for hydrated Nafion membranes at water contents $\lambda \in [5, 10, 15, 20]$ and temperatures between 330 and 420 K. The data reported in this study are shown in Fig. 31. The electric fields applied were in the range 0.05 to 0.10 V/Å while the velocity ratio of water to H_3O^+ ions was determined across different field strengths. PCFF and COMPASS force fields were used to model all interactions. This study showed that the average velocities of both species scaled linearly with the electric field, resulting in a constant velocity ratio and a linear dependence of EOD on hydration level. The EOD increased with λ, reaching up to 7.5 at λ = 20 and 420 K, while showing a slight decrease with temperature. As in the prior studies using classical force fields, proton hopping was not modeled, thus, limiting the accuracy of the computed EOD at high hydration. Nevertheless, the results at lower λ aligned better with experiments as can be observed in Fig. 31.

Wang et al.[98] conducted classical MD simulations to compute the EOD in Nafion membranes with low hydration levels λ = 1, 1.5, and 2 at T = 350 K. The computed EOD coefficients were 0.098, 0.149, and 0.255, respectively. Electric fields ranging from 0.001 to 0.005 V/nm were applied, and EOD coefficients were determined from the average velocities of water and H_3O^+. The results are in excellent agreement with the linear model EOD = $\frac{2.5}{22}\lambda$, confirming the assumption made by Springer et al.[704] that EOD varies linearly with water content at low hydration. This finding is also in line with most experimental and simulation data at low water contents as shown in Fig. 31. Similarly to the prior classical studies, ss the hopping mechanism was not included, the calculated EOD reflects only vehicular proton transport.[94,556] The authors showed that EOD approaches zero as water content vanishes.

The linear increase of the EOD coefficient with hydration level, as predicted by classical MD simulation studies,[94,127] was also confirmed by Sahu and Ali.[705] Consistently with the prior studies, the approach did not include the Grotthuss mechanism (proton hoping). As a result, the computed EOD values were shown to overestimate experimental data, particularly in well-hydrated systems. This overestimation is further amplified by the use of high electric field strengths. The EOD values reported by Sahu et al. are shown in Fig. 31.

In summary, several studies have investigated the EOD in hydrated membranes using molecular simulations (see Table

https://doi.org/10.1021/acs.chemrev.5c00617
Chem. Rev. 2025, 125, 11878−12029

10), providing valuable insights into the underlying transport mechanisms and associated limitations. Collectively, these studies show that while classical force fields can qualitatively reproduce trends in EOD, quantitatively accurate predictions, particularly at high hydration, require explicit modeling of proton hopping and a more realistic description of membrane nanostructure. It is also important to note that there remains considerable variability among experimental EOD measurements; however, a detailed discussion of experimental inconsistencies is beyond the scope of this review. Nevertheless, the major differences and systematic trends between simulation and experimental data can still be identified.

4.1.7. Reactive Systems and Membrane Properties Related to Hydrogen Research. Despite the fact that in this review we primarily focus on the computation of thermophysical propertiers using classical molecular simulations, in many H_2 processes chemical, reactions cannot be ignored to obtain reliable predictions.[706] To this purpose, reactive MD and MC simulations allow for the study of chemical reactivity by explicitly modeling bond formation and breaking, providing a pathway towards understanding complex phenomena in H_2 (and many other) systems. These methods are particularly useful for studying the VLE of reactive systems, the internal workings of MEAs in fuel cells and electrolyzer cells, or any H_2 system where chemical reactions play a crucial role.[707−710] An important example in the context of H_2 systems is the application of reactive MD in modeling ion-exchange membranes, where proton hopping mechanisms, the lifetime of H_3O^+, and the dynamic behavior of reactive species in electrolyte environments are central mechanisms.[118] Unlike classical MD, which relies on predefined force fields (see Section 3.1), reactive MD uses techniques that allow for changes in molecular topology during the simulation. Reactive MD can be implemented within different modeling frameworks, including hybrid quantum-classical models, fully classical approaches, and quantum-based reactive force fields.[707,711]

The prediction of thermodynamic and transport properties of H_2, H_3O^+, and protons in MEAs (see Section 2.1) also requires the use of combined classical/reactive molecular modeling approaches. Relevant properties in such systems include ion diffusion, electrical conductivity, membrane structure, EOD, and thermal conductivity. As discussed in the previous section, accurate modeling of the membrane, serving as the medium for H_2 transport, is essential for understanding and optimizing system performance. Although a detailed analysis of MEAs lies outside the main scope of this review, selected membrane properties relevant to H_2 applications are discussed here to illustrate the depth of insight that can be obtained via molecular simulations.

The review by Arntsen et al.[93] explores the application of reactive MD simulations to study proton transport in polymers commonly used in fuel cells (Nafion 3M and Hyflon). The authors particularly highlight the Multistate Empirical Valence Bond (MS-EVB) method, which can capture the Grotthuss mechanism that classical non-reactive MD simulations fail to model. The application of MS-EVB simulations revealed an anti-correlation between vehicular and Grotthuss transport mechanisms. This anti-correlation was already hinted in Section 4.1.6 and Fig. 31 where our analysis of the collected simulation results revealed that excluding Grotthuss mechanism leads to overpredicting the EOD. The review by Arntsen et al.[93] demonstrates how H^+ conductivity computed from MS-EVB simulations aligns more closely with experimental data,[93] showcasing the accuracy of the MS-EVB method. This study not only captured proton hopping, but also proposed a transport mechanism in which H^+ primarily pass between sulfonate groups, rather than diffusing through the bulk water region.

Awulachew and Nigussa[115] conducted MD simulations of MEAs encountered in fuel cells considering Pd_3Ag electrodes as alternatives to Pt electrodes. Self-diffusion coefficients were computed using the Einstein approach (see Section 3.2.3) to determine H^+ conductivity, while coordination numbers were obtained from radial distribution functions. The conductivity values obtained were comparable to, but slightly higher than, those reported in the literature. A benchmark comparison was performed, and it was concluded that the combination of a Nafion membrane with a Pd_3Ag electrode offers an efficient and cost-effective solution for MEAs. The authors discussed the influence of hydrogen bonding and temperature on H^+ mobility. The authors proposed that including interaction effects between H^+, the electrode, and the electrolyte improves the computation accuracy of H^+ conductivity. Cui et al.[116] performed classical MD simulations of hydrated Nafion membranes at hydration levels corresponding to λ = 3.44, 5.42, 8.63, and 11.83. Water clustering and H_3O^+ diffusion were analyzed as functions of hydration. This study revealed that increasing water content promotes the formation of a connected aqueous network composed of interlinking water channels. Based on the molecular structure, the formation of Eigen-type ions is proposed as hydration increases. The authors attribute the low H^+ conductivity at low water contents to the disconnected morphology of the water network.

Venkatnathan et al.[117] performed MD simualtions to compute the density and diffusion coefficient of H_3O^+ in a nafion membrane at hydration levels λ = 3.5, 6, 11, 16, and temperatures of 300 and 350 K. Consistently with the prior studies, diffusion coefficients were underestimated due to the lack of proton hoping in classical MD framework. The effects of hydration on the structure and vehicular transport of ions and the mobility of water molecules in Nafion membrane were discussed. The authors proposed that H_3O^+ ions do not merely act as passive charge carriers but actively shape the local structure of the hydrated Nafion membrane. At low hydration levels, participation of H_3O^+ in forming hydrogen bonds constrains the mobility of sulfonate, effectively affecting the morphology of the membrane. As hydration increases, these constraints are relaxed due to enhanced solvation, allowing sulfonate groups and H_3O^+ to become more spatially separated.

Hofmann et al.[118] performed reactive MD simulations to compute the diffusion and conductivity of oxygen and hydrogen ions in hydrated Nafion membranes at λ = 6 and λ = 12. The simulations indicated shorter H_3O^+ lifetimes at higher hydration levels. The authors proposed that the time−determining step for proton transfer is the formation of a precursor complex (Zundel-type) prior to rapid proton hopping. This study also showed that the conductivity significantly exceeds the value expected from self-diffusion alone, highlighting the role of collective proton motion. This is reflected in a reduced Haven ratio at higher hydration, indicating enhanced correlated transport and increased conductivity.

Brunello et al.[120] performed fully atomistic MD simulations to study the structure, sulfonate solvation, density, and water

https://doi.org/10.1021/acs.chemrev.5c00617
Chem. Rev. 2025, 125, 11878−12029

Table 11. Brief Overview of Mechanistic Insights Obtained from Molecular Simulation Studies of Hydrated Membranes Relevant to Hydrogen Systems[a]

Reference	Property Studied	Key Insights
Flottat et al.[125]	Water diffusion in Nafion vs. Aquivion	Linear growth of water domains with hydration; earlier percolation in Aquivion; water volume fraction governs structure and dynamics
Awulachew and Nigussa[115]	Proton conductivity in MEAs with Pd_3Ag electrodes	H-bonding enhances proton mobility; electrode-electrolyte interaction boosts conductivity; Pd_3Ag-Nafion outperforms Pt; simulation exceeds literature values
Cha[124]	Side chain length effect on H_3O^+ transport	Shorter side chains improve inter-chain mobility and ion conductivity; contradicts some experimental trends
Zhang et al.[95]	H_3O^+ and H_2O diffusion in Nafion	Na^+, Ca^{2+} disrupt water clusters; Ca^{2+} has stronger binding and impact; reduced H_3O^+, H_2O mobility
Arntsen et al.[93]	Review of proton transport in fuel cell membranes	MS-EVB captures Grotthuss mechanism; anti-correlation with vehicular transport; hopping occurs between sulfonates; matches experiments
Ozmaian and Naghdabadi[101]	Glass transition temperature of Nafion	Hydration lowers T_g significantly; hydration gradients lead to heterogeneous degradation behavior
Brunello et al.[120]	Water transport in S-PEEK	Water content enhances phase segregation and water channel development; consistent with Nafion trends
Lins et al.[122]	Structure and transport in Ph-SPEEKK	Hydration increases sulfonate mobility and spacing; qualitative match with Nafion/SPEEK behavior
Hofmann et al.[118]	Proton transfer mechanisms	High λ shortens H_3O^+ lifetime; precursor (Zundel-type) forms before hopping; collective effects increase conductivity
Venkatnathan et al.[117]	Density and diffusion in Nafion	H_3O^+ shapes local structure; low λ restricts mobility via H-bonding with sulfonates
Cui et al.[116]	Water clustering and hydronium diffusion	Hydration enables channel formation; Eigen-ion structures proposed; disconnected morphology limits conductivity at low λ

[a]The table summarizes key findings on structure-transport relationships, ion coordination, and hydration-dependent phenomena in membrane electrode assemblies.

transport in hydrated sulfonated poly(ether ether ketone) (S-PEEK) at temperatures of 298 to 353 K, and λ = 4.9 and 11.1. The simulations revealed that temperature has limited impact on sulfonate solvation and morphology, while water content significantly enhances nano-phase segregation and the development of water channels. Water diffusion increased with temperature and hydration, though activation energies remained similar, indicating a consistent diffusion mechanism. While explicit experimental validation is not provided, the authors point to qualitative consistencies with previous findings on membranes such as Nafion and Dendrion, suggesting physically plausible trends in structure and transport behavior.

Lins et al.[122] performed MD simulations of fully sulfonated Ph-SPEEKK to evaluate the influence of hydration level (λ = 3.5, 6, 11, 16, 25, 40) on the internal structure of the membrane and H^+ transport. The authors computed diffusion coefficients for water and H_3O^+, as well as hydrogen bond statistics. In the absence of direct experimental data for Ph-SPEEKK, the pair correlation functions was used to assess sulfonate clustering, which revealed that higher hydration leads to greater sulfonate mobility and separation. While explicit validation was not deemed possible at the time of the publication, qualitative agreement with prior findings on SPEEK and Nafion was noted, particularly in hydration–dependent structural trends and the enhancement of diffusion at higher λ.

Ozmaian and Naghdabadi[101] computed the diffusion coefficient of water in hydrated Nafion with λ = 14 at temperatures ranging from 100 to 600 K. The authors investigated the glass transition temperature (T_g) of hydrated Nafion to better understand its thermomechanical stability and performance limits, particularly for applications such as fuel cells and shape–memory devices. This study showed taht increasing hydration significantly lowers T_g; for example, at λ = 20, T_g = 230 K, while for λ = 2, no clear transition is observed below 500 K. Overall, the simulations results show good consistency with experimental T_g values (340 - 350 K). An important insight finding in this study was that membranes with hydration gradients may exhibit heterogeneous thermal and degradation behavior across their thickness, which is relevant for their operational durability.

Cha[124] performed MD simulations to investigate how the morphology of perfluorosulfonic acid (PFSA) membranes, specifically, the length of side chains, affects H_3O^+ conductivity in polymer electrolyte membranes (PEMs), which constitutes a key performance factor in fuel cells. The study was motivated by discrepancies between prior simulation and experimental studies, which reported conflicting results on whether shorter side-chains improve conductivity. To address this, Cha[124] developed tracked H_3O^+ pathways throughout the simulation. The findings showed that shorter side-chains increase the fraction of conductive H_3O^+, and enhance inter-chain ion movement, thus, improving ionic conductivity, contrary to some earlier experimental observations. Despite the motivation of this study, the discrepancies between the simulation and experimental results were not resolved, and follow-up research is proposed.

Flottat et al.[125] conducted MD simulations to elucidate why Aquivion (850 g/equiv) exhibits higher water diffusion than Nafion (850 g/equiv). Motivated by the fact that H^+ conductivity depends on the morphology of the hydrophilic water network (which itself is strongly influenced by hydration), the authors investigated how nanoscale structure governs transport properties. The simulations were shown to reproduce experimental trends for membrane density and water diffusion, while a linear increase in water domain size with hydration was obtained, in qualitative agreement with experimental measurements. A key finding was that the transition from isolated to percolated water networks occurs at a lower hydration level in Aquivion than in Nafion, potentially explaining improved diffusion/conductivity under dry conditions. The study also showed that structural and dynamic properties scale with water volume fraction, identifying it as a more fundamental parameter than hydration number.

https://doi.org/10.1021/acs.chemrev.5c00617
Chem. Rev. 2025, 125, 11878–12029

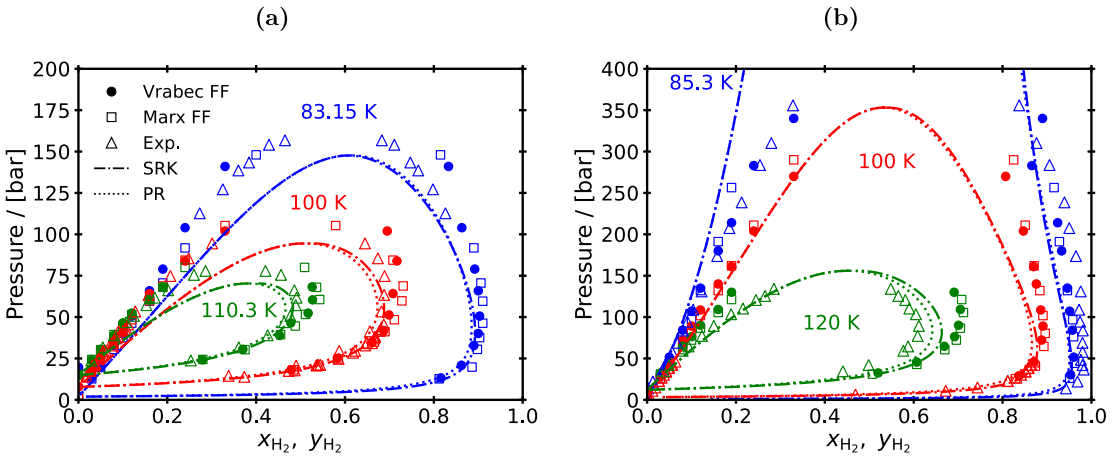

Figure 32. Comparison of molecular simulation results with experimental VLE data for the (a) H_2-N_2 and (b) H_2-Ar binary mixtures using the Vrabec and Marx hydrogen force fields, adapted from Köster et al.[48] The experimental data[712−714] are also presented in Köster et al.[48] The PR and SRK predictions are computed with the Open-Source Fluid Thermodynamics Toolkit Clapeyron.[715] The simulation results of H_2-Ar at 120 seem to deviate significantly from the experimental results, however, these measurements were performed at 122.73 K instead of 120 K.[714]

Zhang et al.[95] investigated the effects of Na^+ and Ca^{2+} ions on the diffusion of H_3O^+ and water in Nafion 117 membranes using MD simulations. The study revealed that both cations significantly reduce H_3O^+ and water diffusivities by associating with sulfonic acid groups and disrupting water cluster connectivity, especially at λ = 16 and temperatures of 298 and 353 K. Ca^{2+} appeared to have a stronger effect than Na^+ due to the higher charge and higher hydration degree, leading to stronger binding with sulfonic groups and greater disruption of water channels. Diffusion coefficients reported for all species confirm that Na^+ diffuses more rapidly than Ca^{2+}. The decline in H_3O^+ and H_2O transport aligned with previous experimental and simulation findings. The computed diffusion of Na^+ was also shown to be in line with with the respective experiments.

This section highlighted how molecular simulations can be used to obtain deep mechanistic insights into the transport and thermodynamic behavior of H_2-related species in hydrated polymer membranes. By considering water content, temperature, ionomer morphology, and contaminant effects, molecular simulations not only provide a means of computation of diffusion coefficients and conductivities but also reveal nanoscale structural phenomena, such as water channel formation, sulfonate-cation interactions, and the role of hydration in enabling or restricting ionic transport. The representative studies reviewed above demonstrate the power of molecular simulations in studying experimentally inaccessible systems/conditions, provided that accurate force fields and methods are used.

Table 11 provides a succinct summary of the key insights obtained from the relevant literature. While our focus here was mainly on transport properties which are relevant to H_2 applications, molecular simulations can also be used to study other membrane features such as thermal conductivity[126] or the impact of contamination on oxygen transport.[96] These topics lie outside the scope of this review but further illustrate the wide applicability of molecular simulation in membrane research.

4.2. Thermodynamic and Transport Properties of Nonaqueous Hydrogen Mixtures

4.2.1. Vapor-Liquid Equilibrium of Pure Hydrogen and Binary and Ternary Mixtures of Hydrogen with Argon, Nitrogen, and Carbon Dioxide. Köster et al.[48] studied various thermophysical properties (including VLE, vapor and liquid densities, and residual enthalpy of vaporization) of binary H_2-N_2 mixtures using the grand equilibrium method (see Section 3.3.1.6). The simulations were conducted at T = [83.15, 100, 110.3] K, with corresponding pressure ranges of [(0.196−14.1), (0.794−10.20), (1.51−8)] MPa. To model H_2, the Vrabec[48] and Marx[310] force fields were used. The results, shown in Fig. 32a, demonstrate that the Vrabec model, which was fitted to pVT and speed of sound data, is in good agreement with experimentally measured VLE data across the whole temperature range considered, outperforming Marx. Deviations are observed as pressure increases. Vapor pressures and saturated liquid densities are accurately captured, particularly at lower temperatures. The Vrabec force field is also shown to yield improved predictions of relative volatilities and residual enthalpies of vaporization compared to Peng−Robinson, SRK, and PC-SAFT EoS (for the PC-SAFT predictions the reader is referred to ref 48), which exhibit significant deviations from reference data in the critical and dense liquid regions. This force field also performs well in predicting homogeneous phase densities of equimolar H_2-N_2 mixtures under cryogenic and near-critical conditions, with mean absolute percentage errors below 1% in some cases.[48]

In the same study, Köster et al.[48] performed simulations also for H_2-Ar binary mixtures to compute the same properties (VLE, densities, and residual enthalpy of vaporization). For this binary mixture, the authors considered T = [85.8, 100, 120] K, with corresponding pressure ranges of [(0.090−34), (0.331−27), (1.220−15.6)] MPa for the Vrabec force field, and [(0.088−25.644), (0.331−29), (1.220−14.3)] MPa for the Marx force field. As shown in Fig. 32b, molecular simulations using the Vrabec[48] force field, demonstrated good agreement with the available experimental VLE data. In particular, the saturated liquid compositions and vapor pressures at cryogenic conditions (90−120 K) are well captured. Although minor deviations were noted in the saturated vapor compositions at lower temperatures, the predictions from the molecular simulations remained within the scatter of the experimental data. Furthermore, in the homogeneous supercritical region, the computed compressibility factors matched experimental values with high accuracy, achieving mean absolute percentage errors below 1% for

https://doi.org/10.1021/acs.chemrev.5c00617
Chem. Rev. 2025, 125, 11878−12029

pressures up to 9 MPa. These findings highlight the reliability of Vrabec force field in describing both phase behavior and volumetric properties of H_2-N_2 and H_2-Ar mixtures under sub- and super-critical conditions.

Raju et al.[716] computed the VLE of the H_2-CO_2 binary mixture using molecular simulations in the CFCGE ensemble (see Section 3.3.1.1). The authors compared the simulation results with data from the GERG-2008[685] EoS and available experiments. The results are illustrated in Fig. 33. Notably, the

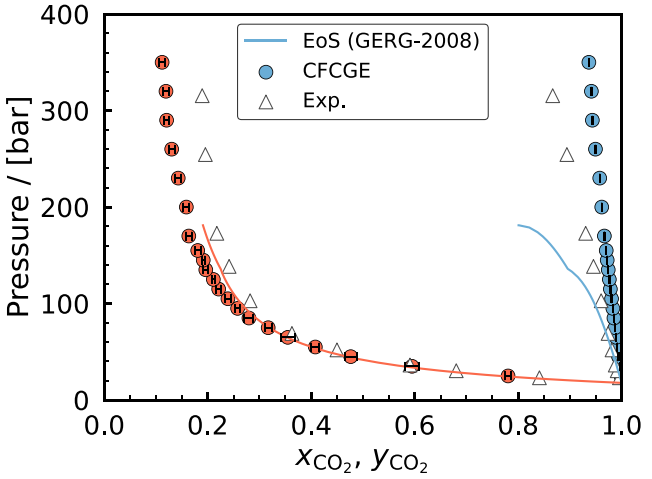

Figure 33. Vapor-liquid equilibrium data for the CO_2-H_2 binary mixture from molecular simulations[716] compared to GERG-2008[685] EoS predictions and experimental measurements.[717]

authors faced convergence issues with GERG-2008 at pressures exceeding 170 bar, as solid lines in Fig. 33 indicate. Moreover, the computed bubble points from GERG-2008 showed significant discrepancies from the experimental measurements. In contrast, the mole fractions obtained from molecular simulations exhibited good agreement with the experimental data by Tsang and Street,[717] with relative deviations remaining below 5% even at elevated pressures.

The VLE of the ternary H_2/Ar/N_2 system at 100 K was studied by Köster et al.[48] using the force field fitted in the same study. As shown in Fig. 34, the simulations accurately captured the vapor and liquid compositions for both pressures of 20 and 30 bar. A particularly large two-phase region is observed due to the presence of H_2. The simulation results show excellent agreement with experimental data, while cubic EoS (SRK and PR) were shown to underestimate the extent of phase separation, and predicted narrower two-phase envelopes. Consistent with the accurate predictions for the binaries discussed earlier, Vrabec force field was also shown to perform well in predicting also the ternary phase behavior of these light gas mixtures.

4.2.2. Pressure–Volume–Temperature and Thermodynamic Factor Computations for Hydrogen, Methane, and Carbon Dioxide Mixtures. Zhang et al.[718] performed MD simulations to compute the pressure of pure H_2, CO_2, CH_4, and their binary mixtures at various temperatures and molar volumes. The results, corresponding to a molar volume of V_m = 0.143 L mol^{-1}, are shown in Fig. 35. For pure-component simulations, the authors reported that the data from MD are in excellent agreement with predictions from GERG-2008 EoS and NIST. However, the reference provided by Zhang et al.[718] (ref 54) for the NIST database does not directly lead to the respective data. The molecular simulation data were subsequently used to parameterize new, computationally efficient analytical equations describing the *pVT* behavior of H_2/CO_2/CH_4 mixtures at pressures up to 1720 bar and temperatures in the range of 310.9 to 470 K.

Zhang et al.[718] reported excellent agreement with available experimental data[719] at temperatures between 300 and 350 K, for 5 to 50% H_2 in CH_4 (see Fig. 36). Also, the $P\rho T$ MD data at 673.1 K are in excellent agreement with the available experiments[720] for the mixture 0.6992 H_2 + 0.3008 CO_2 as shown in Fig. 36. The authors proposed further developing analytical EoS for other binary or multicomponent gas mixtures using MD simulations, potentially augmented with machine learning.

In the recent studies by Hulikal Chakrapani et al.,[576,677] the Marx[310] force field was combined with TraPPE[721] to model the densities, Gibbs excess energies, and thermodynamic factors of H_2/CO_2 mixtures. For an extended collection of raw simulation data for these properties, but also viscosities, compressibility factors, and diffusivities, the reader is referred to the Supporting Information of refs 576 and 677. The authors presented a wide and reliable collection of simulation data spanning gaseous densities of H_2/CO_2 mixtures in the range of 298-423 K, 0-1 mole fraction of H_2, and for pressures up to 500 bar.[677] The thermodynamic factors of H_2/CO_2

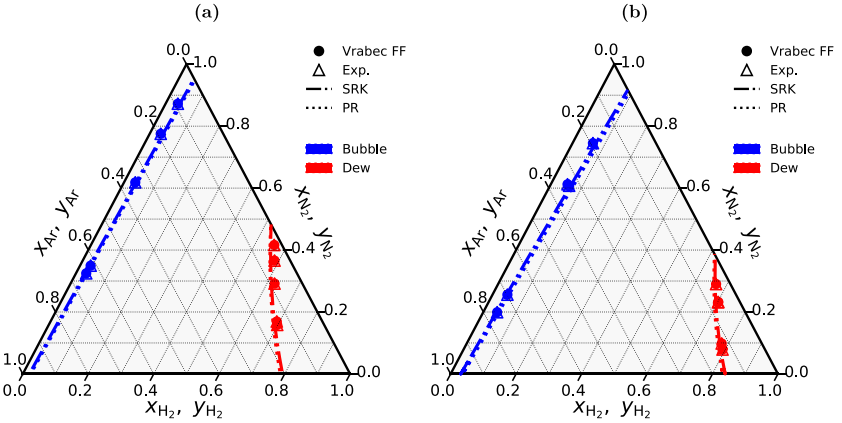

Figure 34. Ternary phase diagrams for the H_2/Ar/N_2 system at 100 K and (a) 20 bar or (b) 30 bar. The simulation data are collected from Köster et al.,[48] the experimental measurements from Xiao et al.,[712] and the SRK and PR EoS datapoints are computed with Clapeyron.[715]

https://doi.org/10.1021/acs.chemrev.5c00617
Chem. Rev. 2025, 125, 11878–12029

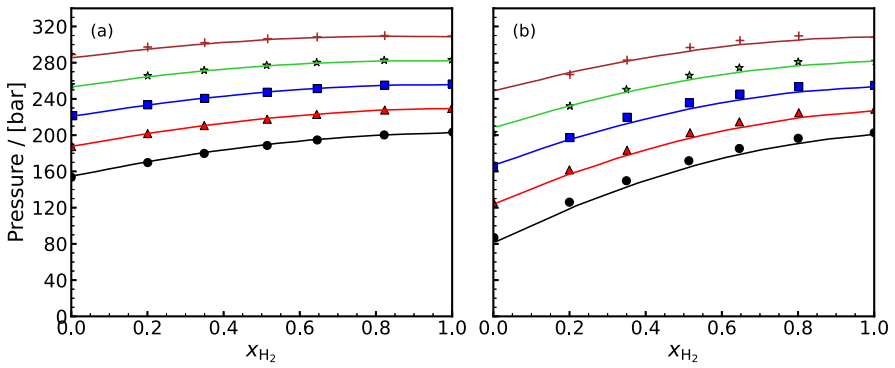

Figure 35. Pressure as a function of mole fraction of H_2 at different temperatures for (a) H_2-CH_4 and (b) H_2-CO_2 binary mixtures. EoS data are shown as lines (black: 310.9 K, red: 350 K, blue: 390 K, green: 430 K, brown: 470 K). Molecular simulation data are shown as symbols (black circles: 310.9 K, red triangles: 350 K, blue squares: 390 K, green stars: 430 K, brown crosses: 470 K).

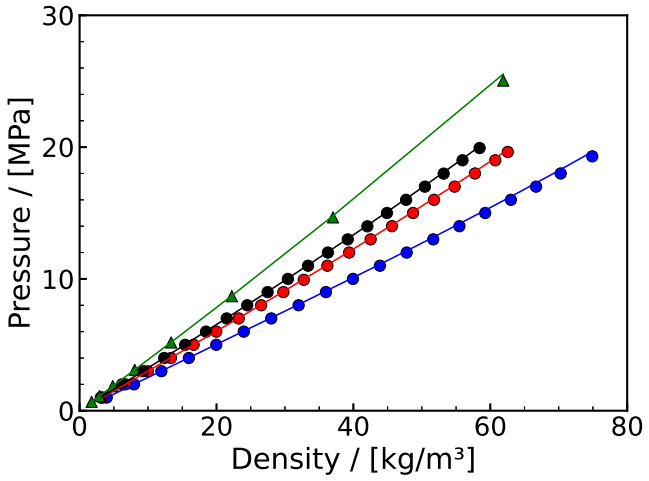

Figure 36. Pressure - density diagrams of an equimolar mixture of H_2 and CH_4 (black, red, and blue circles are molecular simulation data from ref 718. Black, red, and blue lines represent experimental data from ref 719). Additional comparisons for mixtures with H_2 mole fractions of 0.05 and 0.10 are provided in the Supporting Information of ref 718. Here, a H_2-CH_4 mixture with H_2 mole fraction of 0.6992 H_2 at 673.1 K is also shown (simulation data, represented as green triangles are from ref 718 and experimental data, shown as green line, are from ref 720).

systems were computed at 323 K (using CFCMC simulation - see Section 3.3.1.4), and were shown to have excellent agreement (within 3%) compared to values obtained using REFPROP.[352] Hulikal Chakrapani et al.[576] also showed that thermodynamic factors can be computed from simulations of small system sizes (of ca. 100 molecules) even for densely packed systems using the proposed method.

Barraco et al.[309] systematically compared eight classical LJ-based rigid molecular models of pure H_2 gas under thermodynamic conditions relevant to on−board H_2 storage in tanks. The selected temperatures (-50 °C to 90 °C) and pressures (50 to 2000 bar) reflect specifications provided by H_2 tank manufacturers, ensuring that the models are evaluated under realistic, high pressure, operating scenarios. A total of 600 MD simulations were conducted across twenty−five experimentally derived H_2 gas densities per temperature (-50 °C, 20 °C, and 90 °C). For each model, the study presented data for the *pVT* and phase behavior, and self-diffusivities. The raw simulation data are available in the original work.[309] While all models exhibited nearly identical diffusion behavior, clear differences emerged in reproducing phase behavior and solubility, especially at high densities. Among the force fields tested, the two-site model by Yang and Zhong[325] and the single-site model derived from Buch[312] performed most consistently across all conditions. For a detailed discussion on H_2 force fields see Section 3.1.1.

4.2.3. Density, Thermal Expansivity, Heat Capacity, Joule-Thomson Coefficient, and Isothermal Compressibility of the Hydrogen-Light Gas Mixtures. Raju et al.[716] performed MC and MD simulations to compute various thermodynamic properties of CO_2-rich mixtures with different gases (N_2, Ar, CH_4, and H_2) at mole fractions ranging from 0.01 to 0.10 (impurity level), exploring a broad spectrum of state points. The authors used well-known force fields previously validated for the pure components. For an extensive collection of raw simulation data and respective figures, the reader is referred to the main manuscript and Supporting Information of ref 716. To illustrate key trends without redundancy, here, we focus on the binary CO_2-H_2 system at a H_2 mole fraction of 0.05, comparing the data from molecular simulation with predictions from the GERG-2008 EoS obtained from REFPROP. Density predictions closely follow GERG-2008 EoS values as shown in Fig. 37. Under these conditions, the maximum relative deviation is approximately 4.4% in the MC simulation at 313 K and 60 bar, 4.3% in the

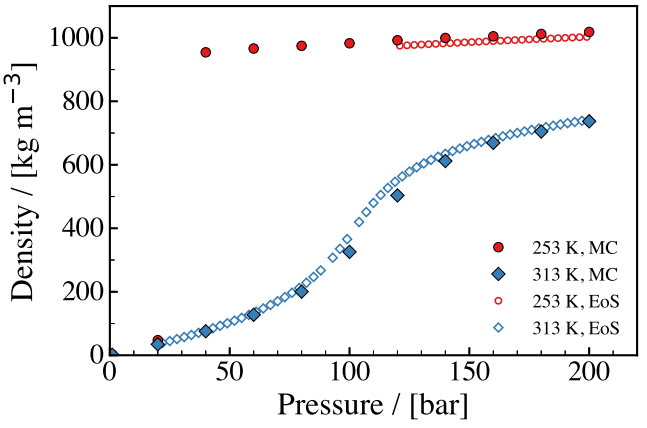

Figure 37. Density of CO_2-H_2 mixture as a function of pressure at a fixed CO_2 mole fraction of 0.05 for two temperatures. The EoS data are from GERG-2008 via REFPROP. Raw simulation data are provided in ref 716.

https://doi.org/10.1021/acs.chemrev.5c00617
Chem. Rev. 2025, 125, 11878−12029

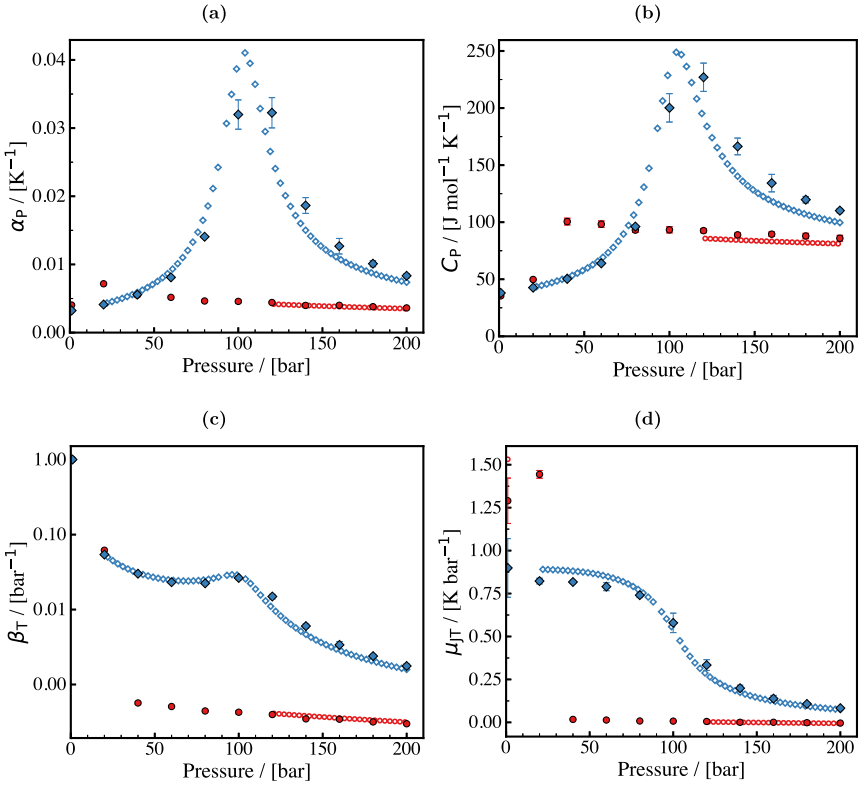

Figure 38. Thermodynamic properties of the CO_2-H_2 mixture at fixed H_2 mole fraction of 0.05: (a) Thermal-expansion coefficient, showing peaks near the saturation pressure at 313 K. (b) Isobaric heat capacity, which surges near saturation, showing increased sampling uncertainty. (c) Isothermal compressibility, also showing maxima at saturation. (d) Joule-Thomson coefficient. In all panels, MC simulation (ensemble-fluctuations) results are plotted with filled colored markers, and GERG-2008 EoS with white-filled markers. Red and blue colors represent 253 and 313 K, respectively.

MD simulation at 253 K and 80 bar, 2.1% in MC at 253 K and 40 bar, and 6.6% in MD at 313 K and 60 bar. Notably, in Fig. 37 the GERG-2008 EoS data are absent for 253 K (near the critical region), reflecting the known limitations of the EoS in that regime.

Raju et al.[716] also showed that CO_2-rich mixtures with H_2 gas as impurity, exhibit the largest reductions in thermal-expansion coefficients, isothermal compressibilities, isobaric heat capacities, and Joule-Thomson coefficients in the gas phase, followed, in decreasing order of effect, by N_2, Ar, and CH_4. Conversely, in the liquid and supercritical regions, H_2 impurities cause the greatest increases in these properties, again with N_2, Ar, and CH_4 having progressively smaller impacts. In contrast to these findings, the addition of H_2 raises gas phase speed of sound, but lowers this property in the liquid and supercritical phases. The respective data are shown in Fig. 38. As can be seen in Fig. 38(a), both the MC simulations and GERG-2008 EoS capture the pronounced maximum in the thermal-expansion coefficient of the CO_2-H_2 mixture at 313 K, as the pressure approaches saturation. At 253 K, the EoS fails to converge in the vicinity of the critical point (hence the missing data), whereas the MC simulations produce valid fluctuations, consistent with the absence of any phase split. The highest discrepancy between simulation and EoS occurs at approximately 120 bar and 313 K (very close to the saturation line of the mixture). Similar peaks are observed for the heat capacity (Fig. 38(b)) and the compressibility factor (Fig. 38(c)). For heat capacities near the saturation pressure, a sharp increase in both the EoS and MC results can be clearly observed. Due to the proximity to saturation, and the resulting spontaneous density fluctuations, sampling becomes more computationally expensive, as reflected by the larger error bars. Therefore, the exact peak value cannot be predicted by MC simulations, unless prohibitively large system sizes are used. In ref 716, it is further concluded that the Joule-Thomson coefficient of CO_2 decreases in the presence of impurities. The JT coefficients for the CO_2-H_2 mixture are shown in Fig. 38(d).

4.2.4. Self-Diffusivity of Hydrogen in Hydrocarbons.

The diffusivity of H_2 in hydrocarbons is a crucial property for industrial processes such as Fischer-Tropsch, coal liquefaction, hydrotreating, hydrogenation, liquid organic hydrogen carriers, and separation of gas mixtures. The diffusivities of H_2 in heavy alkanes can be used to evaluate the mass transfer limitations in chemical reactors, which operate in conditions ranging from 450−550 K and 20−80 bar.[722] As for the diffusivities of H_2 in aqueous solutions (see Section 4.1.5), experimental data of H_2/hydrocarbon systems at a wide range of relevant conditions are scarce. Therefore, analytical models, such as modified Stokes-Einstein relations, are used to estimate these diffusivities. To this end, MD simulations are used to predict both self- and mutual diffusion coefficients for different H_2/hydrocarbon mixtures.

Makrodimitri et al.[722] investigated the self-diffusivities of H_2, CO, and H_2O in alkane mixtures with different chain lengths, ranging from *n*-C_{12} to *n*-C_{96}. The TraPPE[301] and Hirschfelder[321] force fields were used to model the alkanes and H_2, respectively (see more details on these force fields in Section 3.1). The choice of force fields was based on the fact that TraPPE can accurately model the critical point, densities, and

https://doi.org/10.1021/acs.chemrev.5c00617
Chem. Rev. 2025, 125, 11878−12029

melting temperatures for pure solutions and mixtures of alkanes over a wide temperature range, while the Hirschfelder model is simple (only LJ interactions) and accurate for pure H_2 gas properties. While TraPPE force field explicitly accounts for intramolecular interactions and the bond/angle/dihedral changes (modeled using harmonic potentials) for alkanes, for smaller molecules such as H_2, CO, and H_2O intramolecular interactions and bond/angle changes are usually not considered as the vibrational and rotational relaxation times are significantly smaller than the time scales relevant for diffusion. Makrodimitri et al.[722] validated the diffusivities of H_2 and CO in pure C_{12}, C_{16}, and C_{28} alkanes and obtained an agreement of ca. 10% compared to the respective experiments. MD simulations were then used to generate data for self-, Maxwell-Stefan, and Fickian diffusivities of H_2 alkane solutions. The self-diffusivities of H_2 in alkane solutions at constant temperatures and pressures were shown to decrease with the increase in the alkyl chain length. This is expected since large chain alkanes have high viscosities. The authors used SAFT EoS to compute thermodynamic factors and, thereby, the Fick diffusivities of H_2 and CO in C_{12} and C_{28} solutions at 473 K (see the method in Section 3.2.4).

Giraudet et al.[723] performed dynamic light scattering (DLS) experiments and MD simulations to measure/compute self- and mutual diffusivities of binary gas/*n*-alkane mixtures. The authors reported H_2 self-diffusivities in C_6 and C_{10} for temperatures spanning 303−423 K (at pressures of ca. 40 and 10 bar for C_6 and C_{10}, respectively). The H_2 mole fractions in all mixtures were approaching infinite dilution. The Darkrim[327] and Hirschfelder[321] force fields were used to model H_2, while for the alkanes the L-OPLS[420] force field was used. As shown in Fig. 39, the agreement between computed

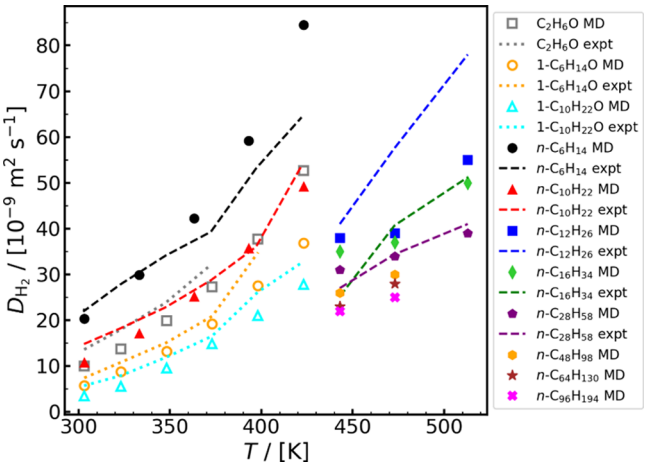

Figure 39. Diffusion coefficients of H_2 in different *n*-alkanes and 1-alcohols. Data sources: n-C_6H_{14} MD and experimental data (expt),[723] n-$C_{10}H_{22}$ MD and expt,[723] alcohols,[725] MD data for n-$C_{12}H_{26}$ up to n-$C_{96}H_{194}$,[722] expt for these systems.[726,727] Details about the force fields are given in Section 4.2.4.

and experimentally measured diffusivities of H_2 in light alkanes is relatively high. Among the gases studied by Giraudet et al.,[723] H_2 showed distinctly higher diffusivities (e.g., compared to mixtures containing N_2 or CO), which follow an Arrhenius-like behavior. Consistent with other studies in literature, diffusivity decreased with increasing carbon chain length of the *n*-alkanes. The authors used the experimental and simulation data to develop semi-empirical correlations (based on the model of Wilke and Chang[724]) with parameters being the temperature, solute and solvent molar masses, and the viscosity of the solvent.

In a consecutive study by the same research group following the same experimental technique (DLS) and simulation approach (methods and force fields), Wu et al.[725] reported H_2 self-diffusivities in 1-alcohols (i.e., C_2H_6O, 1-$C_6H_{14}O$, and 1-$C_{10}H_{22}O$) in the temperature range 303 - 423 K. As in their previous study,[723] the concentration of H_2 was close to the infinite dilution limit. The computed diffusivities are shown in Fig. 39 along with the respective experimental data. The temperature and alkyl chain dependence of H_2 diffusivity was the same as in the previous study, however, the value was lower compared to He diffusivity in the same solvents, despite the latter having a lower molar mass. The study showed that the fraction of hydrogen-bonded alcohol molecules was another factor affecting diffusivity. The fractions ranged from 0.99 at low temperatures to 0.68 at high temperatures for the different alcohol solvents, decreasing with increasing temperature and increasing alkyl chain length. The authors used the data to construct a semi-empirical model for fast estimations of the gas diffusivities in these alcohols. More MD and experimental data of transport and structural properties of H_2-hydrocarbon systems have been reported by Fröba and co-workers.[728−730]

By observing the different datasets collectively shown in Fig. 39, one can conclude that despite the different force fields and simulation protocols used in the different studies, the computed diffusivities show consistent trends, mainly dictated by the molecular weight of the hydrocarbon. Fig. 39 also reveals a lack of MD data for low/near-ambient temperature regimes for long *n*-alkanes, which can possibly be explained by the increased computational effort required to equilibrate and sample properties from these systems.

4.2.5. Mutual Diffusivities of Hydrogen Mixtures. Accurately computing the mutual diffusivities in H_2 mixtures is crucial for various applications including UHS and synthetic fuel production. Mutual diffusivities govern the rate of molecular mixing and mass transport in gas mixtures such as H_2/CO_2, impacting H_2 purity and storage efficiency in subsurface reservoirs. Additionally, H_2 diffusivity in aqueous environments (e.g., brines) affects H_2 losses due to dissolution and potential chemical reactions during UHS as discussed in Section 2.3.4. Since experimental data under relevant high-pressure and temperature conditions are not available or challenging to obtain, molecular simulations provide vital insights and reliable predictions of diffusion behavior, enabling better design and management of H_2 storage systems and related processes. Here, we review articles that report mutual- and self-diffusivities of H_2 binary mixtures with small gases using MD simulations. Contrary to self-diffusivities of aqueous systems, the data on mutual-diffusivities of H_2 mixtures are limited, practically corresponding to two studies, which are listed in Table 12.

Hulikal Chakrapani et al.[677] computed mutual (i.e., MS and Fick) diffusivities of binary gas mixtures of H_2 and CO_2, as well as their solubilities in NaCl brine, over pressures ranging from 5 to 50 MPa, temperatures from 323.15 to 423.15 K, H_2 mole fractions from 0 to 1, and salt concentrations up to 2 mol salt/kg of H_2O. MD simulations were used to compute transport properties, i.e., self-, MS, and Fick diffusivities (methods discussed in Sections 3.2.3 and 3.2.4), while GEMC simulations with the CFC method were conducted to obtain VLE and solubilities. MS diffusivities from MD exhibit

https://doi.org/10.1021/acs.chemrev.5c00617
Chem. Rev. 2025, 125, 11878−12029

Table 12. List of the MD Simulation Studies Investigating the Mutual Diffusivities of H_2-Gas Mixtures along with Information on the Force Fields and Thermodynamic Conditions

Study	System details		Thermodynamic conditions	
	Components	Force field	p/[MPa]	T/[K]
Hulikal Chakrapani et al.[677]	H_2	Marx[328]	5−50	323.15−423.15
	CO_2	TraPPE[678]		
Saric et al.[731]	H_2	Vrabec[48]	9	290−350
	CO_2	Merker et al.[732]		

significant deviations from the Darken relation,[509] which assumes ideal diffusing mixtures. For a H_2 mole fraction of ca. 0.7, Darken underestimates MS diffusivities by up to 30%, whereas deviations drop to about 5% at low or high H_2 concentrations. This underscores the non-ideal behavior of H_2/CO_2 mixtures, as also reflected in the thermodynamic factors, Γ, which quantify the non-ideality of mixtures (see Section 3.2.13). Γ decreases with increasing pressure, and increases with temperature, spanning roughly 0.25 to 1 across the studied conditions. The deviation of Γ from unity in the study by Hulikal Chakrapani et al.,[677] confirms strong non-ideal interactions affecting the MS-Fick relationship. The order of magnitude of Fick diffusivities, which are obtained by multiplying MS diffusivities with Γ, range from approximately 10^{-8} to 10^{-6} m^2/s, with higher values corresponding to lower pressures and elevated temperatures. At 5 MPa and 423.15 K, where mixtures approach ideal behavior, kinetic theory (using the Chapman-Enskog expression) predicts Fick diffusivities within 5% accuracy. However, at lower temperatures and higher pressures, especially in CO_2-rich mixtures, kinetic theory deviates by up to 75%. In contrast, H_2-rich mixtures retain agreement within about 15% even at 50 MPa, owing to their more ideal-gas-like behavior. To remedy kinetic theory's shortcomings at high pressures and low temperatures, the empirical Moggridge correlation is applied. This captures the liquid-like behavior of CO_2-rich mixtures and predicts MS, and thus Fick, diffusivities within 5 to 10% of computed values under such conditions. Yet, for H_2-rich mixtures and low pressures, Moggridge's correlation can err by up to 35%, making it less suitable in those regimes. The observed transport behavior stems from the transition between gas-like and dense-gas-like regimes, with self-diffusivities inversely proportional to mixture density. Molecular size differences also play a key role i.e., H_2 diffuses 2.5 to 6 times faster than CO_2, a discrepancy partially explained by the Stokes-Einstein relation. Comparisons with experimental data at near-atmospheric pressures (indirectly obtained by extrapolating the simulation data via the principle of corresponding states) show agreement within approximately 15%, thereby validating the molecular simulation approach. Although no single general fit function is proposed, established correlations (i.e., Chapman-Enskog kinetic theory, Fuller correlation, and Moggridge correlation) are assessed and recommended according to the relevant pressure, temperature, and composition regimes.

Saric et al.[731] performed MD simulations and EoS modeling to examine thermodynamic, transport, and structural properties of supercritical carbon dioxide ($scCO_2$) mixtures containing solutes such as H_2, CH_4, and various hydrocarbons, over temperatures from approximately 290 to 350 K, and pressures in the range 9 - 12 MPa. The study focused on dilute compositions near the infinite-dilution limit (0.3-1.5 mol%). Here, the Widom region refers to the temperature span near the critical point where the fluid undergoes a continuous crossover from liquid-like to gas-like supercritical behavior. It is marked by pronounced maxima in thermodynamic response functions such as c_p, β_T, and α, and corresponds to enhanced density fluctuations and structural changes. In this context, the temperature dependence of self-diffusion coefficients (also termed intra-diffusion coefficients) in $H_2/scCO_2$ mixtures was analyzed. These coefficients, representing species-specific Fickian self-diffusion, were derived from velocity autocorrelation functions in MD simulations, distinguishing them from MS diffusivities. Across the Widom region, self-diffusion coefficients exhibit a sigmoidal increase with temperature, rising by at least an order of magnitude between roughly 305 and 320 K at 9 MPa. Lighter molecules, such as H_2, diffuse significantly faster than e.g., hydrocarbons, with diffusivities increasing more steeply during the liquid-like to gas-like supercritical crossover. This sigmoidal behavior reflects the transition from a dense, liquid-like regime, dominated by strong intermolecular interactions and low diffusivity, to a low-density, gas-like regime where kinetic effects prevail and diffusivity is high. The crossover temperature aligns with maxima in c_p, β_T, and α, and coincides with microscopic structural changes: a reduction in average coordination number and clustering effects quantified by Kirkwood-Buff integrals. Moreover, near the Widom line, the kinetic contribution to shear viscosity surpasses the configurational component, indicating a shift in molecular transport mechanisms. In the Widom region, simulation data exhibit increased scatter, reflecting the strong density fluctuations characteristic of critical phenomena. Finally, Saric et al.[731] proposed an empirical correlation for predicting the Widom line temperature as a function of pressure, solute mole fraction, and the critical properties of mixture components. Although this correlation yields only the thermodynamic crossover temperature, it enables indirect estimation of mutual diffusivity trends by pinpointing the temperature region where transport properties such as diffusivity change dramatically due to the liquid-to-gas transition in the supercritical phase. Consequently, knowledge of the Widom line location aids in anticipating the temperature range over which molecular transport properties vary strongly.

4.3. Hydrogen Liquefaction and Properties of Liquid Hydrogen Systems

Han et al.[295] investigated H_2 liquefaction on CNT surfaces by performing MD simulations using the reactive force field ReaxFF[707] to model H_2-CNT interactions. Although in this review we do not systematically discuss reactive systems, we cover this study for two reasons: (i) to the best of our knowledge, molecular simulations of H_2 liquefaction are extremely scarce, and (ii) the claim of the authors that the liquefaction of H_2 could be increased by introducing CNTs is both unique and could lead to significant advancements in H_2 transport and storage. The simulations compared H_2 interactions with different CNT systems (bundles, isolated CNTs, single- and multi-walled). The authors report that H_2 liquefaction occurred only on the CNT bundle (not on single CNTs) at 80 K and 100 bar. This phenomenon involves various mechanisms; deformation of the CNT bundle into oval shapes under pressure, charge transfer from low-curvature to

https://doi.org/10.1021/acs.chemrev.5c00617
Chem. Rev. 2025, 125, 11878−12029

high-curvature regions of the deformed CNTs, development of charge polarization in the bundle, long-range electrostatic interactions between the polarized charges and H_2 molecules, and high local-ordering of H_2 gas leading to liquefaction. Single CNTs did not induce liquefaction because they deformed symmetrically under pressure, preventing charge polarization from developing. No chemisorption of H_2 was observed, only physisorption and liquefaction. Han et al.[295] suggest that H_2 gas could potentially be liquefied at temperatures higher than 80 K on more strongly polarized CNT bundles. This study provides insight into the previously unexplained linear increase in H_2 uptake with pressure observed by Ye et al.[733] and explains the discrepancy between the high storage capacity of CNT bundles versus the limited capacity of single CNTs.

Cheng and Frenkel[537] introduced the WAVE method and applied it to calculate the thermal conductivity of liquid H_2 and supercritical water (see the details of the method in Section 3.2.6). The H_2 system studied was highly compressed (33 GPa) at 2000 K. The authors used an ML-derived force field, for which they obtained a thermal conductivity of 5 W/mK. This value is on the same order of magnitude with the value for compressed gaseous H_2 at 1000 bar, obtained from the extrapolation of measurements. The authors note that nuclear quantum effects should probably be considered for more accurate results. For more details on these effects the reader is referred elsewhere.[734,735]

A series of studies, such as the ones by Lenosky et al.,[736] Collins et al.,[737] Holst et al.,[738] Tian et al.,[739] Redmer et al.[740] focused on computing properties of liquid H_2 mainly using quantum mechanical methods (e.g., ab initio MD, tight-binding electronic structure techniques, DFT). These studies report electrical conductivities, *pVT* relations, hopping mechanisms and electronic transport coefficients, atomic/molecular H_2 properties, liquid-liquid phase transitions, shock-compressed H_2. Despite the wealth of physical insights and the useful data provided, a detailed analysis of these papers is not in the scope of this review, which focuses on classical molecular simulation of H_2 systems.

Liu et al.[741] performed MD simulations to study liquid H_2 nucleation and boiling on a flat aluminum heat conducting substrate. The authors used a simple LJ potential for H_2 molecules and an EAM potential for the wall. Bubble nucleation was studied in the temperature range of 100 - 200 K, while liquid H_2 was obtained at 20 K. The authors mention that their MD simulations revealed a complete bubble nucleation, growth, and merging process, while for the H_2 boiling process, nucleate, transition, and film boiling stages were obtained. Higher wall temperatures accelerated bubble growth rate and affected gas film growth rate more than bubble growth rate. Wall temperature was shown to have minimal effect on liquid layer thickness during nucleation. The contact angle computed was ca. 4.9 degrees. While the study by Liu et al.[741] provides some insight into interfacial H_2 properties, the methods used could raise concerns regarding the accuracy of the reported data and conclusions. The LJ potential used for H_2-H_2 interactions may be adequate for gaseous systems, however, since H_2 is a quantum fluid at low temperatures (such as the cryogenic temperature of 20 K used in the study), is highly unlikely to be accurate (techniques such as path-integral MD would be more appropriate). The authors mentioned that the potential validation was performed for density at 20 K and 1 bar, for which the result deviated only 1.37% from the NIST data (ca. 70 kg m^{-3}). While this seems reasonable, density alone is insufficient to validate a model for complex phenomena such as boiling. The authors neither mention the use of quantum corrections nor of a more sophisticated force field which accounts for quantum effects. In addition, the cutoff distance for the interactions is not mentioned. The NEMD simulation performed to study the bubble nucleation was only 26 fs, which is extremely short for observing complete boiling phenomena.

4.4. Hydrogen Solubility, Diffusivity, and Permeability in Polymeric and Composite Materials

The role of molecular simulations the past 40 years in understanding gas sorption and permeation in polymers has been significant. Unlike inorganic materials, polymers experience structural alterations during these processes. Many studies successfully modeled barrier properties in various polymers (e.g., PET, PS, polyimides) and accurately predicted sorption mechanisms, temperature effects, and permeation values. Key qualitative findings include the sorption mechanisms below glass transition temperatures, accessible volume pockets influenced by polymer chemistry, and structural changes during sorption. Research also has been conducted to study mixed-gas penetrants and composite materials (such as MOF-polymers, zeolite-polymers), demonstrating that molecular simulations can reproduce experimental trends, and sometimes, even quantitative predictions of permeation properties.[742,743]

As discussed in Sections 2.2.1, 2.3.1 and 2.4.1, important H_2 technologies, such as storage in tanks, membrane separations, and gas transport via pipelines, may involve polymeric materials. To this purpose, MD and MC studies focusing on H_2 solubilities, diffusivities, and permeabilities in these materials are abundant in the literature. The study by Voyiatzis and Stroeks[407] presents a comprehensive investigation into the solubilities of H_2 and O_2 in two industrially significant polymers (e.g., as liner materials in high-pressure H_2 storage tanks): PA6 and HDPE. The authors used the free energy perturbation and fast-growth thermodynamic insertion methods, to predict H_2 solubilities in both the crystalline and amorphous phases of the polymers. These simulations were conducted in a temperature range of 300 - 360 K and at 700 bar pressure to study H_2 transport behavior under conditions relevant to storage in tanks. The crystalline phases of the PA6 and HDPE polymers consisted of 64 and 40 chains of infinite length, respectively. The crystal structure of PA6 in the simulation box is shown in Fig. 42(a). The amorphous phases comprised 10 PA6 molecules of 160 monomers, and 30 HDPE chains of 110 monomers. The study revealed that the crystalline phases of both PA6 and HDPE are completely impermeable barriers to both H_2 and O_2, despite the small size of these gases. The molecular simulations achieved semi-quantitative agreement with experimental solubility measurements. Discrepancies between predicted and experimental values were attributed primarily to the simulations' inability to fully account for the constraining effects that crystalline regions exert on adjacent amorphous polymer domains. The study also showed that despite H_2 being significantly smaller than O_2, it consistently exhibits lower solubility in both PA6 and HDPE. This is a rather counterintuitive finding, also shown in prior simulation and experimental studies, that can be explained based on the more favorable interactions of the O_2 with both polymer matrices compared to H_2. The findings by Voyiatzis and Stroeks[407] that H_2 migration occurs predominantly

https://doi.org/10.1021/acs.chemrev.5c00617
Chem. Rev. 2025, 125, 11878−12029

through the amorphous regions, with crystalline domains acting as impermeable obstacles, and that intermolecular interactions between the gases and the polymer chains dominate solubility behavior over considerations of accessible volume distribution within the polymer, can be taken into consideration when designing gas barrier materials. The computed solubilities are shown in Fig. 40 and listed in Table 13.

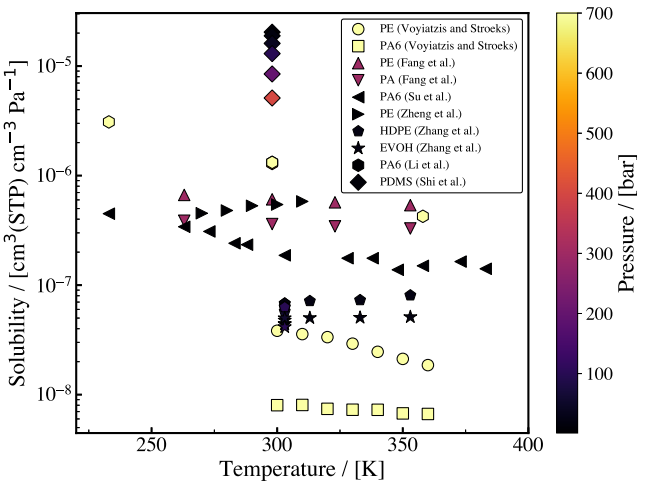

Figure 40. Solubilities of H_2 in different polymers computed via molecular simulations performed in different studies. The raw data and references are listed in Table 13 except for the solubility of H_2 in PDMS.[749]

Zhao et al.[744] performed all-atom MD simulations to study the mass of H_2 in PE, a liner material used in type IV storage tanks (see also Section 2.3.1). The study was performed at a wide pressure (up to 700 bar) and temperature (up to 400 K) range, and focused on different properties including tensile behavior, glass transition temperature, H_2 diffusion in various PE structures, and bubble formation during rapid depressurization. Several systems were considered, i.e., varied PE chain length and structure (branched and unbranched), reinforcement with graphene, the incorporation of small molecules as additives ($C_{20}H_{42}$), and various H_2 concentrations. The number of polymer chains in the systems studied varied from 1 to 16, having degrees of polymerization in the range of 500 to 2000. The authors showed that the presence of H_2 in PE matrices deteriorated tensile performance and decreased the glass transition temperature, compromising the structural integrity of the materials. Several structural factors affected H_2 diffusion in amorphous PE regions. In short, branches and side chains increased H_2 diffusivity by introducing more free volume below glass transition temperature, the chain length variation had minimal effect if chains were sufficiently long, polymer orientation improves barrier properties when aligned against the pressure drop direction, small molecules/additives (acting as plasticizers) increased diffusion rates, while graphene reinforcement has the opposite effect. During rapid depressurization, H_2 molecules aggregated into nano-sized bubbles within the polymer matrix. These bubbles formed in both exclusive and free volume regions, appearing and disappearing during pressure changes before stabilizing at low pressures. To study these bubbling effects, the authors introduced to the systems large number of H_2 molecules. A simulation snapshot showing a H_2 bubble comprising 1000 gas molecules in the polymer is shown in Fig. 42(b). Similarly, for computing diffusivity, 100 H_2 molecules were used. It is important to comment here that such system sizes, which lead to phase separation (gas and polymer), make the control of the pressure of the system an arduous task for the barostat. Additionally, the introduction of rapid changes in pressures in MD simulations, bring the systems in a non-equilibrium state, during which equilibrium properties cannot be accurately sampled. Based on their findings, Zhao et al.[744] indicate that HDPE without branches and without small molecules as additives could deliver superior performance as a H_2 barrier, while graphene reinforcement should be oriented against the pressure drop direction. The computed solubilities are shown in Fig. 40 and listed in Table 13.

The permeation behavior of H_2 in PE and PA was also investigated by Fang and Ji[218]. Since the motivation of this study was also the high-pressure H_2 storage in IV-type tanks, the simulations were performed at representative for the application conditions, i.e., high pressure (300 bar) and at temperatures ranging from ca. 260 to 350 K. Contrary to Voyiatzis and Stroeks,[407] only amorphous phases were considered in this study. The authors state that the molecular weight of the PE cell was 3630, while the respective for PA was 3440. The respective polymerization degrees were 40 and 18. This study focused on several properties affecting H_2 permeation: FFV, and solubility, diffusion, and permeability coefficients. Qualitatively consistent with prior experiments and molecular simulation studies, Fang and Ji[218] showed that increasing temperature causes a decrease in solubilities and increase in diffusivities of H_2 in both polymers. FFV correlated positively with temperature, with PE showcasing an increase of FFV of ca. 50% (in the range 263-353 K) compared to ca. 33% of PA. A schematic representation of the FFV distribution in the PA matrix at 353 K is shown in Fig. 42(c). Permeability coefficients increased with increasing temperature, showing the dominant role of the diffusivity in the computation (see also Section 2.2.1). PE consistently exhibited higher solubilities and diffusivities than PA for all conditions considered. As a consequence, PA is stated to have superior H_2 permeability resistance, performing three to four times better than polyethylene in preventing H_2 permeation. The computed solubilities and permeabilities are shown in Fig. 40 and Fig. 41, and listed in Table 13 and Table 14, respectively. Despite simulations following the general trends of experimental data, quantitatively the simulation data overshoot the experiments by 1 to 2 orders of magnitude, clearly showing that either the simulation scheme and/or the force fields chosen have limited predictive ability. In a similar study, Li et al.[745] studied the barrier performance (via computing solubilities, diffusivities, and permeabilities) of graphene/PA6 composites, having the filler (graphene) composition as a parameter ranging from 3 to 7 wt%. Depending on the graphene content, the number of PA6 monomers varied from 8 to 60. The exact number of polymer chains used is not clearly mentioned, however, the unit cell dimensions for the different systems are provided. A configuration of a model graphene/PA6 system as obtained by the commercial software used by the authors is shown in Fig. 42(d). Similarly to the previous study, conditions relevant to H_2 storage at IV-type tanks were considered, i.e., 233 - 358 K and 1 - 700 bar. In this study, the properties were correlated to different graphene contents except from the different temperatures and pressures. Several insights, relevant to H_2 storage vessel design, were reported. Particularly, it was shown that the

https://doi.org/10.1021/acs.chemrev.5c00617
Chem. Rev. 2025, 125, 11878−12029

Table 13. Solubilities (S) of H_2 in PE/HDPE, PA6/PA, and EVOH Polymeric Matrices Computed in Different Studies[a]

Source	T	p	PE/HDPE	PA6/PA	EVOH
Voyiatzis and Stroeks[407]	300	700	3.83×10^{-8}	8.01×10^{-9}	
	310	700	3.57×10^{-8}	8.05×10^{-9}	
	320	700	3.35×10^{-8}	7.42×10^{-9}	
	330	700	2.92×10^{-8}	7.28×10^{-9}	
	340	700	2.46×10^{-8}	7.27×10^{-9}	
	350	700	2.12×10^{-8}	6.74×10^{-9}	
	360	700	1.86×10^{-8}	6.66×10^{-9}	
Fang and Ji[218]	263	300	6.66×10^{-7}	3.87×10^{-7}	
	298	300	6.07×10^{-7}	3.61×10^{-7}	
	323	300	5.70×10^{-7}	3.44×10^{-7}	
	353	300	5.37×10^{-7}	3.29×10^{-7}	
Su et al.[746]	233	1		4.49×10^{-7}	
	263	1		3.41×10^{-7}	
	273	1		3.09×10^{-7}	
	283	1		2.41×10^{-7}	
	288	1		2.34×10^{-7}	
	303	1		1.87×10^{-7}	
	328	1		1.76×10^{-7}	
	338	1		1.76×10^{-7}	
	348	1		1.38×10^{-7}	
	358	1		1.50×10^{-7}	
	373	1		1.64×10^{-7}	
	383	1		1.41×10^{-7}	
Li et al.[745]	298	1		1.32×10^{-6}	
	298	350		1.31×10^{-6}	
	298	525		1.29×10^{-6}	
	298	700		1.32×10^{-6}	
	233	700		3.09×10^{-6}	
	358	700		4.25×10^{-7}	
Zheng et al.[748]	270	1	4.53×10^{-7}		
	280	1	4.80×10^{-7}		
	290	1	5.30×10^{-7}		
	300	1	5.44×10^{-7}		
	310	1	5.81×10^{-7}		
Zhang et al.[750]	303	25	6.79×10^{-8}		4.40×10^{-8}
	313	25	7.16×10^{-8}		5.02×10^{-8}
	333	25	7.30×10^{-8}		5.05×10^{-8}
	353	25	8.07×10^{-8}		5.12×10^{-8}
	303	25	6.79×10^{-8}		4.43×10^{-8}
	303	40	6.36×10^{-8}		4.755×10^{-8}
	303	60	5.78×10^{-8}		4.995×10^{-8}
	303	100	6.29×10^{-8}		4.148×10^{-8}

[a] T is in units of K, p in bar, and S in $cm^3(STP)\ cm^{-3}\ Pa^{-1}$.

5 wt% graphene/PA6 composite has the optimal barrier performance, achieving a 54.6% reduction in permeability coefficient compared to pure PA6 at ambient conditions. This substantial improvement indicates the effectiveness of graphene as a nanofiller for H_2 barrier applications. Li et al.[745] showed that temperature has a pronounced effect on H_2 diffusion, with the diffusion coefficient of 5 wt% graphene/PA6 increasing by 138% in the range 298 - 358 K at 70 MPa. The authors state that this finding highlights the importance of thermal management in storage vessel design. As in prior studies, H_2 diffusivity was shown to have a linear and inverse relationship with pressure for all materials. Pure PA6 consistently showed the highest diffusion coefficient, while the 4 wt% graphene/PA6 composite displayed the lowest. The addition of graphene was found to restrict polymer chain movement, and disrupt pore continuity within the polymer matrix, creating a more tortuous path for H_2 molecules. FFV directly correlated with diffusion coefficients, providing a mechanistic explanation for the observed barrier improvements. The computed solubilities and permeabilities are shown in Fig. 40 and Fig. 41, and listed in Table 13 and Table 14, respectively.

H_2 permeability in PA6 was also studied via MD and MC simulations performed by Su et al.[746] Similarly to the studies discussed earlier, the authors highlight that H_2 permeation through these polymeric liners is almost inevitable, thus, understanding the behavior of H_2/PA systems under extreme conditions (233-358 K and 1-875 bar) is critical for evaluating long-term performance and safety of storage tanks. The authors claim that their work is the first comprehensive molecular-level investigation of H_2 permeation in PA6 under realistic service conditions. Given that Su et al.[746] performed

https://doi.org/10.1021/acs.chemrev.5c00617
Chem. Rev. 2025, 125, 11878−12029

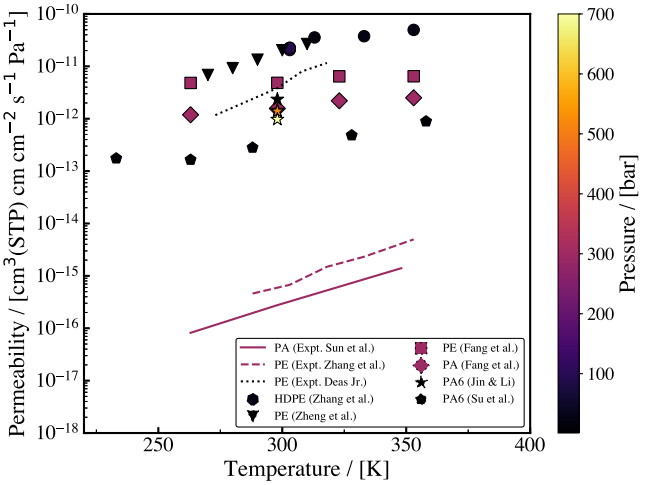

Figure 41. Permeabilities of H_2 in different polymers computed via molecular simulations performed in different studies. Three experimental datasets are shown for comparison (lines). The raw data and references are listed in Table 14.

simulations up to 875 bar, and that correction factors are applied to the results, their claim may be partially justified. However, it is important to comment here that this study uses conventional methods and tools to compute properties that have also been presented earlier for both PA and other polymeric matrices. In more detail, the authors primarily perform GCMC simulations to compute H_2 solubilities, MD simulations to calculate diffusion coefficients, while they apply corrections to account for polymer crystallinity (30%). The corrections used for the solubilities and diffusivites are functions of the volume fractions of the amorphous and crystalline regions, which have been used also in earlier studies.[413,747] In this study, 4 polymer chains comprising 200 monomers, were used. Su et al.[746] discuss the dependence of solubitlies, FFVs, and diffusivities on temperature, which exhibit complex patterns with multiple Arrhenius regions, particularly at ca. PA6's glass transition temperature. The computed solubilities and permeabilities are shown in Fig. 40 and Fig. 41, and listed in Table 13 and Table 14, respectively. The study identified a "hopping" mechanism for H_2 diffusion in PA6, according to which H_2 molecules vibrate within the free volume pores for extended periods with a sudden hop happens to adjacent pores when the thermal motion of the polymer chains creates temporary channels. The simulation trajectory of a H_2 molecule in PA6, indicating the hopping transport mechanism, is shown in Fig. 42(e). Please note that this H_2 hopping mechanism should not be confused with the proton hopping mechanism discussed in e.g., Sections 3.2.12, and 4.1.6. As a conclusive remark, this study showcases that molecular simulations play a crucial role for understanding complex H_2 phenomena at elevated conditions. For example, the identification of multiple Arrhenius regions in the behavior of sorption and diffusivity can lead to improved predictive models for permeation behavior.

Motivated by the use of polymers as building or supporting materials in pipelines, Memari et al.[413] performed experiments and molecular simulations to study the solubility of CH_4+CO_2 and CH_4+H_2 mixtures in semicrystalline PE below its melting temperature. MC simulations in the osmotic ensmeble were performed using PE chains of 70 carbon atoms each. To the best of our knowledge, this is the only H_2/PE study which uses

Table 14. Permeabilities (P) of H_2 in PE/HDPE and PA6/PA Computed in Different Studies[a]

Source	T	p	PA/PA6	PE/HDPE
Fang and Ji[218]	263	300	1.19×10^{-12}	4.82×10^{-12}
	298	300	1.57×10^{-12}	4.84×10^{-12}
	323	300	2.20×10^{-12}	6.43×10^{-12}
	353	300	2.51×10^{-12}	6.46×10^{-12}
Li et al.[745]	298	1	2.35×10^{-12}	
	298	350	1.44×10^{-12}	
	298	525	1.39×10^{-12}	
	298	700	9.70×10^{-13}	
Su et al.[746]	233	1	1.75×10^{-13}	
	263	1	1.65×10^{-13}	
	288	1	2.81×10^{-13}	
	328	1	4.83×10^{-13}	
	358	1	8.91×10^{-13}	
Zheng et al.[748]	270	1		6.84×10^{-12}
	280	1		9.24×10^{-12}
	290	1		1.34×10^{-11}
	300	1		2.03×10^{-11}
	310	1		2.67×10^{-11}
Zhang et al.[750]	303	25		2.16×10^{-11}
	313	25		3.56×10^{-11}
	333	25		3.76×10^{-11}
	353	25		4.96×10^{-11}
	303	40		2.26×10^{-11}
	303	60		2.05×10^{-11}
	303	100		2.24×10^{-11}
Experimental data by Deas-Jr et al.[751]	273	1		1.17×10^{-12}
	298	1		3.84×10^{-12}
	308	1		8.04×10^{-12}
	318	1		1.16×10^{-11}
Experimental data by Na Zhang et al.[752]	288	300		4.60×10^{-16}
	303	300		6.75×10^{-16}
	318	300		1.49×10^{-15}
	333	300		2.32×10^{-15}
	353	300		4.97×10^{-15}
Experimental data by Sun et al.[753]	263	300	8.18×10^{-17}	
	298	300	2.76×10^{-16}	
	348	300	1.40×10^{-15}	

[a]Three experimental datasets are provided for comparison. T is in units of K, p in bar, and P in cm^3(STP) cm cm^{-2} s^{-1} Pa^{-1}.

an anisotropic potential to model the hydrocarbon (AUA4[412]). Interestingly, the force field used for H_2 was developed by Darkrim et al.[327] to study the physisorption of H_2 and N_2 on graphite basal planes. Memari et al.[413] performed the MC simulations at 313 K and two pressures (6 and 21 bar), while a high-pressure (700±100 bar) was also examined to mimic the effect of crystallinity of the permeable zones due to the increase in the density of the polymer matrix as stated by the authors. The simulation results for the concentration of H_2 in PE were shown to be a factor of 2 higher than the respective experimental data. The agreement with experiments for both gas mixtures is significantly better at the high-pressure, while the solubility selectivity S_{CH_4/SH_2}=54 is in agreement with predictive correlations.

Zheng et al.,[748] also motivated by the application of PE as pipeline material, conducted MD and GCMC simulations to predict solubilities, diffusivities, and permeabilities of H_2 in this polymer. The temperatures and pressures considered were in the range 270 - 310 K and 1 - 70 bar, respectively, in an effort

https://doi.org/10.1021/acs.chemrev.5c00617
Chem. Rev. 2025, 125, 11878−12029

Table 15. Experimentally Measured H_2/CH_4 Permeabilities Gathered from Different Literature Sources[a]

Membrane	P_{H_2} (Barrer)	P_{H_2}/P_{CH_4}
ZIF-8[812]	1.38×10^4	20.3
ZIF-8[813]	1.25×10^4	16.2
ZIF-22[814]	2.27×10^4	5.2
LTA[815]	3.76×10^3	3.6
HKUST-1[816]	1.79×10^5	6
ZIF-7[817]	358	5.9
P84/ND[818]	6.7	310
Matrimid/ZIF-11 (10%)[819]	28.11	97
6FDA-TTM/Si-H (5%)[820]	62.6	160.5
MWCNT@GONRs (2%)[821]	42.5	18.5
PLA[822]	25	10
Hyflon AD60X[823]	187	62
ZIF-8/6FDA-durene[824]	4.2×10^3	17
Matrimid-ZIF-8[825]	64	137
MMM-ZIF-8[826]	27.1	123.2
MMM- UiO-66[826]	64.4	153.3
JUC-160[827]	2×10^3	8.5
MEFMEQ mixture[828]	3.7×10^3	7
MEFMEQ single components[828]	4.8×10^3	21
ZIF-8 mixture[828]	6×10^3	9.8
ZIF-8 single components[828]	5.3×10^3	13.4
MOF-5 mixture[828]	4.1×10^3	2
MOF-5 single components[828]	4.6×10^3	2.3
Cu-BTC mixture[828]	2.2×10^3	3.2
Cu-BTC single components[828]	2.4×10^3	4
ZIF-7[829]	15.4	35.8
ZIF-62 glass[830]	4.2×10^3	50
NH2 − MIL−53[831]	1.3×10^5	27.3
ZIF-90[832]	1.7×10^5	70.5
Ni_2(L-asp)$_2$(bipy)[833]	6×10^4	7.77
ZIF-7[829]	14.4	34.6
MOF-5[834]	1.89×10^5	64
SIM-1[835]	6.1×10^3	2.52
Sod-ZMOF-1[836]	36.5	1.4
PSM-MOF[837]	1.18×10^3	11.1
Pebax ZIF-67 NP[838]	10.7	1.444
Pebax ZIF-67 MP[838]	10.8	1.367
Pebax Zif-67 NS[838]	12.1	1.528
Pebax 1675/CuNi[839]	11.5	3.026
PEEK-WC/CuNi[839]	68.01	68.01
6FDA-BI[840]	33.4	278.2
P/Zn[813,840]	31.8	278
6FDA-BI/20%ZIF-8[840]	78.5	223.9
6FDA-BI/20%ZIF-8 0.004 Zn[813,840]	88.2	233.4
6FDA-BI/20%ZIF-8 0.007 Zn[813,840]	110.1	225.2
6FDA-BI/20%ZIF-8 0.01 Zn[813,840]	72.3	318.3
ZIF-67-in-TpPA-1[841]	3.67×10^3	34.9
ZIF-8-in-TpPA-1[841]	3.92×10^3	23.1
ZIF-67-in-TpBD[841]	3.77×10^3	27.9

[a]The data are used in Fig. 5(a) and Fig. 48(a).

to match common operating conditions for urban PE pipelines. The authors used five PE chains each one with a degree of polymerization of 500 (corresponding to $C_{1000}H_{2002}$) to build an amorphous polymer phase. A molecular representation of the PE in the simulation box is shown in Fig. 42(f). In line with the similar studies reviewed earlier, solubilities, diffusivities, and permeabilities increased with temperature, while pressure was shown to have a negligible effect. The computed solubilities and permeabilities are shown in Fig. 40 and Fig. 41, and listed in Table 13 and Table 14, respectively. As in the study by Su et al.,[746] the gas is shown to obey the hopping transport mechanism. The free volume increases with temperature, therefore, enhancing H_2 diffusivity. The computed permeabilities were shown to systematically over-predict the experimental data by 5 to 6 times in the whole temperature range considered, clearly indicating that there is room for improved predictions using molecular simulations. This can be achieved by either using more accurate combination of force fields and/or by fine-tuning the polymer chain characteristics (e.g., molecular weight, number of chains, degree of crystallinity).

Recently, H_2 permeation through HDPE and EVOH was studied by Zhang et al.[750] at conditions relevant to gas transport in polymer pipelines, i.e., 30 °C to 80 °C (303.15 - 353.15 K) and 25 - 100 bar. The authors constructed systems containing 12 HDPE (or EVOH) chains but the degree of polymerization or the molecular weight of the polymer chains is not mentioned. The representativeness of the model was validated by comparing the density of the simulation box containing the polymer matrix with experimental values. Similarly to all the previous studies discussed in this section, temperature was shown to have a strong effect on H_2 properties. In particular, as temperature increased from 30 °C to 80 °C, the solubility, diffusion, and permeability coefficients of H_2 in HDPE increased by 18.7%, 92.9%, and 129.0%, respectively. In EVOH, these coefficients increased by 15.9%, 81.6%, and 112.7%. EVOH exhibited superior H_2 barrier properties compared to HDPE due to the hydroxyl groups in EVOH forming strong hydrogen bonds that impede H_2 movement. The computed solubilities and permeabilities are shown in Fig. 40 and Fig. 41, and listed in Table 13 and Table 14, respectively. Zhang et al.[750] showed that the H_2 permeation mechanism involves two processes: adsorption, where the gas molecules aggregate in low-potential-energy regions; and diffusion, where H_2 molecules vibrate within confined spaces before occasionally transitioning between holes. Comparisons of the simulation data with experimental measurements of H_2 permeability in HDPE are provided, showing an agreement within 7.24% difference.

Except from the study of common thermoplastics such as PE and PA used mainly as liner materials in tanks and pipelines, the sorption and diffusivity of H_2 in poly(chloro-p-xylene)[754] (the simulation box containing the polymer is shown in Fig. 42(g)), PDMS Shi et al.,[749] and in rubbery polymers[755−757] have been reported in the literature. Stalker et al.[758] performed simulations of different cellulose configurations, i.e., purely crystalline (which showed no H_2 sorption), slit pore structures with varying inter-layer spacings (4.67-7.67 Å), amorphous phase, and "pinned" structures with fixed glycosidic oxygens. A molecular simulation snapshot of the slit pore configuration is shown in Fig. 42(h). H_2 molecules within the narrow slit pores were shown to occupy discreet positions, being trapped in the empty spaces between the cellulose layers. The authors showed that in the case of wide slit pores, this behavior is not obeyed, and H_2 has more freedom to move in between the polymer layers. While pure crystalline cellulose was found to be not suitable for H_2 storage, the modified structures showed potential at experimentally accessible pressures (<100 bar), suggesting that engineered cellulose-based materials could be a viable option. Yi et al.[759] performed MD simulations investigating the diffusion of H_2 and its isotopes; deuterium

https://doi.org/10.1021/acs.chemrev.5c00617
Chem. Rev. 2025, 125, 11878−12029

Table 16. Experimentally Measured H_2/CO_2 Permeabilities Gathered from Different Literature Sources[a]

Membrane	P_{H_2} (Barrer)	P_{H_2}/P_{CO_2}
UiO-66-NH2[842]	213.2	6.8
PEI/PVP-UiO-66-NH2[843]	31	0.0787
Matrimid/EDA/ZIF-90[844]	19	9.5
PPO/Silica[845]	257.23	3.6
PI/NH2-MIL-53[846]	384.1	16.7
PI/ZIF-8/EDA[847]	283.5	12
PIL/IL/MIL-53[848]	0.14778	0.07519
PIL/IL/ZIF-8[848]	0.0514	0.2
PEBAX-0H[849]	0.04879	0.13769
PEBAX-2H[849]	0.06889	0.11563
PEBAX-4H[849]	0.07507	0.11055
PEBAX-8H[849]	0.08876	0.10430
PEBAX-12H[849]	0.0808	0.10892
PEBAX-24H[849]	0.07652	0.10732
Glass ZIF-62[830]	4597	2.25
P84/ND[818]	6.7	4.1
Matrimid/ZIF-1 (10%)[819]	28.11	4
6FDA-TTM/Si-H (5%)[820]	62.6	2.1
PI/MWCNT@GONRs (2%)[821]	42.5	1.7
6FDA-DAM-ZIF-11 (10%)[819]	106.7	0.97
6FDA-DAM-ZIF-11 (20%)[819]	272.45	1.06
6FDA-DAM-ZIF-11 (30%)[819]	76.76	1.05
P100G0[850]	0.07465	0.10417
P100G2[850]	0.08241	0.11236
P100G5[850]	0.14525	0.12821
P100G8[850]	0.18277	0.14286
ZIF-8[851]	5411	4.5
CL 6FDA-durene[824]	116.7	24.3
33 MMM[824]	2137	1.4
50 MMM[824]	4157	1.3
CL 33 MMM[824]	394.5	28.6
CL 50 MMM[824]	501	28.8
CL skin alone on 33 MMM[824]	12.5	34.6
CL skin alone on 50 MMM[824]	13.9	32.4
CL skin alone on 6FDA-durene[824]	11.1	31.7
ZIF-67-in-TpPA-1[841]	3618.75	35.71
ZIF-8-in-TpPA-1[841]	3772.04	28.73
ZIF-67-in-TpBD-1[841]	3490.05	23.85
HKUST-1[816]	176844	6.8
ZIF-7[852]	54.2	8.4
ZIF-7[814]	340.8	6.48
ZIF-22[853]	19572	7.2
ZIF-8[854]	3536.4	6
NH2-MIL-53 (Al)[855]	87750	30.9
ZIF-8[856]	2534.8	3.28
Amine-Mg-MOF-74[857]	2240	28
MIL-96 (Al)[858]	12260.8	8.8
Zn_2(Bim)3[859]	19.187	128.4
PIM-EA-TB[860]	7620.1	1.09
PIM-SBI-TB[860]	21697.4	0.76
mPBO[861]	178.5	6.2
PHBOA (8:2)[862]	0	8
PBI[863,864]	12.8	20
PBI[865]	3.6	8.6
PBI[866]	2.9	7.1
PBI[867]	27	16
BILP-101x (400 nm)[868]	9.68	39.5
NUS-2@PBI[869]	2.95	18.78
[COF-300]- [Zn2(bdc)2(dabco)][870]	130368	12.6
[COF-300]- [ZIF-8][870]	105520	13.5
COF-300[870]	107520	6
COF-LZU1[871]	1842.1	6
ACOF-1[871]	1211.34	14.1
COF-LZU1-ACOF-1[871]	660.2	24.2
CTF-1[872]	501	17.4
TpPa-1-30/GO-10[873]	943.47	25.57
[COF-300]- [UiO-66][874]	117310	17.2
COF-LZU1[875]	7309.6	31.6
TFB-BD[875]	7604.4	25.6

[a]The data are used in Fig. 5(b) and Fig. 48(b).

(^{2}H) and tritium (^{3}H) in PS under normal temperature (298 K) and pressure (1 atm). The research is motivated by the use of PS as a target material in Inertial Confinement Fusion (ICF), where understanding gas diffusion is critical for maintaining ^{2}H-^{3}H mixtures within the targets. The authors studied PS models with varying degrees of polymerization (i.e., 60, 120, 180, and 240). Interestingly, the PCFF[406] was used for all species in this study, including H_2 and the isotopes. Diffusion coefficients were shown to decrease with increasing isotope mass (H_2 > ^{2}H > ^{3}H), and decrease with increasing polymer molecular weight. FFV correlates with diffusion behavior, with higher free volume leading to higher diffusion rates. The novel aspect of this study is the investigation of the isotopes diffusion coefficients in PS, which is particularly valuable for ICF research. These gases had not been previously studied in this context despite their importance in fusion applications. The work also establishes relationships between molecular weight, free volume, cohesive energy density, and diffusion behavior that could guide the development of improved target materials with reduced gas permeability. To the best of our knowledge, studies of H_2 permeation in polymers using coarse-grained approaches are limited (e.g., see Zhao et al.[760]) and out of this review.

Synthetic thermoset polymers which are primarily used as components in auxiliary equipment (e.g., gaskets, sealing rings) in H_2 storage infrastructure, with most notable the EPDM rubber, have been studied via molecular simulation. Wilson and Frischknecht[761] used an MC−based method to create a model of cross−linked EPDM. Subsequently, MD simulations using LAMMPS[762] were performed to study the rubber's behavior when filled with high H_2 at near−ambient temperature. The OPLS-AA[428] force field was used for all spcecies. The authors computed H_2 solubilities (as a function of cross−link density) and diffusivities (as a function of the gas concentration). The reported data are in−line with previous simulations and experiments. The authors showed that rapid H_2 depressurization caused system volume to increase, and H_2 − accessible free volume to expand (with effects being more pronounced at high H_2 concentrations). Higher cross-link density increased H_2 − accessible free volume but reduced volume changes during decompression, and produced fewer large pores post−decompression. These findings indicate that higher cross−linking densities might help prevent cavitation in EPDM, though the additional free volume from cross−links could create potential cavitation initiation sites. The authors recommend experimental investigation of crosslinking density

https://doi.org/10.1021/acs.chemrev.5c00617
Chem. Rev. 2025, 125, 11878−12029

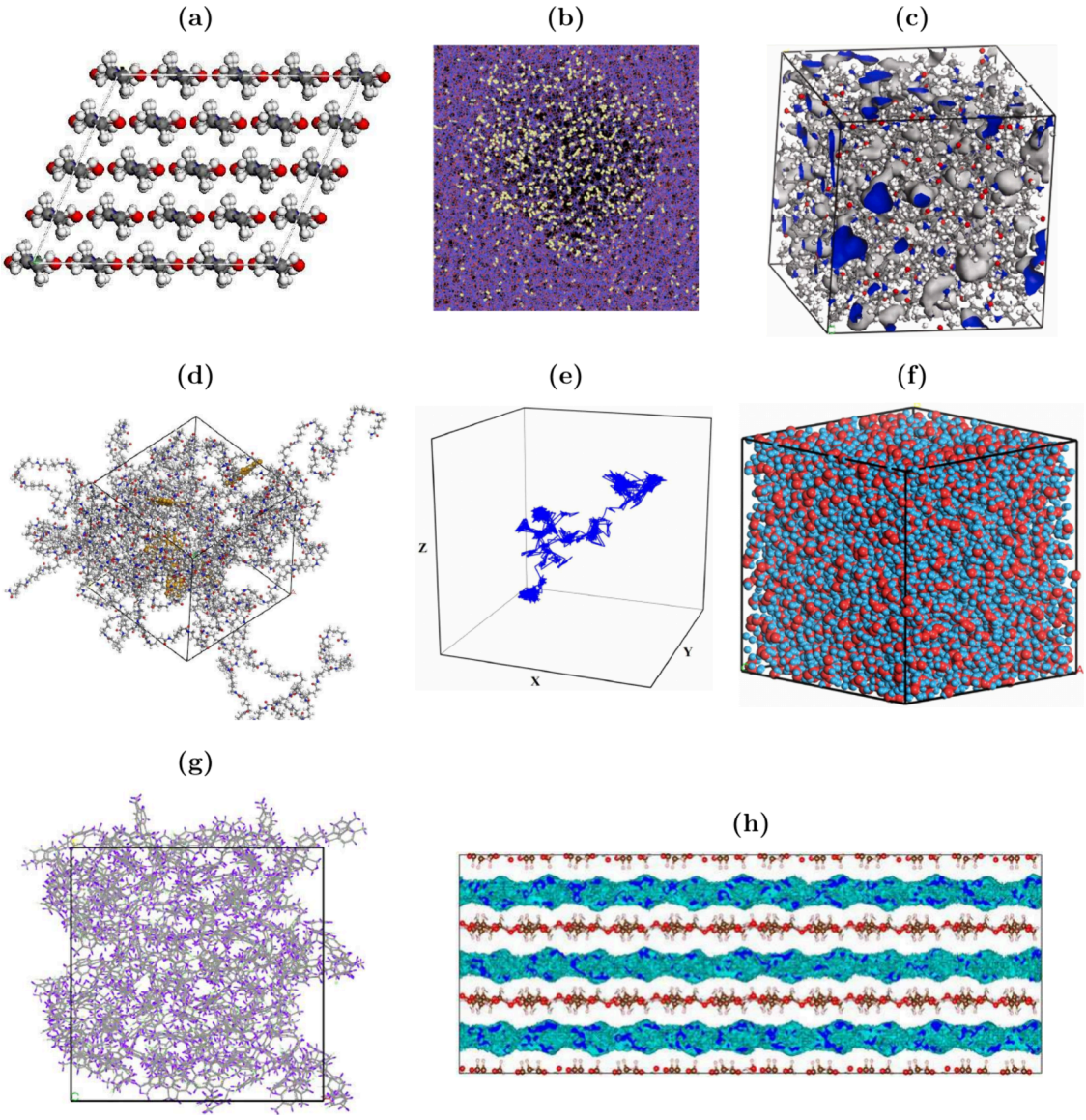

Figure 42. Simulation snapshots and molecular representations collected from different studies of H_2/polymer systems: (a) PA6 crystal structure shown in the x-y plane, (b) H_2 gas bubble in PE. H_2 molecules are shown in yellow; PE is shown in blue (C atoms) and the (H atoms), (c) free volume distribution in PA at 353 K, (d) a model graphene-modified PA6 system. Graphene atoms are shown in yellow, (e) the trajectory of a H_2 molecule in amorphous PA6 328 K and 0.1 MPa, (f) amorphous PE matrix. Carbon atoms are shown in blue and hydrogen atoms in red, (g) amorphous poly(chloro-p-xylylene) matrix, (h) H_2 sorption sites in a cellulose slit pore. [Panel (a) is reprinted with permission from Voyiatzis and Stroeks, Phys. Chem. B 2022, 126, 32, 6102-6111. Copyright 2022, American Chemical Society. Panel (b) is reprinted from International Journal of Hydrogen Energy, Vol 47, Jiawei Zhao et al., Molecular dynamics simulation of H_2 in amorphous polyethylene system: H_2 diffusion in various PE matrices and bubbling during rapid depressurization, 39572−39585, Copyright (2022), with permission from Elsevier. Panel (c) is reprinted from Materials Today Communications, Vol 35, Qing Fang, Dongmei Ji, Molecular simulation of hydrogen permeation behavior in liner polymer materials of Type IV hydrogen storage vessels, 106302, Copyright (2023), with permission from Elsevier. Panel (d) is reprinted from Li et al.,[745] open access article distributed under the terms and conditions of the Creative Commons Attribution (CC BY 4.0) license. Panel (e) is reprinted from International Journal of Hydrogen Energy, Vol 50, Part D, Ying Su et al., Hydrogen permeability of polyamide 6 as the liner material of Type IV hydrogen storage tanks: A molecular dynamics investigation, 1598-1606, Copyright (2024), with permission from Elsevier. Panel (f) is reprinted from Journal of Molecular Liquids, Vol 368, Part B, Dukui Zheng et al., Molecular dynamics investigations into the hydrogen permeation mechanism of polyethylene pipeline material, 120773, Copyright (2022), with permission from Elsevier. Panel (g) is reprinted from Computational Materials Science, Vol 49, Chunhai Lu et al., A molecular modeling study on small molecule gas transportation in poly (chloro-p-xylylene), S65-S69, Copyright (2010), with permission from Elsevier. Panel (f) is from Molecular simulation of hydrogen storage and transport in cellulose Molecular simulation of hydrogen storage and transport in cellulose, Stalker et al., Molecular Simulation, Vol 47, 170−179, Copyright (2010), reprinted by permission of the publisher (Taylor & Francis Ltd, http://www.tandfonline.com).]

effects on high−pressure H_2 − induced EPDM failure as a potential future research direction. In a complementary study by the same research group, Brownell et al.[763] performed all−atom classical MD simulations to examine how compositional changes affect gas diffusion in EPDM, in an effort to guide material design to rubbers less prone to H_2 − induced failure. The simulations revealed anomalous, sub-diffusive H_2 transport. Two distinct gas groups were identified: high−mobility

https://doi.org/10.1021/acs.chemrev.5c00617
Chem. Rev. 2025, 125, 11878−12029

gas and low−mobility gas constrained by polymer interactions. Lower temperatures increased gas localization in the low−mobility group, creating necessary conditions for cavitation damage. At reduced temperatures, higher cross−link density enhanced H_2 mobility and decreased trapped H_2 fraction, suggesting increased cross−linking may minimize cavitation precursors. The authors applied a two−state kinetic model to determine energy requirements for transitions between mobility states.

Recently, Wilson et al.[764] expanded prior studies of EPDM by studying a composite material which incorporates silica into the rubber. The motivation is that elastomers with nano-sized fillers such as silica or carbon black achieve improved mechanical properties. Filler dispersion and filler-polymer interfacial strength are crucial factors in this enhancement. Interfacial strength is vital for component durability in pressurized gas sealing applications e.g., O-rings, where poor filler-polymer binding can create internal void formations. To understand fundamental mechanisms behind pressurized H_2-induced elastomer failure, the authors performed MD simulations to examine H_2 over-saturation effects on filler-polymer interaction strength. Consistently with their prior studies, the OPLS-AA[428] force field was used to model the polymer, while the parameters by[765] were for the silica surface. The authors systematically investigated the interface between EPDM and silica across varying H_2 gas concentrations, cross-link densities, and surface chemistries. The simulations showed that high H_2 concentrations (1000 H_2 molecules) caused significant interfacial failures, including hole formation and complete debonding, while lower concentrations (up to 750 H_2 molecules) did not cause debonding. H_2 preferentially accumulated at silica-EPDM interfaces, creating concentration gradients that persisted after decompression. Higher H_2 concentrations reduced adhesive strength between silica and EPDM, with surface hydroxylation and crosslink density influencing the debonding behavior. The results suggest that dissolved high-pressure H_2 can compromise silica-EPDM interfaces, potentially leading to bubble formation and cavitation-induced failure in H_2 environments.

As shown in Figs. 40 and 41, and the Tables 13 and 14, the simulation data reported in literature regarding H_2 solubilities and permeabilities in different polymeric matrices significantly vary. The computed solubilities and permeabilities collected from different authors span three orders of magnitude. While this is expected up to a degree due to the different pressures and temperatures considered, the fact that most of the studies use the same force fields (primarily COMPASS[316] and PCFF[406]) and similar methods, makes the discrepancies shown in Figs. 40 and 41 interesting. Despite the common elements in these studies, different H_2 force fields, system sizes, polymer chain lengths, and simulation schemes (e.g., for equilibration and production runs) are used, leading to diverging results. Another striking outcome after reviewing these datasets is that while all simulations seem to be able to capture the experimental permeability trend (i.e., qualitative agreement), the quantititative difference is more than three orders of magnitutes as shown in Fig. 41. This finding alone is a strong indication that there is still ground to cover for producing accurate predictions for H_2/polymer systems using molecular simulation. It is also important to mention here that caution should be exercised when interpreting computed results for solubilities and permeabilities due to the inherent difficulties in these simulations having to do with slow dynamics, generic force fields, and computationally demanding systems. Another interesting point is that although we do not show here the collected data on computed diffusivities (which are used to compute permeabilities), none of the studies apply corrections to account for finite size effects.[498−500] It is not clear how big such effects are for the H_2/polymer systems, however, no investigation has been performed to shed light on this.

4.5. Hydrogen Solubility, Diffusivity, Permeability, and Interfacial Properties in Ionic Liquids

Separation of gases using ILs has been an active field in the molecular simulation community the past 20 years. Due to the ever increasing interest in developing carbon capture technologies for environmental and industrial purposes,[766] the vast majority of the ILs simulation studies have focused on both pure and mixtures of CO_2, with a lot of effort put on scrutinizing the diverse families of ILs. Following the same route, various thermodynamic and transport properties of H_2/ILs computed via MC and MD simulations have been reported to date. Shi et al.,[767] motivated by the carbon capture potential of the so-called supported IL membranes, performed molecular simulations to study the solubility, diffusivity, permeability, and partial molar properties of pure H_2, CO_2, and Ar, and their mixtures in 1-*n*-hexyl-3-methylimidazolium bis-(trifluoromethylsulfonyl)amide ([hmim][Tf_2N]). Molecular representations of the ions of these ILs are shown in Fig. 43. Two different H_2 force fields were compared: Buch[312] and Cracknell[311] (see Section 3.1.1). Notably, while the original Cracknell model is rigid, the authors implemented a flexible version to make it compatible with their hybrid MC method which involves a time reversible integrator (the authors explicitly note that traditional constraint dynamics methods for rigid molecules are time reversible, and thus, the original rigid H_2 could not be used in their scheme). Also, the effect of polarizability of H_2 on solubility was investigated, but it was shown to be negligible. The simulations were performed in a temperature range of 313−573 K and for pressures 1−500 bar for pure H_2, and 50−300 bar for mixed gas systems. The simulations showed that H_2 solubility in the IL increased with temperature, contradicting some prior experimental studies. Both force fields gave similar results for thermodynamic properties, though the Cracknell model showed better agreement with experimental data, particularly at high pressures. The molar volume of the ionic liquid was found to be the primary determinant of H_2 solubility, with a clear linear relationship between the Henry coefficient and molar volume. Based on an energy analysis, the interactions between H_2 and IL were shown to be ca. three to six times weaker than the interactions of the other gases with the IL. The selectivity of CO_2 over H_2 decreased from ca. 30 at 313 K to ca. 3 at 573 K. The authors showed that H_2 diffuses 5−12 times faster than CO_2, while the permeability of H_2 was 2.3−3.5 times larger than experiments. Shi et al.[767] highlight substantial differences in experimentally measured H_2 solubilities between research groups. These discrepancies (some showing solubility increasing with temperature, others showing the opposite) indicate difficulties in measuring solubility for such poorly soluble gases. The paper reports negative volume expansion when H_2 dissolves in the ionic liquid at high pressures, suggesting a compression effect. This is somewhat counter-intuitive but can be explained by the high pressures required for appreciable H_2 solubility. The authors conclude that good

https://doi.org/10.1021/acs.chemrev.5c00617
Chem. Rev. 2025, 125, 11878−12029

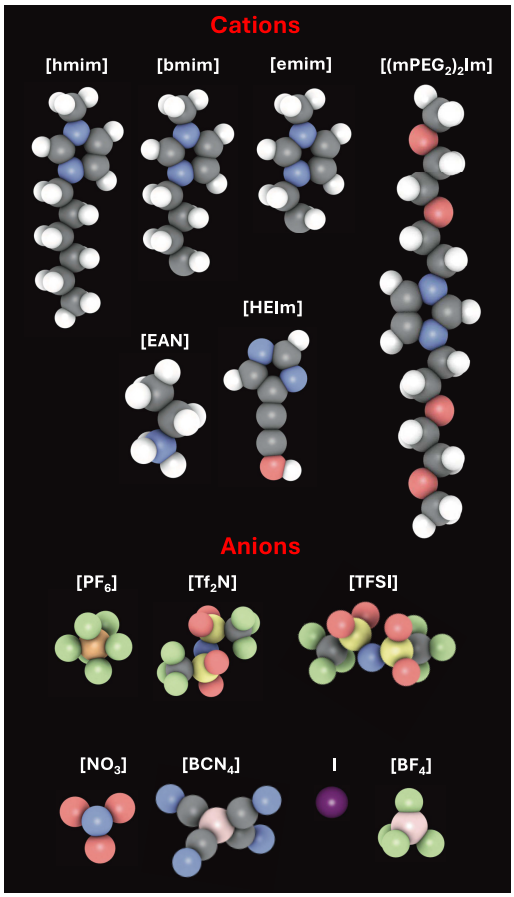

Figure 43. Molecular representations of the cations and anions of the ionic liquids studied in the papers reviewed here (iRaspa[483] visualization software was used). Color code for the atoms: gray: carbon, white: hydrogen, blue: nitrogen, red: oxygen, green: fluorine, dark yellow: phosphorous, yellow: sulfur, pink: boron, purple: iodine.

IL candidates for CO_2/H_2 separation should have low molar volumes (to reduce H_2 solubility) while maintaining high CO_2 solubility through strong interactions. This somewhat contradicts the observation that molar volume is positively correlated with gas solubility in general.

In a follow-up study, Shi and Sorescu[768] investigated how confining [hmim][Tf2N] IL in (20,20 and 9,9) CNTs (composite material) affects gas sorption properties. The authors used the same flexible version of Cracknell model.[767] The simulations were performed at temperatures up to 573 K and pressures up to 400 bar. It was shown that H_2 diffuses ca. 1.5 times faster than CO_2 in the composite material. In contrast, H_2 diffuses almost 10 times faster than CO_2 in both CNT and bulk IL. At 313 K, H_2 in the (20,20) CNT was shown to diffuse ca. 4900 times faster than in the composite material. CNT showed the highest H_2 sorption, followed by composite material and the bulk IL. For increasing temperature H_2 sorption: (i) increased in [hmim][Tf2N], (iii) decreased in CNT, and (iii) and remained almost unaffected in the composite material, which exhibited higher CO_2/H_2 sorption selectivity than both IL and CNT (S_{CO_2/H_2} = 15.0 ± 1.0, 39 ± 2, and 79 ± 2 for CNT, IL, and the composite, respectively). The authors suggest that the composite material would be superior to both IL and CNT for the CO_2/H_2 separation.

Singh et al.[391] presented a MC simulation study of the solubility of CO_2, H_2, and their mixtures in ILs 1-alkyl-3-methylimidazolium bis(trifluoromethanesulfonyl)amide ([$C_n$mim] [Tf2N], n = 4, 6). Molecular representations of the ions of these ILs are shown in Fig. 43. The motivation was the CO_2/H_2 separation in pre-combustion processes, for which understanding S_{CO_2/H_2} in high-pressure/temperature gas mixtures is crucial. The authors have implemented advanced sampling algorithms (e.g., cavity-biased, configurational-biased, and "slow-growth" - for more details on these techniques, the reader is referred to the refs within Singh et al.[391]) to overcome the inherent difficulties in MC simulations of dense and complex systems, such as ILs. Simulations were performed at 333, 413, and 573 K, and pressures up to 300 and 80 bar for pure H_2 and mixtures, respectively. It was shown that H_2 solubility in ILs slightly increases with temperature (positive enthalpy of absorption), while the volume change upon H_2 absorption were negligible (e.g., <1% at 300 bar). S_{CO_2/H_2} was shown to decrease significantly with temperature (from 40-60 at 333 K to 3-4 at 573 K). Interestingly, this study contradicts previous experimental findings by that suggested that CO_2 enhances H_2 solubility at high pressures. The work concludes that CO_2 and H_2 are absorbed almost ideally in these ILs, with no significant interactions between the two gases in the liquid phase at the studied conditions.

Ramdin et al.[769] performed MC simulations to predict the solubility of various pre-combustion gases including H_2 in 1-butyl-3-methylimidazolium bis(trifluoromethylsulfonyl)imide [bmim][Tf2N] (note that [bmim] is a different notation for the [C_4mim] cation, where b stands for butyl). Cracknell[311] force field was used to model H_2 and the model by Liu and Maginn[770] for the IL. The simulations were performed at 333.15 K and pressures up to 150 bar. The authors showed that H_2 has the lowest solubility among all studied gases (H_2S > CO_2 > CH_4 > CO > N_2 > H_2). Simulations under-predicted the H_2 solubility compared to experiments with the difference being 23-33.0%. The computed S_{CO_2/H_2} was reported to be 38.3, while the experimental is 30.4. This value is close to the commercial solvent Selexol which as a respective selectivity of 25. This may indicate that the IL might not offer significant advantages despite its higher cost. This study showcases that despite the quantitative discrepancies between MC simulation and experiment, one should also keep in mind that solubilities of H_2 in ILs are difficult to measure experimentally with uncertainties being as high as 50%.

In their MC study, Wittich and Deiters[771] examined how the choice of simulation box geometry (cubic and orthorhombic) affects H_2 solubilities in ILs computed. The IL studied was 1-n-butyl-3-methyl-imidazolium hexafluorophosphate ([bmim]-[PF_6]) for temperatures ranging from 313 to 373 K at atmospheric pressure. Molecular representations of the ions of this IL are shown in Fig. 43. Similarly to the IL studies discussed earlier, the Cracknell[311] force field was used to model H_2, while the united-atom model by Shah and Maginn[772] was used for [bmim][PF_6]. The cubic simulation box was shown to yield Henry's constant values closer to experimental results for H_2, but still overestimated the experimental data by 14-57%. The authors observed that simulation box geometry significantly affects diffusivity, with the orthorhombic box showing faster diffusion rates. The authors mention that system size effects are present but could not fully investigate them due to computational constraints.

https://doi.org/10.1021/acs.chemrev.5c00617
Chem. Rev. 2025, 125, 11878−12029

Despite this study suggested that for some properties, such as Henry's constants, the orthorhombic box may better represent the system by allowing more configurational freedom, this did not hold true for the case of H_2.

Klein et al.[773] performed DLS experiments and MD simulations to measure/compute the diffusivities (thermal and fick) of binary mixtures of [emim] / [hmim] / [$C_1$0mim] [NTf_2] with H_2, He, N_2, CO_2, and Kr. This work is part of a large number of studies by the research group focusing on thermodynamic and transport properties of gas/liquid mixtures spanning alkanes, alcohols, and ILs. The temperature and pressure ranges covered were 298 - 423 K and 1 - 65 bar, respectively. The authors used various combinations of force fields (details are provided within ref 773) to identify suitable models for predicting densities, viscosities, and diffusivities. Klein et al.[773] reported self- (mentioned as thermal) and fick (component D_{11}) diffusion coefficients. For the whole temperature and pressure ranges, the computed diffusivities were in relatively close agreement (within 12%) with the experiments. The self-diffusivities of H_2 in [emim][NTf_2] ranged from 2.54 to 6.45 × 10^{-9} m s^{-}1 for temperatures 298 to 348 K. For the same temperature range, the respective values for self-diffusivity of H_2 in [hmim][NTf_2] and [$C_1$0mim]-[NTf_2] were similar (deviations of lower than 10% between the different solvents). Unlike in *n*-alkanes, the diffusivities of the gasses in the ILs were not significantly affected by the viscosity of the solvents.

Recently, Zhai et al.[774] investigated how H_2 affects both bulk (viscosity) and interfacial properties (surface tension) of three imidazolium-based ILs using both experiments and MD simulations. The ILs studied were the hydrophobic 1-ethyl-3-methylimidazolium bis(trifluoromethanesulfonyl) imide ([C_2C_1Im][NTf_2], also commonly abbreviated to [emim] [NTf_2] since e refers to the ethyl group) and 1-methyl-3-octylimidazolium hexafluorophosphate ([C_8C_1Im][PF_6]) as well as the hydrophilic 1,3-bis(2-(2-ethoxyethoxy)ethyl) imidazolium iodide ([$(mPEG_2)_2$Im]I). Molecular representations of the ions of these ILs are shown in Fig. 43. To model the ILs, the authors used the force fields by Kelkar and Maginn[388] and Seidl et al.[775] with optimized partial charges. For H_2 the IFF[313] model was used. The conditions examined where 303-393 K and 1 - 310 bar. The authors showed that H_2 has low solubility in all three ILs, with maximum values (in mole fraction units) of χ_{H2} = 0.092 for [C_2C_1Im][NTf_2] at 270 bar and 353 K and χ_{H2} = 0.041 for [$(mPEG_2)_2$Im]I at 310 bar and 393 K. It was shown that H_2 solubility is ca. 3.5 times higher in the hydrophobic [C_2C_1Im][NTf_2] than in the hydrophilic [$(mPEG_2)_2$Im]I at 353 K. Notably, H_2 appeared to only occupy existing voids in the IL rather than creating additional volume It was also shown that H_2 has no significant effect on the viscosities of ILs for pressures up to 80 bar. Nevertheless, the IL force fields overestimate the viscosity by a factor of 2-2.5 compared to experiments, though they capture the qualitative behavior. MD simulations revealed two counterbalancing effects, i.e., increased pressure compresses the liquid (increasing viscosity) while dissolved H_2 has a plasticizing effect (decreasing viscosity). Pressures had a small effect on the gas/liquid surface tension (ca. 6% decrease at 80 bar) which is due to the weak enrichment of the IL-gas interface with H_2. Overall, the effect of H_2 on the IL properties investigated is similar to what has been observed for non-electrolytic organic solvents.

Sharing the motivation with the studies discussed earlier, Rivera-Pousa et al.[776] studied H_2 absorption in the following protic and aprotic ILs: [EAN][NO_3], [HEIm][NO_3], [HEIm] [TFSI], [EMIm] [$B(CN)_4$], [EMIm][TFSI], [EMIm][NO_3], [EMIm] [BF_4], and a series of [C_nMIm][BF_4] with varying alkyl chain lengths (*n* = 2, 4, 6, 8, 10, 12). Molecular representations of the ions of these ILs are shown in Fig. 43. The authors focused on high temperatures (550 K) and pressures (50 bar) because these conditions are relevant for processes such as Fischer-Tropsch synthesis. It was shown that H_2 solubility increased with alkyl chain length in cations. Also, H_2 molecules showed weak interactions with the ILs, while they preferentially occupied the apolar domains of the ILs. However, in ILs with nitrate anions, H_2 also occupied polar regions. Another finding was that the structure of ILs was almost insensitive to the presence of H_2, while free volume and cavity formation appear to be the most important factors affecting solubility. Interestingly, in this study unscaled charges for ions were used instead of scaled charges that are typically used to prevent sluggish dynamics (see also Section 3.1.3). The study revealed that even though nitrate-based ILs show the most favorable solvation enthalpies, they have the lowest H_2 solubility due to limited available void space.

4.6. Hydrogen Sorption and Diffusivity in Metal- and Covalent-Organic Frameworks and Zeolites

Molecular simulations play a central role in the pursuit of understanding the mechanisms underlying sorption, diffusion, and permeability of H_2, and the selectivity of H_2 mixtures in nanoporous media such as MOFs and COFs. For this reason, an extensive literature body is available, making the detailed review of this area here not feasible. Nevertheless, we provide a short overview of important, relevant, and relatively recent studies to showcase the range of applicability of MC and MD simulations in studying H_2 sorption phenomena, especially in light of AI and ML approaches.

As discussed in detail in Section 2.2, accurate modeling of separations of H_2/gas mixtures requires accounting for both sorption and diffusion of the species involved, as membrane permeability is determined by both these phenomena. Early simulation studies focused on such properties in MOFs,[777,778] particularly focusing on separations of H_2 from CO_2 and CH_4. Keskin and Sholl[130] performed GCMC and MD simulations to compute both sorption and diffusion of H_2, CO_2, CH_4, and N_2 in MOF-5. Wu et al.[779] developed a modified force-field for ZIF-8, enabling simulations of H_2 sorption and diffusion alongside other gases. In 2012, Keskin[780] reported simulation results for sorption, diffusion, gas permeability, and membrane selectivity of H_2 over CH_4, focusing on COFs. The authors demonstrated the superior performance of COF-6 compared to zeolites and MOFs. Krokidas et al.[418] explored the potential of functionalization of MOFs to design novel structures for membranes, offering unprecedented H_2/CH_4 separation efficiency.

Song and No[781] used GCMC calculations to study the influence of available volume, surface area, cation types (e.g., Mg, Mn, and Ca), and pre-adsorbed benzene on the H_2 capacity of zeolites. Song and No[781] showed that the available volume and surface area per mass of zeolite are the two parameters having the strongest correlation with H_2 storage capacities, and that pre-adsorbed benzene can significantly decrease H_2 storage capacity by lowering the available volume in the zeolite structure. Deeg et al.[782] investigated H_2

https://doi.org/10.1021/acs.chemrev.5c00617
Chem. Rev. 2025, 125, 11878−12029

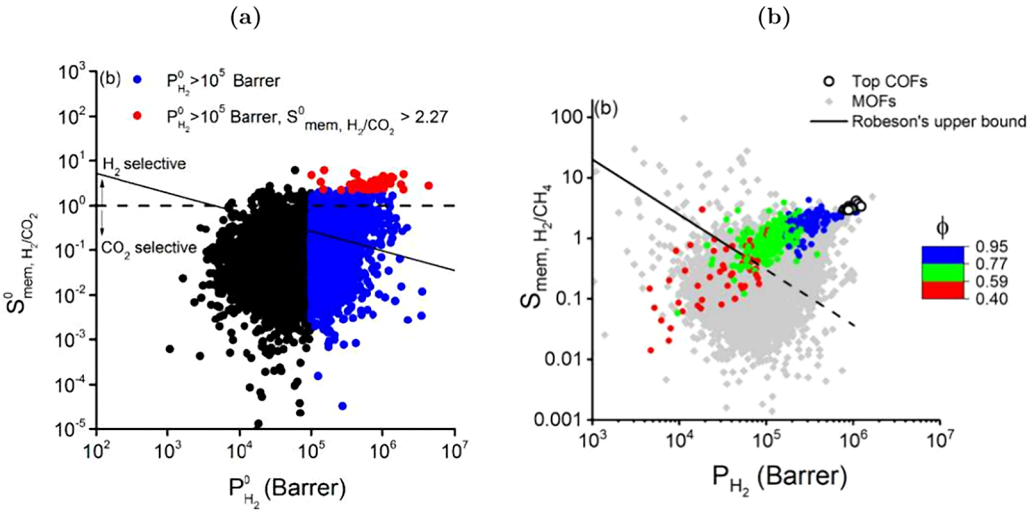

Figure 44. Robeson plots of (a) H_2/CO_2 membrane selectivities as a function of H_2 permeability for the MOFs studied by Avci et al.,[787] and (b) the high-performing CH_4/H_2 COFs, highlighting the importance of porosity, ϕ, as a driving characteristic of separation performance.[789] [Panel (a) is reprinted from Avci et al.,[787] ACS Applied Materials & Interfaces, Vol 12, 41567−41579. Copyright 2020, American Chemical Society. Panel (b) is reprinted from ref 789. Industrial & Engineering Chemistry Research, Vol 60, 12999−13012. Copyright 2020, American Chemical Society (this publication is licensed under CC-BY-NC-ND 4.0)].

adsorption in two all-silica zeolites (i.e., ITQ-29 and MFI) at cryogenic temperatures using molecular simulations. This study revealed that a single-site H_2 force field with an uncharged LJ center can best reproduce experimental adsorption isotherms, while small adjustments to LJ parameters can significantly improved accuracy. It was also shown that in ITQ-29, H_2 preferentially adsorbs onto sodalite cages at low temperatures, creating a unique temperature-dependent pattern in heats of adsorption. In MFI, adsorption occured in sinusoidal channels at low temperatures.[782] The authors also incorporated quantum effects via the Feynman-Hibbs potential (see Section 3.1.1), demonstrating the importance of considering the quantum nature of H_2 to accurately model adsorption, especially at very low temperatures (i.e., 25 K). Extensive reviews of molecular simulations of H_2 adsorption on functionalized nanoporous materials are provided by Getman et al.[317] and Bobbitt and Snurr.[414]

Simulations have also played a crucial role in advancing the study of MMMs, effectively combining the cost-effective and scalable attributes of polymers with the high-performance capabilities of MOFs/COFs as fillers. Yilmaz and Keskin[783] explored diverse combinations of MOFs and polymers for H_2/CH_4 and H_2/CO_2 separations, towards the development of high-performing MMMs. The computed gas selectivity and permeability were compared with experimental data, showing good agreement. The authors also proposed new MOF-based MMMs exhibiting high performance for specific gas separations.

4.6.1. High-Throughput Screening Simulations. So far in this review, insights into H_2 separation mechanisms obtained solely from molecular simulations have been discussed. Nevertheless, the growing availability of structural databases and computational resources enabled a shift towards large-scale, high-throughput screening studies. This approach, comprising massive numbers of simulations, allows for the systematic evaluation of thousands of candidate materials, offering a data-driven perspective on separation performance. Early efforts focused on extracting simple structure-property relations from these datasets, often using visual/manual inspection of simulation results or heuristic approaches based on intuitive structural descriptors such as pore size or surface area.[784] In recent years, however, the adoption of ML and AI has allowed for a more powerful and automated analysis of such relationships, enabling faster and more accurate prediction of material performance across vast chemical spaces. Such data-intensive approaches are efficient since the different structures comprising each family of nanoporous materials are in the order of hundreds of thousands. For example, ca. 100000 different MOF structures have been reported in literature, and more than half a million other MOF structures have been predicted to date.[785]

In the past decade, the significant advancements in high-performance computing have enabled researchers to conduct large-scale screening simulation studies, allowing for the evaluation of numerous material structures in terms of separation performance.[786] For instance, Avci et al.[787] performed high-throughput computational screening on a comprehensive subset of MOFs of the CSD database,[788] exploring the CO_2 capture and H_2 purification potential of 10221 MOFs. These simulations revealed the best-performing materials for PSA, vacuum swing adsorption (VSA), and TSA processes, outperforming commercial zeolites and previously studied MOFs in terms of CO_2/H_2 selectivity (see Fig. 44a).

Similarly, Altintas et al.[790] focused on the comparison of two widely used computation-ready MOF databases, i.e., CoRE[791] and CSDSS.[792] The authors id entified 3490 common MOFs in these databases and conducted simulations to compute their CH_4 and H_2 uptakes. The study also highlighted 'problematic' MOFs exhibiting different gas uptakes depending on the database used, leading to significant variations in ranking and material selection. Aksu et al.[793] focused on COFs for CO_2/H_2 separation using a high-throughput computational screening approach on the CoRE COF.[794] This study covered 288 experimentally synthesized COFs, providing valuable insight into the performance of COFs as adsorbents and membranes for pre-combustion CO_2 capture. Notably, many COFs outperformed traditional zeolites in terms of CO_2 selectivity and working capacities. The structural analysis revealed that

https://doi.org/10.1021/acs.chemrev.5c00617
Chem. Rev. 2025, 125, 11878−12029

COFs with specific pore sizes and porosities are potential adsorbents for selective CO_2/H_2 separation. Aksu et al.[149] extended the screening to a database of hypothetical COFs (hypoCOF). Through an extensive series of molecular simulations, the authors identified top-performing hypoCOFs as adsorbents and membranes for CO_2 capture and H_2 purification. The findings of this study indicated higher CO_2 selectivities and working capacities compared to experimentally synthesized COFs under specific conditions. The study also emphasized the importance of hydrogen bonding between CO_2 and functional groups of linkers for CO_2 selectivity in hypoCOFs. Altundal et al.[789] explored the separation potential of COFs for CH_4 purification from gases such as H_2, N_2, and C_2H_6. By combining GCMC and MD simulations, they assessed adsorption and membrane-based separation performances of 572 COFs. The results demonstrated that COFs have the potential to outperform conventional adsorbents in H_2/CH_4 separations. Additionally, this study identified structural features related to high selectivities and permeabilities, offering a basis for designing COFs with exceptional CH_4 separation performance. For example, Fig. 44b shows that higher porosity values, ϕ, result to higher separation performance. Avci et al.[795] investigated the influence of metal exchange in MOFs on CO_2/H_2 and CO_2/CH_4 separation performances. By exchanging Zn nodes with different metals, they obtained 32 metal-exchanged MOFs (M-MOFs), and showed that the exchange of Zn with V and Cr significantly improved CO_2 uptakes and adsorption selectivities. These molecular-level insights can provide a valuable guide for designing MOFs with enhanced CO_2 separation efficiency.

Zeolites, are another class of porous media similar to MOFs and COFs in many aspects. Zeolites are crystalline aluminosilicate materials characterized by a well-defined, micro-porous structure composed of interconnected channels and cages. These materials have long been studied for applications in gas storage and separation because of their inherent thermal and chemical stability. Despite their attractive structural features, the storage capacities of H_2 in unmodified zeolites (e.g., without structural modifications and doping with metals or other additives) are unsatisfactory (i.e., ca. 0.2-1.1 wt % H_2).[796] Molecular simulations are used in the literature to identify critical features that can enhance H_2 storage capacities and to design new zeolite structures suitable for H_2 storage applications.[781,782,797,798] Manda et al.[797] explored the H_2 storage capacities of 233 zeolites using GCMC simulations combined with ML. An impressive H_2 storage capacity of 4.8 wt% H_2 was reported in the Linde Type A structure, attributed to the low mass of the zeolite and the large gravimetric and volumetric surface area.[797] For a more detailed discussion of H_2 storage in zeolites the reader is referred elsewhere.[796,797,799]

4.6.2. Artificial Intelligence and Machine Learning to Accelerate Material Screening. Building on the advancements of high-throughput screening and the increasing availability of structure databases, such as the aforementioned CoreMOF,[800] hypoCOF,[801] CoRE COF,[802] as well as, the Inorganic Crystal Structure Database (ICSC),[803] Crystallographic Open Database (COD),[804] and the Cambridge Structural Database (CSD),[805] the scientific community has witnessed a flourishing interest in the utilization of AI and ML as a powerful approach for screening and designing H_2-related processes involving MOFs and COFs. Particularly in the context of functionalized, nanoporous solids, these techniques offer a remarkable opportunity to explore and comprehend intricate structure-property correlations.[806] Ahmed et al.[198] evaluated the H_2 storage capacities of ca. 20000 different MOF structures using MC simulations (results are shown in Fig. 45). The authors, then, used the data to train a ML model, which was used to screen nearly half a million different MOF structures.

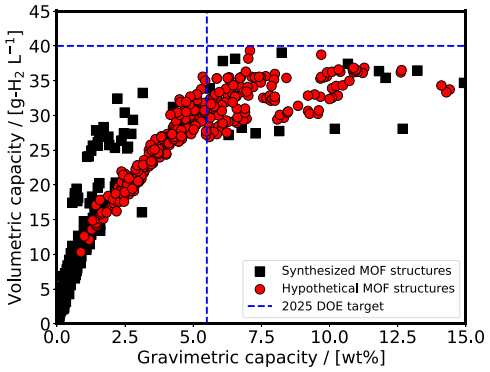

Figure 45. Volumetric and gravimetric capacities of H_2 for different MOFs computed with using GCMC simulations.[198] The volumetric and gravimetric capacities are computed at 77 K for a pressure swing of 100 bar to 5 bar. Various MOF structure databases were utilized for the GCMC simulations conducted by Ahmed et al.,[198] including databases containing synthesized MOF structures as well as databases of hypothetical MOF structures. The data for this plot is obtained from the work of Ahmed et al.[198]

Recently, Chen et al.[151] presented empirical-Morse force fields based on ab-initio calculations for interactions of H_2 with Mg-alkoxides. The empirical force fields are then used to perform high-throughput GCMC simulations of ca. 3000 metal-alkoxide functionalized COF structures, and to develop ML models to predict H_2 capacities.[151] Bucior et al.[807] developed a data-driven approach using sparse regression models to predict gas adsorption in MOFs, enabling rapid exploration of large databases and identification of top-performing candidates like MFU-4l. Similarly, Dureckova et al.[808] used ML to construct quantitative structurerelationship (QSPR) models for CO_2 working capacities and CO_2/H_2 selectivities in MOFs. Their work demonstrated that ML can accurately predict the performance of MOFs, even in topologically diverse databases, while significantly accelerating the screening process. Yang et al.[809] utilized ML algorithms, such as decision trees and random forests, to predict the separation performance of computational-ready MOF membranes for H_2-related separations, such as H_2/CO_2, H_2/CH_4,H_2/N_2 and He/H_2. By analyzing structural feature descriptors and principal components, the authors successfully identified the best-performing MOFs for each binary gas mixture.

Shi et al.[810] summarized recent progress in ML-assisted high-throughput computational screening of MOFs, including applications in CH_4 storage, H_2 storage, and CO_2 separations. The authors showed that the use of ML models improved the screening speed by several orders of magnitude and facilitated the identification of high-performance materials. Bai et al.[811] explored the application of high-throughput computational screening and ML for evaluating the H_2 separation performances of COF membranes. Their models efficiently predicted permeability and selectivity, enabling the identification of top-performing COFs for H_2 separation. Fig. 46 shows the

https://doi.org/10.1021/acs.chemrev.5c00617
Chem. Rev. 2025, 125, 11878−12029

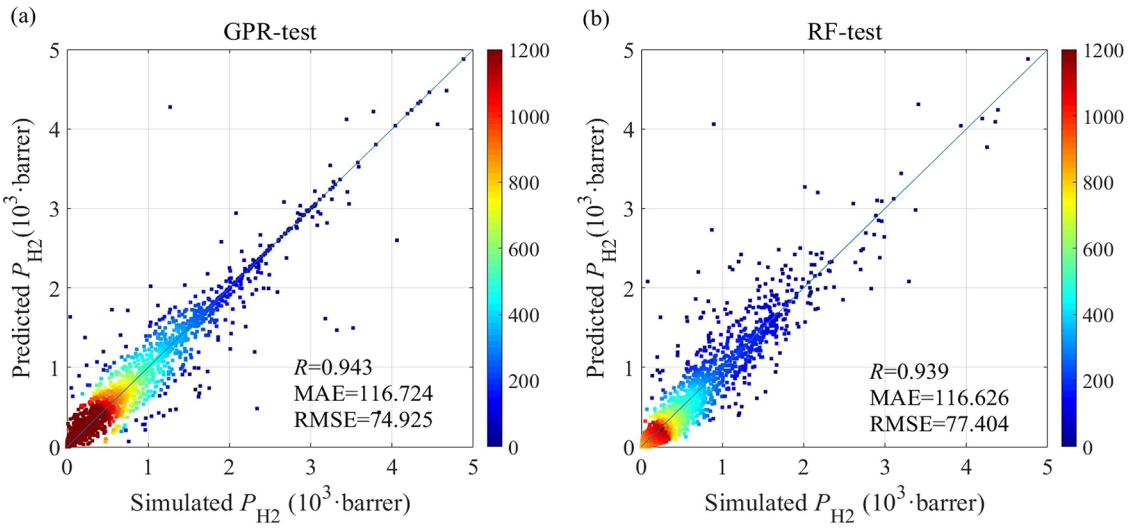

Figure 46. Predictions compared with the data of the test set (simulations) for P_{H_2} made with (a) GP and (b) with RF, from the work of Bai et al.[811] [The figure is reprinted from Chemical Engineering Journal, Vol 446, Xiangning Bai et al., Machine−Learning−Assisted High−Throughput computational screening of Metal−Organic framework membranes for hydrogen separation, Copyright (2022), with permission from Elsevier].

performance of Gaussian Processes (GP) and Random Forest (RF) regression models in predicting the permeability of TMSP of H_2, in the form of parity plots (i.e., predictions vs simulation results). Aksu and Keskin[153] introduced a high-throughput computational screening approach combined with ML for assessing synthesized and hypothetical COFs for CH_4/H_2 separation. By developing ML models based on simulation results on 7700 COFs of the 69800 in total in their dataset, these authors accurately predicted the adsorption properties of hypothetical COFs and identified the top-10 performing COFs in VSA and PSA processes as shown in Fig. 47.

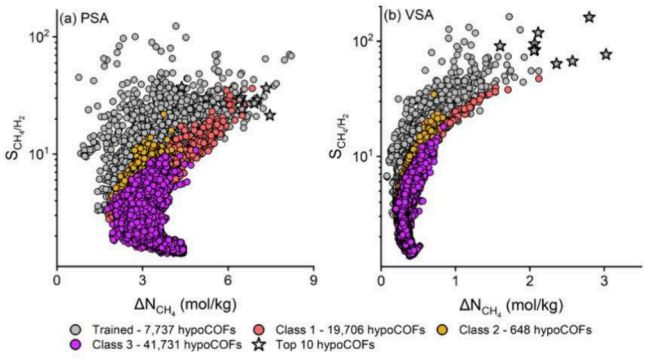

Figure 47. ML predictions of CH_4/H_2 performance for (a) PSA and (b) VSA processes. [The figure is reprinted from Journal of Materials Chemistry A, Aksu and Keskin,[153] Advancing CH_4/H_2 separation with covalent organic frameworks by combining molecular simulations and machine learning (This article is licensed under a Creative Commons Attribution-NonCommercial 3.0 Unported Licence - CC BY-NC 3.0)].

As a concluding remark, it is important to highlight that the design of materials for H_2-gas separations, with molecular simulation as the enabling tool, can pave the way for membranes with unprecedented performance. Fig. 48 illustrates this potential by comparing predicted materials from simulations with state-of-the-art synthesized membranes. These Robeson plots show that *in silico* designed nanoporous materials, such as MOFs and COFs, not only outperform conventional polymer membranes but also exceed the performance of previously studied functionalized porous materials. Notably, many of the predicted structures lie beyond the traditional upper bounds for both H_2/CH_4 and H_2/CO_2 separations, demonstrating that simulation-guided design can expand the accessible membrane performance space. Table 17 provides a list of the available simulation data from high-throughput screenings and ML studies in literature. We provide data for the diffusivity, permeability, and sorption of H_2 mixtures on various functionalized nanoporous materials. It is important to note that most computational studies of MOF/COF membranes assume defect-free, perfectly crystalline, and rigid structures. While this practice is useful for identifying intrinsic transport limits, it represents a highly idealized model which may differ significantly from real, defect-containing, and flexible membranes.

4.7. Adsorption and Diffusivity of Hydrogen in Clay-Rich Reservoirs

Here, we summarize the findings from MD and GCMC studies (also see Table 18) to clarify how the insights presented for mechanisms such as adsorption, solubility, diffusivity, and intercalation processes influence the efficiency of UHS. We first discuss competitive adsorption on rock surfaces, then discuss H_2 solubility in confined water, pore-scale transport dynamics, and intercalation within layered geological structures. Researchers frequently use substrates such as kaolinite and graphite in H_2 storage studies due to their distinct yet complementary properties, enabling systematic exploration of adsorption and diffusion at the molecular scale. Kaolinite, an abundant clay mineral characterized by a 1:1 layered structure, exhibits two distinct surfaces (hydroxylated (gibbsite) and siloxane) resulting in varying H_2−solid interactions. These properties make kaolinite ideal for modeling the heterogeneous pore surfaces found in subsurface reservoirs.[877] Conversely, graphite and its derivative graphene offer high chemical stability, low mass, and a well-defined 2D structure, serving as proxies for organic-rich fractions commonly found in shale formations.[878,879] The utilization of these representative substrates enables the systematic evaluation of how pore size, temperature, and pressure influence adsorption and diffusion,

https://doi.org/10.1021/acs.chemrev.5c00617
Chem. Rev. 2025, 125, 11878−12029

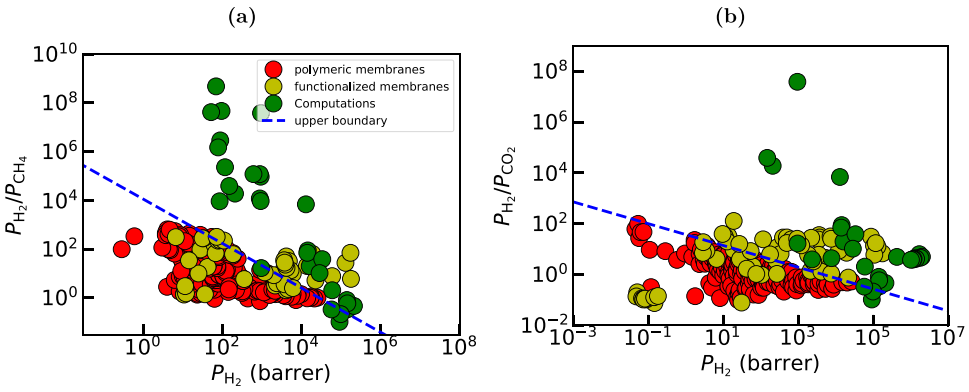

Figure 48. Robeson plots of (a) H_2/CH_4 and (b) H_2/CO_2 separation depict the impact of computational-empowered design. Functionalized nanoporous materials engineered through simulations surpass the current, experimentally measured polymers and functionalized nanoporous materials, showcasing unprecedented gas separation performance. The literature results on polymeric membranes are taken from the seminal work of Robeson.[136] The experimental and computational data for functionalized materials are collected from an extended survey of the authors, and are listed in Tables 15, 16, and 17.

which are key properties for assessing UHS viability. Additionally, the well-characterized nature of materials such as kaolinite and graphite facilitates the validation of molecular simulations against experimental data, thereby refining theoretical models. The distribution of substrates adopted in the reviewed studies is summarized in Fig. 49.

4.7.1. Competitive Adsorption on Organic and Inorganic Substrates. For applications pertaining to subsurface storage like UHS, H_2 must stick to rock surfaces effectively but remain easy to retrieve, often competing with cushion gases like CH_4 and CO_2. We review articles studying the adsorption of gas mixtures in organic and inorganic nanopores. Ho et al.[880] performed molecular simulations to study the adsorption and diffusion of H_2 and CH_4 in shale systems, with a particular focus on kerogen. The study demonstrates that CH_4 exhibits a substantially higher excess adsorption than H_2 over the entire pressure range, with the total CH_4 uptake reaching approximately 3.3 mmol/g at a CH_4 pressure of ca. 100 bar. Moreover, the computed interaction energies indicate that kerogen has a much stronger affinity for CH_4 (with a minimum interaction energy of ca. -4.3 kcal/mol) compared to H_2 (ca. -1.8 kcal/mol), which explains the preferential adsorption of CH_4. When simulating a competitive 1:1 CH_4:H_2 mixture, the kerogen selectivity for CH_4 is found to be more than 10 to 25 times higher than that for H_2, corroborating existing literature and experimental insights. The simulations further reveal that under conditions of low residual CH_4 partial pressure, up to 30−35% of adsorbed CH_4 desorbs upon H_2 injection. The overall H_2 uptake in kerogen is of the same order of magnitude as that observed in coal, reinforcing the broader relevance of the results. The MD simulations also predicted that the diffusion coefficient of H_2 in the kerogen matrix is approximately 20−40 × 10^{-9} m^2/s, which is approximately one order of magnitude higher than that for CH_4 and CO_2, in agreement with comparative studies. These simulation results effectively complement their NMR experiments, which have independently observed distinct signatures for free versus adsorbed H_2 in shale. Overall, the study provides a molecular-level understanding of the competitive adsorption phenomena, highlighting that the dominance of CH_4-kerogen interactions must be considered when designing H_2 geological storage projects.

Zhang et al.[881] performed GCMC simulations to explore H_2 adsorption in shale nano-pores for both organic (kerogen) and inorganic (montmorillonite, MMT) substrates at 333.15 K and pressures up to 180 bar, finding that pure H_2 exhibits nearly twice the excess adsorption on kerogen relative to MMT (yielding a higher absolute storage capacity) while recovery efficiency − defined as the percentage of gas retrieved when pressure is reduced from 180 bar to 3 bar − remains similar between the substrates. In competitive adsorption tests with equimolar mixtures of CH_4 and H_2, CH_4 preferentially adsorbs on kerogen (with selectivity values above one) and, although CH_4 still adsorbs more strongly in MMT, overlapping adsorption layers result in a smaller competitive difference; additionally, the presence of cushion gases dramatically reduces H_2 storage capacity (by about 50% in 5 nm pores and up to 80% in 2 nm pores) due to H_2 dilution and competitive displacement, with the effect intensifying as pore size decreases and CO_2 proving more effective than CH_4 (yielding CO_2/H_2 selectivity values up to 18 in 2 nm pores), thereby underscoring how pore size, substrate type, and specific gas interactions govern adsorption and recovery, which is critical for optimizing UHS processes.

Kahzadvand et al.[882] investigated the partitioning behavior of a H_2 and cushion gas (CO_2 or CH_4) mixture within clay mineral pores to assess caprock integrity during UHS. Using advanced non-equilibrium molecular simulations at 333 K and 150 bar, this study provided molecular-level insights by using constant reservoir composition MD (CRC-MD) which dynamically maintains fixed fluid compositions in designated regions, thereby overcoming limitations such as feed depletion and composition control seen in traditional methods. The results reveal that pores narrower than 0.5 nm are impermeable to both H_2 and cushion gases, while H_2, owing to its superior rotational degrees of freedom, begins to penetrate at pore widths between 0.5 and 0.6 nm, with a notable increase in number density observed at these dimensions. In contrast, cushion gases, particularly CO_2, exhibit a stronger affinity for the clay surfaces and edges, dominating pore occupancy in interlayer spaces up to approximately 2 nm. Quantitatively, the simulations show that in montmorillonite and illite pores, the mole fraction of CO_2 initially exceeds that of H_2 at 0.6 nm for CO_2/H_2 mixtures, with parity reached only at larger pore sizes (around 5 nm in montmorillonite and 7 nm in illite). For H_2/

https://doi.org/10.1021/acs.chemrev.5c00617
Chem. Rev. 2025, 125, 11878−12029

Table 17. Sorption, Diffusivity, and Permeability Data Collected from Molecular Simulation Studies of Pure H_2 and H_2 Mixtures in Different Functionalized Nanoporous Materials

		Sorption Selectivity		Diffusion Selectivity			Permeability Selectivity		
Study	Material	CH_4/H_2	CO_2/H_2	H_2/CH_4	H_2/CO_2	$D_{H_2}(10^{-10}m^2/s)$	H_2/CH_4	H_2/CO_2	P_{H_2} (barrer)
Yang et al.[876]	MOF-5	5							
Liu et al.[778]	Cu-BTC	10							
	IRMOF-9	13.51							
	IRMOF-10	3.48							
	IRMOF-11	18.53							
	IRMOF-12	6.31							
	IRMOF-13	17.15							
	IRMOF-14	5.3							
Wu et al.[779]	ZIF-8			571.43	41.67	2.28			
Keskin[780]	COF-5	9.894		6.06			0.612		
	COF-6	17.223		4.785			0.272		
	COF-10	4.741		7.09			1.484		
Krokidas et al.[418]	ZIF-8	14.1	21.8	277.8	33.3	1.6×10^{-8}	20	1.49	1.62×10^{4}
	ZIF-67	14.1	24.1	2×10^{-3}	9.1	8.7×10^{-9}	16.67	0.09	9.66×10^{2}
	BeIF-1	28.9	49.1	1.1×10^{9}	45.5	9.4×10^{-10}	3.85×10^{7}	0.62	9.55×10^{2}
	ZIF-7-8	23.7	47.4	4.81×10^{5}	238.1	2.4×10^{-10}	1.9×10^{4}	3.15	2.1×10^{2}
	Co-ZIF-7-8	25.1	49.1	9.43×10^{5}	90.9	1.7×10^{-10}	3.9×10^{4}	3.49	1.5×10^{2}
Yilmaz et al.[783]	ZIF-2			2.48	11.7	6.20×10^{-8}	0.104	0.175	9.21×10^{4}
	ZIF-3			7.33	73.3	1.10×10^{-7}	0.343	0.987	1.49×10^{5}
	ZIF-10			5.71	13.3	1.60×10^{-7}	0.465	0.409	2.13×10^{5}
	ZIF-11			9.23	17.1	1.20×10^{-7}	0.812	0.598	1.41×10^{5}
	ZIF-12			1.86×10^{3}	15.3	1.10×10^{-8}	88.3	0.251	1.45×10^{4}
	ZIF-60			1.45×10^{11}	2.16×10^{9}	1.1	70.4	0.460	1.41×10^{4}
	ZIF-65			6.32	23.1	1.20×10^{-7}	0.593	0.658	1.45×10^{5}
	ZIF-67			5.32×10^{2}	8.25×10^{2}	3.30×10^{-8}	38.7	11.6	3.37×10^{4}
	ZIF-69			1.29×10^{5}	22.9	1.10×10^{-8}	6.9×10^{3}	0.409	1.30×10^{4}
	ZIF-78			54.5	1.13×10^{2}	5.40×10^{-8}	2.05	1.67	6.02×10^{4}
	ZIF-79			2.89×10^{2}	2.00×10^{2}	2.80×10^{-8}	10.4	2.02	2.88×10^{4}
	ZIF-81			7.00	91.3	8.40×10^{-8}	0.214	1.34	9.93×10^{4}
	ZIF-90			9.00	2.84×10^{2}	5.40×10^{-8}	0.333	4.03	5.80×10^{4}
Avci et al.[787]	FOTNIN		12		76.05	1.35×10^{-6}		6.34	1.67×10^{6}
	BAZGAM		3.47		17.42	1.51×10^{-6}		5.02	1.97×10^{6}
	PESSUE		3.93		19.42	3.86×10^{-7}		4.94	4.26×10^{5}
	XANLIJ		2.95		13.55	8.39×10^{-7}		4.59	1.83×10^{6}
	AVAJUE02		4.1		18.06	1.01×10^{-6}		4.4	1.33×10^{6}
	XAHQAA		4.52		18.84	1.06×10^{-6}		4.17	1.40×10^{6}
	KAZSIQ		7.25		29.82	9.08×10^{-7}		4.11	1.21×10^{6}
	CEFNOT		5.25		20.94	8.67×10^{-7}		3.99	1.15×10^{6}
	XAHPUT		4.72		18.47	8.83×10^{-7}		3.91	1.16×10^{6}
	NIBJAK		4.78		18.17	7.65×10^{-7}		3.8	1.02×10^{6}
Aksu et al.[793]	PE-COF-I (for PSA)		368.2						
	NPN-2 (for PTSA)		2196.1						
	NPN-2 (VSA)		566.3						
	NPN-1 (TSA)		856.8						
	NPN-1 (VTSA)		936						
Aksu et al.[149]	linker99_C_linker100_C_pts (PSA)		229						
	linker92_C_linker92_C_bpi (VSA)		336						
	linker103_CH_linker89_N_unh (membrane)		0.49		12.5			6.14	
	linker91_CH_linker95_N_bod		0.67		9			6.04	
Altundal et al.[789]	CTF-FUM (VSA)	102.7							
	COF-303	21.84							
Yang et al.[809]	TUMGOX						1.2×10^{4}	4.39	8.9×10^{2} (H_2/CH_4)

https://doi.org/10.1021/acs.chemrev.5c00617
Chem. Rev. 2025, 125, 11878−12029

Table 17. continued

Study	Material	Sorption Selectivity		Diffusion Selectivity			Permeability Selectivity		
		CH_4/H_2	CO_2/H_2	H_2/CH_4	H_2/CO_2	$D_{H_2}(10^{-10}m^2/s)$	H_2/CH_4	H_2/CO_2	P_{H_2} (barrer)
									7.75×10^3 (H_2/CO_2)
	HEDCEA						9.4×10^3	3.95	9.35×10^2 (H_2/CH_4)
									2.35×10^3 (H_2/CO_2)
Bai et al.[811]	IDAZEU						9.4×10^4		935.42
	WENSIS						1.2×10^5		890.06
	YAFGAP						1.2×10^5		614.29
	BEVQUP						4.7×10^7		95.68
	BEVQID						2.3×10^5		117.45
	JASNEX						2.9×10^6		88.9
	NIRDEX						1.5×10^6		78.75
	HIWXER						4.2×10^7		52.27
	NAXKOO01						9.2×10^3		85.78
	EMANAH						4.8×10^8		69.68

CH_4 systems, CH_4 fails to penetrate below 0.6 nm, highlighting a selective permeation linked to molecular size, while at 1 nm, CH_4 occupancy peaks with relative ratios of about 0.6:0.4 compared to H_2, before declining at larger pore sizes. The study underscores that the effectiveness of cushion gas in inhibiting H_2 leakage is strongly dependent on pore thickness and clay surface charge, with CO_2 showing higher adsorption owing to electrostatic interactions with negatively charged sites and exchangeable cations. Furthermore, the detailed analysis via 2D density maps illustrates that gas molecules accumulate preferentially in the mid-interlayer region and near the clay edges, which correlates well with experimental observations and prior simulation studies. New physics uncovered include the dynamic interplay between rotational freedom of H_2 and the surface affinity of cushion gases, leading to qualitatively different partitioning behaviors in nano-pores (pore sizes < 2 nm) versus meso-pores (pore sizes > 2 nm). The CRC-MD approach thus not only clarifies the penetration thresholds (e.g., 0.5, 0.6, and 2 nm) but also reveals that for pore sizes larger than 4 nm, the gas composition approaches bulk behavior. Overall, this work provides a comprehensive molecular explanation for the dual role of cushion gases as both pressure maintenance agents and leakage barriers in H_2 geo-storage applications.

Muther and Dahagi[883] performed a study of H_2 adsorption on kaolinite using GCMC simulations to elucidate adsorption mechanisms under varying geological conditions. The study validates its simulation setup by comparing the computed CO_2 adsorption isotherms with experimental measurements taken at 298.15 K and pressures ranging from 0.2 to 1 bar, thereby establishing a robust basis for subsequent simulations. The results show that under high-pressure (10−500 bar) and elevated temperature (323−403 K) conditions, pure H_2 adsorption on kaolinite ranges from 0.0494 to 2.237 mol/kg; specifically, H_2 uptake increases with pressure and decreases with temperature. When H_2 is mixed with CO_2 or CH_4, the simulations reveal that introducing 10−50 mol% of these gases significantly reduces H_2 uptake because the available adsorption sites on the kaolinite are increasingly occupied by CO_2 or CH_4 molecules. In particular, the simulations indicate that, when present, CO_2 displaces H_2 more effectively than CH_4—as evidenced by lower H_2 density peaks-suggesting that the kaolinite surface exhibits a stronger affinity for CO_2. Furthermore, the RDFs confirm that among the atoms in the kaolinite structure, silicon atoms contribute slightly more to the H_2 adsorption process than do H_2, oxygen, or aluminum atoms. Overall, the quantitative insights obtained-such as the observed linear decrease in the Henry coefficient with increasing temperature-are in good agreement with previous simulation and experimental studies on gas adsorption in clay minerals, and can help guide strategies for underground H_2 storage. The study also demonstrates that the desorption curves closely mirror the adsorption behavior, confirming efficient H_2 recovery without hysteresis effects.

Muther and Dahaghi[884] performed GCMC simulations to compute the adsorption of H_2 on hydroxylated quartz (i.e., a representative geological mineral) across a wide range of pressures and temperatures. The study utilizes a molecular-scale quartz structure that has been hydroxylated to mimic natural subsurface conditions. The simulations explore the response of H_2 in both pure and mixed gas systems. The results show that H_2 uptake increases linearly with pressure, while high temperatures (up to 403 K) reduce adsorption since elevated temperatures weaken the mineral's affinity for H_2 by increasing the kinetic energy of the molecules, reducing the stability of H_2 retention on the quartz surface. To quantify the mineral's affinity for H_2, Henry coefficients were calculated, which were shown to consistently decrease with rising temperature, indicating that adsorption is less favorable when kinetic energy is higher; this decline is accompanied by higher binding energies between H_2 and the quartz surface, reinforcing the observation that elevated temperatures reduce adsorption effectiveness. In mixed gas systems, the presence of CO_2 and CH_4 further displaces H_2, with H_2 uptake reduced to as low as 1.28 mol/kg in a 50:50 gas mixture, mirroring trends observed in other porous materials such as MOFs and zeolites, and the addition of a thin water film (ca. 1 wt%) further reduces H_2 adsorption by ca. 3% due to water molecules preferentially occupying the adsorption sites on the hydroxylated quartz surface, highlighting the crucial role of surface hydroxyl groups in mediating gas interactions. Overall, the study emphasizes that both conditions (i.e., pressure and temperature) and compositional factors (e.g., presence of CO_2, CH_4, and water) are critical in controlling H_2 adsorption on

https://doi.org/10.1021/acs.chemrev.5c00617
Chem. Rev. 2025, 125, 11878−12029

Table 18. Overview of the Literature on H_2 Adsorption in Geological Substrates[a]

Author	Materials/Force Fields	Method	T [K]/P [MPa]	Pore Size [nm]	Mixture(s)
Wang *et al.*[905]	Na-Montmorillonite (CLAYFF)[422,423] H_2 (Cracknell Two-site)[311] CH_4 (TraPPE-UA)[301] H_2O (SPC/E)[346]	EMD and NEMD	343 K /Not mentioned	3.7−8.2	CH_4, H_2, H_2O
Oliver *et al.*[879]	Kaolinite - Gib.[1] and Sil.[2] (CLAYFF)[422,423] Graphene (OPLS)[428] H_2 (Michels Single site)[924]	EMD	300 K / 1.0-50.7 MPa	1−20	H_2
Ho *et al.*[880]	Kerogen (CVFF)[426] H_2 (Buch Single site)[312] CH_4 (TraPPE-UA)[301]	GCMC	338 K / 0−27.6 MPa	Disordered	H_2 and CH_4
Ho *et al.*[921]	Montmorillonite (CLAYFF)[422,423] H_2 (Darkrim Three-site)[327] H_2O (SPC/E)[346]	GCMC	323 K / upto 11.15 MPa	n/a	H_2 and CH_4 H_2, CH_4 and H_2O
Zhang *et al.*[889]	Kaolinite − Gib. and Sil. (CLAYFF)[422,423] H_2 (Cracknell Two-site)[311] CH_4 (TraPPE)[925] H_2O (SPC/E)[346]	GCMC	298.15 K / 0.1−10 MPa	5−200	H_2 and H_2O H_2 and CH_4
Muther *et al.*[884]	Hydroxylated Quartz (CLAYFF)[422,423] H_2 (Darkrim Three-site)[327] CH_{TraPPE}[301] CO_2 (EPM2)[419]	GCMC	323.15−423.15 K / 1−50 MPa	3	H_2 and CH_4 H_2 and CO_2 H_2 and H_2O
Zhao *et al.*[886]	Kaolinite (UFF)[399] Illite (UFF)[399] Dolomite (UFF)[399] Quartz (UFF)[399] Calcite (UFF)[399] H_2 (UFF Two-site)[399]	GCMC and MD	303.15−353.15 K / 0−18 MPa	0.3−0.4	H_2
Liu *et al.*[923]	SiO_2 (PCFF+)[316,406,430] H_2 (PCFF+)[316,406,430] CH_4 (PCFF+)[316,406,430] H_2O (PCFF+)[316,406,430]	MD and MD−MC	300 K / 10−30 MPa	0.5−1.4	H_2 H_2 and CH_4 H_2 and H_2O H_2, CH_4 and H_2O
Li *et al.*[329]	Kaolinite[422,423] H_2 (Three-site Darkrim)[327] CH_4 (TraPPE)[925] CO_2 (TraPPE)[678]	MD	333.15 K / 30 MPa	0.6	H_2, CH_4, and H_2O H_2, CO_2, and H_2O
Kahzadvand *et al.*[882]	Montmorillonite and Illite (CLAYFF)[422,423] H_2 (Three-site Marx)[328] H_2O (SPC/E)[346]	MD	333 K / 15 MPa	0.4−7	H_2 and CH_4 H_2 and CO_2
Bui *et al.*[895]	Kaolinite − Gib. and Siloxane (CLAYFF)[422,423] H_2 (Single-site Buch)[312] H_2O (SPC/E)[346]	MD	298 K / 10 and 20 MPa	1 and 2	H_2 and H_2O
Zheng *et al.*[878]	Calcite (Xiao)[431] Hematite (modified CLAYFF)[424] Quartz (CLAYFF)[422] H_2 (Three-site Alavi)[336]	MD	298−350 K / 1−10 MPa	2 and 20	H_2
Xie *et al.*[887]	Kaolinite[423] and Kerogen (CVFF)[426] H_2[313] CH_4 (TraPPE)[301]	MD	333.15 K / 30−15−10 MPa	2 and 5	H_2 and CH_4
Zhang *et al.*[881]	Kerogen II-D (CVFF)[426] Montmorillonite (CLAYFF)[422,423] H_2 (Single-site Buch)[312] CH_4 (TraPPE)[301] CO_2 (Fully Flexible)[926]	GCMC	333.15 K / 3−18 MPa	2 and 5	H_2 H_2 and CH_4 H_2 and CO_2
Muther and Dahagi[883]	Kaolinite (CLAYFF)[422,423] H_2 (Three-site Darkrim)[327] CH_4 (TraPPE)[301]	GCMC	323−403 K / 1−50 MPa	3	H_2 H_2 and CH_4 H_2 and CO_2

https://doi.org/10.1021/acs.chemrev.5c00617
Chem. Rev. 2025, 125, 11878−12029

Table 18. continued

Author	Materials/Force Fields	Method	T [K]/P [MPa]	Pore Size [nm]	Mixture(s)
	CO_2 (EPM2)[419]				
Chen et al.[885]	Quartz (CLAYFF)[422,423]	GCMC and MD	339−400 K / 1−50 MPa	2, 4, and 10	H_2 and CH_4
	H_2 (Single-site Michels)[924]				H_2, CH_4, and H_2O
	CH_4 (TraPPE-UA)[301]				
	H_2O (TIP4P)[300]				
Shang et al.[877]	Kaolinite : Gib. and Sil. (CLAYFF)[422,423]	GCMC and MD	303−423 K / 1−30 MPa	1−20	H_2
	H_2 (Three-site Darkrim)[327]				
Zhang et al.[896]	Kaolinite (CLAYFF)[422,423]	GCMC	318.15 K / 0.1−30 MPa	0.5−2	H_2 and H_2O
	H_2 (Two-site Cracknell)[311]				CH_4 and H_2O
	CH_4 (TraPPE)[925]				H_2, CH_4, and H_2O
Choudhary and Ho[898]	Pyrophyllite, Gibbsite (CLAYFF)[422,423]	MD	300 K / 0.1 MPa	1.326 and 1.626	H_2 and H_2O
	H_2 (Three-site Darkrim)[327]				CO_2 and H_2O
	CO_2 (TraPPE)[678]				
	H_2O (SPC/E)[346]				
Babaei et al.[888]	Kerogen (CVFF)[426]	GCMC and MD	363.15 K / 0.1−50 MPa	Disordered	H_2
	H_2 (Single-site Buch)[312]				CH_4
	CH_4 (TraPPE-UA)[301]				H_2 and CH_4
Muther and Dahagi[922]	Na-Montmorillonite (CLAYFF)[422,423]	GCMC and MD	298-403 K / 1−50 MPa	1.26−1.55	H_2
	H_2 (Three-site Darkrim)[327]				H_2, CO_2, and H_2O
	CO_2 (Cygan Flexible)[927]				H_2, CH_4, and H_2O
	CH_4 (TraPPE-UA)[301]				
	H_2O (Not mentioned)				
Choudhary and Ho[897]	Kaolinite : Gib. and Sil. (CLAYFF)[422,423]	MD	300 K / 5.1−30.4 MPa	n/a	H_2, CO_2 and Octane
	H_2 (Two-site IFF)[313]				
	CO_2 (TraPPE)[678]				
	C_8H_{18} (OPLS all-atom)[428]				
Ho et al.[894]	MCM-41 Silica (Customized)[429]	GCMC	298 K / 0−1 MPa	3.4 (Cylindrical)	H_2 and OMCTS
	H_2 (Single-site)[894,928]				CO_2 and OMCTS
	CO_2 (EPM)[419]				
	OMCTS (Customized)[928]				
Liu et al.[906]	MMT (CLAYFF)[422,423]	MD	333-413 K / 2−30 MPa	3-40	H_2
	H_2 (Single-site Hirschfelder)[321]				H_2 and H_2O
	H_2O (SPC/E)[346]				
Mashhadzadeh et al.[899]	Kaolinite (INTERFACE)[425]	MD	310−410 K / 30 MPa	1−10	H_2 and H_2O
	H_2 (Two-site Yang)[325]				H_2 and NaCl Brine
	H_2O (SPC/E)[346]				H_2 and $MgCl_2$ Brine
	Na^+,[371] Cl^-, Mg^{2+} [929] [1−5 M]				
Hubao et al.[907]	Calcium Silicate Hydrate (CLAYFF)[425]	MD and GCMC	300−370 K / 2.5−40 MPa	2.5−40	H_2
	H_2 (Single-site Hirschfelder)[321]				
Raza et al.[908]	Kerogen (PCFF++)[427]	MD and GCMC	360 K / 3−41 MPa	0.5 and 2	H_2
	H_2 (Single-site Waldman)[930]				
Kim et al.[909]	Illite (CLAYFF)[422,423] and Kerogen (CVFF)[426]	MD	326 K / 30.4 MPa	n/a	H_2, CH_4, and H_2O
	H_2 (Two-site Wang)[313]				H_2, CH_4, CO_2, and H_2O
	CH_4 (OPLS)[428]				
	CO_2 (Not mentioned)				
	H_2O (SPC/E)[346]				
Ghasemi et al.[910]	Pyrophillite (CLAYFF)[422,423]	MD	368.15 K / 30 MPa	1−8	H_2 and H_2O
	Montmorillonite (CLAYFF)[422,423]				
	Beidellite (CLAYFF)[422,423]				
	H_2 (Two-site Yang)[325]				
	H_2O (SPC/E)[346]				
Li et al.[931]	Calcite[432]	MD	353 K / 20 MPa	8	H_2 and H_2O
	H_2 (Single-site Hirschfelder)[321]				
	H_2O (SPC/E)[346]				
	Na^+, Cl^- [374]				

https://doi.org/10.1021/acs.chemrev.5c00617
Chem. Rev. 2025, 125, 11878−12029

Table 18. continued

Author	Materials/Force Fields	Method	T [K]/P [MPa]	Pore Size [nm]	Mixture(s)
	Mg^{2+},[932] SO_4^{-2} [b 933]				

[a]Gibbsite surfaces have a -OH group : Hydrophilic [b]Siloxane surfaces have an Si-O-Si group : Hydrophobic

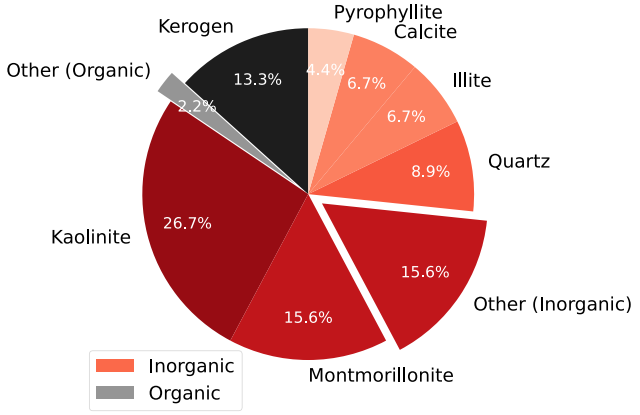

Figure 49. The substrates considered in the molecular simulation studies reviewed in this section. The sectors in shades of red and black represent inorganic and organic materials, respectively.

hydroxylated quartz, with the interplay between these factors ultimately determining the storage capacity and stability of H_2 geo-storage systems. Similarly, Chen et al.[885] used GCMC simulations to study the adsorption of CH_4−H_2 mixtures under conditions representative of shale gas reservoirs. A base-case scenario was set in a 4-nm slit pore at 370 K and 300 bar (in the paper, units of Fahrenheit and psi were used), while simulation conditions spanned temperatures of 339 - 400 K, and pressures up to 500 bar. It is important to note that experimental data are available only for pure CH_4 adsorption; the computed excess adsorption capacities and adsorbed phase densities CH_4 agree with these experiments within a deviation of 3%. The outcomes revealed that when the mole fraction of CH_4 is high (≥50%), CH_4 is preferentially adsorbed on both graphite and quartz surfaces, forming an adsorption layer close to the solid boundary, while H_2 is predominantly distributed in the free phase within the pore. However, when the mole fraction of CH_4 is low (e.g., 20%), the behavior changes: in the graphite layer, the fewer CH_4 molecules present leave sufficient space for H_2 to form its own adsorption layer at the surface. A similar trend is observed for the quartz surface, although the density of the H_2 adsorption layer is notably lower compared to that in the graphite system. When water is present in the system (modeled with TIP4P), water molecules strongly interact with the solid surfaces, particularly with the carbon atoms of the graphite layer and the hydroxylated (100) face of quartz, which further suppresses CH_4 adsorption. This suppression reinforces the free distribution of H_2, with water forming its own distinct adsorption layer and having small direct effect on the behavior of H_2 molecules.

Zhao et al.[886] evaluated the feasibility of using depleted shale gas reservoirs for UHS by combining experiments with molecular simulations. A major finding was that H_2 adsorption is well described by the Langmuir isotherm over temperatures ranging from 303.15 K to 353.15 K and pressures up to 180 bar, which indicates that only a single layer of H_2 molecules is adsorbed on the mineral surfaces. It is noteworthy that the Langmuir fit was applied separately to experimental excess adsorption isotherms as well as simulation data. Both sets of results are in the same order of magnitude, however, slight deviations arise due to the single pore size assumption in the simulations and impurities present in the mineral samples used in the experiments. Quantitatively, the adsorption capacity decreases in the order of kaolinite > illite > calcite > dolomite > quartz. Both experimental measurements and simulations confirm that clay minerals (kaolinite and illite) exhibit capacities approximately two to three times higher than those of common minerals such as calcite, dolomite, and quartz. The overall agreement between experiments and simulations strengthens the comparative framework; yet, any minor discrepancies likely stem from differences in pore size distributions in natural samples versus the idealized models employed in simulations. Furthermore, the computed heat of adsorption was in the range of ca. 9−26 kJ/mol. This range, which lies well below the threshold for chemical adsorption, confirms that the process is dominated by physisorption. Additionally, H_2 diffusion coefficients were computed from MD simulations. It was shown that H_2 has the lowest diffusion coefficient in illite (ca. 0.018×10^{-9} m^2/s) and the highest in dolomite (ca. 25.83×10^{-9} m^2/s). This variation is attributed to the hindering effect of interlayer cations in illite and a relatively more open nano-pore structure in dolomite, which facilitates faster molecular movement. Overall, while the qualitative agreement between experiment and simulation confirms the potential of shale inorganic minerals for H_2 storage, the significant quantitative deviations emphasize the need for further refinement in pore structure modeling, and a more detailed study of additional factors (e.g., organic matter, residual gases, water).

In a similar study, Xie et al.[887] investigated the feasibility of UHS in depleted shale gas reservoirs by performing MD simulations that capture the complete huff-n-puff process. In that work, the simulation conditions mimic reservoir settings (333.15 K and pressures varying from 300 down to 100 bar). The simulations were designed to mimic a reservoir's operational cycle by first reducing pressure from 300 to 150 bar to trigger CH_4 desorption (the *huff* stage), then injecting H_2 until a desired composition is achieved, and finally further lowering the pressure to 100 bar (the *puff* stage) to mobilize the stored H_2. Recovery efficiency is quantified by comparing the computed H_2 densities before and after the final pressure drop. This cyclic injection and production strategy is designed to maximize storage efficiency while enabling later retrieval of H_2. The study compares two types of nano-pore models. The organic nano-pores are modeled using a type II-D kerogen representation derived from previous studies (i.e., a realistic representation of organic matter in shale), while the inorganic nano-pores are represented by kaolinite-based models of clay minerals. The adsorption capacities in these nano-pores are quantified by analyzing the ensemble-averaged density profiles and the distribution of gas molecules (both H_2 and CH_4) along the pore dimensions. In practice, the adsorption capacity is measured in terms of apparent adsorption isotherms and the average density computed from simulation snapshots at equilibrium. Furthermore, the simulations revealed that for the reservoir conditions studied, the organic pores show a

https://doi.org/10.1021/acs.chemrev.5c00617
Chem. Rev. 2025, 125, 11878−12029

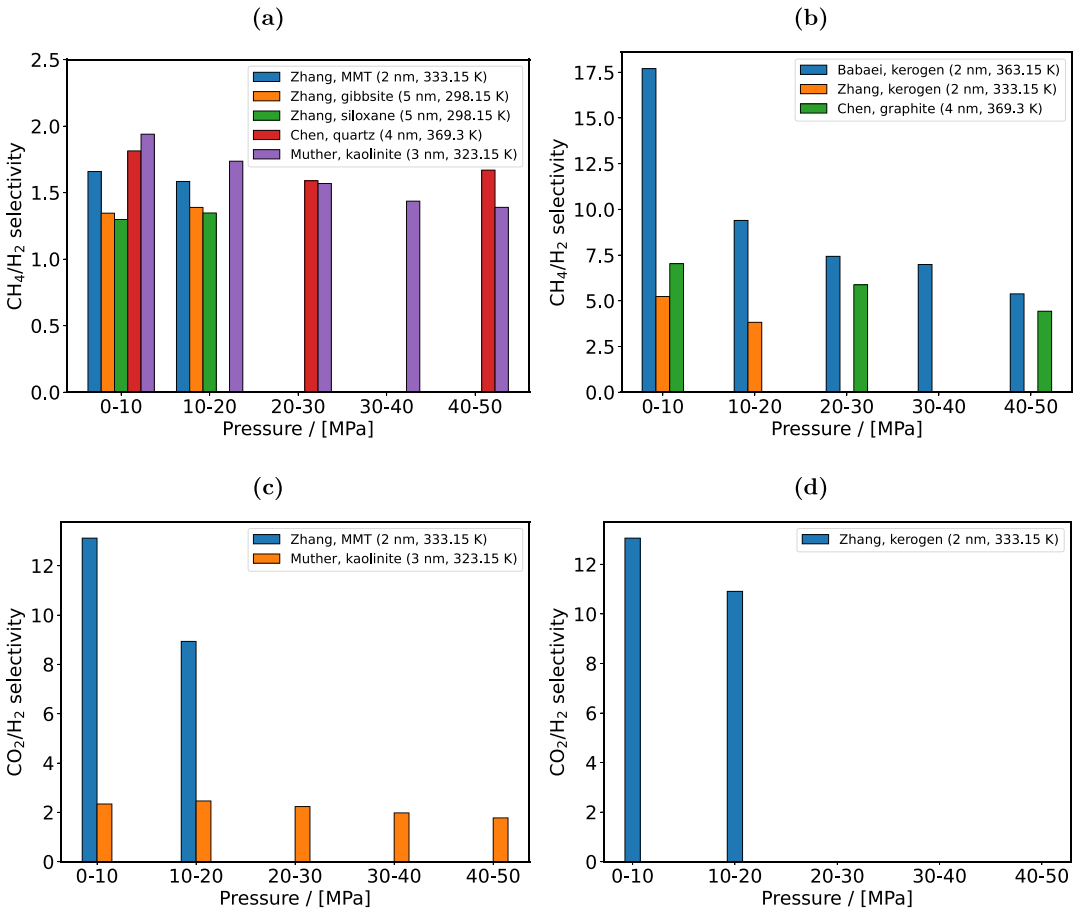

Figure 50. Comparison of CH_4/H_2 selectivities gathered from the literature for (a) inorganic and (b) organic pores. Comparison of CO_2/H_2 selectivities gathered from the literature for (c) inorganic and (d) organic pores. The data are taken from Zhang et al.,[881] Chen et al.,[885] Babaei et al.,[888] and Muther and Dahagi.[883] Each bar represents the mean selectivity within pressure bins of 10 MPa (0-10, 10-20, 20-30, 30-40, 40-50 MPa), calculated from data points in the corresponding pressure range. The legend indicates the study and, where applicable, the pore width (e.g., 2 nm) and temperature. Pressure values were converted from psi to MPa where necessary, and selectivity was inverted for studies where H_2/gas was originally reported. This figure illustrates the variation in selectivity across different geological materials and gas mixtures, highlighting the impact of pore type and pressure on adsorption behavior.

unique density profile for H_2 where the first adsorption peak is lower than the second. This behavior is opposite in inorganic pores, which can be attributed to competitive adsorption with CH_4, which strongly adheres to the organic surface. Density profile analysis clearly corroborated these findings across the different pressure points studied. The simulation results were further validated by comparing the computed bulk densities of pure and binary gas mixtures with NIST data. In the huff-n-puff cycle, recovery efficiency was determined by monitoring the change in the average density of H_2 before and after the puff stage; for example, recovery efficiencies were found to be 49.9% in organic meso-pores and 40.0% in organic micro-pores, in contrast with higher recovery values in inorganic pores (70.0% in meso-pores and 63.3% in micr-opores). These percentages are calculated as the ratio of the recovered H_2 (measured as the drop in average density) to the initial injected H_2 density.

Babaei et al.[888] followed a hybrid GCMC/MD approach at 363.15 K and pressures up to 500 bar to investigate the adsorption and diffusion of H_2, CH_4, and their mixtures in type II-D kerogen, wherein realistic pore size distributions are generated through the incorporation of dummy particles. In this framework, the inherent heterogeneity of the kerogen matrix is captured via three distinct models (Model 1, Model 2, and Model 3) constructed by embedding dummy particles with diameters of 0 nm, 1 nm, and 2 nm, respectively, to represent incremental variations in pore structure. Two computational frameworks were established to quantify adsorption-induced deformation. The "Lagrangian approach" referenced the system to its pre-adsorption state under fixed thermodynamic conditions, maintaining a constant accessible volume as a baseline, whereas the "Eulerian approach" was used to compare the system with and without adsorption under identical mechanical conditions, rendering the pore structure pressure dependent and more sensitive to deformation at high pressures. This detailed representation was critical as variations in pore size not only affect the accessibility of adsorption sites but also determine the extent of swelling induced by gas adsorption, a key factor influencing both the storage capacity and mechanical integrity of the matrix. In the case of CH_4 adsorption, the results indicated that the flexible kerogen models exhibited 1.4, 1.6, and 1.3 times higher adsorption in Models 1, 2, and 3, respectively, compared to their rigid counterparts. The corresponding volumetric strain (a measure of matrix expansion) ranged from 3.25% to 4.54% using the Lagrangian approach, and from 2.97% to 5.92% with the Eulerian approach at high pressures. For H_2 adsorption, however, the kerogen showed negligible deformation overall

https://doi.org/10.1021/acs.chemrev.5c00617
Chem. Rev. 2025, 125, 11878−12029

with the matrix experiencing either slight swelling or even contraction depending on the pore size distribution, an outcome attributed to the H_2's small molecular size and weak adsorption affinity, combined with capillary effects and pore geometry variations. Moreover, the study revealed that H_2 diffuses roughly one order of magnitude faster than CH_4 (6.87×10^{-9} m^2/s for H_2 compared to 0.30×10^{-9} m^2/s for CH_4 at 5 MPa). Although CH_4 was preferentially adsorbed, as evidenced by a selectivity greater than 1 across all pressures, this selectivity decreases with increasing pressure due to the saturation of adsorption sites, thereby reducing the differences between the two gases. Zhang et al.[889] used GCMC simulations to investigate the adsorption behavior of H_2/CH_4 mixtures in two types of kaolinite nano-pores, namely, the hydrophilic gibbsite and the hydrophobic siloxane pores, with pore sizes ranging from 5 to 200 nm, at 298.15 K and pressures between 1 and 100 bar. Under dry conditions, the study demonstrated that increasing the bulk H_2 mole fraction leads to an increased storage density for H_2, with its adsorption varying linearly with pressure, and a corresponding decrease in CH_4 density. Notably, when the injected mixture contained less than 20% H_2, the adsorption process selectively favors H_2. For instance, an injection mixture of 5% H_2 and 95% CH_4 yielded a H_2/CH_4 selectivity of approximately 2. Although both nano-pore types exhibit enhanced H_2 selectivity under low H_2 injection fractions, the surface chemistry plays a critical role: in gibbsite pores, strong interactions between CH_4 molecules and the pore surface result in higher CH_4 densities at low H_2 fractions, whereas in siloxane pores the overall CH_4 capacity is slightly lower, thereby improving the relative selectivity for H_2. In terms of pore size effects, the absolute density of H_2 remains nearly independent of the pore size because most stored H_2 is concentrated in the middle of the pore; however, the relative selectivity, defined as the ratio of the adsorbed H_2 to CH_4, increases in larger pores (particularly those exceeding 100 nm) due to improved enrichment of H_2. The presence of moisture reduces the adsorption densities of both gases in the mixed-gas scenario. In hydrophilic (gibbsite) nano-pores, water molecules are strongly attracted to the surface via hydrogen-bonding, forming a thin film along the walls, whereas in hydrophobic (siloxane) pores, water tends to form clusters that span across the pore, reducing the available free volume. Under moist conditions, for example at a water concentration of 0.2 g/cm^3 and a bulk H_2 mole fraction of 20%, the gibbsite pores are more favorable for H_2 storage than their siloxane counterparts. Although both pore types exhibit reduced overall adsorption densities in the presence of water, the effective storage volume in siloxane pores is more significantly diminished due to the water clusters, which adversely affect the selective adsorption of H_2.

A cross-comparison of these studies reveals several common quantitative trends. Muther and Dahaghi[883,884] reported that with increasing temperature, H_2 molecules possess greater kinetic energy, which they argued weakens attractive interactions with the adsorbent surface, thereby reducing adsorption capacity. While this reflects the interpretation of these authors, a more physically consistent explanation is that the release of H_2 at higher temperatures arises from the increasing dominance of entropic effects, rather than from the weakening of enthalpic attractions. It should also be noted that GCMC simulations, by construction, do not capture kinetic energy and kinetic effects. Thus, the observed reduction in adsorption with temperature in GCMC results should not be attributed to the reduced molecular kinetic energy of H_2 molecules.

Shifting our focus on the adsorption of CH_4/H_2 and CO_2/H_2 on organic and inorganic pores, we compiled Fig. 50 which shows selectivities for these mixtures collected from different simulation studies. Given the potential sensitivity of selectivities to pore size[890] and temperature, the values are selected such that the data can be compared without significant biases introduced from varying thermodynamic conditions. From Fig. 50(a) and (b), it is clear that the selectivity of CH_4 over H_2 remains above one in both organic and inorganic pores. However, the magnitude of this selectivity differs substantially: organic nano-pores (e.g., kerogen) often exhibit values an order of magnitude larger than their inorganic counterparts. Organic nano-pores show higher CH_4 selectivity because their heterogeneous surfaces provide stronger van der Waals interactions, promoting the formation of saturated, well-defined CH_4 adsorption layers that preclude extensive H_2 binding.[881,891] The stronger van der Waals interactions between CH_4 and carbon, compared to H_2 and carbon, arise from differences in the LJ potential parameters, specifically the well-depth. For instance, Kumar et al.[892] illustrated these differences clearly in their interaction profiles (Figure 2 in ref 892), showing that the well-depth for CH_4-carbon interactions is approximately eight times deeper than that for H_2-carbon interactions. This deeper potential well for CH_4 reflects its larger molecular size and greater polarizability,[893] both of which enhance dispersion forces relative to H_2. In contrast, inorganic minerals, with their lower CH_4 affinity and more uniform surfaces, result in less saturation and greater availability of sites for H_2, thus, reducing CH_4 selectivity.

As shown in Fig. 50(a) and (c), S_{CO_2/H_2} selectivities are significantly higher than S_{CH_4/H_2} indicating a strong preferential adsorption of CO_2 over CH_4[890] in inorganic pores. This strong adsorption can be attributed to the strong quadrupole moment and polarizability[890] of CO_2. This substantial preference for CO_2 compared to CH_4/H_2 systems can have significant practical implications. For instance, in underground storage, the intentional use of CO_2 as a cushion gas would result in its retention on pore surfaces, leaving H_2 predominantly in the free (mobile) phase, which is advantageous for recovery and purity. For organic pores, the comparison between Fig. 50(b) and (d) suggests that S_{CO_2/H_2} reported by Zhang et al.[881] generally exceeds S_{CH_4/H_2}, except in the data from Babaei et al.,[888] who studied adsorption in disordered pores, leading to a pore size distribution rather than a single pore size (as in slit-pore studies).

The studies reviewed earlier suggest that beyond surface chemistry and cushion gases, pore size, pressure, and temperature all significantly impact gas/H_2 selectivities. Zhang et al.[890] demonstrated that S_{CO_2/H_2} in Na-Montmorillonite pores vary by a factor of 3 to 4 when pore size increases from 2 to 5 nm. In sharp contrast, S_{CH_4/H_2} in the disordered kerogen pores studied by Babaei et al.[888] hardly show any change despite an increase in mean pore size from 0.4 nm (Model 1) to 2 nm (Model 3). The authors attributed this invariance to the particularly strong CH_4-kerogen interactions overshadowing pore size effects.[888] Another commonly observed behavior across the reviewed studies is the decrease in selectivities with increasing pressure due to the saturation of

https://doi.org/10.1021/acs.chemrev.5c00617
Chem. Rev. 2025, 125, 11878−12029

binding sites. There has not been a systematic investigation of the role of temperature in gas selectivity.

The presence of water films typically reduces H_2 adsorption by 3 to 40%, whereas cushion gases like CO_2 and CH_4 form robust adsorption layers, potentially decreasing H_2 capacity by up to 30%. H_2 interaction energies in pure systems range from approximately −1.5 to −2.0 kcal/mol, while competing gases exhibit stronger binding (e.g., CH_4 at −4.3 kcal/mol). Smaller pore sizes show up to 40% higher adsorption, and the maturity of organic content (kerogen) further modulates these effects. Together, these quantitative findings provide a road-map for understanding and optimizing competitive adsorption and storage performance in geological formations.

4.7.2. Solubility of Hydrogen under Confinement. Solubility under confinement is a crucial topic with direct implications for UHS and other applications. As highlighted by Ho et al.,[894] the confined environment in nano-pores - whether circular, as in some studies, or flat-walled, as in others - not only enhances gas solubility through mechanisms such as cavity formation and solvent layering, but also alters gas diffusion and clustering behavior. The studies focusing on this topic use a variety of molecular models. For example, Ho et al.[894] studied circular pore systems to mimic realistic confined environments, whereas Bui et al.[895] used flat-wall, slit-shaped nano-pore models that represent kaolinite or other clay minerals. Such differences in the molecular systems used allow for a rigorous comparison of how pore geometry and surface chemistry control gas uptake phenomena. A detailed information of the thermodynamic conditions, pore sizes, materials, and the force fields used in the different studies are tabulated in Table 18.

Ho et al.[894] investigated gas uptake in a model meso-porous system where a solvent is confined within well-defined pores, providing a basis for understanding how nano-confinement affects gas-solvent interactions. The paper identifies two distinct mechanisms for over-solubility. For gases that interact strongly with the solid surface (e.g., CO_2 on silica), there is an adsorption-driven uptake, while for gases with weak gas/solid interactions (such as H_2), the predominant mechanism is an enhanced solubility due to the formation of low-density regions arising from solvent layering. For instance, the work explains that when only a single layer of solvent is present inside a meso-pore, adsorption at the gas/liquid interface contributes additionally to the gas uptake. Although no numerical values are provided in this study, the mechanism establishes the baseline for comparison with more detailed quantitative studies in later works, such as Bui et al.[895] The study by Zhang et al.[896] examined H_2 dissolution in water-saturated caprock nano-pores mimicking natural sealing layers. Nano-confinement in these pores was shown to enhance H_2 solubility by up to 27 times relative to bulk water. For example, Zhang et al.[896] report that in pores with an optimal width of 0.55 nm, the dissolved H_2 density reaches 5.614 kmol/m^3 at 318.15 K and 300 bar, corresponding to an enhancement factor of about 27.4 times the bulk value.

In the context of UHS, Bui et al.[895] studied H_2 solubility in water confined within kaolinite nano-pores. Two distinct pore widths were considered: 20 Å and 10 Å. For the 20 Å wide pore, the study reports that under pressures of 100 and 200 bar, H_2 solubility is enhanced by approximately 2.5 times compared to bulk water as shown in Fig. 51. Strikingly, in the 10 Å pore, the solubility is significantly enhanced to nearly 25 times that of the bulk (see Fig. 51). These numbers are

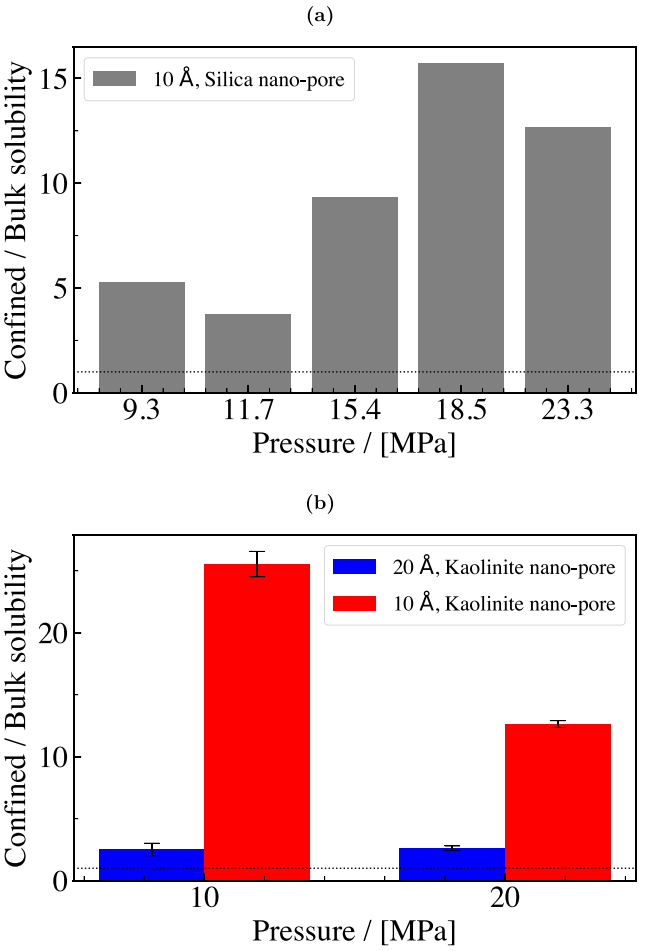

Figure 51. Enhancement of solubility under confinement: Ratio of gas solubility in confined water and bulk water for (a) CH_4 and (b) H_2. H_2 solubilities are taken from Bui et al.[895] and CH_4 solubilities are taken from Phan et al.[900] and Sakamaki et al.[904] The nano-pores are made of Kaolinite in the study by Bui et al.[895] (see Table 18) and Silica in Phan et al.[900] The dotted line serves as a reference where bulk solubility equals confined solubilities.

supported by detailed water density profiles that reveal pronounced hydration layers; H_2 preferentially accumulates in regions of low water density near the hydrophobic siloxane surface, whereas the hydrophilic gibbsite side shows a dense water layer that excludes H_2. The enhancement is attributed to pronounced water density fluctuations that generate regions of low solvent density where H_2 preferentially dissolves. Interestingly, while the confinement retards water diffusion, H_2 diffusion is enhanced due to these fluctuations. The study clearly links the molecular-scale structuring of water under confinement to the observed over-solubility of H_2.

The work by Choudhary and Ho[897] explores a hybrid system designed to mimic depleted oil reservoirs, where oil, gas, and kaolinite interact. The study demonstrates that H_2 dissolves more readily in oil than in water, owing to weaker H_2-oil interactions compared with H_2 - water interactions. Quantitatively, the simulation results indicate that the addition of as little as 5% CO_2 (in mole fraction units) can reduce H_2 dissolution in oil by approximately 15% because of the resulting decrease in interfacial tension. H_2 adsorption is weak and similar on both hydrophilic and hydrophobic faces, whereas it is CO_2 that exhibits a strong preference for the

https://doi.org/10.1021/acs.chemrev.5c00617
Chem. Rev. 2025, 125, 11878−12029

hydrophilic side. These detailed quantitative observations (e.g., the reduction percentage and the role of specific surface terminations) provide a link of the molecular-level interactions with the overall gas uptake behavior. Choudhary and Ho[898] focused on gas clustering within hydrated nano-pores with contrasting surface chemistries. It shows that over-solubility can emerge either through adsorption at the liquid/solid interface or by gas molecules migrating into low-density regions formed by solvent structuring. For example, in hydrophobic nano-pores (represented by pyrophyllite with siloxane rings), CO_2 exhibits a much stronger tendency to form stable dimers and larger clusters due to its higher quadrupole moment (14.2×10^{-40} C m^2) compared to H_2 (1.7×10^{-40} C m^2); as a result, while CO_2 tends to exit the pore as clusters, H_2, with its lower polarizability (0.80×10^{-24} cm^3), shows a lesser degree of clustering. Such molecular insights, supported by free energy calculations, are crucial for understanding how nano-pore dimensions and surface chemistry jointly control the aggregation processes within confined media.

The investigation by Mashhadzadeh and Faroughi[899] used atomistic simulations to study the behavior of dilute H_2 in water-saturated kaolinite-a mineral representative of clay-rich caprocks. Their results indicate that as the pore size decreases, for example from 100 Å down to 10−15 Å, dense layers of water and H_2 form near the clay surface. These structured arrangements lead to a reduction of the H_2 self-diffusion coefficient compared to the bulk phase, even as local H_2 concentrations are elevated. The study further identifies that the presence of divalent ions (with larger hydration shells), such as Mg^{2+}, decreases H_2 mobility more significantly than monovalent ions. These findings offer useful insights into the interplay between nano-scale confinement, salinity, and molecular diffusion.

All studies discussed in this section converge to the notion that both nano-confinement and surface/interface phenomena, ranging from cavity formation, solvent layering, and density fluctuations to specific interaction strengths, are vital in enhancing H_2 solubility (or over-solubility) in confined media. Concrete examples, showcasing the particular nature of confined H_2 are the studies by Zhang et al.,[896] where it was shown that a pore width of 5.5 Å at 318.15 K and 300 bar yields a H_2 solubility enhancement of nearly 27 times relative to bulk, and by Bui et al.,[895] where it was reported that kaolinite nano-pores with a width of 10 Å result in a 25-fold enhancement of hydrogen solubility at pressures of 100−200 bar. In the molecular simulation studies reviewed here, the differences in interfacial behavior were also highlighted, i.e., hydrophobic surfaces such as siloxane and pyrophyllite, foster the formation of gas clusters[898] and low-density solvent regions, whereas hydrophilic surfaces, such as gibbsite and kaolinite, tend to form dense water layers that limit gas uptake. The study addressing oil−clay−gas interactions by Choudhary and Ho[897] underscores the role of interfacial tension and mineral surface properties in modulating gas uptake in hybrid systems. It is also important to emphasize that this confinement-induced over-solubility is not unique to H_2. Similar trends have been reported for other gases, such as CH_4 and CO_2, across a range of systems spanning protein−water and gas−water in industrial catalysis. As reported in the literature, CH_4 solubility in confined water has been reported to be enhanced by up to 50 times relative to its bulk value.[900] Likewise, CO_2 over-solubility in confined solvents has been well documented in studies where confinement and the nature of the solid surface (e.g., hydrophobic and hydrophilic terminations) significantly alter the adsorption−desorption equilibrium.[898]

The influence of confinement on gas solubility is not limited to simple gas−solvent systems. Similar mechanisms-often linked to water density fluctuations, cavity formation, and local solvent structuring-also manifest in more complex media, such as those involving protein - water interactions. Reviews on protein hydration, such as the work by Ball,[901] as well as studies on hydrophobic effects and water density fluctuations discussed by Rego and Patel[902] and Jamadagni et al.,[903] provide additional evidence that enhanced gas uptake under nano-confinement is a universal phenomenon, governed by a delicate balance between solvent layering, cavity formation, and specific gas−solid and gas−solvent interaction strengths.

4.7.3. Diffusivity of Hydrogen under Confinement. Understanding mass transport mechanisms of H_2 in geological environments is essential for evaluating both the feasibility and efficiency for a variety of applications such as UHS. This section reviews recent studies using MD simulations to investigate H_2 transport in nano-pores inspired by geological systems. In the study by Wang et al.,[905] EMD simulations were first used to reveal the behavior of fluid mixtures in Na-montmorillonite nano-pores, showing that water preferentially adsorbs onto the clay surfaces forming water films. At a water content of 10%, both H_2 and CH_4 form two distinct adsorption layers in smaller pores. As water content increases, the water film thickens by 2−3 times, driving the gas molecules into the bulk region, while the calculated selectivity coefficients for H_2/CH_4 (ranging from 0.70 to 0.76) indicate that the cushion gas (CH_4) effectively reduces H_2 loss. In contrast, NEMD simulations captured the dynamic transport behavior under applied pressure gradients, where elevated pressures induce the desorption of water molecules near the pore walls, thereby enhancing the accumulation and mobility of H_2. The self-diffusion coefficient of H_2 was observed to decrease by up to 53% when water content increases from 10% to 30%, with the ratio of H_2 to CH_4 diffusion coefficients decreasing from 2.2 to 1.7. Under high pressure gradients, a notable desorption of water molecules is observed near the pore walls that enhances the accumulation and mobility of H_2 in these regions, a phenomenon that is consistent with recent experimental trends in enhanced multiphase flow through nanoporous media.

The study by Oliver et al.[879] reported MD simulations of H_2 transport in nanoporous media, focusing on both organic (graphene) and inorganic (kaolinite) slit pores under subsurface conditions. The authors investigated how H_2 diffusion is influenced by surface chemistry and pore size (ranging from 2 to 20 nm), and pressure (from 20 to 500 bar). Notably, H_2 adsorption occured as a monolayer (3 Å thick) on both materials, though graphene exhibited ca. 35% higher surface density than kaolinite. Despite the stronger gas−solid interaction in the case of graphene, the self-diffusion coefficients (in the order of 10^{-6} m^2/s) were higher in graphene than in kaolinite at low pressures. This finding, supported also by the density profiles, collision times (with graphene's collision time being approximately 2 ps longer at 20 atm), and lateral velocity autocorrelation functions that reveal more frequent wall-mediated collisions on the rougher kaolinite surface. Both materials demonstrated an exponential decrease in H_2 self-diffusion coefficients with increasing pressure. However, at high pressures (beyond 50-100 atm),

https://doi.org/10.1021/acs.chemrev.5c00617
Chem. Rev. 2025, 125, 11878−12029

the impact of surface chemistry diminishes as gas−gas collisions begin to dominate, leading their transport properties to converge.

Zheng et al.[878] studied the mechanisms of H_2 diffusion in geological slit pores made of calcite, hematite, and quartz, focusing on the effects of temperature, pressure, pore size (confinement), and surface chemistry. The study demonstrated that for all three minerals, the H_2 self−diffusion coefficient increases with temperature in the range of 298 to 350 K, and in 20 nm slit pores at 100 bar the diffusion follows a bulk regime with the relation $D \propto T^{1.5}$ (supported by linear trends in the ln−ln plots with slopes equal to ca. 1.5). In contrast, increasing the pressure from 10 to 100 bar, consistently reduces the diffusion coefficient across all minerals, following a power law with fitted exponents ranging from −0.825 to −0.964, which is corroborated by analyses of normalized interaction energies and density profiles showing enhanced adsorption at higher pressures. When the pore aperture is reduced from 20 nm to 2 nm, the diffusion coefficient decreases substantially due to stronger wall-gas interactions, resulting in a shift from bulk to transition or even surface diffusion regimes. The study showed that surface roughness enhances H_2 diffusion in larger pores by effectively enlarging the pore space while it decreases diffusion in smaller pores due to stronger adsorption. These conclusions were corroborated by comparisons of decay times from velocity autocorrelation functions and 2D density distributions. In a related work, Shang et al.[877] performed simulations to compute the H_2 diffusion and adsorption in confined kaolinite slits using a hybrid MD−GCMC approach. Similarly to the studies reviewed so far, the focus of this work was also on how variations in pore size, temperature, pressure, and surface mineralogy affect H_2 properties. This study showed that when the pore size exceeds 5 nm, H_2 is predominantly located in the bulk phase with minimal adsorption losses, whereas for pores below 5 nm, a rapid decrease in both excess adsorption and diffusion coefficient due to enhanced gas−solid interactions is observed. Increasing temperature from 303 to 423 K reduced the adsorption capacity but concomitantly increased the H_2 diffusion coefficient, following a power law relationship, with corresponding changes in both the density profiles and the gas−solid interaction energy. Meanwhile, elevating pressure from 10 to 300 bar enhanced the storage capacity while diminishing the mobility of H_2, as supported by the observed rise in adsorption peak densities and the inverse trend in diffusion coefficients. In terms of surface chemistry, the study by Shang et al.[877] revealed that the positively charged gibbsite surface promotes H_2 adsorption compared to the negatively charged siloxane surface.

Liu et al.[906] conducted MD simulations to investigate the diffusion of H_2 confined in montmorillonite nano-pores, with the motivation being assessing its leakage risk in geological storage settings. The study systematically examined the dependence of the self−diffusion coefficient (which were shown to be on the order of 10^{-8} m^2/s) on temperature (333−413 K), pressure (20−300 bar), and pore size (with slit apertures ranging from 3 to 40 nm). It was observed that diffusivity increases moderately with temperature and pore size, yet decreases with higher pressures. For example, in an 8 nm slit, the diffusivity increased from approximately 8.08×10^{-8} m^2/s at 353 K to 10.03×10^{-8} m^2/s at 413 K, while an increase in the pressure from 2 to 300 bar led to a reduction from nearly 10×10^{-8} m^2/s to 7.5×10^{-8} m^2/s. The authors further demonstrated anisotropic diffusion by resolving local diffusion coefficients into components parallel and perpendicular to the clay surfaces, with density profile analyses revealing a single adsorption layer at ca. 2.8 Å from the surface. In addition, trends in H_2 diffusion under varying moisture content and brine salinity were explored. As the average water density increases in a 3 nm slit from 0.568 to 0.758 g/cm^3, the self−diffusion coefficient steeply decreases from 8.27×10^{-8} to 4.25×10^{-8} m^2/s. While variations in salinity up to 8 wt% yield minor changes, at 12 wt% the diffusivity drops further (e.g., from 8.67×10^{-8} to 7.21×10^{-8} m^2/s) due to the formation of brine droplets that hinder gas motion. Although similar trends in diffusion modulation have been reported for other fluids such as CH_4, CO_2, octane, and nonadecane, the study implied that the relatively moderate fluid−solid interactions of H_2 render its pore−size sensitivity less pronounced than that of the other materials.

Using MD simulations, Mashhadzadeh and Faroughi[899] computed H_2 diffusion in water-saturated kaolinite nano-pores under conditions relevant to UHS. The study explored how variations in pore size (ranging from 10 to 100 Å), temperature (from 310 to 410 K), and ionic composition (salinities of 1 to 5 M, and the use of monovalent Na^+ versus divalent Mg^{2+} ions) affect the diffusion of H_2 under a fixed pressure of 300 bar. It was shown that reducing pore size leads to denser H_2 and water layers at the kaolinite surface, and consequently, to a significant reduction in H_2 diffusivity. H_2 diffusivities dropped from ca. 7.8×10^{-9} m^2/s at a confinement distance of 60 Å to ca. 2.5×10^{-9} m^2/s at 10 Å. Similarly, the study demonstrated that higher temperatures promote increased H_2 mobility, with diffusion coefficients increasing from apporixmately 4.49×10^{-9} m^2/s at 310 K to 9.27×10^{-9} m^2/s at 410 K. The presence of divalent ions such as Mg^{2+} further restricts H_2 motion compared to monovalent ions (Na^+) due to their larger hydration shells and stronger electrostatic interactions. Overall, these findings underscored the critical roles of pore size, surface chemistry, temperature, and salinity in controlling H_2 transport in confined systems, which are important implications for UHS technologies.

Hubao et al.[907] investigated the diffusion and distribution of H_2 in confined calcium silicate hydrate (C-S-H) nano-pores using MD simulations, covering a wide range of conditions, namely temperatures ranging from 300 to 370 K, pressures from 25 to 400 bar, and pore sizes spanning 2.5−40 nm. The study revealed that H_2 molecules tend to accumulate near the C-S-H walls, forming a high-density adsorption layer. The diffusion of H_2 was shown to be strongly anisotropic, with diffusion parallel to the walls being significantly faster than in the perpendicular direction. Furthermore, increasing pressure notably elevates the density and suppresses the overall diffusion coefficient, whereas higher temperatures reduce the density and enhance mobility. Although similar observations have been already made, for confined fluids, H_2 exhibits a distinct single adsorption layer due to its relatively weak interactions with the surface compared to materials like water and CO_2, for which multi-layer adsorption is often reported. Finally, the work demonstrated that as the pore size increases beyond a critical threshold (ca. 20 nm), the confined diffusion gradually approaches that of the bulk phase.

Raza et al.[908] reported self−diffusivities of H_2 in organic-rich shale, focusing on how H_2 transport behavior changes with pore confinement, pressure, and indirectly with surface chemistry via kerogen type. The study considers two representative kerogen types (II-A, representing immature

https://doi.org/10.1021/acs.chemrev.5c00617
Chem. Rev. 2025, 125, 11878−12029

organic matter, and II-C, representing mature organic matter) with slit pore sizes of 0.5 and 2 nm. The temperature was constant at 360 K while pressures ranged from 30 to 400 bar. The findings indicated that the dominant transport mechanism is "transitional diffusion," characterized by Knudsen numbers between 0.64 and 9.72, where H_2 diffusion is a balanced interplay between slip flow and molecular diffusion. Across both kerogen types, a clear trend emerges where H_2 diffusivity declines with increasing pressure, and, importantly, larger pores (2 nm) consistently yield higher self-diffusion coefficients (ranging from ca. 0.004 to 0.02 cm^2/s for type II-A and 0.0037 to 0.019 cm^2/s for type II-C) compared to the 0.5 nm pores. For a fixed nano-pore size, the thermal maturity of the kerogen does not have a discernible impact on H_2 diffusivity even though type II-A tends to retain greater H_2 density due to stronger adsorption effects. Finally, the diffusion data were successfully regressed to a power-law model with coefficients of determination (R^2) being in the range 79−98%, providing a continuous description of the diffusivity−pressure relationship. Note that while the study explores variations with pore size and pressure in depth, the temperature was kept constant and specific variations in surface chemical properties beyond the kerogen type were not explicitly considered.

Kim et al.[909] also studied the H_2 diffusion within nanoporous shale caprocks. The simulations considered both binary (H_2/CH_4) and ternary ($H_2/CH_4/CO_2$) gas mixtures confined by three distinct pore types i.e., organic pores formed by kerogen, inorganic pores formed by clay, and mixed−wet pores composed of both kerogen and clay. The simulations were carried out at 300 atm and 326 K, focusing on diffusive transport in two directions: perpendicular (x direction) to the pore faces (which, due to periodic boundary conditions, includes diffusion through the kerogen matrix) and parallel (yz direction) to the pore surfaces. Graham's law states that the rate of gas diffusion varies inversely with the square root of its molecular weight (i.e., lighter gases diffuse faster than heavier ones). However, while the expectation is that H_2 (having very low molecular weight) should diffuse much more rapidly than CH_4 and CO_2, the results by Kim et al.[909] showed that the differences are moderated by additional factors such as surface affinity, adsorption by water and ions, and restrictions imposed by the available pore space. In fact, H_2 exhibits a self-diffusivity in the order of 10^{-7} m^2/s in the parallel direction in clay and mixed-wet pores, whereas diffusion through kerogen is reduced by 2−3 orders of magnitude owing to its much smaller pore sizes (ca. 1 to 10 nm). These findings illustrate that, beyond the influence of molecular weight, the interplay between adsorption phenomena and pore geometry is critical for understanding H_2 diffusivity in geologic media.

Ghasemi et al.[910] also performed MD simulations to investigate H_2 diffusion in confined, water−saturated clay minerals, which is a representative caprock system for UHS. The authors systematically explored the effects of pore size, surface chemistry, and interlayer cations under conditions of 368.15 K and 300 bar. The study examined five clay mineral types, namely pyrophyllite (uncharged), Na- and Ca-montmorillonite, and Na- and Ca-beidellite (both negatively charged with different charge distributions), providing insight into how H_2 mobility is affected confinement in the pores. For the charged clays, a critical pore size of ca. 2 nm was observed for which a substantial increase in the H_2 diffusion coefficient occurred (increase of up to 24.06% relative to bulk water), while for pyrophyllite the diffusion coefficient increased monotonically with pore expansion, indicating that is not affected by surface charge. The study also showed that the distribution of negative charges (concentrated in the octahedral layer of montmorillonite versus the tetrahedral sheets in beidellite) significantly influences the positioning of H_2 molecules relative to the clay surfaces, thereby affecting diffusion, whereas the effect of inter-layer cations (with Na^+ allowing slightly higher mobility compared to Ca^{2+} due to their closer association with the clay surface and smaller hydration shell) is comparatively less pronounced. By using the Einstein relation to analyze molecular trajectories, the authors corroborated that confined H_2 diffusion is markedly different from that in bulk water and converges toward bulk behavior as pore size increases beyond 2 nm, with the diffusion coefficient for some clays approaching that in bulk water (ca. 13.07×10^{-9} m^2/s) at larger spacings (up to 8 nm).

A common oversight observed in many of the studies discussed above relates to the subtlety involved in diffusion parallel to interfaces. Determining diffusion coefficients of gases and liquids confined within cavities or at inhomogeneous interfaces, such as air-water or water-solid boundaries, presents unique challenges.[911−913] In confinement, traditional methods like the Einstein or Kubo relations (see Section 3.2.1) become insufficient. For confined liquids, the MSD is inherently limited by the size of the confinement, making it difficult to clearly define a diffusion coefficient. For systems with inhomogeneous regions, particles typically spend a finite duration within a specific area before exploring others (see also the discussion on H_2 diffusivity in polymers in Section 4.4). Consequently, the diffusion coefficient will vary across regions, and the MSD computed for particles initially localized in a particular region will only exhibit linear behavior after sufficient time has elapsed, allowing particles to sample all available regions. Ultimately, the slope of this long-term linear behavior represents an averaged diffusion coefficient across the entire system.

Berne and co-workers developed a methodology to quantify position-dependent diffusion coefficients in interfacial or confined fluids, where conventional MSD or GK approaches fail.[914] The method is based on the anisotropic Smoluchowski equation, which describes molecular diffusion in systems with an inhomogeneous density profile arising from the influence of the solid-liquid or liquid-vapor interface. This spatial variation in density can be expressed as a potential of mean force that enters the Smoluchowski formulation, allowing diffusion to be resolved into diffusivities parallel and perpendicular to the interface. For the parallel component, MD trajectories are analyzed within each layer while imposing virtual absorbing boundaries. The mean lateral displacement of molecules that remain within a layer yields the local in-plane diffusivity. For the perpendicular component, where the location of a molecule from the solid-liquid or liquid-vapor interface strongly affects molecular motion, Langevin dynamics simulations are performed in parallel with MD using the same potential of mean force and boundary conditions. The friction parameter in the Langevin model is adjusted until the survival probability matches that from MD, from which the perpendicular diffusivity is inferred. For layers located well within the bulk phase, where the density is uniform and unaffected by interfacial gradients, the perpendicular diffusivity is readily obtained from the exponential decay of the molecular survival probability within that region. Although accurate and physically motivated, this dual-simulation approach can be

https://doi.org/10.1021/acs.chemrev.5c00617
Chem. Rev. 2025, 125, 11878−12029

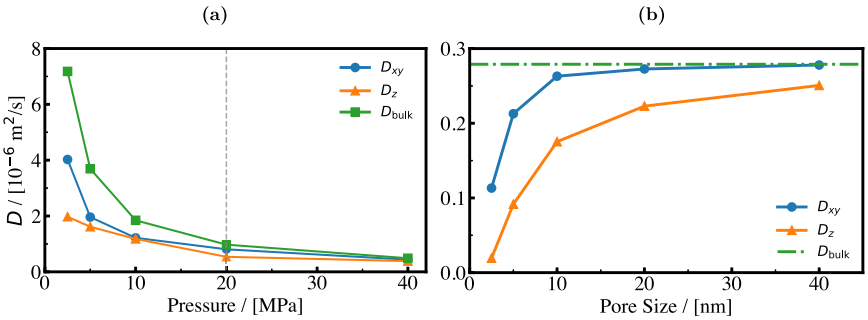

Figure 52. Self-diffusion coefficients of hydrogen in calcium silicate hydrate (C-S-H) pores computed with MD simulations. (a) Lateral (D_{xy}, blue circles), perpendicular (D_z, orange triangles), and bulk (D_{bulk}, green squares) diffusion coefficients as a function of pressure at a fixed pore size of 5 nm and temperature of 340 K. A vertical dashed line indicates 20 MPa, corresponding to the conditions in (b). (b) Lateral (D_{xy}, blue circles), perpendicular (D_z, orange triangles), and bulk (D_{bulk}, green dash-dotted line) diffusion coefficients versus pore size at a fixed pressure of 20 MPa and temperature of 340 K. All data in the plots are taken from Hubao et al.[907].

cumbersome since Langevin dynamics must be solved alongside MD for each spatial region, motivating later efforts toward simpler alternatives for evaluating perpendicular diffusivities.

Of relevance in this context is the work of Mercier Franco et al.,[911] who proposed an analytical alternative to the dual-simulation approach. In their method, the potential of mean force associated with regions of non-uniform density is linearized, allowing the anisotropic Smoluchowski equation to be solved analytically for the perpendicular diffusivity. In this framework, the perpendicular diffusivity is inversely proportional to the molecular residence time, defined as the time integral of the survival probability, within a given layer. Hence, layers where molecules remain trapped for longer times exhibit lower perpendicular diffusivities. The predicted diffusivities for water near the liquid-vapor interface agree closely with those obtained by Liu et al.,[914],validating the underlying approximation. This methodology was later extended by Spera et al.[915] to methane-ethane mixtures confined in calcite nanopores, where steep density gradients arise near the walls. Their study demonstrated that the perpendicular diffusivity in the first adsorbed layer is highly sensitive to the precise definition of the interfacial boundary, highlighting the importance of accurately identifying the starting point of the adsorbed layer. In all such cases, the perpendicular diffusivity remains consistently smaller than the corresponding parallel component. An alternative approach was proposed by Předota et al.,[916] who directly computed spatially resolved diffusivities from molecular dynamics trajectories by tracking mean-square displacements within bins parallel to the interface. To minimize artefacts from molecules crossing between bins, half of the squared displacement was apportioned to the initial and terminal bins, and diffusivities were extracted from the linear regime of the mean-square displacement over intermediate timescales. This pragmatic treatment yields well-behaved perpendicular diffusivities even in finite slab geometries and provides a numerically efficient alternative to dual-simulation or analytical methods.

The methodology proposed by Berne and colleagues (and modifications of this methodology) has successfully been applied in multiple contexts, including the diffusion of water confined within clay materials,[917−919] and more recently in H_2 storage studies. For instance, Bui et al.[895] used this method to computed water diffusion parallel to surfaces at various spatial locations, close to hydrophobic and hydrophilic surfaces, and within the bulk region. Among recent hydrogen diffusion studies, only Liu et al.[906] and Hubao et al.[907] explicitly considered diffusivities within distinct layers, while other studies[877−879,899,905,908−910] did not follow this layered approach.

Considering these insights, we proceed by examining how the wall-parallel (D_{xy} - lateral) and wall-normal (D_z - perpendicular) diffusivities vary with pressure and pore size. Initially, we focus on the results from Liu et al.,[906] since[906] do not explicitly address these diffusion dependencies. In Fig. 52(a), both D_{xy} and D_z decrease with increasing pressure, approaching D_{bulk}. This trend signifies reduced confinement effects at higher pressures, where H_2-H_2 collisions dominate over pore wall interactions. Under all conditions considered, D_{xy} remains significantly higher than D_z, clearly demonstrating anisotropic diffusion due to confinement by the nano-pore walls. At low pressures, diffusion within nano-pores strongly deviates from bulk values due to prominent wall interactions. H_2 molecules become adsorbed on the C-S-H surfaces, significantly restricting mobility, particularly perpendicular to the walls. With increasing pressure, the nano-pores become densely populated, and molecular collisions dominate diffusion behavior, diminishing confinement effects. Consequently, diffusivities (especially the lateral component - D_{xy}) approach bulk-phase values. Fig. 52(b) shows that at larger pore sizes (20−40 nm), D_{xy} approaches bulk values faster than D_z, indicating stronger confinement effects in the perpendicular direction. Overall, larger pore sizes enhance diffusion rates and reduce anisotropy. Liu et al.[906] reported similar anisotropic diffusion behavior in nanoporous montmorillonite, where lateral mobility closely matches bulk-phase diffusion even near surfaces, while perpendicular diffusion is significantly hindered due to confinement and boundary interactions. Lastly, as emphasized by Ghasemi et al.,[910] it is essential to account for hydrodynamic finite-size corrections when evaluating self-diffusivities in confined environments,[499] a point initially highlighted by Rotenberg and colleagues.[920] Among the reviewed studies, only Ghasemi et al.[910] explicitly considered these corrections, reporting a mere 2% impact of confinement on H_2 self-diffusivities. We conclude by urging future studies to consider both anisotropic diffusivities and finite-size hydrodynamic effects when reporting self- or mutual diffusivities of H_2 mixtures under confinement.

4.7.4. Hydrogen Intercalation and Leakage in Geological Nanopores. The behavior of H_2 within geological nano-pores is highly affected by two complementary but

https://doi.org/10.1021/acs.chemrev.5c00617
Chem. Rev. 2025, 125, 11878−12029

distinct phenomena: (1) intercalation of H_2 into hydrated clay nano-pores, and (2) H_2 leakage through nano-pore defects and cracks. While intercalation studies primarily explore how H_2 molecules enter and remain within clay layers, leakage studies focus on identifying mechanisms by which H_2 may escape from these geological barriers. In this section, we first address recent advances in the energetics and molecular interactions governing H_2 intercalation, followed by a discussion of factors influencing H_2 leakage from nanoporous caprocks.

Ho et al.[921] investigated H_2 intercalation mechanisms in hydrated montmorillonite clay, relevant to H_2 geological storage. Using meta-dynamics/MD simulations, the authors showed that dissolving H_2 in bulk water is highly unfavorable (2.3 kcal/mol). Within clay interlayers (with spacings of 12.5 Å and 15 Å), H_2 intercalation remains thermodynamically challenging, though slightly less so in hydrophobic regions near siloxane ring centers due to their lower local charge density. In contrast, regions with higher charge density from isomorphic substitutions (e.g., Mg replacing Al) and interlayer cations strongly repel H_2 intercalation. Compared to H_2, CO_2 demonstrated significantly more favorable energetics, indicating that the limited polarizability and quadrupole moment of H_2 severely restricts its interactions within these environments. Muther and Dahaghi[922] extended this analysis by studying H_2 intercalation in hydrated sodium montmorillonite (Na-MMT) clay under realistic geological conditions (1−50 MPa, 298−403 K). They observed similarly low H_2 intercalation mole fractions (approximately 1.569×10^{-6} to 0.0119), attributed to the limited solubility of H_2 in water, and its weak interactions with clay surfaces. Crucially, intercalation is significantly influenced by the hydration state, with increased uptake generally occurring during the transition from monolayer (1W, ∼12.5 Å) to bilayer hydration (2W, ∼15.5 Å), although slight decreases may result from water filling interlayer spaces. Competitive adsorption with CO_2 and CH_4 further reduces H_2 uptake (by ca. 32% and 52%, respectively), highlighting complex interactions among gases that limit H_2 storage potential but simultaneously mitigate risks to caprock integrity.

Li et al.[329] studied H_2 leakage through nano-cracks in kaolinite caprocks using MD simulations. The focus was on H_2 near hydrophilic gibbsite and hydrophobic siloxane surfaces at 333.15 K and 30 MPa, varying water content and cushion gas compositions. On gibbsite surfaces, increasing water content significantly reduces H_2 leakage—from nearly complete leakage at low water content to below 5% when water is sufficient to form dense adsorption layers. On siloxane surfaces, water distribution is less uniform, leading to variable H_2 retention efficiency. For CO_2, stronger adsorption in gibbsite and kaolinite aquifers enhances its collaboration with H_2O to effectively block cracks. For CH_4, while it helps plug H_2 leakage on hydrophilic gibbsite by hindering entry, its role is minimal on siloxane surfaces, where the non-uniform distribution of H_2O governs leakage control. These findings emphasize surface chemistry, water content, and gas composition as critical factors for leakage prevention. Liu et al.[923] further explored H_2 leakage through nanoporous shale caprock using MD and MC simulations. The authors highlighted that H_2, due to the small molecular size (less than 1 Å), easily leaks through nano-pores, whereas larger molecules such as CH_4 create stable adsorption layers, reducing H_2 contact with rock surfaces. Water further reinforces caprock integrity by forming clusters through H_2 bonding, enhancing the sealing effect in combination with CH_4. Leakage increases with pore size, significantly intensifying beyond approximately 10.5 Å. Higher pressures accelerate leakage through distinct stages of blockage, partial penetration, and eventual breakthrough. Additionally, elevated temperatures weaken water clusters by disrupting H_2 bonds, thereby increasing H_2 leakage. This study underscores the critical interplay between pore geometry, surface chemistry, and environmental conditions in governing H_2 leakage dynamics.

In summary, these studies collectively illuminate the complexities underlying H_2 behavior in nanoporous geological formations. The low affinity of H_2 for water and clay surfaces poses intrinsic barriers to efficient intercalation, while nanopore surface chemistry, water content, gas composition, and operating conditions decisively influence leakage pathways. These insights from molecular simulations can significantly contribute to strategies for safer and more efficient UHS.

4.8. Hydrogen in Pure and Mixed Hydrates

4.8.1. Hydrate−Liquid−Vapor Three-Phase Equilibria of Aqueous Hydrogen Solutions. Frankcombe and Kroes[934] performed MD simulations using 2D, sII clathrate hydrate slabs with an occupancy equal to (1S + 4L) H_2, in contact with a slab of H_2 gas at a pressure of 1500 bar. The authors used different water force fields (SPC/E, TIP3P, TIP4P, TIP4P/2005, TIP4P/Ice, and TIP5P) to compare the predicted stability of the H_2 hydrate in the simulation with the respective experimental data, and concluded that TIP5P yielded the best temperature−pressure stability prediction for the hydrate, predicting a decomposition temperature in the range 245−265 K. It should be noted, however, that this conclusion was the result of a single MD simulation, instead of using multiple replicas as discussed in detail in refs 369 and 578.

The first attempt to calculate the three-phase ($H-L_w-V$) equilibria (see Fig. 8 for notation) for the binary H_2 − water system using the "direct phase coexistence" approach was reported by Luis et al.[935] The authors used TIP4P/Ice and the H_2 force filed proposed by Alavi et al.[336] (see details in Section 3.1), and reported predictions that were underestimating the three-phase equilibrium temperature by ca. 16−20 K. In a subsequent study, Luis et al.[936] examined the effects of externally-applied static electric fields on the stability of H_2 hydrates. The authors concluded that hydrate crystallization is prevented with a certain magnitude of electrical field, which depends on the pressure of the system. Namely, as the pressure increases, an electrical field of lower intensity is needed to inhibit crystallization.

Michalis et al.[342] performed simulations with a modified "direct phase coexistence" approach and reported a significant improvement (i.e., by 10.5 K) in the calculation of the three-phase equilibria temperatures for the pressure range 100−300 MPa compared to the earlier study of Luis et al.[935] The improvement was the direct result of implementing two modifications in the treatment of the H_2 force-field. Namely, (i) the use of H_2 LJ parameters that are a function of temperature, and (ii) the water−H_2 guest energy interaction parameters were optimized further by using the Lorentz-Berthelot combining rules, accounting for the improved description of the solubility of H_2 in water (i.e., Eq. (8) discussed in Section 3.1.1). While the simulations by Michalis et al.[342] currently provide the most accurate description of the $H-L_w-V$ equilibrium temperature for the binary H_2 − water system, using the "direct phase coexistence" approach, there is

https://doi.org/10.1021/acs.chemrev.5c00617
Chem. Rev. 2025, 125, 11878−12029

still room for improvements. In particular, there is still an under-prediction of the three-phase equilibrium temperature of the pure H_2 hydrate by a ΔT that is higher than the value of 3.35 K, that the TIP4P/Ice water model under-predicts the melting point of ice I_h. This is clearly shown in Fig. 53 which is

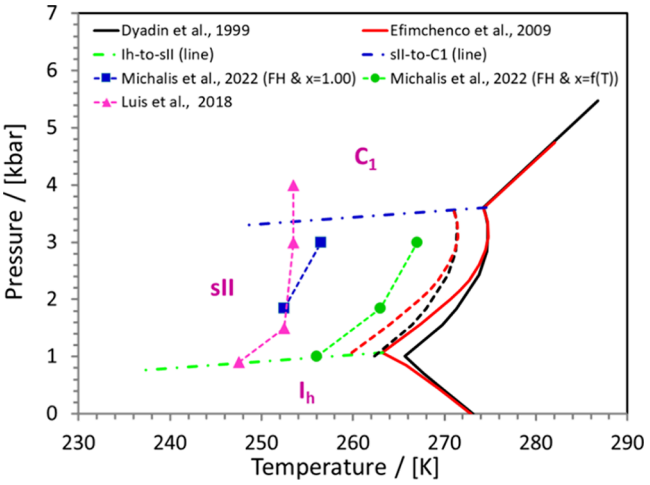

Figure 53. Experimental values (denoted with lines) and MD data from Michalis et al.[342] [blue squares: Feynman–Hibbs (FH) and χ = 1.00; green circles: FH and $\chi = f(T)$] and from Luis et al.[935] (magenta triangles) for the three-phase coexistence temperature of the hydrogen hydrate system. The two dashed lines denote the MD-expected phase equilibrium lines corresponding to the experimental data of Dyadin et al.[244] (black line) and Efimchenko et al.[937] (red line). The MD-expected values presented in the figure are defined as $T_{Eq,expected} = T_{Eq,exp} - 3.35$ K, where $T_{Eq,exp}$ is the experimental three-phase equilibrium temperature. Data extracted from ref 342.

constructed with data from ref 342. Another important observation made by Michalis et al.[342], that needs future experimental/computational investigation, is the reported discrepancy between the experimental data for the three-phase equilibrium conditions for the binary H_2 – water system of Dyadin et al.[244] and Efimchenko et al.,[937] especially at temperatures lower than 268 K (see Fig. 53).

Kang et al.[938] used the "phase coexistence" approach to calculate the three phase equilibria for the mixed H_2 + THF (5.56 mole% THF) hydrate at 100, 250, and 400 bar. The authors considered two different cases for the LJ parameters between the centers of the mass of H_2 and the oxygen of H_2O. Namely, the first case used LJ parameters based on ab initio calculations, while the second used the classical Lorentz-Berthelot mixing rule. As shown in Fig. 54 the ab initio-based parameters produce better agreement with the experimental measurements.

4.8.2. Kinetics of Hydrate Growth/Decomposition. Zhang et al.[594] studied the growth of mixed H_2 + CH_4 hydrate with MD simulations, motivated by the high energy density of the particular gas mixture. The authors reported that the growth mechanism of the mixed hydrate is controlled by the solubility and diffusivity of the guest molecules. The complex interplay of diffusivity and solubility with the increasing temperature results in a growth rate and cage occupancy maximum at 250 K and a pressure equal to 50 MPa. Therefore, by an appropriate selection of P, T conditions certain storage capacities can be achieved. In a similar study Tian and Zhang[595] studied the mixed H_2 + THF hydrate with MD simulations and reported growth rates at (i) 50 MPa and

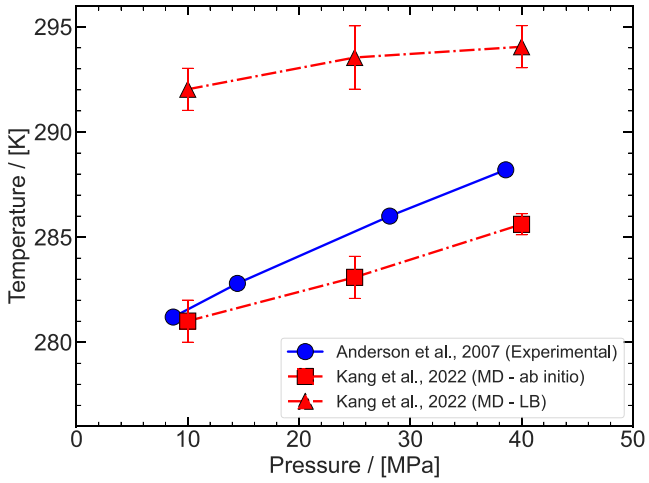

Figure 54. Phase equilibria (H–L_w – V) of H_2 + THF hydrates. Blue circles denote experimental measurements (5.56 mole% THF) by Anderson et al.[939] Red symbols denote the MD "phase coexistence" simulation values of Kang et al.[938] Lines connecting the symbols are guides to the eye only.

temperatures in the range 230–270 K, and (ii) at 250 K and pressures in the range 20–110 MPa, reporting a maximum cage occupancy maximum at 260 K and a pressure equal to 50 MPa. The computed H_2 storage capacity was shown to be correlated with the trend of the growth rate. Fig. 55a shows the hydrate growth rates computed with MD as a function of T (at P = 50 MPa), while Fig. 55b shows the calculated hydrate growth rates as a function of P (at T = 250 K) for the cases of H_2 + CH_4 (Zhang et al.[594]) and H_2 + THF (Tian and Zhang[595]) mixed hydrates. Tian and Zhang[595] observed that in MD simulations at 50 MPa, the mixed H_2 + THF hydrate growth rates exhibit a maximum at 260 K, which is close to the temperature conditions of the maximum growth rates of pure THF hydrate. For temperatures above 260 K, a dramatic decrease is observed in the growth rate (see Fig. 55a). Notice that for the case of H_2 + CH_4 the maximum is obtained at 250 K. Contrary, as shown in Fig. 55b, a practically negligible dependence on pressure is observed (for constant T = 250 K) for the growth rates of the mixed H_2 + THF hydrate. However, for the case of H_2 + CH_4, Zhang et al.[594] reported an increase of almost 300% in the growth rate for the pressure range 20–110 MPa.

While the studies of Zhang et al.[594] and Tian and Zhang[595] reported hydrate growth rates in units of[nm^{-2} ns^{-1}], other MD studies report growth rates in units of [cages/ns]. Such are the studies by Kang et al.[938] for H_2 + THF mixed hydrate, and Hu et al.[940] for H_2 + CH_4 mixed hydrate. The combined results of the two studies are shown in Fig. 56, where the hydrate growth rate is plotted as a function of the THF (or CH_4) concentration in units of [mol%]. From Fig. 56 it becomes evident that as the concentration of THF (or CH_4) increases towards the stoichiometric value, hydrate formation rate decreases in both cases of mixed hydrates. Furthermore, similar to the conclusion reported by Tian and Zhang,[595] a negligible effect of pressure on the growth rate can be seen in the MD simulations of Kang et al.,[938] for the case of H_2 + THF mixed hydrates.

Ghaani and English[941] performed both equilibrium and non-equilibrium MD simulations to study thermal-driven decomposition of mixed H_2 + propane planar clathrate crystals with

https://doi.org/10.1021/acs.chemrev.5c00617
Chem. Rev. 2025, 125, 11878–12029

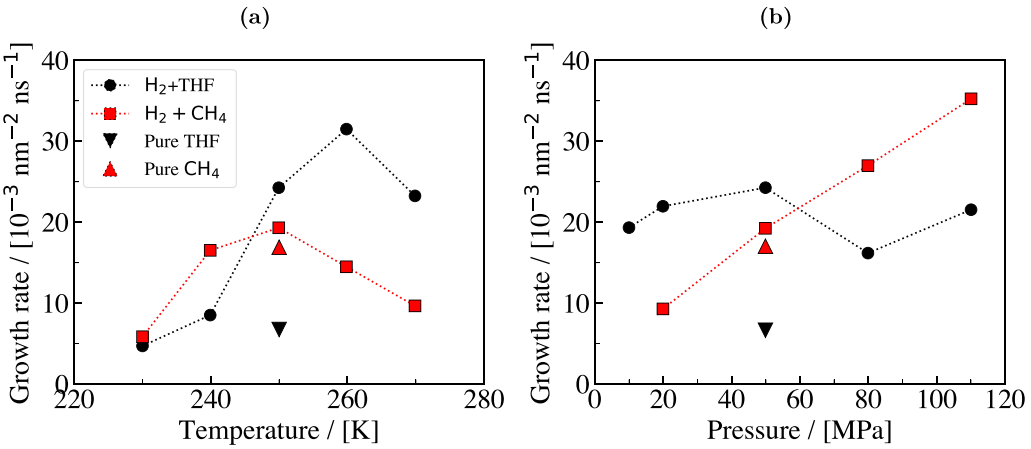

Figure 55. Comparison of computed growth rates of H_2 + THF (black symbols − Tian and Zhang[595]) and H_2 + CH_4 (red symbols − Zhang et al.[594]) binary hydrates: (a) growth rate as a function of temperature at 50 MPa and (b) growth rate as a function of pressure at 250 K. The triangles represent the growth rates of pure THF and CH_4 hydrates, respectively. Lines are drawn to guide the eye. The data are taken from ref 595.

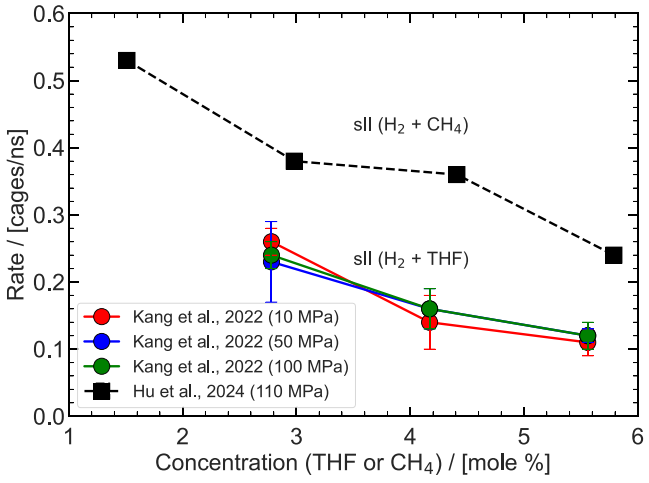

Figure 56. Hydrate growth rate as a function of THF (or CH_4) concentartion. Comparison of growth rates of H_2 + THF (red symbols − Kang et al.[938]) and H_2 + CH_4 (green symbols − Hu et al.[940]) binary hydrates computed with MD simulations. Lines are drawn to guide eye.

liquid water at 260−320 K. The authors concluded that the different surface-cavity terminations result in substantial differences in initial break-up rates. In a subsequent study, Ghaani et al.[942] used non-equilibrium MD simulations to study the H_2 release and uptake from/into propane planar clathrate surfaces a temperatures ranging from 180 to 273 K.[943] reported experimental measurements and MD simulations of the mixed sII H_2 + propane hydrate dissociation by heating or depressurization, and concluded that (i) H_2 release from the hydrate crystal was much faster than that of propane, with experiments and simulations being in agreement, and (ii) simulations showed that hydrate dissociation induced by depressurization was slower than the case induced by heating, an observation which contradicts the experimental measurements reported in the same study. The authors tracked the number of H_2 and propane molecules in the aqueous and hydrate phases. Only complete cages were considered for the counting of H_2 and propane molecules in the hydrate crystal. They also tracked the number of hydrogen bonds and the potential energy. The number of hydrogen bonds was closely associated with the degree of crystallization of water molecules, reflecting, thus, the kinetics of hydrate dissociation.

4.8.3. Structural and Other Properties of Hydrates. Wang et al.[180] combined QM calculations with classical MD to compute average structure and vibrational spectra of H_2 in pure sII H_2 clathrate. The authors reported that the H_2 molecules in the L cages and the singly-occupied S cages are stretched, and the vibrational mode is softened and uncoupled. Contrary, in the case of doubly-occupied S cages, the H_2 molecules were shown to be slightly compressed, with the vibrational frequencies being close or above that of the free gas. Furthermore, a strong vibrational coupling was observed as a result of the short intermolecular distance between the two H_2 in the S cages.

Gorman et al.[944] performed MD simulations to investigate the dynamical and energy-related properties in sII pure H_2 and mixed H_2 + THF hydrates at 30 and 200 K (also at intermediate temperatures) and 0.05 kbar, using SPC/E and TIP4P/2005 water models. The study ignored the quantum effects which are expected to be important at temperatures below 150 K. Mondal et al.[334] performed MD simulations to calculate binding energies and radial distribution functions for various cases of occupancies of the sI pure H_2 hydrate, using the SPC/E water model. By observing the radial distribution functions of H_2 loaded hydrates, the authors concluded that within the time-scale considered (200 fs), the H_2 hydrate cages are not ruptured. In a later study,[945] also performed MD simulations on structure and dynamics of high-pressure ices and filled ices, using TIP4P and TIP5P water models. This study focused on the rotational motions of both H_2O and H_2 molecules in the filled-ice C_2 in addition to those in ice VII.

Rick and Freeman[364] used three water models (SPC/E, TIP4P/Ice, and TIP4P-FQ/Ice) to predict dielectric constants, the proton order parameters, and the molecular volumes for pure Ar and H_2 clathrate systems. The conclusion provided was that the dielectric response arises only from the water molecules as a result of the fact that the guest molecules do not have a dipole moment. English et al.[946] performed equilibrium MD simulations to investigate thermal conduction mechanisms via the GK approach (see Section 3.2.1) for sII pure H_2 hydrate, at 0.05 kbar and temperatures in the range 30−250 K. The authors considered the TIP4P water model, and assumed single or double occupancy of the 5^{12} cages and quadruple

https://doi.org/10.1021/acs.chemrev.5c00617
Chem. Rev. 2025, 125, 11878−12029

occupancy of the $5^{12}6^4$ cages. Consistent with prior literature, in this study it was pointed out that for temperatures of ca. 150 K and below, it is expected that classical MD will not accurately capture the quantum nature of H_2 motion. Zhao et al.[947] performed MD simulation, as well as DFT and AIMD simulations, of spontaneous formation of quasi-one-dimensional (Q1D) H_2 gas hydrates within single-walled carbon nanotubes (SW-CNTs) of nanometer-sized diameter (1−1.3 nm) occurring at near ambient temperature. It was observed that the guest H_2 molecules in the Q1D hydrates are contained within a 1D nanochannel in which the H_2 molecules form a molecule wire, while in conventional H_2 hydrates the guest H_2 molecules are contained in individual 3D cages.

4.8.4. Hydrate Storage Capacities from Molecular Dynamics Simulations. The pioneering work of Alavi et al.[336] was the first one to report anisotropic *NPT* MD simulations of pure sII H_2 hydrates with flexible cages and periodic boundary conditions. H_2 molecules were modeled using the potential developed within this study (see details in Section 3.1.1), while SPC/E force field was used for water. Water molecules of the hydrate lattice were allowed to move about their equilibrium positions. Simulations were performed at 1.013 and 2.5 kbar, temperatures in the range of 100−250 K, and for various H_2 occupancies in each cage type, ranging from (1L + 0S) to (4L + 2S). Alavi et al. showed that the energy per unit cell for each H_2 occupancy makes a large "jump" when going from the single to the double occupancy of the S cage. This was interpreted as a strong indication that the double occupancy in the S cages would not be stable. A subsequent study[343] using MD (*NPT*) simulations of pure sII H_2 hydrates with the SPC/E water model, and a H_2/D_2 potential parameterised to account for QM effects of H_2 motion at low temperatures, resulted in similar conclusions regarding the H_2 occupancies in the L and S cages.

Alavi et al.[948] extended their previous study of pure H_2 hydrates[336] to binary, THF + H_2 sII hydrates to study the energetics of the occupancy of the H_2 guests in the S and L cages, and again reached to similar conclusions regarding the cage occupancies. Furthermore, the simulations revealed that replacing a THF molecule in the L cages of the unit cell by a cluster of four H_2 molecules is accompanied by an increase in unit cell total potential energy and volume. The authors examined the possibility of observing the tuning effect, discussed earlier,[247] and concluded, based on MD data, that the formation of binary THF + H_2 sII hydrates with large fractions of the L cages occupied by the H_2 molecules is not likely to occur if large concentrations of THF are present in the initial hydrate-forming aqueous solution. Such an observation is consistent with MC simulations and experimental studies (e.g., see the detailed discussion in refs 177 and 248). Alavi et al.[949] also performed classical MD simulations for the case of the binary sH methyl-tert-butylether + H_2 clathrate hydrate, and similarly to prior literature,[336,343,948] it was observed that the double H_2 occupancy of the small (S) and medium (M) cages of the sH hydrate leads to a large increase in energy of the unit cell compared to the single H_2 occupancies of these cages.

Daschbach et al.[950] performed MD simulations in order to investigate H_2 storage in β-hydroquinone clathrate and showed that higher storage capacities are obtained at lower temperatures. Zhang et al.[594] studied the mixed sII H_2 + CH_4 hydrate with MD simulations, and reported cage occupancies at (i) 50 MPa and temperatures in the range 230−270 K, and (ii) at 250 K and pressures in the range 20−110 MPa. The findings were single H_2 cage occupancies for the case of 5^{12} cages, while up to triple H_2 occupancies for the case of $5^{12}6^4$ cages. In particular, the simulations indicated that the 5^{12} cages are occupied by either single H_2 or single CH_4 molecules, while the $5^{12}6^4$ cages are occupied by either single CH_4 or single or double or triple H_2 molecules. Note, however that the authors also mentioned the existence of $5^{12}6^4$ cages with simultaneous occupancy of H_2 and CH_4, encountered especially at high temperatures and pressures. The importance of this issue will be further discussed in Section 4.8.8. In similar studies, Tian and Zhang[595] and Kang et al.[938] studied the mixed sII H_2 + THF hydrate with MD simulations, focusing on occupancies at similar temperature and pressure ranges as in ref 594. The observations regarding the cages H_2 occupancy were consistent with the prior studies. Wang et al.[951] performed MD simulations to explore the H_2 storage capacity of the mixed sH H_2 + methylcyclohexane (MCH) hydrate at 240−260 K and 70−110 MPa. A H_2 storage capacity in the range 0.5 to 1.0 wt.% at pressures between 70−110 MPa and temperatures 250 or 260 K was reported, while the storage capacity increased to 1.6−2.0 wt.% at 240 K at the same pressure range. The authors also indicated that the 5^{12} cages at the hydrate crystal boundary can prevent the diffusion of H_2 inside the hydrate crystal phase.

The collective behavior of storage capacities of the three mixed hydrates (i.e., H_2 + CH_4; H_2 + THF; and H_2 + MCH) predicted from MD simulations as a function of pressure/temperature is shown in Fig. 57 and Fig. 58, respectively. As

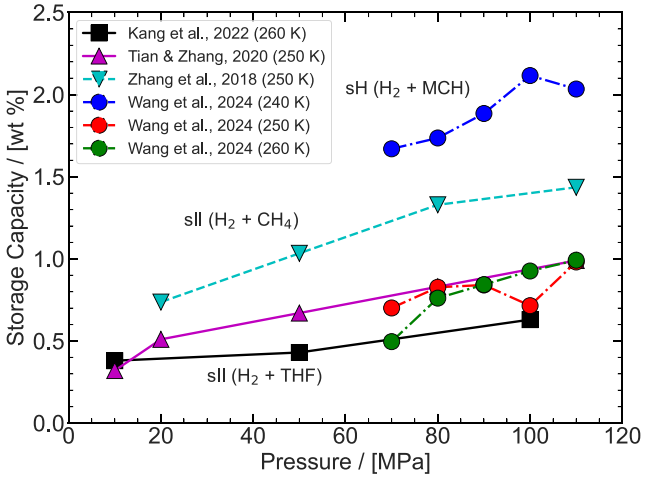

Figure 57. Hydrogen content (storage capacity in wt%) as a function of pressure for various temperatures and mixed hydrate systems (at stoichiometric promoter composition): (i) sII H_2 + CH_4 (Zhang et al.[594] − green triangles), (ii) sII H_2 + THF (Kang et al.[938] − red circles; Tian and Zhang[595] − red triangles), and (iii) sH H_2 + MCH (Wang et al.[951] − blue symbols). Lines connecting the symbols are to guide the eye.

can be observed from Fig. 57, at a fixed temperature, the storage capacity increases with pressure. In contrast, at a fixed pressure, higher storage capacities occur for the lower temperatures. Among the mixed hydrates considered, the hydrate with the highest storage capacity is the mixed sH H_2 + MCH, resulting from the increased amount of H_2 diffusing into the 5^{12} and $4^35^66^3$. Such behavior for the storage capacity will be further discussed in Section 4.8.5, where storage capacities computed via MC simulations are considered. Similar

https://doi.org/10.1021/acs.chemrev.5c00617
Chem. Rev. 2025, 125, 11878−12029

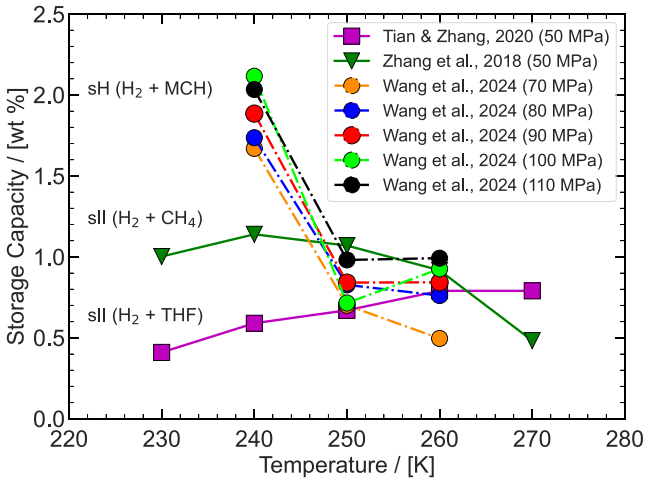

Figure 58. H_2 content (storage capacity) as a function of temperature for various pressures and mixed hydrate systems (at stoichiometric promoter composition): (i) sII H_2 + CH_4 (Zhang et al.[594] – green triangles), (ii) sII H_2 + THF (Tian and Zhang[595] – red circles), and (iii) sH H_2 + MCH (Wang et al.[951] – blue symbols). Lines connecting the symbols are to guide the eye.

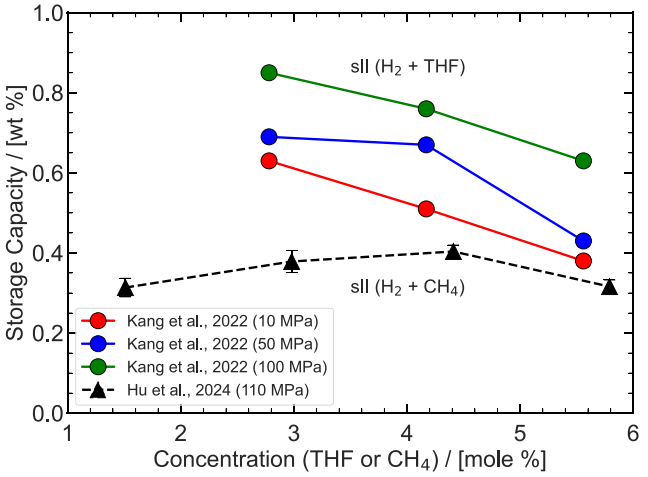

Figure 59. H_2 content (storage capacity) as a function of promoter concentration: (i) sII H_2 + CH_4 (Hu et al.[940] – green squares), (ii) sII H_2 + THF (Kang et al.[938] – red symbols). Lines connecting the symbols are to guide the eye.

conclusions can be drawn from Fig. 58. A notable exception, however, is the study of Tian and Zhang[595] for the mixed hydrate H_2 + THF, where it shown that at 50 MPa, the storage capacity increases as the temperature increases as a result of the tuning effect (i.e., the THF concentration is lower than the stoichiometric one (5.56 THF mol%)). The hydrate tuning effect has been a controversial issue, extensively discussed in the literature (see the reviews by Tsimpanogiannis and Economou[240] and Alavi and Ripmeester[177] for more details on experimental and MC studies). Only limited work has been reported using MD simulations.

Hu et al.[940] studied the mixed H_2 + CH_4 hydrate with MD simulations, and reported the effect of the promoter (i.e., CH_4) concentration on the H_2 cage occupancies. Five types of cage occupancies for H_2 molecules were observed in the MD simulations, namely: (i) single H_2, (ii) single H_2 – single CH_4, (iii) double H_2, (iv) double H_2 – single CH_4, and (v) triple H_2. The 5^{12} cage can only be occupied by a single H_2, while for the $5^{12}6^4$ cage all five of the the above situations can occur. There was no strong tuning effect observed in their study. Kang et al.[938] performed MD simulations for the mixed H_2 + THF hydrate, and explored the effect of the promoter (i.e., THF) concentration on the H_2 cage occupancies. In this study, tuning effect was clearly identified. Fig. 59 shows the H_2 storage capacity of two sII mixed hydrates as a function of the promoter concentration for the two aforementioned studies. Notably, Wang et al.[951] could not identify any tuning behavior for the mixed sH H_2 + MCH hydrate.

As pointed out in the review article by Alavi and Ripmeester[177], a consensus is developing based on experimental, classical MD, and MC studies, indicating that in either pure or mixed H_2 hydrates (sI, sII, sH) the stable hydrate occupancy configuration is the one with a single H_2 molecule in the S cages (or M cage of sH hydrates), while multiple occupancies are possible for the L cages. It should be mentioned that DFT studies (e.g., see discussion in[177]) have reported occupancies higher than classical MD or MC simulations, however, a thorough discussion on this discrepancy is beyond the scope of our review.

4.8.5. Hydrate Storage Capacities from Monte Carlo Simulations. For a clathrate hydrate structure to be used as a gas-storage material, the number of guest gas molecules enclathrated inside each cavity becomes a critical factor that determines the total storage capacity of the specific hydrate structure. If quadruple occupancy of the L ($5^{12}6^4$) cavities and double occupancy of the S (5^{12}) cavities[171] is assmumed, the storage capacity of sII H_2 hydrate is 5.0 wt.%. Contrary, the storage capacity drops to 3.8 wt.% H_2 if single occupancy of the S cavities is assumed while retaining the quadruple occupancy of the L cavities.[952] The multiple occupancy of a single cavity can significantly increase the storage capacity of the particular hydrate structure. Therefore, it is essential to know how the cavity occupancies evolve as a function of temperature, pressure and the possible presence of other co-guests (promoters or inhibitors) to accurately calculate the storage capacity of different clathrate hydrate structures. To this purpose, GCMC simulations have been proven to be a valuable tool.

The first study to report GCMC simulations of the pure sII H_2 hydrate was by Katsumasa et al.[953] Subsequently, Papadimitriou et al.[634] examined the cases of (i) pure sII H_2 hydrate, and (ii) the binary sII H_2 + THF hydrate, Chun and Lee[954] considered the binary sII H_2 + THF hydrate, and Nakayama et al.[955,956] (using the TIP5P water model) studied binary sII H_2 + acetone hydrate. These MC studies computationally proved the single occupancy of the 5^{12} cages of structure sII, which is in good agreement with subsequent experimental measurements. For a detailed discussion on this subject, the reader is referred to ref 248. It should be noted though, that the GCMC simulations by Koh et al.[957] showed the opposite, i.e., double occupancy in the small cages.

Tanaka and co-workers, extended their previous work on H_2 storage in hydrates to various ices (I_c, II), as well.[958,959] After establishing the possibility of forming sII H_2 hydrates, other hydrate structures were examined as well. Duarte et al.[960] reported experiments of sH H_2 hydrate formation in the presence of methylcyclohexane (MCH), 1,1-dimethylcyclohexane (DMCH) and methyl tert-butyl ether (MTBE), followed by GCMC simulations of sH H_2 hydrate with MCH as promoter.[635] Subsequently, sI H_2 hydrates with promoter

https://doi.org/10.1021/acs.chemrev.5c00617
Chem. Rev. 2025, 125, 11878–12029

(ethylene oxide) were studied via means of GCMC simulations in ref 636. Both these GCMC studies, also considered the hypothetical pure sH and sI H_2 hydrates, since they constitute the upper limiting case for the storage capacities of the two particular hydrate structures. Pure sI H_2 hydrate was subsequently experimentally synthesized,[961] thus, confirming the hypothesis of Papadimitriou et al.[636] regarding the existence of the pure sI H_2 hydrate.

Papadimitriou et al.[962] presented an overview and a detailed discussion of the three common H_2 hydrate structures considered in the earlier studies. The case of pure H_2 hydrates was later revisited in a series of GCMC studies.[248,341,640] In these studies, an elaborate and self-consistent MC-based approach was used to relate the chemical potential of the guest with the pressure of the system (see more details about this method in Section 3.3.3). This is important, since earlier studies had used a much simpler approach for the calculation of the chemical potential, based on the use of general-purpose[634−636] or component-specific[638] EoS.

A systematic study and quantification of the effect of the lattice constant of sII H_2 hydrate on the storage capacity of the particular hydrate structure was reported in ref 341 while preliminary results following a simpler approach were presented in ref 634. Both studies were motivated by experimental observations[957] indicating that the presence of different promoters in the binary "H_2 + Promoter" results in sII hydrates with differences in the lattice constant in the range 0.60 − 3.24% comparing to the value (1.7047 nm)[171] of the sII pure H_2 hydrate. The increase in the lattice constant can result in an increase in the H_2 storage capacity by up to 3% when compared to the base case.

The effect of three water force fields (i.e., SPC/E, TIP4P/Ice, and TIP5P) on the computed storage capacities of the three most common pure H_2 hydrates (i.e., sI, sII, and sH) was reported in ref 248. It should be noted that this study did not reveal a significant effect of the different force fields on the cage occupancies and the corresponding storage capacities (i.e., less than 5% differences were reported). In this context, the use of SPC/E for water and the single-site FH effective potential (see Eq. (7) in Section 3.1.1) for H_2 was recommended for the use in GCMC simulations in order to calculate storage capacities. This conclusion is in contrast to the findings of MD simulations studies,[369,578] where it was shown that to accurately calculate the three-phase equilibria conditions, using a water model that can accurately predict the melting point of hexagonal ice, I_h, is essential. Therefore, the use of TIP4P/Ice was proposed in these studies. In a related context, Brumby et al.[633] performed MC simulations in the GE that are in good agreement with the results reported in ref 248.

Currently, there seems to be consensus between the various MC simulation studies regarding the occupancy of the small cavities of the three most common hydrates structures. These cavities are singly occupied and cannot accommodate more than one H_2 molecules even at the highest pressures examined (e.g., 500 MPa). Contrary, the large cavities of the sI, sII, and sH hydrates, may contain up to 2.3, 3.8, and 6.7 H_2 molecules, respectively. The deviation between the water models regarding these occupancy values is less than 4%.

A detailed comparison of the experimental[939,963−965] H_2 storage capacities in binary H_2+THF hydrates with earlier MC simulations[634,954] is shown in Fig. 60, along with a special modification[966] of the classical van der Waals−Platteeuw theory. Using the latter, one is capable of performing

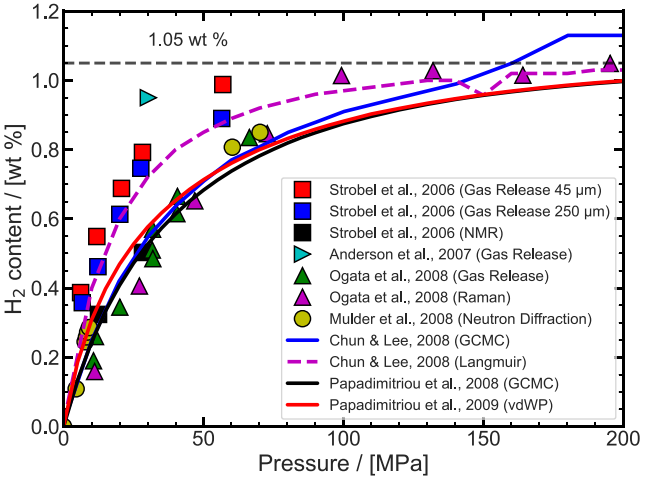

Figure 60. Hydrogen content as a function of pressure for the sII binary H_2 + THF hydrate. Comparison between: (i) experimental measurements (Strobel et al.;[963] Anderson et al.;[939] Ogata et al.;[964] Mulder et al.[965]), (ii) GCMC simulations (Chun and Lee[954], Papadimitriou et al.[634]), and (iii) the modified van der Waals−Platteeuw (vdWP) theory, proposed by Papadimitriou et al.[966] The horizontal black dashed line (at 1.05 wt.%) denotes the case where all small cavities (i.e., 100% occupancy) are occupied by a single H_2 molecule.

calculations at the limit of the 100% occupancy of cages for water-soluble promoters (such as THF). At this limit thermodynamic models based on the classical van der Waals−Platteeuw theory fail to provide any results.

An extensive comparison with results from updated MC simulation studies[248] and additional experimental measurement[967−971] was presented by Papadimitriou et al.[248] for the case of binary H_2 sII hydrates. This study presented comparisons under isothermal (i.e., 268, 274, and 278 K) conditions. Fig. 61 shows the data reported in ref 248 along with the corresponding comparison for the 255 K isotherm, using experimental data from Sugahara et al.[972,973] and Kawamura et al.[974] The GCMC results of Papadimitriou et al.[248] were later used by Tsimpanogiannis et al.[975] to develop engineering−type correlations for the H_2 storage capacity of the three most common hydrate structures. In principle, the considered methodology could be used to examine storage in hydrates with various promoters, using the assumption that there is no change in the lattice constant resulting from the use of different promoters. This is a reasonable assumption based on the conclusions of Papadimitriou et al.,[341] discussed earlier. This assumption could be relaxed in future studies, nevertheless, it would require a significant number of additional MC simulations to be performed to account for the change in the lattice constant of the hydrate crystals resulting from the use of different promoters.

A general observation we can make from all the GCMC simulation studies reviewed here is that the US DOE specifications regarding the H_2 storage capacity of pure H_2 hydrates are not met when considering mobility/vehicular applications.[192,197] Namely, the storage capacity is expected to be lower than 4 wt.%. Even lower storage capacities (i.e., less than 2 wt.%) are expected for the cases of mixed H_2 + promoter hydrates. However, there is still significant scientific interest on H_2 storage in clathrate hydrates for stationary applications.

https://doi.org/10.1021/acs.chemrev.5c00617
Chem. Rev. 2025, 125, 11878−12029

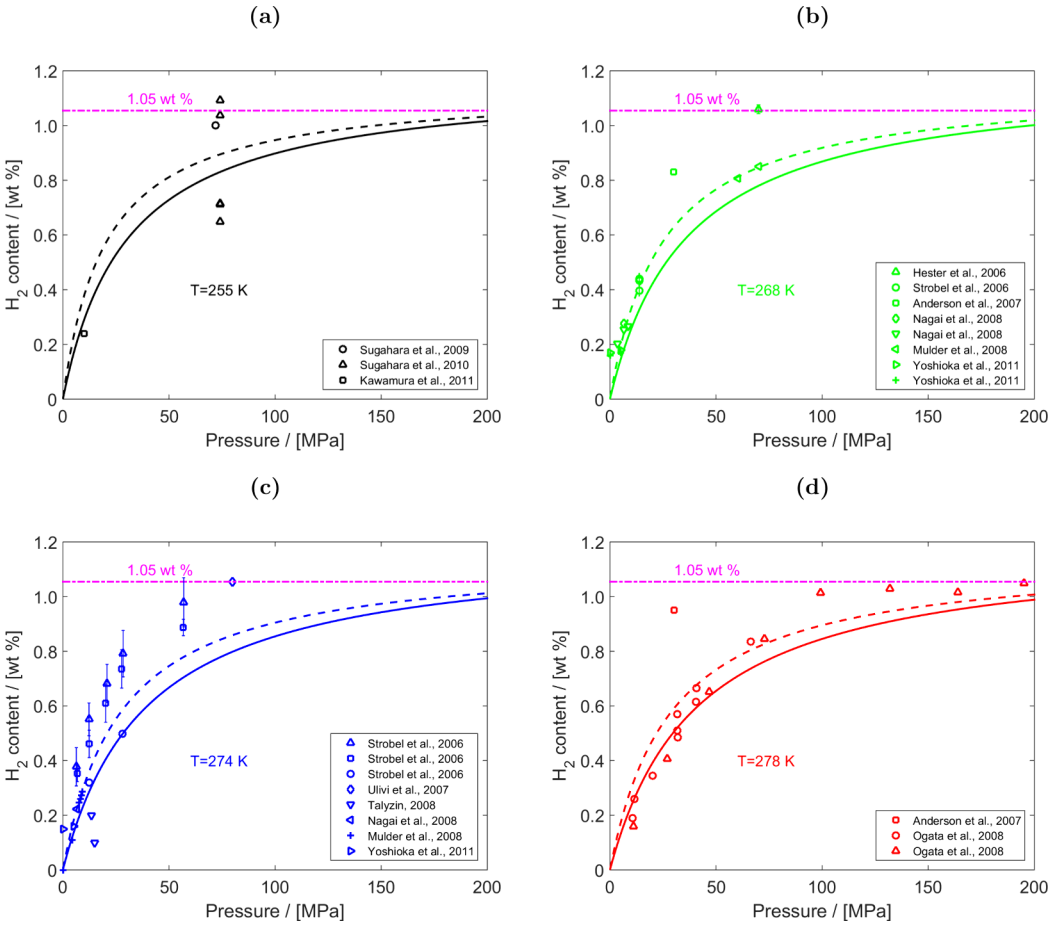

Figure 61. Hydrogen content (wt.%) as a function of pressure for the sII binary hydrate H_2 + THF using the Silvera−Goldman H_2 force field. Comparison between experimental measurements, denoted with symbols (Strobel et al.;[963] Anderson et al.;[939] Ogata et al.;[964] Mulder et al.;[965] Hester et al.;[967] Nagai et al.;[968] Yoshioka et al.;[969] Ulivi et al.;[970] Talyzin[971]), and the MC simulations by Papadimitriou et al.[248] (denoted with lines; solid lines correspond to SPC/E and dashed lines to TIP4P/Ice). The comparison is for four different temperatures: (a) 255 K, (b) 268 K, (c) 274 K, and (d) 278 K. The magenta dashed-dotted line corresponds to the limiting case of 100% of small and large cages occupied with a single H_2 and THF molecule respectively. The figure is reconstructed based on the data of ref 248. Error bars are shown only for cases that were reported in the original studies.

4.8.6. Hydrate-Based Gas Mixture Separation Efficiencies. While a considerable number of studies have focused on the experimental aspects of hydrate-based separation of H_2 − containing mixtures,[976−979] to the best of our knowledge, no relevant MC simulation study has been performed. MC studies for other hydrate mixtures, however, are available in literature: Glavatskiy et al.[980] performed GCMC simulations of mixed CH_4 + CO_2 hydrates, motivated by the possibility of CO_2 replacing CH_4 within hydrate deposits. Such a process has gained significant attention lately due to the fact that it can simultaneously take care of two important issues. Namely, the energy production (i.e., CH_4) and the sequestration of a "green-house" gas (i.e., CO_2) within a single process. In contrast, the study by Papadimitriou et al.,[981] which focused on computing the efficiencies of a hydrate-based gas-mixture separation process (the latter being the motivation), examined the same mixed CH_4 + CO_2 hydrate system, and reported good agreement between the experimental and GCMC simulations.

4.8.7. Hydrate-Promoter Selection. Atamas et al.[982] used the self-referential technique to compute the Gibbs free energy of molecular crystals. The self-referential technique utilizes the principle that the free energy is an extensive quantity. Therefore, it follows that by constructing a reversible path between two systems that contain N and $2N$ particles, respectively, the free energy difference between the two systems can be calculated as well as the free energy of the system itself. Subsequently, the authors examined the storage of H_2 in sII[983] and sH[984] hydrates. The binary H_2 + promoter hydrate with lower Gibbs free energy is more stable. The main purpose of both studies was to identify appropriate promoter molecules. An important conclusion of these studies is the identification of THF as one of the most promising promoters for H_2 hydrates. Hydrate promoters are molecules that shift the hydrate equilibrium curve to more moderate conditions (i.e., lower pressures or higher temperatures). Hydrate promotion acts in the opposite direction to hydrate inhibition (i.e., a hydrate inhibitor results in shifting the hydrate equilibrium curve to higher pressures or lower temperatures).

Motivated by the need to identify promoters for storing H_2 in clathrate hydrates, Frankcombe and Kroes[985] introduced a new predictive computational method for classifying clathrate hydrate promoter molecules, based on the interaction energies between potential promoters and the water networks of sII and sH clathrates. To this purpose, water was modelled using the TIP5P force field. On the other hand, the promoter molecules

https://doi.org/10.1021/acs.chemrev.5c00617
Chem. Rev. 2025, 125, 11878−12029

were frozen at the geometries minimising the MP2/cc-pVTZ energy, either at the global minimum or at a metastable conformer. Ab initio calculations of the electronic structure of the promoter molecules, with the charges constrained to reproduce the calculated dipole moment of the guest molecule were performed using Gaussian 03. Atamas et al.[986] introduced a generalization of the method by Frankcombe and Kroes,[985] extending it to finite temperatures and pressures. The method is based on Gibbs free energy calculations of sI, sII, and sH H_2 clathrates. Atamas et al. reported that the van der Waals volume of a potential promoter is an important parameter which can determine the type (either sII or sH) of clathrate to be formed.

Iwai and Aokawa[987] performed MD simulations for the sII mixed H_2 + promoter hydrates to search for potential promoters to stabilise the H_2 hydrates. Simulations were performed at 10.1 MPa and an initial temperature 260 K (increased at a rate 0.1 K/s). A slow increase of the hydrate cell volume was initially observed, followed by a rapid increase. The temperature at which the cell volumes rapidly increased was identified as the simulated collapse temperature. The promoter (cyclobutane) which gave the highest simulated collapse temperature was identified as the one to best stabilise the hydrates.

Mi et al.[246] performed an extensive series of equilibrium MD simulation to study the effect of various promoters (i.e., CH_4, CO_2, C_2H_6, C_3H_8, C_5H_{10}, and THF) on the nucleation of mixed H_2 + promoter hydrates. Computations, up to 3 μs, were performed at a pressure of 110 MPa and a temperature of 240 K to computate free energies, diffusivities, residence time correlation functions, order parameters, and H_2 uptake. Mi et al. recommended that instead of using individual properties for identifying the suitability of a tentative promoter for enhancing the behavior of H_2-containing hydrates, it is essential to examine the collective control of the aforementioned thermodynamic factors. The authors identified four criteria that an ideal hydrate promoter should possess: (i) High solubility in water for maximizing the guest molecule availability close to the hydrate formation front; (ii) Optimized residence time to enhance nucleation without the need for excessive mobility; (iii) Strong hydrogen bonding interactions to facilitate stable cage formation; (iv) Environmental sustainability to minimize ecological impact.

4.8.8. Self-Diffusivity of Hydrogen in Hydrates. Here, we briefly review the most important experimental work in the area of diffusivity of H_2, to lay the ground for the review of molecular simulation studies. Earlier studies[988] considered that single H_2 molecules were too small to be confined within the hydrate cages, and thus, were unable to provide the required stability to any of the hydrate structures. It was assumed that eventually the H_2 molecules would be able to diffuse through the pentagonal or hexagonal faces of the cages and escape out of the hydrate crystal, ultimately leading to the complete dissociation of the hydrate. However, following the initial experimental synthesis of the H_2 hydrate,[241,244,245] experimental and computational evidence began to accumulate that under reduced pressure conditions, the H_2 content of the hydrate crystal can decrease with time, as a result of H_2 migration, however, without the complete breakdown of the hydrate crystal. The research in this direction was initially driven by the important experimental observation of Okuchi et al.[989] The authors used a pulsed-field gradient NMR method (at high H_2 pressures), and reported that if the pressure on the binary THF + H_2 hydrate phase is relieved for temperatures 250 K or higher, the H_2 guest molecules can diffuse out of the hydrate crystal while the hydrate can still remain stable. On the other hand, upon reversal of the process (i.e., re-pressurisation), H_2 can reversibly fill some of the empty S cages of the THF hydrate by diffusing through the cage faces of the intact hydrate crystal. Okuchi et al.[989] reported experiments for H_2 diffusivity in hydrates for four different temperatures (250, 255, 260, and 265 K) and H_2 pressures in the range 1−20 MPa. The experiments (see Fig. 62) show that the diffusivity

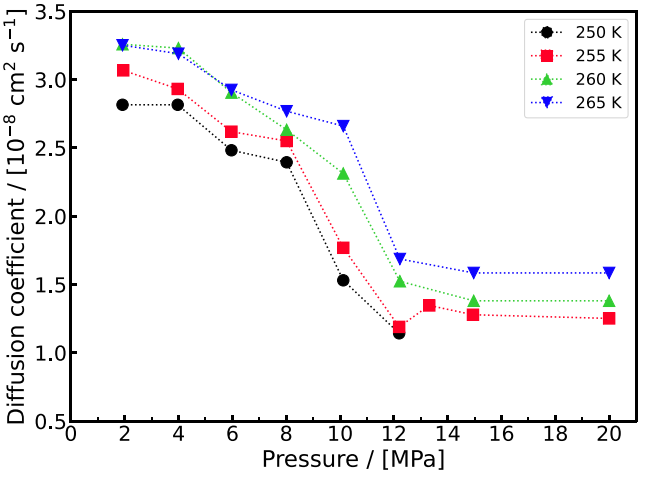

Figure 62. Diffusion coefficient of stored hydrogen in the hydrate as a function of pressure for different temperatures. The data are taken from Okuchi et al.[989] The dotted lines are drawn to guide the eye.

decreases as pressure increases. The decrease is attributed to the hypothesis that H_2 transport occurs only when there is a vacant guest site in the neighboring cage. Recall that at high pressures the cage occupancies increase (see Section 4.8.5), therefore the number of empty cages is reduced. The authors further suggested that the translation of the H_2 through pentagonal H_2O rings between the 5^{12} cages is the most likely path for the activation barrier since all $5^{12}6^4$ cages are occupied by THF. Note, however, that the NMR experiments reported by Senadhere and Conradi[990,991] failed to confirm the previous observations of Okuchi et al.[989] for the H_2 diffusivity via the S cages.

The high mobility of H_2 molecules within the sII S cages has been demonstrated by the inelastic neutron scattering (INS) experiments of the H_2 + THF mixed hydrate reported by Choi et al.[992] The authors argued that the 5^{12} cages alone, form a network of corner−sharing tetrahedral. The channels connecting the S cages are shown in Fig. 63. It is evident that the neighboring S cages line up in a [101] and symmetrical directions to form linear tunnels via which H_2 diffuses, provided unoccupied neighboring cages are present. Information of such diffusion jumps are contained in quasi-elastic neutron scatter (QENS) signals. At low temperatures (i.e., $T <$ 60 K), H_2 molecules have not enough energy to overcome the potential barrier between the S cages. However, a sudden signal jump is observed between 60 and 65 K, persistent also at higher temperatures. This is a clear indication for the beginning of H_2 diffusion via the [101] direction, where the S cages are aligned (i.e., H_2 molecules have gained enough thermal energy to overcome the barrier and cross the pentagonal face connecting the neighboring S cages).

https://doi.org/10.1021/acs.chemrev.5c00617
Chem. Rev. 2025, 125, 11878−12029

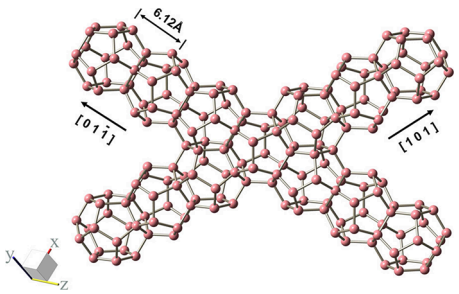

Figure 63. Channels formed by 5^{12} cages. Each S cage is connected to six other S cages through pentagonal faces.[992] [The figure is reprinted from International Journal of Hydrogen Energy, Vol 35, Yong Nam Choi et al., Dynamics of hydrogen molecules in the channels of binary THF-H_2 clathrate hydrate and its physicochemical significance on hydrogen storage, 13068−13072, Copyright (2022), with permission from Elsevier].

In a subsequent experimental study using Raman, Strobel et al.[993] proposed an alternative scheme: Only the $5^{12}6^4$ cages participate in the H_2 diffusion via the hexagonal faces. Fig. 64 is

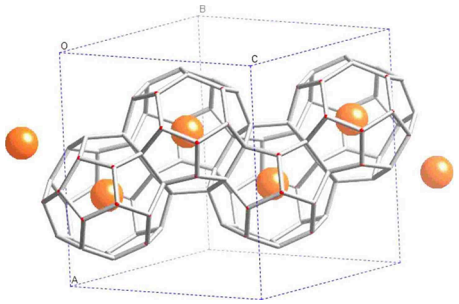

Figure 64. Portion of sII unit cell showing hexagonal face-sharing large cavities.[993] [The figure is reprinted from Journal of Chemical Physics, Vol 130, Strobel and Dendy, Raman spectroscopic studies of hydrogen clathrate hydrates, 014506, Copyright (2009), with permission from AIP Publishing].

a schematic of a portion of the sII hydrate unit cell that shows the hexagonal face-sharing L cages. The proposed scheme takes into account the DFT calculations of Alavi et al., which are discussed further, later in this Section (i.e., barriers for H_2 diffusion equal to 25−29 kcal/mol and 5−6 kcal/mol for the S and L cages respectively).

Russina et al.[994] performed neutron scattering experiments of mixed H_2 + THF. The authors reported significant H_2 diffusive mobility in the L cages even at 10−50 K. Contrary, H_2 confined in S cages were shown to be trapped at the center of the cages and, thus, were available for long range diffusion, independent of the activation barriers for the inter-cage jumps. Pefoute et al.,[995] based on an INS study, reported that under equilibrium conditions, a single H_2 molecule occupying the S cages of the binary THF + H_2 sII clathrate hydrate does not diffuse outside of its cage on pico-second time-scales (i.e., an observation opposite to Choi et al.[992]). Conversely, Mulder et al.[965] using neutron diffraction experiments, reported a value of H_2 diffusion in the S cages of the binary THF + H_2 hydrate equal to " . . .at least 10^{-11} cm^2/s at 264 K", inferred from the time required to enter and leave hydrate crystallites with size equal to 0.4 μm.

Parallel to the experimental work in this field, molecular simulation has played a pivotal role. Frankcombe and Kroes,[934] performed equilibrium MD simulations, and showed that H_2 molecules in the L cages can readily diffuse through the hexagonal faces, and ultimately, reach the bulk gas phase in contact with the hydrate structure. Nevertheless, H_2 guests in the S cages have high energy barriers to migration, and thus, do not diffuse outside their cages. In a similar MD study, Cao et al.[996] performed MD simulations to study the mixed H_2 + THF system. The findings showed that H_2 intercage migration from S cages occurs only during double occupancy of the S cages, while no H_2 migration occurs during single H_2 occupations of the S cages.

Gorman et al.[997] reported MD simulations of the pure H_2 and binary THF + H_2 sII clathrate hydrates at 50 bar and temperatures up to 250 K. The authors detected diffusion of H_2 molecules only when configurations with 2 H_2 in the S cages were used. The S cages were observed to temporarily expand through a "breathing motion" (i.e., one of its pentagonal faces opened temporary) as one H_2 guest migrated to a neighboring cage. The cage structure remained intact during the migration process. Gorman et al. claimed that this migration exhibits an approximate Arrhenius temperature dependence in the range 200−250 K.

Iwai and Hirata[998] performed MD simulations of THF + H_2 clathrates with different H_2 occupancies in the S and L cages, at 300 and 310 K, and 10.1 MPa. The simulations revealed migration of H_2 molecules between S cages and L cages. However, it should be noted that the observed diffusion between cages may be related to the high temperature at which the simulations were performed, which is likely outside the stability range of the binary hydrate (i.e., possible occurrence of hydrate dissociation). Geng et al.[999] also observed the migration of H_2 in the pure H_2 and binary THF + H_2 hydrates using equilibrium MD simulations. The authors concluded that these migration phenomena lead to the hydrate decomposition process. The MD data also showed that the diffusion of H_2 is always larger than that of H_2O molecules. Contrary, THF molecules encaged in the $5^{12}6^4$ cavities perform as stabilisers because of the high interaction energy barrier restricting the motion of THF molecules.

Luis et al.[936] investigated the effects of externally−applied static electric fields on the H_2 diffusion in sII hydrates. The authors reported that the diffusion of H_2 molecules occurs only through the L cages, while the H_2 molecules diffuse, with a slight preference, in the same direction of the applied electric field.

Hasegawa et al.[1000] performed equilibrium MD simulations of sII mixed H_2 + SF_6 hydrates, and reported that the diffusion of H_2 molecules between L cages was found to occur more frequently. However, the presence of SF_6 molecules in the L cages was proved to inhibit H_2 diffusion. Therefore, the authors recommended that an optimal number of L cages should be occupied by SF_6 molecules as a means to increase the H_2 storage capacity of the mixed hydrate. Furthermore, Hasegawa et al. reported that a partial breaking of the hydrate structure was required to make room for the H_2 to diffuse through the open pentagonal ring in the case that a H_2 molecule diffused to/from an S cage. By contrast, no cage distortion was observed in H_2 diffusion via a hexagonal ring from an L cage. Hasegawa et al.[1000] also performed MD simulations of sII mixed H_2 + tert−butylamine hydrate, where the tert−butylamine molecules occupied the L cages. The authors reported that more H_2 molecules diffused into the hydrate as a result of a less stable, and partially distorted,

https://doi.org/10.1021/acs.chemrev.5c00617
Chem. Rev. 2025, 125, 11878−12029

hydrate structure, which created enough space for H_2 molecules to move between adjacent cages.

Zhang et al.[594] studied the growth of mixed H_2 + CH_4 hydrate with MD simulations, and observed that H_2 can hop between the $5^{12}6^4$ cages through the six-membered rings connecting the cages without any distortion of the cages, even for cases that the L cages are occupied by CH_4. The observation of the simultaneous presence of two different guests (i.e., H_2 and CH_4) within the same L cage is of utmost importance since it can have a significant effect on the storage capacity of the hydrate. The possibility of the simultaneous occupancy of the L cages by two different guests was originally reported by Papadimitriou et al.[1001,1002] for the case of the mixed sII He + THF, based on observations from GCMC simulations. Subsequently,[1003] reported similar observations, based on experiments using *in situ* Raman spectroscopy for the mixed sII H_2 + Ar hydrates. Waage et al.[1004] performed MC simulations, which showed that H_2 molecules are capable of coexisting, even in S cages, with any of the other molecules (i.e., CH_4, CO_2, N_2) examined in their study.

In a similar context, Harada et al.[1005] reported MD simulations for the case of H_2 hydrate with crystal structure C_1, namely ice II filled with H_2 molecules. The authors observed fast diffusion of the H_2 molecules in the C_1 crystal. The H_2 molecules were observed to migrate (via a highly anisotropic in space diffusion process) only inside the tube−like voids of the C_1 hydrate. Harada et al. also pointed out the importance of the existence of defects or vacancies in the tube−like voids for H_2 diffusion to occur. In the absence of vacancies no diffusion was observed. In a related study, Arman and Nugroho[1006] reported MD simulations for the case of H_2 hydrate with structure C_2, namely ice I_c filled with H_2 molecules. Additional MD simulations of anomalous H_2 diffusion in various ices have been performed by Smirnov and Stegailov.[1007]

Except from classical MD, other atomistic-scale simulations have been conducted to study the diffusion of H_2 in hydrate systems including, but not limited to the following: Alavi and Ripmeester[1008] performed DFT calculations at the B3LYP and MP2 levels of theory to compute the energy required for the H_2 molecules to migrate through a hexagonal face of the L-type cage or a pentagonal face of the S-type cage, considering both parallel and perpendicular configurations of the H_2 molecules with respect to the examined face. They reported energy barriers to diffusion equal to 5−6 kcal/mol and 25−29 kcal/mol for the L and S cages, respectively.

The calculation of the free−energy barrier for H_2 diffusion between cages has been been achieved using methods such as PIMD[1009] and ab initio simulations. Typical examples can be found in the works of Trinh et al.,[182] Cendagorta et al.,[366] and Burnham et al.[1010−1012] These alternative approaches are especially important at low temperatures, where H_2 molecules are affected by quantum effects.

The molecular simulations by Trinh et al.[182] demonstrated the importance of cage flexibility and cage occupancy on the diffusion of H_2 between cages. Furthermore, they showed that the multiple occupancy of cages helps reduce the free energy barrier for H_2 hopping between cages. Cendagorta et al.[366] used the Ring Polymer Molecular Dynamics (RPMD) rate theory. This work was motivated by the fact that the energy barrier to hopping is significant compared to the thermal energy. Therefore, H_2 diffusion is a rare event process, and thus, amenable to computation using rate theory. The PIMD simulations by Burnham and English[1010] for the case of H_2 diffusion between two L hydrate cages at 200 K also yielded the quantum free−energy barrier higher than the classical one, by about 2 kJ/mol.

Waage et al.[1004] performed MC simulations to calculate the free energy barriers associated with CH_4, CO_2, N_2, and H_2 hopping through rings of water between the cages of the sI hydrate structure. The authors considered intact cages, as well as cages with H_2 vacancies. H_2 was shown to be capable of diffusing out from both the S or L cages.

Ghaani et al.[942] used non-equilibrium MD simulations to examine H_2 diffusion during release/uptake from/into propane planar clathrate surfaces in the temperature range 180−273 K. The simulations revealed that H_2 molecules exhibited higher movement during release studies (with hydrate being in contact with a vacuum) when compared with the uptake studies (with gas H_2 molecules located on top of the hydrate structure).

English and Burnham[1013] considered classical MD and PIMD simulation to study the intra-cage behavior of H_2 and D_2 molecules in doubly occupied L cages of sII hydrates at 100 K. Krishnan et al.[1014] examined transient, non-equilibrium inter-cage hopping, and presented a diffusional activation energy for the four nominal L cage occupancies (1 up to 4) using leakage−rate fits. Markov-chain models were utilized to study the inter-cage hopping of H_2 and D_2, and expressed at different temperatures and large-cage occupancies. Furthermore, the authors computed the free energy of guest "binding" in the L and S cages for all of the occupancies. Krishnan et al.[1015] conducted micro-second-long, non-equilibrium MD simulations, in the temperature range 140−180 K, to elucidate mechanistic effects of electric−field on guest diffusivity control in hydrates. It was found that a judicious selection of the electromagnetic fields (i.e., in the microwave frequency range), could act towards the dramatic enhancement of the H_2 release rate, without any breakup of the hydrate lattice itself. This is an important aspect for the kinetic control of large-scale H_2 storage systems. Krishnan et al.[1016] reported MD calculations exploring both H_2 and D_2 hydrates for cage occupancies and their self-diffusivity via inter−cage hopping. The authors studied these hopping phenomena as a function of temperature using a Markov chain model.

4.9. Interfacial Tensions of Aqueous Hydrogen Systems

Computing and analyzing the interfacial tension (IFT) between H_2 and brine systems is crucial for the effective and safe implementation of UHS in geological formations, such as saline aquifers. IFT directly influences the capillary forces at the interface between H_2 and reservoir fluids, governing H_2 migration, trapping efficiency, and retention capacity within subsurface reservoirs. Accurate knowledge of IFT allows precise prediction and optimization of storage capacities and operational efficiencies, ensuring efficient H_2 injection and withdrawal. IFT values, in addition, depend on thermodynamic and chemical conditions, including temperature, pressure, salinity, ionic composition, and the presence of cushion gases like CO_2 and CH_4, making its study essential for realistic reservoir modeling and design of storage strategies. Accurate IFT data support safety and risk mitigation by evaluating the sealing capability of caprocks, critical for preventing H_2 leakage. Given the challenges associated with experimental IFT measurements under reservoir conditions, MD simulations offer valuable atomic-level insights and extensive predictive

https://doi.org/10.1021/acs.chemrev.5c00617
Chem. Rev. 2025, 125, 11878−12029

ability. Furthermore, understanding IFT helps optimize cushion gas composition and injection strategies, enhancing overall storage performance. The interplay between IFT and rock wettability significantly impacts capillary pressures, determining H_2 stability and displacement behavior in porous formations. Therefore, a comprehensive examination of IFT is fundamental to ensuring secure, efficient and large-scale storage H_2 in geological reservoirs. For a thorough introduction on the role of molecular simulation for designing and optimizing UHS the reader is referred to Section 2.3.4. Details on the computation of IFT via MD are provided in Section 3.2.16. A review of relevant studies is provided below.

van Rooijen et al.[630] computed IFTs of H_2 gas in contact with aqueous NaCl solutions, self-diffusivities and solubilities of H_2 in aqueous NaCl solutions using MD simulations at conditions relevant to UHS and H_2O electrolysis. The IFTs were computed for temperatures of 298 to 523 K, pressures of 1 to 600 bar, and molalities of 0 to 6 mol NaCl/kg H_2O using the TIP4P/2005 water model, Madrid-2019 force field for NaCl, and Vrabec force field for H_2 (for details on these force fields see Section 3.1). The results showed that IFTs do not exhibit significant pressure dependence, increase linearly with salt molality (by ca. 1.44 mN/m per mol NaCl/kg H_2O), and decrease non-linearly with temperature. This behavior is explained by the fact that IFT is related to the density difference between the two phases, with the low density of H_2 relative to water resulting in minimal pressure effects, while the increased density of saline water and the arrangement of ions at the interface (with anions being depleted from the bulk phase and cations being absorbed into it) strengthen the H_2 bond network of H_2O, leading to increased IFT. Temperature has the strongest influence on the IFT, causing a non-linear decrease due to its effect on the density difference between H_2 and aqueous solutions. The computed IFTs were compared with available experimental data from Hosseini et al.,[1017] showing excellent agreement with average deviations lower than 6.4% across the range of conditions studied. The authors proposed an engineering equation for IFT as a function of temperature and molality: $\gamma = c_1 + c_2 m + c_3 T^{c_4}$, valid for temperatures of [298, 523] K, pressures of [1, 600] bar, and molalities of [0, 6] mol NaCl/kg H_2O. The IFT data generated in this work is particularly valuable because experimental measurements for the H_2/H_2O/NaCl system are scarce, especially at high pressures and temperatures, which are highly relevant to H_2 technologies.

Omrani et al.[1018] investigated the IFT, density, and molecular distribution properties of the H_2 − brine systems with various salts including Na^+, K^+, Ca^{2+}, and Mg^{2+}, under reservoir conditions. IFT was computed as a function of pressure (1−30 MPa), temperature (298−373 K), and salt molality/composition (up to 5.02 mol/kg for NaCl and up to 1.91 mol/kg for other salts). The results show that IFT decreases with increasing temperature, slightly decreases with increasing pressure, and increases with higher salinity, with values ranging roughly from 55.85 to 77.54 mN/m, depending on the conditions. Physically, these trends are explained by the interfacial molecular structure where higher temperature broadens the interfacial width and enhances H_2 − H_2O mixing, reducing IFT, while increased salinity enriches H_2 accumulation at the interface, thinning the interface and increasing IFT. Temperature is identified as the strongest factor influencing IFT, followed by salinity, with pressure having a comparatively minor effect. The MD simulation results for IFT showed excellent agreement with available experimental data, with deviations less than 3% when using the combined Marx force field for H_2, TIP4P/2005 model for H_2O, and Smith-Dang parameters for Na^+ and Cl^-. A general correlation for IFT as a function of reduced temperature, density difference between H_2 and brine phases, and NaCl mole fraction was developed using genetic programming, achieving high accuracy with $R^2 = 0.9783$ and absolute average relative deviation below 1%. The effect of cation type was also shown to be significant, with $CaCl_2$ yielding the highest IFT values and K^+ the lowest at comparable concentrations, attributed to differences in ion hydration enthalpy and interfacial distribution.

Xie et al.[1019] focused on accurately predicting the IFT of H_2 + CO_2 gas mixtures in contact with H_2O and brines containing Na^+ and Cl^- ions over a wide range of temperatures, pressures, gas compositions, and salinities. Molecular interactions were analyzed to elucidate the underlying mechanisms affecting IFT, while and ML approach was used to develop a general predictive equation. The parameters used to compute IFT included temperatures from 298 to 373 K, pressures in the range of 50 to 400 bar, gas compositions expressed as H_2 mole fraction, and brine salinities up to 3.15 mol/kg. The IFT was shown to decrease with increasing pressure and CO_2 content, while increasing salinity raised the IFT, with values ranging approximately between 20 and 60 mN/m depending on conditions. These trends arise from the interplay between molecular mobility of gas and water molecules (entropy) and intermolecular interactions primarily between gas molecules and water/brine ions (enthalpy). The higher pressure enhances gas solubility in the aqueous phase, which reduces the IFT, whereas the presence of salt ions (Na^+ and Cl^-) increases electrostatic and van der Waals interactions at the interface, thereby strengthening intermolecular forces and increasing IFT. Among the factors studied, pressure and gas composition exhibit the strongest influence on IFT behavior under the chosen conditions (relevant to UHS), with temperature showing a less dominant but still significant effect. MD simulations of IFT were validated against extensive experimental data, showing good agreement with average relative errors around 4.4%. A ML-based polynomial equation was developed to predict IFT as a function of temperature, pressure, H_2 mole fraction, and salinity, achieving high accuracy with $R^2 = 0.972$ on testing data. This equation outperforms previous empirical models, especially for ternary (H_2 + CO_2)-water/brine systems, and is suitable for reservoir simulation applications.

Yang et al.[602] computed IFT, contact angles, adhesion tension, density distributions, and relative adsorption in multiphase systems of H_2 + H_2O with silica or kerogen under various conditions. IFTs, computed via MD simulations (INTERFACE force field for H_2 and TIP4P/2005 for H_2O) and density gradient theory (with PC-SAFT EoS), range from approximately 25 to 72 mN/m as functions of pressure (1 to 160 MPa) and temperature (298 to 523 K). A general outcome, IFT was shown to decrease with increasing pressure and temperature, but above about 448 K and 60 MPa, IFT increased with pressure due to an inversion of H_2 relative adsorption: at low T and P, adsorption is positive (enrichment at the interface), decreases past a pressure threshold, and becomes negative at high T (depletion at the interface). Temperature most strongly influences IFT by altering molecular distributions and thermal fluctuations. The INTER-

https://doi.org/10.1021/acs.chemrev.5c00617
Chem. Rev. 2025, 125, 11878−12029

FACE + TIP4P/2005 combination of force fields accurately reproduces the surface tension of water, and matches experimental IFTs within 1.7 - 7.4 mN/m, while density gradient theory with PC−SAFT reproduces the same trends seen in both simulations and experiments. The authors note that the value of IFT in H_2+H_2O is close to the surface tensions of pure water, and higher than in CO_2+H_2O, CH_4+H_2O, or N_2+H_2O computed in other studies not reviewed here.

Doan et al.[1020] studied IFT and adsorption in water−H_2, CH_4, and CO_2 mixtures. IFT was computed at 1 to 70 MPa and at 300 and 323 K for pure water and binary gas mixtures. IFT was generally shown to decrease with pressure and temperature; for instance, $\gamma(CO_2 - H_2O)$ value fell from ca. 62 to ca. 34 mN/m, $\gamma(CH_4 - H_2O)$ from ca. 64 to ca. 53 mN/m, while $\gamma(H_2 - H_2O)$ remained equal to 62-63 mN/m, showing greater temperature sensitivity. Thus, H_2 yielded the highest IFT and CO_2 the lowest. This decrease was attributed to enhanced gas adsorption at the water interface, especially stronger CO_2 - water interactions compared to CH_4 or H_2, though detailed molecular mechanisms remain unexplored. The authors reported that pressure dominates IFT behavior, decreasing sharply up to 50 MPa and plateauing above, while temperature has a lesser effect, becoming negligible at high pressure. The computed IFTs agree well with experiments for CO_2-H_2O and CH_4-H_2O, though underestimating low-pressure values by up to 10%, and underestimating H_2-H_2O by 10 to 14%, likely due to the choice of force fields, inaccurate mixing rules for the intermolecular interactions, or system-size limitations. MD simulations show H_2 in ternary H_2 - CH_4 - H_2O mixtures increases IFT relative to CH_4 - H_2O and CO_2 - CH_4 - H_2O, owing to weaker H_2 intermolecular forces and lower interfacial adsorption.

Doan et al.[1021] computed IFT and flow properties of water−H_2 mixtures with cushion gases CO_2, N_2, and CH_4 under geological storage conditions. IFT was computed as a function of pressure [1, 70] MPa, temperature [300, 343] K, and cushion-gas mole fractions [10 to 90]%. For $H_2/CO_2/H_2O$, $H_2/N_2/H_2O$, and $H_2/CH_4/H_2O$ systems, IFT decreased from ca. 64 mN/m at low pressure to ca. 42 mN/m at 70 MPa at higher pressures and temperatures. Higher H_2 content raised IFT: N_2-containing mixtures yield the highest IFT, while CO_2-containing mixtures yield the lowest IFT at fixed conditions. These trends arise from gas adsorption at the H_2O interface i.e., heavier CO_2 reduces IFT due to stronger inter-molecular interactions and higher adsorption, CH_4 moderately lowers IFT, and the light, inert N_2, yields higher IFT. Pressure was shown to most strongly affect IFT, which dropped sharply up to ca. 30 MPa, and then reached a plateau for all CO_2, N_2, and CH_4 mixtures across the 300 - 343 K temperature range. Temperature caused a gradual decrease in IFT (at fixed pressure), but had a weaker effect. The computed IFTs for $H_2/CO_2/H_2O$ agree with experiments within 12% at low pressures. For $H_2/N_2/H_2O$ and $H_2/CH_4/H_2O$ systems, the available experimental data are limited, making the molecular simulation predictions valuable.

Chen et al.[604] performed molecular simulations to study the IFT, surface excess, bubble evolution, and contact angle of CO_2, H_2, and their mixtures with H_2O or brine (Na^+, Cl^-) at 10 MPa and temperatures ranging form 300 to 400 K. CO_2/H_2 mixtures included H_2/CO_2 ratios of 1:10, 2:10, 3:10 (CO_2 − rich) and their inverses (H_2 − rich). IFT was computed isobarically (10 MPa) over 300 to 400 K with 4% NaCl brine. In H_2 − rich mixtures, IFT decreased roughly linearly from ca. 65 mN/m at 300 K to ca. 50 mN/m at 400 K in both pure H_2O and brines. CO_2 − rich systems showed non-monotonic temperature dependence: IFT rose to ca. 20 mN/m at the range 320 - 360 K, and at higher temperatures decreased. The authors qualitatively attributed this peak to phase transitions and temperature-dependent surface adsorption, without though providing a detailed mechanistic explanation. Brine was shown to increase IFT by a few mN/m relative to pure H_2O. CO_2 significantly reduced IFT compared to H_2, which has minimal impact. This is due to the stronger electrostatic and quadrupolar interactions of CO_2 with H_2O, influencing the anisotropy of the tensor of the virial pressure, a concept noted but not elaborated further by Chen et al.[604] The weak van der Waals interactions of H_2 cause smaller IFT changes. The temperature change from 300 to 400 K, yielded a 10 mN/m IFT decrease in H_2-rich systems and non-monotonic variation of 5 mN / m in CO_2 − rich systems, signifying temperature as the prime IFT variable. MD results agreed with experimental CO_2 − H_2O and H_2 − H_2O data (298 - 448 K, ≤ 45 MPa). The experimental data cover pure gas-water, but the trends of the mixture were shown to be consistent with the behavior of the extrapolated pure components. The simulations indicated linear temperature dependence in systems rich in H_2, and non-monotonic in systems rich in CO_2, with a consistently increasing IFT of brine.

Chen and Xia[605] computed transport properties, wettability, IFT, and surface adsorption of H_2, CO_2, and CH_4 interacting with H_2O and silica under reservoir conditions. The IFT calculations were carried out at a fixed temperature of 320 K and pressures up to 60 MPa, considering pure water and silica substrates. Across all conditions, the IFT follows the order $\gamma_{CO_2-H_2O} < \gamma_{CH_4-H_2O} < \gamma_{H_2-H_2O}$. In particular, the CO_2-water IFT dramatically decreased by ca. 42% at 10 MPa before plateauing, the CH_4 − water IFT decreased more gradually with pressure, and the H_2 − water IFT remained nearly constant. These trends arise from differences in density and molecular interactions i.e., the higher density and quadrupole moment of CO_2 enhance its surface activity, while the low density of H_2 and weaker van der Waals forces lead to minimal variation in IFT. The primary factor influencing IFT is the density difference between the gas and water phases, which governs interfacial molecular interactions. MD-computed IFTs agree well with experimental data for CO_2 and CH_4 systems. For H_2, the simulations were shown to slightly underestimate the experimentally measured IFTs, but correctly capture the qualitative behavior. No significant pressure dependence of IFT for H_2 is observed in simulations, consistent with experimental observations of only slight decreases.

The study by Adam et al.[1022] reported data on IFT, structure, and solubility for UHS-relevant brine (NaCl) and gas mixtures of H_2, CO_2, and CH_4. IFTs were computed for pressures of 10−60 MPa, temperatures from 323.15 to 388.15 K, and salt concentrations 10-25 wt%, covering both pure gas-brine and mixed gas-brine systems. Pure gases included brine/H_2, brine/CO_2, and brine/CH_4, while mixtures considered were ternary brine/H_2/CO_2 and quaternary brine/40% mol H_2/60% mol cushion gases (CO_2 or CH_4). Pure brine/H_2 IFT remained nearly constant (around 59 mN/m) across pressures, whereas brine/CO_2 IFT decreased markedly from 44.4 to 30.6 mN/m, and brine/CH_4 showed a minor drop (53.6 to 51.8 mN/m). Mixed gas systems with CO_2 exhibited stronger

https://doi.org/10.1021/acs.chemrev.5c00617
Chem. Rev. 2025, 125, 11878−12029

pressure dependence; brine/40% mol H_2/60% mol CO_2 IFT decreased about 14.6%, compared to a smaller 7.4% decrease with CH_4. Temperature significantly reduced IFT across all systems: brine/H_2 decreased roughly 20% (67.4 to 54.3 mN/m), brine/CO_2 from 37.1 to 31.6 mN/m, and brine/CH_4 from 57.5 to 50.2 mN/m. Similar trends occurred in mixed systems; brine/40% mol H_2/60% mol CO_2 IFT dropped by 8 mN/m, and brine/40% mol H_2/60% mol CH_4 by 12 mN/m. Higher CO_2 content lowered temperature sensitivity due to stronger molecular interactions requiring higher thermal energy to disrupt these intermolecular bonds. Radial distribution function analysis revealed weak hydrogen-bonding between CO_2 oxygen and H_2O hydrogen atoms at the interface, leading to CO_2 clustering and reduced IFT as its mole fraction increased. Increasing salt concentration raised IFT in all systems via the salting-out effect, as ions attracted water molecules, reducing water-gas interactions. For example, increasing NaCl from 10 to 25 wt% raised IFT by approximately 3 mN/m for brine/H_2, 4 mN/m for brine/CO_2, and 7 mN/m for brine/CH_4. Pressure had a moderate impact on IFT, notably in systems with higher CO_2, whereas temperature and salinity exerted stronger effects. The computed IFT values closely agree with experimental data, validating the methodology and force fields used by Adam et al.[1022]. Engineering correlations using polynomial functions were developed to predict IFT based on pressure, temperature, CO_2 concentration, and salinity. It is important to note that the functional form (i.e., actual cubic polynomial) of the devised equations and the coefficients were not provided by the authors, hindering the wide, practical use of the presented model.

4.9.1. Handling Long-Range Dispersion Interactions. Transitioning now from the specific findings presented by the studies reviewed earlier, we collectively address the approaches followed for calculating IFTs. A primary challenge associated with the slab method of determining IFTs in MD simulations is accurately handling long-range dispersion (LJ) interactions. Two principal strategies commonly applied are semi-analytic tail corrections and explicit mesh-based methods. Tail corrections adjust IFT values post-simulation, following the approach developed by Blokhuis et al.[1023] and elaborated by Allen and Tildesley[52], and can significantly impact computed IFT values, sometimes by up to ca. 35% for LJ fluids. Alternatively, explicit mesh-based methods, such as smooth Particle Mesh Ewald (sPME)[1024] and Particle-Particle Particle-Mesh (PPPM),[1025,1026] directly compute long-range dispersion analogously to electrostatic Ewald summation, as comprehensively reviewed by Goujon et al.[1027] Sega and Dellago[1028] compared these approaches across seven water models, demonstrating that explicit mesh-based methods yield more accurate IFT predictions and correctly reproduce liquid and vapor densities. Furthermore, including the full dispersion interactions explicitly shifted the critical temperature of water upwards, a crucial thermodynamic effect not captured by semi-analytic tail corrections, highlighting the importance of explicitly incorporating long-range dispersion interactions.

Several studies have applied these methodologies specifically to H_2-water and H_2-brine systems, adopting various approaches to computing the long-range dispersion. For instance, van Rooijen et al.[630], Xie et al.,[1019] and Yang et al.[602] used explicit mesh-based methods (PPPM[1025] or PME[1029]), with Yang et al.[602] also validating the improved accuracy against NIST data when using PPPM. Omrani et al.[1018] truncated dispersion interactions without applying tail corrections but mitigated potential underestimations in IFT by using an unusually large LJ cutoff (2.9 nm), requiring larger simulation cells and greater computational effort. Adam et al.[1022] also truncated dispersion interactions at 1.28 nm without long-range dispersion interactions. Doan et al.[1020,1021] used semi-analytic tail corrections proposed by Blokhuis et al.,[1023] Chen et al.[604] and Chen and Xia[605] use truncated LJ interactions without explicit tail corrections, potentially underestimating IFT values due to the omission of long-range dispersion effects. Consequently, differences in IFT predictions among these studies can often be attributed to varying treatments of long-range dispersion interactions. Although semi-analytic tail corrections provide computational efficiency, they may overlook important thermodynamic effects, whereas explicit mesh-based methods ensure higher accuracy at the expense of greater computational resources. Thus, consistently addressing long-range dispersion interactions is vital for obtaining reliable IFT predictions in H_2-water and H_2-brine systems.

Although here we focus on long-range dispersion in simulations of interfacial tension for H_2-water, the same considerations arise in nanoporous frameworks (e.g., MOFs, zeolites, COFs). Whether to apply homogeneous long−range (tail) corrections in crystalline hosts remains debated in the literature. One view argues against the use of these corrections because the standard assumption that the radial distribution function approaches unity beyond the interaction cutoff radius often fails in ordered solids (the radial distribution function can remain oscillatory and even peak near the cutoff). Thus, applying a homogeneous correction may introduce spurious energetic contributions.[1030] Moreover, in crystalline materials, the radial distribution function is inherently direction dependent. The opposing view recommends applying tail corrections to solid−fluid and fluid−fluid terms to reduce sensitivity to truncation, and to enable more consistent cross−study comparisons; substantial effects on Henry coefficients and loadings have been reported by Siperstein et al.[1031] and Jablonka et al.[1032]

Tail corrections are, ultimately, a modeling choice. In practice, we suggest: (i) following the force field as originally parametrized (its interaction cutoff radius and any prescribed tail correction), (ii) reporting these choices explicitly in the methodology section of the study, and (iii) where feasible, demonstrating robustness with brief sensitivity tests (for example, one can vary the interaction cutoff radius and toggle the correction on or off). As a way to sidestep the truncation/tail-correction decision entirely, one can use smooth finite−range pair potentials that vanish continuously, for example, the Wang-Ramírez-Dobnikar-Frenkel ("WF") LJ-like potential[1033] keeping in mind that using such potentials generally requires re−fitting parameters to reproduce the target adsorbate-framework interactions.

4.9.2. Importance of Force Field Selection on Interfacial Tension Computations. As extensively discussed thusfar in this review, in MD simulations aimed at accurate predictions, selecting appropriate force fields to describe molecular interactions is essential. Omrani et al.[1018] extensively explored various force fields for H_2 including Vrabec,[48] Hirschfelder,[321] modified Silvera-Goldman,[335] 3-site Alavi,[336] Cracknell,[311] and Marx,[310] and for water TIP4P/2005,[305] TIP4P-μ,[47] TIP4P OPLS/AA,[360] SPC/E,[346] TIP3P,[300] and TIP5P[359] (see Sections 3.1.1 and 3.1.2).

https://doi.org/10.1021/acs.chemrev.5c00617
Chem. Rev. 2025, 125, 11878−12029

Omrani et al.[1018] computed IFTs under pressures of 5 and 20 MPa and temperatures of 323 and 373 K, alongside multiple NaCl models including the ones by Smith and Dang,[374] Joung and Cheatham,[371] the Madrid-2019,[1034] and from Loche et al.[1035] The combination of Marx[310] with TIP4P/2005[305] and Smith and Dang[374] provided the best agreement with the experimental IFT data of Hosseini et al.,[1017] with deviations being consistently lower than 5%. Notably, Omrani et al.[1018] did not include the widely-used IFF[313] force field for H_2, yet emphasized the superior performance of TIP4P/2005, aligning with earlier conclusions by Vega and Miguel.[1036]

Subsequent work by Yang et al.[602] evaluated the performance of the Hirschfelder,[321] IFF,[313] and Alavi[336] H_2 models combined with the TIP4P/2005[305] water model, showing that the IFF model is the most precise in reproducing experimental IFT values. Meanwhile, Xie et al.[1019] tested various force field combinations, observing a consistent underestimation (18%) of IFT when using the SPC/E water model. Adam et al.[1022] also indicated that SPC/E significantly deviated from experimental IFT data when compared to TIP4P/2005. For example, in the H_2O/H_2 system at 323 K and 5-20 MPa, SPC/E showed discrepancies of up to 15 mN/m, whereas TIP4P/2005 remained within ±0.15 mN/m. Similar trends were observed across brine/CO_2, brine/CH_4, and ternary brine/H_2/CO_2 systems, where TIP4P/2005 consistently reproduced experimental IFT values and pressure trends, while SPC/E underestimated IFT and failed to capture its pressure dependence. The results of Xie et al.[1019] and Adam et al.[1022] further highlight the critical role of the water force field, noting that variations between the IFF[313] and Alavi[336] H_2 force fields were less significant compared to those arising from the choice of the water model. Although Yang et al.[602] concluded that the Alavi force field failed to capture the pressure-dependent IFT trend, their conclusion was based on limited data, raising caution. In contrast, the more comprehensive study by Xie et al.[1019] demonstrated that while the 3-site Alavi model slightly underestimates absolute IFT values at 323 K, it does correctly reflect the pressure dependence. Collectively, these studies emphasize that selecting an accurate water force field has a greater impact on IFT predictions than the specific choice of the H_2 force field.

Another important detail to consider when performing MD simulations of non-homogeneous systems (e.g., gas/liquid systems used for the computation of the interfacial tension of H_2/water) is the use (or not) of analytic tail corrections.[51,52] Such corrections are only valid for systems that the radial distribution function converges to 1 at long distances (homogeneous gas and liquid phases).[51,52] Therefore, tail corrections are usually not used in systems containing interfaces, since this choice will produce simulation artifacts.[1037,1038] To minimize the error introduced from not considering the long-tail of the interactions potentials, cutoff radii larger than what the chosen force fields dictate can be used. However, such a choice will increase the computational requirements (since more interaction pairs will be considered in each timestep of the simulation), while it should be explicitly mentioned in the methodology section of the study to enable the reproducibility of the results. MD simulation software packages, such as LAMMPS[762] and GROMACS,[476,477] allow for the computation of the long-range LJ and electrostatic interactions with the PPPM[51] method. For more details on this approach, the reader is referred to the studies by Isele-Holder and co-workers.[1039,1040]

4.9.3. Comparison between Molecular Simulations and Experiments of Hydrogen−Water Interfacial Tensions.

Fig. 65(a) shows a comparison between experimental $H_2 - H_2O$ IFT data from Hosseini et al.[1017] with fitted MD data using the engineering correlations proposed by van Rooijen et al.,[630] Omrani et al.,[1018] and Xie et al.[1019] Notable deviations occur primarily below 325 K. Specifically, Xie et al.[1019] calibrated their model over a temperature range of 298−373 K and pressures of 5−40 MPa, whereas van Rooijen et al.[630] used a broader range of 298−523 K and 0.1−60 MPa. The weak pressure dependence of IFT observed experimentally by Hosseini et al.[1017] is qualitatively captured by Xie et al.,[1019] although their model exhibits roughly a 5% deviation and an overestimation of the pressure sensitivity, evidenced by a steeper slope. Conversely, the model by van Rooijen et al.,[630] assuming pressure independence, exhibits a deviation of ca. 10% from experimental data below 325 K, but aligns well (within 5%) at higher temperatures. Omrani et al.[1018] could not be directly compared due to their fit requiring gas-liquid density differences that were not provided. Fig. 65(b) shows a comparison of the experimental IFTs reported by Chow et al.[1041] with predictions from van Rooijen et al.[630] and Hosseini et al.,[1017] both achieving better than 5% agreement at temperatures above 370 K. Since Chow et al.[1041] also provided gas and liquid densities, Omrani et al.[1018] could be evaluated, revealing the near pressure independence of IFT, consistently with experiments, except for pressures above about 40 MPa, for which a notable decrease is observed. Overall, within their respective calibration ranges, the fit functions from Omrani et al.[1018] and Xie et al.[1019] achieve agreement within 1−10% of experimental values, while van Rooijen et al.[630] cover a broader range but remain within roughly 15%. Despite variability among MD-based predictions, the computed IFT values for $H_2 - H_2O$ systems consistently fall within approximately 10−15% of experimental measurements from Hosseini et al.[1017] and Chow et al.[1041]

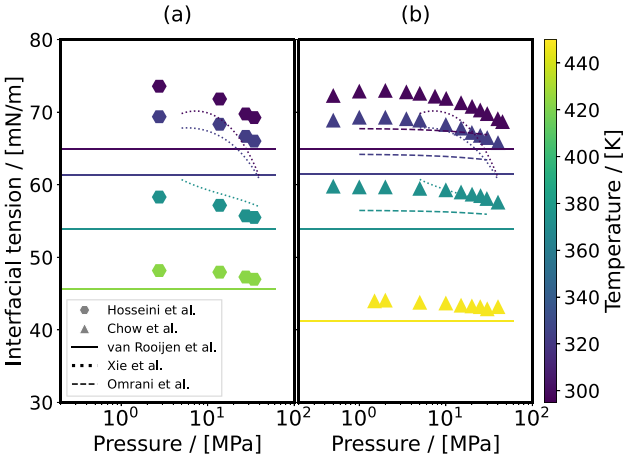

Figure 65. Interfacial tension of H_2-H_2O as a function of pressure. Comparison between experiments (from: (a) Hosseini et al.[1017] and (b) Chow et al.[1041] shown as markers) and engineering equations fitted with data from three different MD simulations(from van Rooijen et al.[630]: solid line, Omrani et al.[1018]: dashed line, and Xie et al.[1019]: dashed dotted line). The colors of the markers represent the temperature at which the interfacial tension is reported. The MD simulation predictions are plotted within the range where the equation remains valid.

https://doi.org/10.1021/acs.chemrev.5c00617
Chem. Rev. 2025, 125, 11878−12029

4.9.4. Interfacial Tensions of Hydrogen−Brine Systems. Fig. 66 illustrates the IFTs of H_2 − NaCl brine systems

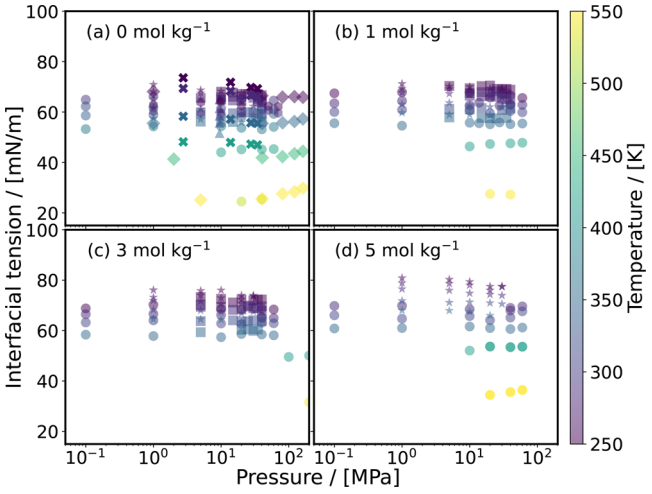

Figure 66. Interfacial tension of aqueous H_2-NaCl mixtures as a function of pressure computed from MD simulations for salt concentrations of (a) 0 mol of NaCl/kg of H_2O, (b) 1 mol of NaCl/kg of H_2O, (c) 3 mol of NaCl/kg of H_2O, and (d) 5 mol of NaCl/kg of H_2O. The colors of the markers represent the temperature at which the interfacial tension is reported. The data are taken from van Rooijen et al.[630] (circle), Omrani et al.[1018] (star), Xie et al.[1019] (square), Yang et al.[602] (diamond), Doan et al.[1021] (hexagon), and Chen et al.[604] (triangle). To facilitate comparison between simulations and experiments for pure water-H_2 system, the experimental data of Hosseini et al.[1017] (shown with marker x) is added in subfigure (a).

compiled from various studies (summarized in Table 19), collectively capturing key experimental observations such as the minimal sensitivity of IFT to pressure, the decreasing IFT with rising temperature, and increasing IFT with salt concentration. Fig. 66(a)-(d) predominantly show data points within pressure ranges of 1−50 MPa and temperatures of 300−400 K, relevant to UHS. For aqueous H_2 − systems, there is notable consistency across multiple studies, largely attributable to the widespread adoption of the TIP4P/2005 water model. Although various H_2 force fields (single-site versus multi-site) were used, the resulting discrepancies among the different studies[602,630,1018,1019] remain modest. However, the presence of salt significantly increases variability among predictions. Notably, at 298 K and 10 MPa, reported IFT values for aqueous H_2 systems without salt range from 64.9 to 68.2 mN/m across studies, whereas at a salt concentration of 3 mol NaCl/kg water yields IFTs in the range of 68.6 and 76.1 mN/m. While Omrani et al.[1018] and Xie et al.[1019] remain closely aligned, van Rooijen et al.[630] deviate by ca. 5%, potentially due to their use of a single-site H_2 model. Additionally, even studies using identical force fields for NaCl differ by around 5%, a discrepancy possibly intensified by the different choices for modeling long-range dispersion interactions relevant for correcting the IFTs (e.g., omitted in ref 1018). Overall, while TIP4P/2005[305] seems to ensure consistent and reliable IFT predictions for aqueous H_2, discrepancies emerge in H_2 − NaCl brine simulations due to variations in H_2 and salt force fields and methodological choices, such as neglecting long-range corrections. Despite these variations, most simulation predictions remain within a 5−10% margin, providing a reliable source of data for further experimentation, modeling, and industrial practice. Future refinements in force field development and selection, and accurate treatment of ionic interactions may further reduce these discrepancies and enhance predictive accuracy.

4.9.5. Interfacial Tensions of Gas Mixture−Hydrogen−Water Systems. Fig. 67 highlights the distinct differences in IFT behavior for gas mixtures involving H_2/CO_2 compared to those containing N_2 or CH_4. Specifically, the H_2/CO_2 mixture displays a notably steeper slope, indicating a more pronounced decrease in IFT with increasing pressure. This behavior primarily arises due to CO_2 being near or above its critical point (7.3773 MPa and 304.15 K), where its density can fluctuate significantly, often changing by an order of magnitude within a narrow pressure interval. For instance, at 323.15 K, the density of CO_2 can increase dramatically from around 100 kg/m^3 at 5 MPa to roughly 1000 kg/m^3 at 20 MPa. Such significant density changes drastically reduce the liquid-vapor density contrast, causing a marked reduction in IFT. In contrast, mixtures involving N_2 or NH_4 remain well within supercritical conditions over comparable pressure ranges, resulting in more moderate density variations and correspondingly flatter IFT profiles. Additionally, the presence of H_2 does not significantly alter these general trends; the substantial decrease in IFT is predominantly driven by the supercritical transition of CO_2. From a practical standpoint, e.g., for subsurface storage and enhanced oil recovery applications, these observations highlight the acute sensitivity of interfacial properties to pressure variations near the critical region of CO_2.

4.10. Contact Angles of Hydrogen−Brine−Solid Systems

Contact angle (CA) is a key metric of wettability, which governs how H_2 gas, brine, and rock interact at nanoscale interfaces in UHS. Wettability controls capillary trapping, migration, and flow efficiency, yet experimental CA measurements under reservoir conditions are often hindered by surface roughness, contamination, and the challenges posed by extreme pressures and temperatures. MD simulations help overcome these limitations by resolving atomistic-scale interfacial structures, capturing gas adsorption, water layering, and ion-specific effects, while systematically varying pressure, temperature, salinity, gas composition, and mineral surface chemistry. When validated with experimental data, accurate force fields enable MD-derived CAs to inform larger-scale reservoir models, bridging molecular-level insights with field-scale performance. In what follows, we review studies that use MD simulations to investigate the CAs of water/brine droplets on different mineral substrates. Among these substrates, quartz surfaces are particularly important due to their prevalence in sandstone formations and their highly variable surface chemistry. To interpret the wettability trends observed in MD studies, it is useful to first outline the different types of quartz surfaces based on their degree of hydroxylation, as defined by Zhuravlev:[1047]

- Q4 Quartz Surface: Dehydroxylated (0 nm^{-2} OH), weakly hydrophobic.
- Q3 Quartz Surface: Partially hydroxylated (≈ 4.7 nm^{-2} OH), strongly hydrophilic.
- Q2 Quartz Surface: Fully hydroxylated (≈ 9.4 nm^{-2} OH), hydrophilic but with some OH-OH hydrogen bonding that slightly reduces water affinity.

Understanding these surface chemistries provides essential context for interpreting how CA, and, by extension, wettability,

https://doi.org/10.1021/acs.chemrev.5c00617
Chem. Rev. 2025, 125, 11878−12029

Table 19. Summary of the MD Simulation Studies Investigating the IFTs of Hydrogen−Gas Mixtures in Contact with Water or Brine[a]

Study	System details		Thermodynamic conditions		
	Phases	Force fields	p / [MPa]	T / [K]	c_{salt} / [molal]
van Rooijen et al.[630]	H_2(g)	Vrabec[48]	0.1 to 60	298 to 523	
	H_2O(l)	TIP4P/2005[1042]	(Logarithmic)		
	Brine(l): Na^+ and Cl^-	Madrid-2019[1034]			0 to 5
Omrani et al.[1018]	H_2(g)	Marx and Nielaba[310]	1 to 30	298 to 373	
	H_2O(l)	TIP4P/2005[1042]	(Logarithmic)		
	Brine(l): K^+, Na^+ and Cl^-	Smith and Dang[374,1043]			0 to 5
	Brine(l): Ca^{2+}, Mg^{2+}	Aqvist[1044]			0 to 5
Xie et al.[1019]	H_2(g)	IFF[313]	5 to 40	298 to 373	
	CO_2(g)	Zhu[926]			
	H_2O(l)	TIP4P/2005[1042]	(steps of 5)		
	Brine(l): Na^+ and Cl^-	Smith and Dang[374,1043]			0 to 3
Yang et al.[602]	H_2(g)	IFF[336]	1 to 160 MPa	298 to 523 K	0
	H_2O(l)	TIP4P/2005[1042]			
Doan et al.[1021]	H_2(g)	IFF[313]	1 to 70	300 to 343	
	CO_2(g)	EPM2[419]			
	N_2(g)	OPLS[360]			
	H_2O(l)	TIP4P/2005[1042]			
Doan et al.[1020]	H_2(g)	IFF[313]	1 to 70	300 and 323	0
	H_2O(l)	TIP4P/2005[1042]			
Chen and Xia [605]	H_2(g)	IFF[313]	1 to 60	320	0
	H_2O(l)	TIP4P/2005[1042]			
Chen et al.[604]	H_2(g)	IFF[313]	9.5	300, 400	2.22 (in unitls of molarity)
	CO_2(g)	TraPPE[1045]			
	H_2O(l)	TIP4P/2005[1042]			
	Brine(l): Na^+ and Cl^-	Madrid-2019[1034]			
Adam et al.[1022]	H_2(g)	Yang[325]	10-60	323-388	1.9-4.75
	CO_2(g)	TraPPE[1045]			
	CH_4(g)	TraPPE[301]			
	H_2O(l)	TIP4P/2005[1042]			
	Na^+	Chen et al.[1046]			
	Cl^-	Chen et al.[1046]			

[a]The salt concentrations in brine are reported in units of molality (mol salt / kg of H_2O). g and l in the parentheses indicate gas and liquid phases, respectively.

responds to changes in thermodynamic conditions and compositions relevant to UHS. The classification also helps prevent confusion when these surface types appear throughout the following sections.

Abdel-Azeim et al.[603] investigated the CA of water droplets in a H_2 gas atmosphere on caprock minerals mica, anhydrite, gypsum, and halite, examining the effects of pressure (5 to 20 MPa), temperature (298 to 323 K), and salinity (deionized water, seawater with 60000 ppm total dissolved solids, and formation water with 213000 ppm TDS). The system focuses on pure H_2 gas without mixtures such as CH_4 or CO_2, and brines containing ions like Na^+, Ca^{2+}, Mg^{2+}, Cl^-, and SO_4^{2-} are used to represent different salinities. The CAs obtained for the water droplet on these mineral surfaces in a H_2 gas environment remain at or near zero degrees across all tested conditions, indicating strongly water-wet surfaces regardless of changes in pressure, temperature, or salinity. For example, in both MD simulations and sessile-drop experiments, the CA for water droplets on mica under H_2 pressure up to 20 MPa at 300 K was consistently zero, and similar behavior was observed on anhydrite, gypsum, and halite surfaces. The physical mechanism underlying these CA trends is attributed to the significantly stronger interactions between water molecules and the mineral surfaces compared to the interactions between H_2 molecules and the mineral surfaces. Water forms strong adsorption and hydrogen bonds especially on calcium sulfate minerals (gypsum and anhydrite) due to divalent cations like Ca^{2+}. In contrast, H_2 is nonpolar and exhibits weak hydrophobic interactions with the mineral surfaces, making it unable to displace water or alter wettability even at elevated pressures. Temperature and salinity influence water diffusion and spreading kinetics but do not affect the ultimate water-wet state. Among the studied factors, the intrinsic molecular interactions between water and mineral surfaces most strongly influence the CA, overriding effects from pressure, temperature, or salinity variations. CAs computed with MD simulations were validated by sessile-drop experiments on plasma-cleaned mineral surfaces, showing excellent agreement with near-zero CAs, whereas higher CAs reported in the literature were attributed to organic surface contamination on uncleaned samples. No general empirical fit function for CA as a function of pressure, temperature, and salt composition was proposed in this study.

Al-Yaseri et al.[607] studied the CAs of water droplets on quartz and calcite mineral surfaces in a pure H_2 gas environment over a pressure range of 3.44 to 206.8 MPa, temperatures from 298 K to 323 K, and brine salinities from deionized water up to 213000 ppm total dissolved solids, with

https://doi.org/10.1021/acs.chemrev.5c00617
Chem. Rev. 2025, 125, 11878−12029

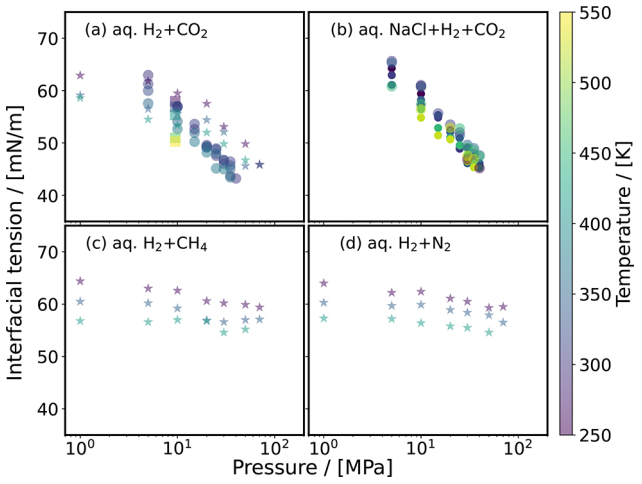

Figure 67. Interfacial tension of aqueous H_2-gas and H_2-gas-NaCl brine systems as a function of pressure computed with MD simulations. Gases considered in the H_2-gas-H_2O system are (a) CO_2, (c) CH_4, and (d) N_2. (b) For the H_2-gas-NaCl brine (3 mol kg^{-1}), we consider only CO_2 for comparison. The colors of the markers represent the temperature at which the interfacial tension is reported. The data are taken from Xie et al.[1019] (circle), Doan et al.[1021] (star), and Chen et al.[604] (square). For comparison, a hydrogen mole fraction of 0.7 is chosen from the three different studies.

no additional gas mixtures such as CH_4 or CO_2 considered. The CAs measured for the water droplet on these mineral surfaces in a H_2 gas environment remain at or near zero degrees across all tested pressures, temperatures, and salinities, indicating a completely water-wet system; for example, CAs on quartz and calcite were zero even at the highest pressure of 206.8 MPa and formation water salinity. The MD simulations reveal that the dominant physical mechanism behind the zero CA is the significantly stronger molecular interactions between water and the mineral surfaces compared to the weaker H_2-water and H_2-mineral interactions, with water diffusion coefficients on quartz and calcite surfaces decreasing with increased salinity and stronger water-calcite interactions resulting in slower spreading times. Surface cleanliness was found to be the most critical factor influencing the CA measurements, as contamination can lead to artificially higher CAs, particularly on calcite surfaces. The CAs obtained experimentally using a carefully controlled cleaning protocol with air plasma treatment were in excellent agreement with MD simulations, both confirming the zero CA findings, resolving discrepancies in the literature reporting higher and variable CAs. No general empirical fit function for CA dependency on pressure, temperature, or salinity was proposed in the study.

Al-Yaseri et al.[606] studied the wettability properties as quantified by CAs of H_2 gas bubbles on quartz surfaces in the presence of brine containing 0.5M Na^+ ions at room temperature and ambient pressure. The study focused on the quartz-brine-H_2 interface, including the effect of organic acids such as Humic acid on wettability alteration. MD simulations were performed to measure the CAs of pure H_2 bubbles on silica surfaces in deionized water and in 0.5M NaCl brine, yielding CAs of approximately 120° and 122°, respectively. These values indicate poor H_2 wettability, consistent with a strongly water-wet quartz surface. In the simulations, the quartz surface was "aged" by introducing a model hydrophobic layer representing Humic acid decomposition products, such as naphthenic acids and hexane, adsorbed onto the silica surface. This "aging" in MD refers to the surface modification step within the simulation framework rather than a physical experimental aging process. After this surface functionalization in the simulations, the CA of the H_2 bubble on the hydrophobized silica surface decreased significantly to about 44°, indicating a shift toward intermediate or H_2-wet conditions. This change is attributed to the hydrophobization of the silica surface by Humic acid, which enhances van der Waals interactions between H_2 molecules and the modified mineral surface, thereby promoting H_2 spreading. Experimentally, natural sandstone cores from the Lesueur Sandstone formation were aged by exposure to an aqueous Humic acid solution (10^{-2}M) for 42 days at 5°C and room pressure. This laboratory aging caused a wettability shift consistent with the MD results: the CA transitioned from strongly water-wet toward an intermediate wetting state. Although exact experimental CAs were not directly measured, the wettability alteration was inferred from changes in H_2 saturation and residual trapping, which are consistent with a CA reduction similar in magnitude to the 44° obtained in simulations. This study shows that the MD simulations capture the essential physics of wettability alteration by Humic acid.

MD simulations were conducted by Ali et al.[1048] to investigate the effects of varying gas compositions, including H_2, CO_2, and CH_4, on the wettability of kaolinite clay surfaces by brine droplets containing 10 wt% NaCl at 323 K and pressures between 5 and 40 MPa. The study focused on two distinct basal planes of kaolinite: the hydrophobic siloxane surface and the hydrophilic gibbsite surface, examining how CAs and IFTs respond to changes in pressure, temperature, and H_2 content. On the hydrophobic siloxane surface, CAs of brine droplets in pure H_2 environments ranged from approximately 91° to 106° over the pressure range studied, indicating an 'intermediate wet' behavior with relatively minor pressure dependence. When CO_2 was introduced as a cushion gas, the CAs increased significantly, ranging from about 118° at 5 MPa to nearly 160° at 40 MPa, corresponding to a transition from weakly gas-wet to strongly gas-wet surfaces. Mixtures of H_2 and CO_2 showed a marked reduction in the wettability of brine compared to pure H_2; for example, at 20 MPa, a system with 90 wt% CO_2 exhibited a CA of approximately 106°, lower than pure CO_2 but substantially higher than pure H_2. The effect of CH_4 as a cushion gas followed similar trends but was less pronounced than CO_2, with CAs increasing by up to 15° relative to pure H_2. Increasing pressure consistently increased CAs across all gas compositions, attributed to enhanced intermolecular interactions between the denser gas phases and the siloxane surface. Atomic density profiles revealed that CO_2 molecules adsorb closer to the siloxane surface (at approximately 2.7 Å) compared to CH_4 (ca. 3.1 Å) or H_2, effectively displacing some water molecules from the surface and reducing brine wettability. Water molecules form two distinct hydration layers near the surface, with gas molecules preferentially located within the first hydration layer; higher gas densities at elevated pressures amplify gas-surface affinity, further increasing CAs. On the hydrophilic gibbsite surface, H_2 formed cylindrical bubbles detached from the surface, indicative of strong water wettability and complete spreading of water. Increasing pressure from 20 to 80 MPa resulted in denser H_2 bubbles with reduced radius (from approximately 50.5 Å to 33.0 Å), reflecting increased water CAs and decreased H_2 affinity with the surface. Temperature increases from 303 K to

https://doi.org/10.1021/acs.chemrev.5c00617
Chem. Rev. 2025, 125, 11878−12029

343 K led to reduced affinity between H_2 and the gibbsite surface, suggesting an increase in wettability at higher temperatures due to a decrease in H_2 density. The presence of CO_2 in H_2 bubbles on the gibbsite surface reduced H_2 density near the surface, further influencing wettability trends. Regarding temperature effects on the gibbsite surface, the study indicated a less pronounced influence compared to pressure. However, higher temperatures tend to reduce gas density, and thus, gas affinity, which would increase wettability, although these effects were secondary to pressure-driven trends. These observations indicate that pressure and temperature influence wettability on the hydrophilic surface in manners similar to those on the hydrophobic siloxane surface but with overall stronger water affinity leading to complete wetting. Overall, the simulations demonstrate that the wettability of kaolinite surfaces by brine is significantly modulated by gas composition and thermodynamic conditions, with CO_2 causing the most substantial increase in gas-wetting behavior on the hydrophobic siloxane surface, followed by CH_4, while pure H_2 maintains intermediate wettability. Pressure predominantly governs these effects by altering gas density and gas-surface interactions, whereas temperature has a subtler role, particularly on the hydrophilic gibbsite surface. The simulated CA trends align well with experimental observations reporting increased CAs with pressure and stronger gas wetting for CO_2 compared to H_2, although some discrepancies exist due to differences in surface basal planes studied.

The study by Alshammari et al.[1049] focused on IFT and wettability of water−H_2 systems-pure and with cushion gases (CH_4, CO_2)-in brines containing Na^+, Mg^{2+}, Ca^{2+}, and Cl^-. Simulations were performed at 298-323 K, 5−20 MPa, and salinities from deionized to formation water. CAs of water on calcite and silica were evaluated up to 20 MPa at ≈ 300 K. pH was represented by tuning the ionization of surface silanol groups on silica slabs: 0% ionization (all silanols protonated) reproduce acidic conditions (pH ≈ 3), whereas 10% ionization (partial deprotonation) correspond to near-neutral pH ≈ 6. This shift from a neutral to a negatively charged surface alters rock-fluid interactions, moving the quartz CA from an intermediate value toward a strongly water-wet state as water molecules increasingly displaced adsorbed CO_2. In H_2 gas, calcite stayed strongly water-wet (CA ≈ 0°); quartz showed CA ≈ 56 - 75°, shifting toward intermediate wetting with changing gas mixtures and surface charge. The highest CA was in H_2/CO_2 at low pH, as CO_2 strongly adsorbs on protonated silica, thickening the interfacial gas layer and slowing water spread. In contrast, CH_4 and pure H_2 interact weakly, keeping CA lower. Barbosa et al.[1050] reported wettability, specifically CAs, of water and brine droplets containing NaCl (up to 20 wt %) on siloxane, gibbsite, and defective siloxane surfaces of kaolinite in the presence of gases including H_2, CH_4, and CO_2 across conditions relevant to underground H_2 storage, with pressure at 10 MPa, temperature at 323 K, and varying defect densities on the substrate. The CAs of brine droplets on the siloxane surface without gas are approximately 93°, indicating hydrophobic behavior, whereas on gibbsite surfaces CAs are about 13°, showing hydrophilicity; the presence of CO_2 significantly increases CAs (e.g., up to 131° on siloxane), while H_2 (95°) and CH_4 (100°) cause smaller increases. Increasing defect density on siloxane surfaces by removing up to 30% of silicon sites reduces CAs for brine droplets, e.g., from 84° to 68° in H_2 environments and from 111° to 83° in CO_2 environments, indicating enhanced wettability with more defects; CAs for pure water are generally lower than for brine and show greater variability. The physical mechanism behind these trends is attributed to stronger adsorption of CO_2 on heterogeneous surfaces displacing water and altering surface hydrophilicity, the formation of silanol nests at defect sites may alter hydrophilicity, and salt ions (Na^+, Cl^-) interacting with the surface to reduce CAs by modifying water-surface interactions. Surface defects, particularly their density and spatial coordination, most strongly influence CAs, with machine learning models showing improved prediction when defect arrangement is considered. The simulation data of CAs for brine on siloxane and gibbsite surfaces agree well with available experimental data, supporting the validity of the MD approach.

Fatah et al.[1051] performed MD simulations to compute the wettability and flow of H_2, CH_4, CO_2, and N_2 against 57-670 ppm brine (Na^+, Mg^{2+}, Ca^{2+}, Cl^-, SO_4^{2-}) on calcite at 25 °C and 1000 psi. In all cases the water droplet spread completely (CA ≈0°), confirming calcite is strongly water-wet; seawater-calcite interaction energies dwarfed gas-rock and water-gas terms. Although CO_2 adsorbed most strongly and its brine IFT was far lower than for H_2, CH_4, or N_2, these differences did not alter the CA. Hence gas type and brine composition exert negligible influence on calcite wettability, which is governed by the mineral's hydrophilicity, an insight vital for underground H_2-storage design.

Ghafari et al.[1052] used MD simulations to examine water CAs on silica surfaces in brine/gas environments under subsurface conditions (10 - 30 MPa, 333 - 413 K), with H_2 mole fractions varying from 0 to 1 and silica surface charges from 0 to -0.12 C m^{-2}. Binary gas mixtures of H_2 with CO_2, CH_4, or N_2 were considered at x_{H_2}=[0.0, 0.3, 0.7, 1.0], showing that increasing the mole fraction of cushion gases, especially CO_2, raises the CA, an effect amplified at higher pressures and lower temperatures. Five distinct silica surface models (Q2, Q3, and Q3/Q4 types) with silanol densities between 2.35 and 9.58 nm^{-2} were tested, with α-quartz (101) at 5.9 nm^{-2} serving as the reference substrate. Surface charges were introduced by deprotonating a fraction of surface silanol (Si-OH) groups: 0% ionization (all silanols protonated) represents acidic conditions, whereas 10% ionization (partial deprotonation) mimics near-neutral pH. On neutral silica in pure H_2, the CA remains low and nearly independent of pressure and temperature. For neutral surfaces, the four cushion gases increase the contact angle in the following order: CO_2 > CH_4 > N_2 > H_2. This trend arises from competitive gas adsorption, CO_2 has the strongest affinity for silica−forming a thicker adsorbed layer that impedes water spreading under high−pressure, low-temperature conditions while CH_4 and N_2 exhibit weaker adsorption, and H_2 the weakest. The surface charge exerts the most pronounced influence: As ionization increases to -0.12 C m^{-2}, the silica becomes strongly water-wet (CA → 0°) regardless of the composition, pressure, or temperature of the gas, because deprotonation enhances the electrostatic interactions between rocks and water that displace the adsorbed gas. Simulations of α-quartz (101) based on the INTERFACE force field closely reproduce experimental CA data, correcting the overestimation of hydrophilicity reported when using CLAYFF or DDEC force fields. These results emphasize that accurate force field selection and realistic

https://doi.org/10.1021/acs.chemrev.5c00617
Chem. Rev. 2025, 125, 11878−12029

surface characterization are essential for predicting wettability in brine−gas−rock systems relevant to UHS.

Atomistic MD simulations were conducted by Phan et al.[1053] to investigate the wetting properties of brine droplets containing 20 wt% Na^+ and 1 wt% K^+ on talc and the hydroxylated basal face of kaolinite (kaoOH) substrates in gas mixtures comprising H_2 and cushion gases (CH_4 or CO_2) at geological conditions of 15 MPa and 333 K, with varying gas compositions including pure H_2, 75 mol% H_2 - 25 mol% cushion gas, 60 mol% H_2 - 40 mol% cushion gas, and pure cushion gas. The CAs of brine droplets on talc surfaces were found to be strongly hydrophobic with values greater than 90°, increasing from approximately 102.6° in pure H_2 to about 143.4° with pure CO_2, and to ca. 112.4° with pure CH_4, whereas on the kaoOH surface the CAs remained consistently low, between 11.4° and 15.8°, regardless of gas composition. The authors attribute these trends to the differences in clay-brine interactions and surface chemistry, where talc's hydrophobic siloxane basal face leads to more favorable cavity formation near the surface (lower free energy) and thus higher CAs, while kaoOH's hydrophilic hydroxylated surface exhibits stronger water adsorption and higher free energy of cavity formation, resulting in lower CAs. Among the factors studied, the nature of the clay surface chemistry most strongly influences the CA. The simulation results for CAs on kaoOH closely agree with experimental data reporting values near 15° to 20°, while differences with some experiments on kaolinite siloxane faces are noted, likely due to variation in the specific basal planes studied.

Yang et al.[602] studied interfacial properties of the H_2 + H_2O and H_2 + H_2O + solid systems with silica and kerogen substrates over a broad range of temperatures (298 to 523K) and pressures (1 to 160 MPa). The study focused on pure H_2 gas mixtures without additional gases such as CH_4 or CO_2 and did not address salt concentration effects in brine; CAs of H_2O droplets on silica and kerogen surfaces in a H_2 gas environment were analyzed. The CAs of the H_2O droplet on silica surfaces ranged from approximately 21.8° to 49.0° and generally increased with pressure while decreasing with temperature, with less pronounced temperature and pressure effects at low temperatures (298 and 373 K). For kerogen surfaces, the CAs ranged from 0° (fully water-wet) to about 61.9°, showing a decrease with increasing temperature and an increase with pressure, with CAs increasing from 0° to 31.4° as pressure rose from 5 to 160 MPa at 523 K. These CA trends were explained through variations in the IFT between H_2O-rich and H_2-rich phases and adhesion tensions representing fluid-solid interactions; the adhesion tension is defined as the difference between the IFT of the solid with the H_2-rich phase and that with the water-rich phase, reflecting the fluid-solid interaction contribution to wettability. Adhesion tensions decreased significantly with temperature and showed moderate pressure dependence on silica but decreased with pressure on kerogen, especially at lower temperatures. The strongest influence on CAs was identified as the balance between fluid-fluid IFT and fluid-solid adhesion tension, which both vary with temperature and pressure. CAs obtained from MD simulations were consistent with previous simulation studies and showed qualitative agreement with experimental trends, although absolute values for silica were somewhat higher likely due to differences in surface silanol group density; no explicit quantitative fit to experimental CAs was reported.

The MD study by Yao et al.[1054] examined bulk and interfacial properties (IFT and water−silica CAs) in H_2/brine systems, i.e., NaCl, KCl, $CaCl_2$, over 323 - 423 K, 14 - 150 MPa, and up to 5.4 mol/kg salt, and provided comparisons with CO_2/brine/silica systems. CAs on silica in H_2/brine span roughly 42.5° to 72.2°, as salt increases from 0 to 5.4 mol/kg in the order KCl < NaCl ≈ $CaCl_2$. Pressure and temperature effects on the angle are otherwise minor. By measuring cos θ (CA) and γ_{WG}(brine-gas surface tension), the authors use Neumann's equation,[1055] with an empirical constant β, to evaluate γ_{SG} (solid-gas surface tension) and γ_{SW} (solid-brine surface tension), though γ_{SG} and γ_{SW} are challenging to directly obtain. They report γ_{SG} remains effectively constant with salinity (whether imposed or derived is unclear from their article), and as a result γ_{SW} decreases as salt concentration rises. Consequently, the adhesion tension ($\gamma_{SG} - \gamma_{SW}$) falls with salinity, explaining the larger CAs. Beyond noting these interdependencies, the study does not draw further conclusions from the trend in γ_{SW} alone. It seems that ion exclusion (negative surface excess) raises γ_{WG} and shifts the force balance at the contact line and drives the wettability behavior. Salt concentration thus most strongly controls the CA by altering adhesion tension. The computed angles and IFTs compared reasonably well with experimental data for H_2/NaCl brine on silica, though some discrepancies remain, likely due to force−field limitations.

Yu et al.[1056] performed MD simulations to compute the CAs of water droplets on organic-rich shale surfaces, represented by graphene, in pure H_2 environments and H_2-CH_4 and H_2-CO_2 gas mixtures, over pressure ranges from 5 to 40 MPa and temperature ranges from 292 to 343 K, with gas mole fractions varying from 25% to 100% H_2; salt concentration and specific brine ion effects are not explicitly modeled but are noted as future considerations. The CA of water on these substrates generally decreases with increasing temperature by up to about 5.8° at an intermediate pressure of 5 MPa and increases with increasing H_2 pressure by roughly 20° from 5 to 40 MPa, indicating a shift toward less water-wet conditions; in CO_2-H_2 mixtures, CAs remain high at 180° (fully gas-wet) when the H_2 fraction is below 25% and sharply decrease to strongly water-wet values around 22° as H_2 fraction approaches 100%, while in CH_4-H_2 mixtures, the system transitions from moderately gas-wet to strongly water-wet as H_2 fraction increases, with a neutrally wet state defined by CAs near 90° at about 75% CH_4. These trends are explained by molecular interactions where increased temperature (292−343 K) reduces H_2 density and adsorption due to higher kinetic energy, weakening H_2-surface interactions and lowering CAs, whereas increased pressure (5−40 MPa) enhances H_2 density and adsorption, increasing CA; competitive adsorption in gas mixtures causes preferential adsorption of CO_2 and CH_4 over H_2, influencing wettability and CA behavior. CA results from molecular simulations agree qualitatively with experimental data on H_2-organic shale systems but show variations attributed to differences in rock composition, surface roughness, and experimental uncertainties.

The study by Zhang et al.[1057] focused on CAs of H_2 with brines of varying salinity (up to about 1 mol/L NaCl) on mineral substrates quartz, calcite, halite, and montmorillonite, across pressure ranges of 5 to 25 MPa and temperatures from 300 to 400 K. The CAs of water on these mineral surfaces in a H_2 gas environment were examined using MD simulations under these reservoir-like conditions. CAs generally increase

https://doi.org/10.1021/acs.chemrev.5c00617
Chem. Rev. 2025, 125, 11878−12029

with pressure; for example, CAs for quartz increased from approximately 25° at 5 MPa to about 40° at 25 MPa. Temperature effects on CAs are less pronounced. For all substrates, CA slightly decreases (by ca. 5°) when temperature increases from 300 to 400 K. Salinity increases tend to raise CAs by ca. 5°, except for calcite where the effect is negligible, less than 1° change up to 1 mol/L NaCl. The authors observe that the variation in the bulk density of H_2 with pressure correlates with the cosine of the contact angle: as the bulk density of H_2 increases with pressure (from ca. 5 kg/m^3 to 20 kg/m^3 between 5 and 25 MPa), the cosine of the contact angle decreases. Electrostatic interactions and the electrical double layer on charged minerals like montmorillonite enhance water wettability strongly, contributing up to 50% of the total interaction energy. Among the investigated factors, pressure, via its effect on H_2 density, exerts the strongest influence on CA. The simulated CAs were compared to various experimental measurements, showing reasonable agreement especially for clean mineral surfaces, with discrepancies attributed to organic surface contamination and surface heterogeneity in experiments. The authors propose a theoretical model based on a sharp-kink approximation that relates CA to H_2 density, IFT, and water-mineral interaction energy, which can predict trends of CA as functions of pressure, temperature, and salinity.

Using MD simulations Zheng et al.[609] studied the wettability of pure water droplets on quartz substrates in the presence of H_2 gas under various geo-storage conditions, covering pressures from 1 to 30 MPa and temperature fixed at 338 K. The study focuses on pure H_2 environments and considers hydroxylation states of quartz surfaces (Q2, Q3, and Q4 quartz). The CA of water on fully hydroxylated quartz surfaces in a H_2 environment fluctuates between approximately 30.7° and 37.1° across the pressure range studied, with CAs increasing from 4.5° on partially hydroxylated quartz (Q3) to 34° on fully hydroxylated quartz (Q2), and reaching 94.7° on dehydroxylated quartz (Q4), indicating a transition from hydrophilic to weakly hydrophobic behavior depending on surface chemistry. The authors attribute these CA trends primarily to the flexibility of the quartz substrate and the arrangement and area density of surface hydroxyl groups, where hydrogen bonding probability between water and hydroxyl groups strongly dictates hydrophilicity; the CA increase with hydroxyl density is nonmonotonic due to intramolecular hydrogen bonding among surface hydroxyls reducing available bonding sites for water. The simulated CAs fall within the range of experimental measurements reported in the literature, confirming the validity of the MD models, although discrepancies in pressure dependence of CA observed experimentally are suggested to arise from surface roughness and experimental conditions. No general empirical fit function for CA as a function of pressure, temperature, or salt composition is proposed in this work.

The study by Zheng et al.[608] focused on the wettability of quartz surfaces with varying surface chemistries and morphologies under subsurface H_2 geo-storage conditions, examining the effects of pressure up to 1000 MPa, temperature at 338 K, NaCl concentrations from 0 to 1.0 mol%, and gas mixtures including pure H_2 and H_2-CH_4 mixtures with CH_4 mole fractions up to 50 mol%. CAs of water droplets on fully hydroxylated, half-methylated, fully methylated, pristine, and rough quartz surfaces in H_2 and H_2-CH_4 environments are quantified to understand wetting behavior. For fully hydroxylated (non-methylated) quartz surfaces, the water CA remains consistently near 34° across NaCl concentrations, showing negligible influence from salinity. Similarly, the addition of CH_4 as cushion gas only slightly increases the CA to about 36.1°, indicating minimal wettability change. With pressure variation up to 30 MPa, the CA on fully hydroxylated quartz fluctuates modestly between approximately 30.7° and 37.1°, driven primarily by the pinning effect due to surface heterogeneity at low pressures, and transitions to H_2-quartz interaction dominance at higher pressures. The fully hydroxylated rough quartz surfaces also exhibit a distinct jump in CA between 38 and 70 MPa, corresponding to a transition in the water film state on the rough surface. Moving to half-methylated quartz surfaces, CAs decrease from about 45.9° to 31.2° as NaCl concentration rises to 0.5 mol%. In H_2-CH_4 mixtures, the half-methylated quartz surfaces show a notable CA decrease from 45.9° to 32° with CH_4 mole fraction increasing to 20 mol%, followed by a slight increase at higher CH_4 content. The variation of CA with pressure on half-methylated quartz is non-monotonic, increasing from 41.2° to 49.3° between 1 and 20 MPa, then slightly decreasing at 30 MPa; this behavior is attributed to a competition between the pinning effect caused by surface heterogeneity (including organic ligand distribution) at low pressures and H_2-quartz interactions at higher pressures. Finally, for fully methylated quartz surfaces, the CA of water increases significantly with methylation degree, rising from about 32° at 12.5% methylation to 96.4° at 87.5% methylation. Interestingly, a slight decrease in CA from 34° to about 32° is observed when methylation increases from 0 to 12.5%, explained by the dual role of methyl groups: while their hydrophobic nature reduces surface hydrophilicity at high methylation, at low methylation they suppress hydrogen bonding among surface hydroxyl groups, thereby enhancing hydrophilicity. The study highlights that methylation degree is the strongest factor influencing the CA, whereas pressure and salinity effects are strongly dependent on the quartz surface chemistry and morphology. Simulated CAs for water on fully hydroxylated quartz in H_2 at 10 MPa and 338 K are ca. 34°, aligning well with experimental values ranging from 30° to 40°. This research reconciles prior experimental discrepancies by considering detailed variations in surface morphology and chemistry.

Chen et al.[604] computed interfacial properties including CA, IFT, surface excess, and bubble morphology of CO_2/H_2 mixtures in contact with brine containing Na^+ and Cl^- ions and hydrophilic silica surfaces, over pressure of 10 MPa and temperature range 300-400 K, with gas mixtures varying in H_2 mole fraction from pure H_2 to CO_2-rich systems and brine salt concentration of ca. 2.22 molal. The CAs of CO_2 and H_2 bubbles on hydrophilic silica in H_2O and brine environments are greater than 100°, with CO_2 showing smaller CAs (e.g., 109.8° to 134.3° for CO_2 and up to 156.8° for H_2) indicating stronger wetting affinity to silica compared to H_2; salts reduce CA, particularly at low temperatures, and CA for CO_2 increases with temperature while that of H_2 is less sensitive. The authors attribute CA trends to molecular interactions where CO_2 has stronger electrostatic and hydrogen bonding interactions with H_2O and silica surfaces due to its quadrupole moment, while H_2 interacts weakly via van der Waals forces; NaCl ions modify surface polarity by forming an electrical double layer reducing CA, and temperature affects dissolution and diffusivity impacting wetting behavior. CAs predicted by MD simulations are consistent with available experimental

https://doi.org/10.1021/acs.chemrev.5c00617
Chem. Rev. 2025, 125, 11878−12029

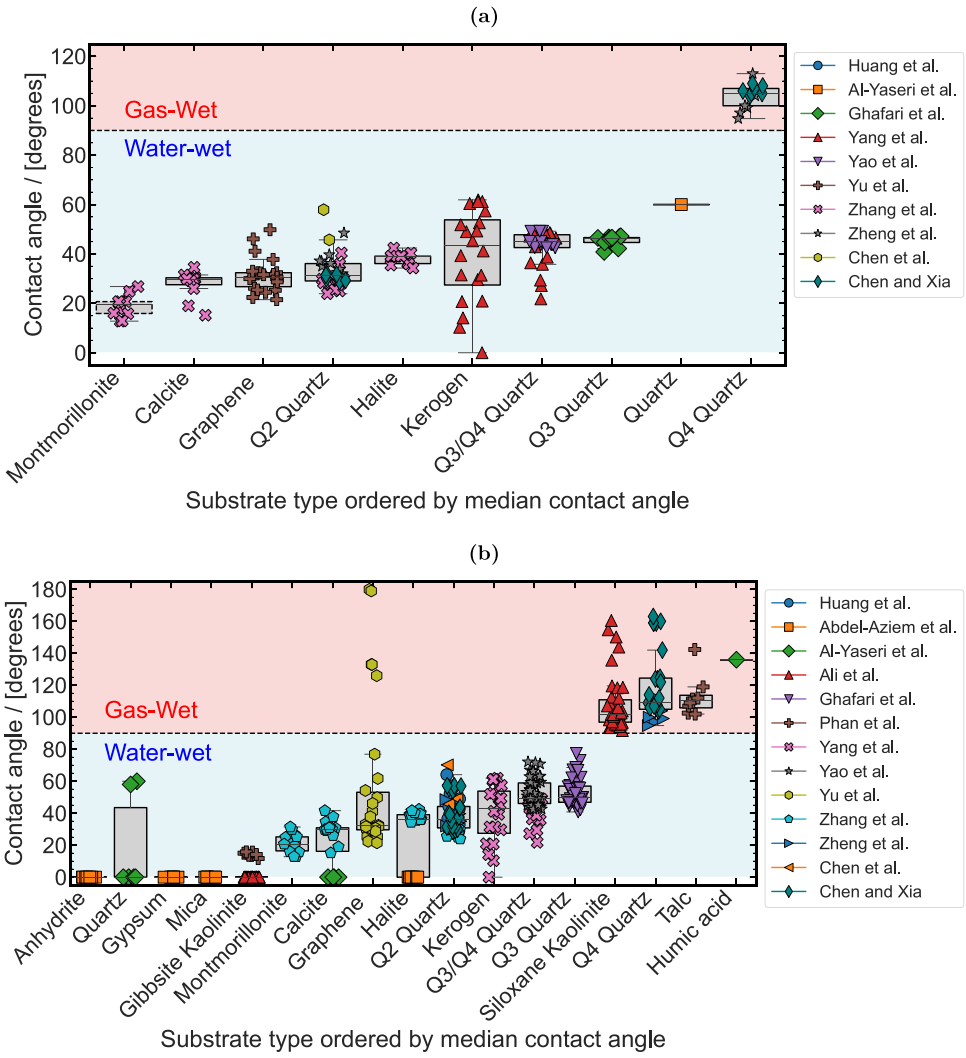

Figure 68. (a) Data for contact angles of pure water droplets immersed in pure H_2 for different substrates collected from multiple studies. Angles below 90° indicate water-wet surfaces, while those above 90° indicate gas-wet surfaces. All reported contact angles are shown regardless of temperature and pressure. (b) Data for contact angles of water/brine droplets immersed in a gas environment (pure H_2, H_2-CO_2, H_2-CH_4) collected from different sources. The complete list of studies and their temperature ranges are listed in Table 20.

data, showing similar trends in temperature and pressure dependence, although direct quantitative comparison is limited by experimental uncertainties and system complexities.

MD simulations were performed by Chen and Xia[605] to investigate the transport and interfacial properties including density, viscosity, diffusion coefficient, wettability, IFT, and surface adsorption of H_2, CO_2, and CH_4 gases interacting with H_2O and silica substrates under typical subsurface reservoir conditions at a temperature of 320 K and pressures up to 60 MPa. The study focused on CAs of water droplets on two types of silica substrates, hydrophilic Q2 and hydrophobic Q4, in environments containing pure H_2, CO_2, or CH_4 gases. The CA of water on both Q2 and Q4 silica substrates generally increased with gas pressure for CO_2 and CH_4, reaching plateaus between 10 and 30 MPa, with CO_2 showing the highest CAs, followed by CH_4, and then H_2, which had minimal effect even up to 60 MPa. For example, the CA on hydrophobic Q4 silica was about 106° without gas and increased to approximately 142° in a CO_2 environment at 10 MPa, whereas H_2 caused negligible changes in CA under all pressures. The physical mechanism explaining these trends arises from the differences in intermolecular interactions: CO_2 exhibits strong electrostatic interactions with silica due to its quadrupole moment, leading to higher wettability and increased CAs, while H_2 interacts weakly via van der Waals forces and has low adsorption capability on silica surfaces, resulting in little alteration of the water CA. The CA correlates inversely with the gas−water IFT, which remains nearly constant for H_2 but decreases significantly with pressure for CO_2. Gas pressure, particularly of CO_2, is the most influential factor affecting CA, while substrate hydrophilicity or hydrophobicity also plays a significant role in baseline CA values. MD results for CAs show good qualitative agreement with available experimental data for CO_2 and CH_4 systems, although some discrepancies exist regarding the pressure dependence of CAs in H_2 environments.

Huang et al.[1058] performed MD simulations to study CAs of deionized water and brine droplets containing Na^+ and Cl^- ions on fully hydroxylated α-quartz (Q2 surface) substrates under varying gas environments including pure H_2, CH_4, and CO_2 gases. The simulations are conducted at a temperature of 333 K and a pressure of 20 MPa, with brine salinities of ca. 1.5 M and 3.5 M, mimicking typical geological conditions relevant for underground gas storage and recovery. The CA of water

https://doi.org/10.1021/acs.chemrev.5c00617
Chem. Rev. 2025, 125, 11878−12029

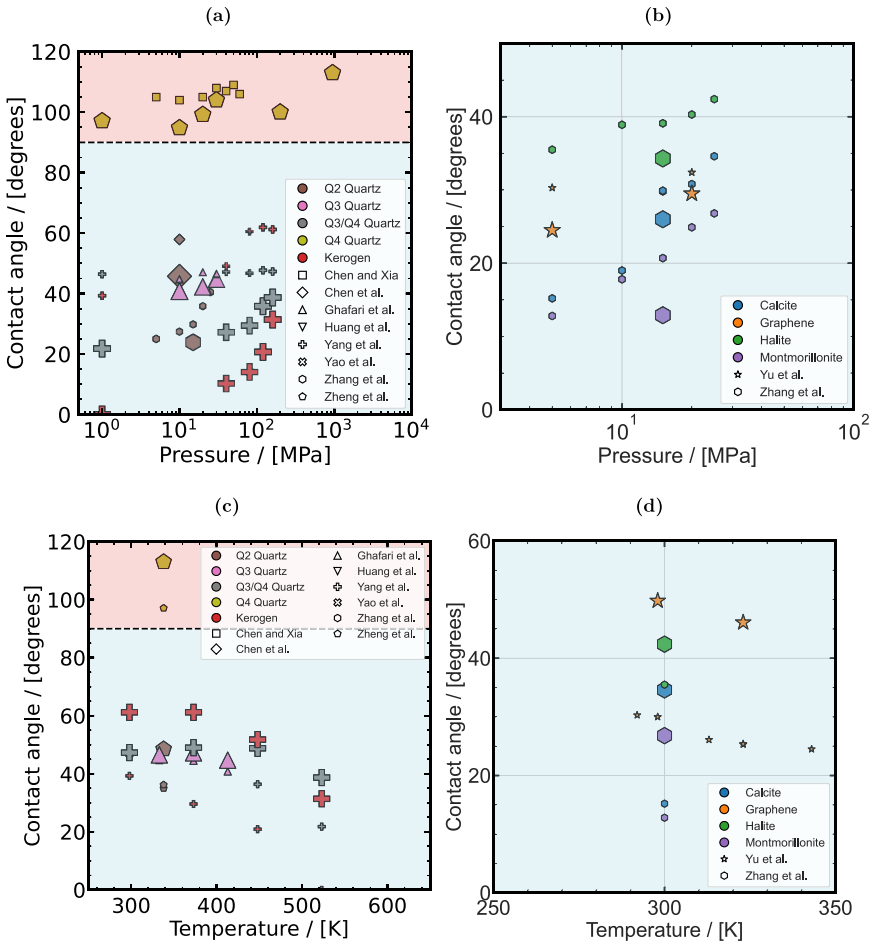

Figure 69. Computed contact angles of pure water droplets immersed in H_2 as a funtion of pressure (a: low pressure data and b: high-pressures data) and temperature (c and d: all pressures reported) compiled from multiple studies. Angles below 90° denote water-wet surfaces, while those above 90° denote gas-wet surfaces. From each study, only the data with the lowest and highest pressures/temperatures are shown. The marker size represents the magnitude of pressure/temperature: In (a) and (b) large and small symbols represent high and low temperatures, respectively, and in (c) and (d) large and small symbols represent high and low pressures, respectively. A complete list of the studies and the respective temperature ranges are provided in Table 20.

droplets on quartz in the presence of different gases follows the order $\theta_{H_2} < \theta_{CH_4} < \theta_{CO_2}$, with all values below 50°, indicating a strongly hydrophilic surface; the presence of salt ions generally increases the CA regardless of the gas type, thus reducing wettability. This trend is explained by the authors through interaction energy analyses showing that gas-quartz interactions decay faster than gas - water interactions, with the gas-quartz interaction energies ordered as $CO_2 > CH_4 > H_2$, while water-quartz interactions remain relatively constant and dominated by electrostatic forces (≈ 95%), minimally affected by salt ions; the increased CA with salinity is attributed primarily to the augmented gas−water IFT caused by salt addition. The gas species type most strongly influences the CA, with CO_2 producing the largest values due to its stronger van der Waals and electrostatic interactions with quartz, and salt concentration also plays a significant role by increasing IFT and thus CA. The computed CAs are consistent with experimental observations showing quartz surfaces are more hydrophilic in H_2 environments and become less hydrophilic with increasing salinity.

4.10.1. Effect of Substrate Material, Pressure, Temperature, and Salinity on the Computation of Contact Angles. Based on the studies reviewed above, it is clear that the CA of a water droplet varies with substrate, salt concentration, pressure, temperature, and surrounding gas composition. In Fig. 68(a), CAs collected from multiple studies[602,604,605,607,609,1052,1054,1056−1058] are shown. These data are shown irrespective of the pressure and temperature conditions to isolate substrate effects. A clear trend emerges where all substrates except Q4 Quartz are hydrophilic (water-wet in UHS terminology), with CAs below 60 degrees. In contrast, Q4 Quartz shows CA values of ca. 100 degrees, indicating weak hydrophobic (gas-wet) behavior. This aligns with its dehydroxylated surface having negligible hydroxyl group density (0 nm^{-2}),[1047] which limits hydrogen bonding. Also evident in Fig. 68(a) is the consistency across studies, i.e., CAs for Q2 Quartz, Q3/Q4 Quartz, and Q4 Quartz agree within 20 degrees. The key message is that CAs can range from 0 to 120 degrees depending on the substrate, with substrate effects outweighing those of pressure and temperature. To further emphasize this, Fig. 68(b) compiles CA data for water or brine droplets, regardless of pressure, temperature, salt concentration, or surrounding gas. Here, CAs span 0 to 180 degrees. Non-wetting substrates such as the siloxane surface of Kaolinite, Q4 Quartz, Talc, and Humic acid stand out clearly. Graphene also shows a non-wetting trend in the study by Yu et al.,[1056] with CAs above 90 degrees due to exposure to CO_2,

https://doi.org/10.1021/acs.chemrev.5c00617
Chem. Rev. 2025, 125, 11878−12029

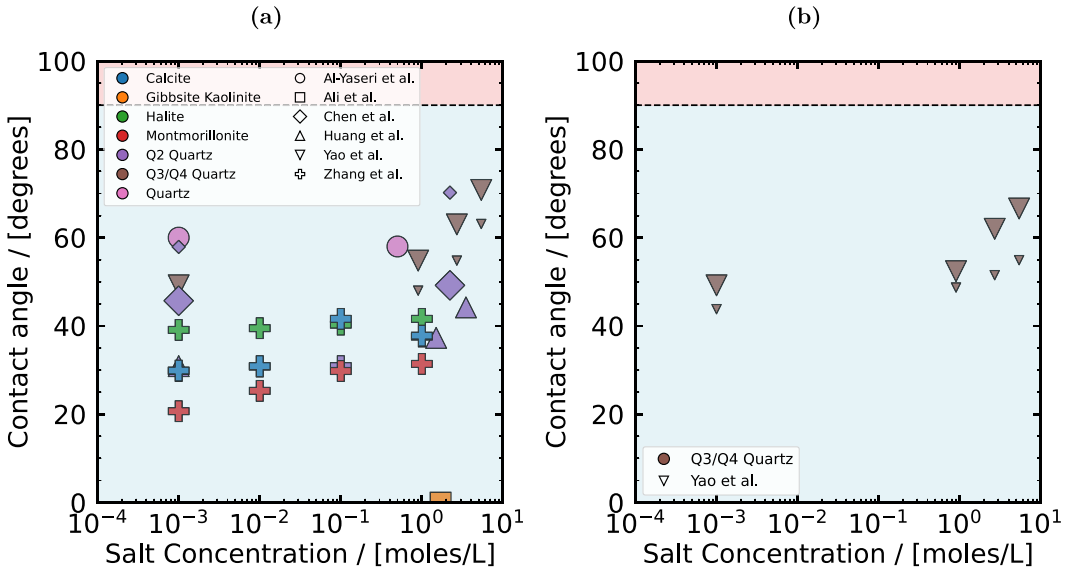

Figure 70. Data for contact angles of pure water droplets immersed in pure H_2 as a function of salt concentration of (a) NaCl and (b) KCl, compiled from multiple studies. Angles below 90° indicate water - wet surfaces (blue shade), while those above 90° indicate gas - wet surfaces (red shade). All reported pure-water CAs from each study are included, regardless of pressure and temperature. The CA data for the largest pressure and largest temperature is represented by larger - sized symbol and the smaller symbol represents the CA at the lowest pressure and lowest temperature by the same study. All CA data at intermediate pressures and temperatures are omitted for visual clarity. The complete list of studies and their pressure ranges are listed in Table 20.

which reduces water adsorption. Similarly, Ali et al.[1048] report brine droplets on Q4 Quartz with CAs ranging from 100 to 180 degrees depending on the CO_2 content in the environment surrounding the bubble. Chen and Xia[605] further show that water on Q4 Quartz in CO_2 exhibits a CA increase of nearly 60 degrees with pressure. In summary, surface chemistry has the strongest influence on CA, followed by the effect of CO_2 composition on substrates like Graphene[1056] and Q4 Quartz.[1048]

In Fig. 69(a) and Fig. 69(b), the effect of pressure across different substrates is shown. Clearly, CA increases with pressure. Data from Yang et al.[602] in Fig. 69(a) (small and large plus symbols) show CA rising from 0 to 30 degrees on Kerogen and from 20 to 40 degrees on Q3/Q4 Quartz as pressure increases from 1 to 160 MPa. A similar trend is reported by Zhang et al.,[1057] where CA increases from 25° to 40° at T = 300 K. Notably, Zheng et al.[608] computed CAs over a wide pressure range (1 - 1000 MPa) on Q4 Quartz and observed a maximum variation of only about 20 degrees. In contrast, Ghafari et al.[1052] have shown that CAs are weakly dependent on pressure shown specifically for water droplets on Q3 Quartz (pink triangles in Fig. 69(a)). In Fig. 69(b), contact angles on Calcite, Montmorillonite, and Halite from Zhang et al.[1057] show a modest increase with pressure. By contrast, Yu et al.[1056] in Fig. 69(b), and Chen et al.[604] in Fig. 69(a), report no clear pressure dependence. Overall, pressure tends to increase CA, although the effect is relatively weak. The underlying mechanism, as suggested by several authors, involves gas adsorption density increasing more strongly near the substrate than that of the liquid, due to gas compressibility. This enhances gas−substrate interactions, shifting the interfacial balance and increasing CA.

The effect of temperature on the CAs of water droplets is shown in Fig. 69(c) and Fig. 69(d). One can observe that increasing temperature reduces CA, enhancing water-wetness. In the study by Yang et al.[602], water droplets on Kerogen show a clear decrease in CA with temperature: at 160 MPa (large plus symbols), CA drops from 60° to 30°, and at 1 MPa (small plus symbols), from 40° to 0°. On Q3/Q4 Quartz, however, the reduction is less pronounced. At 1 MPa, CA decreases from approximately 45° to 20°, and at 160 MPa, from 45° to 40°, indicating substrate-dependent variation with temperature. Yang et al.[602] attribute this trend to weakened H_2 adsorption at higher temperatures, where entropic contributions dominate, allowing water to spread more readily by displacing gas molecules—a mechanism likely applicable to other gases as well. Similarly, CA variation on Q3 Quartz (pink triangles) in Ghafari et al.[1052] is minimal. As shown in Fig. 69(d), Yu et al.[1056] also reported a decrease of about 10° in CA for water on graphene as temperature increases from 260 to 340 K. As a concluding remark we can say that rising temperature weakens gas adsorption, facilitating water spreading and reducing contact angles.

The effect of salt concentration on the CAs of water droplets is shown in Fig. 70. It can be observed that increasing salt concentration raises CA by reducing water-wetness. In Fig. 70(a), the CAs of NaCl brine droplets from Yao et al.[1054] (Q3/Q4 Quartz) and Zhang et al.[1057] (Montmorillonite, Calcite, Halite, and Quartz, overlapping markers) show a clear increasing trend with salt concentration. Huang et al.[1058] reported a similar rise on Q2 Quartz. Thus, despite variations in substrate type, CAs consistently increase with salt concentration. Notable exceptions include Al-Yaseri et al.[607] and Chen et al.,[1046] where CA remains largely unchanged with increasing salt. In Fig. 70(b), Yao et al.[1054] show that KCl exhibits a similar trend on Q3/Q4 Quartz. Therefore, increasing the concentration of either NaCl or KCl appears to similarly increase CA. This rise is attributed to ion accumulation in the water bulk, which lowers the water-H_2 IFT.[1054] At the same time, the adhesion tension (difference between solid-brine and solid-gas interfacial energies) adjusts

https://doi.org/10.1021/acs.chemrev.5c00617
Chem. Rev. 2025, 125, 11878−12029

Table 20. Summary of the MD Simulation Studies Investigating the CAs in aqueous brine-H_2 Gas Mixture-Solid Systems.[a]

Study	System details		Thermodynamic conditions		
	Species	Force field	p [MPa]	T [K]	c_{salt} [mol / L of solvent]
Abdel-Azeim et al.[603]	Flexible H_2	IFF[313]	5 and 20	300 and 323	0
	H_2O	SPC/E[346]			
	$KAl_2(Si_3Al)O_{10}(OH)_2$ (Mica)	ClayFF[422]			
	$CaSO_4.2H_2O$ (Gypsum)	ClayFF[422]			
	$CaSO_4$ (Anhydrite)	ClayFF[422]			
	NaCl (Halite)	ClayFF[422]			
	Brine : Na^+, Ca^{2+}, Mg^{2+}	Aqvist[1044]			0.001, 0.007
	Brine : SO_4^{2-}, Cl^-, HCO_3^-	Chandrashekhar[1059]			0.001, 0.007
Huang et al.[1058]	H_2	Alavi[1060]	20	333	1.5 and 3.5
	CO_2	Aimei et al.[926]			
	CH_4	TraPPE[301]			
	H_2O	OPC4[1061]			
	Na^+Cl^- and	Yagasaki et al.[1062]			
	Quartz (Q2)	INTERFACE[1063]			
Ali et al.[1048]	H_2	Buch[312]	5−80	303−343	1.7
		Marx[310]			
	CO_2	Cygan et al.[927]			
	CH_4	[301]			
	H_2O	SPCE[346]			
	Na^+Cl^- and	Joung and Cheatham [371]			
	Kaolinite	[422]			
Chen and Xia[605]	H_2	IFF[313]	5 to 60	320	0
	H_2O	TIP4P/2005[1042]	(steps of 5)		
	SiO_4 (Q^2 Silica)	INTERFACE[425]			
	SiO_4 (Q^4 Silica)	INTERFACE[425]			
Chen et al.[604]	H_2	IFF[313]	10	300, 400	0 and 2.22
	H_2O	TIP4P/2005[1042]			
	SiO_4 (Q^2 Silica)	INTERFACE[425]			
	Brine : Na^+ and Cl^-	Madrid-2019[1034]	10	300, 400	NA
Al-Yaseri et al.[606]	H_2 (G)	IFF[313]		300	
	H_2O	SPC/E[346]			
	Na^+	Aqvist[1044]			0.5
	Cl^-	Chandrashekhar[1059]			0.5
	Humic Acid	OPLS-AA[360]			
	SiO_4	CLAYFF[422]			
Al-Yaseri et al.[607]	H_2	IFF[313]	5, 20	300, 323	
	H_2O	SPC/E[346]			
	Na^+, Ca^{2+}, Mg^{2+},	Aqvist[1044]			0.001, 0.007
	Cl^-	Chandrashekhar[1059]			
	SiO_4 (S, Silica)	CLAYFF[422]			
	$CaCO_3$ (S, Calcite)	Xiao[1064]			
Yang et al.[602]	H_2	IFF[1060]	1 to 160 MPa	298 to 523 K	0
	H_2O	TIP4P/2005[1042]			
	SiO_4 (Q^3/Q^4 Silica)	INTERFACE[422]			
	$C_{175}H_{102}O_9N_4S_2$ (II-D, Kerogen)	CVFF[427]			
Zheng et al.[608]	H_2	Three-site model[1060]	1 to 30 MPa	338 K	0, 0.5, 1
	CH_4	OPLS-AA[360,1065]			
	H_2O	SPC/E[346]			
	Na^+, Cl^-	Joung and Cheatham[371]			
	SiO_4 (Quartz) (Q^3/Q^4 Silica)	CLAYFF[422]			
Zheng et al.[609]	H_2	Three-site model[1060]	1, 10, 20, and 30	338	0
	H_2O	SPC/E[346]			
	SiO_4 (S, Q^3/Q^4 Silica)	CLAYFF[422]			
Alshammari et al.[1049]	H_2	IFF[313]	0.1−70	293−373	NA
	CH_4	OPLS-AA[360,1059]			
	CO_2	Cygan et al.[927]			
	H_2O	SPCE[346]			
	Na^+Cl^-	OPLS-AA[360]			
	Mg^{2+}	Aqvist [1044]			

https://doi.org/10.1021/acs.chemrev.5c00617
Chem. Rev. 2025, 125, 11878−12029

Table 20. continued

Study	System details		Thermodynamic conditions		
	Species	Force field	p [MPa]	T [K]	c_{salt} [mol / L of solvent]
	Calcite	Xiao et al.[1064]			
	Silica	INTERFACE[1063]			
Barbosa et al.[1050]	H_2	Buch [312]	10	323	20 wt%
	CO_2	Cygan et al.[927]			
	CH_4	TraPPE[301]			
	H_2O	SPCE[346]			
	Na^+Cl^-	Joung and Cheatham [371]			
	Kaolinite (siloxane, gibbsite)	CLAYFF[422]			
Fatah et al.[1051]	H_2	IFF[313]	6.9	298.15	NA
	N_2	IFF[313]			
	CO_2	Cygan et al.[927]			
	CH_4	OPLS-AA[360]			
	Na^+, Mg^{2+}, Ca^{2+}	Aqvist [1044]			
	Cl^-	OPLS-AA[360]			
	SO_4^{2-}	Cannon et al.[1066]			
Ghafari et al.[1052]	H_2	IFF[313]	10−30	333−413	0
	CO_2	Cygan et al.[927]			
	CH_4	TraPPE[301]			
	N_2	IFF[313]			
	H_2O	SPC/E[346]			
	Na^+Cl^-	Smith and Dang [374]			
	Silica	INTERFACE[1063]			
		CLAYFF[422]			
		DDEC[1067]			
		BKS[1068]			
Phan et al.[1053]	H_2	Lopez-Lazaro et al.[675]	15	333	3.4 NaCl and 0.13 KCl
	CO_2	EPM2[419]			
	CH_4	TraPPE[301]			
	H_2O	SPC/E[346]			
	Na^+, K^+, Cl^-	Dang [1043]			
	Talc	CLAYFF[422]			
	Kaolinite	CLAYFF[422]			
Yao et al.[1054]	H_2	IFF[313]	14−150	323−423	0−5.4
	H_2O	TIP4P/2005[305]			
	Na^+, K^+, Cl^-	CLAYFF,[422] Madrid-2019[1034]			
	Silica	INTERFACE[1063]			
Yu et al.[1056]	H_2	Hirschfelder et al.[321]	5−40	292−343	
	CO_2	CVFF[1069]			
	CH_4	CVFF[1069]			
	H_2O	SPC/E[346]			
	Graphene	Not mentioned			
Zhang et al.[1057]	H_2	IFF[313]	5−25	300-400	0−1 mol/L
	H_2O	SPC/E[346]			
	Halite NaCl	Joung and Cheatham [371]			
	Quartz	CLAYFF[422]			
	Calcite	Xiao et al.[1064]			
	Montmorillonite	CLAYFF[422]			
	Na^+Cl^-	Smith and Dang[374]			

[a]The salt concentrations in brine are reported in units of molality, or kgs of salt per kg of solvent (H_2O). The gaseous (G), liquid (L) and the solid (S) phases and the respective force fields used to model the interactions between the like molecules are provided. The final column lists the thermodynamic conditions at which CAs were computed. Note that the salt concentrations reported by Barbosa et al.[1050] and Zhang et al.[1057] are in weight percentage and mol/L, respectively

such that its ratio with the water-H_2 IFT decreases, leading to a higher CA, consistent with Young's equation.

4.11. Atomistic Modeling of Hydrogen Embrittlement

HE poses a critical threat to structural integrity by severely degrading the ductility and toughness of metallic materials, leading to premature brittle fracture even under low external stresses. At the atomistic scale, HE involves several distinct, yet interconnected mechanisms, as shown in Fig. 71, all of which have been intensively studied using MD simulations.

H-enhanced decohesion (HEDE)[1070] occurs when H atoms segregate and accumulate at interfaces, GBs, and atomic-scale defects, significantly lowering the cohesive strength between

https://doi.org/10.1021/acs.chemrev.5c00617
Chem. Rev. 2025, 125, 11878−12029

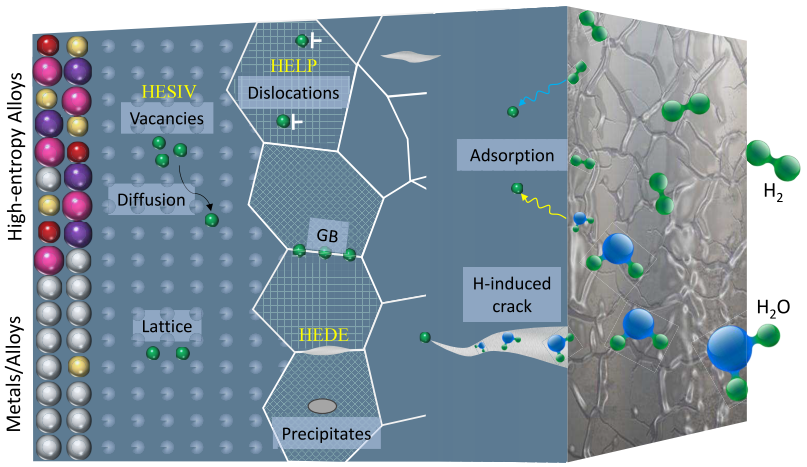

Figure 71. Illustration of hydrogen embrittlement mechanisms in high-performance materials (metals, alloys, and high-entropy alloys) with microstructural defects. Key processes include: (1) hydrogen adsorption, trapping, and diffusion; (2) hydrogen-defect interactions; and (3) the progression of hydrogen-induced damage. The figure emphasizes the interplay of these factors and their role in activating HE mechanisms, HEDE,[1070] HELP,[1071] HESIV.[1072]

atomic planes, and thus, promoting brittle intergranular or cleavage fracture. On the other hand, H-enhanced localized plasticity (HELP)[1071] describes the H-driven reduction of barriers for dislocation motion, leading to increased dislocation activity. While HELP initially facilitates plastic deformation, it ultimately results in severe strain localization and accelerated crack initiation due to locally intense deformation. Additionally, H-enhanced strain-induced vacancy formation (HESIV)[1072] emerges when H atoms stabilize vacancies, effectively lowering vacancy formation energies, which generates a higher density of defects and provides further preferential sites for crack initiation and growth. H also affects crack propagation dynamics directly by promoting dislocation emission or, conversely, inhibiting dislocation nucleation near crack tips, depending on the H concentration and the local stress state. Furthermore, H-dislocation interactions modify dislocation core structures and mobility, affecting overall material plasticity, fracture toughness, and resistance to fatigue crack growth. MD simulations uniquely enable direct visualization and quantification of these atomistic phenomena, providing detailed insights into the role of H at different length scales, defect configurations, and loading conditions. The complexity of H-induced effects is further magnified by the random and complex chemical environments, characteristic of high-entropy alloys (HEAs). For this reason, ML approaches have emerged as critical tools for navigating these complexities. In the following sections, we explore these mechanisms in detail and review the relevant literature.

4.11.1. Atomic Hydrogen Diffusion in Metallic Materials. H diffusion is critical for understanding and mitigating the detrimental effects of HE, as the migration of H atoms within the material microstructure precedes the degradation of mechanical properties. MD and KMC are commonly used to study H diffusion, with the simplest case being diffusion in a perfect lattice. For example, Zhou et al.[545] conducted a parametric study using MD simulations to investigate H diffusion in fcc Al (diffusion barriers and coefficients). This work provides a foundational reference for MD studies of H diffusion. However, MD simulations depend on empirical force fields, such as the EAM potential, which often lack sufficient accuracy as thoroughly discussed in Section 3.1. An alternative approach is KMC simulations with predefined energy barriers obtained from DFT-based NEB calculations. A key advantage of KMC is the ability to incorporate ZPE corrections into the energy barriers, accounting for harmonic quantum effects. Yang and Oyeniyi[1073] performed KMC simualtions with ZPE−corrected barriers to study H diffusion in bcc W, achieving excellent agreement with experimental results. To fully capture quantum effects, e.g., proton tunneling, more advanced techniques such as PIMD and higher-accuracy force fields are required. Kimizuka et al.[546] demonstrated that in bcc Fe, quantum effects not only substantially reduce the H diffusion barrier but also alter the preferred diffusion pathway, even at room temperature.

Defects, such as vacancies, impurities, dislocations, GBs, and other interfaces play a critical role in H diffusion, as they significantly alter the energy landscape of diffusion pathways. MD simulations using EAM potentials have revealed key insights into these effects. The study by Zhu and Oda[1074] revealed that in bcc Fe, vacancies act as strong trapping sites, substantially reducing the effective H diffusivity. The authors showed that while bulk-dissolved H atoms dominate diffusion, trapped H at vacancies contributes negligibly to long−range diffusion of H. Similar suppression of H diffusion due to vacancies and dislocations has been observed in bcc W through MD simulations.[1075] The influence of GBs has also been extensively studied, particularly in nano-grained materials, where a large fraction of atoms resides near interfaces. Zhou et al.[1076] systematically investigated H diffusion in nanograined Fe by means of MD simualtions, and showed that decreasing grain size restricts H diffusion due to the increased density of triple junctions.

Beyond the inherent inaccuracies of empirical force fields, such as EAM, another critical limitation in modeling H diffusion near defects is the constrains of accessible time-scales by MD simulations. Given the femtosecond−scale time steps required to resolve H diffusion, an impractically large number of MD steps would be needed to capture diffusion near defects, particularly at room and low temperatures. To overcome these challenges, KMC simulations incorporating DFT-derived diffusion barriers have emerged as a powerful alternative for studying H-defect interactions. Implementing this approach requires either precomputing all possible H diffusion pathways

https://doi.org/10.1021/acs.chemrev.5c00617
Chem. Rev. 2025, 125, 11878−12029

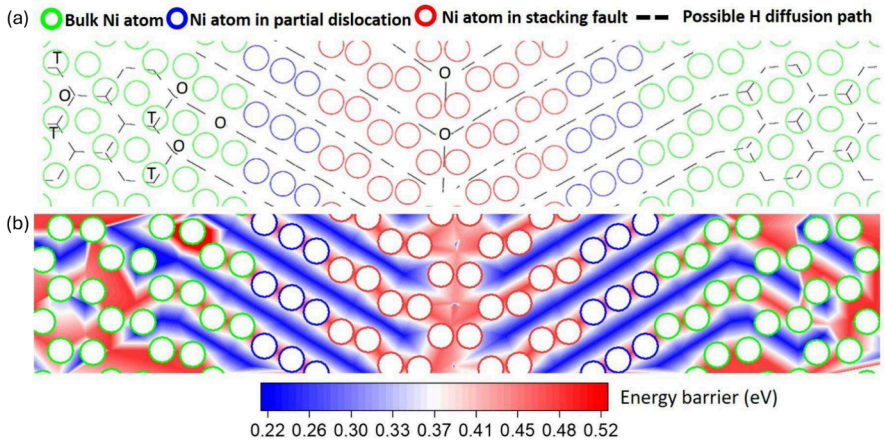

Figure 72. (a) Possible atomic hydrogen diffusion pathways on the glide plane and (b) the corresponding diffusion barrier contour map for an edge dislocation in fcc Ni. Octahedral (O) and tetrahedral (T) sites are indicated, with tetrahedral sites overlapping the host Ni atoms. Diffusion hops between adjacent sites are connected by dashed lines. [Reprinted from Acta Materialia, Vol 268, Xiao Zhou et al., Critical assessment of hydrogen pipe diffusion at dislocations in metals, 119758, Copyright (2024), with permission from Elsevier].

around defects to construct an event table for KMC or using advanced on-the-fly methods like the kinetic Activation-Relaxation Technique (k-ART) to dynamically identify diffusion paths during simulations. Zhou et al.[541] performed classical KMC simulations with DFT-derived barriers to investigate H diffusion across various GBs in fcc Ni. The authors demonstrated that high−angle GBs enhance H diffusion, whereas low-angle GBs hinder it. In a separate study, Zhou et al.[653] combined k-ART with KMC to examine H pipe diffusion along both edge and screw dislocations in fcc Ni (Fig. 72) and bcc Fe. This advanced computational framework enabled simulations spanning micro-second to second time-scales, revealing an unexpected suppression of H diffusion along dislocation cores, a phenomenon inaccessible to conventional MD simulations due to time-scale limitations.

From a methodological standpoint, both MD and KMC present distinct advantages and limitations for studying H diffusion in metals. MD captures the true dynamic evolution of the system, but its accuracy is inherently constrained by the quality of the force field. Moreover, MD becomes computationally prohibitive at low temperatures when high diffusion barriers necessitate excessively long simulation times. In contrast, KMC readily incorporates DFT−derived energy barriers with ZPE corrections, offering improved accuracy for H diffusion processes. Nevertheless, conventional KMC implementations neglect the temperature dependence of diffusion barriers and face two significant challenges: (1) the need to explicitly define all possible H diffusion pathways and the associated barriers within defective regions, and (2) the low−barrier problem where simulations may become trapped in local energy basins as discussed by Andersen et al.[650] These limitations underscore the urgency for advanced MD and KMC approaches capable of addressing such complexities in H diffusion studies. MLIPs (introduced in Section 3.1.5) show promise for addressing these challenges, combining accuracy and efficiency. A detailed discussion of these advanced methods will be presented in Section 4.11.7.

4.11.2. Atomic Hydrogen Trapping and Hydrogen-Mediated Vacancy Behaviors. H diffusion in metals and alloys is strongly governed by trapping phenomena, whereby H atoms become confined in sites with high escape barriers that retard their migration. These traps include interstitial impurities, such as carbon and nitrogen, substitutional solutes (e.g., Nb, Ti, Mg, Sc, and Y), intrinsic crystal defects including vacancies, nanovoids, dislocations, and GBs, and secondary-phase interfaces formed by carbides (TiC, V_4C_3, NbC, Mo_2C) or dispersed oxides, as reveled by Sagar et al.,[1077] Zhang et al.,[1078] Liu et al.[1079] and Wang et al.[1080] H trapping at GBs or precipitate−matrix interfaces can lead to HEDE, in which H reduces the cohesive strength of the GBs and the interfaces. DFT calculations and experimental measurements indicate that lattice defects (dislocations and GBs) and precipitates with coherent interfaces, typically exhibit trapping energies below 50 kJ/mol (often regarded as the reversibility limit), while semi- or incoherent precipitates can trap H much more strongly, with energies reaching up to 129 kJ/mol. For a thorough review of the available DFT and experimental studies the reader is referred elswhere.[1081]

H profoundly alters vacancy behavior in metals. The associated HE mechanism is known as HESIV, which hypothesizes that the density and clustering of vacancies is enhanced in the presence of H. Consequently, the vacancies can coalesce to form micro-voids, which in turn may combine to form larger voids leading to a decrease in ductile crack growth resistance. Hayward and Fu[544] combined MD and DFT to show that in bcc Fe, vacancy formation energies drop sharply as local H concentration increases, becoming negative at high coverage, and thus, provide an atomistic explanation for HESIV. Echeverri Restrepo et al.[1082] used parallel-replica dynamics alongside NEB calculations to quantify mono-vacancy diffusivity in bcc Fe with 0−3 H atoms. This study revealed that a single H raises the activation energy, slowing diffusion, whereas two to three H atoms lower the barrier, restoring or even enhancing vacancy mobility. Du et al.[1083] used a potential-of-mean-force method to investigate vacancies in Cu and Pd, and demonstrated that H enrichment at the saddle point (positive H Gibbs excess energy) lubricates vacancy migration, and significantly boosts diffusivity. These studies demonstrate that H creates superabundant vacancies by lowering formation energies, traps them at low coverage but enhances their diffusion at high coverage via saddle-point enrichment, and therefore, accelerates void nucleation and growth, leading to HE.

https://doi.org/10.1021/acs.chemrev.5c00617
Chem. Rev. 2025, 125, 11878−12029

4.11.3. Dislocation Nucleation and Mobility. H exerts a dual, system−dependent influence on incipient plasticity. In many fcc metals it facilitates dislocation nucleation by lowering the shear modulus, the line energy, and—when it enters the lattice—the intrinsic and extrinsic stacking-fault energies. These trends underlie the HELP signature reported by Barnoush and Vehoff[1084] during nano-indentation, where the first "pop-in" event is a direct measure of the nucleation of dislocation half-loops beneath the indenter. The MD study by Zhou et al.[547] refined this picture: in fcc Ni and Pd the pop-in load drops, primarily because interstitial H produces an isotropic lattice swelling that acts as a pre-strain, while little direct H−dislocation interaction is required. The GCMC simulations of Yu et al.[552] revealed that the H-induced increase in the core radius and decrease in the core energy of dislocations are the key factors affecting dislocation activities including dislocation nucleation, emission, mobility, and reaction that leads to HE. Equally well documented are cases where H suppresses dislocation nucleation. Early NEB calculations for fcc Ni crack tips performed by Wen et al.[1085] showed that adsorbed H raises the activation energy, and therefore, the stress-intensity factor for loop emission, an effect traced to a marked reduction in the activation volume when H decorates the embryo (i.e., the initial, critical-sized nucleus of a dislocation loop). Yin et al.[548] studied Ag−H nanowires both experimentally and by means of MD/NEB. The authors showed that surface−adsorbed H at ledges and steps increases the critical stress for loop formation, with the computed activation barrier rising accordingly. Here, H lowers the local surface energy, and relaxes the tensile stress concentration, effectively "locking" the most efficient surface sources. Using MD simulations coupled with NEB calculations, Li et al.[549] systematically elucidated the dual effect of H on dislocation nucleation: surface-segregated H raises the activation barrier, thus, inhibiting dislocation emission, while bulk-dissolved H lowers the barrier, thereby, promoting nucleation.

H can also profoundly alter the mobility of preexisting dislocations in metals, a topic that has been extensively explored using MD and other atomistic simulation approaches. Early DFT calculations combined with a line tension model by Itakura et al.[1086] showed that the effect of H on screw dislocation glide in bcc Fe depends sensitively on temperature, H concentration and applied stress. In that study, H both promoted kink nucleation, thereby softening the lattice, and trapped kinks behind the dislocation core, thereby producing a hardening effect. For a bulk H concentration of 0.1 parts per million (ppm), the softening window extended from ca. 200 to 300 K; at ten ppm it shifted to a range of 300 to 400 K. The subsequent NEB calculations and room temperature MD simulations of Yin et al.[548] confirmed these predictions. At a H line density of 0.4 per nanometer, the kink nucleation barrier decreased from 0.47 to 0.42 eV, and the critical shear stress for glide decreased from 32 to 22 MPa, consistent with experimental observations of H enhanced screw dislocation mobility. MD simulations by Song and Curtin[1087] revealed that H slows edge dislocation motion in bcc Fe by rapidly forming Cottrell atmospheres, which exert a strong solute drag effect over a wide concentration range. Kapci et al.[550] conducted GCMC simulations coupled with MD to further show that increasing the H concentration raises the critical stress required for edge dislocation depinning, underscoring the pervasive influence of H on dislocation based plasticity in Fe.

4.11.4. Crack Propagation and Grain Boundary Decohesion. Song and Curtin[276] used atomistic MD and GCMC to show that, under stress, H concentrates at crack tips in single- and bi-crystal Ni to form nano-scale hydrides that suppress dislocation emission and inhibit crack-tip blunting. Song and Curtin[1088] then integrated H diffusion kinetics with criteria for dislocation emission and cleavage into a single nondimensional parameter that, without any fitting constants, predicts the ductile-to-brittle transition across different Fe-based alloys based on H concentration, temperature and loading rate. For fcc Ni, Tehranchi and Curtin[442] showed that H segregation reduces both the critical stress for dislocation emission and the cleavage fracture stress intensity at a range of GBs, yet under conditions of only initial equilibrium segregation, and no active diffusion, a ductile-to-brittle transition was not observed, and the Σ3(111) twin boundary remained essentially immune to HE. In a follow-up study, Tehranchi et al.[1089] explicitly coupled H nano-diffusion onto freshly-created crack surfaces with mechanical, thermodynamic and kinetic modelling to derive a quantitative, parameter-free criterion that predicts the onset of HE for both crack propagation and GB cleavage. The mechanistic and predictive frameworks developed in these studies are essential for guiding the design of HE−resistant materials. Jung et al.[553] conducted systematic MD simulations of crack propagation along GBs in bcc Fe, with and without H. The findings showed that the effects of H on crack growth vary significantly with GB character. Specifically, the Σ3 coherent twin boundary (CTB) markedly retards crack propagation, owing to its capacity to accommodate plastic deformation, indicating that CTBs can substantially enhance resistance to HE. These results underscore the promise of GB engineering as a strategy for improving materials resistance to HE.

Several atomistic MD studies have quantitatively assessed H−induced decohesion in Ni GBs. Tehranchi and Curtin[1090] systematically investigated 110 symmetric−tilt boundaries in fcc Ni, computing both the theoretical strength (rigid separation) and the yield strength (onset of dislocation emission), and showed that equilibrium H segregation has negligible impact on either metric. Li et al.[1091] extended this analysis to a broader spectrum of GB characters, reporting that, under equilibrium H coverage, the maximum tensile strength and fracture energy of the Σ5(210)100 and Σ17(530)100 boundaries decrease by only 6.6% and 15.8%, respectively. Crucially, by incorporating plastic deformation into the simulations, Li et al.[1091] demonstrated that the synergy between H−facilitated decohesion and dislocation activity can notably amplify embrittlement. Huang et al.[1092] further combined a polyhedral packing−unit identification of all interstitial trap sites with atomistic segregation energies and Rice−Wang thermodynamics to predict work−of−separation reductions under different fracture rates: in the fast−fracture (constant concentration) limit H lowers the work of separation by 10%, whereas the reduction approaches 50% in the slow-fracture (constant chemical potential) limit. Collectively, these works show that equilibrium H segregation alone weakens Ni GBs only modestly, while H diffusion kinetics and plasticity critically govern the full extent of HE.

4.11.5. Hydrogen Effects on Complex Deformations

MD simulations have become indispensable for clarifying how H modulates nanoscale plasticity and fracture. Focusing on dislocation-GB interactions, Adlakha and Solanki[1093] showed

https://doi.org/10.1021/acs.chemrev.5c00617
Chem. Rev. 2025, 125, 11878−12029

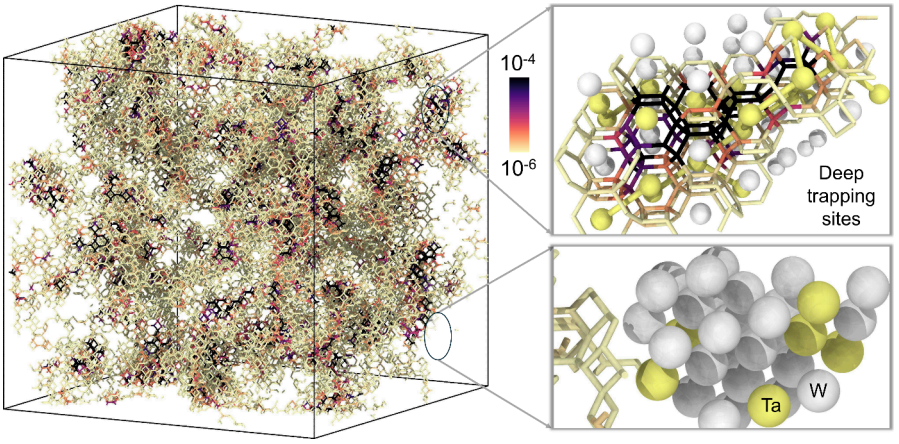

Figure 73. Visualization of H visitation frequencies at accessible tetrahedral (T) interstitial sites in $Ta_{20}W_{80}$ at 500 K. Frequencies are calculated by normalizing the visitation count of each T site by the total number of jumps in KMC simulations. The top-right and bottom-right panels highlight the metallic environments near trapping sites and inaccessible sites, respectively. H diffusion pathways between adjacent T sites are represented as atomic bonds. [Reprinted from Acta Materialia, Vol 289, Shuang et al.,[468] Decoding the hidden dynamics of super-Arrhenius hydrogen diffusion in multi-principal element alloys via machine learning, 120924, Copyright Elsevier (2025) (open access article distributed under the terms of the Creative Commons license - CC BY 4.0)].

that interstitial H raises the activation barrier for screw-dislocation transmission across 111 tilt GBs in bcc Fe. Using [110] symmetric tilt GBs, Li et al.[1094] showed that H shifts the reaction pathway from dislocation transmission to dislocation absorption, concomitantly increasing the initiation barrier. Tensile loading of H-segregated bicrystals conducted by Wan et al.[1095] further reveals complex coupled deformation mechanisms, providing an atomistic basis for embrittlement scenarios governed by dislocation-GB interactions. In polycrystalline models, the H effects on the mechanical properties become even richer. Zhou et al.[1096] demonstrated that decreasing the grain size in bcc Fe enhances resistance to HE, both by diluting H concentration at GBs and by activating a broader spectrum of GB-mediated deformation modes. For fcc Ni, Kuhr et al.[1097] observed an H-induced increase in yield strength at small strains, followed by accelerated dislocation emission from GB sources at larger strains. MD simulations of penta-twinned Ag nanowires by Yin et al.[548] revealed that surface-adsorbed H not only elevates the yield strength but also shifts the failure mode from distributed plasticity to localized necking. Surprisingly, MD simulations of HCP Mg polycrystals by Ji et al.[1098] revealed that H can enhance ductility without sacrificing strength.

From the perspective of multiscale modeling, Peng et al.[292] employed a concurrent atomistic−continuum (CAC) framework to simulate crack initiation at H-charged GBs in bicrystalline bcc Fe, bridging atomistic H diffusion, nanoscale GB cavitation/cracking, and mesoscale dislocation activity in a single model. The authors showed that tensile loading drives H toward the GB, where plasticity-induced clustering of H (PICH) acts as a mechanistic link between HELP and HEDE, greatly increasing local stress concentrations and weakening GB cohesion. Distinct failure modes emerge depending on GB character: Σ3 boundaries undergo micro-twinning−assisted void nucleation and coalescence, while Σ9 boundaries fail via crack initiation and growth concurrent with dislocation emission. By capturing long-range stress fields at sub-micron scales, their CAC simulations predict significantly lower GB cohesive strengths than conventional MD, and provides parameters for cohesive zone models, underscoring the necessity of multiscale simulation to reliably describe HE.

4.11.6. HE in High-Entropy Alloys

High-entropy alloys (HEAs), also known as multi-principal element alloys (MPEAs), have garnered significant research attention across various hydrogen-related fields, spanning H production, storage, and HE prevention. Recent experimental studies demonstrate exceptional HE resistance in HEAs, where H-charged specimens maintain higher strength while retaining comparable plasticity to their H-free counterparts (Luo et al.[1099,1100] and Li et al.[1101]). Two primary mechanisms have been proposed to explain this behavior: (1) significantly reduced H diffusion due to the complex chemical environment in HEAs, and (2) H-induced reduction in stacking fault energy, promoting stacking fault formation during deformation. These findings have spurred extensive investigations into H solubility, diffusion behavior, and deformation mechanisms in HEAs with H.

Unlike conventional metals and simple alloys, HEAs exhibit a non-uniform distribution of H solution energies even within an otherwise pristine lattice. The random spatial arrangement of multiple metallic elements produces a correspondingly random potential-energy landscape for interstitial H. DFT has therefore become the method of choice for quantifying site-to-site variations in solution energies and migration barriers. For equiatomic FeCuCrMnMo, Ren et al.[1102] demonstrated that the pronounced lattice distortion intrinsic to HEAs leads to large fluctuations in H migration barriers. In fcc FeMnCrCoNi, Xie et al.[1103] likewise reported a broad distribution of local solution energies; trapping in low-energy sites raises the effective diffusion barrier and thus slows long-range diffusion. Extending these insights, Yin et al.[1104] showed that chemical short-range order (CSRO) in fcc CrCoNi provides particularly deep traps, making CSRO an additional and tunable determinant of H diffusivity.

H diffusion in HEAs is inherently more intricate than in elemental metals. Because the governing timescales far exceed those accessible to direct AIMD, a variety of ML approaches have been developed to retain DFT-level fidelity at tractable cost. A comprehensive survey of ML techniques is given in Section 4.11.7. In fcc FeMnCrCoNi, Zhou et al.[654] trained ML models on DFT data to predict H solution energies and

https://doi.org/10.1021/acs.chemrev.5c00617
Chem. Rev. 2025, 125, 11878−12029

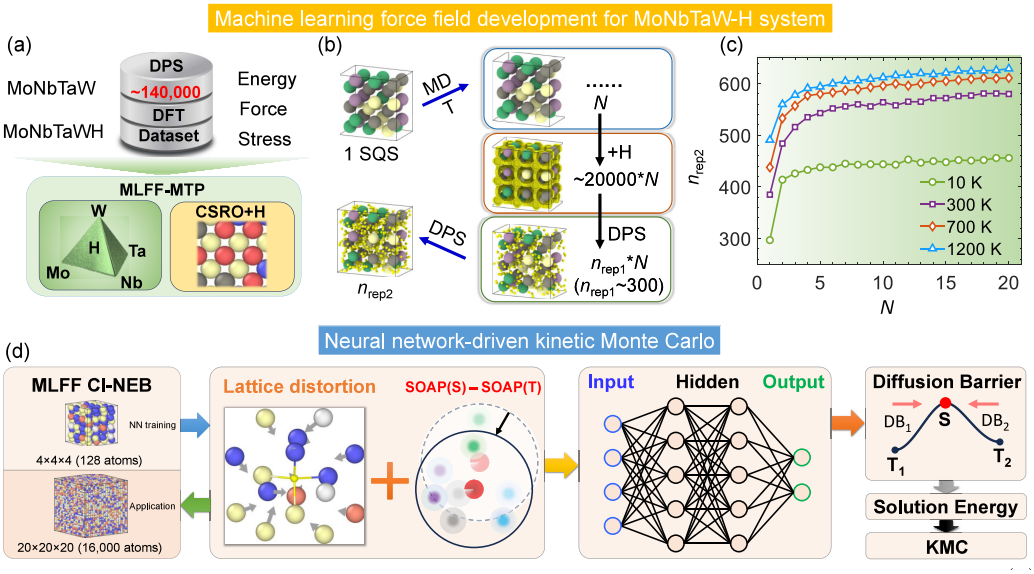

Figure 74. Machine learning-driven exploration of H diffusion with DFT-level accuracy. (a) Workflow for MLIP development. (b) Schematic of the distorted pathway sampling (DPS) method at various temperatures, where n_{rep1} and n_{rep2} denote selected configurations after initial and secondary DPS operations, respectively, and N represents the number of distorted high-entropy alloy (HEA) configurations at temperature T. Large colored spheres indicate metallic atoms, while small yellow spheres represent H atoms. (c) Evolution of representative configurations (n_{rep2}) through a two-stage DPS process, showing the count of distorted HEA configurations (N) at different temperatures. (d) Neural network-driven KMC (NN-KMC) methodology flowchart. [Reprinted from Acta Materialia, Vol 289, Shuang et al.[468] Decoding the hidden dynamics of super-Arrhenius hydrogen diffusion in multi-principal element alloys via machine learning, 120924, Copyright Elsevier (2025) (open access article distributed under the terms of the Creative Commons license - CC BY 4.0)].

migration barriers within the random chemical environment; these energetics subsequently informed KMC simulations of long-range diffusion. Their analysis shows that H most stably occupies the octahedral site, while larger Co, Cr, and Mn fractions reduce the diffusion coefficient, whereas additional Fe or Ni has the opposite effect. In bcc MoNbTaW, Shuang et al.[468] integrated an MLIP, neural-network KMC, and symbolic regression into a unified framework capable of accessing experimental timescales for H diffusion. The study reveals a previously unreported super-Arrhenius temperature dependence, traced to the spontaneous emergence of nanoscale clusters enriched in H-favourable elements (Nb, Ta), as shown in Fig. 73. Disruption of these clusters by CSRO accelerates H diffusivity, thereby underscoring the critical interplay between local chemical order and diffusion kinetics.

H profoundly alters the deformation mechanisms and mechanical properties of HEAs. Using an EAM potential parameterized for FeNiCr-H, Zhou et al.[444] showed through extensive MD simulations that H statistically widens stacking faults by lowering both intrinsic and extrinsic stacking-fault energies. Building on the same potential, Guo et al.[1105] uncovered a dual influence of H on twinning: it facilitates homogeneous twin nucleation yet suppresses surface-initiated twinning. To provide higher-fidelity benchmarks beyond classical potentials, DFT calculations have long been employed. Xie et al.[1103] demonstrated that electron transfer from H to the lattice reduces both unstable and stable stacking-fault energies, thereby favoring deformation twinning. Systematic DFT calculations by Zhou and Curtin[1106] for 304/316 stainless steels and FeMnCrCoNi HEAs quantified H adsorption, surface energies, and GB fracture energies, illuminating the atomistic origins of HE resistance. The same DFT-guided strategy, coupled with mechanistic modelling, subsequently identified CoNiV as an exceptionally HE resistant alloy.[1107] In a related study, Tan et al.[1108] showed that CTBs in fcc HEAs retard crack propagation and thus enhance HE resistance. To combine MD length- and time-scales with DFT accuracy, Zhou et al.[469] recently developed a MLIP for FeCoNiCrMn-H. Their simulations revealed that H lowers stacking-fault energy and promotes twinning, while dynamically formed local chemical ordering (LCO) traps H to create LCO−H complexes that pin dislocations more effectively than LCO alone. Moreover, segregation-induced Cr enrichment and Fe depletion at GBs raise the GB fracture energy, further improving HE resistance.

4.11.7. Machine Learning in Hydrogen Embrittlement Studies

The emergence of AI has revolutionized materials research (see also Section 4.6.2), with ML becoming a major tool for advancing our understanding of HE in metallic systems. ML techniques are transforming all aspects of HE research, spanning all scales from atomistic simulations of H diffusion to macroscopic predictions of mechanical properties in H-charged materials. Among various ML applications, the development of MLIP represents one of the most significant advances, enabling accurate large-scale simulations while maintaining near-DFT level accuracy. MLIPs typically require sophisticated ML architectures containing approximately 10^3 trainable parameters that are optimized against extensive DFT datasets. Widely used MLIPs are the neural network potential (NNP),[460] Gaussian approximation potential (GAP),[461] spectral neighbor analysis potential (SNAP),[1109] moment tensor potential (MTP),[462] and atomic cluster expansion (ACE).[1110]

Kwon et al.[465] developed MTPs to investigate H diffusion in pristine bcc metals (Nb, Fe, W), using PIMD to demonstrate the significant influence of nuclear quantum effects below 500 K across a 100−1000 K temperature range. Similar progress in

https://doi.org/10.1021/acs.chemrev.5c00617
Chem. Rev. 2025, 125, 11878−12029

fcc systems includes NNPs coupled with PIMD, which captured the quantum mechanical aspects of nonlinear H isotope diffusion in Pd.[464] The Bravais-Inspired Gradient-Domain Machine Learning (BIGDML) approach[1111] achieved comparable accuracy for H diffusion in Pd, while utilizing compact DFT datasets (10−200 structures). Other applications include H diffusion in hcp Mg and Ti hydrides using MTP, MACE, and CHGNet potentials.[466] Complementing these diffusion studies, Meng et al.[467] created a general-purpose MLIP for Fe-H systems capable of modeling diverse phenomena including surface processes, defect-mediated diffusion, and H-influenced plasticity.

Additionally, MLIPs have emerged as particularly powerful tools for investigating HE in HEAs, where they successfully capture the complex chemical interactions between H and multiple elements. The field advanced significantly through the work of Shuang et al.[468] who used D-optimality-based dataset construction to develop a high-accuracy MTP that comprehensively describes H-MoNbTaW interactions across the whole compositional space, including chemical short-range ordering effects (Fig. 74a-c). This MTP enabled the discovery of super-Arrhenius H diffusion behavior in bcc HEAs. Subsequent developments include a Deep Potential model capable of simulating coupled H diffusion and H-influenced plastic deformation in fcc FeMnCrCoNi HEAs, demonstrating the expanding capabilities of ML approaches for these challenging multicomponent systems.[469]

The significance of ML in HE studies extends beyond MLIP applications. Leveraging large-scale DFT datasets and the Sure Independence Screening and Sparsifying Operator (SISSO) algorithm, Korostelev et al.[1112] developed robust analytical models for accurate prediction of H absorption and migration energetics in metal alloys. For H diffusion specifically, Shuang et al.[468] implemented a neural-network KMC framework capable of computing hundreds of millions of DFT-accurate diffusion barriers (Fig. 74d), enabling unprecedented long-timescale simulations. The same work further applied SISSO to derive analytical models for H diffusivity in bcc HEAs, providing fundamental insights into diffusion mechanisms within complex chemical environments. Another work by Zhou et al.[654] established an ML−KMC framework to investigate H diffusion in fcc FeMnCrCoNi HEAs, employing whale optimization algorithms to identify atomic configurations with minimized H diffusivity. Tang et al.[1113] developed a reinforcement learning−guided transition kinetics simulator and a low-energy state sampler that leverage neural networks to predict transition rates, automatically uncovering the most probable diffusion pathways without explicit barrier calculations and enabling efficient long-timescale atomistic simulations.

5. CHALLENGES AND FUTURE OUTLOOK

5.1. Future Considerations on Molecular Simulation of Hydrogen in Geological Formations: From Molecules to Reservoir-Scale

Accurate prediction of H_2-brine IFTs, adsorption energies, and transport properties requires high-quality experimental data, mainly for training force fields and validating MD simulations. Based on, but not only limited to, our analysis of the available molecular simulation literature reviewed in Sections 4.7.1, 4.9, and 4.10, significant discrepancies in MD results can be seen. These often stem from the varying treatment of electrostatic interactions, cut-off distances, choice of force fields, surface model, all of which must be carefully validated against experiments. These discrepancies become more pronounced when modeling multicomponent systems (e.g., H_2 mixed with H_2O, CO_2, CH_4, and N_2) across an extended range of pressures, temperatures, and salinities. Therefore, a key research direction that we are confident should be explored in the future is the systematic investigation of IFTs, contact angles, and other interfacial properties under varying conditions, using both MD simulations and experimental measurements to refine interaction parameters. In parallel, ML methods, such as the approach demonstrated by Omrani et al.[1114], show great potential for developing predictive models that capture the dependencies of e.g., IFT on gas composition, thermodynamic conditions, and salinity. Nevertheless, robust experimental datasets for a wide range of H_2 properties (both for the pure component and mixtures) remain essential to validate these computational frameworks, ensuring accuracy and applicability for real−world processes such as UHS and CO_2 sequestration.

A thorough understanding of H_2 wettability in subsurface environments requires accurate experimental measurements, molecular modeling, and reservoir-scale simulations. Although significant progress has been made in molecular modeling, particularly in the parameterization of force fields and the characterization of mineral surface functionalities, important challenges remain. Addressing these is crucial for advancing H_2 storage technologies and improving our predictive capability of H_2 behavior at reservoir-scales. Some existing studies have already highlighted discrepancies in pressure-dependent behavior (e.g., Alavi[336] vs. IFF Wang et al.[313] models). Thus, future work should focus on systematically validating and refining force fields, especially for high-pressure regimes, against comprehensive experimental datasets. Efforts could include re-parameterizing H_2 models to better capture the pressure sensitivity observed in H_2−H_2O interfacial systems. Also, many simulations assume uniform silanol distributions (e.g., Q^2, Q^3, Q^4). This approach, although providing a simple foundation, it does not reflect the actual rock surfaces (i.e., natural formations exhibit heterogeneous surfaces and multi-mineral interfaces). Extending MD simulations to capture such compositional complexities spanning organic matter, multivalent ions, and varying functional-group densities, will yield more accurate predictions of in-situ wettability. Discrepancies between simulation papers in contact-angle computations (e.g., Q^2 silica) emphasize the importance of robust sampling and sufficient equilibration. Although some experimental data exist for H_2−H_2O−solid contact angles, coordinated efforts where experiments and simulations target identical minerals, surface treatments, and thermodynamic conditions are urgently needed. Such collaborative studies would reduce uncertainties in force-field validation and identify key parameters controlling H_2 wettability under realistic subsurface conditions.

While molecular simulations have greatly helped the community in understanding the intrinsic H_2 − H_2O − solid interactions, they are still almost exclusively performed in ideal, nm-scale slit pores or on perfectly flat crystal faces. Since molecular simulation cannot reach the cm-scale representative elementary volumes (REVs), multiphase transport modelling cannot be accurately performed. Natural reservoir rocks exhibit tortuous pore networks, angular throats, surface roughness, and mosaics of mineral and organic coatings. Together these features generate broad, hysteretic distributions of apparent

https://doi.org/10.1021/acs.chemrev.5c00617
Chem. Rev. 2025, 125, 11878−12029

contact angles that may depart markedly from the single, intrinsic value obtained on a smooth, chemically uniform surface.

Lastly, it is important to point out is the scarcity of atomistic work on dynamic phenomena directly relevant to H_2 storage, e.g., advancing/receding contact angles, meniscus motion, and capillary trapping. In classical MD, Newton's equations of motion are integrated and momentum is conserved, thereby, recovering Navier−Stokes hydrodynamics at the nm−scale. Thus, MD could in principle capture such processes without added constitutive assumptions. However, in practice, the required length− and time−scales are prohibitive since even a simple cylindrical pore with a length of a few mm would contain on the order of billions of atoms. Moreover, the reliability of existing force fields for transient, far-from-equilibrium configurations, such as rapidly moving three-phase contact lines, has not been evaluated. Systematic benchmarks that compare dynamic contact angles and capillary entry pressures predicted from MD with well-controlled microfluidic experiments, are therefore, urgently needed (even before tackling complex rock geometries). In practice, this means using MD to supply key inputs such as the variation of interfacial tension and contact angle with pressure, temperature, and fluid composition to larger-scale solvers (e.g., pore network, lattice Boltzmann, or volume-of-fluid models) that run on cm−scale digital rock geometries. Reliable predictions of H_2 migration, trapping efficiency, and long−term storage security in geological formations are only possible if the atomistic inputs are carefully validated and combined with simulations at the pore scale and continuum, while guided by experiments.

5.2. Machine Learning Perspective on Atomistic Modeling of Hydrogen Embrittlement

ML has significantly advanced our ability to study H diffusion and HE in metals and alloys by providing interatomic potentials that approach first-principles accuracy. As discussed in Section 4.11.7, traditional studies have largely relied on empirical force fields, most commonly variants of EAM or modified EAM potentials, to describe H-metal interactions. While these potentials can capture qualitative trends, they often fail to reproduce quantitatively accurate H binding energies and diffusion barriers, particularly in the presence of crystalline defects such as vacancies, dislocations, and GBs. The emergence of MLIPs, such as NNP,[460] GAP,[461] SNAP,[1109] MTP,[462] and ACE,[1110] has begun to address these shortcomings. By training on diverse data sets of H-metal atomic configurations (drawn from DFT), MLIPs can reliably predict H interactions with pristine lattices and with a variety of defects. In practice, this means that vacancy formation energies, dislocation core structures, and GB binding sites can be characterized with near-DFT accuracy, enabling more predictive modeling of H diffusion coefficients and embrittlement mechanisms.

One major challenge in developing MLIPs for H-metal systems is adequately sampling the vast configurational space that arises from complex H-metal environments—particularly around defects and during dynamic processes. Domain expertise alone cannot exhaustively enumerate all relevant local environments. Active learning techniques, which iteratively identify and add the most informative new configurations during MD, have proven useful in accelerating potential development.[1115] More advanced strategies, such as uncertainty−driven active learning, further enhance efficiency by focusing the sampling on rare events and underrepresented local environments,[1116] thus, reducing the total number of required DFT calculations. An alternative sampling strategy is to generate a broad, pre-computed pool of H-metal configurations before any DFT calculations are performed.[466] Universal MLIPs (uMLIPs) can serve as "sampling engines", driving MD simulations at scale to explore configurational space. Table 21 provides a list with the most important uMLIPs to date, along with information of the associated datasets and archtectures. Although these uMLIPs do not match the accuracy of DFT, they excel at rapidly producing physically relevant atomic structures. Once a diverse pool of configurations is generated, single-point DFT calculations on these snapshots suffice to train a specialized H-metal MLIP, streamlining the workflow.

Table 21. State-of-the-Art uMLIP Architectures and DFT Datasets

Architecture	Organization	Dataset	# of structures
M3GNet[1117]	UC San Diego	MPtri	1.58M
CHGNet[1118]	UC Berkeley		
MACE[1119]	University of Cambridge	Alex(sAlex)	30.50M (10.45M)
Orb[1120,1121]	Orbital Materials		
MatterSim[1122]	Microsoft Research AI for Science	OMat24	100.82M
GRACE[1123]	ICAMS, RUB		
SevenNet[1124]	Seoul National University	MatPES-PBE	40M
DPA3[1125]	AI for Science Institute, Beijing		
eqV2[1126]	FairChem at Meta	MatPES-r2SCAN	40M
eSEN[1127]	FairChem at Meta		

uMLIPs are MLIPs trained on extensive datasets spanning diverse elements, chemical environments, and material classes. Unlike specialized MLIPs (e.g., ACE or MTP) tailored to specific systems, uMLIPs prioritize broad transferability, achieved through training on hundreds of millions of DFT-labeled structures and architectures with hundreds of millions of parameters. Despite their general-purpose nature, modern uMLIPs can approach the accuracy of specialized MLIPs,[1128] enabling applications ranging from high-throughput materials screening to defect dynamics simulations. Prominent uMLIPs include M3GNet,[1117] CHGNet,[1118] Orb,[1120,1121] eqV2,[1126] MACE,[1119] DPA3,[1125] SevenNet,[1124] MatterSim[1122] and eSEN,[1127] all built on comprehensive DFT collections exceeding one hundred million structures. These collections include the Materials Project trajectory (MPtrj) dataset with 1.58 million structures,[1118] the Alexandria (Alex) dataset with 30.5 million structures or its subsampled version sAlex with 10.45 million structures,[1129] as well as the Open Materials 2024 (OMat24) dataset with 100.82 million structures.[1126] Whereas MPtrj and Alex (sAlex) focus primarily on near equilibrium configurations, OMat24 emphasizes far from equilibrium structures, making it the most extensive inorganic materials dataset to date. More recently two new datasets computed with the Perdew Burke Ernzerhof (PBE) functional (MatPES-PBE) and the revised regularized strongly constrained and appropriately normed (r2SCAN) functional (MatPES-r2SCAN) have become available to further improve consistency and accuracy of next generation uMLIPs.[1130] Among current models, the eqV2 and eSEN variants trained

https://doi.org/10.1021/acs.chemrev.5c00617
Chem. Rev. 2025, 125, 11878−12029

on OMat24 by the FairChem group at Meta rank among the best for modeling general defects and hydrogen−metal interactions.[1128] These developments underscore the transformative potential of uMLIP-driven computational modeling in the materials science community by delivering accuracy comparable to DFT and enabling high fidelity predictions of H related trapping, embrittlement, storage and production processes at unprecedented scales.

The main limitation in developing specialized MLIPs is the vast amount of DFT data required, while uMLIPs face inference-speed constraints that typically limit them to systems of tens of thousands of atoms.[1131] A promising avenue to overcome both challenges is model distillation—deriving a smaller, task specific MLIP from a pretrained uMLIP can bypass much of the DFT sampling effort.[1132] The critical challenge which lies here is quantifying the uncertainty of uMLIP predictions in order to ensure that the distilled model inherits accurate energy and force predictions without introducing significant errors. Developing robust uncertainty metrics for uMLIPs will therefore be essential. Furthermore, ML techniques extend beyond interatomic potentials to higher-level property predictions. For example, supervised learning models can predict H-trapping energies and migration barriers directly from local structural and chemical descriptors. This capability is especially valuable for studying H diffusion and trapping in complex alloys—such as random solid solutions and HEAs, where enumerating every local environment and associated DFT calculation becomes impractical.[468] By combining ML-based property estimators with MLIPs, the community can build multiscale frameworks that predict H diffusion, trapping, and HE susceptibility in real-world engineering alloys with unprecedented accuracy.

5.3. Challenges in Force Field and Method Development for Predicting Properties of Liquid Hydrogen and Hydrogen Bubbles

This review highlighted many studies investigating the bulk fluid behavior of H_2. Based on our survey and analysis, clear knowledge gaps can be identified. Some of these gaps are especially relevant for technological applications and, thus, of interest to the chemical industry. Such a case is molecular modeling H_2 liquefaction. This requires force fields that can accurately capture phase transitions and the ortho-to-para conversion of H_2. To achieve this accuracy, a force field should automatically adjust the interaction parameters, for example as a function of the temperature. Classical models with such features could be inspired by the approach of Buch,[312] which uses a quadrupole interaction term to model H_2 at very low temperatures (1 to 3 K) (see Section 3.1.1). MLIPs can also provide approaches to simulate this behavior. Recent advances in MLIPs for magnetic materials resulted to inter-atomic potentials that are spin-state aware.[1133] A similar approach could provide accurate predictions of the ortho-to-para conversion as this would directly address the physical change within the H_2 molecule. Such an advanced model can then be combined with PIMD techniques to predict H_2 properties relevant to H_2 liquifaction and transport (i.e. heat capacity, thermal conductivity, viscosity, self-diffusion).

While the main focus of this review is on classical simulation methods of H_2, we are convinced that MLIPs will blur the barrier between classical and quantum simulations. MLIPs allow for large scale simulations of reactive systems, the modeling of which was limited to AIMD simulations. Recent studies into Grotthuss transfer in water[105,1134−1137] have shown that MLIPs show a great potential in studying reactive systems. These studies revealed that both the details of the Grotthuss transfer events (i.e., energy barriers, local environment required for Grotthuss transfer), as well as the effects of these reactions on transport properties (i.e., self-diffusion coefficients and electrical conductivities) can be predicted. As discussed in Section 4.1.6, the electro-osmotic drag of H_2 in nafion membranes also requires accurate modeling of Grotthuss transfer. Only the study by Choe et al.[129] showed success in computing the EOD, as it combined AIMD and classical MD methods. Reactive MLIPs could provide a more efficient way to compute the EOD for larger system sizes. This will accelerate the simulations by orders of magnitude, and could lead to optimized membrane designs where the structure of the membrane promotes Grotthuss transfer, while minimizing the drag the H_2 experiences from the membrane.

H_2 dissolution in aqueous solutions is another area of great interest for advancing H_2 economy (e.g., for water electrolysis, subsurface storage, fuel cells). The development of fast polarizable force fields for H_2, H_2O, and ions (such as the water force field) can lead to accurate descriptions of H_2 bubble formation in aqueous electrolyte solutions. Capturing bubble formation provides valuable insight into the amount of water that can be dissolved in H_2 gas. The pressure inside H_2 bubbles is the highest at the moment of formation, as it inversely scales with bubble radius. Rahbari et al.[110] demonstrated that water solubility in H_2 decreases with increasing pressure, making the initial stages of bubble formation critical for predicting water impurities in the H_2 gas produced by the electrolyzer. Accurate molecular simulations if bubble formation under varying electrolyte compositions can lead to better informed design decisions for electrolysis setups. While MLIPs have shown great promise, we believe that there are still fundamental challenges that need to be addressed before MLIPs can be used in such simulations. Simulating bubble formation requires large systems, and while MLIPs provide significant speed-up compared to AIMD, they still require significant computational resources compared to classical force fields. Additionally, the long-ranged interactions in such systems pose challenges for MLIPs, since many of them implement a (smoothened) cut-off distance for all inter-atomic interactions. This leads to inaccuracies in systems where electrostatic interactions are dominant.[1138] Some support for long-ranged interactions has been implemented into several MLIPs.[1138−1140] Further development into MLIPs with less computational requirements, while maintaining the accuracy of the long-ranged interactions, is needed to make MLIPs suitable for simulating bubble formation in aqueous solutions. Lastly, MLIPs require accurate DFT data to train the model. While modern ab initio exchange correlation functionals (i.e. metaGGA and hybrid density functionals) have shown great improvement, they still have significant limitations. Recent studies showed that MLIPs trained on metaGGA functionals yield accurate trends in the computed properties. However, a relatively constant shift in temperature is observed with computations using MLIPs, for example in viscosity[1141] or melting temperature.[1142] While theses MLIPs are useful for predicting trends or providing insight into the underlying physics, they might not yet be suitable for predicting properties for industrial applications. Therefore, for MLIPs to become more broadly applicable, a key breakthrough will be the development of training frameworks that incorporate both

https://doi.org/10.1021/acs.chemrev.5c00617
Chem. Rev. 2025, 125, 11878−12029

DFT data and experimental measurements instead of relying on more and more accurate and expensive DFT methods.

5.4. Pathways to Advance Research on Hydrogen Hydrates through Molecular Simulation

As thoroughly discussed in Section 4.8, molecular simulation is an indispensable tool for studying H_2 hydrates. As such, advancing H_2 technologies utilizing hydrate systems can be aided by exploring novel simulation routes. For example, investigating hydrate structural effects as a result of using different promoters could lead to increased H_2 storage capacities. Such studies can be coupled with conventional/novel crystal engineering approaches and techniques. The partial replacement of H_2O molecules by another species could result in modifying the lattice in way that larger cages could provide increased storage capacity. Other routes towards increasing H_2 storage capacity in hydrates are the screening of hypothetical structures (following the example of nanoporous materials such as MOFs and zeolites) and developing techniques which can reduce H_2 "leakage" rate out of the hydrate structure. Reducing the number of faces in a given hydrate crystal would function towards the reduction of "leakage". Alternatively, the use of certain ice structures could provide a solution, since channels can be more efficient storage structures than cages with faces. Studying the effect of flexible cages on H_2 storage capacity and leakage with molecular simulations, is another promising route.

To reliably predict thermophysical properties of hydrate systems requires a multi-scale approach, i.e., from the atomistic up to the continuum-level. To this end, developing hybrid computational tools, which couple multi-scale modeling methods is essential. Such tools can incorporate information obtained from ab-initio calculations, classical molecular and coarse-grained simulations, and ML predictive methods (e.g., using MLIPs (see also Sections 3.1.5 and 5.2) and/or physics-informed ML approaches).

Other promising future directions for molecular simulation research on H_2 hydrates are the investigation of confinement effects on the kinetics and thermodynamics of pure and mixed H_2 hydrate in solid materials, systematic exploration of semiclathrates and hydrate-based H_2 + CO_2 gas mixture separations, and coupling hydrate formation/dissociation with industrial processes such as LNG gasification and desalination.

5.5. Importance of Open-Source Software for Studying Properties of H_2 in Polymeric and Composite Materials

Evidently, the vast majority of the studies reviewed in Section 4.4 were conducted using commercial software (mainly Materials Studio[1143]). The use of commercial software instead of open-source comes with advantages and disadvantages. Major advantages are the ease of setting systems up (which is especially useful in the study of polymers and other highly viscous systems), the available pre- and post-processing options, access to a user interface (which may be particularly important in a corporate setting), professional support, and the overall less steep learning curve compared to an open-source code. Additionally, commercial software, such as Materials Studio[1143] and MAPS,[1144] provides access to proprietary force fields (e.g., COMPASS[316]). However, the relatively high price and the inaccessibility to the source code, and therefore, the inherent limitation in expanding, debugging, or modifying the scientific software, are the major drawbacks of commercial molecular simulation codes.

Another important point to consider is that since the early days of molecular simulation, algorithms and methods have been developed with an open-knowledge/source mentality, and mainly financed via national funds in United States and EU. Later on, when molecular simulations became more popular and commercial software arose, these algorithms and methods were incorporated in proprietary software. A characteristic example is the pioneering work by Theodorou and Suter,[1145−1148] who developed efficient methods for modeling polymeric systems, essentially allowing for the creation of initial configurations and relaxation of long hydrocarbons. Another, broader, example showcasing how open-source can aid the progress in the simulation community is LAMMPS,[473,475] one of the most widely used MD simulators, which is maintained by Sandia National Laboratories. As a final remark, codes such as LAMMPS and GROMACS,[476,477] being open to modification and enrichment by the simulation community worldwide, usually offer high performance, a plethora of features, access to new methods sooner, and easier implementation of new force fields compared to commercial software. Therefore, open-source software is considered one of the cornerstones of the molecular simulation field. The expansion and maintenance of open-source software should continue to be a priority of both research universities and governmental education bodies.

5.6. Transparency and Reproducibility in Molecular Simulation Workflows

In our review, we encountered several challenges related to the clarity and consistency of force field parametrizations in the literature of H_2 molecular simulation. In some studies, the rationale behind the choice of molecular models or interaction parameters was insufficiently explained. While such choices may be driven by computational efficiency, availability in simulation packages, or alignment with specific properties (e.g., density, viscosity, or interfacial tension), a clear and explicit justification is essential for scientific transparency. Ideally, this should include reference to the properties against which the force field was tuned, as well as known limitations in transferability or range of validity. Moreover, we observed that some studies do not cite the original source of the force field, but instead reference secondary literature that cited the original work. A notable example is the widely used force field from Hirschfelder,[321] which in its original formulation includes four different parameter variants (see relevant discussion in Section 3.1.1). In cases where studies cite a derivative reference rather than the primary source, it remains unclear whether the authors are fully aware of the specific force field variant used or its original context. We strongly recommend that future studies consult and cite the original work when reporting force field parameters and their origin, to ensure both scientific accuracy and reproducibility.

Another critical issue we observed is the limited availability of raw simulation data. While some studies commendably include detailed results (in tabulated or other form) along with uncertainty estimates, others provide only plots with densely populated data points and no accessible underlying values. This practice significantly hampers reproducibility, introduces uncertainty in data extraction, and complicates efforts to benchmark or validate results across independent studies. We therefore advocate for rigorous data reporting standards, wherein all key outputs (e.g., pressure, energy, interfacial tension, contact angle, diffusion coefficients) are made

https://doi.org/10.1021/acs.chemrev.5c00617
Chem. Rev. 2025, 125, 11878−12029

available in machine−readable formats, along with metadata describing simulation settings. Such transparency not only enhances the credibility of the published work but also prevents unnecessary duplication of computational efforts in future studies. Promoting reproducibility and interpretability through open, well−documented datasets is essential if molecular simulation is to serve as a reliable and cumulative tool for advancing H_2 technologies.

AUTHOR INFORMATION

Corresponding Author

Othonas A. Moultos − *Engineering Thermodynamics, Process & Energy Department, Faculty of Mechanical Engineering, Delft University of Technology, 2628 CB Delft, The Netherlands;* orcid.org/0000-0001-7477-9684; Email: o.moultos@wtudelft.nl

Authors

Ahmadreza Rahbari − *Headquarters, XINTC B.V., 6961 EK Eerbeek, The Netherlands; Engineering Thermodynamics, Process & Energy Department, Faculty of Mechanical Engineering, Delft University of Technology, 2628 CB Delft, The Netherlands;* orcid.org/0000-0002-6474-3028

Thejas Hulikal Chakrapani − *Institute for Multiscale Thermofluids, School of Engineering, University of Edinburgh, Edinburgh EH9 3FB, United Kingdom*

Fei Shuang − *Department of Materials Science and Engineering, Faculty of Mechanical Engineering, Delft University of Technology, 2628 CD Delft, The Netherlands;* orcid.org/0000-0001-6333-9237

Panagiotis Krokidas − *National Centre for Scientific Research "Demokritos", 15310 Aghia Paraskevi Attikis, Greece*

Parsa Habibi − *Engineering Thermodynamics, Process & Energy Department, Faculty of Mechanical Engineering, Delft University of Technology, 2628 CB Delft, The Netherlands; Department of Materials Science and Engineering, Faculty of Mechanical Engineering, Delft University of Technology, 2628 CD Delft, The Netherlands*

V. Jelle Lagerweij − *Engineering Thermodynamics, Process & Energy Department, Faculty of Mechanical Engineering, Delft University of Technology, 2628 CB Delft, The Netherlands;* orcid.org/0009-0000-6839-530X

Mahinder Ramdin − *Engineering Thermodynamics, Process & Energy Department, Faculty of Mechanical Engineering, Delft University of Technology, 2628 CB Delft, The Netherlands;* orcid.org/0000-0002-8476-7035

Thijs J. H. Vlugt − *Engineering Thermodynamics, Process & Energy Department, Faculty of Mechanical Engineering, Delft University of Technology, 2628 CB Delft, The Netherlands;* orcid.org/0000-0003-3059-8712

Hadi Hajibeygi − *Geoscience and Engineering Department, Faculty of Civil Engineering and Geosciences, Delft University of Technology, 2628 CN Delft, The Netherlands;* orcid.org/0000-0002-8517-8283

Poulumi Dey − *Department of Materials Science and Engineering, Faculty of Mechanical Engineering, Delft University of Technology, 2628 CD Delft, The Netherlands;* orcid.org/0000-0003-4679-1752

Ioannis N. Tsimpanogiannis − *Chemical Process & Energy Resources Institute (CPERI), Centre for Research & Technology Hellas (CERTH), 57001 Thermi-Thessaloniki, Greece;* orcid.org/0000-0002-3466-1873

Complete contact information is available at: https://pubs.acs.org/10.1021/acs.chemrev.5c00617

Author Contributions

○A.R. and T.H.C. contributed equally to this work.

Notes

The authors declare no competing financial interest.

Biographies

Ahmadreza Rahbari is Director of Research & Development at XINTC (The Netherlands) and visiting staff at Delft University of Technology. He obtained his Ph.D. in Computational Physical Chemistry from TU Delft in 2020 under the supervision of Professors Thijs J. H. Vlugt and David Dubbeldam, developing advanced Monte Carlo methodologies for phase equilibria of reactive mixtures, with applications to hydrogen and ammonia systems. He subsequently worked as a postdoctoral researcher at TU Delft and HyET Hydrogen, focusing on electrochemical hydrogen compression and high-pressure vapor-liquid equilibria of hydrogen mixtures. At XINTC, his work bridges process modeling and market-driven innovation, leading product development and techno-economic research on modular alkaline electrolyzer systems for green hydrogen production. He received his M.Sc. in Mechanical Engineering from the Norwegian University of Science and Technology (NTNU) in 2014.

Thejas Hulikal Chakrapani received his Ph.D. in Computational Physics from the University of Twente, where he developed coarse-grained models to study fluid transport in porous materials. He subsequently worked as a postdoctoral researcher at Delft University of Technology, employing molecular simulations to compute thermophysical properties of hydrogen mixtures relevant to subsurface hydrogen storage. He is currently a Research Associate at the University of Edinburgh, investigating nanoscale heat transfer at solid-liquid interfaces using non-equilibrium molecular dynamics. His research combines coarse-grained and atomistic simulations to explore fluid mechanics and transport phenomena at the nanoscale.

Fei Shuang is a postdoctoral researcher in Materials Science and Engineering department at Delft University of Technology. He received a Ph.D. in Mechanical Engineering from the University of Florida in 2021 and previously held postdoctoral roles at UF and the University of Texas at San Antonio. His work develops machine-learning interatomic potentials and atomistic simulations for complex alloys and 2D materials, focusing on deformation, defects, hydrogen transport, and efficient energy-minimization methods.

Panagiotis Krokidas received his B.Sc. in Physics and his M.Sc. and Ph.D. in Computational Chemistry from the University of Patras, Greece. He is currently an Associate Researcher at the Institute of Informatics and Telecommunications, NCSR "Demokritos". His research focuses on machine learning and artificial intelligence methods for inverse materials design, with emphasis on efficient optimization and data-driven discovery of functional materials. He has participated in research projects in Greece, Stockholm, and at Texas A&M University at Qatar. In 2020, he was awarded a Marie Skłodowska-Curie Fellowship for developing an AI-enhanced design tool for metal−organic frameworks (MOFs).

Parsa Habibi received his PhD in Computational Chemistry from TU Delft in 2025 (thesis advisors: Thijs J. H. Vlugt, Poulumi Dey, and Othonas A. Moultos). His PhD research focused on performing molecular simulations to assess the hydrogen storage capacities of 2D materials and to predict thermodynamic and transport properties of hydrogen in aqueous electrolyte solutions. He obtained his BSc

degree in Molecular Science and Technology and his MSc degree in Chemical Engineering from TU Delft with distinction. After a short postdoctoral research period on hydrogen embrittlement (supervised by Poulumi Dey), he is currently working as a researcher/scientist in the industry.

V. Jelle Lagerweij is a PhD candidate in the Engineering Thermodynamics group at TU Delft, supervised by Thijs J. H. Vlugt and Othonas A. Moultos. He obtained his BSc and MSc degrees in Mechanical Engineering from TU Delft with distinction. His research focuses on the Grotthuss mechanism of proton transfer in aqueous solutions (computation of self-diffusion coefficients and electrical conductivities of these mixtures using ab initio and classical m1aq1ar dynamics simulations). His research interests also include the application of machine learning techniques for developing interatomic potentials.

Mahinder Ramdin is an assistant professor in Engineering Thermodynamics at the Process and Energy Department of the Delft University of Technology. His research focuses on process design, thermodynamic modeling, and techno-economics of renewable processes, including green hydrogen and CO_2 conversion to chemicals. He received an MSc degree in Chemical Engineering in 2010 and a PhD degree in Thermodynamics in 2015, both from the Delft University of Technology. After two postdocs, the first one in Molecular Simulations at the Delft University of Technology and the second one in Electrochemistry at the Antwerp University of Technology, he started his independent career as a tenure-track assistant professor in 2020 at the Delft University of Technology.

Thijs J. H. Vlugt obtained his MSc degree at Eindhoven University of Technology in the Netherlands in 1997. After a PhD degree at the University of Amsterdam in 2000 (thesis advisors: Rajamani Krishna and Berend Smit) he was postdoc in Mainz (Germany) and Leiden (the Netherlands). In 2003 he has appointed as assistant professor at Utrecht University (the Netherlands), and in 2007 he moved to Delft University of Technology, first as associate professor and since 2010 as full professor and chair Engineering Thermodynamics. He research is focused on molecular simulation, nanoporous materials, and applied thermodynamics.

Hadi Hajibeygi is Energi Simulation Chair and full professor of Geo-Energy Solid and Fluid Mechanics at TU Delft, where he also leads the Subsurface Storage Theme. He holds a PhD degree from ETH Zurich, Institute of Fluid Dynamics, for which he was awarded the ETH Zurich PhD medal. After completing his PhD in 2011, he became postdoctoral fellow at Stanford University, Department of Energy Resources Engineering, until 2013 when he joined TU Delft. Hadi was also a guest professor at the Institute for Modeling Hydraulic and Environmental Systems at the University of Stuttgart between 2017−2020 and served as the deputy/science lead of the IEA Technology Collaboration Program 42 on Underground Hydrogen Storage. His research interests include multiscale modeling and simulation of multiphase flow and mechanics in porous systems relevant to geoscience and geo-energy applications.

Poulumi Dey is an Associate Professor in the Department of Materials Science and Engineering at Delft University of Technology. She obtained her PhD degree in the field of theoretical Condensed Matter Physics from IITG in 2011. In 2012, she joined Max-Planck-Institut für Eisenforschung GmbH (Germany) as post-doctoral scientist. Dr. Dey's research focusses on computation-guided design of materials for sustainable and renewable energy applications. The research activities of her group are focused on the identification and optimization of materials for efficient hydrogen storage and hydrogen production based on simulation approach combining quantum mechanical Density Functional Theory (DFT) calculations and Molecular Dynamics simulations with machine learning and DFT based materials designing e.g., steels to make them better resistant to hydrogen embrittlement.

Ioannis N. Tsimpanogiannis is since 2019 a Research Scientist at the Centre for Research & Technology Hellas/Chemical Process & Energy Resources Institute (CERTH/CPERI), Thessaloniki, Greece. He received a Diploma of Chemical Engineering (1993) from the National Technical University of Athens, Greece and a Ph.D. Degree (2002) from the Chemical Engineering Department of the University of Southern California (USC), Los Angeles, CA, USA. He has worked as a postdoctoral research associate (2003-2006) at the Earth and Environmental Sciences Division of the Los Alamos National Laboratory (LANL), Los Alamos, NM, USA. He has also worked (2007-2019) at the National Center for Scientific Research (NCSR) "Demokritos", Athens, Greece. His research interests include: Flow, Phase Change, and Reactions in Porous Media; Hydrate Science and Technology; CO_2 Capture & Sequestration; Applied Thermodynamics, and Multiscale Modeling (Atomistic, Mesoscopic, and Macroscopic).

Othonas A. Moultos is an Associate Professor in the Mechanical Engineering Faculty at TU Delft. Before joining TU Delft, he worked as a research scientist on molecular modeling of chemical mixtures relevant to CCUS under the supervision of Prof. Ioannis Economou (Chem. Eng. TAMUQ, Qatar) and Prof. Athanassios Panagiotopoulos (Chem. Eng. Princeton, USA). In 2013, Dr. Moultos obtained a PhD in Physical Chemistry of Polymers from University of Ioannina, Greece (supervisor Prof. Costas Vlahos). In 2008, he graduated with a Diploma in Materials Engineering from the same university. His research and teaching activities focus on the application of molecular simulation to Process & Energy Engineering focusing primarily on hydrogen storage, purification and transportation, and towards designing sustainable adsorbents for the removal of organic pollutants from water. His work involves large-scale high-performance computing and takes advantage of powerful molecular simulation methods such as on-the-fly calculations of thermodynamic and transport properties using molecular dynamics, and phase-, adsorption- and reaction-equilibria using Monte Carlo.

ACKNOWLEDGMENTS

This work was sponsored by NWO Domain Science for the use of supercomputer facilities. The authors acknowledge the use of computational resources of DelftBlue supercomputer, provided by Delft High Performance Computing Centre (https://www.tudelft.nl/dhpc). O.A.M. is thankful to Prof. Luis F. M. Franco (UNICAMP) and Darshan Raju (TU Delft) for providing raw simulation data.

REFERENCES

(1) Palo, D. R.; Dagle, R. A.; Holladay, J. D. Methanol Steam Reforming for Hydrogen Production. *Chemical Reviews* **2007**, *107*, 3992−4021.

(2) Gunathilake, C.; Soliman, I.; Panthi, D.; Tandler, P.; Fatani, O.; Ghulamullah, N. A.; Marasinghe, D.; Farhath, M.; Madhujith, T.; Conrad, K.; Du, Y.; Jaroniec, M. A comprehensive review on hydrogen production, storage, and applications. *Chem. Soc. Rev.* **2024**, *53*, 10900−10969.

(3) Juangsa, F. B.; Irhamna, A. R.; Aziz, M. Production of ammonia as potential hydrogen carrier: Review on thermochemical and electrochemical processes. *International Journal of Hydrogen Energy* **2021**, *46*, 14455−14477.

(4) Aziz, M. Liquid Hydrogen: A Review on Liquefaction, Storage, Transportation, and Safety. *Energies* **2021**, *14*, 5917.

https://doi.org/10.1021/acs.chemrev.5c00617
Chem. Rev. 2025, 125, 11878−12029

(5) Cecere, D.; Giacomazzi, E.; Ingenito, A. A review on hydrogen industrial aerospace applications. *International Journal of Hydrogen Energy* **2014**, *39*, 10731−10747.
(6) Boldrini, A.; Koolen, D.; Crijns-Graus, W.; van den Broek, M. The impact of decarbonising the iron and steel industry on European power and hydrogen systems. *Applied Energy* **2024**, *361*, 122902.
(7) Nemmour, A.; Inayat, A.; Janajreh, I.; Ghenai, C. Green hydrogen-based E-fuels (E-methane, E-methanol, E-ammonia) to support clean energy transition: A literature review. *International Journal of Hydrogen Energy* **2023**, *48*, 29011−29033.
(8) Bacatelo, M.; Capucha, F.; Ferrão, P.; Margarido, F.; Bordado, J. Carbon-neutral cement: The role of green hydrogen. *International Journal of Hydrogen Energy* **2024**, *63*, 382−395.
(9) Bailera, M.; Kezibri, N.; Romeo, L. M.; Espatolero, S.; Lisbona, P.; Bouallou, C. Future applications of hydrogen production and CO_2 utilization for energy storage: Hybrid Power to Gas-Oxycombustion power plants. *International Journal of Hydrogen Energy* **2017**, *42*, 13625−13632.
(10) Hydrogen, International Renewable Energy Agency (IRENA). https://www.irena.org/Energy-Transition/Technology/Hydrogen#:~:text=Hydrogen%20is%20produced%20on%20a,of%20a%20mix%20of%20gases.. Accessed: 2024-07-22.
(11) Hydrogen Production Processes, Office of Energy Efficiency & Renewable Energy, U.S. Department of Energy. https://energy.sandia.gov/programs/fossil-energy/subsurface-storage/geologic-hydrogen-capabilities/geologic-hydrogen/, Accessed: 2024-07-22.
(12) Hasiuk, F.; Conley, D. M. Exploring Geologic Hydrogen: A New Frontier for Affordable, Reliable Energy Security, Sandia National Laboratories. https://www.energy.gov/eere/fuelcells/hydrogen-production-processes, Accessed: 2025-7-12.
(13) Lamy, C.; Millet, P. A critical review on the definitions used to calculate the energy efficiency coefficients of water electrolysis cells working under near ambient temperature conditions. *Journal of Power Sources* **2020**, *447*, 227350.
(14) Boettcher, S. W. Introduction to Green Hydrogen. *Chemical Reviews* **2024**, *124*, 13095−13098.
(15) Brauns, J.; Turek, T. Alkaline Water Electrolysis Powered by Renewable Energy: A Review. *Processes* **2020**, *8*, 248.
(16) Mazloomi, K.; Gomes, C. Hydrogen as an energy carrier: Prospects and challenges. *Renewable and Sustainable Energy Reviews* **2012**, *16*, 3024−3033.
(17) Nazir, H.; Muthuswamy, N.; Louis, C.; Jose, S.; Prakash, J.; Buan, M. E.; Flox, C.; Chavan, S.; Shi, X.; Kauranen, P.; Kallio, T.; Maia, G.; Tammeveski, K.; Lymperopoulos, N.; Carcadea, E.; Veziroglu, E.; Iranzo, A.; Kannan, A. M. Is the H_2 economy realizable in the foreseeable future? Part II: H_2 storage, transportation, and distribution. *International Journal of Hydrogen Energy* **2020**, *45*, 20693−20708.
(18) Holladay, J.; Hu, J.; King, D.; Wang, Y. An overview of hydrogen production technologies. *Catalysis Today* **2009**, *139*, 244−260.
(19) Lim, D.-W.; Ha, J.; Oruganti, Y.; Moon, H. R. Hydrogen separation and purification with MOF-based materials. *Materials Chemistry Frontiers* **2021**, *5*, 4022−4041.
(20) Morales-Ospino, R.; Celzard, A.; Fierro, V. Strategies to recover and minimize boil-off losses during liquid hydrogen storage. *Renewable and Sustainable Energy Reviews* **2023**, *182*, 113360.
(21) Yu, H.; Díaz, A.; Lu, X.; Sun, B.; Ding, Y.; Koyama, M.; He, J.; Zhou, X.; Oudriss, A.; Feaugas, X.; Zhang, Z. Hydrogen Embrittlement as a Conspicuous Material Challenge-Comprehensive Review and Future Directions. *Chemical Reviews* **2024**, *124*, 6271−6392.
(22) Jena, P. Materials for Hydrogen Storage: Past, Present, and Future. *Journal of Physical Chemistry Letters* **2011**, *2*, 206−211.
(23) Züttel, A. Materials for Hydrogen Storage. *Materials Today* **2003**, *6*, 24−33.
(24) Chalk, S. G.; Miller, J. F. Key challenges and recent progress in batteries, fuel cells, and hydrogen storage for clean energy systems. *Journal of Power Sources* **2006**, *159*, 73−80.
(25) Haug, P.; Koj, M.; Turek, T. Influence of process conditions on gas purity in alkaline water electrolysis. *International Journal of Hydrogen Energy* **2017**, *42*, 9406−9418.
(26) Zarghami, A.; Deen, N.; Vreman, A. CFD modeling of multiphase flow in an alkaline water electrolyzer. *Chemical Engineering Science* **2020**, *227*, 115926.
(27) Directive 2014/34/EU of the European Parliament and of the Council of 26 February 2014 on the harmonisation of the laws of the Member States relating to equipment and protective systems intended for use in potentially explosive atmospheres (recast) Text with EEA relevance. *Official Journal of the European Union* **2014-02-26**, *L 96/309*.
(28) Directive 2014/68/EU of the European Parliament and of the Council of 15 May 2014 on the harmonisation of the laws of the Member States relating to the making available on the market of pressure equipment (recast) Text with EEA relevance. *Official Journal of the European Union* **2014-05-15**, *L 189/164*.
(29) Tham, M. J.; Walker, R. D., Jr; Gubbins, K. E. Diffusion of oxygen and hydrogen in aqueous potassium hydroxide solutions. *The Journal of Physical Chemistry* **1970**, *74*, 1747−1751.
(30) Zhang, C.; Fan, F.-R. F.; Bard, A. J. Electrochemistry of oxygen in concentrated NaOH solutions: solubility, diffusion coefficients, and superoxide formation. *Journal of the American Chemical Society* **2009**, *131*, 177−181.
(31) Shi, K.; Meng, X.; Xiao, S.; Chen, G.; Wu, H.; Zhou, C.; Jiang, S.; Chu, P. K. MXene Coatings: Novel Hydrogen Permeation Barriers for Pipe Steels. *Nanomaterials* **2021**, *11*, 2737.
(32) Alanazi, A.; Ali, M.; Bawazeer, S.; Yekeen, N.; Hoteit, H. Evaluation of cubic, PC-SAFT, and GERG2008 equations of state for accurate calculations of thermophysical properties of hydrogen-blend mixtures. *Energy Reports* **2022**, *8*, 13876−13899.
(33) Alanazi, A.; Bawazeer, S.; Ali, M.; Keshavarz, A.; Hoteit, H. Thermodynamic modeling of hydrogen-water systems with gas impurity at various conditions using cubic and PC-SAFT equations of state. *Energy Conversion and Management: X* **2022**, *15*, 100257.
(34) Hassanpouryouzband, A.; Joonaki, E.; Edlmann, K.; Heinemann, N.; Yang, J. Thermodynamic and transport properties of hydrogen containing streams. *Scientific Data* **2020**, *7*, 222.
(35) van Westen, T.; Bauer, G.; Gross, J. Corresponding-states framework for classical and quantum fluids—Beyond Feynman-Hibbs. *The Journal of Chemical Physics* **2025**, *162*, 031101.
(36) Nasrifar, K. Comparative study of eleven equations of state in predicting the thermodynamic properties of hydrogen. *International Journal of Hydrogen Energy* **2010**, *35*, 3802−3811.
(37) Figueroa, J. D.; Bayona, S. G.; Orozco, G. A. A study of the thermodynamic properties of H_2 using EOS and molecular simulation methods. *International Journal of Hydrogen Energy* **2025**, *155*, 150074.
(38) Leachman, J. W.; Jacobsen, R. T.; Penoncello, S. G.; Lemmon, E. W. Fundamental Equations of State for Parahydrogen, Normal Hydrogen, and Orthohydrogen. *Journal of Physical and Chemical Reference Data* **2009**, *38*, 721−748.
(39) Bai-gang, S.; Dong-heng, Z.; Fu-Shui, L. A new equation of state for hydrogen gas. *International Journal of Hydrogen Energy* **2012**, *37*, 932−935.
(40) Lozano-Martín, D.; Moreau, A.; Chamorro, C. R. Thermophysical properties of hydrogen mixtures relevant for the development of the hydrogen economy: Review of available experimental data and thermodynamic models. *Renewable Energy* **2022**, *198*, 1398−1429.
(41) Park, B. H.; Chae, C. K. Development of correlation equations on hydrogen properties for hydrogen refueling process by machine learning approach. *International Journal of Hydrogen Energy* **2022**, *47*, 4185−4195.
(42) Economou, I. G. Statistical Associating Fluid Theory: A Successful Model for the Calculation of Thermodynamic and Phase Equilibrium Properties of Complex Fluid Mixtures. *Industrial & Engineering Chemistry Research* **2002**, *41*, 953−962.

https://doi.org/10.1021/acs.chemrev.5c00617
Chem. Rev. 2025, 125, 11878−12029

(43) Diamantonis, N. I.; Boulougouris, G. C.; Mansoor, E.; Tsangaris, D. M.; Economou, I. G. Evaluation of cubic, SAFT, and PC-SAFT equations of state for the vapor-liquid equilibrium modeling of CO_2 mixtures with other gases. *Ind. Eng. Chem. Res.* **2013**, *52*, 3933−3942.
(44) Gross, J.; Sadowski, G. Perturbed-Chain SAFT: An equation of state based on a perturbation theory for chain molecules. *Ind. Eng. Chem. Res.* **2001**, *40*, 1244−1260.
(45) Li, K.; Ye, Z.; Liang, X. PC-SAFT-Type Equations of State Revisited: Quantifying the Value of Base Model Adjustments through Universal Criteria Benchmarks. *Industrial & Engineering Chemistry Research* **2025**, *64*, 16873−16888.
(46) Rahbari, A.; Brenkman, J.; Hens, R.; Ramdin, M.; Van Den Broeke, L. J.; Schoon, R.; Henkes, R.; Moultos, O. A.; Vlugt, T. J. H. Solubility of water in hydrogen at high pressures: a molecular simulation study. *Journal of Chemical & Engineering Data* **2019**, *64*, 4103−4115.
(47) Rahbari, A.; Garcia-Navarro, J. C.; Ramdin, M.; van den Broeke, L. J. P.; Moultos, O. A.; Dubbeldam, D.; Vlugt, T. J. H. Effect of Water Content on Thermodynamic Properties of Compressed Hydrogen. *J. Chem. Eng. Data* **2021**, *66*, 2071−2087.
(48) Köster, A.; Thol, M.; Vrabec, J. Molecular models for the hydrogen age: hydrogen, nitrogen, oxygen, argon, and water. *J. Chem. Eng. Data* **2018**, *63*, 305−320.
(49) Sesé, L. M. Study of the Feynman-Hibbs effective potential against the path-integral formalism for Monte Carlo simulations of quantum many-body Lennard-Jones systems. *Mol. Phys.* **1994**, *81*, 1297−1312.
(50) Chen, J.; Li, X.-Z.; Zhang, Q.; Probert, M. I.; Pickard, C. J.; Needs, R. J.; Michaelides, A.; Wang, E. Quantum simulation of low-temperature metallic liquid hydrogen. *Nature communications* **2013**, *4*, 2064.
(51) Frenkel, D.; Smit, B. *Understanding Molecular Simulation: From Algorithms to Applications*, 3rd ed.; Elsevier: San Diego, United States, 2023.
(52) Allen, M. P.; Tildesley, D. J. *Computer Simulation of Liquids*, 2nd ed.; Oxford University Press: Oxford, 2017.
(53) McQuarrie, D. A.; Simon, J. D. *Physical Chemistry: A Molecular Approach*; University Science Books: Sausalito, California, 1997.
(54) Vega, C.; Sanz, E.; Abascal, J. L. F.; Noya, E. G. Determination of phase diagrams via computer simulation: methodology and applications to water, electrolytes and proteins. *J. Phys.: Condens. Matt.* **2008**, *20*, 153101.
(55) Allen, M. P. Long-range behaviour in liquid crystals by computer simulation. *J. Mol. Liq.* **2000**, *85*, 161−171.
(56) Chew, P. Y.; Reinhardt, A. Phase diagrams—Why they matter and how to predict them. *J. Chem. Phys.* **2023**, *158*, 030902.
(57) Reinhardt, A.; Cheng, B. Quantum-mechanical exploration of the phase diagram of water. *Nature Communications* **2021**, *12*, 588.
(58) Reinhardt, A.; Bethkenhagen, M.; Coppari, F.; Millot, M.; Hamel, S.; Cheng, B. Thermodynamics of high-pressure ice phases explored with atomistic simulations. *Nature Communications* **2022**, *13*, 4707.
(59) Marrink, S. J.; Risselada, H. J.; Yefimov, S.; Tieleman, D. P.; de Vries, A. H. The MARTINI Force Field: Coarse Grained Model for Biomolecular Simulations. *The Journal of Physical Chemistry B* **2007**, *111*, 7812−7824.
(60) Souza, P. C. T.; Alessandri, R.; Barnoud, J.; Thallmair, S.; Faustino, I.; Grunewald, F.; Patmanidis, I.; Abdizadeh, H.; Bruininks, B. M. H.; Wassenaar, T. A.; Kroon, P. C.; Melcr, J.; Nieto, V.; Corradi, V.; Khan, H. M.; Domański, J.; Javanainen, M.; Martinez-Seara, H.; Reuter, N.; Best, R. B.; Vattulainen, I.; Monticelli, L.; Periole, X.; Tieleman, D. P.; de Vries, A. H.; Marrink, S. J. Martini 3: a general purpose force field for coarse-grained molecular dynamics. *Nature Methods* **2021**, *18*, 382−388.
(61) Hoogerbrugge, P. J.; Koelman, J. M. V. A. Simulating Microscopic Hydrodynamic Phenomena with Dissipative Particle Dynamics. *Europhysics Letters* **1992**, *19*, 155.
(62) Jenko, F. Accelerating fusion research via supercomputing. *Nature Reviews Physics* **2025**, *7*, 365.
(63) Lu, G.-H.; Zhou, H.-B.; Becquart, C. S. A review of modelling and simulation of hydrogen behaviour in tungsten at different scales. *Nuclear Fusion* **2014**, *54*, 086001.
(64) Wang, X.-Y.; Wang, Y.-N.; Xu, K.; Dai, F.-Z.; Liu, H.-F.; Lu, G.-H.; Wang, H. Deep neural network potential for simulating hydrogen blistering in tungsten. *Physical Review Materials* **2023**, *7*, 093601.
(65) Li, X.-C.; Li, Y.-W.; Huang, H.-X.; Li, Y.-H.; Zhou, H.-B.; Lu, G.-H.; Deng, H.; Zhou, H.-S.; Luo, G.-N. Analytical WH, HH and HHe interatomic potentials for a WH-He system. *Journal of Nuclear Materials* **2025**, *607*, 155666.
(66) Brenner, D. W. Empirical potential for hydrocarbons for use in simulating the chemical vapor deposition of diamond films. *Physical review B* **1990**, *42*, 9458.
(67) Li, X.-C.; Shu, X.; Liu, Y.-N.; Gao, F.; Lu, G.-H. Modified analytical interatomic potential for a W-H system with defects. *Journal of Nuclear Materials* **2011**, *408*, 12−17.
(68) Thompson, A. P.; Swiler, L. P.; Trott, C. R.; Foiles, S. M.; Tucker, G. J. Spectral neighbor analysis method for automated generation of quantum-accurate interatomic potentials. *Journal of Computational Physics* **2015**, *285*, 316−330.
(69) El-Adawy, M.; Dalha, I. B.; Ismael, M. A.; Al-Absi, Z. A.; Nemitallah, M. A. Review of Sustainable Hydrogen Energy Processes: Production, Storage, Transportation, and Color-Coded Classifications. *Energy & Fuels* **2024**, *38*, 22686−22718.
(70) Incer-Valverde, J.; Korayem, A.; Tsatsaronis, G.; Morosuk, T. "Colors" of hydrogen: Definitions and carbon intensity. *Energy Conversion and Management* **2023**, *291*, 117294.
(71) Manabe, A.; Kashiwase, M.; Hashimoto, T.; Hayashida, T.; Kato, A.; Hirao, K.; Shimomura, I.; Nagashima, I. Basic study of alkaline water electrolysis. *Electrochimica Acta* **2013**, *100*, 249−256.
(72) Haug, P.; Kreitz, B.; Koj, M.; Turek, T. Process modelling of an alkaline water electrolyzer. *Int. J. Hydrogen Energy* **2017**, *42*, 15689−15707.
(73) de Groot, M. T.; Kraakman, J.; Garcia Barros, R. L. Optimal operating parameters for advanced alkaline water electrolysis. *Int. J. Hydrogen Energy* **2022**, *47*, 34773−34783.
(74) Oikonomidis, S.; Ramdin, M.; Moultos, O. A.; Bos, A.; Vlugt, T. J. H.; Rahbari, A. Transient modelling of a multi-cell alkaline electrolyzer for gas crossover and safe system operation. *Int. J. Hydrogen Energy* **2023**, *48*, 34210−34228.
(75) Abdin, Z.; Webb, C.; Gray, E. Modelling and simulation of an alkaline electrolyser cell. *Energy* **2017**, *138*, 316−331.
(76) Hammoudi, M.; Henao, C.; Agbossou, K.; Dubé, Y.; Doumbia, M. New multi-physics approach for modelling and design of alkaline electrolyzers. *International Journal of Hydrogen Energy* **2012**, *37*, 13895−13913.
(77) Bouwman, P. Electrochemical Hydrogen Compression (EHC) solutions for hydrogen infrastructure. *Fuel Cells Bulletin* **2014**, *2014*, 12−16.
(78) Bampaou, M.; Panopoulos, K. D.; Papadopoulos, A. I.; Seferlis, P.; Voutetakis, S. An electrochemical hydrogen compression model. *Chem. Eng. Trans.* **2018**, *70*, 1213−1218.
(79) de Miguel, N.; Acosta, B.; Moretto, P.; Ortiz Cebolla, R. Influence of the gas injector configuration on the temperature evolution during refueling of on-board hydrogen tanks. *Int. J. Hydrogen Energy* **2016**, *41*, 19447−19454.
(80) NASA, Fueling Protocols for Light Duty Gaseous Hydrogen Surface Vehicles. https://www.sae.org/standards/content/j2601_202005/, 2020; Accessed: 01-12-2020.
(81) Ji, M.; Wei, Z. A review of water management in polymer electrolyte membrane fuel cells. *Energies* **2009**, *2*, 1057−1106.
(82) Chatenet, M.; Pollet, B. G.; Dekel, D. R.; Dionigi, F.; Deseure, J.; Millet, P.; Braatz, R. D.; Bazant, M. Z.; Eikerling, M.; Staffell, I.; Balcombe, P.; Shao-Horn, Y.; Schäfer, H. Water electrolysis: from textbook knowledge to the latest scientific strategies and industrial developments. *Chem. Soc. Rev.* **2022**, *51*, 4583−4762.

(83) Haug, P.; Koj, M.; Turek, T. Influence of process conditions on gas purity in alkaline water electrolysis. *Int. J. Hydrogen Energy* **2017**, *42*, 9406−9418.
(84) Haug, P.; Kreitz, B.; Koj, M.; Turek, T. Process modelling of an alkaline water electrolyzer. *Int. J. Hydrogen Energy* **2017**, *42*, 15689−15707.
(85) Bodner, M.; Hofer, A.; Hacker, V. H_2 generation from alkaline electrolyzer. *Wiley Interdisciplinary Reviews: Energy and Environment* **2015**, *4*, 365−381.
(86) David, M.; Ocampo-Martínez, C.; Sánchez-Peña, R. Advances in alkaline water electrolyzers: A review. *Journal of Energy Storage* **2019**, *23*, 392−403.
(87) Solovey, V.; Shevchenko, A.; Zipunnikov, M.; Kotenko, A.; Khiem, N. T.; Tri, B. D.; Hai, T. T. Development of high pressure membraneless alkaline electrolyzer. *International Journal of Hydrogen Energy* **2022**, *47*, 6975−6985.
(88) Ulleberg, Ø. Modeling of advanced alkaline electrolyzers: a system simulation approach. *International Journal of Hydrogen Energy* **2003**, *28*, 21−33.
(89) Merle, G.; Wessling, M.; Nijmeijer, K. Anion exchange membranes for alkaline fuel cells: A review. *Journal of Membrane Science* **2011**, *377*, 1−35.
(90) Haug, P.; Kreitz, B.; Koj, M.; Turek, T. Process modelling of an alkaline water electrolyzer. *International Journal of Hydrogen Energy* **2017**, *42*, 15689−15707.
(91) Himmelblau, D. M. Diffusion of Dissolved Gases in Liquids. *Chemical Reviews* **1964**, *64*, 527−550.
(92) Kusoglu, A.; Weber, A. Z. New Insights into Perfluorinated Sulfonic-Acid Ionomers. *Chem. Rev.* **2017**, *117*, 987−1104.
(93) Arntsen, C.; Savage, J.; Tse, Y.-L.; Voth, G. A. Simulation of proton transport in proton exchange membranes with reactive molecular dynamics. *Fuel Cells* **2016**, *16*, 695−703.
(94) Rahbari, A.; Hartkamp, R.; Moultos, O. A.; Bos, A.; van den Broeke, L. J. P.; Ramdin, M.; Dubbeldam, D.; Lyulin, A. V.; Vlugt, T. J. H. Electro-osmotic Drag and Thermodynamic Properties of Water in Hydrated Nafion Membranes from Molecular Dynamics. *J. Phys. Chem. C* **2022**, *126*, 8121−8133.
(95) Zhang, G.; Yang, G.; Shen, Q.; Li, S.; Li, Z.; Liao, J.; Jiang, Z.; Wang, H.; Zhang, H.; Ye, W. Study on the transport performance degradation of Nafion membrane due to the presence of Na^+ and Ca^{2+} using molecular dynamics simulations. *Journal of Power Sources* **2022**, *542*, 231740.
(96) Li, H.; You, J.; Cheng, X.; Yan, X.; Shen, S.; Zhang, J. New insight into the effect of Co^{2+} contamination on local oxygen transport in PEMFCs. *Chemical Engineering Journal* **2023**, *453*, 139945.
(97) Zhu, Z.; Paddison, S. J. Perspective: Morphology and ion transport in ion-containing polymers from multiscale modeling and simulations. *Frontiers in Chemistry* **2022**, *10*, 981508.
(98) Wang, Y.; Si, C.; Zhang, X.; Wang, X.; He, W. Electro-osmotic drag coefficient of Nafion membrane with low water Content for Proton exchange membrane fuel cells. *Energy Reports* **2022**, *8*, 598−612.
(99) Sengupta, S.; Lyulin, A. V. Molecular Modeling of Structure and Dynamics of Nafion Protonation States. *J. Phys. Chem. B* **2019**, *123*, 6882−6891.
(100) Lyulin, A. V.; Sengupta, S.; Varughese, A.; Komarov, P.; Venkatnathan, A. Effect of Annealing on Structure and Diffusion in Hydrated Nafion Membranes. *ACS Appl. Polym. Mater.* **2020**, *2*, 5058−5066.
(101) Ozmaian, M.; Naghdabadi, R. Molecular dynamics simulation study of glass transition in hydrated Nafion. *Journal of Polymer Science Part B: Polymer Physics* **2014**, *52*, 907−915.
(102) Tuckerman, M. E.; Laasonen, K.; Sprik, M.; Parrinello, M. Ab initio simulations of water and water ions. *Journal of Physics: Condensed Matter* **1994**, *6*, A93.
(103) Tuckerman, M. E.; Marx, D.; Parrinello, M. The nature and transport mechanism of hydrated hydroxide ions in aqueous solution. *Nature* **2002**, *417*, 925−929.
(104) Marx, D. Proton Transfer 200 Years after von Grotthuss: Insights from Ab Initio Simulations. *ChemPhysChem* **2006**, *7*, 1848−1870.
(105) Lagerweij, V. J.; Bougueroua, S.; Habibi, P.; Dey, P.; Gaigeot, M.-P.; Moultos, O. A.; Vlugt, T. J. H. From Grotthuss Transfer to Conductivity: Machine Learning Molecular Dynamics of Aqueous KOH. *The Journal of Physical Chemistry B* **2025**, *129*, 6093−6099.
(106) Dohrn, R.; Brunner, G. High-pressure fluid-phase equilibria: Experimental methods and systems investigated (1988-1993). *Fluid Phase Equilib.* **1995**, *106*, 213−282.
(107) Christov, M.; Dohrn, R. High-pressure fluid phase equilibria: Experimental methods and systems investigated (1994-1999). *Fluid Phase Equilib.* **2002**, *202*, 153−218.
(108) Dohrn, R.; Peper, S.; Fonseca, J. M. High-pressure fluid-phase equilibria: Experimental methods and systems investigated (2000-2004). *Fluid Phase Equilib.* **2010**, *288*, 1−54.
(109) Fonseca, J. M.; Dohrn, R.; Peper, S. High-pressure fluid-phase equilibria: Experimental methods and systems investigated (2005-2008). *Fluid Phase Equilib.* **2011**, *300*, 1−69.
(110) Rahbari, A.; Brenkman, J.; Hens, R.; Ramdin, M.; Broeke, L. J. V. D.; Schoon, R.; Henkes, R.; Moultos, O. A.; Vlugt, T. J. H. Solubility of water in hydrogen at high pressures: A Molecular Simulation study. *J. Chem. Eng. Data* **2019**, *64*, 4103−4115.
(111) Habibi, P.; Dey, P.; Vlugt, T. J. H.; Moultos, O. A. Effect of Dissolved KOH and NaCl on the solubilities of water in Hydroen: A Monte Carlo Study. *The Journal of Chemical Physics* **2024**, *161*, 054304.
(112) Habibi, P.; Rahbari, A.; Blazquez, S.; Vega, C.; Dey, P.; Vlugt, T. J. H.; Moultos, O. A. A New Force Field for OH- for Computing Thermodynamic and Transport Properties of H_2 and O_2 in Aqueous NaOH and KOH Solutions. *J. Phys. Chem. B* **2022**, *126*, 9376−9387.
(113) Habibi, P.; Postma, J. R. T.; Padding, J. T.; Dey, P.; Vlugt, T. J. H.; Moultos, O. A. Thermodynamic and Transport Properties of $H_2/H_2O/NaB(OH)_4$ Mixtures Using the Delft Force Field (DFF/$B(OH)_4^-$). *Industrial & Engineering Chemistry Research* **2023**, *62*, 11992−12005.
(114) Kwon, S. H.; Kang, H.; Sohn, Y.-J.; Lee, J.; Shim, S.; Lee, S. G. Molecular dynamics simulation study on the effect of perfluorosulfonic acid side chains on oxygen permeation in hydrated ionomers of PEMFCs. *Scientific Reports* **2021**, *11*, 8702.
(115) Awulachew, S.; Nigussa, K. Molecular dynamics simulation of ion dynamics within PEM Fuel Cells. *Chemical Physics Letters* **2023**, *816*, 140380.
(116) Cui, S.; Liu, J.; Selvan, M. E.; Keffer, D. J.; Edwards, B. J.; Steele, W. V. A Molecular Dynamics Study of a Nafion Polyelectrolyte Membrane and the Aqueous Phase Structure for Proton Transport. *J. Phys. Chem. B* **2007**, *111*, 2208−2218.
(117) Venkatnathan, A.; Devanathan, R.; Dupuis, M. Atomistic Simulations of Hydrated Nafion and Temperature Effects on Hydronium Ion Mobility. *J. Phys. Chem. B* **2007**, *111*, 7234−7244.
(118) Hofmann, D. W.; Kuleshova, L.; D'Aguanno, B. Molecular dynamics simulation of hydrated Nafion with a reactive force field for water. *Journal of Molecular Modeling* **2008**, *14*, 225−235.
(119) Hofmann, D.; Kuleshova, L.; D'Aguanno, B. Theoretical simulations of proton conductivity: Basic principles for improving the proton conductor. *Journal of Power Sources* **2010**, *195*, 7743−7750.
(120) Brunello, G. F.; Mateker, W. R.; Lee, S. G.; Choi, J. I.; Jang, S. S. Effect of temperature on structure and water transport of hydrated sulfonated poly (ether ether ketone): A molecular dynamics simulation approach. *Journal of Renewable and Sustainable Energy* **2011**, 3.043111
(121) Brunello, G.; Lee, S. G.; Jang, S. S.; Qi, Y. A molecular dynamics simulation study of hydrated sulfonated poly (ether ether ketone) for application to polymer electrolyte membrane fuel cells: Effect of water content. *Journal of Renewable and Sustainable Energy* **2009**, *1*, 033101.
(122) Lins, R. D.; Devanathan, R.; Dupuis, M. Modeling the nanophase structural dynamics of phenylated sulfonated poly ether

https://doi.org/10.1021/acs.chemrev.5c00617
Chem. Rev. 2025, 125, 11878−12029

ether ketone ketone (Ph-SPEEKK) membranes as a function of hydration. *J. Phys. Chem. B* **2011**, *115*, 1817−1824.
(123) Devanathan, R.; Idupulapati, N.; Dupuis, M. Molecular modeling of the morphology and transport properties of two direct methanol fuel cell membranes: Phenylated sulfonated poly (ether ether ketone ketone) versus Nafion. *Journal of Materials Research* **2012**, *27*, 1927−1938.
(124) Cha, J. Morphological effect of side chain on H_3O^+ transfer inside polymer electrolyte membranes across polymeric chain via molecular dynamics simulation. *Scientific Reports* **2020**, *10*, 22014.
(125) Flottat, T.; Latour, B.; Goujon, F.; Hauret, P.; Malfreyt, P. Investigating percolation and clustering effects on aquivion and nafion membranes at the molecular scale. *Int. J. Hydrogen Energy* **2023**, *48*, 33283−33296.
(126) Xian, L.; Li, Z.; Li, S.; Chen, L.; Tao, W.-Q. Elucidating the impact mechanism of temperature and water content on thermal conductivity of hydrated Nafion membranes by molecular dynamics simulation. *International Journal of Heat and Mass Transfer* **2023**, *208*, 124034.
(127) Din, X.-D.; Michaelides, E. E. Transport processes of water and protons through micropores. *AIChE Journal* **1998**, *44*, 35−47.
(128) Yan, L.; Ji, X.; Lu, W. Molecular Dynamics Simulations of Electroosmosis in Perfluorosulfonic Acid Polymer. *J. Phys. Chem. B* **2008**, *112*, 5602−5610.
(129) Choe, Y.-K.; Tsuchida, E.; Ikeshoji, T.; Yamakawa, S.; Hyodo, S.-a. Nature of Water Transport and Electro-Osmosis in Nafion: Insights from First-Principles Molecular Dynamics Simulations under an Electric Field. *J. Phys. Chem. B* **2008**, *112*, 11586−11594.
(130) Keskin, S.; Sholl, D. S. Assessment of a Metal-Organic Framework Membrane for Gas Separations Using Atomically Detailed Calculations: CO_2, CH_4, N_2, H_2 Mixtures in MOF-5. *Industrial & Engineering Chemistry Research* **2009**, *48*, 914−922.
(131) Bayati, B.; Ghorbani, A.; Ghasemzadeh, K.; Iulianelli, A.; Basile, A. Study on the Separation of H_2 from CO_2 Using a ZIF-8 Membrane by Molecular Simulation and Maxwell-Stefan Model. *Molecules* **2019**, *24*, 4350.
(132) Duan, S.; Li, D.; Yang, X.; Niu, C.; Sun, S.; He, X.; Shan, M.; Zhang, Y. Experimental and molecular simulation study of a novel benzimidazole-linked polymer membrane for efficient H_2/CO_2 separation. *Journal of Membrane Science* **2023**, *671*, 121396.
(133) Hiscock, K. M.; Bense, V. F. *Hydrogeology: Principles and Practice*, 3rd Edition; Wiley-Blackwell, 2021.
(134) Barrer, R. M.; Chio, H. T. Solution and diffusion of gases and vapors in silicone rubber membranes. *Journal of Polymer Science Part C: Polymer Symposia* **1965**, *10*, 111−138.
(135) Karki, S.; Hazarika, G.; Yadav, D.; Ingole, P. G. Polymeric membranes for industrial applications: Recent progress, challenges and perspectives. *Desalination* **2024**, *573*, 117200.
(136) Robeson, L. M. The upper bound revisited. *Journal of Membrane Science* **2008**, *320*, 390−400.
(137) Koros, W. J.; Zhang, C. Materials for next-generation molecularly selective synthetic membranes. *Nature Materials* **2017**, *16*, 289−297.
(138) Krishna, R. Methodologies for screening and selection of crystalline microporous materials in mixture separations. *Separation and Purification Technology* **2018**, *194*, 281−300.
(139) Adil, K.; Belmabkhout, Y.; Pillai, R. S.; Cadiau, A.; Bhatt, P. M.; Assen, A. H.; Maurin, G.; Eddaoudi, M. Gas/vapour separation using ultra-microporous metal-organic frameworks: insights into the structure/separation relationship. *Chem. Soc. Rev.* **2017**, *46*, 3402−3430.
(140) Perez-Carbajo, J.; Matito-Martos, I.; Balestra, S. R. G.; Tsampas, M. N.; van de Sanden, M. C. M.; Delgado, J. A.; Águeda, V. I.; Merkling, P. J.; Calero, S. Zeolites for CO_2-CO-O_2 Separation to Obtain CO_2-Neutral Fuels. *ACS Applied Materials & Interfaces* **2018**, *10*, 20512−20520.
(141) Ackley, M. W.; Rege, S. U.; Saxena, H. Application of natural zeolites in the purification and separation of gases. *Microporous and Mesoporous Materials* **2003**, *61*, 25−42.
(142) Sircar, S.; Golden, T.; Rao, M. Activated carbon for gas separation and storage. *Carbon* **1996**, *34*, 1−12.
(143) Erdos, M.; Geerdink, D. F.; Martin-Calvo, A.; Pidko, E. A.; van den Broeke, L. J. P.; Calero, S.; Vlugt, T. J. H.; Moultos, O. A. In Silico Screening of Zeolites for High-Pressure Hydrogen Drying. *ACS Applied Materials & Interfaces* **2021**, *13*, 8383−8394.
(144) Jeong, H.-K. Metal-organic framework membranes: Unprecedented opportunities for gas separations. *AIChE Journal* **2021**, *67*, No. e17258.
(145) Beuerle, F.; Gole, B. Covalent Organic Frameworks and Cage Compounds: Design and Applications of Polymeric and Discrete Organic Scaffolds. *Angewandte Chemie International Edition* **2018**, *57*, 4850−4878.
(146) Yang, Z.; Wu, Z.; Peh, S. B.; Ying, Y.; Yang, H.; Zhao, D. Mixed-Matrix Membranes Containing Porous Materials for Gas Separation: From Metal-Organic Frameworks to Discrete Molecular Cages. *Engineering* **2023**, *23*, 40−55.
(147) Li, W. Metal-organic framework membranes: Production, modification, and applications. *Progress in Materials Science* **2019**, *100*, 21−63.
(148) Ahmad, N. N. R.; Lee, Y.; Abdul Hamid, M. R.; Mohd Ghazi, T. I.; Nasir, R.; Leo, C. P.; Koh, S. P.; Pasupuleti, J.; Tiong, S. K. Unlocking the potential of metal-organic frameworks-based mixed matrix membranes for hydrogen separation and purification. *Journal of Industrial and Engineering Chemistry* **2023**, *128*, 143−160.
(149) Aksu, G. O.; Erucar, I.; Haslak, Z. P.; Keskin, S. Accelerating discovery of COFs for CO_2 capture and H_2 purification using structurally guided computational screening. *Chemical Engineering Journal* **2022**, *427*, 131574.
(150) Ignacz, G.; Bader, L.; Beke, A. K.; Ghunaim, Y.; Shastry, T.; Vovusha, H.; Carbone, M. R.; Ghanem, B.; Szekely, G. Machine learning for the advancement of membrane science and technology: A critical review. *Journal of Membrane Science* **2025**, *713*, 123256.
(151) Chen, Y.; Zhao, G.; Yoon, S.; Habibi, P.; Hong, C. S.; Li, S.; Moultos, O. A.; Dey, P.; Vlugt, T. J. H.; Chung, Y. G. Computational Exploration of Adsorption-Based Hydrogen Storage in Mg-Alkoxide Functionalized Covalent-Organic Frameworks (COFs): Force-Field and Machine Learning Models. *ACS Applied Materials & Interfaces* **2024**, *16*, 61995−62009.
(152) Chung, Y. G.; Camp, J.; Haranczyk, M.; Sikora, B. J.; Bury, W.; Krungleviciute, V.; Yildirim, T.; Farha, O. K.; Sholl, D. S.; Snurr, R. Q. Computation-Ready, Experimental Metal-Organic Frameworks: A Tool To Enable High-Throughput Screening of Nanoporous Crystals. *Chemistry of Materials* **2014**, *26*, 6185−6192.
(153) Aksu, G. O.; Keskin, S. Advancing CH_4/H_2 separation with covalent organic frameworks by combining molecular simulations and machine learning. *J. Mater. Chem. A* **2023**, *11*, 14788−14799.
(154) Daglar, H.; Keskin, S. Combining Machine Learning and Molecular Simulations to Unlock Gas Separation Potentials of MOF Membranes and MOF/Polymer MMMs. *ACS Applied Materials & Interfaces* **2022**, *14*, 32134−32148.
(155) Aksu, G. O.; Keskin, S. The COF Space: Materials Features, Gas Adsorption, and Separation Performances Assessed by Machine Learning. *ACS Materials Letters* **2025**, *7*, 954−960.
(156) Altintas, C.; Keskin, S. On the shoulders of high-throughput computational screening and machine learning: Design and discovery of MOFs for H_2 storage and purification. *Materials Today Energy* **2023**, *38*, 101426.
(157) Demir, H.; Daglar, H.; Gulbalkan, H. C.; Aksu, G. O.; Keskin, S. Recent advances in computational modeling of MOFs: From molecular simulations to machine learning. *Coordination Chemistry Reviews* **2023**, *484*, 215112.
(158) Altintas, C.; Altundal, O. F.; Keskin, S.; Yildirim, R. Machine Learning Meets with Metal Organic Frameworks for Gas Storage and Separation. *Journal of Chemical Information and Modeling* **2021**, *61*, 2131−2146.
(159) Park, Y.; Kang, J.-H.; Moon, D.-K.; Jo, Y. S.; Lee, C.-H. Parallel and series multi-bed pressure swing adsorption processes for

https://doi.org/10.1021/acs.chemrev.5c00617
Chem. Rev. 2025, 125, 11878−12029

H2 recovery from a lean hydrogen mixture. *Chemical Engineering Journal* **2021**, *408*, 127299.
(160) Ribeiro, A. M.; Grande, C. A.; Lopes, F. V.; Loureiro, J. M.; Rodrigues, A. E. A parametric study of layered bed PSA for hydrogen purification. *Chemical Engineering Science* **2008**, *63*, 5258−5273.
(161) Sloan, E. D. J.; Koh, C. A. *Clathrate Hydrates of Natural Gases*, 3rd ed.; Taylor & Francis Group: Boca Raton, FL, 2008.
(162) Sloan, E. D., Jr Fundamental principles and applications of natural gas hydrates. *Nature* **2003**, *426*, 353−359.
(163) Khokhar, A.; Gudmundsson, J.; Sloan, E. Gas storage in structure H hydrates. *Fluid Phase Equilibria* **1998**, *150-151*, 383−392.
(164) Thomas, S.; Dawe, R. A. Review of ways to transport natural gas energy from countries which do not need the gas for domestic use. *Energy* **2003**, *28*, 1461−1477.
(165) Mi, F.; He, Z.; Pang, J.; Moultos, O. A.; Vlugt, T. J. H.; Ning, F. Molecular Insights into Hybrid CH_4 Physisorption-Hydrate Formation in Spiral Halloysite Nanotubes: Implications for Energy Storage. *ACS Applied Materials & Interfaces* **2024**, *16*, 67587−67596.
(166) Fang, B.; Lü, T.; Li, W.; Moultos, O. A.; Vlugt, T. J. H.; Ning, F. Microscopic insights into poly- and mono-crystalline methane hydrate dissociation in Na-montmorillonite pores at static and dynamic fluid conditions. *Energy* **2024**, *288*, 129755.
(167) Brewer, P. G.; Friederich, G.; Peltzer, E. T.; Orr, F. M., Jr Direct experiments on the ocean disposal of fossil fuel CO_2. *Science* **1999**, *284*, 943−945.
(168) Mi, F.; Li, W.; Pang, J.; Moultos, O. A.; Ning, F.; Vlugt, T. J. H. Molecular Insights into the Microscopic Behavior of CO_2 Hydrates in Oceanic Sediments: Implications for Carbon Sequestration. *The Journal of Physical Chemistry C* **2024**, *128*, 18588−18597.
(169) Ngan, Y. T.; Englezos, P. Concentration of mechanical pulp mill effluents and NaCl solutions through propane hydrate formation. *Industrial & Engineering Chemistry Research* **1996**, *35*, 1894−1900.
(170) Babu, P.; Nambiar, A.; He, T.; Karimi, I. A.; Lee, J. D.; Englezos, P.; Linga, P. A review of clathrate hydrate based desalination to strengthen energy-water nexus. *ACS Sustainable Chemistry & Engineering* **2018**, *6*, 8093−8107.
(171) Mao, W. L.; Mao, H.-k.; Goncharov, A. F.; Struzhkin, V. V.; Guo, Q.; Hu, J.; Shu, J.; Hemley, R. J.; Somayazulu, M.; Zhao, Y. Hydrogen clusters in clathrate hydrate. *Science* **2002**, *297*, 2247−2249.
(172) Veluswamy, H. P.; Kumar, R.; Linga, P. Hydrogen storage in clathrate hydrates: Current state of the art and future directions. *Applied Energy* **2014**, *122*, 112−132.
(173) Babu, P.; Linga, P.; Kumar, R.; Englezos, P. A review of the Hydrate Based Gas Separation (HBGS) process for carbon dioxide pre-combustion capture. *Energy* **2015**, *85*, 261−279.
(174) Kastanidis, P.; Tsimpanogiannis, I. N.; Romanos, G. E.; Stubos, A. K.; Economou, I. G. Recent advances in experimental measurements of mixed-gas three-phase hydrate equilibria for gas mixture separation and energy-related applications. *Journal of Chemical & Engineering Data* **2019**, *64*, 4991−5016.
(175) Tsimpanogiannis, I. N.; Costandy, J.; Kastanidis, P.; El Meragawi, S.; Michalis, V. K.; Papadimitriou, N. I.; Karozis, S. N.; Diamantonis, N. I.; Moultos, O. A.; Romanos, G. E. Using clathrate hydrates for gas storage and gas-mixture separations: Experimental and computational studies at multiple length scales. *Molecular Physics* **2018**, *116*, 2041−2060 others.
(176) Hassanpouryouzband, A.; Joonaki, E.; Farahani, M. V.; Takeya, S.; Ruppel, C.; Yang, J.; English, N. J.; Schicks, J. M.; Edlmann, K.; Mehrabian, H.; Aman, Z. M.; Tohidi, B. Gas hydrates in sustainable chemistry. *Chemical Society Reviews* **2020**, *49*, 5225−5309.
(177) Alavi, S.; Ripmeester, J. A. Simulations of hydrogen gas in clathrate hydrates. *Molecular Simulation* **2017**, *43*, 808−820.
(178) Patchkovskii, S.; Tse, J. S. Thermodynamic stability of hydrogen clathrates. *Proceedings of the National Academy of Sciences* **2003**, *100*, 14645−14650.
(179) Tribello, G. A.; Slater, B. A theoretical examination of known and hypothetical clathrate hydrate materials. *The Journal of Chemical Physics* **2009**, *131*, 024703.
(180) Wang, J.; Lu, H.; Ripmeester, J. A.; Becker, U. Molecular-dynamics and first-principles calculations of raman spectra and molecular and electronic structure of hydrogen clusters in hydrogen clathrate hydrate. *The Journal of Physical Chemistry C* **2010**, *114*, 21042−21050.
(181) Willow, S. Y.; Xantheas, S. S. Enhancement of hydrogen storage capacity in hydrate lattices. *Chemical Physics Letters* **2012**, *525-526*, 13−18.
(182) Trinh, T. T.; Waage, M. H.; Van Erp, T. S.; Kjelstrup, S. Low barriers for hydrogen diffusion in sII clathrate. *Physical Chemistry Chemical Physics* **2015**, *17*, 13808−13812.
(183) van der Waals, J.; Platteeuw, J. Clathrate solutions. *Advances in Chemical Physics* **1958**, *2* (Wiley), 1−57.
(184) Parrish, W. R.; Prausnitz, J. M. Dissociation pressures of gas hydrates formed by gas mixtures. *Industrial & Engineering Chemistry Process Design and Development* **1972**, *11*, 26−35.
(185) Holder, G.; Zetts, S.; Pradhan, N. Phase behavior in systems containing clathrate hydrates: a review. *Reviews in Chemical Engineering* **1988**, *5*, 1−70.
(186) Ballard, A.; Sloan, E., Jr The next generation of hydrate prediction: I. Hydrate standard states and incorporation of spectroscopy. *Fluid Phase Equilibria* **2002**, *194-197*, 371−383.
(187) Medeiros, F. D. A.; Segtovich, I. S. V.; Tavares, F. W.; Sum, A. K. Sixty years of the van der Waals and Platteeuw model for clathrate hydrates—A critical review from its statistical thermodynamic basis to its extensions and applications. *Chemical Reviews* **2020**, *120*, 13349−13381.
(188) Baltus, R. E.; Counce, R. M.; Culbertson, B. H.; Luo, H.; DePaoli, D. W.; Dai, S.; and, D. C. D. Examination of the Potential of Ionic Liquids for Gas Separations. *Separation Science and Technology* **2005**, *40*, 525−541.
(189) Ramdin, M.; de Loos, T. W.; Vlugt, T. J. H. State-of-the-Art of CO_2 Capture with Ionic Liquids. *Industrial & Engineering Chemistry Research* **2012**, *51*, 8149−8177.
(190) Designer Solvents. *Chemical & Engineering News Archive* **1998**, *76*, 32−37.
(191) Han, X.; Armstrong, D. W. Ionic Liquids in Separations. *Accounts of Chemical Research* **2007**, *40*, 1079−1086.
(192) U.S. Department of Energy, Hydrogen and Fuel Cell Technologies Office. https://www.energy.gov/eere/fuelcells/hydrogen-storage, 2023; Accessed: 03-01-2024.
(193) U.S. Department of Energy, Hydrogen Storage Fact Sheet. https://www.energy.gov/eere/fuelcells/articles/hydrogen-storage-fact-sheet, 2017; Accessed: 03-01-2024.
(194) Bell, I. H.; Wronski, J.; Quoilin, S.; Lemort, V. Pure and Pseudo-pure Fluid Thermophysical Property Evaluation and the Open-Source Thermophysical Property Library CoolProp. *Industrial & Engineering Chemistry Research* **2014**, *53*, 2498−2508.
(195) Pizzutilo, E.; Acher, T.; Reuter, B.; Will, C.; Schäfer, S. Subcooled liquid hydrogen technology for heavy-duty trucks. *World Electric Vehicle Journal* **2024**, *15*, 22.
(196) Safe, Fast and Simple: Daimler Truck and Linde Set New Standard for Liquid Hydrogen Refueling Technolog. https://www.daimlertruck.com/en/newsroom/pressrelease/safe-fast-and-simple-daimler-truck-and-linde-set-new-standard-for-liquid-hydrogen-refueling-technology-52581266#:~:text=Daimler%20Truck%20and%20Linde%20Engineering,costs%20and%20superior%20energy%20efficiency.. Accessed: October 15, 2025.
(197) DOE Technical Targets for Onboard Hydrogen Storage for Light-Duty Vehicles. https://www.energy.gov/eere/fuelcells/doe-technical-targets-onboard-hydrogen-storage-light-duty-vehicles, Accessed: October 15, 2025.
(198) Ahmed, A.; Seth, S.; Purewal, J.; Wong-Foy, A. G.; Veenstra, M.; Matzger, A. J.; Siegel, D. J. Exceptional hydrogen storage achieved by screening nearly half a million metal-organic frameworks. *Nature communications* **2019**, *10*, 1568.

https://doi.org/10.1021/acs.chemrev.5c00617
Chem. Rev. 2025, 125, 11878−12029

(199) Durbin, D.; Malardier-Jugroot, C. Review of Hydrogen Storage Techniques for on Board Vehicle Applications. *International Journal of Hydrogen Energy* **2013**, *38*, 14595−14617.
(200) Eberle, U.; Felderhoff, M.; Schueth, F. Chemical and Physical Solutions for Hydrogen Storage. *Angewandte Chemie International Edition* **2009**, *48*, 6608−6630.
(201) Sdanghi, G.; Maranzana, G.; Celzard, A.; Fierro, V. Review of the current technologies and performances of hydrogen compression for stationary and automotive applications. *Renew. Sust. Energy Rev.* **2019**, *102*, 150−170.
(202) Abe, J.; Popoola, A.; Ajenifuja, E.; Popoola, O. Hydrogen energy, economy and storage: Review and recommendation. *International Journal of Hydrogen Energy* **2019**, *44*, 15072−15086.
(203) Perspective on hydrogen energy carrier and its automotive applications. *International Journal of Hydrogen Energy* **2014** *39*, 8482−8494.
(204) Møller, K. T.; Jensen, T. R.; Akiba, E.; wen Li, H. Hydrogen - A sustainable energy carrier. *Progress in Natural Science: Materials International* **2017**, *27*, 34−40.
(205) Staffell, I.; Scamman, D.; Abad, A. V.; Balcombe, P.; Dodds, P. E.; Ekins, P.; Shah, N.; Ward, K. R. The role of hydrogen and fuel cells in the global energy system. *Energy & Environmental Science* **2019**, *12*, 463−491.
(206) Schlapbach, L.; Züttel, A. Hydrogen-storage materials for mobile applications. *Nature* **2001**, *414*, 353−358.
(207) Kuroki, T.; Sakoda, N.; Shinzato, K.; Monde, M.; Takata, Y. Prediction of transient temperature of hydrogen flowing from pre-cooler of refueling station to inlet of vehicle tank. *Int. J. Hydrogen Energy* **2018**, *43*, 1846−1854.
(208) Najdi, R. A.; Shaban, T. G.; Mourad, M. J.; Karaki, S. H. Hydrogen production and filling of fuel cell cars. 2016 3rd International Conference on Advances in Computational Tools for Engineering Applications (ACTEA). 2016; pp 43-48.
(209) de Miguel, N.; Acosta, B.; Baraldi, D.; Melideo, R.; Ortiz Cebolla, R.; Moretto, P. The role of initial tank temperature on refuelling of on-board hydrogen tanks. *Int. J. Hydrogen Energy* **2016**, *41*, 8606−8615.
(210) Adolf, J.; Balzer, C.; Louis, J. Energy of the future? Sustainable mobility through fuel cells and H_2;*Shell Hydrogen Study* **2017**; DOI: *Technical Report* DOI: 10.13140/RG.2.2.31848.57604.
(211) Manoharan, Y.; Hosseini, S. E.; Butler, B.; Alzhahrani, H.; Senior, B. T. F.; Ashuri, T.; Krohn, J. Hydrogen Fuel Cell Vehicles; Current Status and Future Prospect. *Applied Sciences* **2019**, *9*, 2296.
(212) Hammerschlag, R.; Mazza, P. Questioning hydrogen. *Energy Policy* **2005**, *33*, 2039−2043.
(213) Das, L. On-board hydrogen storage systems for automotive application. *Int. J. Hydrogen Energy* **1996**, *21*, 789−800.
(214) Bauer, A.; Mayer, T.; Semmel, M.; Guerrero Morales, M. A.; Wind, J. Energetic evaluation of hydrogen refueling stations with liquid or gaseous stored hydrogen. *Int. J. Hydrogen Energy* **2019**, *44*, 6795−6812.
(215) Rivard, E.; Trudeau, M.; Zaghib, K. Hydrogen Storage for Mobility: A Review. *Materials* **2019**, *12*, 1973.
(216) Moradi, R.; Groth, K. M. Hydrogen storage and delivery: Review of the state of the art technologies and risk and reliability analysis. *Int. J. Hydrogen Energy* **2019**, *44*, 12254−12269.
(217) Smolinka, T.; Garche, J. *Electrochemical power sources: fundamentals, systems, and applications: hydrogen production by water electrolysis*; Elsevier: Radarweg 29, PO Box 211, 1000 AE Amsterdam, The Netherlands, 2021.
(218) Fang, Q.; Ji, D. Molecular simulation of hydrogen permeation behavior in liner polymer materials of Type hydrogen storage vessels. *Materials Today Communications* **2023**, *35*, 106302.
(219) Preuster, P.; Papp, C.; Wasserscheid, P. Liquid Organic Hydrogen Carriers (LOHCs): Toward a Hydrogen-free Hydrogen Economy. *Accounts of Chemical Research* **2017**, *50*, 74−85.
(220) Ghotia, S.; Kumar, P.; Srivastava, A. K. A review on 2D materials: unveiling next-generation hydrogen storage solutions, advancements and prospects. *Journal of Materials Science* **2025**, *60*, 1071−1097.
(221) Sunnardianto, G. K.; Bokas, G.; Hussein, A.; Walters, C.; Moultos, O. A.; Dey, P. Efficient Hydrogen Storage in Defective Graphene and its Mechanical Stability: A Combined Density Functional Theory and Molecular Dynamics Simulation Study. *International Journal of Hydrogen Energy* **2021**, *46*, 5485−5494.
(222) Habibi, P.; Vlugt, T. J. H.; Dey, P.; Moultos, O. A. Reversible Hydrogen Storage in Metal-Decorated Honeycomb Borophene Oxide. *ACS Applied Materials & Interfaces* **2021**, *13*, 43233−43240.
(223) Bhatia, S. K.; Myers, A. L. Optimum Conditions for Adsorptive Storage. *Langmuir* **2006**, *22*, 1688−1700.
(224) Chan, K. S.; Miller, M. A.; Peng, X. First-Principles Computational Study of Hydrogen Storage in Silicon Clathrates. *Materials Research Letters* **2018**, *6*, 72−78.
(225) Lee, H.; Choi, W. I.; Nguyen, M. C.; Cha, M.-H.; Moon, E.; Ihm, J. Ab Initio Study of Dihydrogen Binding in Metal-Decorated Polyacetylene for Hydrogen Storage. *Phys. Rev. B* **2007**, *76*, 195110.
(226) Wang, L.; Chen, X.; Du, H.; Yuan, Y.; Qu, H.; Zou, M. First-Principles Investigation on Hydrogen Storage Performance of Li, Na and K Decorated Borophene. *Applied Surface Science* **2018**, *427*, 1030−1037.
(227) Suh, M. P.; Park, H. J.; Prasad, T. K.; Lim, D.-W. Hydrogen Storage in Metal-Organic Frameworks. *Chemical Reviews* **2012**, *112*, 782−835.
(228) Zhang, X.; Liu, P.; Zhang, Y. The application of MOFs for hydrogen storage. *Inorganica Chimica Acta* **2023**, *557*, 121683.
(229) Klopčič, N.; Grimmer, I.; Winkler, F.; Sartory, M.; Trattner, A. A review on metal hydride materials for hydrogen storage. *Journal of Energy Storage* **2023**, *72*, 108456.
(230) Schneemann, A.; White, J. L.; Kang, S.; Jeong, S.; Wan, L. F.; Cho, E. S.; Heo, T. W.; Prendergast, D.; Urban, J. J.; Wood, B. C.; Allendorf, M. D.; Stavila, V. Nanostructured Metal Hydrides for Hydrogen Storage. *Chemical Reviews* **2018**, *118*, 10775−10839.
(231) Lai, Q.; Sun, Y.; Wang, T.; Modi, P.; Cazorla, C.; Demirci, U. B.; Ares Fernandez, J. R.; Leardini, F.; Aguey-Zinsou, K.-F. How to Design Hydrogen Storage Materials? Fundamentals, Synthesis, and Storage Tanks. *Advanced Sustainable Systems* **2019**, *3*, 1900043.
(232) Sordakis, K.; Tang, C.; Vogt, L. K.; Junge, H.; Dyson, P. J.; Beller, M.; Laurenczy, G. Homogeneous Catalysis for Sustainable Hydrogen Storage in Formic Acid and Alcohols. *Chemical Reviews* **2018**, *118*, 372−433.
(233) Orimo, S.-i.; Nakamori, Y.; Eliseo, J. R.; Zuttel, A.; Jensen, C. M. Complex Hydrides for Hydrogen Storage. *Chemical Reviews* **2007**, *107*, 4111−4132.
(234) Park, J.; Ha, J.; Muhammad, R.; Lee, H. K.; Balderas-Xicohtencatl, R.; Cheng, Y.; Ramirez-Cuesta, A. J.; Streppel, B.; Hirscher, M.; Moon, H. R.; Oh, H. 20 K H_2 Physisorption on Metal-Organic Frameworks with Enhanced Dormancy Compared to Liquid Hydrogen Storage. *ACS Applied Energy Materials* **2023**, *6*, 9057−9064.
(235) Habibi, P.; Saji, T. H.; Vlugt, T. J. H.; Moultos, O. A.; Dey, P. Hydrogen dissociation in Li-decorated borophene and borophene hydride: An ab-initio study. *Applied Surface Science* **2022**, *603*, 154323.
(236) Hector, L.; Herbst, J. Density functional theory for hydrogen storage materials: successes and opportunities. *Journal of Physics: Condensed Matter* **2008**, *20*, 064229.
(237) Peng, B.; Zhang, H.; Shao, H.; Xu, Y.; Ni, G.; Zhang, R.; Zhu, H. Phonon transport properties of two-dimensional group-IV materials from ab initio calculations. *Physical Review B* **2016**, *94*, 245420.
(238) Memarian, F.; Fereidoon, A.; Darvish Ganji, M. Graphene Young's modulus: Molecular mechanics and DFT treatments. *Superlattices and Microstructures* **2015**, *85*, 348−356.
(239) Kuhs, W.; Chazallon, B.; Radaelli, P.; Pauer, F. Cage occupancy and compressibility of deuterated N_2-clathrate hydrate by neutron diffraction. *Journal of Inclusion Phenomena and Molecular Recognition in Chemistry* **1997**, *29*, 65−77.

https://doi.org/10.1021/acs.chemrev.5c00617
Chem. Rev. 2025, 125, 11878−12029

(240) Tsimpanogiannis, I. N.; Economou, I. G. Monte Carlo simulation studies of clathrate hydrates: A review. *The Journal of Supercritical Fluids* **2018**, *134*, 51−60.
(241) Vos, W. L.; Finger, L. W.; Hemley, R. J.; Mao, H.-k. Novel H_2-H_2O clathrates at high pressures. *Physical Review Letters* **1993**, *71*, 3150−3153.
(242) Udachin, K. A.; Lipkowski, J.; Tkacz, M. Double clathrate hydrates with helium and hydrogen. *Supramolecular Chemistry* **1994**, *3*, 181−183.
(243) Dyadin, Y. A.; Aladko, E. Y. The phase diagram of the water-hydrogen system in the crystallization field of solid solutions based on ices Ih and II at high pressures. *Journal of Inclusion Phenomena and Molecular Recognition in Chemistry* **1995**, *20*, 115−121.
(244) Dyadin, Y. A.; Larionov, E. G.; Manakov, A. Y.; Zhurko, F. V.; Aladko, E. Y.; Mikina, T. V.; Komarov, V. Y. Clathrate hydrates of hydrogen and neon. *Mendeleev Communications* **1999**, *9*, 209−210.
(245) Florusse, L. J.; Peters, C. J.; Schoonman, J.; Hester, K. C.; Koh, C. A.; Dec, S. F.; Marsh, K. N.; Sloan, E. D. Stable low-pressure hydrogen clusters stored in a binary clathrate hydrate. *Science* **2004**, *306*, 469−471.
(246) Mi, F.; Ning, F.; Vlugt, T. J. H.; Moultos, O. A. Molecular insight into hydrogen storage in clathrate hydrates: The effect of different promoters on the spontaneous nucleation of hydrogen hydrates studied via microsecond-scale molecular dynamics simulations. *Chemical Engineering Journal* **2025**, *512*, 162253.
(247) Lee, H.; Lee, J.-w.; Kim, D. Y.; Park, J.; Seo, Y.-T.; Zeng, H.; Moudrakovski, I. L.; Ratcliffe, C. I.; Ripmeester, J. A. Tuning clathrate hydrates for hydrogen storage. *Nature* **2005**, *434*, 743−746.
(248) Papadimitriou, N. I.; Tsimpanogiannis, I. N.; Economou, I. G.; Stubos, A. K. Storage of H_2 in clathrate hydrates: Evaluation of different force-fields used in Monte Carlo simulations. *Molecular Physics* **2017**, *115*, 1274−1285.
(249) Struzhkin, V. V.; Militzer, B.; Mao, W. L.; Mao, H.-k.; Hemley, R. J. Hydrogen storage in molecular clathrates. *Chemical Reviews* **2007**, *107*, 4133−4151.
(250) Manakov, A. Y.; Skiba, S. Application of clathrate compounds for hydrogen storage. *Russian Journal of General Chemistry* **2007**, *77*, 740−751.
(251) English, N. J.; MacElroy, J. Perspectives on molecular simulation of clathrate hydrates: Progress, prospects and challenges. *Chemical Engineering Science* **2015**, *121*, 133−156.
(252) Both, A. K.; Gao, Y.; Zeng, X. C.; Cheung, C. L. Gas hydrates in confined space of nanoporous materials: new frontier in gas storage technology. *Nanoscale* **2021**, *13*, 7447−7470.
(253) Davoodabadi, A.; Mahmoudi, A.; Ghasemi, H. The potential of hydrogen hydrate as a future hydrogen storage medium. *Iscience* **2021**, *24*, 101907.
(254) Gupta, A.; Baron, G. V.; Perreault, P.; Lenaerts, S.; Ciocarlan, R.-G.; Cool, P.; Mileo, P. G.; Rogge, S.; Van Speybroeck, V.; Watson, G. Hydrogen clathrates: Next generation hydrogen storage materials. *Energy Storage Materials* **2021**, *41*, 69−107 others.
(255) Moon, S.; Lee, Y.; Seo, D.; Lee, S.; Hong, S.; Ahn, Y.-H.; Park, Y. Critical hydrogen concentration of hydrogen-natural gas blends in clathrate hydrates for blue hydrogen storage. *Renewable and Sustainable Energy Reviews* **2021**, *141*, 110789.
(256) Zhang, Y.; Bhattacharjee, G.; Kumar, R.; Linga, P. Solidified hydrogen storage (Solid-HyStore) via clathrate hydrates. *Chemical Engineering Journal* **2022**, *431*, 133702.
(257) Tanaka, H.; Matsumoto, M. Statistical mechanical approach to the thermodynamic stability of clathrate hydrates. *Liquid Polymorphism* **2013**, *152* (Advances in Chemical Physics; Wiley), 421−462.
(258) Enerdata, 2022 Edition: Annual benchmarks and long-term impacts. 2022; https://www.enerdata.net/publications/reports-presentations/world-energy-trends.html, Accessed: October 15, 2025.
(259) Hematpur, H.; Abdollahi, R.; Rostami, S.; Haghighi, M.; Blunt, M. J. Review of underground hydrogen storage: Concepts and challenges. *Adv. Geo-Energy Res.***2023**, *7*, 111-131.
(260) Hassanpouryouzband, A.; Joonaki, E.; Edlmann, K.; Haszeldine, R. S. Offshore geological storage of hydrogen: is this our best option to achieve net-zero? *ACS Energy Letters* **2021**, *6*, 2181−2186.
(261) Heinemann, N.; Alcalde, J.; Miocic, J. M.; Hangx, S. J.; Kallmeyer, J.; Ostertag-Henning, C.; Hassanpouryouzband, A.; Thaysen, E. M.; Strobel, G. J.; Schmidt-Hattenberger, C. Enabling large-scale hydrogen storage in porous media-the scientific challenges. *Energy & Environmental Science* **2021**, *14*, 853−864 others.
(262) Krevor, S.; De Coninck, H.; Gasda, S. E.; Ghaleigh, N. S.; de Gooyert, V.; Hajibeygi, H.; Juanes, R.; Neufeld, J.; Roberts, J. J.; Swennenhuis, F. Subsurface carbon dioxide and hydrogen storage for a sustainable energy future. *Nat. Rev. Earth Environ.* **2023**, *4*, 102−118.
(263) Zivar, D.; Kumar, S.; Foroozesh, J. Underground hydrogen storage: A comprehensive review. *Int. J. Hydrogen Energy* **2021**, *46*, 23436−23462.
(264) Pan, B.; Yin, X.; Ju, Y.; Iglauer, S. Underground hydrogen storage: Influencing parameters and future outlook. *Adv. Colloid Interface Sci.* **2021**, *294*, 102473.
(265) Fernandez-Prini, R.; Harvey, A.; Palmer, D. *Aqueous Systems at Elevated Temperatures and Pressures* 1st Edition; 2004.
(266) Taylor, R.; Krishna, R. *Multicomponent mass transfer*, 1st ed.; John Wiley & Sons, 1993; Vol. 2.
(267) Krishna, R.; Wesselingh, J. The Maxwell-Stefan approach to mass transfer. *Chemical Engineering Science* **1997**, *52*, 861−911.
(268) Wang, L.; Jin, Z.; Huang, X.; Liu, R.; Su, Y.; Zhang, Q. Hydrogen Adsorption in Porous Geological Materials: A Review. *Sustainability* **2024**, *16*, 1958.
(269) Gong, Y.; Wang, S.-H.; Zhang, Z.-Y.; Yang, X.-L.; Yang, Z.-G.; Yang, H.-G. Degradation of sunlight exposure on the high-density polyethylene (HDPE) pipes for transportation of natural gases. *Polymer Degradation and Stability* **2021**, *194*, 109752.
(270) Wang, H.; Shah, J.; Hawwat, S.-E.; Huang, Q.; Khatami, A. A comprehensive review of polyethylene pipes: Failure mechanisms, performance models, inspection methods, and repair solutions. *Journal of Pipeline Science and Engineering* **2024**, *4*, 100174.
(271) Yersak, T. A.; Baker, D. R.; Yanagisawa, Y.; Slavik, S.; Immel, R.; Mack-Gardner, A.; Herrmann, M.; Cai, M. Predictive model for depressurization-induced blistering of type IV tank liners for hydrogen storage. *International Journal of Hydrogen Energy* **2017**, *42*, 28910−28917.
(272) Johnson, W. H. On some remarkable changes produced in iron and steel by the action of hydrogen and acids. *Nature* **1875**, *11*, 393.
(273) Pressouyre, G. Trap theory of hydrogen embrittlement. *Acta Metallurgica* **1980**, *28*, 895−911.
(274) Louthan, M., Jr; Caskey, G., Jr; Donovan, J.; Rawl, D., Jr Hydrogen embrittlement of metals. *Materials Science and Engineering* **1972**, *10*, 357−368.
(275) Seita, M.; Hanson, J. P.; Gradečak, S.; Demkowicz, M. J. The dual role of coherent twin boundaries in hydrogen embrittlement. *Nature Communications* **2015**, *6*, 6164.
(276) Song, J.; Curtin, W. A nanoscale mechanism of hydrogen embrittlement in metals. *Acta Materialia* **2011**, *59*, 1557−1569.
(277) Murakami, Y.; Kanezaki, T.; Mine, Y. Hydrogen effect against hydrogen embrittlement. *Metallurgical and Materials Transactions A* **2010**, *41*, 2548−2562.
(278) Wang, M.; Akiyama, E.; Tsuzaki, K. Effect of hydrogen on the fracture behavior of high strength steel during slow strain rate test. *Corrosion Science* **2007**, *49*, 4081−4097.
(279) Park, G. T.; Koh, S. U.; Jung, H. G.; Kim, K. Y. Effect of microstructure on the hydrogen trapping efficiency and hydrogen induced cracking of linepipe steel. *Corrosion Science* **2008**, *50*, 1865−1871.
(280) Turnbull, A. Perspectives on hydrogen uptake, diffusion and trapping. *International Journal of Hydrogen Energy* **2015**, *40*, 16961−16970.

https://doi.org/10.1021/acs.chemrev.5c00617
Chem. Rev. 2025, 125, 11878−12029

(281) Suzuki, N.; Ishii, N.; Miyagawa, T.; Harada, H. Estimation of delayed fracture property of steels. *Tetsu-to-Hagané* **1993**, *79*, 227−232.
(282) Han, Y.; Jing, H.; Xu, L. Welding heat input effect on the hydrogen permeation in the X80 steel welded joints. *Materials Chemistry and Physics* **2012**, *132*, 216−222.
(283) Bhadeshia, H. K. D. H. Prevention of hydrogen embrittlement in steels. *ISIJ international* **2016**, *56*, 24−36.
(284) Young, K. T.; Smith, C.; Krentz, T. M.; Hitchcock, D. A.; Vogel, E. M. Graphene synthesized by chemical vapor deposition as a hydrogen isotope permeation barrier. *Carbon* **2021**, *176*, 106−117.
(285) Takahashi, J.; Kawakami, K.; Tarui, T. Direct observation of hydrogen-trapping sites in vanadium carbide precipitation steel by atom probe tomography. *Scripta Materialia* **2012**, *67*, 213−216.
(286) Haley, D.; Merzlikin, S. V.; Choi, P.; Raabe, D. Atom probe tomography observation of hydrogen in high-Mn steel and silver charged via an electrolytic route. *international journal of hydrogen energy* **2014**, *39*, 12221−12229.
(287) Chen, Y.-S.; Haley, D.; Gerstl, S. S.; London, A. J.; Sweeney, F.; Wepf, R. A.; Rainforth, W. M.; Bagot, P. A.; Moody, M. P. Direct observation of individual hydrogen atoms at trapping sites in a ferritic steel. *Science* **2017**, *355*, 1196−1199.
(288) Chen, Y.-S.; Lu, H.; Liang, J.; Rosenthal, A.; Liu, H.; Sneddon, G.; McCarroll, I.; Zhao, Z.; Li, W.; Guo, A.; Cairney, J. M. Observation of hydrogen trapping at dislocations, grain boundaries, and precipitates. *Science* **2020**, *367*, 171−175.
(289) Maxelon, M.; Pundt, A.; Pyckhout-Hintzen, W.; Barker, J.; Kirchheim, R. Interaction of hydrogen and deuterium with dislocations in palladium as observed by small angle neutron scattering. *Acta materialia* **2001**, *49*, 2625−2634.
(290) Malard, B.; Remy, B.; Scott, C.; Deschamps, A.; Chene, J.; Dieudonné, T.; Mathon, M. Hydrogen trapping by VC precipitates and structural defects in a high strength Fe-Mn-C steel studied by small-angle neutron scattering. *Materials Science and Engineering: A* **2012**, *536*, 110−116.
(291) Yu, H.; Díaz, A.; Lu, X.; Sun, B.; Ding, Y.; Koyama, M.; He, J.; Zhou, X.; Oudriss, A.; Feaugas, X.; Zhang, Z. Hydrogen Embrittlement as a Conspicuous Material ChallengeComprehensive Review and Future Directions. *Chemical Reviews* **2024**, *124*, 6271−6392.
(292) Peng, Y.; Phan, T.; Zhai, H.; Xiong, L.; Zhang, X. Multiscale computational analysis of crack initiation at the grain boundaries in hydrogen-charged bi-crystalline alpha-iron. *International Journal of Plasticity* **2025**, *184*, 104182.
(293) Falcone, P. M.; Hiete, M.; Sapio, A. Hydrogen economy and sustainable development goals: Review and policy insights. *Current Opinion in Green and Sustainable Chemistry* **2021**, *31*, 100506.
(294) Al Ghafri, S. Z.; Munro, S.; Cardella, U.; Funke, T.; Notardonato, W.; Trusler, J. P. M.; Leachman, J.; Span, R.; Kamiya, S.; Pearce, G.; Swanger, A.; Rodriguez, E. D.; Bajada, P.; Jiao, F.; Peng, K.; Siahvashi, A.; Johns, M. L.; May, E. F. Hydrogen liquefaction: a review of the fundamental physics, engineering practice and future opportunities. *Energy Environ. Sci.* **2022**, *15*, 2690−2731.
(295) Han, S. S.; Kang, J. K.; Lee, H. M.; van Duin, A. C. T.; Goddard, I.; William, A. Liquefaction of H_2 molecules upon exterior surfaces of carbon nanotube bundles. *Applied Physics Letters* **2005**, *86*, 203108.
(296) Tuckerman, M. *Statistical Mechanics: Theory and Molecular Simulation*; Oxford Graduate Texts; OUP Oxford, 2010.
(297) Rapaport, D. *The Art of Molecular Dynamics Simulation*, 2nd ed.; Cambridge University Press, 2004.
(298) Landau, D. P.; Binder, K. *A Guide to Monte Carlo Simulations in Statistical Physics*, 4th ed.; Cambridge University Press: Cambridge, United Kingdom, 2015.
(299) Evans, D.; Morriss, G. *Statistical Mechanics of Nonequilibrium Liquids*, 2nd ed.; Cambridge University Press, 2008.
(300) Jorgensen, W. L.; Chandrasekhar, J.; Madura, J. D.; Impey, R. W.; Klein, M. L. Comparison of simple potential functions for simulating liquid water. *J. Chem. Phys.* **1983**, *79*, 926−935.
(301) Martin, M. G.; Siepmann, J. I. Transferable Potentials for Phase Equilibria. 1. United-Atom Description of n-Alkanes. *The Journal of Physical Chemistry B* **1998**, *102*, 2569−2577.
(302) Blazquez, S.; Conde, M. M.; Abascal, J. L. F.; Vega, C. The Madrid-2019 force field for electrolytes in water using TIP4P/2005 and scaled charges: Extension to the ions F^-, Br^-, I^-, Rb^+, and Cs^+. *The Journal of Chemical Physics* **2022**, *156*, 044505.
(303) Wallqvist, A.; Mountain, R. D. *Reviews in Computational Chemistry*; John Wiley & Sons, Ltd, 1999; pp 183−247.
(304) Stillinger, F. H.; Rahman, A. Improved simulation of liquid water by molecular dynamics. *The Journal of Chemical Physics* **1974**, *60*, 1545−1557.
(305) Abascal, J. L. F.; Vega, C. A general purpose model for the condensed phases of water: TIP4P/2005. *J. Chem. Phys.* **2005**, *123*, 234505.
(306) Jorgensen, W. L.; Tirado-Rives, J. The OPLS [optimized potentials for liquid simulations] potential functions for proteins, energy minimizations for crystals of cyclic peptides and crambin. *Journal of the American Chemical Society* **1988**, *110*, 1657−1666.
(307) Wang, J.; Wolf, R. M.; Caldwell, J. W.; Kollman, P. A.; Case, D. A. Development and testing of a general amber force field. *J. Comput. Chem.* **2004**, *25*, 1157−1174.
(308) Bartolomeu, R. A.; Franco, L. F. Thermophysical properties of supercritical H_2 from Molecular Dynamics simulations. *International Journal of Hydrogen Energy* **2020**, *45*, 16372−16380.
(309) Barraco, M.; Neyertz, S.; Benes, N. E.; Brown, D. Comparison of Eight Classical Lennard-Jones-Based H_2 Molecular Models in the Gas Phase at Temperatures and Pressures Relevant to Hydrogen On-Board Storage Tanks. *The Journal of Physical Chemistry A* **2023**, *127*, 6335−6346.
(310) Marx, D.; Nielaba, P. Path-integral Monte Carlo techniques for rotational motion in two dimensions: quenched, annealed, and no-spin quantum-statistical averages. *Phys. Rev. A* **1992**, *45*, 8968−8971.
(311) Cracknell, R. F. Molecular simulation of hydrogen adsorption in graphitic nanofibres. *Phys. Chem. Chem. Phys.* **2001**, *3*, 2091−2097.
(312) Buch, V. Path integral simulations of mixed para-D_2 and ortho-D_2 clusters: The orientational effects. *J. Chem. Phys.* **1994**, *100*, 7610−7629.
(313) Wang, S.; Hou, K.; Heinz, H. Accurate and Compatible Force Fields for Molecular Oxygen, Nitrogen, and Hydrogen to Simulate Gases, Electrolytes, and Heterogeneous Interfaces. *Journal of Chemical Theory and Computation* **2021**, *17*, 5198−5213.
(314) Śmiechowski, M. Molecular hydrogen solvated in water-A computational study. *The Journal of Chemical Physics* **2015**, *143*, 244505.
(315) Yang, J.; Ren, Y.; Tian, A.-m.; Sun, H. COMPASS Force Field for 14 Inorganic Molecules, He, Ne, Ar, Kr, Xe, H_2, O_2, N_2, NO, CO, CO_2, NO_2, CS_2, and SO_2, in Liquid Phases. *The Journal of Physical Chemistry B* **2000**, *104*, 4951−4957.
(316) Sun, H. COMPASS: an ab initio force-field optimized for condensed-phase applications overview with details on alkane and benzene compounds. *The Journal of Physical Chemistry B* **1998**, *102*, 7338−7364.
(317) Getman, R. B.; Bae, Y.-S.; Wilmer, C. E.; Snurr, R. Q. Review and Analysis of Molecular Simulations of Methane, Hydrogen, and Acetylene Storage in Metal Organic Frameworks. *Chemical Reviews* **2012**, *112*, 703−723.
(318) Boccara, N. *Essentials of Mathematica: With Applications to Mathematics and Physics*; Springer: New York, 2007; pp 445−448.
(319) Mason, E. A.; Rice, W. E. The Intermolecular Potentials of Helium and Hydrogen. *The Journal of Chemical Physics* **1954**, *22*, 522−535.
(320) Lenhard, J.; Stephan, S.; Hasse, H. On the History of the Lennard-Jones Potential. *Annalen der Physik* **2024**, *536*, 2400115.
(321) Hirschfelder, J. O.; Curtiss, C. F.; Bird, R. B. *Molecular Theory of Gases and Fluids*; Wiley: New York, 1954.
(322) Rzepka, M.; Lamp, P.; de la Casa-Lillo, M. A. Physisorption of Hydrogen on Microporous Carbon and Carbon Nanotubes. *J. Phys. Chem. B* **1998**, *102*, 10894−10898.

https://doi.org/10.1021/acs.chemrev.5c00617
Chem. Rev. 2025, 125, 11878−12029

(323) Ferrando, N.; Ungerer, P. Hydrogen/hydrocarbon phase equilibrium modelling with a cubic equation of state and a Monte Carlo method. *Fluid Phase Equilib.* **2007**, *254*, 211−223.
(324) Caviedes, D.; Cabria, I. Grand Canonical Monte Carlo simulations of the hydrogen storage capacities of slit-shaped pores, nanotubes and torusenes. *Int. J. Hydrogen Energy* **2022**, *47*, 11916−11928.
(325) Yang, Q.; Zhong, C. Molecular simulation of adsorption and diffusion of hydrogen in metal- organic frameworks. *The Journal of Physical Chemistry B* **2005**, *109*, 11862−11864.
(326) Engin, C.; Vrabec, J.; Hasse, H. On the difference between a point multipole and an equivalent linear arrangement of point charges in force field models for vapour-liquid equilibria; partial charge based models for 59 real fluids. *Mol. Phys.* **2011**, *109*, 1975−1982.
(327) Darkrim, F.; Vermesse, J.; Malbrunot, P.; Levesque, D. Monte Carlo simulations of nitrogen and hydrogen physisorption at high pressures and room temperature. Comparison with experiments. *J. Chem. Phys.* **1999**, *110*, 4020−4027.
(328) Marx, D.; Nielaba, P. Path-integral Monte Carlo techniques for rotational motion in two dimensions: Quenched, annealed, and no-spin quantum-statistical averages. *Physical Review A* **1992**, *45*, 8968.
(329) Li, Z.; Li, T.; Meng, L.; Wang, X.; Sun, H.; Zhang, M.; Kou, J. Molecular mechanisms of hydrogen leakage and blockage in kaolinite nano-cracks for underground hydrogen storage. *Physics of Fluids* **2025**, *37*, 012023.
(330) Bouanich, J.-P. Site-site Lennard-Jones potential parameters for N_2, O_2, H_2, CO and CO_2. *Journal of Quantitative Spectroscopy and Radiative Transfer* **1992**, *47*, 243−250.
(331) Sun, Y.; DeJaco, R. F.; Li, Z.; Tang, D.; Glante, S.; Sholl, D. S.; Colina, C. M.; Snurr, R. Q.; Thommes, M.; Hartmann, M.; Siepmann, J. I. Fingerprinting diverse nanoporous materials for optimal hydrogen storage conditions using meta-learning. *Science Advances* **2021**, *7*, No. eabg3983.
(332) Belof, J. L.; Stern, A. C.; Space, B. An accurate and transferable intermolecular diatomic hydrogen potential for condensed phase simulation. *J. Chem. Theory Comput.* **2008**, *4*, 1332−1337.
(333) Belof, J. L.; Stern, A. C.; Space, B. A predictive model of hydrogen sorption for metal-organic materials. *The Journal of Physical Chemistry C* **2009**, *113*, 9316−9320.
(334) Mondal, S.; Ghosh, S.; Chattaraj, P. A molecular dynamics study on sI hydrogen hydrate. *Journal of Molecular Modeling* **2013**, *19*, 2785−2790.
(335) Silvera, I. F.; Goldman, V. V. The isotropic intermolecular potential for H_2 and D_2 in the solid and gas phases. *J. Chem. Phys.* **1978**, *69*, 4209−4213.
(336) Alavi, S.; Ripmeester, J.; Klug, D. Molecular-dynamics study of structure II hydrogen clathrates. *The Journal of Chemical Physics* **2005**, *123*, 024507.
(337) Levesque, D.; Gicquel, A.; Darkrim, F. L.; Kayiran, S. B. Monte Carlo simulations of hydrogen storage in carbon nanotubes. *Journal of Physics: Condensed Matter* **2002**, *14*, 9285.
(338) Gu, C.; Gao, G.-H.; Yu, Y.-X.; Nitta, T. Simulation for separation of hydrogen and carbon monoxide by adsorption on single-walled carbon nanotubes. *Fluid Phase Equilibria* **2002**, *194*, 297−307.
(339) Sesé, L. M. Feynman-Hibbs quantum effective potentials for Monte Carlo simulations of liquid neon. *Molecular Physics* **1993**, *78*, 1167−1177.
(340) Kumar, A. A.; Bhatia, S. K. Quantum effect induced reverse kinetic molecular sieving in microporous materials. *Physical Review Letters* **2005**, *95*, 245901.
(341) Papadimitriou, N. I.; Tsimpanogiannis, I. N.; Economou, I. G.; Stubos, A. K. The effect of lattice constant on the storage capacity of hydrogen hydrates: a Monte Carlo study. *Molecular Physics* **2016**, *114*, 2664−2671.
(342) Michalis, V. K.; Economou, I. G.; Stubos, A. K.; Tsimpanogiannis, I. N. Phase equilibria molecular simulations of hydrogen hydrates via the direct phase coexistence approach. *The Journal of Chemical Physics* **2022**, *157*, 154501.
(343) Alavi, S.; Klug, D.; Ripmeester, J. Simulations of structure II H_2 and D_2 clathrates: potentials incorporating quantum corrections. *The Journal of Chemical Physics* **2008**, *128*, 064506.
(344) Wang, W. Atomic-potential parameters for H_2 and D_2: quantum corrections in the calculation of second-virial coefficients. *Journal of Quantitative Spectroscopy and Radiative Transfer* **2003**, *76*, 23−30.
(345) Vega, C.; Abascal, J. L. Simulating water with rigid non-polarizable models: a general perspective. *Phys. Chem. Chem. Phys.* **2011**, *13*, 19663−19688.
(346) Berendsen, H. J. C.; Grigera, J. R.; Straatsma, T. P. The missing term in effective pair potentials. *Journal of Physical Chemistry* **1987**, *91*, 6269−6271.
(347) Zeron, I.; Abascal, J.; Vega, C. A force field of Li^+, Na^+, K^+, Mg^{2+}, Ca^{2+}, Cl^-, and SO_4^{2-} in aqueous solution based on the TIP4P/2005 water model and scaled charges for the ions. *The Journal of Chemical Physics* **2019**, *151*, 134504.
(348) Tsimpanogiannis, I. N.; Moultos, O. A.; Franco, L. F. M.; Spera, M. B. M.; Erdos, M.; Economou, I. G. Self-diffusion coefficient of bulk and confined water: a critical review of classical molecular simulation studies. *Molecular Simulation* **2019**, *45*, 425−453.
(349) Abascal, J. L.; Vega, C. A general purpose model for the condensed phases of water: TIP4P/2005. *The Journal of Chemical Physics* **2005**, *123*, 234505.
(350) Habibi, P.; Polat, H. M.; Blazquez, S.; Vega, C.; Dey, P.; Vlugt, T. J. H.; Moultos, O. A. Accurate Free Energies of Aqueous Electrolyte Solutions from Molecular Simulations with Non-polarizable Force Fields. *The Journal of Physical Chemistry Letters* **2024**, *15*, 4477−4485.
(351) Wagner, W.; Pruß, A. The IAPWS formulation 1995 for the thermodynamic properties of ordinary water substance for general and scientific use. *J. Phys. Chem. Ref. Data* **2002**, *31*, 387−535.
(352) Lemmon, E. W.; Huber, M. L.; McLinden, M. O. NIST reference fluid thermodynamic and transport properties-REFPROP. *NIST Standard Reference Database* 2002, *23*, v7.
(353) Rick, S. W. A reoptimization of the five-site water potential (TIP5P) for use with Ewald sums. *J. Chem. Phys.* **2004**, *120*, 6085−6093.
(354) Jiang, H.; Moultos, O. A.; Economou, I. G.; Panagiotopoulos, A. Z. Hydrogen-Bonding Polarizable Intermolecular Potential Model for Water. *Journal of Physical Chemistry B* **2016**, *120*, 12358−12370.
(355) Kiss, P. T.; Baranyai, A. A Systematic Development of a Polarizable Potential of Water. *Journal of Chemical Physics* **2013**, *138*, 204507.
(356) Laury, M. L.; Wang, L.-P.; Pande, V. S.; Head-Gordon, T.; Ponder, J. W. Revised parameters for the AMOEBA polarizable atomic multipole water model. *J. Phys. Chem. B* **2015**, *119*, 9423−9437.
(357) Xiong, Y.; Izadi, S.; Onufriev, A. V. Fast Polarizable Water Model for Atomistic Simulations. *J. Chem. Theory Comput.* **2022**, *18*, 6324−6333.
(358) Abascal, J. L. F.; Sanz, E.; García Fernández, R.; Vega, C. A potential model for the study of ices and amorphous water: TIP4P/Ice. *The Journal of Chemical Physics* **2005**, *122*, 234511.
(359) Mahoney, M. W.; Jorgensen, W. L. A five-site model for liquid water and the reproduction of the density anomaly by rigid, nonpolarizable potential functions. *J. Chem. Phys.* **2000**, *112*, 8910−8922.
(360) Jorgensen, W. L.; Maxwell, D. S.; Tirado-Rives, J. Development and testing of the OPLS all-atom force field on conformational energetics and properties of organic liquids. *J. Amer. Chem. Soc.* **1996**, *118*, 11225−11236.
(361) Mark, P.; Nilsson, L. Structure and dynamics of the TIP3P, SPC, and SPC/E water models at 298 K. *J. Phys. Chem. A* **2001**, *105*, 9954−9960.

https://doi.org/10.1021/acs.chemrev.5c00617
Chem. Rev. 2025, 125, 11878−12029

(362) Habershon, S.; Markland, T. E.; Manolopoulos, D. E. Competing quantum effects in the dynamics of a flexible water model. *The Journal of Chemical Physics* **2009**, *131*, 024501.
(363) Rick, S. W. Simulations of ice and liquid water over a range of temperatures using the fluctuating charge model. *The Journal of Chemical Physics* **2001**, *114*, 2276−2283.
(364) Rick, S. W.; Freeman, D. L. Proton disorder and the dielectric constant of type II clathrate hydrates. *The Journal of Chemical Physics* **2010**, *132*, 054509.
(365) Rick, S. W.; Stuart, S. J.; Berne, B. J. Dynamical fluctuating charge force fields: Application to liquid water. *The Journal of Chemical Physics* **1994**, *101*, 6141−6156.
(366) Cendagorta, J. R.; Powers, A.; Hele, T. J.; Marsalek, O.; Bačić, Z.; Tuckerman, M. E. Competing quantum effects in the free energy profiles and diffusion rates of hydrogen and deuterium molecules through clathrate hydrates. *Physical Chemistry Chemical Physics* **2016**, *18*, 32169−32177.
(367) García Fernández, R.; Abascal, J. L.; Vega, C. The melting point of ice Ih for common water models calculated from direct coexistence of the solid-liquid interface. *The Journal of Chemical Physics* **2006**, *124*, 144506.
(368) Conde, M.; Rovere, M.; Gallo, P. High precision determination of the melting points of water TIP4P/2005 and water TIP4P/Ice models by the direct coexistence technique. *The Journal of Chemical Physics* **2017**, *147*, 244506.
(369) Conde, M.; Vega, C. Determining the three-phase coexistence line in methane hydrates using computer simulations. *The Journal of Chemical Physics* **2010**, *133*, 064507.
(370) Zeron, I. M.; Abascal, J. L. F.; Vega, C. A force field of Li^+, Na^+, K^+, Mg^{2+}, Ca^+, Cl^-, and SO_4^{2-} in aqueous solution based on the TIP4P/2005 water model and scaled charges for the ions. *J. Chem. Phys.* **2019**, *151*, 104501.
(371) Joung, I. S.; Cheatham, T. E. Determination of alkali and halide monovalent ion parameters for use in explicitly solvated biomolecular simulations. *The Journal of Physical Chemistry B* **2008**, *112*, 9020−9041.
(372) Kiss, P. T.; Baranyai, A. A new polarizable force field for alkali and halide ions. *The Journal of Chemical Physics* **2014**, *141*, 114501.
(373) Dočkal, J.; Lísal, M.; Moučka, F. Polarizable force fields for accurate molecular simulations of aqueous solutions of electrolytes, crystalline salts, and solubility: Li^+, Na^+, K^+, Rb^+, F^-, Cl^-, Br^-, I^-. *Journal of Molecular Liquids* **2022**, *362*, 119659.
(374) Smith, D. E.; Dang, L. X. Computer simulations of NaCl association in polarizable water. *The Journal of Chemical Physics* **1994**, *100*, 3757−3766.
(375) Jensen, K. P.; Jorgensen, W. L. Halide, Ammonium, and Alkali Metal Ion Parameters for Modeling Aqueous Solutions. *Journal of Chemical Theory and Computation* **2006**, *2*, 1499−1509.
(376) Straatsma, T. P.; Berendsen, H. J. C. Free energy of ionic hydration: Analysis of a thermodynamic integration technique to evaluate free energy differences by molecular dynamics simulations. *J. Chem. Phys.* **1988**, *89*, 5876−5886.
(377) Dang, L. X. Development of nonadditive intermolecular potentials using molecular dynamics: Solvation of Li^+ and F^- ions in polarizable water. *The Journal of Chemical Physics* **1992**, *96*, 6970−6977.
(378) Reif, M. M.; Hünenberger, P. H. Computation of methodology-independent single-ion solvation properties from molecular simulations. IV. Optimized Lennard-Jones interaction parameter sets for the alkali and halide ions in water. *The Journal of Chemical Physics* **2011**, *134*, 144104.
(379) Leontyev, I. V.; Stuchebrukhov, A. A. Electronic continuum model for molecular dynamics simulations. *The Journal of Chemical Physics* **2009**, *130*, 085102.
(380) Leontyev, I. V.; Stuchebrukhov, A. A. Electronic Continuum Model for Molecular Dynamics Simulations of Biological Molecules. *Journal of Chemical Theory and Computation* **2010**, *6*, 1498−1508.
(381) Leontyev, I. V.; Stuchebrukhov, A. A. Polarizable Mean-Field Model of Water for Biological Simulations with AMBER and CHARMM Force Fields. *Journal of Chemical Theory and Computation* **2012**, *8*, 3207−3216.
(382) Leontyev, I.; Stuchebrukhov, A. Accounting for electronic polarization in non-polarizable force fields. *Phys. Chem. Chem. Phys.* **2011**, *13*, 2613−2626.
(383) Kostal, V.; Jungwirth, P.; Martinez-Seara, H. Nonaqueous Ion Pairing Exemplifies the Case for Including Electronic Polarization in Molecular Dynamics Simulations. *J. Phys. Chem. Lett.* **2023**, *14*, 8691−8696.
(384) Blazquez, S.; Conde, M. M.; Vega, C. Scaled charges for ions: An improvement but not the final word for modeling electrolytes in water. *The Journal of Chemical Physics* **2023**, *158*, 054505.
(385) Blazquez, S.; Zeron, I.; Conde, M.; Abascal, J.; Vega, C. Scaled charges at work: Salting out and interfacial tension of methane with electrolyte solutions from computer simulations. *Fluid Phase Equilib.* **2020**, *513*, 112548.
(386) Shi, W.; Maginn, E. J. Atomistic Simulation of the Absorption of Carbon Dioxide and Water in the Ionic Liquid 1-n-Hexyl-3-methylimidazolium Bis(trifluoromethylsulfonyl)imide ([hmim][Tf2N]. *The Journal of Physical Chemistry B* **2008**, *112*, 2045−2055.
(387) Shi, W.; Maginn, E. J. Molecular Simulation and Regular Solution Theory Modeling of Pure and Mixed Gas Absorption in the Ionic Liquid 1-n-Hexyl-3-methylimidazolium Bis-(Trifluoromethylsulfonyl)amide ([hmim][Tf2N]). *The Journal of Physical Chemistry B* **2008**, *112*, 16710−16720.
(388) Kelkar, M. S.; Maginn, E. J. Calculating the Enthalpy of Vaporization for Ionic Liquid Clusters. *The Journal of Physical Chemistry B* **2007**, *111*, 9424−9427.
(389) Sambasivarao, S. V.; Acevedo, O. Development of OPLS-AA Force Field Parameters for 68 Unique Ionic Liquids. *Journal of Chemical Theory and Computation* **2009**, *5*, 1038−1050.
(390) Koller, T.; Ramos, J.; Garrido, N. M.; Fröba, A. P.; and, I. G. E. Development of a united-atom force field for 1-ethyl-3-methylimidazolium tetracyanoborate ionic liquid. *Molecular Physics* **2012**, *110*, 1115−1126.
(391) Singh, R.; Marin-Rimoldi, E.; Maginn, E. J. A Monte Carlo Simulation Study To Predict the Solubility of Carbon Dioxide, Hydrogen, and Their Mixture in the Ionic Liquids 1-Alkyl-3-methylimidazolium bis(trifluoromethanesulfonyl)amide ([Cnmim+][Tf2N-], n = 4, 6). *Industrial & Engineering Chemistry Research* **2015**, *54*, 4385−4395.
(392) Doherty, B.; Zhong, X.; Acevedo, O. Virtual Site OPLS Force Field for Imidazolium-Based Ionic Liquids. *The Journal of Physical Chemistry B* **2018**, *122*, 2962−2974.
(393) Cui, K.; Yethiraj, A.; Schmidt, J. R. Influence of Charge Scaling on the Solvation Properties of Ionic Liquid Solutions. *The Journal of Physical Chemistry B* **2019**, *123*, 9222−9229.
(394) Celebi, A. T.; Vlugt, T. J. H.; Moultos, O. A. Structural, Thermodynamic, and Transport Properties of Aqueous Reline and Ethaline Solutions from Molecular Dynamics Simulations. *The Journal of Physical Chemistry B* **2019**, *123*, 11014−11025.
(395) Celebi, A. T.; Vlugt, T. J. H.; Moultos, O. A. Thermal conductivity of aqueous solutions of reline, ethaline, and glyceline deep eutectic solvents; a molecular dynamics simulation study. *Molecular Physics* **2021**, *119*, No. e1876263.
(396) Verma, A. K.; Thorat, A. S.; Shah, J. K. Predicting Ionic Conductivity of Imidazolium-Based Ionic Liquid Mixtures Using Quantum-Mechanically Derived Partial Charges in the Condensed Phase. *The Journal of Physical Chemistry B* **2025**, *129*, 2546−2559.
(397) Habibi, P.; Rahbari, A.; Blazquez, S.; Vega, C.; Dey, P.; Vlugt, T. J. H.; Moultos, O. A. A New Force Field for OH^- for Computing Thermodynamic and Transport Properties of H_2 and O_2 in Aqueous NaOH and KOH Solutions. *J. Phys. Chem. B* **2022**, *126*, 9376−9387.
(398) Nezbeda, I.; Moučka, F.; Smith, W. R. Recent progress in molecular simulation of aqueous electrolytes: force fields, chemical potentials and solubility. *Molecular Physics* **2016**, *114*, 1665−1690.
(399) Rappe, A. K.; Casewit, C. J.; Colwell, K. S.; Goddard, W. A. I.; Skiff, W. M. UFF, a full periodic table force field for molecular

https://doi.org/10.1021/acs.chemrev.5c00617
Chem. Rev. 2025, 125, 11878−12029

mechanics and molecular dynamics simulations. *Journal of the American Chemical Society* **1992**, *114*, 10024−10035.
(400) Mayo, S. L.; Olafson, B. D.; Goddard, W. A. DREIDING: a generic force field for molecular simulations. *The Journal of Physical Chemistry* **1990**, *94*, 8897−8909.
(401) Vanduyfhuys, L.; Vandenbrande, S.; Verstraelen, T.; Schmid, R.; Waroquier, M.; Van Speybroeck, V. QuickFF: A program for a quick and easy derivation of force fields for metal-organic frameworks from ab initio input. *Journal of Computational Chemistry* **2015**, *36*, 1015−1027.
(402) Coupry, D. E.; Addicoat, M. A.; Heine, T. Extension of the Universal Force Field for Metal-Organic Frameworks. *Journal of Chemical Theory and Computation* **2016**, *12*, 5215−5225.
(403) Verploegh, R. J.; Kulkarni, A.; Boulfelfel, S. E.; Haydak, J. C.; Tang, D.; Sholl, D. S. Screening Diffusion of Small Molecules in Flexible Zeolitic Imidazolate Frameworks Using a DFT-Parameterized Force Field. *The Journal of Physical Chemistry C* **2019**, *123*, 9153−9167.
(404) Weng, T.; Schmidt, J. R. Flexible and Transferable ab Initio Force Field for Zeolitic Imidazolate Frameworks: ZIF-FF. *The Journal of Physical Chemistry A* **2019**, *123*, 3000−3012.
(405) Sun, H.; Jin, Z.; Yang, C.; Akkermans, R. L. C.; Robertson, S. H.; Spenley, N. A.; Miller, S.; Todd, S. M. COMPASS II: extended coverage for polymer and drug-like molecule databases. *Journal of Molecular Modeling* **2016**, *22*, 47.
(406) Sun, H.; Mumby, S. J.; Maple, J. R.; Hagler, A. T. An ab initio CFF93 all-atom force field for polycarbonates. *Journal of the American Chemical society* **1994**, *116*, 2978−2987.
(407) Voyiatzis, E.; Stroeks, A. Atomistic Modeling of Hydrogen and Oxygen Solubility in Semicrystalline PA-6 and HDPE Materials. *The Journal of Physical Chemistry B* **2022**, *126*, 6102−6111.
(408) Direct Force Field. https://www.aeontechnology.com/index.php, Accessed: October 15, 2025.
(409) O'Connor, T. C.; Andzelm, J.; Robbins, M. O. AIREBO-M: A reactive model for hydrocarbons at extreme pressures. *The Journal of Chemical Physics* **2015**, *142*, 024903.
(410) Mabuchi, T.; Tokumasu, T. Effect of bound state of water on hydronium ion mobility in hydrated Nafion using molecular dynamics simulations. *The Journal of Chemical Physics* **2014**, *141*, 104904.
(411) Smith, J. S.; Borodin, O.; Smith, G. D. A Quantum Chemistry Based Force Field for Poly(dimethylsiloxane). *The Journal of Physical Chemistry B* **2004**, *108*, 20340−20350.
(412) Ungerer, P.; Beauvais, C.; Delhommelle, J.; Boutin, A.; Rousseau, B.; Fuchs, A. H. Optimization of the anisotropic united atoms intermolecular potential for n-alkanes. *The Journal of Chemical Physics* **2000**, *112*, 5499−5510.
(413) Memari, P.; Lachet, V.; Klopffer, M.-H.; Flaconneche, B.; Rousseau, B. Gas mixture solubilities in polyethylene below its melting temperature: Experimental and molecular simulation studies. *Journal of Membrane Science* **2012**, *390-391*, 194−200.
(414) Bobbitt, N. S.; Snurr, R. Q. Molecular modelling and machine learning for high-throughput screening of metal-organic frameworks for hydrogen storage. *Molecular Simulation* **2019**, *45*, 1069−1081.
(415) Heinen, J.; Dubbeldam, D. On flexible force fields for metal-organic frameworks: Recent developments and future prospects. *Wiley Interdisciplinary Reviews: Computational Molecular Science* **2018**, *8*, No. e1363.
(416) Franz, D.; Forrest, K. A.; Pham, T.; Space, B. Accurate H_2 Sorption Modeling in the rht-MOF NOTT-112 Using Explicit Polarization. *Crystal Growth & Design* **2016**, *16*, 6024−6032.
(417) Krokidas, P.; Moncho, S.; Brothers, E. N.; Castier, M.; Economou, I. G. Tailoring the gas separation efficiency of metal organic framework ZIF-8 through metal substitution: A computational study. *Physical Chemistry Chemical Physics* **2018**, *20*, 4879−4892.
(418) Krokidas, P.; Moncho, S.; Brothers, E. N.; Economou, I. G. Defining New Limits in Gas Separations Using Modified ZIF Systems. *ACS Applied Materials & Interfaces* **2020**, *12*, 20536−20547.
(419) Harris, J. G.; Yung, K. H. Carbon Dioxide's Liquid-Vapor Coexistence Curve And Critical Properties as Predicted by a Simple Molecular Model. *The Journal of Physical Chemistry* **1995**, *99*, 12021−12024.
(420) Siu, S. W. I.; Pluhackova, K.; Böckmann, R. A. Optimization of the OPLS-AA Force Field for Long Hydrocarbons. *Journal of Chemical Theory and Computation* **2012**, *8*, 1459−1470.
(421) Gonzalez-Salgado, D.; Vega, C. A new intermolecular potential for simulations of methanol: The OPLS/2016 model. *J. Chem. Phys.* **2016**, *145*, 034508.
(422) Cygan, R. T.; Liang, J.-J.; Kalinichev, A. G. Molecular models of hydroxide, oxyhydroxide, and clay phases and the development of a general force field. *J. Phys. Chem. B* **2004**, *108*, 1255−1266.
(423) Cygan, R. T.; Greathouse, J. A.; Kalinichev, A. G. Advances in clayff molecular simulation of layered and nanoporous materials and their aqueous interfaces. *The Journal of Physical Chemistry C* **2021**, *125*, 17573−17589.
(424) Kerisit, S. Water structure at hematite-water interfaces. *Geochimica et Cosmochimica Acta* **2011**, *75*, 2043−2061.
(425) Heinz, H.; Lin, T.-J.; Kishore, R. M.; Emami, F. S. Thermodynamically consistent force fields for the assembly of inorganic, organic, and biological nanostructures: the INTERFACE force field. *Langmuir* **2013**, *29*, 1754−1765.
(426) Hagler, A.; Lifson, S.; Dauber, P. Consistent force field studies of intermolecular forces in hydrogen-bonded crystals. 2. A benchmark for the objective comparison of alternative force fields. *Journal of the American Chemical Society* **1979**, *101*, 5122−5130.
(427) Ungerer, P.; Collell, J.; Yiannourakou, M. Molecular modeling of the volumetric and thermodynamic properties of kerogen: Influence of organic type and maturity. *Energy & Fuels* **2015**, *29*, 91−105.
(428) Jorgensen, W. L.; Maxwell, D. S.; Tirado-Rives, J. Development and testing of the OPLS all-atom force field on conformational energetics and properties of organic liquids. *J. Amer. Chem. Soc.* **1996**, *118*, 11225−11236.
(429) Siboulet, B.; Coasne, B.; Dufreche, J.-F.; Turq, P. Hydrophobic transition in porous amorphous silica. *The Journal of Physical Chemistry B* **2011**, *115*, 7881−7886.
(430) Ungerer, P.; Rigby, D.; Leblanc, B.; Yiannourakou, M. Sensitivity of the aggregation behaviour of asphaltenes to molecular weight and structure using molecular dynamics. *Molecular Simulation* **2014**, *40*, 115−122.
(431) Xiao, S.; Edwards, S. A.; Grater, F. A new transferable forcefield for simulating the mechanics of $CaCO_3$ crystals. *The Journal of Physical Chemistry C* **2011**, *115*, 20067−20075.
(432) Raiteri, P.; Gale, J. D.; Quigley, D.; Rodger, P. M. Derivation of an accurate force-field for simulating the growth of calcium carbonate from aqueous solution: A new model for the calcite- water interface. *The Journal of Physical Chemistry C* **2010**, *114*, 5997−6010.
(433) Daw, M. S.; Baskes, M. I. Semiempirical, Quantum Mechanical Calculation of Hydrogen Embrittlement in Metals. *Phys. Rev. Lett.* **1983**, *50*, 1285−1288.
(434) Daw, M. S.; Baskes, M. I. Embedded-atom method: Derivation and application to impurities, surfaces, and other defects in metals. *Phys. Rev. B* **1984**, *29*, 6443−6453.
(435) Hale, L. M.; Wong, B. M.; Zimmerman, J. A.; Zhou, X. W. Atomistic potentials for palladium-silver hydrides. *Modelling and Simulation in Materials Science and Engineering* **2013**, *21*, 045005.
(436) Angelo, J. E.; Moody, N. R.; Baskes, M. I. Trapping of hydrogen to lattice defects in nickel. *Modelling and Simulation in Materials Science and Engineering* **1995**, *3*, 289.
(437) Ramasubramaniam, A.; Itakura, M.; Carter, E. A. Interatomic potentials for hydrogen in α-iron based on density functional theory. *Phys. Rev. B* **2009**, *79*, 174101.
(438) Wen, M. A new interatomic potential describing Fe-H and H-H interactions in bcc iron. *Computational Materials Science* **2021**, *197*, 110640.

https://doi.org/10.1021/acs.chemrev.5c00617
Chem. Rev. 2025, 125, 11878−12029

(439) Kumar, P.; Ludhwani, M. M.; Das, S.; Gavini, V.; Kanjarla, A.; Adlakha, I. Effect of hydrogen on plasticity of α-Fe: A multi-scale assessment. *International Journal of Plasticity* **2023**, *165*, 103613.
(440) Zhou, X.; Zimmerman, J.; Wong, B.; Hoyt, J. An embedded-atom method interatomic potential for Pd-H alloys. *Journal of Materials Research* **2008**, *23*, 704−718.
(441) Bonny, G.; Grigorev, P.; Terentyev, D. On the binding of nanometric hydrogen-helium clusters in tungsten. *Journal of Physics: Condensed Matter* **2014**, *26*, 485001.
(442) Tehranchi, A.; Curtin, W. Atomistic study of hydrogen embrittlement of grain boundaries in nickel: I. Fracture. *Journal of the Mechanics and Physics of Solids* **2017**, *101*, 150−165.
(443) Mason, D. R.; Nguyen-Manh, D.; Lindblad, V. W.; Granberg, F. G.; Lavrentiev, M. Y. An empirical potential for simulating hydrogen isotope retention in highly irradiated tungsten. *Journal of Physics: Condensed Matter* **2023**, *35*, 495901.
(444) Zhou, X.; Nowak, C.; Skelton, R.; Foster, M.; Ronevich, J.; San Marchi, C.; Sills, R. An Fe-Ni-Cr-H interatomic potential and predictions of hydrogen-affected stacking fault energies in austenitic stainless steels. *International Journal of Hydrogen Energy* **2022**, *47*, 651−665.
(445) Baskes, M. I. Modified embedded-atom potentials for cubic materials and impurities. *Phys. Rev. B* **1992**, *46*, 2727−2742.
(446) Lee, B.-J.; Baskes, M. I. Second nearest-neighbor modified embedded-atom-method potential. *Phys. Rev. B* **2000**, *62*, 8564−8567.
(447) Ko, W.-S.; Shim, J.-H.; Lee, B.-J. Atomistic modeling of the Al-H and Ni-H systems. *Journal of Materials Research* **2011**, *26*, 1552−1560.
(448) Shim, J.-H.; Ko, W.-S.; Kim, K.-H.; Lee, H.-S.; Lee, Y.-S.; Suh, J.-Y.; Cho, Y. W.; Lee, B.-J. Prediction of hydrogen permeability in V-Al and V-Ni alloys. *Journal of Membrane Science* **2013**, *430*, 234−241.
(449) Lee, B.-J.; Jang, J.-W. A modified embedded-atom method interatomic potential for the Fe-H system. *Acta Materialia* **2007**, *55*, 6779−6788.
(450) Shim, J.-H.; Lee, Y.-S.; Fleury, E.; Cho, Y. W.; Ko, W.-S.; Lee, B.-J. A modified embedded-atom method interatomic potential for the V-H system. *Calphad* **2011**, *35*, 302−307.
(451) Lee, B.-M.; Lee, B.-J. A Comparative Study on Hydrogen Diffusion in Amorphous and Crystalline Metals Using a Molecular Dynamics Simulation. *Metallurgical and Materials Transactions A* **2014**, *45*, 2906−2915.
(452) Mishin, Y.; Mehl, M.; Papaconstantopoulos, D. Phase stability in the Fe-Ni system: Investigation by first-principles calculations and atomistic simulations. *Acta Materialia* **2005**, *53*, 4029−4041.
(453) Apostol, F.; Mishin, Y. Angular-dependent interatomic potential for the aluminum-hydrogen system. *Phys. Rev. B* **2010**, *82*, 144115.
(454) Starikov, S.; Smirnova, D.; Pradhan, T.; Gordeev, I.; Drautz, R.; Mrovec, M. Angular-dependent interatomic potential for large-scale atomistic simulation of the Fe-Cr-H ternary system. *Phys. Rev. Mater.* **2022**, *6*, 043604.
(455) Smirnova, D.; Starikov, S.; Vlasova, A. New interatomic potential for simulation of pure magnesium and magnesium hydrides. *Computational Materials Science* **2018**, *154*, 295−302.
(456) Pettifor, D. G.; Oleinik, I. I. Analytic bond-order potentials beyond Tersoff-Brenner. I. Theory. *Phys. Rev. B* **1999**, *59*, 8487−8499.
(457) Ward, D. K.; Zhou, X. W.; Wong, B. M.; Doty, F. P.; Zimmerman, J. A. Analytical bond-order potential for the cadmium telluride binary system. *Phys. Rev. B* **2012**, *85*, 115206.
(458) Zhou, X. W.; Ward, D. K.; Foster, M. E. A bond-order potential for the Al-Cu-H ternary system. *New J. Chem.* **2018**, *42*, 5215−5228.
(459) Zhou, X. W.; Ward, D. K.; Foster, M.; Zimmerman, J. A. An analytical bond-order potential for the copper-hydrogen binary system. *Journal of Materials Science* **2015**, *50*, 2859−2875.
(460) Behler, J.; Parrinello, M. Generalized Neural-Network Representation of High-Dimensional Potential-Energy Surfaces. *Phys. Rev. Lett.* **2007**, *98*, 146401.
(461) Bartok, A. P.; Payne, M. C.; Kondor, R.; Csányi, G. Gaussian Approximation Potentials: The Accuracy of Quantum Mechanics, without the Electrons. *Phys. Rev. Lett.* **2010**, *104*, 136403.
(462) Shapeev, A. V. Moment Tensor Potentials: A Class of Systematically Improvable Interatomic Potentials. *Multiscale Modeling & Simulation* **2016**, *14*, 1153−1173.
(463) Mishin, Y. Machine-learning interatomic potentials for materials science. *Acta Materialia* **2021**, *214*, 116980.
(464) Kimizuka, H.; Thomsen, B.; Shiga, M. Artificial neural network-based path integral simulations of hydrogen isotope diffusion in palladium. *Journal of Physics: Energy* **2022**, *4*, 034004.
(465) Kwon, H.; Shiga, M.; Kimizuka, H.; Oda, T. Accurate description of hydrogen diffusivity in bcc metals using machine-learning moment tensor potentials and path-integral methods. *Acta Materialia* **2023**, *247*, 118739.
(466) Qi, J.; Ko, T. W.; Wood, B. C.; Pham, T. A.; Ong, S. P. Robust training of machine learning interatomic potentials with dimensionality reduction and stratified sampling. *npj Computational Materials* **2024**, *10*, 43.
(467) Meng, F.-S.; Du, J.-P.; Shinzato, S.; Mori, H.; Yu, P.; Matsubara, K.; Ishikawa, N.; Ogata, S. General-purpose neural network interatomic potential for the α-iron and hydrogen binary system: Toward atomic-scale understanding of hydrogen embrittlement. *Phys. Rev. Mater.* **2021**, *5*, 113606.
(468) Shuang, F.; Ji, Y.; Wei, Z.; Dong, C.; Gao, W.; Laurenti, L.; Dey, P. Decoding the hidden dynamics of super-Arrhenius hydrogen diffusion in multi-principal element alloys via machine learning. *Acta Materialia* **2025**, *289*, 120924.
(469) Zhou, X.-Y.; Wu, H.-H.; Zhou, M.; Wang, L.; Lookman, T.; Mao, X. Enhanced hydrogen embrittlement resistance of FeCoNiCrMn multi-principal element alloys via local chemical ordering and grain boundary segregation. *Acta Materialia* **2025**, *296*, 121209.
(470) Pun, G. P. P.; Batra, R.; Ramprasad, R.; Mishin, Y. Physically informed artificial neural networks for atomistic modeling of materials. *Nature Communications* **2019**, *10*, 2339.
(471) Pun, G. P. P.; Yamakov, V.; Hickman, J.; Glaessgen, E. H.; Mishin, Y. Development of a general-purpose machine-learning interatomic potential for aluminum by the physically informed neural network method. *Phys. Rev. Mater.* **2020**, *4*, 113807.
(472) Lin, Y.-S.; Pun, G. P. P.; Mishin, Y. Development of a physically-informed neural network interatomic potential for tantalum. *Computational Materials Science* **2022**, *205*, 111180.
(473) Thompson, A. P.; Aktulga, H. M.; Berger, R.; Bolintineanu, D. S.; Brown, W. M.; Crozier, P. S.; in 't Veld, P. J.; Kohlmeyer, A.; Moore, S. G.; Nguyen, T. D.; Shan, R.; Stevens, M. J.; Tranchida, J.; Trott, C.; Plimpton, S. J. LAMMPS - a flexible simulation tool for particle-based materials modeling at the atomic, meso, and continuum scales. *Comp. Phys. Comm.* **2022**, *271*, 108171.
(474) Shuang, F.; Liu, K.; Ji, Y.; Gao, W.; Laurenti, L.; Dey, P. Modeling extensive defects in metals through classical potential-guided sampling and automated configuration reconstruction. *npj Computational Materials* **2025**, *11*, 118.
(475) Plimpton, S. Fast parallel algorithms for short-range molecular dynamics. *Journal of Computational Physics* **1995**, *117*, 1−19.
(476) Berendsen, H. J.; van der Spoel, D.; van Drunen, R. GROMACS: A message-passing parallel molecular dynamics implementation. *Computer physics communications* **1995**, *91*, 43−56.
(477) Hess, B.; Kutzner, C.; Van Der Spoel, D.; Lindahl, E. GROMACS 4: algorithms for highly efficient, load-balanced, and scalable molecular simulation. *J. Chem. Theory Comput.* **2008**, *4*, 435−447.
(478) LAMMPS Development Team, LAMMPS Documentation. https://docs.lammps.org/Intro_website.html, 2025; Large-scale Atomic/Molecular Massively Parallel Simulator.
(479) Todorov, I. T.; Smith, W.; Trachenko, K.; Dove, M. T. DL_POLY_3: new dimensions in molecular dynamics simulations via massive parallelism. *Journal of Materials Chemistry* **2006**, *16*, 1911−1918.

(480) Dubbeldam, D.; Calero, S.; Ellis, D. E.; Snurr, R. Q. RASPA: molecular simulation software for adsorption and diffusion in flexible nanoporous materials. *Mol. Simul.* **2016**, *42*, 81−101.
(481) Humphrey, W.; Dalke, A.; Schulten, K. VMD - Visual Molecular Dynamics. *Journal of Molecular Graphics* **1996**, *14*, 33−38.
(482) Hanwell, M. D.; Curtis, D. E.; Lonie, D. C.; Vandermeersch, T.; Zurek, E.; Hutchison, G. R. Avogadro: an advanced semantic chemical editor, visualization, and analysis platform. *Journal of Cheminformatics* **2012**, *4*, 17.
(483) Dubbeldam, D.; Calero, S.; Vlugt, T. J. H. iRASPA: GPU-accelerated visualization software for materials scientists. *Mol. Simul.* **2018**, *44*, 653−676.
(484) Stukowski, A. Visualization and analysis of atomistic simulation data with OVITO-the Open Visualization Tool. *Modelling and Simulation in Materials Science and Engineering* **2010**, *18*, 015012.
(485) Cummings, P. T.; Evans, D. J. Nonequilibrium molecular dynamics approaches to transport properties and non-Newtonian fluid rheology. *Industrial & Engineering Chemistry Research* **1992**, *31*, 1237−1252.
(486) Maginn, E. J.; Messerly, R. A.; Carlson, D. J.; Roe, D. R.; Elliot, J. R. Best Practices for Computing Transport Properties 1. Self-Diffusivity and Viscosity from Equilibrium Molecular Dynamics [Article v1.0]. *Living Journal of Computational Molecular Science* **2018**, *1*, 6324.
(487) Zwanzig, R. Time-Correlation Functions and Transport Coefficients in Statistical Mechanics. *Annu. Rev. Phys. Chem.* **1965**, *16*, 67−102.
(488) Hagen, M. H. J.; Lowe, C. P.; Frenkel, D. Long Time Tails in Stress Correlation Functions. 25 Years Non-Equilibrium Stat. *25 Years of Non-Equilibrium Statistical Mechanics* **1995**, *445* (Springer: Berlin), 240−249.
(489) van der Hoef, M. A.; Frenkel, D. Long-time Tails of the Velocity Autocorrelation Function in Two- and Three-dimensional Lattice-gas Cellular Automata: A Test of Mode-Coupling Theory. *Phys. Rev. A* **1990**, *41*, 4277−4284.
(490) Maginn, E. J.; Messerly, R. A.; Carlson, D. J.; Roe, D. R.; Elliot, J. R. Best practices for computing transport properties 1. Self-diffusivity and viscosity from equilibrium molecular dynamics [article v1. 0]. *Living Journal of Computational Molecular Science* **2020**, *1*, 6324−6324.
(491) Jamali, S. H.; Wolff, L.; Becker, T. M.; Groen, M. D.; Ramdin, M.; Hartkamp, R.; Bardow, A.; Vlugt, T. J. H.; Moultos, O. A. OCTP: A Tool for On-the-Fly Calculation of Transport Properties of Fluids with the Order- n Algorithm in LAMMPS. *J. Chem. Inf. Model.* **2019**, *59*, 1290−1294.
(492) Humbert, M. T.; Zhang, Y.; Maginn, E. J. PyLAT: Python LAMMPS Analysis Tools. *Journal of Chemical Information and Modeling* **2019**, *59*, 1301−1305.
(493) Dubbeldam, D.; Ford, D. C.; Ellis, D. E.; Snurr, R. Q. A new perspective on the order-n algorithm for computing correlation functions. *Mol. Simul.* **2009**, *35*, 1084−1097.
(494) Cussler, E. L. *Diffusion Coefficients and Diffusion of Interacting Species*, 2nd ed.; Cambridge University Press: Cambridge, 2009.
(495) Kärger, J.; Valiullin, R.; Brandani, S.; Caro, J.; Chmelik, C.; Chmelka, B. F.; Coppens, M.-O.; Farooq, S.; Freude, D.; Jobic, H.; Kruteva, M.; Mangano, E.; Pini, R.; Price, W. S.; Rajendran, A.; Ravikovitch, P. I.; Sastre, G.; Snurr, R. Q.; Stepanov, A. G.; Vasenkov, S.; Wang, Y.; Weckhuysen, B. M. Diffusion in nanoporous materials with special consideration of the measurement of determining parameters (IUPAC Technical Report). *Pure and Applied Chemistry* **2025**, *97*, 1−89.
(496) Moultos, O. A.; Zhang, Y.; Tsimpanogiannis, I. N.; Economou, I. G.; Maginn, E. J. System-size corrections for self-diffusion coefficients calculated from molecular dynamics simulations: The case of CO_2, n-alkanes, and poly (ethylene glycol) dimethyl ethers. *J. Chem. Phys.* **2016**, *145*, 074109.
(497) Dunweg, B.; Kremer, K. Molecular dynamics simulation of a polymer chain in solution. *The Journal of Chemical Physics* **1993**, *99*, 6983−6997.
(498) Yeh, I.-C.; Hummer, G. System-size dependence of diffusion coefficients and viscosities from molecular dynamics simulations with periodic boundary conditions. *J. Phys. Chem. B* **2004**, *108*, 15873−15879.
(499) Celebi, A. T.; Jamali, S. H.; Bardow, A.; Vlugt, T. J. H.; Moultos, O. A. Finite-size effects of diffusion coefficients computed from molecular dynamics: a review of what we have learned so far. *Molecular Simulation* **2021**, *47*, 831−845.
(500) Jamali, S. H.; Bardow, A.; Vlugt, T. J. H.; Moultos, O. A. Generalized form for finite-size corrections in mutual diffusion coefficients of multicomponent mixtures obtained from equilibrium molecular dynamics simulation. *J. Chem. Theory Comput.* **2020**, *16*, 3799−3806.
(501) Erdos, M.; Frangou, M.; Vlugt, T. J. H.; Moultos, O. A. Diffusivity of α-, β-, γ-cyclodextrin and the inclusion complex of β-cyclodextrin: Ibuprofen in aqueous solutions; A molecular dynamics simulation study. *Fluid Phase Equilibria* **2021**, *528*, 112842.
(502) Jamali, S. H.; Hartkamp, R.; Bardas, C.; Sohl, J.; Vlugt, T. J. H.; Moultos, O. A. Shear viscosity computed from the finite-size effects of self-diffusivity in equilibrium molecular dynamics. *J. Chem. Theory Comput.* **2018**, *14*, 5959−5968.
(503) Jamali, S. H.; Wolff, L.; Becker, T. M.; Bardow, A.; Vlugt, T. J. H.; Moultos, O. A. Finite-size effects of binary mutual diffusion coefficients from molecular dynamics. *J. Chem. Theory Comput.* **2018**, *14*, 2667−2677.
(504) Fick, A. Über Diffusion. *Annalen der Physik* **1855**, *170*, 59−86.
(505) Liu, X.; Schnell, S. K.; Simon, J.-M.; Bedeaux, D.; Kjelstrup, S.; Bardow, A.; Vlugt, T. J. H. Fick Diffusion Coefficients of Liquid Mixtures Directly Obtained from Equilibrium Molecular Dynamics. *J. Phys. Chem. B* **2011**, *115*, 12921.
(506) Liu, X.; Martín-Calvo, A.; McGarrity, E.; Schnell, S. K.; Calero, S.; Simon, J.-M.; Bedeaux, D.; Kjelstrup, S.; Bardow, A.; Vlugt, T. J. H. Fick Diffusion Coefficients in Ternary Liquid Systems from Equilibrium Molecular Simulations. *Ind. Eng. Chem. Res.* **2012**, *51*, 10247.
(507) Liu, X.; Schnell, S. K.; Simon, J.-M.; Krüger, P.; Bedeaux, D.; Kjelstrup, S.; Bardow, A.; Vlugt, T. J. H. Diffusion Coefficients from Molecular Dynamics Simulations in Binary and Ternary Mixtures. *Int. J. Thermophys.* **2013**, *34*, 1169.
(508) Keffer, D. J.; Gao, C. Y.; Edwards, B. J. On the relationship between Fickian diffusivities at the continuum and molecular levels. *J. Phys. Chem. B* **2005**, *109*, 5279−5288.
(509) Wolff, L.; Jamali, S. H.; Becker, T. M.; Moultos, O. A.; Vlugt, T. J. H.; Bardow, A. Prediction of Composition-Dependent Self-Diffusion Coefficients in Binary Liquid Mixtures: The Missing Link for Darken-Based Models. *Industrial & Engineering Chemistry Research* **2018**, *57*, 14784−14794.
(510) Taylor, R.; Kooijman, H. A. Composition derivatives of activity coefficient models (for the estimation of thermodynamic factors in diffusion). *Chem. Eng. Commun.* **1991**, *102*, 87−106.
(511) Liu, X.; Bardow, A.; Vlugt, T. J. H. Multicomponent Maxwell-Stefan Diffusivities at Infinite Dilution. *Ind. Eng. Chem. Res.* **2011**, *50*, 4776.
(512) Maginn, E. J.; Bell, A. T.; Theodorou, D. N. Transport diffusivity of methane in silicalite from equilibrium and non-equilibrium simulations. *J. Phys. Chem.* **1993**, *97*, 4173−4181.
(513) Tsige, M.; Grest, G. S. Molecular dynamics simulation of solvent-polymer interdiffusion: Fickian diffusion. *J. Comput. Phys.* **2004**, *120*, 2989−2995.
(514) Tsige, M.; Grest, G. S. Interdiffusion of solvent into glassy polymer films: A molecular dynamics study. *J. Comput. Phys.* **2004**, *121*, 7513−7519.
(515) Jamali, S. H.; Wolff, L.; Becker, T. M.; De Groen, M.; Ramdin, M.; Hartkamp, R.; Bardow, A.; Vlugt, T. J. H.; Moultos, O. A. OCTP: A tool for on-the-fly calculation of transport properties of fluids with the order-n algorithm in LAMMPS. *Journal of Chemical Information and Modeling* **2019**, *59*, 1290−1294.
(516) Jamali, S. H.; Wolff, L.; Becker, T. M.; Bardow, A.; Vlugt, T. J. H.; Moultos, O. A. Finite-Size Effects of Binary Mutual Diffusion

Coefficients from Molecular Dynamics. *Journal of Chemical Theory and Computation* **2018**, *14*, 2667−2677.
(517) Bird, R. B.; Stewart, W. E.; Lightfoot, E. N. *Transport Phenomena*, 2nd ed.; John Wiley & Sons, New York, 2007.
(518) Cussler, E. L. *Diffusion: Mass transfer in Fluid Systems*, 3rd ed.; Cambridge University Press: Cambridge, 2009.
(519) Krishna, R.; van Baten, J. M. Describing diffusion in fluid mixtures at elevated pressures by combining the Maxwell-Stefan formulation with an equation of state. *Chemical Engineering Science* **2016**, *153*, 174−187.
(520) Liu, X.; Schnell, S. K.; Simon, J.-M.; Krüger, P.; Bedeaux, D.; Kjelstrup, S.; Bardow, A.; Vlugt, T. J. H. Diffusion Coefficients from Molecular Dynamics Simulations in Binary and Ternary Mixtures. *International Journal of Thermophysics* **2013**, *34*, 1169−1196.
(521) Liu, X.; Schnell, S. K.; Simon, J.-M.; Bedeaux, D.; Kjelstrup, S.; Bardow, A.; Vlugt, T. J. H. Fick Diffusion Coefficients of Liquid Mixtures Directly Obtained From Equilibrium Molecular Dynamics. *The Journal of Physical Chemistry B* **2011**, *115*, 12921−12929.
(522) Liu, X.; Martín-Calvo, A.; McGarrity, E.; Schnell, S. K.; Calero, S.; Simon, J.-M.; Bedeaux, D.; Kjelstrup, S.; Bardow, A.; Vlugt, T. J. H. Fick Diffusion Coefficients in Ternary Liquid Systems from Equilibrium Molecular Dynamics Simulations. *Industrial & Engineering Chemistry Research* **2012**, *51*, 10247−10258.
(523) Liu, X.; Vlugt, T. J. H.; Bardow, A. Maxwell-Stefan Diffusivities in Binary Mixtures of Ionic Liquids with Dimethyl Sulfoxide (DMSO) and H_2O. *The Journal of Physical Chemistry B* **2011**, *115*, 8506−8517.
(524) Liu, X.; Bardow, A.; Vlugt, T. J. H. Multicomponent Maxwell-Stefan Diffusivities at Infinite Dilution. *Industrial & Engineering Chemistry Research* **2011**, *50*, 4776−4782.
(525) Kozlova, S.; Mialdun, A.; Ryzhkov, I.; Janzen, T.; Vrabec, J.; Shevtsova, V. Do ternary liquid mixtures exhibit negative main Fick diffusion coefficients? *Physical Chemistry Chemical Physics* **2019**, *21*, 2140−2152.
(526) Su, Y.; Saric, D.; Guevara-Carrion, G.; Zhang, Y.; He, M.; Vrabec, J. Fick and Maxwell-Stefan diffusion of the liquid mixture cyclohexane + toluene + acetone + methanol and its subsystems. *Chemical Engineering Science* **2025**, *301*, 120662.
(527) Karger, J.; Ruthven, M. D. *Diffusion in Zeolites and Other Microporous Solids*; Wiley: New York, 1992.
(528) Skoulidas, A. I.; Sholl, D. S. Molecular Dynamics Simulations of Self-Diffusivities, Corrected Diffusivities, and Transport Diffusivities of Light Gases in Four Silica Zeolites To Assess Influences of Pore Shape and Connectivity. *The Journal of Physical Chemistry A* **2003**, *107*, 10132−10141.
(529) Gulbalkan, H. C.; Haslak, Z. P.; Altintas, C.; Uzun, A.; Keskin, S. Assessing CH_4/N_2 separation potential of MOFs, COFs, IL/MOF, MOF/Polymer, and COF/Polymer composites. *Chemical Engineering Journal* **2022**, *428*, 131239.
(530) Ruiz-Montero, M. J.; Frenkel, D.; Brey, J. J. Efficient schemes to compute diffusive barrier crossing rates. *Molecular Physics* **1997**, *90*, 925−942.
(531) June, R. L.; Bell, A. T.; Theodorou, D. N. Transition-state studies of xenon and sulfur hexafluoride diffusion in silicalite. *The Journal of Physical Chemistry* **1991**, *95*, 8866−8878.
(532) Kästner, J. Umbrella sampling. *WIREs Computational Molecular Science* **2011**, *1*, 932−942.
(533) Verploegh, R. J.; Nair, S.; Sholl, D. S. Temperature and Loading-Dependent Diffusion of Light Hydrocarbons in ZIF-8 as Predicted Through Fully Flexible Molecular Simulations. *Journal of the American Chemical Society* **2015**, *137*, 15760−15771.
(534) Voter, A. F.; Doll, J. D. Dynamical corrections to transition state theory for multistate systems: Surface self-diffusion in the rare-event regime. *The Journal of Chemical Physics* **1985**, *82*, 80−92.
(535) Dubbeldam, D.; Beerdsen, E.; Vlugt, T. J. H.; Smit, B. Molecular simulation of loading-dependent diffusion in nanoporous materials using extended dynamically corrected transition state theory. *The Journal of Chemical Physics* **2005**, *122*, 224712.
(536) Krokidas, P.; Moncho, S.; Brothers, E. N.; Castier, M.; Jeong, H. K.; Economou, I. G. On the Efficient Separation of Gas Mixtures with the Mixed-Linker Zeolitic-Imidazolate Framework-7-8. *ACS Applied Materials and Interfaces* **2018**, *10*, 39631−39644.
(537) Cheng, B.; Frenkel, D. Computing the Heat Conductivity of Fluids from Density Fluctuations. *Phys. Rev. Lett.* **2020**, *125*, 130602.
(538) Ding, Y.; Yu, H.; Lin, M.; Ortiz, M.; Xiao, S.; He, J.; Zhang, Z. Hydrogen trapping and diffusion in polycrystalline nickel: The spectrum of grain boundary segregation. *Journal of Materials Science & Technology* **2024**, *173*, 225−236.
(539) Ito, K.; Tanaka, Y.; Tsutsui, K.; Sawada, H. Analysis of grain-boundary segregation of hydrogen in bcc-Fe polycrystals via a nano-polycrystalline grain-boundary model. *Computational Materials Science* **2023**, *225*, 112196.
(540) Zhou, X.; Marchand, D.; McDowell, D. L.; Zhu, T.; Song, J. Chemomechanical Origin of Hydrogen Trapping at Grain Boundaries in fcc Metals. *Phys. Rev. Lett.* **2016**, *116*, 075502.
(541) Zhou, X.; Mousseau, N.; Song, J. Is Hydrogen Diffusion along Grain Boundaries Fast or Slow? Atomistic Origin and Mechanistic Modeling. *Phys. Rev. Lett.* **2019**, *122*, 215501.
(542) Wang, S.; Martin, M. L.; Robertson, I. M.; Sofronis, P. Effect of hydrogen environment on the separation of Fe grain boundaries. *Acta Materialia* **2016**, *107*, 279−288.
(543) Jiang, D. E.; Carter, E. A. Diffusion of interstitial hydrogen into and through bcc Fe from first principles. *Phys. Rev. B* **2004**, *70*, 064102.
(544) Hayward, E.; Fu, C.-C. Interplay between hydrogen and vacancies in α-Fe. *Phys. Rev. B* **2013**, *87*, 174103.
(545) Zhou, X. W.; El Gabaly, F.; Stavila, V.; Allendorf, M. D. Molecular Dynamics Simulations of Hydrogen Diffusion in Aluminum. *The Journal of Physical Chemistry C* **2016**, *120*, 7500−7509.
(546) Kimizuka, H.; Mori, H.; Ogata, S. Effect of temperature on fast hydrogen diffusion in iron: A path-integral quantum dynamics approach. *Phys. Rev. B* **2011**, *83*, 094110.
(547) Zhou, X.; Ouyang, B.; Curtin, W.; Song, J. Atomistic investigation of the influence of hydrogen on dislocation nucleation during nanoindentation in Ni and Pd. *Acta Materialia* **2016**, *116*, 364−369.
(548) Yin, S.; Cheng, G.; Chang, T.-H.; Richter, G.; Zhu, Y.; Gao, H. Hydrogen embrittlement in metallic nanowires. *Nature Communications* **2019**, *10*, 2004.
(549) Li, J.; Gu, T.; Zhang, Y.; Chen, D. Dual Role of Hydrogen Effect on Surface Dislocation Nucleation in Nickel. *Journal of Applied Mechanics* **2025**, *92*, 051004.
(550) Kapci, M. F.; Yu, P.; Marian, J.; Liu, G.; Shen, Y.; Li, Y.; Bal, B. Edge dislocation depinning from hydrogen atmosphere in α-iron. *Scripta Materialia* **2024**, *247*, 116094.
(551) Sofronis, P.; McMeeking, R. Numerical analysis of hydrogen transport near a blunting crack tip. *Journal of the Mechanics and Physics of Solids* **1989**, *37*, 317−350.
(552) Yu, P.; Cui, Y.; zhen Zhu, G.; Shen, Y.; Wen, M. The key role played by dislocation core radius and energy in hydrogen interaction with dislocations. *Acta Materialia* **2020**, *185*, 518−527.
(553) Jung, S.-P.; Kwon, Y.; Lee, C. S.; Lee, B.-J. Influence of hydrogen on the grain boundary crack propagation in bcc iron: A molecular dynamics simulation. *Computational Materials Science* **2018**, *149*, 424−434.
(554) Marx, D. Proton Transfer 200 Years after von Grotthuss: Insights from Ab Initio Simulations. *ChemPhysChem* **2006**, *7*, 1848−1870.
(555) Hassanali, A.; Prakash, M. K.; Eshet, H.; Parrinello, M. On the Recombination of Hydronium and Hydroxide Ions in Water. *Proceedings of the National Academy of Sciences* **2011**, *108*, 20410−20415.
(556) Jiao, K.; Li, X. Water transport in polymer electrolyte membrane fuel cells. *Progress in Energy and Combustion Science* **2011**, *37*, 221−291.

https://doi.org/10.1021/acs.chemrev.5c00617
Chem. Rev. 2025, 125, 11878−12029

(557) Ise, M.; Kreuer, K.; Maier, J. Electroosmotic drag in polymer electrolyte membranes: an electrophoretic NMR study. *Solid State Ionics* **1999**, *125*, 213−223.
(558) Dickinson, E. J. F.; Smith, G. Modelling the Proton-Conductive Membrane in Practical Polymer Electrolyte Membrane Fuel Cell (PEMFC) Simulation: A Review. *Membranes* **2020**, *10*, 310.
(559) Zawodzinski, T. A.; Davey, J.; Valerio, J.; Gottesfeld, S. The water content dependence of electro-osmotic drag in proton-conducting polymer electrolytes. *Electrochim. Acta.* **1995**, *40*, 297−302.
(560) Pivovar, B. S. An overview of electro-osmosis in fuel cell polymer electrolytes. *Polymer* **2006**, *47*, 4194−4202.
(561) Kirkwood, J. G.; Buff, F. P. The statistical mechanical theory of solutions. I. *J. Chem. Phys.* **1951**, *19*, 774−777.
(562) Schnell, S. K.; Vlugt, T. J. H.; Simon, J.-M.; Bedeaux, D.; Kjelstrup, S. Thermodynamics of small systems embedded in a reservoir: a detailed analysis of finite size effects. *Mol. Phys.* **2012**, *110*, 1069−1079.
(563) Schnell, S. K.; Liu, X.; Simon, J.-M.; Bardow, A.; Bedeaux, D.; Vlugt, T. J. H.; Kjelstrup, S. Calculating Thermodynamic Properties from Fluctuations at Small Scales. *J. Phys. Chem. B* **2011**, *115*, 10911−10918.
(564) Schnell, S. K.; Vlugt, T. J. H.; Simon, J.-M.; Bedeaux, D.; Kjelstrup, S. Thermodynamics of a small system in a μT reservoir. *Chem. Phys. Lett.* **2011**, *504*, 199−201.
(565) Wedberg, R.; O'Connell, J. P.; Peters, G. H.; Abildskov, J. Accurate Kirkwood-Buff integrals from molecular simulations. *Mol. Simul.* **2010**, *36*, 1243−1252.
(566) Wedberg, R.; O'Connell, J. P.; Peters, G. H.; Abildskov, J. Total and direct correlation function integrals from molecular simulation of binary systems. *Fluid Phase Equilib.* **2011**, *302*, 32−42.
(567) Krüger, P.; Schnell, S. K.; Bedeaux, D.; Kjelstrup, S.; Vlugt, T. J. H.; Simon, J.-M. Kirkwood-Buff Integrals for Finite Volumes. *J. Phys. Chem. Lett.* **2013**, *4*, 235−238.
(568) Simon, J.-M.; Krüger, P.; Schnell, S. K.; Vlugt, T. J. H.; Kjelstrup, S.; Bedeaux, D. Kirkwood-Buff Integrals: From fluctuations in finite volumes to the thermodynamic limit. *J. Comput. Phys.* **2022**, *157*, 130901.
(569) Dawass, N.; Krüger, P.; Schnell, S. K.; Moultos, O. A.; Economou, I. G.; Vlugt, T. J. H.; Simon, J.-M. Kirkwood-Buff Integrals Using Molecular Simulation: Estimation of Surface Effects. *Nanomaterials* **2020**, *10*, 771.
(570) Dawass, N.; Krüger, P.; Schnell, S. K.; Simon, J.-M.; Vlugt, T. J. H. Kirkwood-Buff integrals from molecular simulation. *Fluid Phase Equilib.* **2019**, *486*, 21−36.
(571) Schnell, S. K.; Englebienne, P.; Simon, J.-M.; Krüger, P.; Balaji, S. P.; Kjelstrup, S.; Bedeaux, D.; Bardow, A.; Vlugt, T. J. H. How to apply the Kirkwood-Buff theory to individual species in salt solutions. *Chem. Phys. Lett.* **2013**, *582*, 154−157.
(572) Balaji, S. P.; Schnell, S. K.; McGarrity, E. S.; Vlugt, T. J. H. A direct method for calculating thermodynamic factors for liquid mixtures using the Permuted Widom Test Particle Insertion Method. *Mol. Phys.* **2013**, *111*, 287−296.
(573) Balaji, S. P.; Schnell, S. K.; Vlugt, T. J. H. Calculating thermodynamic factors of ternary and multicomponent mixtures using the Permuted Widom Test Particle Insertion Method. *Theor. Chem. Acc.* **2013**, *132*, 1333.
(574) Ben-Naim, A. *Molecular Theory of Solutions*; Oxford University Press, 2006.
(575) Widom, B. Some topics in the theory of fluids. *J. Comput. Phys.* **1963**, *39*, 2808−2812.
(576) Hulikal Chakrapani, T.; Hajibeygi, H.; Moultos, O. A.; Vlugt, T. J. H. Calculating Thermodynamic Factors for Diffusion Using the Continuous Fractional Component Monte Carlo Method. *Journal of Chemical Theory and Computation* **2024**, *20*, 333−347.
(577) Ladd, A.; Woodcock, L. Triple-point coexistence properties of the Lennard-Jones system. *Chemical Physics Letters* **1977**, *51*, 155−159.
(578) Michalis, V. K.; Costandy, J.; Tsimpanogiannis, I. N.; Stubos, A. K.; Economou, I. G. Prediction of the phase equilibria of methane hydrates using the direct phase coexistence methodology. *The Journal of Chemical Physics* **2015**, *142*, 044501.
(579) Costandy, J.; Michalis, V. K.; Tsimpanogiannis, I. N.; Stubos, A. K.; Economou, I. G. The role of intermolecular interactions in the prediction of the phase equilibria of carbon dioxide hydrates. *The Journal of Chemical Physics* **2015**, *143*, 094506.
(580) Michalis, V. K.; Tsimpanogiannis, I. N.; Stubos, A. K.; Economou, I. G. Direct phase coexistence molecular dynamics study of the phase equilibria of the ternary methane-carbon dioxide-water hydrate system. *Physical Chemistry Chemical Physics* **2016**, *18*, 23538−23548.
(581) Mohr, S.; Pétuya, R.; Wylde, J.; Sarria, J.; Purkayastha, N.; Ward, Z.; Bodnar, S.; Tsimpanogiannis, I. N. Size dependence of the dissociation process of spherical hydrate particles via microsecond molecular dynamics simulations. *Physical Chemistry Chemical Physics* **2021**, *23*, 11180−11185.
(582) Mak, T. C.; McMullan, R. K. Polyhedral clathrate hydrates. X. Structure of the double hydrate of tetrahydrofuran and hydrogen sulfide. *The Journal of Chemical Physics* **1965**, *42*, 2732−2737.
(583) McMullan, R. K.; Jeffrey, G. Polyhedral clathrate hydrates. IX. Structure of ethylene oxide hydrate. *The Journal of Chemical Physics* **1965**, *42*, 2725−2732.
(584) Bernal, J. D.; Fowler, R. H. A theory of water and ionic solution, with particular reference to hydrogen and hydroxyl ions. *The Journal of Chemical Physics* **1933**, *1*, 515−548.
(585) Sarupria, S.; Debenedetti, P. G. Molecular dynamics study of carbon dioxide hydrate dissociation. *The Journal of Physical Chemistry A* **2011**, *115*, 6102−6111.
(586) Takeuchi, F.; Hiratsuka, M.; Ohmura, R.; Alavi, S.; Sum, A. K.; Yasuoka, K. Water proton configurations in structures I, II, and H clathrate hydrate unit cells. *The Journal of Chemical Physics* **2013**, *138*, 124504.
(587) English, N. J.; Lauricella, M.; Meloni, S. Massively parallel molecular dynamics simulation of formation of clathrate-hydrate precursors at planar water-methane interfaces: Insights into heterogeneous nucleation. *The Journal of Chemical Physics* **2014**, *140*, 204714.
(588) Blazquez, S.; M Conde, M.; Vega, C.; Sanz, E. Growth rate of CO_2 and CH_4 hydrates by means of molecular dynamics simulations. *The Journal of Chemical Physics* **2023**, *159*, 064503.
(589) Vatamanu, J.; Kusalik, P. G. Heterogeneous crystal growth of methane hydrate on its sII [001] crystallographic face. *The Journal of Physical Chemistry B* **2008**, *112*, 2399−2404.
(590) Yagasaki, T.; Matsumoto, M.; Tanaka, H. Mechanism of slow crystal growth of tetrahydrofuran clathrate hydrate. *The Journal of Physical Chemistry C* **2016**, *120*, 3305−3313.
(591) Báez, L. A.; Clancy, P. Computer simulation of the crystal growth and dissolution of natural gas hydrates. *Annals of the New York Academy of Sciences* **1994**, *715*, 177−186.
(592) Fidler, J.; Rodger, P. Solvation structure around aqueous alcohols. *The Journal of Physical Chemistry B* **1999**, *103*, 7695−7703.
(593) Rodger, P.; Forester, T.; Smith, W. Simulations of the methane hydrate/methane gas interface near hydrate forming conditions conditions. *Fluid Phase Equilibria* **1996**, *116*, 326−332.
(594) Zhang, Z.; Kusalik, P. G.; Guo, G.-J. Molecular insight into the growth of hydrogen and methane binary hydrates. *The Journal of Physical Chemistry C* **2018**, *122*, 7771−7778.
(595) Tian, H.; Zhang, Z. Revealing the growth of H_2 + THF binary hydrate through molecular simulations. *Energy & Fuels* **2020**, *34*, 15004−15010.
(596) Guo, G.-J.; Zhang, Y.-G.; Liu, C.-J.; Li, K.-H. Using the face-saturated incomplete cage analysis to quantify the cage compositions and cage linking structures of amorphous phase hydrates. *Physical Chemistry Chemical Physics* **2011**, *13*, 12048−12057.
(597) Ghoufi, A.; Malfreyt, P.; Tildesley, D. J. Computer modelling of the surface tension of the gas-liquid and liquid-liquid interface. *Chem. Soc. Rev.* **2016**, *45*, 1387−1409.

https://doi.org/10.1021/acs.chemrev.5c00617
Chem. Rev. 2025, 125, 11878−12029

(598) Irving, J.; Kirkwood, J. G. The statistical mechanical theory of transport processes. IV. The equations of hydrodynamics. *J. Chem. Phys.* **1950**, *18*, 817−829.
(599) Hill, T. L. Statistical thermodynamics of the transition region between two phases. I. Thermodynamics and quasi-thermodynamics. *J. Phys. Chem.* **1952**, *56*, 526−531.
(600) Kirkwood, J. G.; Buff, F. P. The statistical mechanical theory of surface tension. *J. Chem. Phys.* **1949**, *17*, 338−343.
(601) Javanbakht, G.; Sedghi, M.; Welch, W.; Goual, L. Molecular dynamics simulations of CO_2/water/quartz interfacial properties: impact of CO_2 dissolution in water. *Langmuir* **2015**, *31*, 5812−5819.
(602) Yang, Y.; Nair, A. K. N.; Zhu, W.; Sang, S.; Sun, S. Molecular Perspectives of Interfacial Properties of the Hydrogen+ Water Mixture in Contact with Silica or Kerogen. *J. Mol. Liq.* **2023**, *385*, 122337.
(603) Abdel-Azeim, S.; Al-Yaseri, A.; Norrman, K.; Patil, P.; Qasim, A.; Yousef, A. Wettability of Caprock-H_2-Water: Insights from Molecular Dynamic Simulations and Sessile-Drop Experiment. *Energy & Fuels* **2023**, *37*, 19348−19356.
(604) Chen, C.; Xia, J.; Bahai, H. Effect of the Temperature on Interfacial Properties of CO_2/H_2 Mixtures Contacting with Brine and Hydrophilic Silica by Molecular Dynamics Simulations. *Energy & Fuels* **2023**, *37*, 18986−18995.
(605) Chen, C.; Xia, J. A comparative study on transport and interfacial physics of $H_2/CO_2/CH_4$ interacting with H_2O and/or silica by molecular dynamics simulation. *Phys. Fluids* **2024**, *36*, 016606.
(606) Al-Yaseri, A.; Esteban, L.; Giwelli, A.; Abdel-Azeim, S.; Sarout, J.; Sarmadivaleh, M. Impact of wettability on storage and recovery of hydrogen gas in the lesueur sandstone formation (Southwest hub project, Western Australia). *Int. J. Hydrogen Energy* **2023**, *48*, 23581−23593.
(607) Al-Yaseri, A.; Abdel-Azeim, S.; Al-Hamad, J. Wettability of water-H_2-quartz and water-H_2-calcite experiment and molecular dynamics simulations: Critical assessment. *Int. J. Hydrogen Energy* **2023**, *48*, 34897−34905.
(608) Zheng, R.; Germann, T. C.; Huang, L.; Mehana, M. Driving mechanisms of quartz wettability alteration under in-situ H2 geo-storage conditions: Role of organic ligands and surface morphology. *International Journal of Hydrogen Energy* **2024**, *59*, 1388−1398.
(609) Zheng, R.; Germann, T. C.; Gross, M.; Mehana, M. Molecular insights into the impact of surface chemistry and pressure on quartz wettability: resolving discrepancies for hydrogen geo-storage. *ACS Sustainable Chemistry & Engineering* **2024**, *12*, 5555−5563.
(610) Martin, M. G. MCCCS Towhee: a tool for Monte Carlo molecular simulation. *Molecular Simulation* **2013**, *39*, 1212−1222.
(611) Hens, R.; Rahbari, A.; Caro-Ortiz, S.; Dawass, N.; Erdos, M.; Poursaeidesfahani, A.; Salehi, H. S.; Celebi, A. T.; Ramdin, M.; Moultos, O. A.; Dubbeldam, D.; Vlugt, T. J. H. Brick-CFCMC: Open Source Software for Monte Carlo Simulations of Phase and Reaction Equilibria Using the Continuous Fractional Component Method. *J. Chem. Inf. Model.* **2020**, *60*, 2678−2682.
(612) Polat, H. M.; Salehi, H. S.; Hens, R.; Wasik, D. O.; Rahbari, A.; de Meyer, F.; Houriez, C.; Coquelet, C.; Calero, S.; Dubbeldam, D.; Moultos, O. A.; Vlugt, T. J. H. New Features of the Open Source Monte Carlo Software Brick-CFCMC: Thermodynamic Integration and Hybrid Trial Moves. *J. Chem. Inf. Model.* **2021**, *61*, 3752−3757.
(613) Dubbeldam, D.; Torres-Knoop, A.; Walton, K. S. On the inner workings of Monte Carlo codes. *Mol. Simul.* **2013**, *39*, 1253−1292.
(614) Binder, K. *Monte Carlo Methods in Statistical Physics*; Springer-Verlag: Berlin, 1986.
(615) Fichthorn, K. A.; Weinberg, W. H. Theoretical foundations of dynamical Monte Carlo simulations. *The Journal of Chemical Physics* **1991**, *95*, 1090−1096.
(616) Panagiotopoulos, A. Z. Direct determination of phase coexistence properties of fluids by Monte Carlo simulation in a new ensemble. *Mol. Phys.* **1987**, *61*, 813−826.
(617) Widom, B. Some topics in the theory of fluids. *The Journal of Chemical Physics* **1963**, *39*, 2808−2812.
(618) Rahbari, A.; Hens, R.; Ramdin, M.; Moultos, O. A.; Dubbeldam, D.; Vlugt, T. J. H. Recent advances in the continuous fractional component Monte Carlo methodology. *Mol. Simul.* **2021**, *47*, 804−823.
(619) Sandler, S. I. *An Introduction to Applied Statistical Thermodynamics*; John Wiley & Sons: Hoboken, New Jersey, 2011.
(620) Widom, B. Potential-distribution theory and the statistical mechanics of fluids. *J. Phys. Chem.* **1982**, *86*, 869−872.
(621) Boulougouris, G. C.; Economou, I. G.; Theodorou, D. N. Calculation of the chemical potential of chain molecules using the staged particle deletion scheme. *J. Chem. Phys.* **2001**, *115*, 8231−8237.
(622) Boulougouris, G. C.; Economou, I. G.; Theodorou, D. N. On the calculation of the chemical potential using the particle deletion scheme. *Mol. Phys.* **1999**, *96*, 905−913.
(623) Coskuner, O.; Deiters, U. K. Hydrophobic interactions by Monte Carlo simulations. *Zeitschrift für Phys. Chem.* **2006**, *220*, 349−369.
(624) Rahbari, A.; Poursaeidesfahani, A.; Torres-Knoop, A.; Dubbeldam, D.; Vlugt, T. J. H. Chemical potentials of water, methanol, carbon dioxide and hydrogen sulphide at low temperatures using Continuous Fractional Component Gibbs ensemble Monte Carlo. *Mol. Simul.* **2018**, *44*, 405−414.
(625) Lu, N.; Singh, J. K.; Kofke, D. A. Appropriate methods to combine forward and reverse free-energy perturbation averages. *J. Chem. Phys.* **2003**, *118*, 2977−2984.
(626) Shi, W.; Maginn, E. J. Continuous Fractional Component Monte Carlo: an adaptive biasing method for open system atomistic simulations. *J. Chem. Theory Comput.* **2007**, *3*, 1451−1463.
(627) Nezbeda, I.; Kolafa, J. A new version of the insertion particle method for determining the chemical Potential by Monte Carlo simulation. *Mol. Simul.* **1991**, *5*, 391−403.
(628) Escobedo, F. A.; de Pablo, J. J. Expanded grand canonical and Gibbs ensemble Monte Carlo simulation of polymers. *J. Chem. Phys.* **1996**, *105*, 4391−4394.
(629) Shi, W.; Maginn, E. J. Continuous Fractional Component Monte Carlo: An adaptive biasing method for open system atomistic simulations. *J. Chem. Theory Comput.* **2007**, *3*, 1451−1463.
(630) van Rooijen, W. A.; Habibi, P.; Xu, K.; Dey, P.; Vlugt, T. J. H.; Hajibeygi, H.; Moultos, O. A. Interfacial Tensions, Solubilities, and Transport Properties of the H_2/H_2O/NaCl System: A Molecular Simulation Study. *Journal of Chemical & Engineering Data* **2024**, *69*, 307−319.
(631) Wang, F.; Landau, D. P. Efficient, multiple-range random walk algorithm to calculate the density of states. *Phys. Rev. Lett.* **2001**, *86*, 2050−2053.
(632) Rahbari, A.; Hens, R.; Dubbeldam, D.; Vlugt, T. J. H. Improving the accuracy of computing chemical potentials in CFCMC simulations. *Mol. Phys.* **2019**, *117*, 3493−3508.
(633) Brumby, P. E.; Yuhara, D.; Hasegawa, T.; Wu, D. T.; Sum, A. K.; Yasuoka, K. Cage occupancies, lattice constants, and guest chemical potentials for structure II hydrogen clathrate hydrate from Gibbs ensemble Monte Carlo simulations. *The Journal of Chemical Physics* **2019**, *150*, 134503.
(634) Papadimitriou, N.; Tsimpanogiannis, I.; Papaioannou, A. T.; Stubos, A. Evaluation of the hydrogen-storage capacity of pure H_2 and binary H_2-THF hydrates with Monte Carlo simulations. *The Journal of Physical Chemistry C* **2008**, *112*, 10294−10302.
(635) Papadimitriou, N.; Tsimpanogiannis, I.; Peters, C.; Papaioannou, A. T.; Stubos, A. Hydrogen storage in sH hydrates: A Monte Carlo study. *The Journal of Physical Chemistry B* **2008**, *112*, 14206−14211.
(636) Papadimitriou, N.; Tsimpanogiannis, I.; Stubos, A. Monte Carlo study of sI hydrogen hydrates. *Molecular Simulation* **2010**, *36*, 736−744.
(637) Tsimpanogiannis, I. N.; Papadimitriou, N. I.; Stubos, A. K. On the limitation of the van der Waals-Platteeuw-based thermodynamic models for hydrates with multiple occupancy of cavities. *Molecular Physics* **2012**, *110*, 1213−1221.

https://doi.org/10.1021/acs.chemrev.5c00617
Chem. Rev. 2025, 125, 11878−12029

(638) Papadimitriou, N. I.; Tsimpanogiannis, I. N.; Papaioannou, A. T.; Stubos, A. K. Monte Carlo study of sII and sH argon hydrates with multiple occupancy of cages. *Molecular Simulation* **2008**, *34*, 1311−1320.
(639) Papadimitriou, N. I.; Tsimpanogiannis, I. N.; Economou, I. G.; Stubos, A. K. Influence of combining rules on the cavity occupancy of clathrate hydrates by Monte Carlo simulations. *Molecular Physics* **2014**, *112*, 2258−2274.
(640) Papadimitriou, N.; Tsimpanogiannis, I.; Economou, I.; Stubos, A. Evaluation of the efficiency of clathrate hydrates in storing energy gases. *Journal of Physics: Conference Series* **2015**, *640*, 012026.
(641) Papadimitriou, N. I.; Tsimpanogiannis, I. N.; Economou, I. G.; Stubos, A. K. Storage of methane in clathrate hydrates: Monte Carlo simulations of sI hydrates and comparison with experimental measurements. *Journal of Chemical & Engineering Data* **2016**, *61*, 2886−2896.
(642) Sandler, S. I. *Chemical, biochemical, and engineering thermodynamics*, 4th ed.; John Wiley & Sons: Hoboken, N.J., USA, 2006.
(643) Moran, M. J.; Shapiro, H. N. *Fundamentals of Engineering thermodynamics*, 5th ed.; John Wiley & Sons: West Sussex, England, 2006.
(644) Jorgensen, W. L. Optimized intermolecular potential functions for liquid alcohols. *J. Phys. Chem.* **1986**, *90*, 1276−1284.
(645) Lagache, M.; Ungerer, P.; Boutin, A.; Fuchs, A. H. Prediction of thermodynamic derivative properties of fluids by Monte Carlo simulation. *Phys. Chem. Chem. Phys.* **2001**, *3*, 4333−4339.
(646) Reid, R. C.; Prausnitz, J. M.; Poling, B. E. *The Properties of Gases and Liquids*, 5th ed.; McGraw-Hill: New York, 2001.
(647) Johnson, R. D., III 2019; NIST Computational Chemistry Comparison and Benchmark Database. *NIST Standard Reference Database Number 101 Release 20*, Editor: Johnson, R. D., III http://cccbdb.nist.gov/.
(648) Rahbari, A.; Josephson, T. R.; Sun, Y.; Moultos, O. A.; Dubbeldam, D.; Siepmann, J. I.; Vlugt, T. J. H. Multiple Linear Regression and Thermodynamic Fluctuations are Equivalent for Computing Thermodynamic Derivatives from Molecular Simulation. *Fluid Phase Equilib.* **2020**, *523*, 112785.
(649) Voter, A. F. INTRODUCTION TO THE KINETIC MONTE CARLO METHOD. *Radiation Effects in Solids. Dordrecht* **2007**, *235*, 1−23.
(650) Andersen, M.; Panosetti, C.; Reuter, K. A Practical Guide to Surface Kinetic Monte Carlo Simulations. *Frontiers in Chemistry* **2019**, *7*, DOI: 10.3389/fchem.2019.00202.
(651) Henkelman, G.; Uberuaga, B. P.; Jonsson, H. A climbing image nudged elastic band method for finding saddle points and minimum energy paths. *The Journal of Chemical Physics* **2000**, *113*, 9901−9904.
(652) Vineyard, G. H. Frequency factors and isotope effects in solid state rate processes. *Journal of Physics and Chemistry of Solids* **1957**, *3*, 121−127.
(653) Zhou, X.; Ou, P.; Mousseau, N.; Song, J. Critical assessment of hydrogen pipe diffusion at dislocations in metals. *Acta Materialia* **2024**, *268*, 119758.
(654) Zhou, X.-Y.; Zhu, J.-H.; Wu, Y.; Yang, X.-S.; Lookman, T.; Wu, H.-H. Machine learning assisted design of FeCoNiCrMn high-entropy alloys with ultra-low hydrogen diffusion coefficients. *Acta Materialia* **2022**, *224*, 117535.
(655) Zhang, J.; Clennell, M. B.; Sagotra, A.; Pascual, R. Molecular dynamics simulation and machine learning for predicting hydrogen solubility in water: Effects of temperature, pressure, finite system size and choice of molecular force fields. *Chemical Physics* **2023**, *564*, 111725.
(656) Chabab, S.; Théveneau, P.; Coquelet, C.; Corvisier, J.; Paricaud, P. Measurements and predictive models of high-pressure H_2 solubility in brine (H_2O+NaCl) for underground hydrogen storage application. *Int. J. Hydrogen Energy* **2020**, *45*, 32206−32220.
(657) *Hydrogen in Water and Aqueous Electrolyte Solutions*; Haynes, W. M., Ed.; Pergamon Press, 1981; Vol. *5/6*; IUPAC Solubility Data Series.
(658) Alvarez, J.; Crovetto, R.; Fernández-Prini, R. The Dissolution of N_2 and of H_2 in Water from Room Temperature to 640 K. *Berichte der Bunsengesellschaft für physikalische Chemie* **1988**, *92*, 935−940.
(659) Sabo, D.; Rempe, S. B.; Greathouse, J. A.; Martin, M. G. Molecular studies of the structural properties of hydrogen gas in bulk water. *Molecular Simulation* **2006**, *32*, 269−278.
(660) Sabo, D.; Varma, S.; Martin, M. G.; Rempe, S. B. Studies of the Thermodynamic Properties of Hydrogen Gas in Bulk Water. *The Journal of Physical Chemistry B* **2008**, *112*, 867−876.
(661) Buch, V.; Devlin, J. P. Preferential adsorption of ortho-H_2 with respect to para-H_2 on the amorphous ice surface. *J. Chem. Phys.* **1993**, *98*, 4195−4206.
(662) Urukova, I.; Vorholz, J.; Maurer, G. Solubility of CO_2, CO, and H_2 in the Ionic Liquid [bmim][PF6] from Monte Carlo Simulations. *J. Phys. Chem. B* **2005**, *109*, 12154−12159.
(663) Salehi, H. S.; Hens, R.; Moultos, O. A.; Vlugt, T. J. H. Computation of gas solubilities in choline chloride urea and choline chloride ethylene glycol deep eutectic solvents using Monte Carlo simulations. *J. Mol. Liq.* **2020**, *316*, 113729.
(664) Liu, X.; Bara, J. E.; Turner, C. H. Understanding Gas Solubility of Pure Component and Binary Mixtures within Multivalent Ionic Liquids from Molecular Simulations. *J. Phys. Chem. B* **2021**, *125*, 8165−8174.
(665) Steele, W. A. The physical interaction of gases with crystalline solids: I. Gas-solid energies and properties of isolated adsorbed atoms. *Surface Science* **1973**, *36*, 317−352.
(666) Tjatjopoulos, G. J.; Feke, D. L.; Mann, J. A. J. Molecule-micropore interaction potentials. *J. Phys. Chem.* **1988**, *92*, 4006−4007.
(667) Siderius, D. W.; Gelb, L. D. Extension of the Steele 10-4-3 potential for adsorption calculations in cylindrical, spherical, and other pore geometries. *J. Chem. Phys.* **2011**, *135*, 084703.
(668) Hendriks, E.; Kontogeorgis, G. M.; Dohrn, R.; de Hemptinne, J.-C.; Economou, I. G.; Zilnik, L. F.; Vesovic, V. Industrial Requirements for Thermodynamics and Transport Properties. *Industrial & Engineering Chemistry Research* **2010**, *49*, 11131−11141.
(669) de Hemptinne, J.-C.; Kontogeorgis, G. M.; Dohrn, R.; Economou, I. G.; ten Kate, A.; Kuitunen, S.; Fele Zilnik, L.; De Angelis, M. G.; Vesovic, V. A View on the Future of Applied Thermodynamics. *Industrial & Engineering Chemistry Research* **2022**, *61*, 14664−14680.
(670) Naseri Boroujeni, S.; Maribo-Mogensen, B.; Liang, X.; Kontogeorgis, G. M. Theoretical and practical investigation of ion-ion association in electrolyte solutions. *The Journal of Chemical Physics* **2024**, *160*, 154509.
(671) Novak, N.; Yang, F.; Olsen, M. D.; Liang, X.; von Solms, N.; Economou, I. G.; Castier, M.; de Hemptinne, J.-C.; Panagiotopoulos, A. Z.; Kontogeorgis, G. M. Contributions to ionic activity coefficients: A review and comparison of equations of state with molecular simulations. *Fluid Phase Equilibria* **2025**, *594*, 114339.
(672) Kerkache, H.; Hoang, H.; Cézac, P.; Galliéro, G.; Chabab, S. The solubility of H_2 in NaCl brine at high pressures and high temperatures: Molecular simulation study and thermodynamic modeling. *Journal of Molecular Liquids* **2024**, *400*, 124497.
(673) Weisenberger, S.; Schumpe, A. Estimation of gas solubilities in salt solutions at temperatures from 273 K to 363 K. *AIChE J.* **1996**, *42*, 298−300.
(674) Torín-Ollarves, G. A.; Trusler, J. M. Solubility of hydrogen in sodium chloride brine at high pressures. *Fluid Phase Equilib.* **2021**, *539*, 113025.
(675) Lopez-Lazaro, C.; Bachaud, P.; Moretti, I.; Ferrando, N. Predicting the phase behavior of hydrogen in NaCl brines by Molecular Simulation for geological applications. *BSGF-Earth Sci. Bulletin* **2019**, *190*, 7.
(676) Zhang, J.; Clennell, M. B.; Dewhurst, D. N. Transport Properties of NaCl in Aqueous Solution and Hydrogen Solubility in Brine. *The Journal of Physical Chemistry B* **2023**, *127*, 8900−8915.

(677) Hulikal Chakrapani, T.; Hajibeygi, H.; Moultos, O. A.; Vlugt, T. J. H. Mutual Diffusivities of Mixtures of Carbon Dioxide and Hydrogen and Their Solubilities in Brine: Insight from Molecular Simulations. *Industrial & Engineering Chemistry Research* **2024**, *63*, 10456−10481.
(678) Potoff, J. J.; Siepmann, J. I. Vapor-liquid equilibria of mixtures containing alkanes, carbon dioxide, and nitrogen. *AIChE Journal* **2001**, *47*, 1676−1682.
(679) Setschenow, J. Über die konstitution der salzlösungen auf grund ihres verhaltens zu kohlensäure. *Zeitschrift für Physikalische Chemie* **1889**, *4*, 117−125.
(680) Postma, J. R. T.; Habibi, P.; Dey, P.; Vlugt, T. J. H.; Moultos, O. A.; Padding, J. T. Densities, Viscosities, and Self-Diffusion Coefficients of Aqueous Mixtures of $NaBH_4$, $NaB(OH)_4$, and NaOH Using the BH_4^- Delft Force Field (DFF/BH_4^-). *Journal of Chemical & Engineering Data* **2025**, *70*, 1830−1842.
(681) Maslennikova, V. Y.; Goryunova, N.; Subbotina, L.; Tsiklis, D. The solubility of water in compressed hydrogen. *Russian Journal of Physical Chemistry* **1976**, *50*, 240−243.
(682) Bartlett, E. P. The concentration of water vapor in compressed hydrogen, Nitrogen and a mixture of these gases in the presence of condensed water. *J. Amer. Chem. Soc.* **1927**, *49*, 65−78.
(683) Wiebe, R.; Gaddy, V. L. The Solubility of Hydrogen in Water at 0, 50, 75 and 100° from 25 to 1000 Atmospheres. *J. Am. Chem. Soc.* **1934**, *56*, 76−79.
(684) Rouha, M.; Nezbeda, I.; Hruby, J.; Moučka, F. Higher Virial Coefficients of Water. *J. Mol. Liq.* **2018**, *270*, 81−86.
(685) Kunz, O.; Wagner, W. The GERG-2008 Wide-Range Equation of State for Natural Gases and Other Mixtures: An Expansion of GERG-2004. *Journal of Chemical & Engineering Data* **2012**, *57*, 3032−3091.
(686) Yang, X.; Xu, J.; Wu, S.; Yu, M.; Hu, B.; Cao, B.; Li, J. A molecular dynamics simulation study of PVT properties for $H_2O/H_2/CO_2$ mixtures in near-critical and supercritical regions of water. *International Journal of Hydrogen Energy* **2018**, *43*, 10980−10990.
(687) Zhao, X.; Jin, H. Investigation of hydrogen diffusion in supercritical water: A molecular dynamics simulation study. *Int. J. Heat Mass Transfer* **2019**, *133*, 718−728.
(688) Tsimpanogiannis, I. N.; Maity, S.; Celebi, A. T.; Moultos, O. A. Engineering Model for Predicting the Intradiffusion Coefficients of Hydrogen and Oxygen in Vapor, Liquid, and Supercritical Water based on Molecular Dynamics Simulations. *Journal of Chemical & Engineering Data* **2021**, *66*, 3226−3244.
(689) Polat, H. M.; Coelho, F. M.; Vlugt, T. J. H.; Mercier Franco, L. F.; Tsimpanogiannis, I. N.; Moultos, O. A. Diffusivity of CO_2 in H_2O: A Review of Experimental Studies and Molecular Simulations in the Bulk and in Confinement. *Journal of Chemical & Engineering Data* **2024**, *69*, 3296−3329.
(690) Wang, S.; Zhou, T.; Pan, Z.; Trusler, J. P. M. Diffusion Coefficients of N_2O and H_2 in Water at Temperatures between 298.15 and 423.15 K with Pressures up to 30 MPa. *Journal of Chemical & Engineering Data* **2023**, *68*, 1313−1319.
(691) Kallikragas, D. T.; Plugatyr, A. Y.; Svishchev, I. M. High temperature diffusion coefficients for O_2, H_2, and OH in water, and for pure water. *J. Chem. Eng. Data* **2014**, *59*, 1964−1969.
(692) Abascal, J. L.; Vega, C. A general purpose model for the condensed phases of water: TIP4P/2005. *J. Chem. Phys.* **2005**, *123*, 234505.
(693) Vega, C. Water: one molecule, two surfaces, one mistake. *Mol. Phys.* **2015**, *113*, 1145−1163.
(694) Moultos, O. A.; Tsimpanogiannis, I. N.; Panagiotopoulos, A. Z.; Economou, I. G. Atomistic Molecular Dynamics Simulations of CO_2 Diffusivity in H_2O for a Wide Range of Temperatures and Pressures. *The Journal of Physical Chemistry B* **2014**, *118*, 5532−5541.
(695) Zhang, C.; Lu, C.; Jing, Z.; Wu, C.; Piquemal, J.-P.; Ponder, J. W.; Ren, P. AMOEBA Polarizable Atomic Multipole Force Field for Nucleic Acids. *Journal of Chemical Theory and Computation* **2018**, *14*, 2084−2108.
(696) Moultos, O. A.; Tsimpanogiannis, I. N. Predictive model for the intra-diffusion coefficients of H_2 and O_2 in vapour H_2O based on data from molecular dynamics simulations. *Molecular Physics* **2023**, *121*, No. e2211889.
(697) Tsimpanogiannis, I. N.; Jamali, S. H.; Economou, I. G.; Vlugt, T. J. H.; Moultos, O. A. On the validity of the Stokes-Einstein relation for various water force fields. *Molecular Physics* **2020**, *118*, No. e1702729.
(698) Tsimpanogiannis, I. N.; Moultos, O. A. Is Stokes-Einstein relation valid for the description of intra-diffusivity of hydrogen and oxygen in liquid water? *Fluid Phase Equilibria* **2023**, *563*, 113568.
(699) Kerkache, H.; Hoang, H.; Nguyen, T. K. N.; Geoffroy-Neveux, A.; Nieto-Draghi, C.; Cézac, P.; Chabab, S.; Galliéro, G. Assessment of H_2 diffusivity in water and brine for underground storage: A molecular dynamics approach. *International Journal of Hydrogen Energy* **2025**, *128*, 279−290.
(700) Blazquez, S.; Abascal, J. L. F.; Lagerweij, J.; Habibi, P.; Dey, P.; Vlugt, T. J. H.; Moultos, O. A.; Vega, C. Computation of Electrical Conductivities of Aqueous Electrolyte Solutions: Two Surfaces, One Property. *Journal of Chemical Theory and Computation* **2023**, *19*, 5380−5393.
(701) Avula, N. V. S.; Klein, M. L.; Balasubramanian, S. Understanding the Anomalous Diffusion of Water in Aqueous Electrolytes Using Machine Learned Potentials. *The Journal of Physical Chemistry Letters* **2023**, *14*, 9500−9507.
(702) Zhu, S.; Robinson, G. W. Structure and dynamics of liquid water between plates. *J. Comput. Phys.* **1991**, *94*, 1403−1410.
(703) Yan, L.; Zhu, S.; Ji, X.; Lu, W. Proton Hopping in Phosphoric Acid Solvated Nafion Membrane: A Molecular Simulation Study. *J. Phys. Chem. B* **2007**, *111*, 6357−6363.
(704) Springer, T. E.; Zawodzinski, T. A.; Gottesfeld, S. Polymer Electrolyte Fuel Cell Model. *J. Electrochem. Soc.* **1991**, *138*, 2334.
(705) Sahu, P.; Ali, S. M. Electric Field Assisted Migration of H^+ and Cu^+/Cu^{2+} Ions through the Nafion in Cu-Cl Electrolyzer for Hydrogen Generation: Molecular Dynamics Simulations. *Journal of Electroanalytical Chemistry* **2025**, *994*, 119267.
(706) Lasala, S.; Samukov, K.; Mert Polat, H.; Lachet, V.; Herbinet, O.; Privat, R.; Jaubert, J.-N.; Moultos, O. A.; De Ras, K.; Vlugt, T. J. H. Application of thermodynamics at different scales to describe the behaviour of fast reacting binary mixtures in vapour-liquid equilibrium. *Chemical Engineering Journal* **2024**, *483*, 148961.
(707) van Duin, A. C. T.; Dasgupta, S.; Lorant, F.; Goddard, W. A. ReaxFF: A Reactive Force Field for Hydrocarbons. *The Journal of Physical Chemistry A* **2001**, *105*, 9396−9409.
(708) Senftle, T. P.; Hong, S.; Islam, M. M.; Kylasa, S. B.; Zheng, Y.; Shin, Y. K.; Junkermeier, C.; Engel-Herbert, R.; Janik, M. J.; Aktulga, H. M.; Verstraelen, T.; Grama, A.; van Duin, A. C. T. The ReaxFF reactive force-field: development, applications and future directions. *npj Computational Materials* **2016**, *2*, 15011.
(709) Brenner, D. W.; Shenderova, O. A.; Harrison, J. A.; Stuart, S. J.; Ni, B.; Sinnott, S. B. A second-generation reactive empirical bondorder (REBO) potential energy expression for hydrocarbons. *Journal of Physics: Condensed Matter* **2002**, *14*, 783.
(710) Polat, H. M.; Lasala, S.; de Meyer, F.; Houriez, C.; Moultos, O. A.; Vlugt, T. J. H. Scaling towards the critical point in the combined reaction/Gibbs ensemble. *Fluid Phase Equilibria* **2024**, *582*, 114084.
(711) Stuart, S. J.; Tutein, A. B.; Harrison, J. A. A reactive potential for hydrocarbons with intermolecular interactions. *The Journal of Chemical Physics* **2000**, *112*, 6472−6486.
(712) Xiao, J.; Liu, K.; Du, Y.; Jin, Z.; Lu, H. Measurement on and Correlation of VLE of H_2-N_2-Ar System. *Chemical Engineering (China)* **1990**, *18*, 8−12.
(713) Streett, W.; Calado, J. Liquid-vapour equilibrium for hydrogen + nitrogen at temperatures from 63 to 110 K and pressures to 57 MPa. *The Journal of Chemical Thermodynamics* **1978**, *10*, 1089−1100.
(714) Calado, J.; Streett, W. Liquid—-vapor equilibrium in the system H_2 Ar at temperatures from 83 to 141 K and pressures to 52 MPa. *Fluid Phase Equilibria* **1979**, *2*, 275−282.

https://doi.org/10.1021/acs.chemrev.5c00617
Chem. Rev. 2025, 125, 11878−12029

(715) Pierre, J.; Walker, H.-W. Y.; Riedemann, A. Clapeyron.jl: An Extensible, Open-Source Fluid Thermodynamics Toolkit. *Ind. Eng. Chem. Res.* **2022**, *61*, 7130−7153.
(716) Raju, D.; Ramdin, M.; Vlugt, T. J. H. Thermophysical Properties and Phase Behavior of CO_2 with Impurities: Insight from Molecular Simulations. *Journal of Chemical & Engineering Data* **2024**, *69*, 2735−2755.
(717) Tsang, C.; Street, W. Phase equilibria in the H_2/CO_2 system at temperatures from 220 to 290 K and pressures to 172 MPa. *Chemical Engineering Science* **1981**, *36*, 993−1000.
(718) Zhang, J.; Clennell, M. B.; Chen, Y. New analytical thermodynamic models developed for pure H_2, CH_4, CO_2 and H_2 containing mixtures based on molecular simulations. *International Journal of Hydrogen Energy* **2024**, *69*, 687−697.
(719) Hernández-Gomez, R.; Tuma, D.; Pérez, E.; Chamorro, C. R. Accurate Experimental (p, ρ, and T) Data for the Introduction of Hydrogen into the Natural Gas Grid (II): Thermodynamic Characterization of the Methane-Hydrogen Binary System from 240 to 350 K and Pressures up to 20 MPa. *Journal of Chemical & Engineering Data* **2018**, *63*, 1613−1630.
(720) Cheng, S.; Shang, F.; Ma, W.; Jin, H.; Sakoda, N.; Zhang, X.; Guo, L. Density Data of Two (H_2 + CO_2) Mixtures and a (H_2 + CO_2 + CH_4) Mixture by a Modified Burnett Method at Temperature 673 K and Pressures up to 25 MPa. *Journal of Chemical & Engineering Data* **2019**, *64*, 1693−1704.
(721) Chen, B.; Potoff, J. J.; Siepmann, J. I. Monte Carlo calculations for alcohols and their mixtures with alkanes. Transferable potentials for phase equilibria. 5. united-atom description of primary, secondary, and tertiary alcohols. *J. Phys. Chem. B* **2001**, *105*, 3093−3104.
(722) Makrodimitri, Z. A.; Unruh, D. J. M.; Economou, I. G. Molecular Simulation of Diffusion of Hydrogen, Carbon Monoxide, and Water in Heavy n-Alkanes. *Journal of Physical Chemistry B* **2011**, *115*, 1429−1439.
(723) Giraudet, C.; Klein, T.; Zhao, G.; Rausch, M. H.; Koller, T. M.; Fröba, A. P. Thermal, Mutual, and Self-Diffusivities of Binary Liquid Mixtures Consisting of Gases Dissolved in n-Alkanes at Infinite Dilution. *The Journal of Physical Chemistry B* **2018**, *122*, 3163−3175.
(724) Wilke, C. R.; Chang, P. Correlation of diffusion coefficients in dilute solutions. *AIChE Journal* **1955**, *1*, 264−270.
(725) Wu, W.; Klein, T.; Kerscher, M.; Rausch, M. H.; Koller, T. M.; Giraudet, C.; Fröba, A. P. Diffusivities in 1-Alcohols Containing Dissolved H_2, He, N_2, CO, or CO_2 Close to Infinite Dilution. *The Journal of Physical Chemistry B* **2019**, *123*, 8777−8790.
(726) Rodden, J. B.; Erkey, C.; Akgerman, A. Diffusion Coefficients for Binary Supercritical Mixtures of n-Alcohols in Carbon Dioxide. *Journal of Chemical Engineering Data* **1988**, *33*, 450−453.
(727) Matthews, M. A.; Rodden, J. B.; Akgerman, A. High-Temperature Diffusion, Viscosity, and Density Measurements in n-Hexadecane. *Journal of Chemical Engineering Data* **1987**, *32*, 319−322.
(728) Klein, T.; Lenahan, F. D.; Kerscher, M.; Jander, J. H.; Rausch, M. H.; Koller, T. M.; Fröba, A. P. Viscosity and Interfacial Tension of Binary Mixtures of n-Hexadecane with Dissolved Gases Using Surface Light Scattering and Equilibrium Molecular Dynamics Simulations. *Journal of Chemical & Engineering Data* **2021**, *66*, 3205−3218.
(729) Klein, T.; Lenahan, F. D.; Zhai, Z.; Kerscher, M.; Jander, J. H.; Koller, T. M.; Rausch, M. H.; Fröba, A. P. Viscosity and Interfacial Tension of Binary Mixtures Consisting of Linear, Branched, Cyclic, or Oxygenated Hydrocarbons with Dissolved Gases Using Surface Light Scattering and Equilibrium Molecular Dynamics Simulations. *International Journal of Thermophysics* **2022**, *43*, 88.
(730) Kerscher, M.; Klein, T.; Preuster, P.; Wasserscheid, P.; Koller, T. M.; Rausch, M. H.; Fröba, A. P. Influence of dissolved hydrogen on the viscosity and interfacial tension of the liquid organic hydrogen carrier system based on diphenylmethane by surface light scattering and molecular dynamics simulations. *International Journal of Hydrogen Energy* **2022**, *47*, 39163−39178.
(731) Saric, D.; Guevara-Carrion, G.; Vrabec, J. Thermodynamics of supercritical carbon dioxide mixtures across the Widom line. *Phys. Chem. Chem. Phys.* **2022**, *24*, 28257−28270.
(732) Merker, T.; Engin, C.; Vrabec, J.; Hasse, H. Molecular model for carbon dioxide optimized to vapor-liquid equilibria. *The Journal of Chemical Physics* **2010**, *132*, 234512.
(733) Ye, Y.; Ahn, C. C.; Witham, C.; Fultz, B.; Liu, J.; Rinzler, A. G.; Colbert, D.; Smith, K. A.; Smalley, R. E. Hydrogen adsorption and cohesive energy of single-walled carbon nanotubes. *Applied Physics Letters* **1999**, *74*, 2307−2309.
(734) Morales, M. A.; McMahon, J. M.; Pierleoni, C.; Ceperley, D. M. Nuclear Quantum Effects and Nonlocal Exchange-Correlation Functionals Applied to Liquid Hydrogen at High Pressure. *Phys. Rev. Lett.* **2013**, *110*, 065702.
(735) Cheng, B.; Paxton, A. T.; Ceriotti, M. Hydrogen Diffusion and Trapping in α-Iron: The Role of Quantum and Anharmonic Fluctuations. *Phys. Rev. Lett.* **2018**, *120*, 225901.
(736) Lenosky, T. J.; Kress, J. D.; Collins, L. A.; Kwon, I. Molecular dynamics simulations of compressed liquid hydrogen. *Journal of Quantitative Spectroscopy and Radiative Transfer* **1997**, *58*, 743−755.
(737) Collins, L. A.; Kress, J. D.; Bickham, S. R.; Lenosky, T. J.; N, J. T. Molecular dynamics simulations of compressed hydrogen. *High Pressure Research* **2000**, *16*, 313−329.
(738) Holst, B.; Redmer, R.; Gryaznov, V. K.; Fortov, V. E.; Iosilevskiy, I. L. Hydrogen and deuterium in shock wave experiments, ab initio simulations and chemical picture modeling. *The European Physical Journal D* **2012**, *66*, 104.
(739) Tian, C.; Liu, F.; Yuan, H.; Chen, H.; Kuan, A. First-order liquid-liquid phase transition in compressed hydrogen and critical point. *The Journal of Chemical Physics* **2019**, *150*, 204114.
(740) Redmer, R.; Röpke, G.; Kuhlbrodt, S.; Reinholz, H. Hopping conductivity in dense hydrogen fluid. *Phys. Rev. B* **2001**, *63*, 233104.
(741) Liu, X.; Yu, Y.; Hou, C.; Ding, J. Effects of the wall temperature on the boiling process and the molecular dynamics behavior of the liquid hydrogen on a flat aluminum wall. *Int. J. Hydrogen Energy* **2024**, *51*, 1130−1141.
(742) Greenfield, M. L. Representing polymer molecular structure using molecular simulations for the study of liquid sorption and diffusion. *Current Opinion in Chemical Engineering* **2020**, *28*, 144−151.
(743) Vergadou, N.; Theodorou, D. N. Molecular Modeling Investigations of Sorption and Diffusion of Small Molecules in Glassy Polymers. *Membranes* **2019**, *9*, 98.
(744) Zhao, J.; Wang, X.; Yang, Q.; Yin, H.; Zhao, B.; Zhang, S.; Wu, C. Molecular dynamics simulation of H_2 in amorphous polyethylene system: H_2 diffusion in various PE matrices and bubbling during rapid depressurization. *International Journal of Hydrogen Energy* **2022**, *47*, 39572−39585.
(745) Li, J.; Zhao, X.; Liang, J.; Zhao, C.; Feng, N.; Guo, G.; Zhou, Z. Molecular Dynamics Simulation of Hydrogen Barrier Performance of Modified Polyamide 6 Lining of IV Hydrogen Storage Tank with Graphene. *Polymers* **2024**, *16*, 2185.
(746) Su, Y.; Lv, H.; Feng, C.; Zhang, C. Hydrogen permeability of polyamide 6 as the liner material of Type IV hydrogen storage tanks: A molecular dynamics investigation. *International Journal of Hydrogen Energy* **2024**, *50*, 1598−1606.
(747) Pant, P. V. K.; Boyd, R. H. Molecular-dynamics simulation of diffusion of small penetrants in polymers. *Macromolecules* **1993**, *26*, 679−686.
(748) Zheng, D.; Li, J.; Liu, B.; Yu, B.; Yang, Y.; Han, D.; Li, J.; Huang, Z. Molecular dynamics investigations into the hydrogen permeation mechanism of polyethylene pipeline material. *Journal of Molecular Liquids* **2022**, *368*, 120773.
(749) Shi, W.; Siefert, N. S.; Morreale, B. D. Molecular Simulations of CO_2, H_2, H_2O, and H_2S Gas Absorption into Hydrophobic Poly(dimethylsiloxane) (PDMS) Solvent: Solubility and Surface Tension. *J. Phys. Chem. C* **2015**, *119*, 19253−19265.
(750) Zhang, X.; Zhai, L.; Li, H.; Qi, G.; Gao, X.; Yang, W. Molecular Simulation Study on the Hydrogen Permeation Behavior and Mechanism of Common Polymers. *Polymers* **2024**, *16*, 953.
(751) Deas, T. M., Jr; Hofer, H. H.; Dole, M. Solubility of Hydrogen in Polyethylene by a Semimicro Method. *Macromolecules* **1972**, *5*, 223−226.

https://doi.org/10.1021/acs.chemrev.5c00617
Chem. Rev. 2025, 125, 11878−12029

(752) Na Zhang, D.; Ding, N.; Zhang, Z.; Cai, X.; Dong Shao, X.; Bu Li, H. Hydrogen Permeation Behavior of Polyethylene Liner for Type IV Vessel. *Advances in New and Renewable Energy* **2022**, *10*, 15−19.
(753) Sun, Y.; Lv, H.; Zhou, W.; Zhang, C. Research on hydrogen permeability of polyamide 6 as the liner material for type IV hydrogen storage tank. *International Journal of Hydrogen Energy* **2020**, *45*, 24980−24990.
(754) Lu, C.; Ni, S.; Chen, W.; Liao, J.; Zhang, C. A molecular modeling study on small molecule gas transportation in poly (chloro-p-xylylene). *Computational Materials Science* **2010**, *49*, S65−S69.
(755) Kucukpinar, E.; Doruker, P. Molecular simulations of gas transport in nitrile rubber and styrene butadiene rubber. *Polymer* **2006**, *47*, 7835−7845.
(756) Tan, J.; Chen, C.; Liu, Y.; Wu, J.; Wu, D.; Zhang, X.; He, X.; She, Z.; He, R.; Zhang, H. Molecular simulations of gas transport in hydrogenated nitrile butadiene rubber and ethylene-propylene-diene rubber. *RSC Adv.* **2020**, *10*, 12475−12484.
(757) Tan, J.-H.; Chen, C.-L.; Liu, Y.-W.; Wu, J.-Y.; Wu, D.; Zhang, X.; She, Z.-H.; He, R.; Zhang, H.-L. Molecular simulations of gas transport in hydrogenated nitrile butadiene rubber. *Journal of Polymer Research* **2020**, *27*, 277.
(758) Stalker, M. R.; Grant, J.; Yong, C. W.; Ohene-Yeboah, L. A.; Mays, T. J.; S, C. P. Molecular simulation of hydrogen storage and transport in cellulose. *Molecular Simulation* **2021**, *47*, 170−179.
(759) Yi, Y.; Bi, P.; Zhao, X.; Wang, L. Molecular dynamics simulation of diffusion of hydrogen and its isotopic molecule in polystyrene. *Journal of Polymer Research* **2018**, *25*, 43.
(760) Zhao, J.; Li, X.; Wang, X.; Zhang, Q.; Yang, Q.; Yin, H.; Zhang, S.; Wu, C. Insights into the solubility of H_2 in various polyethylene matrices at high pressure: A coarse-grained MC/MD study. *International Journal of Hydrogen Energy* **2023**, *48*, 19619−19632.
(761) Wilson, M. A.; Frischknecht, A. L. High-pressure hydrogen decompression in sulfur crosslinked elastomers. *International Journal of Hydrogen Energy* **2022**, *47*, 15094−15106.
(762) Plimpton, S. Fast parallel algorithms for short-range molecular dynamics. *J. Comput. Phys.* **1995**, *117*, 1−19.
(763) Brownell, M.; Frischknecht, A. L.; Wilson, M. A. Subdiffusive High-Pressure Hydrogen Gas Dynamics in Elastomers. *Macromolecules* **2022**, *55*, 3788−3800.
(764) Wilson, M. A.; Winter, I. S.; Frischknecht, A. L. Effects of high-pressure hydrogen exposure on filler-elastomer adhesion. *International Journal of Hydrogen Energy* **2025**, *144*, 19−29.
(765) Lorenz, C.; Webb, E.; Stevens, M.; Chandross, M.; Grest, G. Frictional dynamics of perfluorinated self-assembled monolayers on amorphous SiO_2. *Tribology Letters* **2005**, *19*, 93−98.
(766) Ramdin, M.; de Loos, T. W.; Vlugt, T. J. H. State-of-the-art of CO_2 capture with ionic liquids. *Ind. Eng. Chem. Res.* **2012**, *51*, 8149−8177.
(767) Shi, W.; Sorescu, D. C.; Luebke, D. R.; Keller, M. J.; Wickramanayake, S. Molecular Simulations and Experimental Studies of Solubility and Diffusivity for Pure and Mixed Gases of H_2, CO_2, and Ar Absorbed in the Ionic Liquid 1-n-Hexyl-3-methylimidazolium Bis(Trifluoromethylsulfonyl)amide ([hmim][Tf_2N]). *J. Phys. Chem. B* **2010**, *114*, 6531−6541.
(768) Shi, W.; Sorescu, D. C. Molecular simulations of CO_2 and H_2 sorption into ionic liquid 1-n-Hexyl-3-methylimidazolium Bis-(trifluoromethylsulfonyl)amide ([hmim][Tf_2N]) confined in carbon nanotubes. *J. Phys. Chem. B* **2010**, *114*, 15029−15041.
(769) Ramdin, M.; Balaji, S. P.; Vicent-Luna, J. M.; Gutiérrez-Sevillano, J. J.; Calero, S.; de Loos, T. W.; Vlugt, T. J. H. Solubility of the precombustion Gases CO_2, CH_4, CO, H_2, N_2, and H_2S in the ionic liquid [bmim][Tf2N] from Monte Carlo simulations. *J. Phys. Chem. C* **2014**, *118*, 23599−23604.
(770) Liu, H.; Maginn, E. A molecular dynamics investigation of the structural and dynamic properties of the ionic liquid 1-n-butyl-3-methylimidazolium bis(trifluoromethanesulfonyl)imide. *The Journal of Chemical Physics* **2011**, *135*, 124507.
(771) Wittich, B.; Deiters, U. K. Calculating Thermodynamic Properties of an Ionic Liquid with Monte Carlo Simulations with an Orthorhombic and a Cubic Simulation Box. *The Journal of Physical Chemistry B* **2010**, *114*, 8954−8960.
(772) Shah, J. K.; Maginn, E. J. A Monte Carlo simulation study of the ionic liquid 1-n-butyl-3-methylimidazolium hexafluorophosphate: liquid structure, volumetric properties and infinite dilution solution thermodynamics of CO_2. *Fluid Phase Equilibria* **2004**, *222-223*, 195−203.
(773) Klein, T.; Piszko, M.; Lang, M.; Mehler, J.; Schulz, P. S.; Rausch, M. H.; Giraudet, C.; Koller, T. M.; Fröba, A. P. Diffusivities in Binary Mixtures of [AMIM][NTf2] Ionic Liquids with the Dissolved Gases H_2, He, N_2, CO, CO_2, or Kr Close to Infinite Dilution. *Journal of Chemical & Engineering Data* **2020**, *65*, 4116−4129.
(774) Zhai, Z.; Hantal, G.; Cherian, A.; Bergen, A.; Chu, J.; Wick, C. R.; Meyer, K.; Smith, A.-S.; Koller, T. M. Influence of molecular hydrogen on bulk and interfacial properties of three imidazolium-based ionic liquids by experiments and molecular dynamics simulations. *International Journal of Hydrogen Energy* **2024**, *72*, 1091−1104.
(775) Seidl, V.; Bosch, M.; Paap, U.; Livraghi, M.; Zhai, Z.; Wick, C. R.; Koller, T. M.; Wasserscheid, P.; Maier, F.; Smith, A.-S.; Bachmann, J.; Steinrück, H.-P.; Meyer, K. Bis-polyethylene glycol-functionalized imidazolium ionic liquids: A multi-method approach towards bulk and surface properties. *Journal of Ionic Liquids* **2022**, *2*, 100041.
(776) Rivera-Pousa, A.; Lois-Cuns, R.; Otero-Lema, M.; Montes-Campos, H.; Méndez-Morales, T.; Varela, L. M. Size Matters: A Computational Study of Hydrogen Absorption in Ionic Liquids. *Journal of Chemical Information and Modeling* **2024**, *64*, 164−177.
(777) Yang, Q.; Zhong, C. Molecular Simulation of Carbon Dioxide/Methane/Hydrogen Mixture Adsorption in Metal-Organic Frameworks. *The Journal of Physical Chemistry B* **2006**, *110*, 17776−17783.
(778) Liu, B.; Yang, Q.; Xue, C.; Zhong, C.; Chen, B.; Smit, B. Enhanced Adsorption Selectivity of Hydrogen/Methane Mixtures in Metal-Organic Frameworks with Interpenetration: A Molecular Simulation Study. *The Journal of Physical Chemistry C* **2008**, *112*, 9854−9860.
(779) Wu, X.; Huang, J.; Cai, W.; Jaroniec, M. Force field for ZIF-8 flexible frameworks: atomistic simulation of adsorption, diffusion of pure gases as CH_4, H_2, CO_2 and N_2. *RSC Adv.* **2014**, *4*, 16503−16511.
(780) Keskin, S. Adsorption, Diffusion, and Separation of CH_4/H_2 Mixtures in Covalent Organic Frameworks: Molecular Simulations and Theoretical Predictions. *The Journal of Physical Chemistry C* **2012**, *116*, 1772−1779.
(781) Song, M. K.; No, K. T. Molecular simulation of hydrogen adsorption in organic zeolite. *Catalysis Today* **2007**, *120*, 374−382.
(782) Deeg, K. S.; Gutiérrez-Sevillano, J. J.; Bueno-Pérez, R.; Parra, J. B.; Ania, C. O.; Doblaré, M.; Calero, S. Insights on the Molecular Mechanisms of Hydrogen Adsorption in Zeolites. *J. Phys. Chem. C* **2013**, *117*, 14374−14380.
(783) Yilmaz, G.; Keskin, S. Predicting the Performance of Zeolite Imidazolate Framework/Polymer Mixed Matrix Membranes for CO_2, CH_4, and H_2 Separations Using Molecular Simulations. *Industrial & Engineering Chemistry Research* **2012**, *51*, 14218−14228.
(784) Bobbitt, N. S.; Chen, J.; Snurr, R. Q. High-Throughput Screening of Metal-Organic Frameworks for Hydrogen Storage at Cryogenic Temperature. *Journal of Physical Chemistry C* **2016**, *120*, 27328−27341.
(785) Moosavi, S. M.; Nandy, A.; Jablonka, K. M.; Ongari, D.; Janet, J. P.; Boyd, P. G.; Lee, Y.; Smit, B.; Kulik, H. J. Understanding the diversity of the metal-organic framework ecosystem. *Nature communications* **2020**, *11*, 4068.
(786) Wilmer, C. E.; Leaf, M.; Lee, C. Y.; Farha, O. K.; Hauser, B. G.; Hupp, J. T.; Snurr, R. Q. Large-scale screening of hypothetical metal-organic frameworks. *Nature Chemistry* **2012**, *4*, 83−89.

https://doi.org/10.1021/acs.chemrev.5c00617
Chem. Rev. 2025, 125, 11878−12029

(787) Avci, G.; Erucar, I.; Keskin, S. Do New MOFs Perform Better for CO_2 Capture and H_2 Purification? Computational Screening of the Updated MOF Database. *ACS Applied Materials & Interfaces* **2020**, *12*, 41567−41579.
(788) Allen, F. H. The Cambridge Structural Database: a quarter of a million crystal structures and rising. *Acta Crystallographica B* **2002**, *B58*, 380−388.
(789) Altundal, O. F.; Haslak, Z. P.; Keskin, S. Combined GCMC, MD, and DFT Approach for Unlocking the Performances of COFs for Methane Purification. *Industrial & Engineering Chemistry Research* **2021**, *60*, 12999−13012.
(790) Altintas, C.; Avci, G.; Daglar, H.; Nemati Vesali Azar, A.; Erucar, I.; Velioglu, S.; Keskin, S. An extensive comparative analysis of two MOF databases: high-throughput screening of computation-ready MOFs for CH_4 and H_2 adsorption. *J. Mater. Chem. A* **2019**, *7*, 9593−9608.
(791) Chung, Y. G.; Camp, J.; Haranczyk, M.; Sikora, B. J.; Bury, W.; Krungleviciute, V.; Yildirim, T.; Farha, O. K.; Sholl, D. S.; Snurr, R. Q. Computation-ready, experimental metal-organic frameworks: A tool to enable high-throughput screening of nanoporous crystals. *Chemistry of Materials* **2014**, *26*, 6185−6192.
(792) Moghadam, P. Z.; Li, A.; Wiggin, S. B.; Tao, A.; Maloney, A. G.; Wood, P. A.; Ward, S. C.; Fairen-Jimenez, D. Development of a Cambridge Structural Database Subset: A Collection of Metal-Organic Frameworks for Past, Present, and Future. *Chemistry of Materials* **2017**, *29*, 2618−2625.
(793) Aksu, G. O.; Daglar, H.; Altintas, C.; Keskin, S. Computational Selection of High-Performing Covalent Organic Frameworks for Adsorption and Membrane-Based CO_2/H_2 Separation. *The Journal of Physical Chemistry C* **2020**, *124*, 22577−22590.
(794) Yan, T.; Lan, Y.; Tong, M.; Zhong, C. Screening and Design of Covalent Organic Framework Membranes for CO_2/CH_4 Separation. *ACS Sustainable Chemistry and Engineering* **2019**, *7*, 1220−1227.
(795) Avci, G.; Altintas, C.; Keskin, S. Metal Exchange Boosts the CO_2 Selectivity of Metal Organic Frameworks Having Zn-Oxide Nodes. *The Journal of Physical Chemistry C* **2021**, *125*, 17311−17322.
(796) Abdulkadir, B.; Mohd Zaki, R.; Abd Wahab, A.; Miskan, S.; Nguyen, A.-T.; Vo, D.-V. N.; Setiabudi, H. A concise review on surface and structural modification of porous zeolite scaffold for enhanced hydrogen storage. *Chinese Journal of Chemical Engineering* **2024**, *70*, 33−53.
(797) Manda, T.; Barasa, G. O.; Louis, H.; Irfan, A.; Agumba, J. O.; Lugasi, S. O.; Pembere, A. M. A data-guided approach for the evaluation of zeolites for hydrogen storage with the aid of molecular simulations. *Journal of Molecular Modeling* **2024**, *30*, 43.
(798) Liang, P.; Cao, Y.; Tai, B.; Zhang, L.; Shu, H.; Li, F.; Chao, D.; Du, X. Is borophene a suitable anode material for sodium ion battery? *Journal of Alloys and Compounds* **2017**, *704*, 152−159.
(799) Osman, A. I.; Nasr, M.; Eltaweil, A. S.; Hosny, M.; Farghali, M.; Al-Fatesh, A. S.; Rooney, D. W.; Abd El-Monaem, E. M. Advances in hydrogen storage materials: harnessing innovative technology, from machine learning to computational chemistry, for energy storage solutions. *International Journal of Hydrogen Energy* **2024**, *67*, 1270−1294.
(800) Chung, Y. G.; Haldoupis, E.; Bucior, B. J.; Haranczyk, M.; Lee, S.; Zhang, H.; Vogiatzis, K. D.; Milisavljevic, M.; Ling, S.; Camp, J. S.; Slater, B.; Siepmann, J. I.; Sholl, D. S.; Snurr, R. Q. Advances, Updates, and Analytics for the Computation-Ready, Experimental Metal-Organic Framework Database: CoRE MOF 2019. *Journal of Chemical & Engineering Data* **2019**, *64*, 5985−5998.
(801) Deeg, K. S.; Damasceno Borges, D.; Ongari, D.; Rampal, N.; Talirz, L.; Yakutovich, A. V.; Huck, J. M.; Smit, B. In Silico Discovery of Covalent Organic Frameworks for Carbon Capture. *ACS Applied Materials & Interfaces* **2020**, *12*, 21559−21568.
(802) Exploring the structure-property relationships of covalent organic frameworks for noble gas separations. *Chemical Engineering Science* **2017**, *168*, 456−464.
(803) Hellenbrandt, M. The Inorganic Crystal Structure Database (ICSD)-Present and Future. *Crystallography Reviews* **2004**, *10*, 17−22.
(804) Grazulis, S.; Chateigner, D.; Downs, R. T.; Yokochi, A. F. T.; Quiros, M.; Lutterotti, L.; Manakova, E.; Butkus, J.; Moeck, P.; Le Bail, A. Crystallography Open Database - an open-access collection of crystal structures. *Journal of Applied Crystallography* **2009**, *42*, 726−729.
(805) Groom, C. R.; Bruno, I. J.; Lightfoot, M. P.; Ward, S. C. The Cambridge Structural Database. *Acta Crystallographica Section B* **2016**, *72*, 171−179.
(806) Moosavi, S. M.; Jablonka, K. M.; Smit, B. The Role of Machine Learning in the Understanding and Design of Materials. *Journal of the American Chemical Society* **2020**, *142*, 20273−20287.
(807) Bucior, B. J.; Bobbitt, N. S.; Islamoglu, T.; Goswami, S.; Gopalan, A.; Yildirim, T.; Farha, O. K.; Bagheri, N.; Snurr, R. Q. Energy-based descriptors to rapidly predict hydrogen storage in metal-organic frameworks. *Mol. Syst. Des. Eng.* **2019**, *4*, 162−174.
(808) Dureckova, H.; Krykunov, M.; Aghaji, M. Z.; Woo, T. K. Robust Machine Learning Models for Predicting High CO_2 Working Capacity and CO_2/H_2 Selectivity of Gas Adsorption in Metal Organic Frameworks for Precombustion Carbon Capture. *The Journal of Physical Chemistry C* **2019**, *123*, 4133−4139.
(809) Yang, W.; Liang, H.; Peng, F.; Liu, Z.; Liu, J.; Qiao, Z. Computational screening of metal-organic framework membranes for the separation of 15 gas mixtures. *Nanomaterials* **2019**, *9*, 467.
(810) Shi, Z.; Yang, W.; Deng, X.; Cai, C.; Yan, Y.; Liang, H.; Liu, Z.; Qiao, Z. Machine-learning-assisted high-throughput computational screening of high performance metal-organic frameworks. *Mol. Syst. Des. Eng.* **2020**, *5*, 725−742.
(811) Bai, X.; Shi, Z.; Xia, H.; Li, S.; Liu, Z.; Liang, H.; Liu, Z.; Wang, B.; Qiao, Z. Machine-Learning-Assisted High-Throughput computational screening of Metal-Organic framework membranes for hydrogen separation. *Chemical Engineering Journal* **2022**, *446*, 136783.
(812) Hertäg, L.; Bux, H.; Caro, J.; Chmelik, C.; Remsungnen, T.; Knauth, M.; Fritzsche, S. Diffusion of CH_4 and H_2 in ZIF-8. *Journal of Membrane Science* **2011**, *377*, 36−41.
(813) He, G.; Dakhchoune, M.; Zhao, J.; Huang, S.; Agrawal, K. V. Electrophoretic Nuclei Assembly for Crystallization of High-Performance Membranes on Unmodified Supports. *Advanced Functional Materials* **2018**, *28*, 1707427.
(814) Li, Y.-S.; Liang, F.-Y.; Bux, H.; Feldhoff, A.; Yang, W.-S.; Caro, J. Molecular Sieve Membrane: Supported Metal-Organic Framework with High Hydrogen Selectivity. *Angewandte Chemie International Edition* **2010**, *49*, 548−551.
(815) Huang, A.; Liang, F.; Steinbach, F.; Caro, J. Preparation and separation properties of LTA membranes by using 3-amino-propyltriethoxysilane as covalent linker. *Journal of Membrane Science* **2010**, *350*, 5−9.
(816) Guo, H.; Zhu, G.; Hewitt, I. J.; Qiu, S. "Twin Copper Source" Growth of Metal-Organic Framework Membrane: $Cu_3(BTC)_2$ with High Permeability and Selectivity for Recycling H_2. *Journal of the American Chemical Society* **2009**, *131*, 1646−1647.
(817) Chang, H.; Wang, Y.; Xiang, L.; Liu, D.; Wang, C.; Pan, Y. Improved H_2/CO_2 separation performance on mixed-linker ZIF-7 polycrystalline membranes. *Chemical Engineering Science* **2018**, *192*, 85−93.
(818) Pulyalina, A.; Polotskaya, G.; Rostovtseva, V.; Pientka, Z.; Toikka, A. Improved hydrogen separation using hybrid membrane composed of nanodiamonds and P84 copolyimide. *Polymers* **2018**, *10*, 828.
(819) Safak Boroglu, M.; Yumru, A. B. Gas separation performance of 6FDA-DAM-ZIF-11 mixed-matrix membranes for H_2/CH_4 and CO_2/CH_4 separation. *Separation and Purification Technology* **2017**, *173*, 269−279.
(820) Lanč, M.; Sysel, P.; Soltys, M.; Stepánek, F.; Fonod, K.; Klepic, M.; Vopička, O.; Lhotka, M.; Ulbrich, P.; Friess, K. Synthesis, preparation and characterization of novel hyperbranched 6FDA-TTM based polyimide membranes for effective CO_2 separation: Effect of

https://doi.org/10.1021/acs.chemrev.5c00617
Chem. Rev. 2025, 125, 11878−12029

embedded mesoporous silica particles and siloxane linkages. *Polymer* **2018**, *144*, 33−42.
(821) Xue, Q.; Pan, X.; Li, X.; Zhang, J.; Guo, Q. Effective enhancement of gas separation performance in mixed matrix membranes using core/shell structured multi-walled carbon nanotube/graphene oxide nanoribbons. *Nanotechnology* **2017**, *28*, 065702.
(822) Iulianelli, A.; Algieri, C.; Donato, L.; Garofalo, A.; Galiano, F.; Bagnato, G.; Basile, A.; Figoli, A. New PEEK-WC and PLA membranes for H_2 separation. *International Journal of Hydrogen Energy* **2017**, *42*, 22138−22148.
(823) Macchione, M.; Jansen, J. C.; De Luca, G.; Tocci, E.; Longeri, M.; Drioli, E. Experimental analysis and simulation of the gas transport in dense Hyflon® AD60X membranes: Influence of residual solvent. *Polymer* **2007**, *48*, 2619−2635.
(824) Wijenayake, S. N.; Panapitiya, N. P.; Nguyen, C. N.; Huang, Y.; Balkus, K. J.; Musselman, I. H.; Ferraris, J. P. Composite membranes with a highly selective polymer skin for hydrogen separation. *Separation and Purification Technology* **2014**, *135*, 190−198.
(825) Song, Q.; Nataraj, S. K.; Roussenova, M. V.; Tan, J. C.; Hughes, D. J.; Li, W.; Bourgoin, P.; Alam, M. A.; Cheetham, A. K.; Al-Muhtaseb, S. A.; Sivaniah, E. Zeolitic imidazolate framework (ZIF-8) based polymer nanocomposite membranes for gas separation. *Energy Environ. Sci.* **2012**, *5*, 8359−8369.
(826) Kim, E. Y.; Kim, H. S.; Kim, D.; Kim, J.; Lee, P. S. Preparation of mixed matrix membranes containing ZIF-8 and UiO-66 for multicomponent light gas separation. *Crystals* **2019**, *9*, 15.
(827) Li, Z.; Yang, P.; Yan, S.; Fang, Q.; Xue, M.; Qiu, S. A Robust Zeolitic Imidazolate Framework Membrane with High H_2/CO_2 Separation Performance under Hydrothermal Conditions. *ACS Applied Materials & Interfaces* **2019**, *11*, 15748−15755.
(828) Velioglu, S.; Keskin, S. Simulation of H_2/CH_4 mixture permeation through MOF membranes using non-equilibrium molecular dynamics. *J. Mater. Chem. A* **2019**, *7*, 2301−2314.
(829) Cacho-Bailo, F.; Catalán-Aguirre, S.; Etxeberría-Benavides, M.; Karvan, O.; Sebastian, V.; Téllez, C.; Coronas, J. Metal-organic framework membranes on the inner-side of a polymeric hollow fiber by microfluidic synthesis. *Journal of Membrane Science* **2015**, *476*, 277−285.
(830) Wang, Y.; Jin, H.; Ma, Q.; Mo, K.; Mao, H.; Feldhoff, A.; Cao, X.; Li, Y.; Pan, F.; Jiang, Z. A MOF Glass Membrane for Gas Separation. *Angewandte Chemie International Edition* **2020**, *59*, 4365−4369.
(831) Li, W.; Su, P.; Zhang, G.; Shen, C.; Meng, Q. Preparation of continuous NH_2-MIL-53 membrane on ammoniated polyvinylidene fluoride hollow fiber for efficient H_2 purification. *Journal of Membrane Science* **2015**, *495*, 384−391.
(832) Huang, A.; Wang, N.; Kong, C.; Caro, J. Organosilica-Functionalized Zeolitic Imidazolate Framework ZIF-90 Membrane with High Gas-Separation Performance. *Angewandte Chemie International Edition* **2012**, *51*, 10551−10555.
(833) Kang, Z.; Fan, L.; Wang, S.; Sun, D.; Xue, M.; Qiu, S. In situ confinement of free linkers within a stable MOF membrane for highly improved gas separation properties. *CrystEngComm* **2017**, *19*, 1601−1606.
(834) Kong, C.; Du, H.; Chen, L.; Chen, B. Nanoscale MOF/organosilica membranes on tubular ceramic substrates for highly selective gas separation. *Energy Environ. Sci.* **2017**, *10*, 1812−1819.
(835) Aguado, S.; Nicolas, C.-H.; Moizan-Baslé, V.; Nieto, C.; Amrouche, H.; Bats, N.; Audebrand, N.; Farrusseng, D. Facile synthesis of an ultramicroporous MOF tubular membrane with selectivity towards CO_2. *New J. Chem.* **2011**, *35*, 41−44.
(836) Al-Maythalony, B. A.; Shekhah, O.; Swaidan, R.; Belmabkhout, Y.; Pinnau, I.; Eddaoudi, M. Quest for Anionic MOF Membranes: Continuous sod-ZMOF Membrane with CO_2 Adsorption-Driven Selectivity. *Journal of the American Chemical Society* **2015**, *137*, 1754−1757.
(837) Qian, Q.; Wu, A. X.; Chi, W. S.; Asinger, P. A.; Lin, S.; Hypsher, A.; Smith, Z. P. Mixed-Matrix Membranes Formed from Imide-Functionalized UiO-66-NH_2 for Improved Interfacial Compatibility. *ACS Applied Materials & Interfaces* **2019**, *11*, 31257−31269.
(838) Feng, S.; Bu, M.; Pang, J.; Fan, W.; Fan, L.; Zhao, H.; Yang, G.; Guo, H.; Kong, G.; Sun, H.; Kang, Z.; Sun, D. Hydrothermal stable ZIF-67 nanosheets via morphology regulation strategy to construct mixed-matrix membrane for gas separation. *Journal of Membrane Science* **2020**, *593*, 117404.
(839) Esposito, E.; Bruno, R.; Monteleone, M.; Fuoco, A.; Ferrando Soria, J.; Pardo, E.; Armentano, D.; Jansen, J. C. Glassy PEEK-WC vs. rubbery Pebax® 1657 polymers: Effect on the gas transport in CuNi-MOF based mixed matrix membranes. *Applied Sciences* **2020**, *10*, 1310.
(840) Fan, Y.; Yu, H.; Xu, S.; Shen, Q.; Ye, H.; Li, N. Zn(II)-modified imidazole containing polyimide/ZIF-8 mixed matrix membranes for gas separations. *Journal of Membrane Science* **2020**, *597*, 117775.
(841) Fan, H.; Peng, M.; Strauss, I.; Mundstock, A.; Meng, H.; Caro, J. MOF-in-COF molecular sieving membrane for selective hydrogen separation. *Nature Communications* **2021**, *12*, 38.
(842) Gao, X.; Zhang, J.; Huang, K.; Zhang, J. ROMP for Metal-Organic Frameworks: An Efficient Technique toward Robust and High-Separation Performance Membranes. *ACS Applied Materials & Interfaces* **2018**, *10*, 34640−34645.
(843) Ashtiani, S.; Khoshnamvand, M.; Bouša, D.; Sturala, J.; Sofer, Z.; Shaliutina-Kolešová, A.; Gardenö, D.; Friess, K. Surface and interface engineering in CO_2-philic based UiO-66-NH2-PEI mixed matrix membranes via covalently bridging PVP for effective hydrogen purification. *International Journal of Hydrogen Energy* **2021**, *46*, 5449−5458.
(844) Diestel, L.; Wang, N.; Schulz, A.; Steinbach, F.; Caro, J. Matrimid-Based Mixed Matrix Membranes: Interpretation and Correlation of Experimental Findings for Zeolitic Imidazolate Frameworks as Fillers in H_2/CO_2 Separation. *Industrial & Engineering Chemistry Research* **2015**, *54*, 1103−1112.
(845) Zhuang, G.-L.; Wey, M.; hsin Tseng, H. Theand Polyimide in MOF-Incorporated PPO-silica mixed-matrix membranes produced via the in situ sol-gel method for H_2/CO_2 separation. II: Effect of thermal annealing treatment. *Chemical Engineering Research & Design* **2015**, *104*, 319−332.
(846) Jia, Y.; Liu, P.; Liu, Y.; Zhang, D.; Ning, Y.; Xu, C.; Zhang, Y. In-situ interfacial crosslinking of NH_2-MIL-53 and polyimide in MOF-incorporated mixed matrix membranes for efficient H_2 purification. *Fuel* **2023**, *339*, 126938.
(847) Wijenayake, S. N.; Panapitiya, N. P.; Versteeg, S. H.; Nguyen, C. N.; Goel, S.; Balkus, K. J. J.; Musselman, I. H.; Ferraris, J. P. Surface Cross-Linking of ZIF-8/Polyimide Mixed Matrix Membranes (MMMs) for Gas Separation. *Industrial & Engineering Chemistry Research* **2013**, *52*, 6991−7001.
(848) Nabais, A. R.; Martins, A. P.; Alves, V. D.; Crespo, J. G.; Marrucho, I. M.; Tomé, L. C.; Neves, L. A. Poly(ionic liquid)-based engineered mixed matrix membranes for CO_2/H_2 separation. *Separation and Purification Technology* **2019**, *222*, 168−176.
(849) Cheng, J.; Wang, Y.; Liu, N.; Hou, W.; Zhou, J. Enhanced CO_2 selectivity of mixed matrix membranes with carbonized Zn/Co zeolitic imidazolate frameworks. *Applied Energy* **2020**, *272*, 115179.
(850) Zhao, D.; Ren, J.; Qiu, Y.; Li, H.; Hua, K.; Li, X.; Deng, M. Effect of graphene oxide on the behavior of poly(amide-6-b-ethylene oxide)/graphene oxide mixed-matrix membranes in the permeation process. *Journal of Applied Polymer Science* **2015**, *132*, 42624.
(851) Bux, H.; Liang, F.; Li, Y.; Cravillon, J.; Wiebcke, M.; Caro, J. Zeolitic Imidazolate Framework Membrane with Molecular Sieving Properties by Microwave-Assisted Solvothermal Synthesis. *Journal of the American Chemical Society* **2009**, *131*, 16000−16001.
(852) Li, Y.-S.; Bux, H.; Feldhoff, A.; Li, G.-L.; Yang, W.-S.; Caro, J. Controllable Synthesis of Metal-Organic Frameworks: From MOF Nanorods to Oriented MOF Membranes. *Advanced Materials* **2010**, *22*, 3322−3326.
(853) Huang, A.; Bux, H.; Steinbach, F.; Caro, J. Molecular-Sieve Membrane with Hydrogen Permselectivity: ZIF-22 in LTA Topology

https://doi.org/10.1021/acs.chemrev.5c00617
Chem. Rev. 2025, 125, 11878−12029

Prepared with 3-Aminopropyltriethoxysilane as Covalent Linker. *Angewandte Chemie International Edition* **2010**, *49*, 4958−4961.
(854) Bux, H.; Feldhoff, A.; Cravillon, J.; Wiebcke, M.; Li, Y.-S.; Caro, J. Oriented Zeolitic Imidazolate Framework-8 Membrane with Sharp H_2/C_3H_8 Molecular Sieve Separation. *Chemistry of Materials* **2011**, *23*, 2262−2269.
(855) Zhang, F.; Zou, X.; Gao, X.; Fan, S.; Sun, F.; Ren, H.; Zhu, G. Hydrogen Selective NH2-MIL-53(Al) MOF Membranes with High Permeability. *Advanced Functional Materials* **2012**, *22*, 3583−3590.
(856) Huang, K.; Dong, Z.; Li, Q.; Jin, W. Growth of a ZIF-8 membrane on the inner-surface of a ceramic hollow fiber via cycling precursors. *Chem. Commun.* **2013**, *49*, 10326−10328.
(857) Wang, N.; Mundstock, A.; Liu, Y.; Huang, A.; Caro, J. Amine-modified Mg-MOF-74/CPO-27-Mg membrane with enhanced H_2/CO_2 separation. *Chemical Engineering Science* **2015**, *124*, 27−36.
(858) Knebel, A.; Friebe, S.; Bigall, N. C.; Benzaqui, M.; Serre, C.; Caro, J. Comparative Study of MIL-96(Al) as Continuous Metal-Organic Frameworks Layer and Mixed-Matrix Membrane. *ACS Applied Materials & Interfaces* **2016**, *8*, 7536−7544.
(859) Peng, Y.; Li, Y.; Ban, Y.; Yang, W. Two-Dimensional Metal-Organic Framework Nanosheets for Membrane-Based Gas Separation. *Angewandte Chemie International Edition* **2017**, *56*, 9757−9761.
(860) Carta, M.; Malpass-Evans, R.; Croad, M.; Rogan, Y.; Jansen, J. C.; Bernardo, P.; Bazzarelli, F.; McKeown, N. B. An Efficient Polymer Molecular Sieve for Membrane Gas Separations. *Science* **2013**, *339*, 303−307.
(861) Han, S. H.; Kwon, H. J.; Kim, K. Y.; Seong, J. G.; Park, C. H.; Kim, S.; Doherty, C. M.; Thornton, A. W.; Hill, A. J.; Lozano, A. E.; Berchtold, K. A.; Lee, Y. M. Tuning microcavities in thermally rearranged polymer membranes for CO_2 capture. *Phys. Chem. Chem. Phys.* **2012**, *14*, 4365−4373.
(862) Do, Y. S.; Seong, J. G.; Kim, S.; Lee, J. G.; Lee, Y. M. Thermally rearranged (TR) poly(benzoxazole-co-amide) membranes for hydrogen separation derived from 3,3'-dihydroxy-4,4'-diamino-biphenyl (HAB), 4,4'-oxydianiline (ODA) and isophthaloyl chloride (IPCl). *Journal of Membrane Science* **2013**, *446*, 294−302.
(863) Pesiri, D. R.; Jorgensen, B.; Dye, R. C. Thermal optimization of polybenzimidazole meniscus membranes for the separation of hydrogen, methane, and carbon dioxide. *Journal of Membrane Science* **2003**, *218*, 11−18.
(864) Scholes, C. A.; Smith, K. H.; Kentish, S. E.; Stevens, G. W. CO_2 capture from pre-combustion processes—Strategies for membrane gas separation. *International Journal of Greenhouse Gas Control* **2010**, *4*, 739−755.
(865) Yang, T.; Shi, G. M.; Chung, T.-S. Symmetric and Asymmetric Zeolitic Imidazolate Frameworks (ZIFs)/Polybenzimidazole (PBI) Nanocomposite Membranes for Hydrogen Purification at High Temperatures. *Advanced Energy Materials* **2012**, *2*, 1358−1367.
(866) Yang, T.; Xiao, Y.; Chung, T.-S. Poly-/metal-benzimidazole nano-composite membranes for hydrogen purification. *Energy Environ. Sci.* **2011**, *4*, 4171−4180.
(867) Zhu, L.; Swihart, M. T.; Lin, H. Unprecedented size-sieving ability in polybenzimidazole doped with polyprotic acids for membrane H_2/CO_2 separation. *Energy Environ. Sci.* **2018**, *11*, 94−100.
(868) Shan, M.; Liu, X.; Wang, X.; Yarulina, I.; Seoane, B.; Kapteijn, F.; Gascon, J. Facile manufacture of porous organic framework membranes for precombustion CO_2 capture. *Science Advances* **2018**, *4*, No. eaau1698.
(869) Kang, Z.; Peng, Y.; Qian, Y.; Yuan, D.; Addicoat, M. A.; Heine, T.; Hu, Z.; Tee, L.; Guo, Z.; Zhao, D. Mixed Matrix Membranes (MMMs) Comprising Exfoliated 2D Covalent Organic Frameworks (COFs) for Efficient CO_2 Separation. *Chemistry of Materials* **2016**, *28*, 1277−1285.
(870) Fu, J.; Das, S.; Xing, G.; Ben, T.; Valtchev, V.; Qiu, S. Fabrication of COF-MOF Composite Membranes and Their Highly Selective Separation of H_2/CO_2. *Journal of the American Chemical Society* **2016**, *138*, 7673−7680.
(871) Fan, H.; Mundstock, A.; Feldhoff, A.; Knebel, A.; Gu, J.; Meng, H.; Caro, J. Covalent Organic Framework-Covalent Organic Framework Bilayer Membranes for Highly Selective Gas Separation. *Journal of the American Chemical Society* **2018**, *140*, 10094−10098.
(872) Ying, Y.; Liu, D.; Ma, J.; Tong, M.; Zhang, W.; Huang, H.; Yang, Q.; Zhong, C. A GO-assisted method for the preparation of ultrathin covalent organic framework membranes for gas separation. *J. Mater. Chem. A* **2016**, *4*, 13444−13449.
(873) Tang, Y.; Feng, S.; Fan, L.; Pang, J.; Fan, W.; Kong, G.; Kang, Z.; Sun, D. Covalent organic frameworks combined with graphene oxide to fabricate membranes for H_2/CO_2 separation. *Separation and Purification Technology* **2019**, *223*, 10−16.
(874) Das, S.; Ben, T. A [COF-300]-[UiO-66] composite membrane with remarkably high permeability and H_2/CO_2 separation selectivity. *Dalton Trans.* **2018**, *47*, 7206−7212.
(875) Fan, H.; Peng, M.; Strauss, I.; Mundstock, A.; Meng, H.; Caro, J. High-Flux Vertically Aligned 2D Covalent Organic Framework Membrane with Enhanced Hydrogen Separation. *Journal of the American Chemical Society* **2020**, *142*, 6872−6877.
(876) Yang, Q.; Zhong, C. Molecular simulation of carbon dioxide/methane/hydrogen mixture adsorption in metal-organic frameworks. *J. Phys. Chem. B* **2006**, *110*, 17776−17783.
(877) Shang, Z.; Yang, Y.; Zhang, L.; Sun, H.; Zhong, J.; Zhang, K.; Yao, J. Hydrogen adsorption and diffusion behavior in kaolinite slit for underground hydrogen storage: A hybrid GCMC-MD simulation study. *Chemical Engineering Journal* **2024**, *487*, 150517.
(878) Zheng, R.; Germann, T. C.; Gross, M.; Mehana, M. Hydrogen Diffusion in Slit Pores: Role of Temperature, Pressure, Confinement, and Roughness. *Energy & Fuels* **2024**, *38*, 21642−21650.
(879) Oliver, M. C.; Zheng, R.; Huang, L.; Mehana, M. Molecular simulations of hydrogen diffusion in underground porous media: Implications for storage under varying pressure, confinement, and surface chemistry conditions. *International Journal of Hydrogen Energy* **2024**, *65*, 540−547.
(880) Ho, T. A.; Dang, S. T.; Dasgupta, N.; Choudhary, A.; Rai, C. S.; Wang, Y. Nuclear magnetic resonance and molecular simulation study of H_2 and CH_4 adsorption onto shale and sandstone for hydrogen geological storage. *International Journal of Hydrogen Energy* **2024**, *51*, 158−166.
(881) Zhang, M.; Yang, Y.; Pan, B.; Liu, Z.; Jin, Z.; Iglauer, S. Molecular simulation on H_2 adsorption in nanopores and effects of cushion gas: Implications for underground hydrogen storage in shale reservoirs. *Fuel* **2024**, *361*, 130621.
(882) Kahzadvand, K.; Ghasemi, M.; Yazaydin, A. O.; Babaei, M. Risk of H_2 Leakage into Caprock and the Role of Cushion Gas as a Barrier in H_2 Geo-Storage: A Molecular Simulation Study. *The Journal of Physical Chemistry C* **2024**, *128*, 16161−16171.
(883) Muther, T.; Dahagi, A. K. Monte-Carlo simulations on H_2 adsorption in kaolinite nanopore in the presence of CO_2 and CH_4 gases. *Fuel* **2024**, *365*, 131249.
(884) Muther, T.; Dahaghi, A. K. Calculation of hydrogen adsorption isotherms and Henry coefficients with mixed CO_2 and CH_4 gases on hydroxylated quartz surface: Implications to hydrogen geo-storage. *Journal of Energy Storage* **2024**, *87*, 111425.
(885) Chen, F.; Wang, S.; Dejam, M.; Nasrabadi, H. Molecular Simulation of Competitive Adsorption of Hydrogen and Methane: Analysis of Hydrogen Storage Feasibility in Depleted Shale Gas Reservoirs. *SPE Journal* **2024**, *29*, 3412−3422.
(886) Zhao, Y.; Quan, D.; Wang, C.; Wu, R.; Zhang, K.; Bi, J. Experiments and molecular simulations study on hydrogen adsorption and diffusion behavior of the inorganic mineral surfaces of shale. *International Journal of Hydrogen Energy* **2025**, *97*, 1302−1315.
(887) Xie, C.; Huang, J.; Li, Y.; Tian, S.; Zhao, H. Molecular Simulation on H_2 Huff-n-Puff in a Depleted Shale Gas Reservoir and Its Implications on Underground Hydrogen Storage. *Energy & Fuels* **2025**, *39*, 362−375.
(888) Babaei, S.; Coasne, B.; Ostadhassan, M. Adsorption-Induced Deformation in Microporous Kerogen by Hydrogen and Methane: Implications for Underground Hydrogen Storage. *Langmuir* **2025**, *41*, 6364−6375.

https://doi.org/10.1021/acs.chemrev.5c00617
Chem. Rev. 2025, 125, 11878−12029

(889) Zhang, H.; Diao, R.; Luo, X.; Xie, Q. Molecular Simulation of H_2/CH_4 Mixture Storage and Adsorption in Kaolinite Nanopores for Underground Hydrogen Storage. *ACS Omega* **2023**, *8*, 45801−45816.
(890) Zhang, M.; Yang, Y.; Pan, B.; Liu, Z.; Jin, Z.; Iglauer, S. Molecular simulation on H_2 adsorption in nanopores and effects of cushion gas: Implications for underground hydrogen storage in shale reservoirs. *Fuel* **2024**, *361*, 130621.
(891) Xie, C.; Huang, J.; Li, Y.; Tian, S.; Zhao, H. Molecular Simulation on H_2 Huff-n-Puff in a Depleted Shale Gas Reservoir and Its Implications on Underground Hydrogen Storage. *Energy & Fuels* **2025**, *39*, 362−375.
(892) Kumar, K. V.; Müller, E. A.; Rodriguez-Reinoso, F. Effect of pore morphology on the adsorption of methane/hydrogen mixtures on carbon micropores. *The Journal of Physical Chemistry C* **2012**, *116*, 11820−11829.
(893) Selim, M.; El-Nabarawy, T. A. A general relationship between adsorption of hydrocarbons and their polarizabilities on activated carbon. *Carbon* **1980**, *18*, 287−290.
(894) Ho, L. N.; Clauzier, S.; Schuurman, Y.; Farrusseng, D.; Coasne, B. Gas uptake in solvents confined in mesopores: Adsorption versus enhanced solubility. *The Journal of Physical Chemistry Letters* **2013**, *4*, 2274−2278.
(895) Bui, K. Q.; Bao Le, T. T.; Barbosa, G. D.; Papavassiliou, D. V.; Razavi, S.; Striolo, A. Molecular Density Fluctuations Control Solubility and Diffusion for Confined Aqueous Hydrogen. *The Journal of Physical Chemistry Letters* **2024**, *15*, 8114−8124.
(896) Zhang, H.; Luo, X.; Yang, D.; Liu, K.; Xie, Q.; Diao, R. Molecular simulation of H_2 loss by dissolution in caprock water-saturated nanopores under the nanoconfinement effect for underground hydrogen storage. *Energy & Fuels* **2023**, *37*, 19357−19368.
(897) Choudhary, A.; Ho, T. A. Roles of kaolinite-oil-gas molecular interactions in hydrogen storage within depleted reservoirs. *Chemical Engineering Journal* **2024**, *499*, 156452.
(898) Choudhary, A.; Ho, T. A. Confinement-induced clustering of H_2 and CO_2 gas molecules in hydrated nanopores. *Physical Chemistry Chemical Physics* **2024**, *26*, 10506−10514.
(899) Mashhadzadeh, A. H.; Faroughi, S. A. Atomistic simulation of dilute hydrogen in water-saturated kaolinite nanopores: Implications for underground hydrogen storage. *International Journal of Hydrogen Energy* **2025**, *109*, 1358−1371.
(900) Phan, A.; Cole, D. R.; Striolo, A. Aqueous methane in slit-shaped silica nanopores: high solubility and traces of hydrates. *The Journal of Physical Chemistry C* **2014**, *118*, 4860−4868.
(901) Ball, P. Water as an active constituent in cell biology. *Chemical reviews* **2008**, *108*, 74−108.
(902) Rego, N. B.; Patel, A. J. Understanding hydrophobic effects: Insights from water density fluctuations. *Annual Review of Condensed Matter Physics* **2022**, *13*, 303−324.
(903) Jamadagni, S. N.; Godawat, R.; Garde, S. Hydrophobicity of proteins and interfaces: Insights from density fluctuations. *Annual review of chemical and biomolecular engineering* **2011**, *2*, 147−171.
(904) Sakamaki, R.; Sum, A. K.; Narumi, T.; Ohmura, R.; Yasuoka, K. Thermodynamic properties of methane/water interface predicted by molecular dynamics simulations. *The Journal of Chemical Physics* **2011**, *134*, 144702.
(905) Wang, S.; Pan, S.; Tang, Y.; Mu, Y.; Gao, Y.; Wang, K. Hydrogen-methane transport in clay nanopores: Insights from molecular dynamics simulations. *International Journal of Hydrogen Energy* **2024**, *69*, 1450−1459.
(906) Liu, J.; Wang, S.; Javadpour, F.; Feng, Q.; Cha, L. Hydrogen diffusion in clay slit: Implications for the geological storage. *Energy & Fuels* **2022**, *36*, 7651−7660.
(907) A, H.; Yang, Z.; Chen, Y.; Hu, R.; Wood, C. D.; Kang, Q.; Chen, Y.-F. H_2 diffusion in cement nanopores and its implication for underground hydrogen storage. *Journal of Energy Storage* **2024**, *102*, 113926.
(908) Raza, A.; Alafnan, S.; Glatz, G.; Arif, M.; Mahmoud, M.; Rezk, M. G. Hydrogen diffusion in organic-rich porous media: implications for hydrogen geo-storage. *Energy & Fuels* **2022**, *36*, 15013−15022.
(909) Kim, C.; Devegowda, D.; Dang, S. T.; Mehana, M. Modeling the diffusivity of hydrogen and the associated cushion gas in depleted hydrocarbon reservoir caprocks. *International Journal of Hydrogen Energy* **2025**, *105*, 248−257.
(910) Ghasemi, M.; Omrani, S.; Mahmoodpour, S.; Zhou, T. Molecular dynamics simulation of hydrogen diffusion in water-saturated clay minerals; implications for Underground Hydrogen Storage (UHS). *International Journal of Hydrogen Energy* **2022**, *47*, 24871−24885.
(911) Mercier Franco, L. F.; Castier, M.; Economou, I. G. Diffusion in Homogeneous and in Inhomogeneous Media: A New Unified Approach. *Journal of Chemical Theory and Computation* **2016**, *12*, 5247−5255.
(912) Franco, L. F. M.; Castier, M.; Economou, I. G. Anisotropic parallel self-diffusion coefficients near the calcite surface: A molecular dynamics study. *The Journal of Chemical Physics* **2016**, *145*, 084702.
(913) Santos, M. S.; Franco, L. F. M.; Castier, M.; Economou, I. G. Molecular Dynamics Simulation of n-Alkanes and CO_2 Confined by Calcite Nanopores. *Energy & Fuels* **2018**, *32*, 1934−1941.
(914) Liu, P.; Harder, E.; Berne, B. On the calculation of diffusion coefficients in confined fluids and interfaces with an application to the liquid- vapor interface of water. *The Journal of Physical Chemistry B* **2004**, *108*, 6595−6602.
(915) Spera, M. B.; Braga, F. N.; Bartolomeu, R. A.; Economou, I. G.; Franco, L. F. Diffusion of fluids confined in carbonate minerals: A molecular dynamics simulation study for carbon dioxide and methane-ethane mixture within calcite. *Fuel* **2022**, *325*, 124800.
(916) Předota, M.; Bandura, A.; Cummings, P.; Kubicki, J.; Wesolowski, D.; Chialvo, A.; Machesky, M. L. Electric double layer at the rutile (110) surface. 1. Structure of surfaces and interfacial water from molecular dynamics by use of ab initio potentials. *The Journal of Physical Chemistry B* **2004**, *108*, 12049−12060.
(917) Botan, A.; Rotenberg, B.; Marry, V.; Turq, P.; Noetinger, B. Hydrodynamics in clay nanopores. *The Journal of Physical Chemistry C* **2011**, *115*, 16109−16115.
(918) Marry, V.; Rotenberg, B.; Turq, P. Structure and dynamics of water at a clay surface from molecular dynamics simulation. *Physical Chemistry Chemical Physics* **2008**, *10*, 4802−4813.
(919) Rotenberg, B.; Marry, V.; Vuilleumier, R.; Malikova, N.; Simon, C.; Turq, P. Water and ions in clays: Unraveling the interlayer/micropore exchange using molecular dynamics. *Geochimica et Cosmochimica Acta* **2007**, *71*, 5089−5101.
(920) Simonnin, P.; Noetinger, B.; Nieto-Draghi, C.; Marry, V.; Rotenberg, B. Diffusion under confinement: Hydrodynamic finite-size effects in simulation. *Journal of Chemical Theory and Computation* **2017**, *13*, 2881−2889.
(921) Ho, T. A.; Jove-Colon, C. F.; Wang, Y. Low hydrogen solubility in clay interlayers limits gas loss in hydrogen geological storage. *Sustainable Energy & Fuels* **2023**, *7*, 3232−3238.
(922) Muther, T.; Dahaghi, A. K. Molecular insights into hydrogen intercalation with carbon dioxide and methane in hydrated clay: Implications for hydrogen geo-storage seal integrity. *International Journal of Hydrogen Energy* **2024**, *110*, 386−400.
(923) Liu, J.; Zhang, T.; Sun, S. Molecular mechanisms of hydrogen leakage through caprock in moisture and residual gas conditions: A Molecular Dynamics-Monte Carlo study. *Physics of Fluids* **2024**, *36*, 022024.
(924) Michels, A.; De Graaff, W.; Ten Seldam, C. Virial coefficients of hydrogen and deuterium at temperatures between -175 °C and +150 °C. Conclusions from the second virial coefficient with regards to the intermolecular potential. *Physica* **1960**, *26*, 393−408.
(925) Chen, B.; Siepmann, J. I. Transferable potentials for phase equilibria. 3. Explicit-hydrogen description of normal alkanes. *The Journal of Physical Chemistry B* **1999**, *103*, 5370−5379.
(926) Zhu, A.; Zhang, X.; Liu, Q.; Zhang, Q. A fully flexible potential model for carbon dioxide. *Chinese Journal of Chemical Engineering* **2009**, *17*, 268−272.
(927) Cygan, R. T.; Romanov, V. N.; Myshakin, E. M. Molecular simulation of carbon dioxide capture by montmorillonite using an

https://doi.org/10.1021/acs.chemrev.5c00617
Chem. Rev. 2025, 125, 11878−12029

accurate and flexible force field. *The Journal of Physical Chemistry C* **2012**, *116*, 13079−13091.
(928) Ayappa, K.; Mishra, R. K. Freezing of fluids confined between mica surfaces. *The Journal of Physical Chemistry B* **2007**, *111*, 14299−14310.
(929) Chen, B.; Jiang, H.; Liu, X.; Hu, X. Molecular insight into water desalination across multilayer graphene oxide membranes. *ACS Applied Materials & Interfaces* **2017**, *9*, 22826−22836.
(930) Waldman, M.; Hagler, A. T. New combining rules for rare gas van der Waals parameters. *Journal of Computational Chemistry* **1993**, *14*, 1077−1084.
(931) Li, X.; Huo, T.; Wei, K.; Yan, Z.; Zhu, L.; Xue, Q. The feasibility of hydrogen storage in aquifers: A molecular dynamics simulation. *Fuel* **2024**, *367*, 131469.
(932) Nan, Y.; Li, W.; Jin, Z. Ion valency and concentration effect on the structural and thermodynamic properties of brine-decane interfaces with anionic surfactant (SDS). *The Journal of Physical Chemistry B* **2021**, *125*, 9610−9620.
(933) Williams, C. D.; Burton, N. A.; Travis, K. P.; Harding, J. H. The Development of a Classical Force Field To Determine the Selectivity of an Aqueous Fe^{3+}-EDA Complex for TcO_4^- and SO_4^{2-}. *Journal of Chemical Theory and Computation* **2014**, *10*, 3345−3353.
(934) Frankcombe, T. J.; Kroes, G.-J. Molecular dynamics simulations of type-sII hydrogen clathrate hydrate close to equilibrium conditions. *The Journal of Physical Chemistry C* **2007**, *111*, 13044−13052.
(935) Luis, D.; Romero-Ramirez, I.; González-Calderon, A.; Lopez-Lemus, J. The coexistence temperature of hydrogen clathrates: A molecular dynamics study. *The Journal of Chemical Physics* **2018**, *148*, 114503.
(936) Luis, D.; González-Calderon, A.; Lopez-Lemus, J. Effects of externally-applied static electric fields on hydrogen hydrates: a molecular dynamics study. *Molecular Simulation* **2023**, *49*, 1552−1560.
(937) Efimchenko, V.; Antonov, V.; Barkalov, O.; Klyamkin, S.; Tkacz, M. Two triple points in the H_2O-H_2 system. *High Pressure Research* **2009**, *29*, 250−253.
(938) Kang, D. W.; Lee, W.; Ahn, Y.-H.; Lee, J. W. Exploring tuning phenomena of THF-H_2 hydrates via molecular dynamics simulations. *Journal of Molecular Liquids* **2022**, *349*, 118490.
(939) Anderson, R.; Chapoy, A.; Tohidi, B. Phase relations and binary clathrate hydrate formation in the system H_2-THF-H_2O. *Langmuir* **2007**, *23*, 3440−3444.
(940) Hu, W.; Tian, X.; Chen, C.; Cheng, C.; Zhu, S.; Zhang, J.; Qi, T.; Jin, T.; Wu, X. Molecular dynamic simulation of H_2-CH_4 binary hydrate growth induced by methane hydrate. *Fuel* **2024**, *360*, 130554.
(941) Ghaani, M. R.; English, N. J. Hydrogen-/propane-hydrate decomposition: thermodynamic and kinetic analysis. *Molecular Physics* **2019**, *117*, 2434−2442.
(942) Ghaani, M. R.; Takeya, S.; English, N. J. Hydrogen storage in propane-hydrate: Theoretical and experimental study. *Applied Sciences* **2020**, *10*, 8962.
(943) Wang, P.; Li, K.; Yang, J.; Zhu, J.; Zhao, Y.; Teng, Y. Experimental and theoretical study on dissociation thermodynamics and kinetics of hydrogen-propane hydrate. *Chemical Engineering Journal* **2021**, *426*, 131279.
(944) Gorman, P. D.; English, N. J.; MacElroy, J. Dynamical and energetic properties of hydrogen and hydrogen-tetrahydrofuran clathrate hydrates. *Physical Chemistry Chemical Physics* **2011**, *13*, 19780−19787.
(945) Yagasaki, T.; Himoto, K.; Nakamura, T.; Matsumoto, M.; Tanaka, H. Structure, dynamics and thermodynamic stability of high-pressure ices and clathrate hydrates. *Molecular Simulation* **2015**, *41*, 868−873.
(946) English, N. J.; Gorman, P. D.; MacElroy, J. Mechanisms for thermal conduction in hydrogen hydrate. *The Journal of Chemical Physics* **2012**, *136*, 044501.
(947) Zhao, W.; Wang, L.; Bai, J.; Francisco, J. S.; Zeng, X. C. Spontaneous formation of one-dimensional hydrogen gas hydrate in carbon nanotubes. *Journal of the American Chemical Society* **2014**, *136*, 10661−10668.
(948) Alavi, S.; Ripmeester, J.; Klug, D. Molecular-dynamics simulations of binary structure II hydrogen and tetrahydrofurane clathrates. *The Journal of Chemical Physics* **2006**, *124*, 014704.
(949) Alavi, S.; Ripmeester, J.; Klug, D. Molecular dynamics simulations of binary structure H hydrogen and methyl-tert-butylether clathrate hydrates. *The Journal of Chemical Physics* **2006**, *124*, 204707.
(950) Daschbach, J. L.; Chang, T.-M.; Corrales, L. R.; Dang, L. X.; McGrail, P. Molecular mechanisms of hydrogen-loaded β-hydroquinone clathrate. *The Journal of Physical Chemistry B* **2006**, *110*, 17291−17295.
(951) Wang, Y.; Yin, K.; Lang, X.; Fan, S.; Li, G.; Yu, C.; Wang, S. Hydrogen storage in sH binary hydrate: Insights from molecular dynamics simulation. *International Journal of Hydrogen Energy* **2021**, *46*, 15748−15760.
(952) Lokshin, K. A.; Zhao, Y.; He, D.; Mao, W. L.; Mao, H.-K.; Hemley, R. J.; Lobanov, M. V.; Greenblatt, M. Structure and dynamics of hydrogen molecules in the novel clathrate hydrate by high pressure neutron diffraction. *Physical Review Letters* **2004**, *93*, 125503.
(953) Katsumasa, K.; Koga, K.; Tanaka, H. On the thermodynamic stability of hydrogen clathrate hydrates. *The Journal of Chemical Physics* **2007**, *127*, 044509.
(954) Chun, D.-H.; Lee, T.-Y. Molecular simulation of cage occupancy and selectivity of binary THF-H_2 sII hydrate. *Molecular Simulation* **2008**, *34*, 837−844.
(955) Nakayama, T.; Koga, K.; Tanaka, H. Augmented stability of hydrogen clathrate hydrates by weakly polar molecules. *The Journal of Chemical Physics* **2009**, *131*, 214506.
(956) Nakayama, T.; Matsumoto, M.; Tanaka, H. On the thermodynamic stability of hydrogen hydrates in the presence of promoter molecules. *AIP Conference Proceedings*. 2013; pp 46−52.
(957) Koh, D.-Y.; Kang, H.; Jeon, J.; Ahn, Y.-H.; Park, Y.; Kim, H.; Lee, H. Tuning cage dimension in clathrate hydrates for hydrogen multiple occupancy. *The Journal of Physical Chemistry C* **2014**, *118*, 3324−3330.
(958) Hakim, L.; Koga, K.; Tanaka, H. Phase behavior of different forms of ice filled with hydrogen molecules. *Physical Review Letters* **2010**, *104*, 115701.
(959) Hakim, L.; Koga, K.; Tanaka, H. Thermodynamic stability of hydrogen hydrates of ice Ic and II structures. *Physical Review B* **2010**, *82*, 144105.
(960) Duarte, A. R. C.; Shariati, A.; Rovetto, L. J.; Peters, C. J. Water cavities of sH clathrate hydrate stabilized by molecular hydrogen: Phase equilibrium measurements. *The Journal of Physical Chemistry B* **2008**, *112*, 1888−1889.
(961) Grim, R. G.; Kerkar, P. B.; Shebowich, M.; Arias, M.; Sloan, E. D.; Koh, C. A.; Sum, A. K. Synthesis and characterization of sI clathrate hydrates containing hydrogen. *The Journal of Physical Chemistry C* **2012**, *116*, 18557−18563.
(962) Papadimitriou, N.; Tsimpanogiannis, I.; Stubos, A. Computational approach to study hydrogen storage in clathrate hydrates. *Colloids and Surfaces A: Physicochemical and Engineering Aspects* **2010**, *357*, 67−73.
(963) Strobel, T. A.; Taylor, C. J.; Hester, K. C.; Dec, S. F.; Koh, C. A.; Miller, K. T.; Sloan, E. Molecular hydrogen storage in binary THF-H_2 clathrate hydrates. *The Journal of Physical Chemistry B* **2006**, *110*, 17121−17125.
(964) Ogata, K.; Hashimoto, S.; Sugahara, T.; Moritoki, M.; Sato, H.; Ohgaki, K. Storage capacity of hydrogen in tetrahydrofuran hydrate. *Chemical Engineering Science* **2008**, *63*, 5714−5718.
(965) Mulder, F. M.; Wagemaker, M.; Van Eijck, L.; Kearley, G. J. Hydrogen in porous tetrahydrofuran clathrate hydrate. *ChemPhysChem* **2008**, *9*, 1331−1337.
(966) Papadimitriou, N.; Tsimpanogiannis, I.; Stubos, A. Gas content of binary clathrate hydrates with promoters. *The Journal of Chemical Physics* **2009**, *131*, 044102.

https://doi.org/10.1021/acs.chemrev.5c00617
Chem. Rev. 2025, 125, 11878−12029

(967) Hester, K. C.; Strobel, T. A.; Sloan, E. D.; Koh, C. A.; Huq, A.; Schultz, A. J. Molecular hydrogen occupancy in binary THF-H_2 clathrate hydrates by high resolution neutron diffraction. *The Journal of Physical Chemistry B* **2006**, *110*, 14024−14027.
(968) Nagai, Y.; Yoshioka, H.; Ota, M.; Sato, Y.; Inomata, H.; Smith, R. L., Jr; Peters, C. J. Binary hydrogen-tetrahydrofuran clathrate hydrate formation kinetics and models. *AIChE Journal* **2008**, *54*, 3007−3016.
(969) Yoshioka, H.; Ota, M.; Sato, Y.; Watanabe, M.; Inomata, H.; Smith, R. L., Jr; Peters, C. J. Decomposition kinetics and recycle of binary hydrogen-tetrahydrofuran clathrate hydrate. *AIChE Journal* **2011**, *57*, 265−272.
(970) Ulivi, L.; Celli, M.; Giannasi, A.; Ramirez-Cuesta, A.; Bull, D.; Zoppi, M. Quantum rattling of molecular hydrogen in clathrate hydrate nanocavities. *Physical Review B—Condensed Matter and Materials Physics* **2007**, *76*, 161401.
(971) Talyzin, A. Feasibility of H_2-THF-H_2O clathrate hydrates for hydrogen storage applications. *International Journal of Hydrogen Energy* **2008**, *33*, 111−115.
(972) Sugahara, T.; Haag, J. C.; Prasad, P. S.; Warntjes, A. A.; Sloan, E. D.; Sum, A. K.; Koh, C. A. Increasing hydrogen storage capacity using tetrahydrofuran. *Journal of the American Chemical Society* **2009**, *131*, 14616−14617.
(973) Sugahara, T.; Haag, J. C.; Warntjes, A. A.; Prasad, P. S.; Sloan, E. D.; Koh, C. A.; Sum, A. K. Large-cage occupancies of hydrogen in binary clathrate hydrates dependent on pressures and guest concentrations. *The Journal of Physical Chemistry C* **2010**, *114*, 15218−15222.
(974) Kawamura, T.; Takeya, S.; Ohtake, M.; Yamamoto, Y. Enclathration of hydrogen by organic-compound clathrate hydrates. *Chemical Engineering Science* **2011**, *66*, 2417−2420.
(975) Tsimpanogiannis, I. N.; Economou, I. G.; Stubos, A. K. A Practical Methodology to Estimate the H_2 Storage Capacity of Pure and Binary Hydrates Based on Monte Carlo Simulations. *Journal of Chemical & Engineering Data* **2020**, *65*, 1289−1299.
(976) Luo, Y.; Liu, A.; Guo, X.; Sun, Q.; Yang, L. Experiment on the continuous recovery of H_2 from hydrogenation plant off-gas via hydrate formation in tetra-n-butyl ammonium bromide solution. *International Journal of Hydrogen Energy* **2015**, *40*, 16248−16255.
(977) Li, Q.; Fan, S.; Chen, Q.; Yang, G.; Chen, Y.; Li, L.; Li, G. Experimental and process simulation of hydrate-based CO_2 capture from biogas. *Journal of Natural Gas Science and Engineering* **2019**, *72*, 103008.
(978) Misawa, T.; Ishikawa, T.; Takeya, S.; Alavi, S.; Ohmura, R. Continuous hydrate-based CO_2 separation from H_2 + CO_2 gas mixture using cyclopentane as co-guest. *Journal of Industrial and Engineering Chemistry* **2023**, *121*, 228−234.
(979) Lee, Y.; Lee, S.; Seo, D.; Moon, S.; Ahn, Y.-H.; Park, Y. Highly efficient separation and equilibrium recovery of H_2/CO_2 in hydrate-based pre-combustion CO_2 capture. *Chemical Engineering Journal* **2024**, *481*, 148709.
(980) Glavatskiy, K.; Vlugt, T. J. H.; Kjelstrup, S. Toward a possibility to exchange CO_2 and CH_4 in sI clathrate hydrates. *The Journal of Physical Chemistry B* **2012**, *116*, 3745−3753.
(981) Papadimitriou, N. I.; Tsimpanogiannis, I. N.; Economou, I. G.; Stubos, A. K. Monte Carlo simulations of the separation of a binary gas mixture (CH_4 + CO_2) using hydrates. *Physical Chemistry Chemical Physics* **2018**, *20*, 28026−28038.
(982) Atamas, A.; Koudriachova, M. V.; de Leeuw, S. W.; Sweatman, M. B. Monte Carlo calculations of the free energy of ice-like structures using the self-referential method. *Molecular Simulation* **2011**, *37*, 284−292.
(983) Atamas, A. A.; Cuppen, H. M.; Koudriachova, M. V.; de Leeuw, S. W. Monte Carlo calculations of the free energy of binary sII hydrogen clathrate hydrates for identifying efficient promoter molecules. *The Journal of Physical Chemistry B* **2013**, *117*, 1155−1165.
(984) Atamas, A. A.; Koudriachova, M. V.; de Leeuw, S. W.; Cuppen, H. M. Free energy calculations for identifying efficient promoter molecules of binary sH hydrogen clathrates. *The Journal of Physical Chemistry C* **2014**, *118*, 22211−22220.
(985) Frankcombe, T. J.; Kroes, G.-J. A new method for screening potential sII and sH hydrogen clathrate hydrate promoters with model potentials. *Physical Chemistry Chemical Physics* **2011**, *13*, 13410−13420.
(986) Atamas, A. A.; de Leeuw, S. W.; Cuppen, H. M. A method distinguishing between guest molecules that can form sI, sII, and sH hydrogen clathrates. *RSC Advances* **2015**, *5*, 26376−26382.
(987) Iwai, Y.; Aokawa, R. Stability analysis for binary sII hydrogen-promoter hydrates by molecular dynamics simulation. *Molecular Simulation* **2015**, *41*, 735−740.
(988) Davidson, D. In *Water in Crystalline Hydrates Aqueous Solutions of Simple Nonelectrolytes*; Franks, F., Ed.; Plenum: New York, 1973; pp 115−234.
(989) Okuchi, T.; Moudrakovski, I. L.; Ripmeester, J. Efficient storage of hydrogen fuel into leaky cages of clathrate hydrate. *Applied Physics Letters* **2007**, *91*, 171903.
(990) Senadheera, L.; Conradi, M. S. Rotation and diffusion of H_2 in hydrogen-ice clathrate by 1H NMR. *The Journal of Physical Chemistry B* **2007**, *111*, 12097−12102.
(991) Senadheera, L.; Conradi, M. S. Hydrogen NMR of H_2-TDF-D_2O Clathrate. *The Journal of Physical Chemistry B* **2008**, *112*, 13695−13700.
(992) Choi, Y. N.; Park, J. S.; Strässle, T.; Yeon, S.-H.; Park, Y.; Lee, H. Dynamics of hydrogen molecules in the channels of binary THF-H_2 clathrate hydrate and its physicochemical significance on hydrogen storage. *International Journal of Hydrogen Energy* **2010**, *35*, 13068−13072.
(993) Strobel, T. A.; Sloan, E. D.; Koh, C. A. Raman spectroscopic studies of hydrogen clathrate hydrates. *The Journal of Chemical Physics* **2009**, *130*, 014506.
(994) Russina, M.; Kemner, E.; Mezei, F. Intra-cage dynamics of molecular hydrogen confined in cages of two different dimensions of clathrate hydrates. *Scientific Reports* **2016**, *6*, 27417.
(995) Pefoute, E.; Kemner, E.; Soetens, J.; Russina, M.; Desmedt, A. Diffusive motions of molecular hydrogen confined in THF clathrate hydrate. *The Journal of Physical Chemistry C* **2012**, *116*, 16823−16829.
(996) Cao, H.; English, N. J.; MacElroy, J. Diffusive hydrogen inter-cage migration in hydrogen and hydrogen-tetrahydrofuran clathrate hydrates. *The Journal of Chemical Physics* **2013**, *138*, 094507.
(997) Gorman, P. D.; English, N. J.; MacElroy, J. Dynamical cage behaviour and hydrogen migration in hydrogen and hydrogen-tetrahydrofuran clathrate hydrates. *The Journal of Chemical Physics* **2012**, *136*, 044506.
(998) Iwai, Y.; Hirata, M. Molecular dynamics simulation of diffusion of hydrogen in binary hydrogen-tetrahydrofuran hydrate. *Molecular Simulation* **2012**, *38*, 333−340.
(999) Geng, C.-Y.; Han, Q.-Z.; Wen, H.; Dai, Z.-Y.; Song, C.-H. Molecular dynamics simulation on the decomposition of type SII hydrogen hydrate and the performance of tetrahydrofuran as a stabiliser. *Molecular Simulation* **2010**, *36*, 474−483.
(1000) Hasegawa, T.; Brumby, P. E.; Yasuoka, K.; Sum, A. K. Mechanism for H_2 diffusion in sII hydrates by molecular dynamics simulations. *The Journal of Chemical Physics* **2020**, *153*, 054706.
(1001) Papadimitriou, N. I.; Tsimpanogiannis, I. N.; Stubos, A. K.; Martin, A.; Rovetto, L. J.; Peters, C. J. Unexpected behavior of helium as guest gas in sII binary hydrates. *The Journal of Physical Chemistry Letters* **2010**, *1*, 1014−1017.
(1002) Papadimitriou, N. I.; Tsimpanogiannis, I. N.; Stubos, A. K.; Martín, A.; Rovetto, L. J.; Florusse, L. J.; Peters, C. J. Experimental and computational investigation of the sII binary He-THF hydrate. *The Journal of Physical Chemistry B* **2011**, *115*, 1411−1415.
(1003) Amano, S.; Tsuda, T.; Hashimoto, S.; Sugahara, T.; Ohgaki, K. Competitive cage occupancy of hydrogen and argon in structure-II hydrates. *Fluid Phase Equilibria* **2010**, *298*, 113−116.
(1004) Waage, M. H.; Trinh, T. T.; van Erp, T. S. Diffusion of gas mixtures in the sI hydrate structure. *The Journal of Chemical Physics* **2018**, *148*, 214701.

https://doi.org/10.1021/acs.chemrev.5c00617
Chem. Rev. 2025, 125, 11878−12029

(1005) Harada, A.; Arman, Y.; Miura, S. Molecular dynamics study on fast diffusion of hydrogen molecules in filled ice II. *Journal of Molecular Liquids* **2019**, *292*, 111316.
(1006) Arman, Y.; Nugroho, B. Molecular dynamics study of hydrogen diffusion in the C2 Hydrogen Hydrates. *Journal of Physics: Conference Series* **2021**, *1816*, 012084.
(1007) Smirnov, G. S.; Stegailov, V. V. Anomalous diffusion of guest molecules in hydrogen gas hydrates. *High Temperature* **2015**, *53*, 829−836.
(1008) Alavi, S.; Ripmeester, J. Hydrogen-gas migration through clathrate hydrate cages. *Angewandte Chemie - International Edition* **2007**, *46*, 6102.
(1009) Parrinello, M.; Rahman, A. Study of an F center in molten KCl. *The Journal of Chemical Physics* **1984**, *80*, 860−867.
(1010) Burnham, C. J.; English, N. J. Free-energy calculations of the intercage hopping barriers of hydrogen molecules in clathrate hydrates. *The Journal of Physical Chemistry C* **2016**, *120*, 16561−16567.
(1011) Burnham, C. J.; Futera, Z.; English, N. J. Quantum and classical inter-cage hopping of hydrogen molecules in clathrate hydrate: Temperature and cage-occupation effects. *Physical Chemistry Chemical Physics* **2017**, *19*, 717−728.
(1012) Burnham, C. J.; Futera, Z.; English, N. J. Study of hydrogen-molecule guests in type II clathrate hydrates using a force-matched potential model parameterised from ab initio molecular dynamics. *The Journal of Chemical Physics* **2018**, *148*, 102323.
(1013) English, N. J.; Burnham, C. J. Intra-cage structure, vibrations and tetrahedral-site hopping of H_2 and D_2 in doubly-occupied $5^{12}6^4$ cages in sII clathrate hydrates from path-integral and classical molecular dynamics. *Applied Sciences* **2021**, *11*, 54.
(1014) Krishnan, Y.; Ghaani, M. R.; English, N. J. Hydrogen and deuterium molecular escape from clathrate hydrates:"Leaky" micro-second-molecular-dynamics predictions. *The Journal of Physical Chemistry C* **2021**, *125*, 8430−8439.
(1015) Krishnan, Y.; Rosingana, P. G.; Ghaani, M. R.; English, N. J. Controlling hydrogen release from remaining-intact Clathrate hydrates by electromagnetic fields: molecular engineering via microsecond non-equilibrium molecular dynamics. *RSC Advances* **2022**, *12*, 4370−4376.
(1016) Krishnan, Y.; Ghaani, M. R.; Desmedt, A.; English, N. J. Hydrogen inter-cage hopping and cage occupancies inside hydrogen hydrate: Molecular-dynamics analysis. *Applied Sciences* **2021**, *11*, 282.
(1017) Hosseini, M.; Fahimpour, J.; Ali, M.; Keshavarz, A.; Iglauer, S. H_2-brine interfacial tension as a function of salinity, temperature, and pressure; implications for hydrogen geo-storage. *Journal of Petroleum Science and Engineering* **2022**, *213*, 110441.
(1018) Omrani, S.; Ghasemi, M.; Singh, M.; Mahmoodpour, S.; Zhou, T.; Babaei, M.; Niasar, V. Interfacial Tension-Temperature-Pressure-Salinity Relationship for the Hydrogen-Brine System under Reservoir Conditions: Integration of Molecular Dynamics and Machine Learning. *Langmuir* **2023**, *39*, 12680−12691.
(1019) Xie, M.; Zhang, M.; Jin, Z. Machine Learning-Based Interfacial Tension Equations for (H_2 + CO_2)-Water/Brine Systems over a Wide Range of Temperature and Pressure. *Langmuir* **2024**, *40*, 5369−5377.
(1020) Doan, Q. T.; Keshavarz, A.; Miranda, C. R.; Behrenbruch, P.; Iglauer, S. Molecular dynamics simulation of interfacial tension of the CO_2-CH_4-water and H_2-CH_4-water systems at the temperature of 300 K and 323 K and pressure up to 70 MPa. *Journal of Energy Storage* **2023**, *66*, 107470.
(1021) Doan, Q. T.; Keshavarz, A.; Miranda, C. R.; Behrenbruch, P.; Iglauer, S. A prediction of interfacial tension by using molecular dynamics simulation: A study on effects of cushion gas (CO_2, N_2 and CH_4) for Underground Hydrogen Storage. *Int. J. Hydrogen Energy* **2024**, *50*, 1607−1615.
(1022) Adam, A. M.; Bahamon, D.; Al Kobaisi, M.; Vega, L. F. Molecular dynamics simulations of the interfacial tension and the solubility of brine/H_2/CO_2 systems: Implications for underground hydrogen storage. *International Journal of Hydrogen Energy* **2024**, *78*, 1344−1354.
(1023) Blokhuis, E. M.; Bedeaux, D.; Holcomb, C. D.; Zollweg, J. A. Tail corrections to the surface tension of a Lennard-Jones liquid-vapour interface. *Mol. Phys.* **1995**, *85*, 665−669.
(1024) Essmann, U.; Perera, L.; Berkowitz, M. L.; Darden, T.; Lee, H.; Pedersen, L. G. A smooth particle mesh Ewald method. *J. Comput. Phys.* **1995**, *103*, 8577−8593.
(1025) Hockney, R.; Eastwood, J. *Computer Simulation Using Particles*; CRC Press: New York, 1988.
(1026) Isele-Holder, R. E.; Mitchell, W.; Ismail, A. E. Development and application of a particle-particle particle-mesh Ewald method for dispersion interactions. *J. Chem. Phys.* **2012**, *137*, 174107.
(1027) Goujon, F.; Ghoufi, A.; Malfreyt, P.; Tildesley, D. J. Controlling the long-range corrections in atomistic Monte Carlo simulations of two-phase systems. *J. Chem. Theory Comput.* **2015**, *11*, 4573−4585.
(1028) Sega, M.; Dellago, C. Long-range dispersion effects on the water/vapor interface simulated using the most common models. *J. Phys. Chem. B* **2017**, *121*, 3798−3803.
(1029) Wennberg, C. L.; Murtola, T.; Páll, S.; Abraham, M. J.; Hess, B.; Lindahl, E. Direct-space corrections enable fast and accurate Lorentz-Berthelot combination rule Lennard-Jones lattice summation. *J. Chem. Theory Comput.* **2015**, *11*, 5737−5746.
(1030) Macedonia, M. D.; Maginn, E. J. A biased grand canonical Monte Carlo method for simulating adsorption using all-atom and branched united atom models. *Mol. Phys.* **1999**, *96*, 1375−1390.
(1031) Siperstein, F.; Myers, A.; Talu, O. Long range corrections for computer simulations of adsorption. *Mol. Phys.* **2002**, *100*, 2025−2030.
(1032) Jablonka, K. M.; Ongari, D.; Smit, B. Applicability of tail corrections in the molecular simulations of porous materials. *J. Chem. Theory Comput.* **2019**, *15*, 5635−5641.
(1033) Wang, X.; Ramírez-Hinestrosa, S.; Dobnikar, J.; Frenkel, D. The Lennard-Jones potential: when (not) to use it. *Physical Chemistry Chemical Physics* **2020**, *22*, 10624−10633.
(1034) Zeron, I. M.; Abascal, J. L. F.; Vega, C. A force field of Li^+, Na^+, K^+, Mg^{2+}, Ca^{2+}, Cl^-, and SO_4^{2-} in aqueous solution based on the TIP4P/2005 water model and scaled charges for the ions. *J. Chem. Phys.* **2019**, *151*, 134504.
(1035) Loche, P.; Steinbrunner, P.; Friedowitz, S.; Netz, R. R.; Bonthuis, D. J. Transferable Ion Force Fields in Water from a Simultaneous Optimization of Ion Solvation and Ion-Ion Interaction. *J. Phys. Chem. B* **2021**, *125*, 8581−8587.
(1036) Vega, C.; Miguel, E. D. Surface tension of the most popular models of water by using the test-area simulation method. *J. Chem. Phys.* **2007**, *126*, 154707.
(1037) Papavasileiou, K. D.; Moultos, O. A.; Economou, I. G. Predictions of water/oil interfacial tension at elevated temperatures and pressures: A molecular dynamics simulation study with biomolecular force fields. *Fluid Phase Equilib.* **2018**, *476*, 30−38.
(1038) Salehi, H. S.; Moultos, O. A.; Vlugt, T. J. H. Interfacial Properties of Hydrophobic Deep Eutectic Solvents with Water. *J. Phys. Chem. B* **2021**, *125*, 12303−12314.
(1039) Isele-Holder, R. E.; Mitchell, W.; Hammond, J. R.; Kohlmeyer, A.; Ismail, A. E. Reconsidering Dispersion Potentials: Reduced Cutoffs in Mesh-Based Ewald Solvers Can Be Faster Than Truncation. *Journal of Chemical Theory and Computation* **2013**, *9*, 5412−5420.
(1040) Isele-Holder, R. E.; Mitchell, W.; Ismail, A. E. Development and application of a particle-particle particle-mesh Ewald method for dispersion interactions. *The Journal of Chemical Physics* **2012**, *137*, 174107.
(1041) Chow, Y. F.; Maitland, G. C.; Trusler, J. M. Interfacial tensions of (H_2O + H_2) and (H_2O + CO_2 + H_2) systems at temperatures of (298-448) K and pressures up to 45 MPa. *Fluid Phase Equilibria* **2018**, *475*, 37−44.

https://doi.org/10.1021/acs.chemrev.5c00617
Chem. Rev. 2025, 125, 11878−12029

(1042) Abascal, J. L. F.; Vega, C. A general purpose model for the condensed phases of water: TIP4P/2005. *J. Comput. Phys.* **2005**, *123*, 234505.
(1043) Dang, L. X. Mechanism and thermodynamics of ion selectivity in aqueous solutions of 18-crown-6 ether: a molecular dynamics study. *Journal of the American Chemical Society* **1995**, *117*, 6954−6960.
(1044) Aqvist, J. Ion-water interaction potentials derived from free energy perturbation simulations. *J. Phys. Chem.* **1990**, *94*, 8021−8024.
(1045) Potoff, J. J.; Siepmann, J. I. Vapor-liquid equilibria of mixtures containing alkanes, carbon dioxide, and nitrogen. *AIChE J.* **2001**, *47*, 1676−1682.
(1046) Chen, C.; Dong, B.; Zhang, N.; Li, W.; Song, Y. Pressure and Temperature Dependence of Contact Angles for CO_2/Water/Silica Systems Predicted by Molecular Dynamics Simulations. *Energy & Fuels* **2016**, *30*, 5027−5034.
(1047) Zhuravlev, L. The surface chemistry of amorphous silica. Zhuravlev model. *Colloids and Surfaces A: Physicochemical and Engineering Aspects* **2000**, *173*, 1−38.
(1048) Ali, A.; Cole, D. R.; Striolo, A. Cushion gas effects on clay-hydrogen-brine wettability at conditions relevant to underground gas storage. *International Journal of Hydrogen Energy* **2024**, *58*, 668−677.
(1049) Alshammari, S.; Abdel-Azeim, S.; Al-Yaseri, A.; Qasim, A. The Influence of CH_4 and CO_2 on the Interfacial Tension of H_2-Brine, Water-H_2-Rock Wettability, and Their Implications on Geological Hydrogen Storage. *Energy Fuels* **2024**, *38*, 15834−15847.
(1050) Barbosa, G. D.; Bui, K. Q.; Papavassiliou, D. V.; Razavi, S.; Striolo, A. Wettability of Chemically Heterogeneous Clay Surfaces: Correlation between Surface Defects and Contact Angles as Revealed by Machine Learning. *ACS Appl. Mater. Interfaces* **2025**, *17*, 21916−21928.
(1051) Fatah, A.; Al-Yaseri, A.; Alshammari, S.; Al-Qasim, A. S. Gas Injection Dynamics and Hydrogen Storage in Carbonate Reservoirs: Core-Flooding and Molecular Simulation Study. *Energy Fuels* **2024**, *38*, 20951−20966.
(1052) Ghafari, M. A.; Ghasemi, M.; Niasar, V.; Babaei, M. Wetting Preference of Silica Surfaces in the Context of Underground Hydrogen Storage: A Molecular Dynamics Perspective. *Langmuir* **2024**, *40*, 20559−20575.
(1053) Phan, A.; Barker, V.; Hassanpouryouzband, A.; Ho, T. A. Simulation insights into wetting properties of hydrogen-brine-clay for hydrogen geo-storage. *Journal of Energy Storage* **2025**, *112*, 115477.
(1054) Yao, X.; Narayanan Nair, A. K.; Che Ruslan, M. F. A.; Sun, S.; Yan, B. Interfacial properties of the hydrogen+brine system in the presence of hydrophilic silica. *International Journal of Hydrogen Energy* **2025**, *101*, 741−749.
(1055) Kwok, D. Y.; Neumann, A. W. Contact angle measurement and contact angle interpretation. *Advances in colloid and interface science* **1999**, *81*, 167−249.
(1056) Yu, X.; Rao, S.; Zhang, L.; Li, Y.; Liu, C.; Yang, M.; Chen, Z. In-situ wettability alteration of organic-rich shale caprock in hydrogen with cushion gas: Implications for hydrogen geo-storage. *International Journal of Hydrogen Energy* **2025**, *103*, 75−86.
(1057) Zhang, S.; Tan, D.; Zhu, H.; Zhang, W. Molecular dynamic simulations on the hydrogen wettability of caprock: Considering effects of mineralogy, pressure, temperature and salinity. *International Journal of Hydrogen Energy* **2025**, *109*, 367−382.
(1058) Huang, F.; Yang, Y.; Kang, S.; Wang, K.; Zhang, M. Microscopic insights into water wetting behaviors and physical origin on α-quartz exposed to varying underground gas species. *Chemical Engineering Journal* **2024**, *498*, 155128.
(1059) Chandrasekhar, J.; Spellmeyer, D. C.; Jorgensen, W. L. Energy component analysis for dilute aqueous solutions of lithium (1+), sodium (1+), fluoride (1-), and chloride (1-) ions. *J. Am. Chem. Soc.* **1984**, *106*, 903−910.
(1060) Alavi, S.; Ripmeester, J.; Klug, D. Molecular-dynamics study of structure II hydrogen clathrates. *J. Chem. Phys.* **2005**, *123*, 024507.
(1061) Izadi, S.; Anandakrishnan, R.; Onufriev, A. V. Building water models: A different approach. *J. Phys. Chem. Lett.* **2014**, *5*, 3863−3871.
(1062) Yagasaki, T.; Matsumoto, M.; Tanaka, H. Lennard-Jones parameters determined to reproduce the solubility of NaCl and KCl in SPC/E, TIP3P, and TIP4P/2005 water. *Journal of Chemical Theory and Computation* **2020**, *16*, 2460−2473.
(1063) Emami, F. S.; Puddu, V.; Berry, R. J.; Varshney, V.; Patwardhan, S. V.; Perry, C. C.; Heinz, H. Force field and a surface model database for silica to simulate interfacial properties in atomic resolution. *Chemistry of Materials* **2014**, *26*, 2647−2658.
(1064) Xiao, S.; Edwards, S. A.; Gräter, F. A new transferable forcefield for simulating the mechanics of $CaCO_3$ crystals. *J. Phys. Chem. C* **2011**, *115*, 20067−20075.
(1065) Kaminski, G.; Duffy, E. M.; Matsui, T.; Jorgensen, W. L. Free energies of hydration and pure liquid properties of hydrocarbons from the OPLS all-atom model. *The Journal of Physical Chemistry* **1994**, *98*, 13077−13082.
(1066) Cannon, W. R.; Pettitt, B. M.; McCammon, J. A. Sulfate anion in water: model structural, thermodynamic, and dynamic properties. *The Journal of Physical Chemistry* **1994**, *98*, 6225−6230.
(1067) Senanayake, H. S.; Wimalasiri, P. N.; Godahewa, S. M.; Thompson, W. H.; Greathouse, J. A. Ab initio-derived force field for amorphous silica interfaces for use in molecular dynamics simulations. *The Journal of Physical Chemistry C* **2023**, *127*, 16567−16578.
(1068) Van Beest, B.; Kramer, G. J.; Van Santen, R. Force fields for silicas and aluminophosphates based on ab initio calculations. *Physical review letters* **1990**, *64*, 1955.
(1069) Dauber-Osguthorpe, P.; Roberts, V. A.; Osguthorpe, D. J.; Wolff, J.; Genest, M.; Hagler, A. T. Structure and energetics of ligand binding to proteins: Escherichia coli dihydrofolate reductase-trimethoprim, a drug-receptor system. *Proteins: Structure, Function, and Bioinformatics* **1988**, *4*, 31−47.
(1070) Pfeil, L. B. The effect of occluded hydrogen on the tensile strength of iron. *Proceedings of the Royal Society of London. Series A, Containing Papers of a Mathematical and Physical Character* **1926**, *112*, 182−195.
(1071) Beachem, C. A new model for hydrogen-assisted cracking (hydrogen "embrittlement"). *Metallurgical Transactions* **1972**, *3*, 441−455.
(1072) Nagumo, M.; Nakamura, M.; Takai, K. Hydrogen thermal desorption relevant to delayed-fracture susceptibility of high-strength steels. *Metallurgical and Materials Transactions A* **2001**, *32*, 339−347.
(1073) Yang, X.; Oyeniyi, W. O. Kinetic Monte Carlo simulation of hydrogen diffusion in tungsten. *Fusion Engineering and Design* **2017**, *114*, 113−117.
(1074) Zhu, D.; Oda, T. Trap effect of vacancy on hydrogen diffusivity in bcc-Fe. *Journal of Nuclear Materials* **2016**, *469*, 237−243.
(1075) Wang, L.-F.; Shu, X.; Lin, D.-Y.; Lu, G.-H.; Song, H.-F. Molecular dynamics studies of hydrogen diffusion in tungsten at elevated temperature: Concentration dependence and defect effects. *International Journal of Hydrogen Energy* **2020**, *45*, 822−834.
(1076) Zhou, X.-Y.; Zhu, J.-H.; Wu, H.-H. Molecular dynamics studies of the grain-size dependent hydrogen diffusion coefficient of nanograined Fe. *International Journal of Hydrogen Energy* **2021**, *46*, 5842−5851.
(1077) Sagar, S.; Sluiter, M. H.; Dey, P. First - Principles study of hydrogen - Carbide interaction in bcc Fe. *International Journal of Hydrogen Energy* **2024**, *50*, 211−223.
(1078) Zhang, B.; Xiong, K.; Wang, M.; Liu, Z.; Shen, K.; Mao, Y.; Chen, H. Grain boundary alloying segregation to resist hydrogen embrittlement in BCC-Fe steels: Atomistic insights into solute-hydrogen interactions. *Scripta Materialia* **2024**, *238*, 115757.
(1079) Liu, P.-Y.; Zhang, B.; Niu, R.; Lu, S.-L.; Huang, C.; Wang, M.; Tian, F.; Mao, Y.; Li, T.; Burr, P. A.; Lu, H.; Guo, A.; Yen, H.-W.; Cairney, J. M.; Chen, H.; Chen, Y.-S. Engineering metal-carbide hydrogen traps in steels. *Nature Communications* **2024**, *15*, 724.
(1080) Wang, Y.; Sharma, B.; Xu, Y.; Shimizu, K.; Fujihara, H.; Hirayama, K.; Takeuchi, A.; Uesugi, M.; Cheng, G.; Toda, H.

https://doi.org/10.1021/acs.chemrev.5c00617
Chem. Rev. 2025, 125, 11878−12029

Switching nanoprecipitates to resist hydrogen embrittlement in high-strength aluminum alloys. *Nature Communications* **2022**, *13*, 6860.
(1081) Chen, Y.-S.; Huang, C.; Liu, P.-Y.; Yen, H.-W.; Niu, R.; Burr, P.; Moore, K. L.; Martínez-Pañeda, E.; Atrens, A.; Cairney, J. M. Hydrogen trapping and embrittlement in metals - A review. *International Journal of Hydrogen Energy* **2025**, *136*, 789−821.
(1082) Echeverri Restrepo, S.; Lambert, H.; Paxton, A. T. Effect of hydrogen on vacancy diffusion. *Phys. Rev. Mater.* **2020**, *4*, 113601.
(1083) Du, J.-P.; Geng, W. T.; Arakawa, K.; Li, J.; Ogata, S. Hydrogen-Enhanced Vacancy Diffusion in Metals. *The Journal of Physical Chemistry Letters* **2020**, *11*, 7015−7020.
(1084) Barnoush, A.; Vehoff, H. Recent developments in the study of hydrogen embrittlement: Hydrogen effect on dislocation nucleation. *Acta Materialia* **2010**, *58*, 5274−5285.
(1085) Wen, M.; Li, Z.; Barnoush, A. Atomistic Study of Hydrogen Effect on Dislocation Nucleation at Crack Tip. *Advanced Engineering Materials* **2013**, *15*, 1146−1151.
(1086) Itakura, M.; Kaburaki, H.; Yamaguchi, M.; Okita, T. The effect of hydrogen atoms on the screw dislocation mobility in bcc iron: A first-principles study. *Acta Materialia* **2013**, *61*, 6857−6867.
(1087) Song, J.; Curtin, W. Mechanisms of hydrogen-enhanced localized plasticity: An atomistic study using α-Fe as a model system. *Acta Materialia* **2014**, *68*, 61−69.
(1088) Song, J.; Curtin, W. A. Atomic mechanism and prediction of hydrogen embrittlement in iron. *Nature Materials* **2013**, *12*, 145−151.
(1089) Tehranchi, A.; Zhou, X.; Curtin, W. A decohesion pathway for hydrogen embrittlement in nickel: Mechanism and quantitative prediction. *Acta Materialia* **2020**, *185*, 98−109.
(1090) Tehranchi, A.; Curtin, W. A. Atomistic study of hydrogen embrittlement of grain boundaries in nickel: II. Decohesion. *Modelling and Simulation in Materials Science and Engineering* **2017**, *25*, 075013.
(1091) Li, J.; Lu, C.; Pei, L.; Zhang, C.; Wang, R. Atomistic investigation of hydrogen induced decohesion of Ni grain boundaries. *Mechanics of Materials* **2020**, *150*, 103586.
(1092) Huang, S.; Chen, D.; Song, J.; McDowell, D. L.; Zhu, T. Hydrogen embrittlement of grain boundaries in nickel: an atomistic study. *Npj Comput. Mater.* **2017**, *3*, 28.
(1093) Adlakha, I.; Solanki, K. N. Critical assessment of hydrogen effects on the slip transmission across grain boundaries in α-Fe. *Proceedings of the Royal Society A: Mathematical, Physical and Engineering Sciences* **2016**, *472*, 20150617.
(1094) Li, J.; Lu, C.; Pei, L.; Zhang, C.; Wang, R. Hydrogen-modified interaction between lattice dislocations and grain boundaries by atomistic modelling. *International Journal of Hydrogen Energy* **2020**, *45*, 9174−9187.
(1095) Wan, L.; Geng, W. T.; Ishii, A.; Du, J.-P.; Mei, Q.; Ishikawa, N.; Kimizuka, H.; Ogata, S. Hydrogen embrittlement controlled by reaction of dislocation with grain boundary in alpha-iron. *International Journal of Plasticity* **2019**, *112*, 206−219.
(1096) Zhou, X.-Y.; Yang, X.-S.; Zhu, J.-H.; Xing, F. Atomistic simulation study of the grain-size effect on hydrogen embrittlement of nanograined Fe. *International Journal of Hydrogen Energy* **2020**, *45*, 3294−3306.
(1097) Kuhr, B.; Farkas, D.; Robertson, I. M. Atomistic studies of hydrogen effects on grain boundary structure and deformation response in FCC Ni. *Computational Materials Science* **2016**, *122*, 92−101.
(1098) Ji, Y.; Shuang, F.; Ni, Z.; Yao, C.; Li, X.; Fu, X.; Chen, Z.; Li, X.; Dong, C. Discerning the duality of H in Mg: H-induced damage and ductility. *International Journal of Plasticity* **2024**, *181*, 104084.
(1099) Luo, H.; Lu, W.; Fang, X.; Ponge, D.; Li, Z.; Raabe, D. Beating hydrogen with its own weapon: Nano-twin gradients enhance embrittlement resistance of a high-entropy alloy. *Materials Today* **2018**, *21*, 1003−1009.
(1100) Luo, H.; Sohn, S. S.; Lu, W.; Li, L.; Li, X.; Soundararajan, C. K.; Krieger, W.; Li, Z.; Raabe, D. A strong and ductile medium-entropy alloy resists hydrogen embrittlement and corrosion. *Nature Communications* **2020**, *11*, 3081.
(1101) Li, X.; Yin, J.; Zhang, J.; Wang, Y.; Song, X.; Zhang, Y.; Ren, X. Hydrogen embrittlement and failure mechanisms of multi-principal element alloys: A review. *Journal of Materials Science & Technology* **2022**, *122*, 20−32.
(1102) Ren, X.; Shi, P.; Zhang, W.; Wu, X.; Xu, Q.; Wang, Y. Swamps of hydrogen in equiatomic FeCuCrMnMo alloys: First-principles calculations. *Acta Materialia* **2019**, *180*, 189−198.
(1103) Xie, Z.; Wang, Y.; Lu, C.; Dai, L. Sluggish hydrogen diffusion and hydrogen decreasing stacking fault energy in a high-entropy alloy. *Materials Today Communications* **2021**, *26*, 101902.
(1104) Yin, X.; Liu, X.; Chen, H.; Chen, S. Hydrogen segregation by local chemical ordering structure in CrCoNi medium-entropy alloys: A first principle study. *Materials Today Communications* **2023**, *34*, 105306.
(1105) Guo, J.; Xu, S.; Chen, D. Elucidating the hydrogen influence on twin nucleation in FeNiCr medium-entropy alloy. *Extreme Mechanics Letters* **2023**, *65*, 102107.
(1106) Zhou, X.; Curtin, W. A. First principles study of the effect of hydrogen in austenitic stainless steels and high entropy alloys. *Acta Materialia* **2020**, *200*, 932−942.
(1107) Zhou, X.; Tehranchi, A.; Curtin, W. A. Mechanism and Prediction of Hydrogen Embrittlement in fcc Stainless Steels and High Entropy Alloys. *Phys. Rev. Lett.* **2021**, *127*, 175501.
(1108) Tan, A. M. Z.; Li, Z.; Zhao, Y.; Ramamurty, U.; Gao, H. Modeling the improved hydrogen embrittlement tolerance of twin boundaries in face-centered cubic complex concentrated alloys. *Journal of the Mechanics and Physics of Solids* **2024**, *188*, 105657.
(1109) Thompson, A.; Swiler, L.; Trott, C.; Foiles, S.; Tucker, G. Spectral neighbor analysis method for automated generation of quantum-accurate interatomic potentials. *Journal of Computational Physics* **2015**, *285*, 316−330.
(1110) Drautz, R. Atomic cluster expansion for accurate and transferable interatomic potentials. *Phys. Rev. B* **2019**, *99*, 014104.
(1111) Sauceda, H. E.; Gálvez-González, L. E.; Chmiela, S.; Paz-Borbon, L. O.; Muller, K.-R.; Tkatchenko, A. BIGDML-Towards accurate quantum machine learning force fields for materials. *Nature Communications* **2022**, *13*, 3733.
(1112) Korostelev, V.; Wagner, J.; Klyukin, K. Simple local environment descriptors for accurate prediction of hydrogen absorption and migration in metal alloys. *J. Mater. Chem. A* **2023**, *11*, 23576−23588.
(1113) Tang, H.; Li, B.; Song, Y.; Liu, M.; Xu, H.; Wang, G.; Chung, H.; Li, J. Reinforcement Learning-Guided Long-Timescale Simulation of Hydrogen Transport in Metals. *Advanced Science* **2024**, *11*, 2304122.
(1114) Omrani, S.; Ghasemi, M.; Mahmoodpour, S.; Shafiei, A.; Rostami, B. Insights from molecular dynamics on CO_2 diffusion coefficient in saline water over a wide range of temperatures, pressures, and salinity: CO_2 geological storage implications. *J. Mol. Liq.* **2022**, *345*, 117868.
(1115) Zhang, L.; Lin, D.-Y.; Wang, H.; Car, R.; E, W. Active learning of uniformly accurate interatomic potentials for materials simulation. *Phys. Rev. Mater.* **2019**, *3*, 023804.
(1116) Kulichenko, M.; Barros, K.; Lubbers, N.; Li, Y. W.; Messerly, R.; Tretiak, S.; Smith, J. S.; Nebgen, B. Uncertainty-driven dynamics for active learning of interatomic potentials. *Nature Computational Science* **2023**, *3*, 230−239.
(1117) Chen, C.; Ong, S. P. A universal graph deep learning interatomic potential for the periodic table. *Nature Computational Science* **2022**, *2*, 718−728.
(1118) Deng, B.; Zhong, P.; Jun, K.; Riebesell, J.; Han, K.; Bartel, C. J.; Ceder, G. CHGNet as a pretrained universal neural network potential for charge-informed atomistic modelling. *Nature Machine Intelligence* **2023**, *5*, 1031−1041.
(1119) Batatia, I. et al. A foundation model for atomistic materials chemistry. *arXiv* 2024, DOI: 10.48550/arXiv.2401.00096 .
(1120) Neumann, M.; Gin, J.; Rhodes, B.; Bennett, S.; Li, Z.; Choubisa, H.; Hussey, A.; Godwin, J. Orb: A Fast, Scalable Neural Network Potential. *arXiv*2024, DOI: 10.48550/arXiv.2410.22570.

(1121) Rhodes, B.; Vandenhaute, S.; Simkus, V.; Gin, J.; Godwin, J.; Duignan, T.; Neumann, M. Orb-v3: atomistic simulation at scale. *arXiv* 2025, DOI: 10.48550/arXiv.2504.06231.
(1122) Yang, H.; Hu, C.; Zhou, Y.; Liu, X.; Shi, Y.; Li, J.; Li, G.; Chen, Z.; Chen, S.; Zeni, C.; Horton, M.; Pinsler, R.; Fowler, A.; Zugner, D.; Xie, T.; Smith, J.; Sun, L.; Wang, Q.; Kong, L.; Liu, C.; Hao, H.; Lu, Z. MatterSim: A Deep Learning Atomistic Model Across Elements, Temperatures and Pressures. *arXiv* 2024, DOI: 10.48550/arXiv.2504.04967.
(1123) Bochkarev, A.; Lysogorskiy, Y.; Drautz, R. Graph Atomic Cluster Expansion for Semilocal Interactions beyond Equivariant Message Passing. *Phys. Rev. X* **2024**, *14*, 021036.
(1124) Park, Y.; Kim, J.; Hwang, S.; Han, S. Scalable Parallel Algorithm for Graph Neural Network Interatomic Potentials in Molecular Dynamics Simulations. *Journal of Chemical Theory and Computation* **2024**, *20*, 4857−4868.
(1125) Zhang, D.; Peng, A.; Cai, C.; Li, W.; Zhou, Y.; Zeng, J.; Guo, M.; Zhang, C.; Li, B.; Jiang, H.; Zhu, T.; Jia, W.; Zhang, L.; Wang, H. A Graph Neural Network for the Era of Large Atomistic Models. *arXiv* 2025, DOI: 10.48550/arXiv.2506.01686.
(1126) Barroso-Luque, L.; Shuaibi, M.; Fu, X.; Wood, B. M.; Dzamba, M.; Gao, M.; Rizvi, A.; Zitnick, C. L.; Ulissi, Z. W. Open Materials 2024 (OMat24) Inorganic Materials Dataset and Models. *arXiv* 2024, DOI: 10.48550/arXiv.2410.12771.
(1127) Fu, X.; Wood, B. M.; Barroso-Luque, L.; Levine, D. S.; Gao, M.; Dzamba, M.; Zitnick, C. L. Learning Smooth and Expressive Interatomic Potentials for Physical Property Prediction. *arXiv* 2025, DOI: 10.48550/arXiv.2502.12147.
(1128) Shuang, F.; Wei, Z.; Liu, K.; Gao, W.; Dey, P. Universal machine learning interatomic potentials poised to supplant DFT in modeling general defects in metals and random alloys. *Machine Learning: Science and Technology* **2025**, *6*, 030501.
(1129) Schmidt, J.; Cerqueira, T. F.; Romero, A. H.; Loew, A.; Jäger, F.; Wang, H.-C.; Botti, S.; Marques, M. A. Improving machine-learning models in materials science through large datasets. *Materials Today Physics* **2024**, *48*, 101560.
(1130) Kaplan, A. D.; Liu, R.; Qi, J.; Ko, T. W.; Deng, B.; Riebesell, J.; Ceder, G.; Persson, K. A.; Ong, S. P. A Foundational Potential Energy Surface Dataset for Materials. *arXiv* 2025, DOI: 10.48550/arXiv.2503.04070.
(1131) Wines, D.; Choudhary, K. CHIPS-FF: Evaluating Universal Machine Learning Force Fields for Material Properties. *ACS Materials Letters* **2025**, *7*, 2105−2114.
(1132) Zhang, D.; Liu, X.; Zhang, X.; Zhang, C.; Cai, C.; Bi, H.; Du, Y.; Qin, X.; Peng, A.; Huang, J. DPA-2: a large atomic model as a multi-task learner. *npj Computational Materials* **2024**, *10*, 293.
(1133) Novikov, I.; Grabowski, B.; Körmann, F.; Shapeev, A. Magnetic Moment Tensor Potentials for Collinear Spin-Polarized Materials Reproduce Different Magnetic States of Bcc Fe. *npj Computational Materials* **2022**, *8*, 13.
(1134) Hellström, M.; Behler, J. Structure of aqueous NaOH solutions: insights from neural-network-based molecular dynamics simulations. *Physical Chemistry Chemical Physics* **2017**, *19*, 82−96.
(1135) Hellström, M.; Behler, J. Concentration-Dependent Proton Transfer Mechanisms in Aqueous NaOH Solutions: From Acceptor-Driven to Donor-Driven and Back. *Journal of Physical Chemistry Letters* **2016**, *7*, 3302−3306.
(1136) Gomez, A.; Thompson, W. H.; Laage, D. Neural-Network-Based Molecular Dynamics Simulations Reveal That Proton Transport in Water Is Doubly Gated by Sequential Hydrogen-Bond Exchange. *Nature Chemistry* **2024**, *16*, 1838−1844.
(1137) Shao, Y.; Hellström, M.; Yllö, A.; Mindemark, J.; Hermansson, K.; Behler, J.; Zhang, C. Temperature Effects on the Ionic Conductivity in Concentrated Alkaline Electrolyte Solutions. *Physical Chemistry Chemical Physics* **2020**, *22*, 10426−10430.
(1138) Cheng, B. Latent Ewald Summation for Machine Learning of Long-Range Interactions. *npj Computational Materials* **2025**, *11*, 80.
(1139) Anstine, D. M.; Isayev, O. Machine Learning Interatomic Potentials and Long-Range Physics. *The Journal of Physical Chemistry A* **2023**, *127*, 2417−2431.
(1140) Zhang, L.; Wang, H.; Muniz, M. C.; Panagiotopoulos, A. Z.; Car, R.; E, W. A Deep Potential Model with Long-Range Electrostatic Interactions. *Journal of Chemical Physics* **2022**, *156*, 124107.
(1141) Malosso, C.; Zhang, L.; Car, R.; Baroni, S.; Tisi, D. Viscosity in Water from First-Principles and Deep-Neural-Network Simulations. *npj Computational Materials* **2022**, *8*, 139.
(1142) Zhang, L.; Wang, H.; Car, R.; E, W. Phase Diagram of a Deep Potential Water Model. *Physical Review Letters* **2021**, *126*, 236001.
(1143) *Materials Studio*; D.S. BIOVIA, Dassault Systèmes: San Diego. https://www.3ds.com/products/biovia/materials-studio, Accessed October 15, 2025.
(1144) *Maps Platform, SCIENOMICS*. https://www.scienomics.com/maps-platform/, Accessed October 15, 2025.
(1145) Theodorou, D. N.; Suter, U. W. Detailed molecular structure of a vinyl polymer glass. *Macromolecules* **1985**, *18*, 1467−1478.
(1146) Theodorou, D. N.; Suter, U. W. Shape of unperturbed linear polymers: polypropylene. *Macromolecules* **1985**, *18*, 1206−1214.
(1147) Theodorou, D. N.; Suter, U. W. Geometrical considerations in model systems with periodic boundaries. *The Journal of Chemical Physics* **1985**, *82*, 955−966.
(1148) Theodorou, D. N.; Suter, U. W. Atomistic modeling of mechanical properties of polymeric glasses. *Macromolecules* **1986**, *19*, 139−154.